CONTENTS

Transactions A: Basics

International Journal of Engineering

Journal Homepage: www.ije.ir

Probabilistic Twin Support Vector Machine for Solving Unclassifiable Region Problem

J. A. Nasiri[a], H. Shakibian*[b]

[a] Faculty of Mathematical Sciences, Ferdowsi University of Mashhad, Mashhad, Iran
[b] Department of Computer Engineering, Faculty of Engineering, Alzahra University, Tehran, Iran

A B S T R A C T

Support Vector Machine classifiers are widely used in many classification tasks. However, they have two considerable weaknesses, Unclassifiable Region (UR) in multiclass classification and outliers. In this research, we address these problems by introducing Probabilistic Least Square Twin Support Vector Machine (PLS-TSVM). The proposed algorithm introduces continuous and probabilistic outputs over the model obtained by Least-Square Twin Support Vector Machine (LS-TSVM) method with both linear and polynomial kernel functions. PLS-TSVM not only solves the unclassifiable region problem by introducing a continuous output value membership function, but it also reduces the adverse effects of noisy data and outliers. For showing the superiority of our proposed method, we have conducted experiments on various UCI datasets. In the most cases, higher or competitive accuracy to other methods have been obtained such that in some UCI datasets, PLS-TSVM could obtain up to 99.90% of classification accuracy. Moreover, PLS-TSVM has been evaluated against "one-against-all" and "one-against-one" approaches on several well-known video datasets such as Weizmann, KTH, and UCF101 for human action recognition task. The results show the higher accuracy of PLS-TSVM compared to its counterparts. Specifically, the proposed algorithm could improve respectively about 12.2%, 2.8%, and 12.1% of classification accuracy in three video datasets compared to the standard SVM and LS-TSVM classifiers. The final results indicate that the proposed algorithm could achieve better overall performances than the literature.

doi: 10.5829/ije.2022.35.01a.01

1. INTRODUCTION

Pattern recognition and classification methods are applied to a vast range of real-world applications such as image classification [1-3], disease detection [4], text classification [5], and so on. The significant growth in these applications shows the necessity of fast and classifiers.

For classification tasks, different machine learning classifiers have been applied. The recent research indicates that Support Vector Machines has better performance among other classifiers in most cases [6-11]. However, SVM-based classifiers suffer from several major problems. The first problem is that they are very sensitive to noisy data and outliers. The reason is optimal hyperplane obtained by only a small part of samples (support vectors) [12]. Second, the class-boundary-skew

will be met when SVM is applied to the problem of learning from imbalanced datasets when for instance, one class (suppose negative data) strongly outnumber the other class (positive samples) [13]. In that case, the class boundary can be skewed towards the Negative class. As a result, the false-negative rate can be very high and can make SVM ineffective in identifying the targets that belong to the positive class, which results in the class-boundary-skew problem. Third, the occurrence of unclassifiable regions (URs) when SVM classifiers are applied to multiclass problems.

UR occurs when a multiclass classification application assigns two or more classes to one data sample. In another word, it appears when the classifier can not distinguish between the actual class corresponding to the data-sample and other classes. This may also happen as a result of an imbalance dataset or

*Corresponding Author Institutional Email: h.shakibian@alzahra.ac.ir (H. Shakibiani)

general noises in image recognition tasks. For instance, suppose an application has to distinguish between daily human activities from a set of short videos. The case study videos may suffer from problems such as viewpoint change, ambient occlusion, illumination change, and intra-class action variations [14] that generally occur in image and video classification tasks. Consequently, the application may face difficulty in discriminating between two similar classes, such as "walking" and "running", and it results in an inaccurate classification.

The problem of unclassifiable regions has been addressed in a number of stuides. A weighted voting mechanism formulated by a base classifier has been proposed to eliminate the unclassifiable area [15]. The results based on the logistic regression and support vector machine show higher accuracy and efficiency by modifying the basic classifier. In some of the works, an optimized continuous decision function based on fuzzy support vector machine (FSVM) has been developed to enhance the classification performance [16-18]. A truncated polyhedral pyramidal membership function has been proposed over the decision functions obtained by training the SVM for each class [19]. As the methods obtain the same classification results, for the data points within the classifiable regions, the generalization ability of the FSVM is the same with or better than that of the SVM. A fuzzy classifier based on the support vector machine has been proposed by introducing the concepts of fuzzy linear separability and fuzzy hyperplanes. The proposed fuzzy classifier is robust to the class label perturbation and have been applied in the medical diagnosis. It can obtain a good generalization performance and meanwhile can solve the unclassifiable regions by finding the membership that an example belongs to the positive or negative class [20]. A decision margin based fuzzy output SVM approach has been proposed by Yang [21] to reduce the unclassifiable regions and improve the accuracy of the incident ticket classification. The multiclass support vector machine (SVM) has also been used following decision-directed acyclic graph (DDAG) to address the unclassifable regions for predicting the unkown fault prediction [22]. Nesting-One-Against-One algorithm [23] and vector projection method [24] are the other methods to handle the unclassifable region problem.

The proposed algortihms to solve the UR problem are mainly based on the standard SVM algorithm and there are a few corresponding works on the TWSVM. Moreover, since the TWSVM and the SVM have different mechanisms, the approach of modifying the latter cannot be used directly to the former one. Therefore, we aimed to study the UR problem of TWSVM-type algorithms. Accordingly, following the line of research conducted by Khemchandani and Suresh [25], Liu and Yen-Ting [26], a novel Probabilistic Output

Multi-class Least Square Twin Support Vector Machine (PLS-TSVM) algorithm was proposed in which a contineous decision function has been introduced to the outputs of the LS-TSVM hyperplane [27].

To validate our proposed method, we conducted experiments on a set of UCI datasets to compare PLS-TSVM with SVM, TWSVM, and LS-TSVM. Then, PLS-TSVM has been applied on three well-known and widely-used video datasets, namely Weizmann, KTH and UCF101 to compare it with the literature.

2. PROBABILISTIC LEAST SQUARE TWIN SUPPORT VECTOR MACHINE

Although much research based on least square twin support vector machine has been presented [28-33] they are incapable of eliminating the consequences of unclassifiable regions. Therefore as it was also mentioned previously, our motivation in this research is to propose a classifier based on LS-TSVM that addresses the unclassifiable regions (URs).

The proposed algorithm consists of two main steps. Firstly, two nonparallel separating hyperplanes are obtained as the solutions of the Quadratic Programming Problems (QPPs) problems in TSVMs. In this step, we introduced both linear and nonlinear models. Secondly, the classification decision rule is defined probabilitically according to the linear and nonlinear models, repectively. In following, we present PLS-TSVM in more details.

2. 1. Linear PLS-TSVM   Given a dataset D, we denote the training data of class +1 and class -1 by matrix A and B, respectively. If d^+ and d^- denote the training sets with label +1 and -1, respectively, then A would be $\in R^{d^+ \times m}$ and matrix $B \in R^{d^+ \times m}$, where m is the problem dimension.

In PLS-TSVM, the primal problem as well as the equality constraints are the same as that of LS-TSVM [27]:

$$
\begin{aligned}
&\underset{w_{(1)}, b_{(1)}}{Min} && \frac{1}{2} \left|\left| Aw_{(1)} + eb_{(1)} \right|\right|^2 + \frac{c_1}{2} y^T y \\
&s.t. && -\left(Bw_{(1)} + eb_{(1)} \right) + y = e
\end{aligned}
\tag{1}
$$

where $c_1 > 0$ are penalty parameters, e is the **1**'s vectors, and y is vectors of slack variables, respectively. Substituting the equality constraints into Equation (1), we have:

$$
\underset{w_{(1)}, b_{(1)}}{Min} \quad \frac{1}{2} \left|\left| Aw_{(1)} + eb_{(1)} \right|\right|^2 + \frac{c_1}{2} \left|\left| Bw_{(1)} + eb_{(1)} + e \right|\right|^2
\tag{2}
$$

Next, the gradient of Equation (2) with respect to $(w)_1$ and $(b)_1$ is set to zero and we have:

$$A^T \left(Aw_{(1)} + eb_{(1)} \right) + c_1 B^T \left(Bw_{(1)} + eb_{(1)} + e \right) = 0e, \quad (3)$$

$$e^T \left(Aw_{(1)} + eb_{(1)} \right) + c_1 e^T \left(Bw_{(1)} + eb_{(1)} + e \right) = 0e, \quad (4)$$

Now, arranging Equations (3) and (4) in matrix form and solving for $(w)_1$ and $(b)_1$ gives:

$$c_1 \begin{bmatrix} B^T B & B^T e \\ e^T B & e_2 \end{bmatrix} \begin{bmatrix} w_{(1)} \\ b_{(1)} \end{bmatrix} + \begin{bmatrix} A^T A & A^T e \\ e^T A & e_1 \end{bmatrix} \begin{bmatrix} w_{(1)} \\ b_{(1)} \end{bmatrix} + c_1 \begin{bmatrix} B^T \\ e_2 \end{bmatrix} = 0e \quad (5)$$

$$\begin{bmatrix} w_{(1)} \\ b_{(1)} \end{bmatrix} = \begin{bmatrix} c_1 B^T B + A^T A & c_1 B^T e + A^T e \\ c_1 e^T B + e^T A + & c_1 m_2 + m_1 \end{bmatrix}^{-1} \times \begin{bmatrix} -c_1 B^T \\ -c_1 e^T \end{bmatrix} \quad (6)$$

$$\begin{bmatrix} w_{(1)} \\ b_{(1)} \end{bmatrix} = - \left[c_1 \begin{bmatrix} B^T \\ e^T \end{bmatrix} [B\ e] + \begin{bmatrix} A^T \\ e^T \end{bmatrix} [A\ e] \right]^{-1} \times \left[c_1 \begin{bmatrix} B^T \\ e^T \end{bmatrix} \right] \quad (7)$$

Lets $P = [A\ e]$ and $Q = [B\ e]$, the solution becomes as:

$$\begin{bmatrix} w_{(1)} \\ b_{(1)} \end{bmatrix} = - \left[c_1 Q^T Q + P^T P \right]^{-1} c_1 Q^T e. \quad (8)$$

Similarly, the solution of QPP Equation (9) can be found as shown in Equation (10):

$$\underset{w_{(2)}, b_{(2)}}{Min} \quad \frac{1}{2} \left|\left| Bw_{(2)} + eb_{(2)} \right|\right|^2 + \frac{c_2}{2} y^T y$$
$$s.t. \quad \left(Aw_{(2)} + eb_{(2)} \right) + y = e, \quad (9)$$

$$\begin{bmatrix} w_{(2)} \\ b_{(2)} \end{bmatrix} = \left[c_2 P^T P + Q^T Q \right]^{-1} c_2 P^T e. \quad (10)$$

In this way, two nonparallel separating hyperplanes are obtained. As we know the linear LS-TSVM completely solves the classification problem with just two systems of linear equation as opposed to solving two QPPs in TSVM or one in QPP in SVM which helps the proposed PLS-TSVM to be faster than the other two algorithm in the training phase.

2. 2. Nonlinear PLS-TSVM

To obtain the nonlinear model, the following kernel generated surfaces are introduced:

$$K \left(x^T, C^T \right) u_{(1)} + \gamma_{(1)} = 0$$
$$K \left(x^T, C^T \right) u_{(2)} + \gamma_{(2)} = 0 \quad (11)$$

where $C = [A; B]$ and K is an arbitrary kernel. Now, the primal problems of the nonlinear PLS-TSVM is defined with 2-norm of slack variables. The equality constraints corresponding to surfaces Equation (11) are given in Equations (12) and (13), respectively.

$$\underset{u_{(1)}, \gamma_{(1)}}{Min} \quad \frac{1}{2} \left|\left| K \left(A, C^T \right) u_{(1)} + e\gamma_{(1)} \right|\right|^2 + \frac{c_1}{2} y^T y$$
$$s.t. \quad - \left(K \left(B, C^T \right) u_{(1)} + e\gamma_{(1)} \right) + y = e \quad (12)$$

and:

$$\underset{u_{(2)}, \gamma_{(2)}}{Min} \quad \frac{1}{2} \left|\left| K \left(B, C^T \right) u_{(2)} + e\gamma_{(2)} \right|\right|^2 + \frac{c_2}{2} y^T y$$
$$s.t. \quad \left(K \left(A, C^T \right) u_{(2)} + e\gamma_{(2)} \right) + y = e \quad (13)$$

If the constraints are substituted into the objective function, the QPPs take the following form:

$$\underset{u_{(1)}, \gamma_{(1)}}{Min} \quad \frac{1}{2} \left|\left| K \left(A, C^T \right) u_{(1)} + e\gamma_{(1)} \right|\right|^2 +$$
$$\frac{c_1}{2} \left|\left| K \left(B, C^T \right) u_{(1)} + e\gamma_{(1)} + e \right|\right|^2 \quad (14)$$

$$\underset{u_{(2)}, \gamma_{(2)}}{Min} \quad \frac{1}{2} \left|\left| K \left(B, C^T \right) u_{(2)} + e\gamma_{(2)} \right|\right|^2 +$$
$$\frac{c_2}{2} \left|\left| -K \left(A, C^T \right) u_{(2)} - e\gamma_{(2)} + E_{(2)} \right|\right|^2 \quad (15)$$

Finally, the solutions of Equations (14) and (15) is derived as:

$$\begin{bmatrix} u_{(1)} \\ \gamma_{(1)} \end{bmatrix} = - \left[c_1 N^T N + M^T M \right]^{-1} \left[c_1 N^T e \right] \quad (16)$$

$$\begin{bmatrix} u_{(2)} \\ \gamma_{(2)} \end{bmatrix} = \left[c_2 M^T M + N^T N \right]^{-1} \left[c_2 M^T e \right] \quad (17)$$

where $M = [K(A, C^T)e]$ and $N = [K(B, C^T); e]$

2. 3. Classification Decision Rule

The second step of PLS-TSVM is defining a decision rule for each of the proposed linear and nonlinear model. For a new testing point x, the corresponding class label is assigned by the following decision function in the linear case where $i \in \{1, 2, \ldots, k\}$:

$$f_i(x) = \begin{cases} +1 & \text{if} \quad \left| \frac{xw_{(1)} + eb_{(1)}}{xw_{(2)} + eb_{(2)}} \right| \le 1 \\ \\ 0 & \text{if} \quad \left| \frac{xw_{(1)} + eb_{(1)}}{xw_{(2)} + eb_{(2)}} \right| > 1 \end{cases} \quad (18)$$

In nonlinear PLS-TSVM, the function $f_i(.)$ is defined as follow:

$$f_i(x) = \begin{cases} +1 & \text{if} \quad \left| \frac{K(x, C^T)u_{(1)} + e\gamma_{(1)}}{K(x, C^T)u_{(2)} + e\gamma_{(2)}} \right| \le 1 \\ \\ 0 & \text{if} \quad \left| \frac{K(x, C^T)u_{(1)} + e\gamma_{(1)}}{K(x, C^T)u_{(2)} + e\gamma_{(2)}} \right| > 1 \end{cases} \quad (19)$$

The class which earns the highest voting number will be the final output. If more than one class earns the highest voting number, probabilistic output function Equations (20) and (21) will be used to convert the discrete output to the continuous case. Let n present index of classes earn the highest voting number. In other words, when the decision function outputs the same highest numbers for various classes, it results in unclassifiable regions arisen. Therefore, Equations (20) or (21), will be used for each

individual, and the final decision will be made by comparing the output numbers of the probabilistic decision function Equation (22).

In the case of linear PLS-TSVM, the corresponding decision function is defined as follow $n \in \{argmax(f_i(x))\}$:

$$f_n(x) = \begin{cases} M_n(x) & \text{if} \quad |\frac{xw_{(1)}+eb_{(1)}}{xw_{(2)}+eb_{(2)}}| \le 1 \\ \\ 0 & \text{if} \quad |\frac{xw_{(1)}+eb_{(1)}}{xw_{(2)}+eb_{(2)}}| > 1 \end{cases} \qquad (20)$$

And in the case of nonlinear PLS-TSVM, the decision function is as follows:

$$f_n(x) = \begin{cases} M_n(x) & \text{if} \quad |\frac{K(x,C^T)u_{(1)}+e\gamma_{(1)}}{K(x,C^T)u_{(2)}+e\gamma_{(2)}}| \le 1 \\ \\ 0 & \text{if} \quad |\frac{K(x,C^T)u_{(1)}+e\gamma_{(1)}}{K(x,C^T)u_{(2)}+e\gamma_{(2)}}| > 1 \end{cases} \qquad (21)$$

where the membership function is computed as follow:

$$M_n(x) = \frac{1}{1+e^{-aD_n(x)+b}} \qquad (22)$$

$$D_n(x) = ||xw_{(1)}+eb_{(1)}| - |xw_{(2)}+eb_{(2)}|| \qquad (23)$$

Similary, for the nonlinear PLS-TSVM we have:

$$D_n(x) = ||K(x,C^T)u_{(1)}+e\gamma_{(1)}| - |K(x,C^T)u_{(2)}+e\gamma_{(2)}|| \qquad (24)$$

The final classification decision of the improved voting strategy is made with Equation (22). Figure 1(a). shows the decision function of LS-TSVM and Figure 1(b). shows $f(x)$ in PLS-TSVM calculated by Equation (20). for positive and negative samples, the farther from the separating hyperplanes, the greater probabilistic output value $|f(x)|$ will be obtained. This is to say that $f(x)$ is a suitable continuous output for LS-TSVM. Similar to the continuous output in SVM and TWSVM, the values range of $M(x)$ in our model also from negative infinity to positive infinity [34]. In Figure 2, the proposed algorithm has been illustrated whithin the human action recognition framework.

2. 4. Discussion on PLS-TSVM   PLS-TSVM is an extension of LS-TSVM based on a probabilistic output function to solve unclassifiable regions (URs) problem in multiclass classification.

The constraints of LS-TSVM require the hyperplane to be at a distance of exactly one from the points of the other class. In PLS-SVM, a continuous probabilistic output has been defined. The samples in URs are handled with different degrees of memberships for different classes. We selected the UCI Wine dataset with two of its features to show the effect of PLS-TSVM's decision

function. Figure 3 shows the proposed PLS-TSVM classifier with its probabilistic decision function within the human action recognition framework based on the one-against-one strategy. Linear kernel and polynomial kernel of degree 4 have been used in this figure. The illustrated black region does not belong to any class (URs). We can observe that the decision function of PLS-TSVM has a high effect on resolving the unclassified region.

3. EXPERIMENTAL RESULTS

In this section, we evaluated the test results of PLS-TSVM's experiments on UCI datasets. Then we applied PLS-TSVM on human activity recognition application. We first compared the accuracy of PLS-TSVM with

(a)

(b)
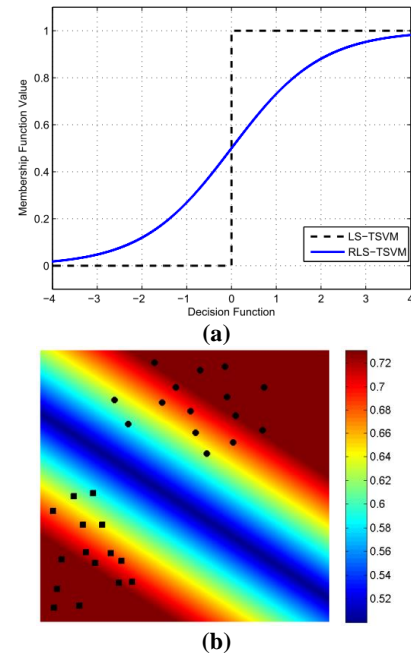
Figure 1. (a) indicates decision function of LS-TSVM, (b) illustrates f(x) calculated by Equation (20) in PLS-TSVM
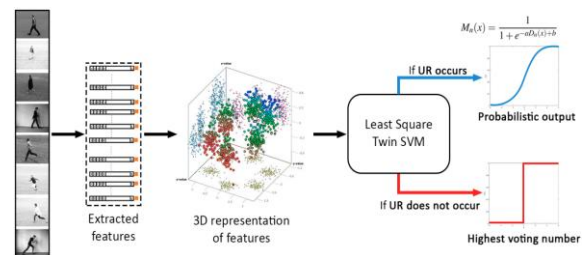
Figure 2. The human action recognition framework based on the proposed algorithm, PLS-TSVM is illus-trated in this figure

LS-TSVM   PLS-TSVM

Polynomial TSVM   Polynomial PLS-TSVM
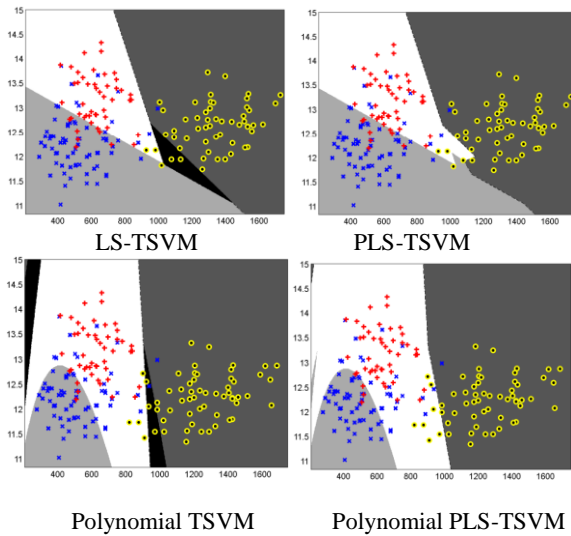
Figure 3. Geometric interpretation of multi-class LS-TSVM and PLS-TSVM

SVM, TWSVM, and LS-TSVM, then compared the obtained results from video datasets, namely, Weizmann, KTH, UCF101 with the literature to show the good performance of PLS-TSVM. The experiments were performed on an Intel Core i7 processor with 32 GB RAM. The optimal values for the parameters were found by the grid search method. In this regard, the optimal values for C and γ parameters where selected from the range $\{2^i| i = -5, -3, -1, 0, 1, 3, 5\}$.

3. 1. UCI Data Sets   In this subsection, the performance of PLS-TSVM is compared with LS-TSVM, TSVM, and SVM. For these experiments, we utilized 9 UCI data sets, which their 141 characteristics are provided in Table 1. The results of these experiments with Linear and RBF kernels are provided in Tables 2 and 3, respectively, using 5-fold cross-validation method. Optimal C, $γ$ parameters were also provided in both tables. In the Tables 2 and 3, the third value in each cell shows the rank of each algorithm based on the corresponding dataset. For example, PLS-TSVM has the rank of 3 in terms of the prediction accuracy among the four SVM-based algorithms using Balance dataset. The average of these ranks have been reported as the overall rank in the last row of the Tables 2 and 3 [30]. As can be seen in both tables, our proposed method obtained the least rank score among the three other algorithms.

As it can be observed in Table 2, PLS-TSVM outperformed other competitors in 6 data sets out of 9. It should also be pointed out that in cases which UR has not occurred, PLS-TSVM has obtained the same accuracy with that of LS-TSVM in both kernels. The results in Table 3 show that our prosed algorithm had better or equal performance in 7 data sets. It can be concluded that PLS-TSVM was successful in the case of improving the

performance of classification in the face of the Unclassifiable region's occurrence.

3. 2. Human Action Video Datasets   The reason why we employ the human activity datasets is that in human action recognition (HAR), a strong occurrence of outliers is highly probable due to the errors in key-point detection, noisy data, occlusion, etc. However, there are no capabilities in SVM, TSVM, and LS-TSVM to handle it. The other problem is that these algorithms were originally designed for binary classification, while HAR is practically a problem of multiclass classification. In SVM and TWSVM family framework, "one-against-all" and "one-against-one" approaches are usually solve multiclass classification. They suffer from the unclassifiable region (UR) problem. However, PLS-TSVM resolved unclassifiable region (UR) problem by continuous decision function.

According to the above reasons, PLS-TSVM has been employed to understand human actions. For this purpose, we have compared our PLS-TSVM method with other related methods on the Weizmann, KTH, and UCF101 action datasets.

Figures 4 and 5 provide some sample frames of action datasets. In our experiments, the leave-one-out cross-validation approach was used on Weizmann and KTH to evaluate the performance of the proposed method. In UCF101 experiments, we have used the predefined splits by authors for training-testing and report the average accuracy. The linear kernel has been utilized in all experiments. we set a = b = 1 in membership function to reduce the computational complexity of parameter selection.

3. 2. 1. Weizmann Dataset   In this dataset, there are 90 low-resolution (180×144 pixels) video sequences from 10 natural actions perfromed by nine persons. The actions (classes) are: walking (walk), running (run), jumping (jump), galloping sideways (side), bending

TABLE 1. Characteristics of selected UCI data sets for the experiments

Dataset	# of features	# of features	# of classes
Balance	626	4	3
Dermatology	367	34	6
Glass	215	10	6
Ecoli	328	7	5
Iris	151	4	3
Teaching Evaluation	152	5	3
Wine	179	13	3
Vowels	991	13	10
Vehicle	847	18	4

TABLE 2. Experiment results on UCI datasets with Linear Kernel. The optimal values for the parameters (C_1, C_2) have been found using grid search method in the range of $\{2^i | i = -5,-3,-1,0,1,3,5\}$. The accuracy rank of each algorithm has also been computed and averaged in the last row

Dataset	SVM (C) Acc $\pm$ std Rank	TSVM (C_1, C_2) Acc $\pm$ std Rank	LS-TSVM (C_1, C_2) Acc $\pm$ std Rank	PLS-TSVM (C_1, C_2) Acc $\pm$ std Rank
Balance	2^{-1} 91.70%±0.02% 1	$2^{-3}, 2^2$ 90.72 %±1.93 % 2	$2^{-2}, 2^{-5}$ 89.68 %±3.34 % 3	$2^{-2}, 2^{-5}$ 89.68 %±3.34 % 3
Dermatology	2^{-3} 97.80 %±0.01 % 2	$2^{-4}, 2^{-2}$ 97.56 %±3.66 % 3	$2^3, 2^3$ 97.60 %±3.25 % 3	$2^5, 2^3$ 98.44 %±2.98 % 1
Ecoli	2^4 89.60 %±0.02 % 3	$2^{-2}, 2^{-1}$ 89.58 %±3.80 % 4	$2^{-3}, 2^{-3}$ 89.67 %±3.69 % 2	$2^{-3}, 2^{-3}$ 89.71 %±3.40 % 1
Glass	2^2 95.30 %±0.03 % 1	$2^2, 2^{-5}$ 91.12 %±3.98 % 4	$2^{-3}, 2^{-4}$ 93.94 %±5.00 % 3	$2^{-3}, 2^{-4}$ 94.15 %±3.81 % 2
Iris	2^{-3} 98.04 %±0.04 % 1	$2^{-2}, 2^{-3}$ 98.00 %±1.63 % 2	$2^{-2}, 2^{-3}$ 98.00 %±1.63 % 2	$2^{-2}, 2^{-3}$ 98.00 %±1.63 % 2
Optdigits	2^4 89.64 %±0.02 % 3	$2^{-2}, 2^{-1}$ 89.36 %±3.77 % 4	$2^{-3}, 2^{-3}$ 89.78 %±3.15 % 2	$2^{-3}, 2^{-3}$ 90.18 %±3.40 % 1
Teaching Evaluation	2^1 56.30 %±0.09 % 3	$2^1, 2^0$ 55.65 %±9.40 % 1	$2^{-2}, 2^{-2}$ 53.05 %±11.61 % 4	$2^{-2}, 2^{-2}$ 56.35 %±11.54 % 2
Wine	2^{-5} 98.90 %±0.02 % 1	$2^{-1}, 2^{-4}$ 97.76 %±2.08 % 2	$2^{-4}, 2^{-3}$ 98.73 %±2.13 % 3	$2^{-4}, 2^{-3}$ 98.73 %±2.13 % 3
Vehicle	2^{-4} 81.10 %±0.01 % 4	$2^{-1}, 2^{-1}$ 81.20 %±1.11 % 3	$2^{-2}, 2^{-2}$ 81.56 %±1.99 % 2	$2^{-2}, 2^{-2}$ 82.74 %±1.80 % 1
Vowel	2^4 82.60 %±0.03 % 2	$2^{-2}, 2^{-1}$ 75.45 %±2.42 % 4	$2^0, 2^{-1}$ 76.96 %±2.84 % 3	$2^0, 2^{-1}$ 83.02 %±2.48 % 1
Overall Rank	2.33	3.33	3.00	1.88

(bend), one-hand-waving (wave1), two-hands-waving (wave2), jumping in place (pjump), jumping jack (jack), and skipping (skip). To compute the recognition rates,

(a)

(b)

Figure 4. Some examples of video sequences in (a) Weizmann and (b) KTH datasets

TABLE 3. Experiment results on UCI datasets with RBF Kernel. The optimal values for the parameters (C_1, C_2, γ) have been found using grid search method in the range of $\{2^i | i = -5,-3,-1,0,1,3,5\}$. The accuracy rank of each algorithm has also been computed and averaged in the last row.

Dataset	SVM (C, γ) Acc $\pm$ std Rank	TSVM (C_1, C_2, γ) Acc $\pm$ std Rank	LS-TSVM (C_1, C_2, γ) Acc $\pm$ std Rank	PLS-TSVM (C_1, C_2, γ) Acc $\pm$ std Rank
Balance	$2^3, 2^{-3}$ 96.18 %$\pm$0.02 % 4	$2^{-3}, 2^{-1}, 2^{-5}$ 95.36 %$\pm$0.78 % 3	$2^{-3}, 2^{-3}, 2^{-5}$ 99.52 %$\pm$0.39 % 2	$2^{-3}, 2^{-3}, 2^{-5}$ 99.84 %$\pm$0.41 % 1
Dermatology	$2^{-1}, 2^{-1}$ 91.70 %$\pm$0.02 % 1	$2^{-3}, 2^2, 2^{-1}$ 90.72 %$\pm$1.93 % 2	$2^{-2}, 2^{-5}, 2^{-1}$ 89.68 %$\pm$3.34 % 3	$2^{-2}, 2^{-5}, 2^{-1}$ 89.68 %$\pm$2.74 % 3
Ecoli	$2^{-1}, 2^2$ 88.00 %$\pm$0.00 % 3	$2^{-3}, 2^{-1}, 2^{-4}$ 89.89 %$\pm$1.93 % 1	$2^{-3}, 2^{-1}, 2^{-4}$ 89.29 %$\pm$2.55 % 1	$2^{-3}, 2^{-1}, 2^{-4}$ 89.29 %$\pm$2.55 % 1
Glass	$2^4, 2^{-4}$ 93.00 %$\pm$ 0.00% 4	$2^{-5}, 2^4, 2^{-5}$ 97.19 %$\pm$1.75 % 3	$2^{-2}, 2^{-5}, 2^{-1}$ 99.44 %$\pm$1.11 % 2	$2^{-2}, 2^{-5}, 2^{-1}$ 99.90 %$\pm$1.11 % 1
Iris	$2^2, 2^{-4}$ 97.00 %$\pm$0.00 % 3	$2^{-4}, 2^{-5}, 2^{-5}$ 98.00 %$\pm$1.63 % 2	$2^{-1}, 2^{-1}, 2^4$ 98.66 %$\pm$1.63 % 1	$2^{-1}, 2^{-1}, 2^4$ 98.66 %$\pm$1.63 % 1
Optdigits	$2^1, 2^{-5}$ 99.28 %$\pm$0.00 % 2	$2^{-4}, 2^{-4}, 2^{-5}$ 98.89 %$\pm$1.00 % 3	$2^0, 2^{-2}, 2^{-5}$ 99.50 %$\pm$0.59 % 1	$2^0, 2^{-2}, 2^{-5}$ 99.50 %$\pm$0.59 % 1
Teaching Evaluation	$2^5, 2^2$ 60.30 %$\pm$0.02 % 4	$2^{-2}, 2^{-1}, 2^{-1}$ 66.79 %$\pm$8.37 % 1	$2^0, 2^0, 2^{-4}$ 62.50 %$\pm$10.85 % 3	$2^0, 2^0, 2^{-4}$ 64.50 %$\pm$9.99 % 1
Wine	$2^{-1}, 2^{-5}$ 98.90 %$\pm$0.02 % 2	$2^{-5}, 2^{-4}, 2^{-5}$ 97.19 %$\pm$1.75 % 3	$2^0, 2^{-1}, 2^{-4}$ 99.44 %$\pm$1.12 % 1	$2^0, 2^{-1}, 2^{-4}$ 99.44 %$\pm$1.12 % 1
Vehicle	$2^5, 2^{-5}$ 82.51 %$\pm$0.04 % 4	$2^{-3}, 2^{-3}, 2^{-5}$ 83.46 %$\pm$2.86 % 3	$2^{-5}, 2^{-4}, 2^{-5}$ 84.99 %$\pm$2.29 % 2	$2^{-5}, 2^{-4}, 2^{-5}$ 87.69 %$\pm$2.46 % 1
Vowel	$2^{-5}, 2^{-3}$ 99.6 %$\pm$0.0 % 1	$2^{-5}, 2^{-3}, 2^{-5}$ 86.96 %$\pm$2.12 % 4	$2^4, 2^4, 2^{-5}$ 95.45 %$\pm$2.30 % 3	$2^4, 2^4, 2^{-5}$ 95.55 %$\pm$2.30 % 1
Overall Rank	3.11	2.77	2.11	1.55

leave-one-out cross-validation has been employed in which the videos of 8 actors are used as the training dataset and one person for the test.

The results of PLS-TSVM has been reported in Table 4 which are the average accuracy rate of 9 independent runs. As it has been shown, the accuracy rate of PLS-TSVM is higher than most of the state-of-the-art methods. However, some approaches, such as [35-41] reported more accurate predictions. In this regard, it should be noted that these later approaches used additional data founded by tracking or background subtraction. Furthermore, the training time of some methods such as Ada-boost based classifiers is considerably higher than PLS-TSVM.

Figure 5. Example frames from video sequences of UCF101 datasets

TABLE 4. Accuracy rates of different methods on the Weizmann dataset (*Background subtraction has been used to localize actors)

Method	Classifier	Average Accuracy
Niebles [42]	SVM	72.80%
Liu [43]	KNN	71.69%
Fathi [40]	Adaboost	100% *
Bregonzio [44]	SVM-NN	96.66%
Wang [45]	SVM	92.1 %
Jiang (motion) [41]	Tree Learning+KNN	88.89% *
Jiang (shape) [41]	Tree Learning+KNN	81.11% *
Jiang (shape+motion) [41]	Tree Learning+KNN	100% *
Chou [46]	NNC-GMMC	95.56%
Goudelis [47]	SVM	95.42%
Arunnehru [48]	3D-CNN	96.37%
Nasiri [27]	LS-TSVM	85.56%
Singh [49]	SVM	97.66%
Aslan [50]	KNN	91.11%
Vishwakarma [51]	SVM	97.50 %
Vishwakarma [52]	SVM-HMM	96.00%
Ramya [53]	NN	92.50%
Our method	PLS-TSVM	97.78%

In order to demonstrate the capabilities of PLS-TSVM, the accuracy rate and training time between SVM, LS-TSVM, and PLS-TSVM has also been compared in Table 5. As it is shown, the Haris3D detector and HOG/HOF descriptor are similarly conducted in the experiment. We observe that PLS-TSVM outperformed the LS-TSVM result by 12% on Weizmann. Also, PLS-TSVM performed several orders of magnitude faster than SVM. Figure 6 (a,b) shows the confusion matrices for the Weizmann dataset with the LS-TSVM and PLS-TSVM classifiers, respectively.

3. 2. 2. KTH Dataset KTH dataset was introduced in literature [54] which has six types of human actions namely: walking, jogging, running, boxing, hand waving, and hand clapping, performed several times by 25 subjects. Similar to the Weizmann dataset, leave-one-out cross-validation has been employed. The confusion matrix of LS-TSVM and PLS-TSVM has been shown in Figure 6 (c,d). It shows more accurate predictions found by PLS-TSVM in comparison with the LS-TSVM. Overall accuracy is 95.21% on average. The accuracy rates of different methods on the KTH dataset are shown in Table 6.

The computional time of PLS-TSVM has been shown in Table 7 according to one-against-one protocol for multiclass classification. From the table, it is observed that the training time of all leave-one-out cross-validation
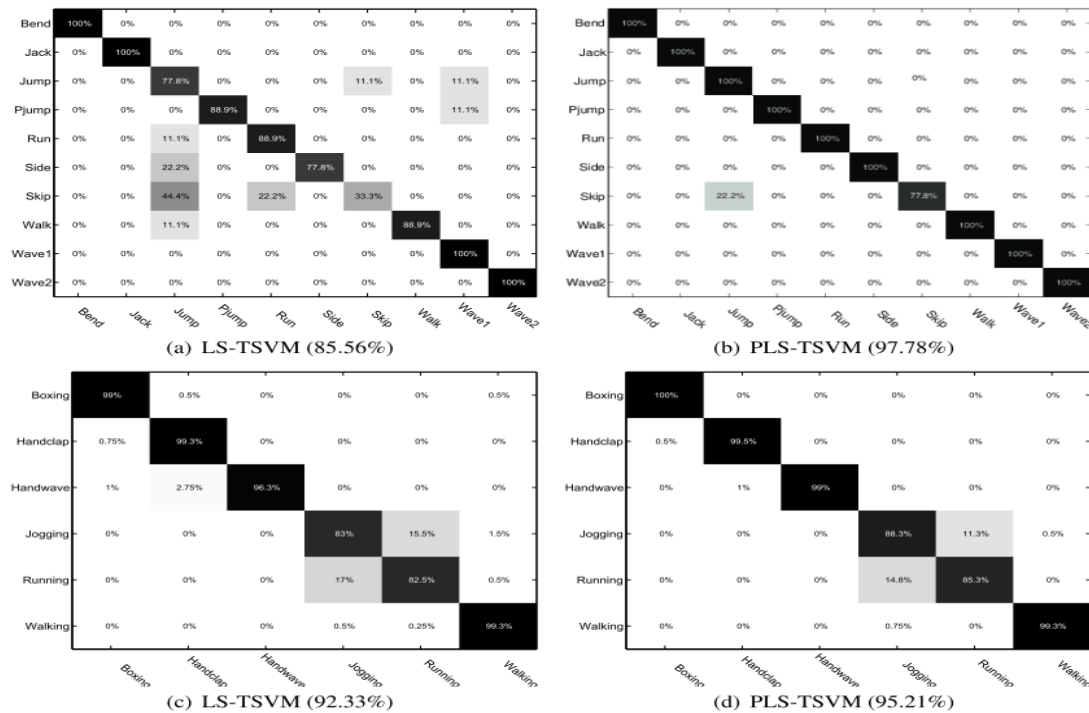
Figure 6. Confusion matrix of PLS-TSVM compared to LS-TSVM: (a, b) the Weizmann dataset, (c,d) the KTH dataset.me examples of video sequences in (a) Weizmann and (b) KTH datasets

TABLE 5. Performance on the Weizmann with Harris3D detector and HOG/HOF descriptor

Classifier	SVM	LS-TSVM	PLS-TSVM
Computational Time	Time(s)	Time(s)	Time(s)
Harris3D+HOG/HOF	84.4%	85.56%	97.78%
	2.9497	0.1082	0.1259

is about 8 minutes and 5 hours for PLS-TSVM and SVM, respectively. This is because PLS-TSVM does not require any special optimizers, whereas SVM has been implemented with fast interior-point solvers of the Mosek optimization toolbox for MATLAB. It is also interesting to mention that using two nonparallel hyperplanes in PLS-TSVM gives an accurate model for human activity.

TABLE 6. Accuracy rates of different methods on KTH dataset

Method	Classifier	Average Accuracy
Schuldt [54]	SVM	71%
Dollar [55]	KNN	81%
Wong [56]	WX-SVM	91.6%
Jhuang [57]	Bio-Inspired	91.7%
Niebles [42]	pLSA	83%
Fathi [40]	AdaBoost	90.5%
Klaser [58]	SVM	91.4%
Liu [59]	VWC-Correlation	94.16%
Wang [45]	SVM	92.1 %
Kovashka [60]	SVM	94.53%
Shao [61]	SVM	93.89%
ghodrati [62]	clustering+KNN	93%
Jiang [41]	Tree Learning+KNN	93.4%
Liu [37]	Boosted NBNN	92.7%
Goudelis [47]	SVM	93.14%
Chou [46]	NNC-GMMC	90.58%
An [63]	Deep Model	91.2%
Arunnehru [48]	3D-CNN	93.43%
Nasiri [27]	LS-TSVM	92.33%
Singh [49]	SVM	94.50%
Aslan [50]	KNN	96.14%
Vishwakarma [51]	SVM	96.60 %
Vishwakarma [52]	SVM-HMM	96.66%
Ramya [53]	NN	91.40%
Our method	PLS-TSVM	95.21%

TABLE 7. Performance on the KTH with Harris3D detector and HOG/HOF descriptor

Classifier	SVM	LS-TSVM	PLS-TSVM
Computational Time	Time (s)	Time (s)	Time (s)
Harris3D+HOG/	91.8 %	92.33%	95.21%
HOF	≃18340 (5h)	448.1872 (8min)	443.1907 (8min)

3. 2. 3. UCF101   UCF101 is one of the largest realistic datasets for human activity recognition, collected from YouTube [64]. The dataset is composed of 13,320 videos from 101 action categories. It gives the largest diversity in terms of actions in the presence of large variations in camera motion, object appearance and pose, object scale, viewpoint, cluttered background, illumination conditions, etc. Each of the 101 action classes belongs to one of five class types: Human-Object Interaction, Body-Motion Only, Human-Human Interaction, Playing Music Instruments, and Sports (see Figure 5). In these experiments, we have used the predefined splits by authors for training-testing and report the average accuracy.

We measure the overall performance of PLS-TSVM using three standard partitions. Also, the PLS-TSVM classifier is compared to an LS-TSVM classifier in Table 8. We observe that PLS-TSVM outperformed the LS-TSVM results by 12% on UCF101. It seems, PLS-TSVM is a robust classifier that could eliminate the unclassifiable regions (URs) and be more robust in the face of outliers of each class. To further show the advantage of PLS-TSVM with researches that have been published using the same features, we have compared accuracy rates in Table 9. It could be found that the accuracy rate of PLS-TSVM is higher than several state-of-the-art methods. It is worth to mention that we have also provided a variety of deep models in the benchmark tables for all three datasets. However, the comparison of these models with the experimental method used in this paper is unfair since most of the human action recognition methods extract high-level features simultaneously with classification, while in this research, we focused only on the classification performance rather than feature extraction.

TABLE 8. Details performance on the UCF101 with Harris3D detector and HOG/HOF descriptor

splits	LS-TSVM	PLS-TSVM
split 1	59.73%	71.75%
split 2	63.50 %	71.21 %
split 3	55.40 %	72.00 %
overall	59.55%	71.66%

TABLE 9. Accuracy rates of different methods on UCF101 dataset with HOG/HOF descriptor

Method	Classifier	Average Accuracy
Schuldt [64]	SVM	43.90%
Karpathy [65]	Neural Net	65.40%
Hou [66]	DaMN	57.60%
Boyraz [67]	Neural Net	53.35%
Kihl (baseline HOG) [68]	SVM	65.30%
Kihl (baseline HOF) [68]	SVM	68.60%
Peng [69]	Deep Model	39.94%
Chang [70]	Deep Model	70.94%
Nasiri [27]	LS-TSVM	59.55%
Hua (2D geometry-based) [71]	Deep	62.03%
Francisco [72]	Naive-Bayes	62.03%
Leyva [73]	Fisher Vector	71.60 %
Prakash [74]	Rand. Tree	65.11%
Our method	PLS-TSVM	71.66%

4. CONCLUSION

In this paper, Probabilistic Least Square Twin Support Vector Machine (PLS-TSVM) has been introduced. PLS-TSVM addressed several problems that may occur in TSVM-based algorithms such as unclassifiable regions (URs) and their sensitivity to outliers when they are applied to multiclass classification tasks such as human activity recognition. PLS-TSVM classifier performs classification by the use of two nonparallel hyperplanes similar to TSVM, unlike SVM, which uses a single hyperplane. Finally, a continuous output value is defined by comparing the distances between the samples and two separating hyperplanes to handle URs. In this research, we had two approaches to evaluate our proposed method. We first conducted experiments with PLS-TSVM on a set of UCI data sets and compared the results with SVM, TSVM, and LS-TSVM. Then we applied PLS-TSVM to 3 well-known human action video data sets and provided the results to be able to compare with the literature. For these experiments, we have used the HOG/HOF descriptor to present each video sequence in the bag of words (BoW) model. The results indicate that our proposed PLS-TSVM reaches a better performance on UCI data sets compared to the other three algorithms and also produces a significant improvement in action recognition while the computational time of the method is several orders of magnitude faster than SVM and AdaBoost classification based methods.

5. REFERENCES

1. Cen, Feng, Xiaoyu Zhao, Wuzhuang Li, and Guanghui Wang. "Deep feature augmentation for occluded image classification." *Pattern Recognition* 111, (2021), 107737, doi: 10.1016/j.patcog.2020.107737.

2. AlyanNezhadi, M. M., H. Qazanfari, A. Ajam, and Z. Amiri. "Content-based Image Retrieval Considering Colour Difference Histogram of Image Texture and Edge Orientation." *International Journal of Engineering, Transactions B: Applications,* Vol. 33, No. 5, (2020), 949-958, doi: 10.5829/ije.2020.33.05b.28.

3. Sezavar, A., H. Farsi, and Sajad Mohamadzadeh. "A modified grasshopper optimization algorithm combined with cnn for content-based image retrieval." *International Journal of Engineering, Transactions A: Basics,* Vol. 32, No. 7, (2019), 924-930, doi: 10.5829/ije.2019.32.07a.04.

4. Sharma, Parul, Yash Paul Singh Berwal, and Wiqas Ghai. "Performance analysis of deep learning CNN models for disease detection in plants using image segmentation." *Information Processing in Agriculture* 7, No. 4 (2020), 566-574, doi: 10.1016/j.inpa.2019.11.001

5. Chen, Long, Liangxiao Jiang, and Chaoqun Li. "Modified DFS-based term weighting scheme for text classification." *Expert Systems with Applications* 168, (2021), 114438, doi: 10.1016/j.eswa.2020.114438

6. Rahmanimanesh, Mohammad, Jalal A. Nasiri, Saeed Jalili, and N. Moghaddam Charkari. "Adaptive three-phase support vector data description." *Pattern Analysis and Applications* 22, No. 2, (2019), 491-504, doi: 10.1007/s10044-017-0646-3

7. Refahi, Mohammad S., Jalal A. Nasiri, and S. M. Ahadi. "Ecg arrhythmia classification using least squares twin support vector machines." In Electrical Engineering (ICEE), Iranian Conference on, 1619-1623. IEEE, 2018.

8. Okwuashi, Onuwa, and Christopher E. Ndehedehe. "Deep support vector machine for hyperspectral image classification." *Pattern Recognition* 103, (2020), 107298, doi: 10.1016/j.patcog.2020.107298

9. Sivaram, M., E. Laxmi Lydia, Irina V. Pustokhina, Denis Alexandrovich Pustokhin, Mohamed Elhoseny, Gyanendra Prasad Joshi, and K. Shankar. "An optimal least square support vector machine-based earnings prediction of blockchain financial products." *IEEE Access* 8, (2020), 120321-120330, doi: 10.1109/ACCESS.2020.3005808

10. Gao, Zheming, Shu-Cherng Fang, Jian Luo, and Negash Medhin. "A kernel-free double well potential support vector machine with applications." *European Journal of Operational Research* 290, No. 1 (2021), 248-262, doi: 10.1016/j.ejor.2020.10.040

11. Badaghei, R., H. Hassanpour, and T. Askari. "Detection of Bikers without Helmet Using Image Texture and Shape Analysis." *International Journal of Engineering, Transactions C: Aspects,* Vol. 34, No. 3 (2021): 650-655, doi: 10.5829/ije.2021.34.03c.09

12. Wang, Kuaini, Wenxin Zhu, and Ping Zhong. "Robust support vector regression with generalized loss function and applications." *Neural Processing Letters* 41, No. 1 (2015), 89-106, doi: 10.1007/s11063-013-9336-3

13. Qu, Hai-Ni, Guo-Zheng Li, and Wei-Sheng Xu. "An asymmetric classifier based on partial least squares." *Pattern Recognition* 43, No. 10 (2010), 3448-3457, doi: 10.1016/j.patcog.2010.05.002

14. Guo, Guodong, and Alice Lai. "A survey on still image based human action recognition." *Pattern Recognition* 47, No. 10 (2014), 3343-3361, doi: 10.1016/j.patcog.2014.04.018

15. Xiao, Yanghao, Yucheng Liu, Yuanyuan Deng, and Haoxuan Li. "Enhancing Multi-Class Classification in One-Versus-One Strategy: A Type of Base Classifier Modification and Weighted

Voting Mechanism." In 2021 International Conference on Communications, Information System and Computer Engineering (CISCE), 303-307. IEEE, 2021.

16. Wu, Yuanyuan, Liyong Shen, and Sanguo Zhang. "Fuzzy multiclass support vector machines for unbalanced data." In 2017 29th Chinese Control and Decision Conference (CCDC), 2227-2231. IEEE, 2017.

17. Pruengkarn, Ratchakoon, Kok Wai Wong, and Chun Che Fung. "Imbalanced data classification using complementary fuzzy support vector machine techniques and SMOTE." In 2017 IEEE International Conference on Systems, Man, and Cybernetics (SMC), 978-983. IEEE, 2017.

18. Liu, Jie, and Enrico Zio. "A scalable fuzzy support vector machine for fault detection in transportation systems." *Expert Systems with Applications* 102 (2018), 36-43, doi: 10.1016/j.eswa.2018.02.017

19. Inoue, Takuya, and Shigeo Abe. "Fuzzy support vector machines for pattern classification." In IJCNN'01. International Joint Conference on Neural Networks. Proceedings (Cat. No. 01CH37222), Vol. 2, 1449-1454. IEEE, 2001.

20. Ji, Ai-bing, Songcan Chen, and Qiang Hua. "Fuzzy classifier based on fuzzy support vector machine." *Journal of Intelligent & Fuzzy Systems* 26, No. 1 (2014), 421-430, doi: 10.3233/IFS-130819.

21. Yang, Libo. "Fuzzy Output Support Vector Machine Based Incident Ticket Classification." *IEICE Transactions on Information and Systems* 104, No. 1 (2021), 146-151, doi: 10.1587/transinf.2020EDP7044

22. Thakur, Arunava Kabiraj, Palash Kumar Kundu, and Arabinda Das. "Prediction of Unknown Fault of Induction Motor using SVM following Decision-Directed Acyclic Graph." *Journal of The Institution of Engineers (India)*: *Series B*, 102, No. 3, (2021), 573-583, doi: 10.1007/s40031-021-00536-2

23. Liu, Bo, Zhifeng Hao, and Eric CC Tsang. "Nesting one-against-one algorithm based on SVMs for pattern classification." *IEEE Transactions on Neural Networks* 19, No. 12, (2008), 2044-2052, doi: 10.1109/TNN.2008.2003298.

24. Li, Renbing, Aihua Li, Tao Wang, and Liang Li. "Vector projection method for unclassifiable region of support vector machine." *Expert Systems with Applications* 38, No. 1, (2011), 856-861, doi: 10.1016/j.eswa.2010.07.046.

25. Khemchandani, Reshma, and Suresh Chandra. "Twin support vector machines for pattern classification." *IEEE Transactions on Pattern Analysis and Machine Intelligence* 29, No. 5, (2007), 905-910, doi: 10.1109/TPAMI.2007.1068

26. Liu, Yi-Hung, and Yen-Ting Chen. "Face recognition using total margin-based adaptive fuzzy support vector machines.*" IEEE Transactions on Neural Networks* 18, No. 1, (2007), 178-192, doi: 10.1109/TNN.2006.883013.

27. Nasiri, Jalal A., Nasrollah Moghadam Charkari, and Saeed Jalili. "Least squares twin multi-class classification support vector machine." *Pattern Recognition* 48, No. 3, (2015), 984-992, doi: 10.1016/j.patcog.2014.09.020.

28. Gao, Zheming, Shu-Cherng Fang, Xuerui Gao, Jian Luo, and Negash Medhin. "A novel kernel-free least squares twin support vector machine for fast and accurate multi-class classification." *Knowledge-Based Systems* 226 (2021), 107123, doi: 10.1016/j.knosys.2021.107123.

29. Xu, Yitian, Xianli Pan, Zhijian Zhou, Zhiji Yang, and Yuqun Zhang. "Structural least square twin support vector machine for classification." *Applied Intelligence* 42, No. 3, (2015), 527-536, doi: 10.1007/s10489-014-0611-4.

30. Mir, A., and Jalal A. Nasiri. "KNN-based least squares twin support vector machine for pattern classification." *Applied

31. Nasiri, Jalal A., Nasrollah Moghadam Charkari, and Kourosh Mozafari. "Energy-based model of least squares twin support vector machines for human action recognition." *Signal Processing* 104 (2014), 248-257, doi: 10.1016/j.sigpro.2014.04.010.

32. Chen, Xiaobo, Jian Yang, Qiaolin Ye, and Jun Liang. "Recursive projection twin support vector machine via within-class variance minimization." *Pattern Recognition* 44, No. 10-11, (2011), 2643-2655, doi: 10.1016/j.patcog.2011.03.001.

33. Chen, Su-Gen, and Xiao-Jun Wu. "Multiple birth least squares support vector machine for multi-class classification." *International Journal of Machine Learning and Cybernetics* 8, No. 6, (2017), 1731-1742, doi: 10.1007/s13042-016-0554-7.

34. Shao, Yuan-Hai, Nai-Yang Deng, Zhi-Min Yang, Wei-Jie Chen, and Zhen Wang. "Probabilistic outputs for twin support vector machines." *Knowledge-Based Systems* 33, (2012), 145-151, doi: 10.1016/j.knosys.2012.04.006.

35. Bottou, Léon, Corinna Cortes, John S. Denker, Harris Drucker, Isabelle Guyon, Larry D. Jackel, Yann LeCun et al. "Comparison of classifier methods: a case study in handwritten digit recognition." In Proceedings of the 12th IAPR International Conference on Pattern Recognition, Vol. 3-Conference C: Signal Processing (Cat. No. 94CH3440-5), Vol. 2, 77-82. IEEE, 1994.

36. KRESSEL, Ulrich HG. "Pairwise classification and support vector machines." Advances in Kernel Methods: Support Vector Learning (2002).

37. Liu, Li, Ling Shao, and Peter Rockett. "Human action recognition based on boosted feature selection and naive Bayes nearest-neighbor classification." *Signal Processing* 93, No. 6, (2013), 1521-1530, doi: 10.1016/j.sigpro.2012.07.017.

38. Lu, Zhiwu, and Yuxin Peng. "Latent semantic learning with structured sparse representation for human action recognition." *Pattern Recognition* 46, No. 7, (2013), 1799-1809, doi: 10.1016/j.patcog.2012.09.027.

39. Laptev, Ivan, Marcin Marszalek, Cordelia Schmid, and Benjamin Rozenfeld. "Learning realistic human actions from movies." In 2008 IEEE Conference on Computer Vision and Pattern Recognition, 1-8. IEEE, 2008.

40. Fathi, Alireza, and Greg Mori. "Action recognition by learning mid-level motion features." In 2008 IEEE Conference on Computer Vision and Pattern Recognition, 1-8. IEEE, 2008.

41. Jiang, Zhuolin, Zhe Lin, and Larry Davis. "Recognizing human actions by learning and matching shape-motion prototype trees." *IEEE Transactions on Pattern Analysis and Machine Intelligence* 34, No. 3, (2012), 533-547, doi: 10.1109/TPAMI.2011.147.

42. Niebles, Juan Carlos, Hongcheng Wang, and Li Fei-Fei. "Unsupervised learning of human action categories using spatial-temporal words." *International Journal of Computer Vision* 79, No. 3, (2008), 299-318, doi: 10.1007/s11263-007-0122-4.

43. Liu, Jingen, Saad Ali, and Mubarak Shah. "Recognizing human actions using multiple features." In 2008 IEEE Conference on Computer Vision and Pattern Recognition, 1-8. IEEE, 2008.

44. Bregonzio, Matteo, Shaogang Gong, and Tao Xiang. "Recognising action as clouds of space-time interest points." In 2009 IEEE conference on computer vision and pattern recognition, 1948-1955. IEEE, 2009.

45. Wang, Heng, Muhammad Muneeb Ullah, Alexander Klaser, Ivan Laptev, and Cordelia Schmid. "Evaluation of local spatio-temporal features for action recognition." In Bmvc 2009-british machine vision conference, pp. 124-1. BMVA Press, 2009.

46. Chou, Kuang-Pen, Mukesh Prasad, Di Wu, Nabin Sharma, Dong-Lin Li, Yu-Feng Lin, Michael Blumenstein, Wen-Chieh Lin, and

Chin-Teng Lin. "Robust feature-based automated multi-view human action recognition system." *IEEE Access* 6, (2018), 15283-15296, doi: 10.1109/ACCESS.2018.2809552.

47. Goudelis, Georgios, Konstantinos Karpouzis, and Stefanos Kollias. "Exploring trace transform for robust human action recognition." *Pattern Recognition* 46, No. 12, (2013), 3238-3248, doi: 10.1016/j.patcog.2013.06.006.

48. Arunnehru, J., G. Chamundeeswari, and S. Prasanna Bharathi. "Human action recognition using 3D convolutional neural networks with 3D motion cuboids in surveillance videos." *Procedia Computer Science* 133 (2018), 471-477, doi: 10.1016/j.procs.2018.07.059.

49. Singh, Tej, and Dinesh Kumar Vishwakarma. "A hybrid framework for action recognition in low-quality video sequences." arXiv preprint arXiv:1903.04090 (2019),

50. Aslan, Muhammet Fatih, Akif Durdu, and Kadir Sabanci. "Human action recognition with bag of visual words using different machine learning methods and hyperparameter optimization." *Neural Computing and Applications* 32, No. 12, (2020), 8585-8597, doi: 10.1007/s00521-019-04365-9.

51. Vishwakarma, Dinesh Kumar, and Chhavi Dhiman. "A unified model for human activity recognition using spatial distribution of gradients and difference of Gaussian kernel." *The Visual Computer* 35, No. 11, (2019), 1595-1613, doi: 10.1007/s00371-018-1560-4.

52. Vishwakarma, Dinesh Kumar. "A two-fold transformation model for human action recognition using decisive pose." *Cognitive Systems Research* 61, (2020), 1-13, doi: 10.1016/j.cogsys.2019.12.004.

53. Ramya, P., and Rajendran Rajeswari. "Human action recognition using distance transform and entropy-based features." *Multimedia Tools and Applications* 80, No. 6, (2021), 8147-8173, doi: 10.1007/s11042-020-10140-z.

54. Schuldt, Christian, Ivan Laptev, and Barbara Caputo. "Recognizing human actions: a local SVM approach." In Proceedings of the 17th International Conference on Pattern Recognition, 2004. ICPR 2004., Vol. 3, 32-36. IEEE, 2004.

55. Dollár, Piotr, Vincent Rabaud, Garrison Cottrell, and Serge Belongie. "Behavior recognition via sparse spatio-temporal features." In 2005 IEEE International Workshop on Visual Surveillance and Performance Evaluation of Tracking and Surveillance, 65-72. IEEE, 2005.

56. Wong, Shu-Fai, Tae-Kyun Kim, and Roberto Cipolla. "Learning motion categories using both semantic and structural information." In 2007 IEEE Conference on Computer Vision and Pattern Recognition, 1-6. IEEE, 2007.

57. Jhuang, Hueihan, Thomas Serre, Lior Wolf, and Tomaso Poggio. "A biologically inspired system for action recognition." In 2007 IEEE 11th international conference on computer vision, 1-8. Ieee, 2007.

58. Klaser, Alexander, Marcin Marszałek, and Cordelia Schmid. "A spatio-temporal descriptor based on 3d-gradients." In BMVC 2008-19th British Machine Vision Conference, 275-301. British Machine Vision Association, 2008.

59. Liu, Jingen, and Mubarak Shah. "Learning human actions via information maximization." In 2008 IEEE Conference on Computer Vision and Pattern Recognition, 1-8. IEEE, 2008.

60. Kovashka, Adriana, and Kristen Grauman. "Learning a hierarchy of discriminative space-time neighborhood features for human

action recognition." In 2010 IEEE computer society conference on computer vision and pattern recognition, 2046-2053. IEEE, 2010.

61. Shao, Ling, Ruoyun Gao, Yan Liu, and Hui Zhang. "Transform based spatio-temporal descriptors for human action recognition." *Neurocomputing* 74, No. 6, (2011), 962-973, doi: 10.1016/j.neucom.2010.11.013.

62. Ghodrati, Amir, and Shohreh Kasaei. "Human action categorization using discriminative local spatio-temporal feature weighting." *Intelligent Data Analysis* 16, No. 4, (2012), 537-550, doi: 10.3233/IDA-2012-0538.

63. An, Feng-Ping. "Human action recognition algorithm based on adaptive initialization of deep learning model parameters and support vector machine." *IEEE Access* 6, (2018), 59405-59421, doi: 10.1109/ACCESS.2018.2874022.

64. Soomro, Khurram, Amir Roshan Zamir, and Mubarak Shah. "UCF101: A dataset of 101 human actions classes from videos in the wild." arXiv preprint arXiv:1212.0402 (2012).

65. Karpathy, Andrej, George Toderici, Sanketh Shetty, Thomas Leung, Rahul Sukthankar, and Li Fei-Fei. "Large-scale video classification with convolutional neural networks." In Proceedings of the IEEE conference on Computer Vision and Pattern Recognition, 1725-1732. 2014.

66. Hou, Rui, Amir Roshan Zamir, Rahul Sukthankar, and Mubarak Shah. "Damn–discriminative and mutually nearest: Exploiting pairwise category proximity for video action recognition." In European Conference on Computer Vision, 721-736. Springer, Cham, 2014.

67. Boyraz12, Hakan, Syed Zain Masood13, Baoyuan Liu, Marshall Tappen12, and Hassan Foroosh. "Action recognition by weakly-supervised discriminative region localization." (2014).

68. Kihl, Olivier, David Picard, and Philippe-Henri Gosselin. "A unified framework for local visual descriptors evaluation." *Pattern Recognition* 48, No. 4, (2015), 1174-1184, doi: 10.1016/j.patcog.2014.11.013.

69. Peng, Xiaojiang, and Cordelia Schmid. "Multi-region two-stream R-CNN for action detection." In European conference on computer vision, pp. 744-759. Springer, Cham, 2016.

70. Chang, Xiaojun, Yao-Liang Yu, and Yi Yang. "Robust top-k multiclass SVM for visual category recognition." In Proceedings of the 23rd ACM SIGKDD International Conference on Knowledge Discovery and Data Mining, 75-83. 2017.

71. Hua, Michelle, Mingqi Gao, and Zichun Zhong. "SCN: Dilated silhouette convolutional network for video action recognition." *Computer Aided Geometric Design* 85, (2021), 101965, doi: 10.1016/j.cagd.2021.101965.

72. dos S Silva, Francisco H., Gabriel M. Bezerra, Gabriel B. Holanda, J. Wellington M. de Souza, Paulo AL Rego, Aloísio V. Lira Neto, Victor Hugo C. de Albuquerque, and Pedro P. Rebouças Filho. "A novel feature extractor for human action recognition in visual question answering." *Pattern Recognition Letters* 147, (2021), 41-47, doi: 10.1016/j.patrec.2021.04.002.

73. Leyva, Roberto, Victor Sanchez, and Chang-Tsun Li. "Compact and low-complexity binary feature descriptor and Fisher vectors for video analytics." *IEEE Transactions on Image Processing* 28, No. 12 (2019): 6169-6184, doi: 10.1109/TIP.2019.2922826.

74. Sahoo, Suraj Prakash, and Samit Ari. "On an algorithm for human action recognition." *Expert Systems with Applications* 115, (2019), 524-534, doi: 10.1016/j.eswa.2018.08.014

Persian Abstract

چکیده

در این مقاله، یک دسته بند جدید مبتنی بر ماشین بردار پشتیبان دوقلو خطی برای مواجهه با مشکل نواحی غیرقابل دسته بندی در مسائل دسته بندی چندکلاسه ارائه شده است. الگوریتم پیشنهادی با عنوان ماشین بردار پشتیبان دوقلوی احتمالاتی روی مدل حاصل از ماشین بردار پشتیبان دوقلوی خطی یک خروجی پیوسته و احتمالاتی تولید می کند. این الگوریتم میتواند مشکل نواحی غیرقابل دسته بندی را با بکارگیری یک تابع عضویت برطرف کرده، اثرات نامطلوب داده های نویزی را کاهش دهد. کارایی الگوریتم پیشنهادی به کمک چندین مجموعه داده شامل دادگان تشخیص رفتار انسان ارزیابی شده است. نتایج بیانگر کارایی بهتر الگوریتم پیشنهادی نسبت به روش های مشابه است.

International Journal of Engineering

J o u r n a l   H o m e p a g e :   w w w . i j e . i r

Role of Praseodymium Addition in the Microstructure and Magnetic Properties of ZnCo Ferrite Nanopowders: Positive or Negative?

B. Shahbahrami[a], S. M. Rabiee[a*], R. Shidpoor[a], H. Salimi-Kenari[b]

[a] Department of Materials Engineering, Babol Noshirvani University of Technology, Babol, Iran
[b] Faculty of Engineering & Technology, University of Mazandaran, Babolsar, Iran

P A P E R   I N F O

A B S T R A C T

In order to investigate the effect of praseodymium (Pr) addition on the microstructure and magnetic properties of cobalt-zinc ferrite nanoparticles (NPs), different values of Pr element (x=0.2, 0.4 and 0.6) were added to the initial composition ($Co_{0.6}Zn_{0.4}Fe_{2-x}Pr_xO_4$) in the co-precipitation method, and the prepared precipitates calcined at 750 °C for 2 h. The synthesized powders were characterized by X-ray diffraction (XRD), field emission electron microscopy (FESEM), Fourier transform infrared spectroscopy (FTIR), and vibrating sample magnetometer (VSM). XRD pattern revealed the formation of a secondary phase of Pr-Fe oxide in addition to the ZnCo ferrite phase in the samples. FESEM images showed changes in the morphology and size of the particles by adding Pr to the composition. For specimen with x=0.2, the homogeneous spherical like particles with the size about less than 60 nm was formed. Whereas, for composition containing x=0.6 of Pr, a non-uniform powder with plate like particles was obtained and NPs had a thickness of approximately less than 30 nm. VSM analysis indicated that by increasing the element Pr to the cobalt-zinc ferrite composition, especially for values higher than x=0.2, the powder become a completely non-magnetic material.

doi: *10.5829/ije.2022.35.01a.02*

NOMENCLATURE

XRD	X-ray diffraction	H_C	Coercive force
FESEM	Field emission scanning electron microscopy	n_B	Bohr magneton
VSM	Vibrating sample magnetometer	Mr	Remanence magnetization
M_S	Saturation magnetization	a	Lattice parameter (Å)
K	Anisotropic constant	D	Crystallite size (Å)

1. INTRODUCTION

The magnetic properties of ferrites with spinel structure and their application depend on the composition and distribution of the cations at the tetrahedral (A) and octahedral (B) spaces [1-4]. Accordingly, many researchers have replaced various elements in the spinel structure and have studied changes in magnetic properties such as the saturation magnetism (Ms), coercive force (Hc), anisotropy constant (K), remanence magnetization (M_r), and the magnetic moment (n_B). Cobalt ferrite is an interesting material due to its high magnetic permeability, high coercive force, good

saturation magnetization (Ms) and usability in a wide range of applications such as telecommunications and medicine [2, 5]. Therefore, research is underway to study the effect of element substitution on cobalt ferrite materials. For example, Topkaya et al. [6] synthesized cobalt ferrite nanoparticles (NPs) substituted with zinc element ($Zn_xCo_{1-x}Fe_2O_4$) by hydrothermal method. The highest M_S of 76.5 emu/g reported for ferrite containing x=0.2. In addition, they stated that Zn^{2+} ion is located in A site, forcing Fe^{3+} ions to move from the A position to the B space. Dalal et al. [7] also synthesized $Ni_{0.4}Zn_{0.4}Co_{0.2}Fe_2O_4$ NPs by co-precipitation method and obtained crystallites with a size of about 34.7 nm and

*Corresponding Author Institutional Email: rabiee@nit.ac.ir (S. M. Rabiee)

high magnetization (84 emu/g) at room temperature. Ramakrishna et al. [8] synthesized $Co_{0.5}Zn_{0.37}Cu_{0.13}Fe_2O_4$ NPs with crystallite diameters 82.41 nm via sol-gel method. They reported Ms, H_c, K and n_B of the NPs equal to 50.35 emu/g, 198.9 Oe, 1.7 x 10^4 erg/Oe and 2.9 µB, respectively.

In another study by Naik and, Salker [9], the effect of adding Dy and Gd elements on magnetic properties of the cobalt ferrite NPs at room temperature (300 K) and very low temperature (5 K) investigated. With analysis of their results, it was found that firstly, lowering the temperature increased the saturation magnetization and the coercive field. The reason for this is activation of the magnetic moments of Dy and Gd ions at temperatures below 40 K. By substituting Dy^{3+} and Gd^{3+}ions instead of Fe^{3+}, the magnetic moment of the B sties, saturation magnetization and the coercive field increases. In addition, it observed that the amount of M_S in Dy-doped cobalt ferrite NPs (70.29 emu/g) is higher than that of Gd-doped specimen (60.85 emu/g) at room temperature. The higher magnetic moment in Dy ions than Gd ions mentioned for this difference.

In the work of Xavier et al. [10], the effect of samarium on the structural and magnetic properties of cobalt ferrite NPs ($CoFe_{2-x}Sm_xO_4$) investigated. They stated that with increasing Sm^{3+} concentration to x=0.25, the crystallites size increases from 11.26 to 16.53 nm, which is due to the higher ionic radius of the samarium than the iron element. For this reason, the coercive force reduced from 1372.2 Oe to 814.73 Oe, which is due to the easier movement of magnetic domains.

Alves et al. [11] studied the effect of adding Y^{3+} ions on the structural and magnetic properties of cobalt ferrite NPs ($CoY_xFe_{2-x}O_4$). By increasing the Y^{3+} ion values to 0.04, the grain size of the sample decreased from 35.32 to 16.05 nm. The saturation magnetization also decreased from 69 emu/g to 33 emu/g, while the coercive force increased from 1100 Oe to 1900 Oe.

In order to control particle size at high calcination temperatures and improve magnetic properties, Panda et al. [12] doped rare earth elements Pr or Gd in cobalt ferrite compositions and calcined them at different temperatures. They stated that the single-domain size of the pure cobalt ferrite materials is 70 nm. On the other hand, with increasing the calcination temperature to more than 500 ° C, the size of the crystallites significantly increases, so the presence of rare earth elements in the ferrite structure prevents their growth. The crystallite sizes of the samples synthesized by them for the compounds $CoGd_{0.1}Fe_{1.9}O_4$, $CoPr_{0.1}Fe_{1.9}O_4$, $CoGd_{0.2}Fe_{1.8}O_4$ and $CoPr_{0.2}Fe_{1.8}O_4$ at 900 °C were equal to 41.4, 33.2, 65.6 and 57.5 nm, respectively, while for pure cobalt ferrite it was 87.5 nm.

We know that the particle size plays a role in the relaxation time according to Equation (1), and the rapid switching of magnetic behavior occurs with smaller particles [13-15].

$$\tau_N = \tau_0 e^{(KV/k_BT)} \tag{1}$$

where τ_N is the Neel relaxation time, τ_0 is the exponential parameter ($\tau_0 = 10^{-9}$-10^{-3} s^{-1}), K is the anisotropy constant, V is the volume of NPs, K_B is Boltzmann constant, and T is the temperature (K_BT is thermal energy).

n the other hand, the amount of magnetic moment theoretically depends on the difference in magnetic moment between the tetrahedral and octahedral spaces according to Equation (2) [6, 16, 17]. Therefore, with the introduce of an even non-magnetic element into the ferrite composition and its replacement instead of one of the elements in A or B spaces, the initial order of ions is disturbed and may lead to a difference in the magnetic moment of the material.

$$nB(cal.) = MB(x) - MA(x) \tag{2}$$

Therefore, in the present work, the element praseodymium is added to the zinc cobalt ferrite composition and its effect on the microstructure and magnetic properties is studied, which has not been investigated by others. In this composition, by doping Zn in cobalt ferrite structure, it is expected to increase the crystallite sizes and saturation magnetization, and reduce the coercive force. By adding Pr to the composition, this element is located in the octahedral spaces instead of iron element and acts like non-magnetic atoms at room temperature. However, it is used for this research for two reasons; first, due to the unpaired electrons in the *4f* layer, it has a single ion anisotropy in the crystal lattice, which may be useful. Second, by changing the particle size and surface effects due to inhibiting the growth of particles and the crystallite diameters beyond the range of single-domain size (70 nm) may improve the microstructure and magnetic properties.

2. EXPERIMENTAL

Nanocrystalline powders ($Co_{0.6}Zn_{0.4}Fe_{2-x}Pr_xO_4$, x=0.2, 0.4 and 0.6) were prepared by co-precipitation method using raw materials of iron nitrate ($Fe(NO_3)_3.9H_2O$) (Merck), cobalt nitrate ($Co(NO_3)_2.6H_2O$) (Merck), zinc nitrate ($Zn(NO_3)_2.4H_2O$) (Merck), and praseodymium nitrate ($Pr(NO_3)_3.6H_2O$) (Merck). Using deionized water (DI), 0.5 M solutions were prepared from each of the starting materials. The solutions were stirred for 10 m on a magnetic stirrer (50 °C, 400 rpm). These solutions were mixed together. The pH of the mixture was raised to 11 using NaOH (Merck) and stirred again (5 h, 80 °C, 700 rpm). The resulting precipitates were dried (110 °C, 24 h), then calcinated (750 °C, 2 h). The phase formation and strain created in the particles were studied by XRD (D8 ADVANCE, BRUKER, Germany) technique. FESEM (Mira 3-XMU) was used to investigate the

morphology and size of the particles, and FTIR (Shimadzu Co., Japan) was performed in order to evaluate the chemical bonds in the synthesized specimens. Also magnetic properties of the prepared samples were identified using VSM (Danesh Pajooh Co., Iran) analysis. From now on, specimens with different Pr values are introduced as Pr0 to Pr6 according to Pr content (x).

3. RESULTS AND DISCUSSION

The XRD results of the synthesized samples at 750 °C for 2 h are shown in Figure 1. It should be noted that in order to compare and evaluate the effect of adding Pr to the composition, XRD analysis of the Pr free sample is also provided.

In the sample without Pr (Pr0) (Figure 1-a), the appearance of planes (220), (311), (222), (400), (422), (511), (440), (622) and (533) according to JCPDS card 00-022-1086 confirms the formation of single-phase ZnCo ferrite with cubic spinel structure. By adding Pr to the composition equal to x= 0.2 (Pr2) (Figure 1-b), it can be seen that in addition to the previously appeared peaks, other peaks are formed at other angles, which according to JCPDS 01-074-1472 belong to the new phase of Pr-Fe oxide ($PrFeO_3$). As the amount of praseodymium increased, the intensity of the new phase peaks also increased, and the height of the initial spectra in the Pr-free sample was significantly reduced, and even many peaks were removed (Figure 1-d). In fact, the predominant phase in these specimens is $PrFeO_3$. This means that contrary to expectations, with the presence of praseodymium in the reaction system, no solid solution of CoZnPr ferrite is formed. This result contradicts the findings reported by Panda et al. [12] that synthesized cobalt ferrite substituted with Pr^{3+} ($CoFe_{1-x}Pr_xO_4$) using citrate raw materials by sol-gel method and obtained $CoPr_{0.1}Fe_{1.9}O_4$ and $CoPr_{0.2}Fe_{1.8}O_4$. This is probably due to the higher ionic radius of praseodymium (1.13 Å) than iron (0.67 Å) [16], which makes it difficult to place as a substituent or interstitial element within the structure.
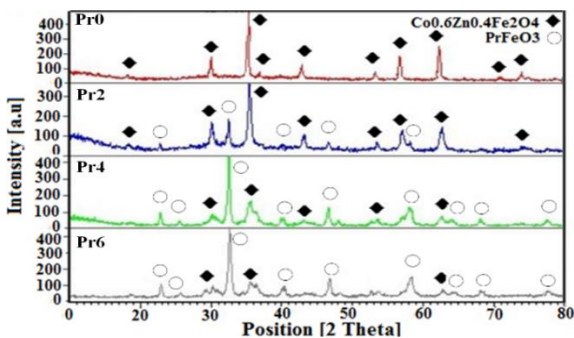
The Bertaut method was used to calculate the amount of phases which is based on the intensity of the scattered peaks and is summarized in Table 1. It is observed that in the composition with x=0.2, equivalent to 30.94 wt. % of the new phase ($PrFeO_3$) is formed. This amount increased to 84.23 wt. % in the composition containing x=0.6, which means a reduction of the initial phase ($Co_{0.6}Zn_{0.4}Fe_2O_4$) to 15.77 wt.% in the powder.

The crystallite diameters and the strain created inside the crystalline particles were obtained by Williamson-Hall equation [18-20] as follows:

$$B.cos(\theta)= (0.9.\lambda / D) + 4 \varepsilon \sin(\theta) \qquad (3)$$

where, D is the grain size (Å), λ is the wavelength of $Cu_{k\alpha}$ (1.54056 Å), B is the broadening line at half the peak height (rad.), ε is the lattice strain, and θ is the Bragg angle of the scattered peak.

The results of the Williamson-Hall equation for the synthesized samples are summarized in Table 2.

It is observed that the sample without Pr has a crystallite diameter of 47.81 nm and a compressive strain equal to 10^{-4}. When praseodymium introduce to the composition, the strain created in the ZnCo ferrite is tensile type and this strain increases with increasing amount of Pr element. Due to the increase in tensile strain, the diameter of its crystallites also decreases further. On the other hand, the strain created in the Pr-Fe oxide phase is compressive type. As a result, the diameter of its crystallites increases. The diagram of changes in the crystallite diameters in terms of the Pr value for each of the phases is given in Figure 2.

The lattice parameter of the synthesized powders was also obtained using extrapolate function $cos^2\theta/sin\theta$ [21] (Table 3).

The chemical bonds in the synthesized specimens are shown in Figure 3. The vibrational modes appeared at 450 cm^{-1} and 590 cm^{-1} are related to M-O bonds in the B and A spaces of the ferrite phase, respectively. The stretching modes at 1650 cm^{-1} and 3450 cm^{-1} are belong to hydroxyl groups which can help to establish the surface bonds of the particles. The frequency band around 2350 cm^{-1} is attributed to C-H bond. Weak bands in the range 1250-1700 cm^{-1} are also related to –C=C– bonds [22-25].

Figure 1. XRD analysis of the synthesized powders at 750 °C for 2 h

TABLE 1. The relative intensity of the spectra appearing (I_{100}) and the amount of phases formed in the synthesized powders

Sample	Pr0	Pr2	Pr4	Pr6
Relative intensity (I_{100}) of ($Co_{0.6}Zn_{0.4}Fe_2O_4$)	100	100	31.83	18.72
Relative intensity (I_{100}) of ($PrFeO_3$)	0	44.81	100	100
$I_{PrFeO3}/I_{Co0.6Zn0.4Fe2O4}$	0	0.45	3.14	5.34
$PrFeO_3$ (Wt. %)	0	30.94	75.86	84.23
$Co_{0.6}Zn_{0.4}Fe_2O_4$ (Wt. %)	100	69.06	24.14	15.77

TABLE 2. Strain and crystallite size of the synthesized nanopowders at 750 °C for 2 h

Sample	Pr0	Pr2		Pr4		Pr6	
		Zn- Co Ferrite	Pr –Fe Oxide	Zn- Co Ferrite	Pr –Fe Oxide	Zn- Co Ferrite	Pr –Fe Oxide
$2\Theta_1$ (°)	35.37	35.48	32.53	35.48	32.56	35.78	32.68
$2\Theta_2$ (°)	62.46	30.15	46.66	62.69	46.68	30.23	46.81
$2\Theta_3$ (°)	56.88	62.67	58.23	30.22	58.27	62.90	58.34
$2\Theta_4$ (°)	30.04	57.10	22.79	57.05	22.86	58.34	22.95
B_1 (°)	0.26	0.45	0.28	0.93	0.34	0.70	0.41
B_2 (°)	0.32	0.46	0.33	0.61	0.37	0.62	0.42
B_3 (°)	0.34	0.51	0.35	0.64	0.64	0.31	0.64
B_4 (°)	0.22	0.48	0.19	0.46	0.31	0.64	0.38
ε	10^{-4}	$-2*10^{-4}$	$16.5*10^{-4}$	$-6.6*10^{-4}$	$35*10^{-4}$	$-45*10^{-4}$	$24*10^{-4}$
D (nm)	47.81	17.55	57.77	9.29	72.97	8.56	33.01
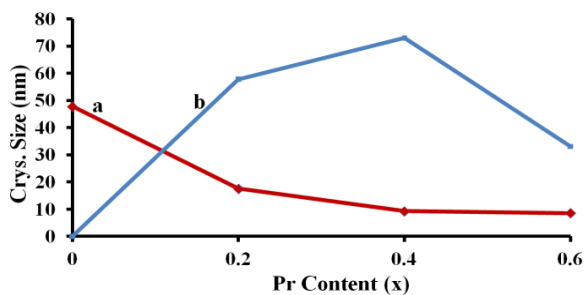
Figure 2. The crystallite diameter of the synthesized samples as a function of Pr value; (a) Crystallite diameter of ZnCo ferrite, and (b) Crystallite diameter of Pr-Fe oxide

The FESEM images of the synthesized samples are shown in Figure 4. It is seen that the morphology of the particles with the increase of praseodymium for content of x=0.4 and 0.6 is deviates from the spherical state and appears as a plate like. The non-uniformity in morphology and particle size is especially evident in Figure 4-c. The larger particles seems to be related to the Pr-Fe oxide phase, which appears mainly in the form of plates with the thickness about less than 30 nm and diameter approximately more than 100 nm. EDS analysis of samples and the weight percent of the elements are presented in Figure 5 and Table 4, respectively. It is

TABLE 3. Lattice parameter of the synthesized NPs with different concentrations of Pr value

Sample	Pr0	Pr2		Pr4		Pr6	
		Zn- Co Ferrite	Pr –Fe Oxide	Zn- Co Ferrite	Pr –Fe Oxide	Zn- Co Ferrite	Pr –Fe Oxide
$2\Theta_1$ (°)	35.37	35.48	32.53	35.48	32.56	35.78	32.68
$2\Theta_2$ (°)	62.46	30.15	46.66	62.69	46.68	30.23	46.81
$2\Theta_3$ (°)	56.88	62.67	58.23	30.22	58.27	62.90	58.34
d_1 (Å)	2.54	2.53	2.75	2.53	2.75	2.51	2.74
d_2 (Å)	1.49	2.96	1.95	1.48	1.94	2.95	1.94
d_3 (Å)	1.62	1.48	1.59	2.96	1.59	1.48	1.58
a (Å)	8.4	8.38	6.47	8.39	6.48	8.35	6.47
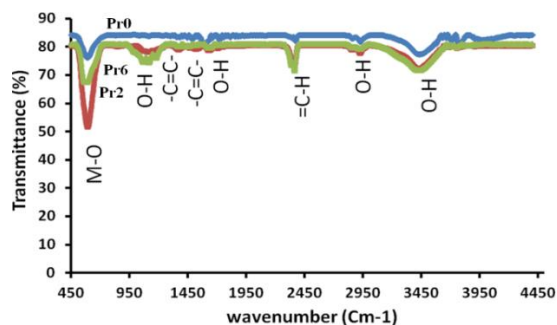
Figure 3. FTIR spectra of the synthesized samples as a function of Pr value

natural that by substituting Pr instead of iron in the composition and increasing its concentration, the presence of this element also increases and the concentration of Fe decreases. The concentrations of other elements (Co, Zn, O) are also changed by maintaining their atomic ratio in the composition. The extracted data are close to the stoichiometric state of the desired compounds.

Magnetic properties of the synthesized samples were investigated using VSM analysis (Figure 6) and the results are given in Table 5.
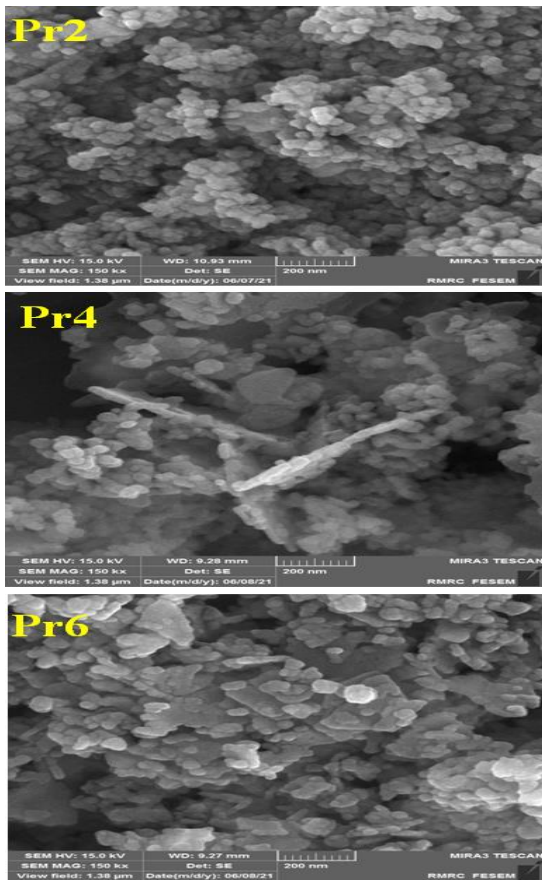
Figure 4. FESEM images of the synthesized samples with different Pr values
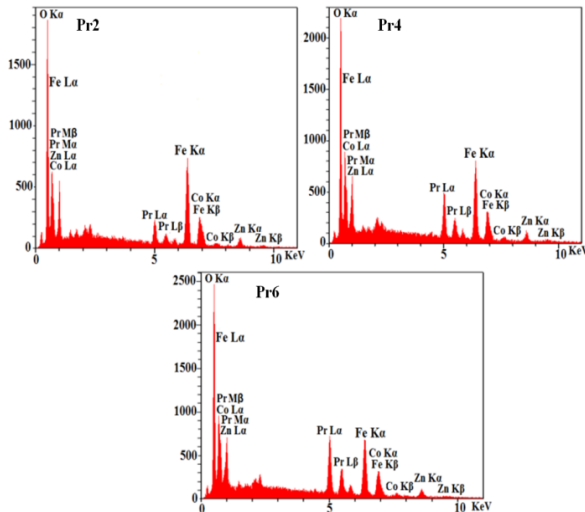
Figure 5. EDS analysis of NPs with different concentration of Pr element

The composition without the element praseodymium (cobalt-zinc ferrite; Pr0) has excellent magnetic properties, so that its saturation magnetization and coercive force at 10^4 Oe are 100.34 emu/g and 150 Oe,

TABLE 4. Weight percent of elements in synthesized samples containing various praseodymium

Sample	O	Fe	Co	Zn	Pr
Pr2	32.30	31.09	13.47	8.81	14.32
Pr4	29.07	24.78	12.39	8.04	25.72
Pr6	29.64	18.73	10.88	7.58	33.16
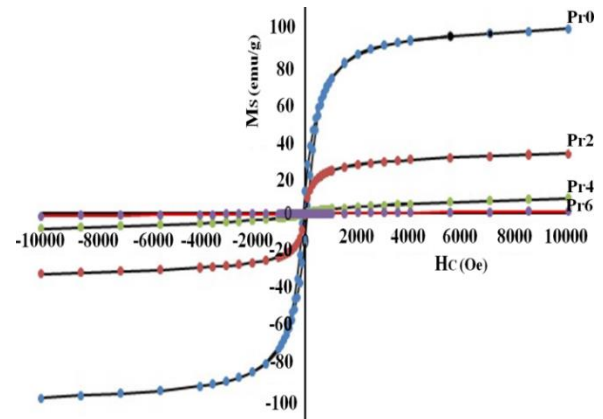
Figure 6. Magnetic hysteresis loops of the synthesized NPs as a function of Pr value

TABLE 5. Magnetic properties obtained from the hysteresis loops in terms of different concentrations of the Pr element

Magnetic properties	Pr0	Pr2	Pr4	Pr6
M (emu/g) at (3000 Oe)	91.54	28.22	4.58	0.43
M (emu/g) at (4000 Oe)	94.16	29.26	5.31	0.56
M (emu/g) at (5500 Oe)	96.48	30.37	6.23	0.76
M (emu/g) at (7000 Oe)	98.01	31.32	6.99	0.94
M (emu/g) at (8500 Oe)	99.18	32.03	7.67	1.12
Ms (emu/g) at (10000 Oe)	100.34	32.72	8.34	1.31
Hc (Oe)	150	~ 0	~ 0	~ 0
Mr (emu/g)	12.16	0.07	0.03	0.01
Mr /Ms	0.121	0.002	0.004	0.008

respectively. By adding the element Pr to the composition, the magnetic properties are drastically reduced and the sample becomes a completely non-magnetic material. The question is, what is the reason for these drastic changes? It should be noted that if the powders were a single phase (as in the Pr0 sample), since this phase (ZnCo ferrite) is a magnetic material, changes in magnetic properties could be attributed to changes in microstructure such as crystallite diameter and particle size. In this case, due to the decrease in crystallite diameter (Table 2) and particle size (Figure 4), it was expected that the Ms would decrease and the Hc would

increase. However, we see here that the coercive forces are completely eliminated and are almost zero, and the saturation magnetization of the samples are very negligible, especially for composition containing Pr equal to x=0.6 (1.31 emu/g). Therefore, it is concluded that this change is due to the magnetic nature of the powder and its conversion to a non-magnetic material with the formation of $PrFeO_3$ phase, and not the microstructure. However, the microstructure of the samples, as shown in Figure 4, had non-uniform particles containing ZnCo ferrites and Pr-Fe oxides which made effect on the magnetic properties.

4. CONCLUSIONS

Contrary to the initial predictions of solid solution formation with the entry of the element praseodymium into the crystal lattice, in the present study this does not happen at least for Pr values higher than x=0.2 and a secondary phase of $PrFeO_3$ forms next to the primary ZnCo ferrite phase. By increasing the presence of Pr in the composition, especially at x=0.6, about 84% by weight of the $PrFeO_3$ phase is formed and a completely non-magnetic material with zero coercive force and almost negligible saturation magnetization (1.13 emu/g) is produced. It has no positive effect on improving magnetic properties. However, the formation of plate like particles with the thickness about less than 30 nm can be seen in the sample containing Pr with x=0.6. Due to the magnetic properties of the Pr-doped sample with x= 0.2, it seems that if smaller amounts of this additive are used in the initial compositions, it is possible to create a solid solution of the initial ferrite and improve the microstructure because of particle size control.

5. ACKNOWLEDGEMENTS

6. REFERENCES

1. Manohar, A., Krishnamoorthi, C., "Synthesis and magnetic hyperthermia studies on high susceptible Fe$_{1-x}$Mg$_x$Fe$_2$O$_4$ superparamagnetic nanospheres", *Journal of Magnetism and Magnetic Materials* 443, (2017), 267-274. DOI: 10.1016/j.jmmm.2017.07.065

2. Puspitasari, P., Budi, L.S., "Physical and magnetic properties comparison of cobalt ferrite nanopowders using sol-gel and sonochemical methods", *International Journal of Engineering, Transactions B: Applications,* Vol. 33, No. 5, (2020), 877-884. DOI:10.5829/ije.2020.33.05b.20

3. Linh, P.H., Anh, N.T.N., Nam, P.H., Bach, T.N., Lam, V.D., Manh, D.H., "A Facile Ultrasound Assisted Synthesis of Dextran-

Stabilized Co$_{0.2}$Fe$_{0.8}$Fe$_2$O$_4$ Nanoparticles for Hyperthermia Application", *IEEE Transactions on Magnetics* 54, No. 6, (2018), 1-4. DOI: 10.1109/TMAG.2018.2815080

4. Nekouee, Kh.A., Rahimi, A.H., Alineghad, M., Ehsani, N., "The effect of Bismuth oxide on microstructures and magnetic properties of Mn-Mg-Al ferrites", *Journal of Electronic Materials* 47, No. 7, (2018), 4078-4084. DOI: 10.1007/s11664-018-6297-3

5. Yazdani, B., Nikzad, L., Vaezi, M.R., "Synthesis of CoFe$_2$O$_4$-polyaniline nanocomposite and evaluation it's magnetic properties", *International Journal of Engineering, Transactions B: Applications,* Vol. 22, No. 4, (2009), 381-386.

6. Topkaya, R., Baykal, A., Demir, A., "Yafet–Kittel-type magnetic order in Zn-substituted cobalt ferrite nanoparticles with uniaxial anisotropy", *Journal of Nanoparticle Research* 15, No. 1, (2013), 1954-1962. DOI 10.1007/s11051-012-1359-6

7. Dalal, M., Das, A., Das, D., Ningthoujam, R.S., Chakrabarti, P.K., "Studies of magnetic, Mössbauer spectroscopy, microwave absorption and hyperthermia behaviour of Ni-Zn-Co-ferrite nanoparticles encapsulated in multi-walled carbon nanotubes", *Journal of Magnetism and Magnetic Materials,* (2018). DOI: 10.1016/j.jmmm.2018.03.048

8. Ramakrishna, A., Murali, N., Margarette, S.J., Mammo, T.W., Joythi, N., Sailaja, B., Kumari, C.C., Samatha, K., Veeraiah, V., "Studies on structural, magnetic, and DC electrical resistivity properties of Co$_{0.5}$M$_{0.37}$Cu$_{0.13}$Fe$_2$O$_4$ (M = Ni, Zn and Mg) ferrite nanoparticle systems", *Advanced Powder Technology* 29, (2018), 2601-2607. DOI: 10.1016/j.apt.2018.07.005

9. Naik, S.R., Salker, A.V., "Change in the magneto structural properties of rare earth doped cobalt ferrites relative to the magnetic anisotropy", *Journal of Materials Chemistry* 22, (2012), 2740-2750. DOI: 10.1039/C2JM15228B

10. Xavier, S., Thankachan, S., Jacob, B., Mohammed, E., "Effect of Samarium Substitution on the Structural and Magnetic Properties of Nanocrystalline Cobalt Ferrite", *Journal of Nanoscience,* (2013), 1-7. DOI: 10.1155/2013/524380

11. Alves, T., Pessoni, H., Franco, A., "The effect of Y^{3+} substitution on the structural, optical band-gap, and magnetic properties of cobalt ferrite nanoparticles", *Physical Chemistry Chemical Physics,* (2017), 1-12. DOI: 10.1039/C7CP02167D

12. Panda, R.N., Shih, L.C., Chin, T.S., "Magnetic properties of nano-crystalline Gd-or Pr-substituted CoFe$_2$O$_4$ synthesized by the citrate precursor technique", *Journal of Magnetism and Magnetic Materials* 257, (2003), 79-86. DOI: 10.1016/S0304-8853(02)01036-3

13. Shahbahrami, B., Rabiee, S.M., Shidpoor, R., "An Overview of Cobalt Ferrite Core-Shell Nanoparticles for Magnetic Hyperthermia Applications", *Advanced Ceramics Progress* 6, (2020), 1-15. DOI: 10.30501/acp.2020.105923

14. Deatsch, A.E., Evans, B.A., "Heating efficiency in magnetic nanoparticle hyperthermia", *Journal of Magnetism and Magnetic Materials* 354, (2014), 163-172. DOI:10.1016/j.jmmm.2013.11

15. Mallick, A., Mahapatra, A.S., Mitra, A., Greneche, J.M., Ningthoujam, R.S., Chakrabarti, P.K., "Magnetic properties and bio-medical applications in hyperthermia of lithium zinc ferrite nanoparticles integrated with reduced graphene oxide", *Journal of Applied Physics,* 123, No. 5, (2018), 1-9. DOI: 10.1063/1.5009823

16. Pachpinde, A.M., Langade, M.M., Lohar, K.S., Shirsath, S.E., "Impact of larger rare earth Pr^{3+} ions on the physical properties of chemically derived Pr$_x$CoFe$_{2-x}$O$_4$ nanoparticles", *Chemical Physics* 429, (2014), 20-26. DOI:10.1016/j.chemphys.2013.11.018

17. Mahdikhah, V., Ataie, A., Babaei, A., Sheibani, S., Yang, C.W.O., Abkenar, S.K., "Control of structural and magnetic

characteristics of cobalt ferrite by post calcination mechanical milling", *Journal of Physics and Chemistry of Solids* 134, (2019) 286-294. DOI: 10.1016/j.jpcs.2019.06.018

18. Dhiwahar, A.T., Sundararajan, M., Sakthivel, P., Dash, C.S., Yuvaraj, S., "Microwave-assisted combustion synthesis of pure and zinc-doped copper ferrite nanoparticles: Structural, morphological, optical, vibrational, and magnetic behaviour", *Journal of Physics and Chemistry of Solids* 138, (2020), 109257. DOI: 10.1016/j.jpcs.2019.109257

19. Sinfroni, F.S.M., Santana, P.Y.C., Coelho, S.F.N., Silva, F.C., Menezes, A.S.D., Sharma, S.K., "Magnetic and structural properties of cobalt- and zinc-substituted nickel ferrite synthesized by microwave-assisted hydrothermal method", *Journal of Electronic Materials* 46, No. 2, (2017), 1145-1154. DOI: 10.1007/s11664-016-5081-5

20. Hanish, H.H., Edrees, S.J. Shukur, M.M., "The Effect of Transition Metals Incorporation on the Structural and Magnetic Properties of Magnesium Oxide Nanoparticles", *International Journal of Engineering, Transactions A: Basics,* Vol. 33, No. 4, (2020), 647-656. DOI: 10.5829/ije.2020.33.04a.16

21. Cullity, B.D., Elements of X-ray Diffraction, Massachusetts: Addison-Wesley Publishing Company, 1978.

22. Pilati, V., Gomes, R.C., Gomide, G., Coppola, P., Silva, F.G., Paula, F.L.O., Perzynski, R., Goya, G.F., Aquino, R., Depeyrot, J., "Core/Shell Nanoparticles of Non-Stoichiometric Zn-Mn and Zn-Co Ferrites as thermo sensitive Heat Sources for Magnetic Fluid Hyperthermia", *Journal of Physical Chemistry C* 122, No. 5, (2018), 3028-3038. DOI:10.1021/acs.jpcc.7b11014.

23. Asogekar, P.A., Verenkar, V.M.S., "Structural and magnetic properties of nanosized $Co_xZn_{(1-x)}Fe_2O_4$ (x= 0.0, 0.5, 1.0) synthesized via autocatalytic thermal decomposition of hydrazinated cobalt zinc ferrous succinate", *Ceramics International* 45, (2019), 21793-21803. DOI: 10.1016/j.ceramint.2019.07.182

24. Moravvej-Farshi, F., Amishi, M., Nekouee, Kh.A., "Influence of different milling time on synthesized Ni-Zn ferrite properties by mechanical alloying method", *Journal of Materials Science: materials in Electronics* 31, (2020), 13610-13619. DOI: 10.1007/s10854-020-03917-3

25. Moslehi-Niasar, M., Molaei, M.J., Aghaei, A., "Electromagnetic Wave Absorption Properties of Barium Ferrite/Reduced Graphene Oxide Nanocomposites", *International Journal of Engineering, Transactions C: Aspects,* Vol. 34, No. 6, (2021) 1505-1513. DOI: 10.5829/ije.2021.34.06c.14

Persian Abstract

چکیده

به منظور بررسی اثر Pr بر ریزساختار و خواص مغناطیسی ترکیب فریت کبالت-روی، مقادیر مختلف از Pr (x معادل ۰/۲، ۰/۴ و ۰/۶) با استفاده از مواد اولیه نیتراتی و به روش همرسوبی به ترکیب اولیه ($Co_{0.6}Zn_{0.4}Fe_{2-x}Pr_xO_4$) افزوده شد. رسوبات حاصل در دمای ۷۵۰ °C به مدت ۲ ساعت کلسینه شدند. نمونه‌های سنتز شده با آنالیزهای الگوی پراش اشعه ایکس (XRD)، میکروسکپ الکترونی نشر میدانی (FESEM)، طیف‌نگاری فوریه (FTIR) و مگنتومتر نمونه ارتعاشی (VSM) مشخصه‌یابی شدند. بررسی XRD نشان داد که با افزودن Pr به ترکیب $Co_{0.6}Zn_{0.4}Fe_2O_4$ علاوه بر فاز فریت کبالت- روی، فاز ثانویه اکسید آهن--پرازئودمیم نیز تشکیل می‌شود. تصاویر میکروگراف پودرهای سنتز شده تغییراتی را در شکل و اندازه ذرات سنتز شده با افزودن Pr به ترکیب نشان دادند. برای نمونه با x=۰/۲، ذرات کروی شکل یکنواختی با اندازه حدوداً کمتر از ۶۰ nm تشکیل شدند. در حالیکه، برای ترکیب با x=۰/۶، پودری غیریکنواخت با ذرات صفحه‌ای شکل بدست آمد و نانو ذرات ضخامتی کمتر از ۳۰ nm داشتند. آنالیز مگنتومتر نمونه ارتعاشی (VSM) حکایت از تغییر خواص مغناطیسی قابل توجه فریت کبالت- روی به یک ماده کاملاً غیر مغناطیس با افزودن پرازئودمیم به ویژه برای مقادیر بالاتر از x=۰/۲ دارد.

International Journal of Engineering

J o u r n a l   H o m e p a g e :   w w w . i j e . i r

Synthesis and Characterization Unsaturated Polyester Resin Nanocomposites Reinforced by Fe_2O_3+ Ni Nanoparticles: Influence on Mechanical and Magnetic Properties

K. D. Salman*

Department of Electromechanical Engineering, University of Technology, Iraq

P A P E R I N F O	*A B S T R A C T*
	This investigation aims to study the effect of Fe_2O_3, Ni nanoparticles as a reinforcement material on the mechanical properties of unsaturated polyester (UPR) as a matrix to produce a nanocomposite material using a casting route. Various examinations and tests were conducted to define the characteristics of the manufactured nanocomposite, such as Field Emission Scanning Electron Microscopy (FESEM), Energy Dispersive Spectrometry (EDS), and Fourier Transform Infrared Spectrometer (FTIR) analysis. The mechanical tests, including tensile, bending and hardness were performed on samples at the room temperature according to ASTM standards, while the magnetic characteristics were defined by vibrating sample magnetometer (VSM). Fe_2O_3 nanoparticles were incorporation into unsaturated polyester resin by different weight percentages that vary from 0 wt% to 20 wt% and a constant concentration 3 wt% of Ni nanoparticles. The images of FESEM and EDS evinced the homogeneity of F_2O_3, Ni nanoparticles into the pure unsaturated polyester resin (UPR). While, the improvement in Young's modulus, tensile strength, bending strength, and hardness was compared with those for the UPR. The improvement was 10.02% in young's modulus, 44.08% in tensile strength, 13.55% in bending strength, and strength in hardness. Also, the magnetic properties, including saturation magnetization (Ms), residual magnetization (Mr) and coercivity force (Hc) enhanced with an increase in the concentration of nanoparticles. The preferred percentage to improve the mechanical properties was found at 15 wt% of Fe_2O_3 and then decreased above this concentration, whereas the enhancement in hardness was achieved at 20 wt% of Fe_2O_3.

doi: 10.5829/ije.2022.35.01a.02 |

NOMENCLATURE

UPR	unsaturated polyester resin	W t%	Weight percent
FESEM	Field Emission Scanning Electron Microscopy	FTIR	Fourier Transform Infrared Spectrometer
EDS	Energy Dispersive Spectrometry	Hc	Coercivity field
Mr	residual magnetization	VSM	Vibrating sample magnetometer

1. INTRODUCTION

In recent years, polymer nanocomposites (PNCs) have become an interest for many researchers because of their ability to manipulate the thermal, electrical, and thermomechanical properties [1]. Thermosetting as polymer matrix are characterized as a low molecular weight solids and low viscosity liquids which they need reinforcement materials as a cross-linking agent to be cured and formulated. Also, thermosetting polymer can be incorporated with nanoparticles of fibers reinforcements to improve the mechanical, thermal, electrical and magnetics properties [2].

The polyester resin was used as a matrix owing to its network structure, resistance to moisture and toxin [3]. Polymer nanocomposites (PNCs) consisting of unsaturated polyester (UPRs) have been widely used for the automotive and electrical fields, structural,

Corresponding Author Institutional Email: 50123@uotechnology.edu.iq (K. D. Salman)

biomedical and tribological applications [4]. PNCs are an important type of a hybrid material comprising a reinforcement material (inorganic) in nanoscale incorporated into (organic) polymer matrix [5]. Different nanoparticles have been used as fillers in nanocomposites, including ZnO, Fe_2O_3, SiO_2, Al_2O_3, TiO_2, and $CaCO_3$. Owing to their excellent stability, inertness, biocompatibility, non-toxicity, low cost, iron oxide (Fe_2O_3) nanoparticles are very popular among them [6].

It is worth noting that Fe_2O_3 is stable in different ambient conditions, low cost, non-toxicity and high resistance to the corrosion. Polymer/Fe_2O_3 nanocomposites are particularly interested owing to the combination of properties between polymer matrix (organic) and Fe_2O_3 nanoparticles (inorganic) [7, 8]. A highly cross-linking thermoset polymer, such as the unsaturated polyester resins (UPRs), is used as the matrix in nanocomposites. The reinforcement unsaturated polyester resins are basically used in marine and transportation industries. UPRs offer many advantages comparing with other thermosetting resins, like thermal and mechanical properties, easy to cure at room temperature, can be molded at low pressure and temperature, and low cost. Although UPRs are very brittle owing to their covalently bonding network, they are low inhibitors to the initiated cracks and their propagation. However, many researches have been able to improve many properties with addition of organic and inorganic materials [9]. The magnetic nanoparticles have been extremely used as a reinforcement material into many polymers owing to their characteristics and applications, the magnetic iron oxide (Fe_3O_4) is an important oxide nanoparticle having special properties in manufacturing nanocomposites. Its unique properties, such as a high ratio of the spin polymerization, ferromagnetic ordering, high magnetic moment and high conductivity are important to choose this material as reinforcements to prepare nanocomposites [10]. However, the disadvantages of polyester like low toughness limits its industrial applications for engineering components subjected to the impact energy [11]. There are many investigations published in this field, Rahman et al. [12] investigated the effect of different gamma radiation doses about 0-15 KGy on the mechanical properties of (UPR) unsaturated polyester resin reinforced by Fe_2O_3 nanoparticles. Fe_2O_3 nanoparticles were prepared by sol-gel route, while the nanocomposite UPR/Fe_2O_3 nanoparticles were manufactured by solution casting route. The results of this work showed that increasing the dose of gamma radiation to 5 KGy will increase the Young's modulus, tensile strength and decrease the elongation. In another study by Rahman et al. [13] depicted the effect of $NiFe_2O_4$, TiO_2 and Fe_2O_3 nanoparticles on the electrical, optical and mechanical properties of the unsaturated

polyester resin (UPR). Results of this investigation revealed the improvement in the DC electrical conductivity and low resistivity for $NiFe_2O_4 + Fe_2O_3 + TiO_2$, and the enhancement in the optical properties for Fe_2O_3 was about 30.38%. Finally, the improvement in the mechanical properties developed was about 6.56% in Young's modulus, about 21.62% in tensile strength, and the highest microhardness obtained for $NiFe_2O_4$. While Seyhan et al. [14] investigated the effect of CNTs carbon nanotubes on the mechanical, thermal and electrical properties of unsaturated polyester resin (UPRs) with and without NH_2 amine functional groups. The results of this study showed that the polyester resin incorporated by carbon nanotubes with amine has better mechanical properties comparing with the carbon nanotubes. Also, the images of the TEM examination revealed a homogeneous dispersion of carbon nanotubes into the unsaturated polyester resin. The main objective of this paper is to improve the mechanical and magnetic properties of (polyester/Fe_2O_3 + Ni) nanocomposites.

2. 1. Materials Used   In this work, the materials used are unsaturated polyester resin (UPR) supplied by Petrochemicals Pvt. Ltd., India with accelerator methyl-ethyl-ketone-peroxide (MEKP, Turkey). The reinforcement materials are Fe_2O_3 nanoparticles (with an average diameter of 15-20 nm and the purity ratio at 97.5%, specific surface area (SSA) 40-45 m^2/g) supplied by USA research nanomaterial, while the Ni nanoparticles (at size 40 nm, specific surface area (SSA) at 40-60 m^2/g and the purity ratio at 99.9%) provided by (Hongwu International Group Ltd, China) are further reinforcing material. Tables (1-3) list the properties of the all used materials in this work.

2. 2. Nanocomposite Fabrication   The UPR/Fe_2O_3 nanocomposites were fabricated by the casting route. At first, the nanoparticles of Fe_2O_3 and Ni were added to the unsaturated polyester with different weight percentages and stirred for 10 minutes to ensure

TABLE 1. Properties of unsaturated polyester used in this work

Average Particle size (APS)	Purity	Specific Surface Area (SSA)	Density	Color	Morphology
30 nm	99.5%	40-60 m^2/g	5.24 g/cm^3	Red brown	Spherical

TABLE 2. Properties Fe_2O_3 nanomaterial used in this work

Density (gm/cm³)	Tensile strength (MPa)	Elongation (EL%)	Thermal conductivity W/m.ºC	Viscosity at 25ºC
1.2	65-100	< 2.8	0.17	200-300 cps

TABLE 3. Properties Ni nanomaterial used in this work

Average Particle size (APS)	Purity	Specific Surface Area (SSA)	Density	Color	Morphology
40 nm	99.9%	12-16 m²/g	8.9 g/cm³	Black	Spherical

the better mixing of Fe_2O_3 and Ni nanoparticles with the unsaturated polyester resins. Then, a hardener about 5 wt% of methyl ethyl ketone peroxide (MEKP) was added to the mixture. Afterward, the mixture was stirred by hand at a slow rate in an ultrasonication bath for 10 min to obtain a homogeneous dispersion of Fe_2O_3, Ni nanoparticles into a polymer. The mixture was poured into templets of silicon molds with standard dimensions according to ASTM specifications for each mechanical test's specimen to be tested and cured for 72h at room temperature [15-18]. The as-received sample of unsaturated polyester resin (UPR) with hardener (MEKP) was prepared by mixing process as mentioned above.

2. 3. Microstructural Examinations

2. 3. 1. FESEM and EDS Examinations   Field emission scanning electron microscopy (FESEM) type (MIRA3 TESCAN) operating at 10 kV was used to examine the surface morphology of the manufactured polymer nanocomposites. While, the EDS examination was done using SEM analysis for the same sample.

2. 3. 2. FTIR Examination   The chemical structure of nanocomposites and the bonding between the oxide nanoparticles and the unsaturated polyester resin were examined by Fourier-transform infrared spectrometer) (FTIR) type (Shimadzu IRAffinity-1, Japan) in the 400–4000 cm⁻¹ range. FTIR was used to show the interaction between the nanoparticles and the polymer matrix.

2. 4. Mechanical Properties

The mechanical tests, including tensile, bending, and hardness tests were performed for the samples prepared in the present work. The tensile test was conducted using a computerized universal testing machine (Laryee Company) with full capacity (50 KN). Bending test was carried out using a bending apparatus type Microcomputer Controlled Electronic Universal Machine, and the shore (D) hardness device type Bareiss to measure the hardness of the samples. All specimens were tested according to ASTM standards, comprising (ASTM D 638) for the tensile test specimens, (ASTM D 790) for the bending test specimens (ASTM D 790), and (ASTM 2240) for hardness test specimens (ASTM 2240).

2. 5. Magnetic Properties

At ambient temperature, the magnetic characteristics of (UPR/Fe_2O_3+Ni) nanocomposite were examined using a vibrating sample magnetometer (VSM) measuring device. The curves of the magnetic hysteresis loops were used to calculate the residual magnetization (Mr), saturation magnetization (Ms), and coercivity field (Hc) values for each specimen. The saturation magnetization manifests the specimen's response to the external magnetic field, whereas the coercivity field represents the force necessary when the specimen is subjected to an external magnetic field that is the polar opposite of the initial external magnetic field. The coercivity field (Hc) is utilized to minimize the magnetization of the specimen and then the external magnetic field; the magnetization returns to the zero, while the residual magnetization is not reduced to zero [19].

3. RESULTS AND DISCUSSION

3. 1. Microstructural Analysis (FESEM and EDS)
FESEM and EDS analysis of the manufactured nanocomposites manifested a good dispersion and homogeneous distribution of Fe_2O_3 and Ni nanoparticles into a polymer matrix. This is due to mechanical and chemical techniques which in turn improve the dispersion of Fe_2O_3 and Ni nanoparticles into polymer matrix [20], and the main factor increases the interaction between the nanoparticles and polymer matrix depending on the chacteristics of nanoparticles, such as the size, shape and surface area. However, the dispersion mechanism depends on the characteristics of polymer matrix like the molecules of polymer and how they are reacted together to improve the dispersion of nanoparticles in it. In the present work, the ultrasonication stirring also helps the dispersion of nanoparticles in the polymer due to creating a homogenous dispersion [21]. Moreover, in all samples, a limited agglomeration is present. This is attributed to a heterogeneous dispersion and causes stress concentration and interfacial failure; such phenomena were reported by Kim et al. [22]. Figure 1 shows the images of FESEM and EDS.

(a)   (b)
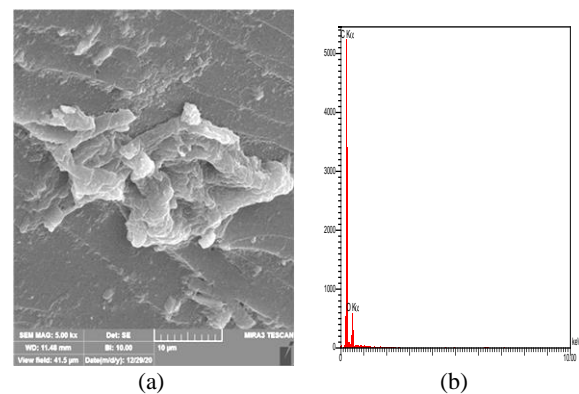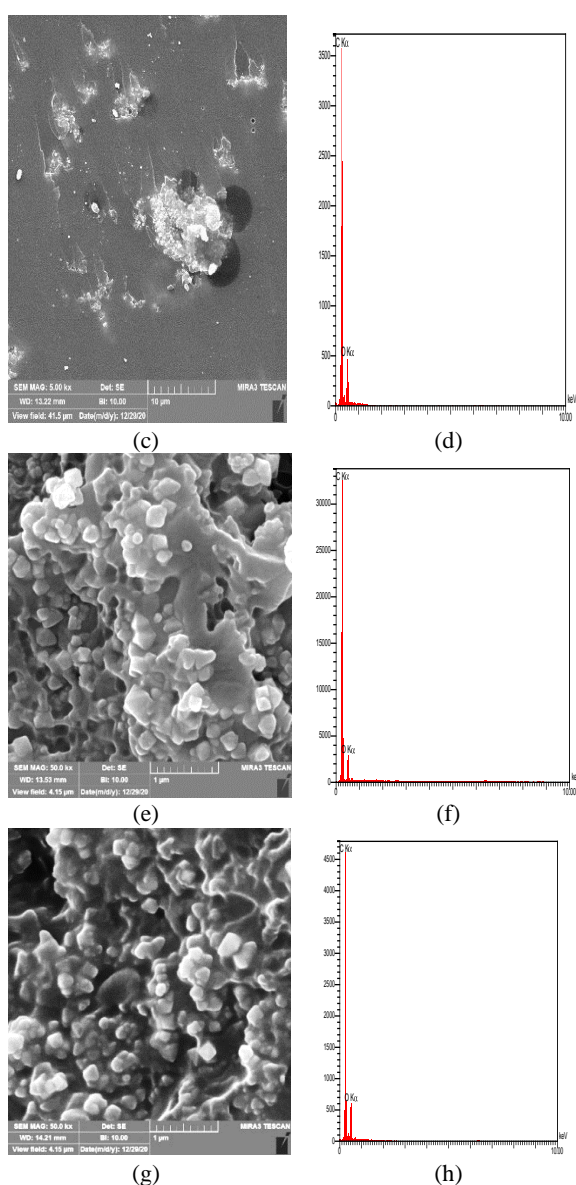
Figure 1. FESEM image and EDS for polymer nanocomposites with different weights (a, b) FESEM and EDS for 5wt% Fe_2O_3 + 3wt% Ni, (c, d) FESEM and EDS for 10wt% Fe_2O_3 + 3wt% Ni, (e, f) FESEM and EDS for 15wt% Fe_2O_3 + 3wt% Ni, and (g, h) FESEM and EDS for 20wt% Fe_2O_3 + 3wt% Ni

3. 2. FTIR Analysis of the Nanocomposite   The FTIR range of the polyester with different weight percentages of Fe_2O_3 nanoparticles and the constant weight percentage of Ni is shown in Figure 2. The stretching vibration modes of the Fe–O functional groups bonds in Fe_2O_3 are similar to the bands of absorption peaks at wavelengths around (450–480 cm^{-1}) and (500–600 cm^{-1}). The vibrations of the following chemical bonds/groups produce IR bands in the range of (700 – 4000 cm^{-1}), which are observed in the range of (700 – 4000 cm^{-1}). The stretching of asymmetrical aromatic C-

O with vibrations is at (1029.99–1035 cm^{-1}) and (1234.44–1292.31 cm^{-1}). The asymmetrical aliphatic C-O is stretching at (1111-1180.44 cm^{-1}), while the symmetrical aliphatic C-O is stretching at (1111-1180.44 cm^{-1}). The vibration is at (1450–1850 cm^{-1}) during the C-C stretching. C-H stretching bands were observed at around (2850.79 - 2920.23 cm^{-1}). The aliphatic and aromatic C–H bond stretching is at (2330.01-2366.87 cm^{-1}). The peaks at around (3738.04 -3741.90 cm^{-1}) are assigned to the stretching vibration of the OH group.
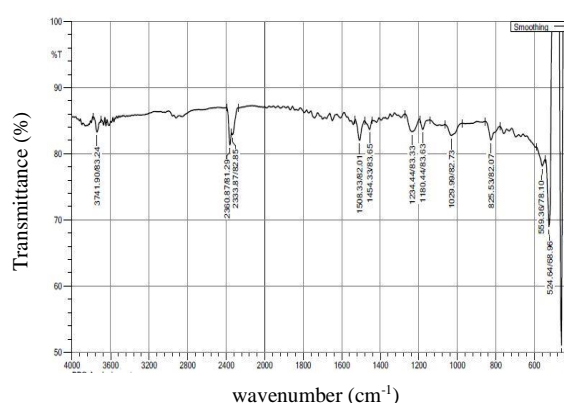
(a) FTIR spectroscopy of 15wt% Fe_2O_3 + 3wt% Ni
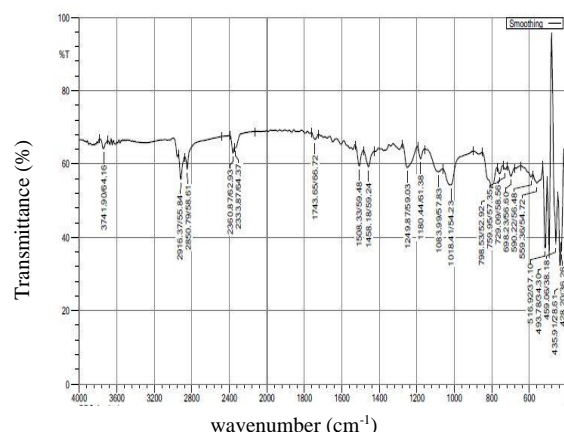
(b) FTIR spectroscopy of 10wt% Fe_2O_3 + 3wt% Ni
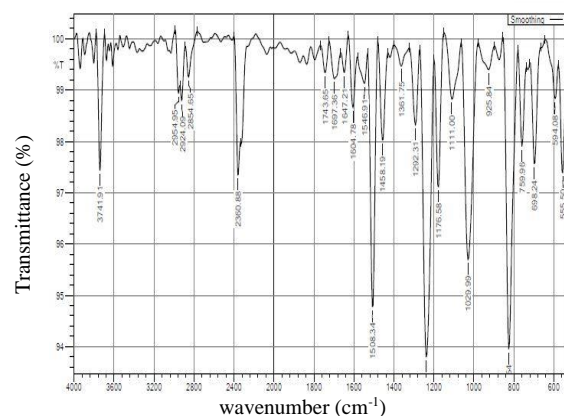
(c) FTIR spectroscopy of 15wt% Fe_2O_3 + 3wt% Ni
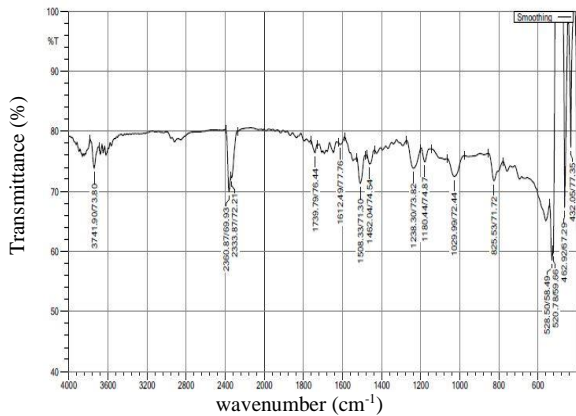
(d) FTIR spectroscopy of 15wt% Fe₂O₃ + 3wt% Ni

Figure 2. FTIR spectroscopy of (UPR /Fe₂O₃ + Ni) nanocomposites with different weights (a, b) FTIR for 5wt% Fe₂O₃ + 3wt% Ni and 10wt% Fe₂O₃ + 3wt% Ni, and (c, d) for 15wt% Fe2O3 + 3wt% Ni and 20 wt% Fe₂O₃ + 3wt% Ni

3. 3. Mechanical Tests Results

In general, the aim of incorporating ceramic nanoparticles Fe₂O₃, Ni into unsaturated polyester resin is to enhance the mechanical properties, including Young's modulus, tensile strength, bend strength and hardness through reinforcement mechanisms defined by nanocomposites theories. Table 4 shows the mechanical properties of the all manufactured samples of (UPR /Fe₂O₃+ Ni) nanocomposites.

3. 2. 1. Results of Tensile Test

The tensile test is one of the most important mechanical tests, and this test was done to assess the improvement in the tensile properties of nanocomposites with different percentages of reinforcement materials. The role of surface area for Fe₂O₃ and Ni nanoparticles is extremely affected on the Young's modulus and tensile strength for the manufactured nanocomposites. As shown in Table 1, the Young's modulus and tensile strength of pure polyester are about 810 MPa and 18.6 MPa, respectively. While,

TABLE 4. Mechanical properties of (UPR/Fe₂O₃+ Ni) nanocomposite

Material (Polyester+ Fe₂O₃)	Young's Module (MPa)	Tensile Strength (MPa)	Bending Strength (MPa)	Hardness Shore D
Pure Polyester (UPR)	810	18.6	59	68
Polyester + 5 wt% Fe₂O₃ +3wt% Ni	865.3	22.2	61	72
Polyester + 10 wt% Fe₂O₃ +3wt% Ni	871.3	25.3	65.3	75
Polyester + 15 wt% Fe₂O₃ +3wt% Ni	891.2	26.8	67	82
Polyester + 20 wt% Fe₂O₃ +3wt% Ni	775.6	19.7	62.9	85

an increase in the weight percentage of Fe₂O₃ by 5, 10 and 15 wt% as well as a constant percentage of Ni (3wt, %) leads to increase the Young's modulus about 865.3, 871.3 and 891.2 MPa, respectively. Moreover, the tensile strength increases about 22.2, 25.3 and 26.8 MPa, respectively. This is owing to the increasing of cross linking of unsaturated polyester molecules and then the enhancement of the interfacial bonding between the hybrid nanoparticles (Fe₂O₃, Ni) and the unsaturated polyester matrix. When the concentration of nanoparticles is increased to 20 wt%, the Young's modulus and tensile strength decreased to 775.6 MPa, 19.7 MPa, respectively. This is attributed to the aggregation of the hybrid nanoparticles (Fe₂O₃, Ni) into the unsaturated polyester matrix [21]. Additionally, it can be seen that the Young's modulus of the synthesized UPRNCs firstly increased till 15wt% of Fe₂O₃ nanoparticles and then decreased at 20wt% of Fe₂O₃ as displayed in Figure 3(a and b).

3. 2. 2. Results of Bending Test

The Fe₂O₃ nanoparticles have the same effect on the polymer in the bending test. Also, the bending strength increases with an increase in weight percentage of Fe₂O₃ nanoparticles till
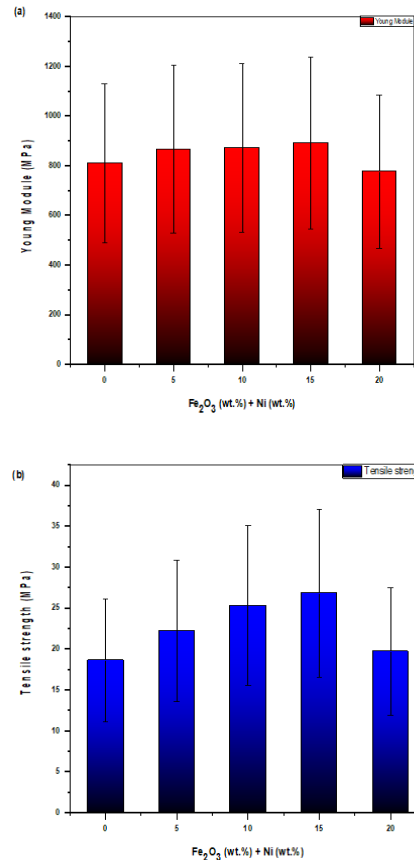
Figure 3. (a) Young's modulus vs wt% of Fe₂O₃ + Ni and (b) tensile strength vs wt% of Fe₂O₃ + Ni

15wt% and decreases above this ratio. This is owing to the same reasons mentioned in tensile test. Figure 4 evices the bending strength of (UPR/Fe$_2$O$_3$+Ni) nanocomposites.

3. 2. 3. Results of Hardness Test
The hardness test was done using hardness shore D. Figure 5 reveals the results of hardness for nanocomposite samples. Four readings were recorded for each sample, and then an average of these readings was calculated to define the accuracy value of hardness. The hardness (Shore D) value also increased with an increase in the weight percentage of Fe$_2$O$_3$, and the maximum value for the unsaturated polyester resin was obtained with 20wt% of Fe$_2$O$_3$ nanoparticles. This is attributed to the stiffness and rigidity for the (UPR/Fe$_2$O$_3$ + Ni) nanocomposites and the strong bonding between unsaturated polyester molecules and Fe$_2$O$_3$ + Ni nanoparticles.
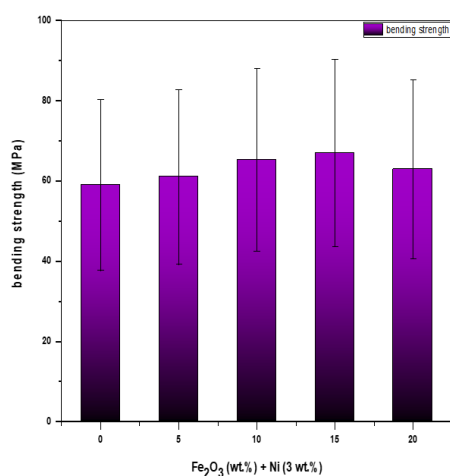
Figure 4. Bending strength *vs* wt% of Fe$_2$O$_3$ + Ni
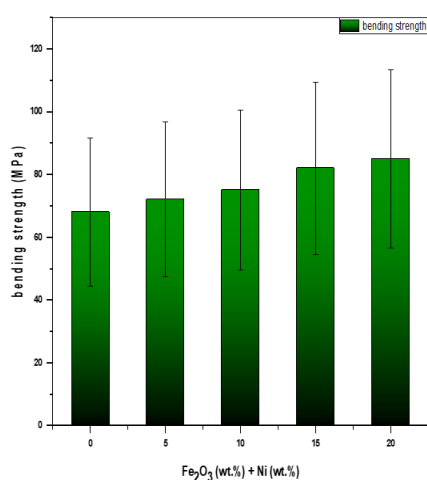
Figure 5. Hardness *vs* wt% of Fe$_2$O$_3$

3. 3. Magnetic Characterization
Figure 6 elucidates the magnetic hysteresis loops (M-H) at the room temperature for the pure unsaturated polyester resins and (UPR/Fe$_2$O$_3$+Ni) nanocomposites. The residual magnetization, saturation magnetization and coercivity field values were extracted from the curves of hysteresis loop to describe the magnetic behavior of each sample. The results demonstrated that increasing the amount of Fe$_2$O$_3$, Ni nanoparticles into the unsaturated polyester resins improved the residual magnetization, saturation magnetization and coercivity field values. The maximum values of (Ms), (Mr) and (Hc) were obtained at (20wt% Fe$_2$O$_3$ + 3wt%. Ni) as 1.23 emu/g, 12.19 emu/g and 99.7 Oe, respectively. Magnetic characteristics of the manufactured nanocomposites are listed in Table 5.
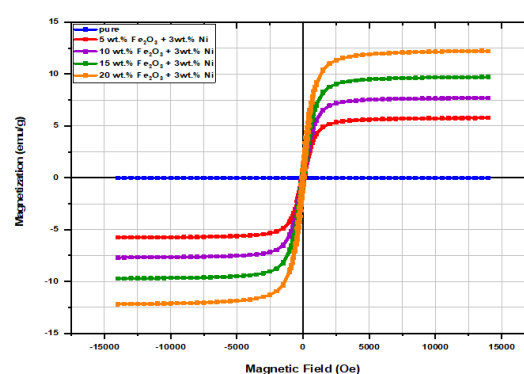
Figure 6. Magnetic hysteresis loops for (UPR/Fe$_2$O$_3$+Ni) nanocomposite

TABLE 5. Magnetic properties of (UPR/Fe$_2$O$_3$+Ni).

Specimens No.	Fe$_2$O$_3$ wt%	Ni wt%	Saturation Magnetization (M$_s$) (emu/g)	Residual Magnetization (M$_r$) (emu/g)	Coercivity Field (H$_c$) (Oe)
1	0	0	0	0	0
2	5	3	5.77	0.40	94.18
3	10	3	7.72	0.79	95.5
4	15	3	9.66	1.02	97.05
5	20	3	12.19	1.23	99.7

4. CONCLUSIONS

In this work, the nanocomposites UPR/Fe$_2$O$_3$+Ni were successfully manufactured by casting technique using different weight percentages (5, 10, 15 and 20wt%) of Fe$_2$O$_3$ nanoparticles and a constant weight (3wt%) of Ni nanoparticles dispersed in the unsaturated polyester resins matrix. FESEM, EDS and FTIR examinations were conducted for all samples. The mechanical and magnetic properties of the synthesized nanocomposites

were defined. The best mechanical properties were achieved at 15wt% Fe_2O_3 + 3wt% Ni (UPR/Fe_2O_3 + Ni) nanocomposites having (891.2 MPa) Young modulus, (26.8 MPa) tensile strength, (67 MPa) bending strength and (82 shore D) hardness and then decreased for the samples containing Fe_2O_3 more than 15wt%. This is perhaps attributed to the agglomeration of Fe_2O_3, Ni nanoparticles during the long pouring period and causes heterogeneous dispersion of Fe_2O_3, Ni nanoparticles into the unsaturated polyester resins. While, the maximum improvement in the hardness (85 shore D) was obtained at 20wt% of (UPR/Fe_2O_3+Ni) nanocomposites. Magnetic experiments manifested that the improvement of magnetic characteristics, including residual magnetization (Mr), saturation magnetization (Ms), and coercivity field (Hc) was obtained at 20wt% Fe_2O_3 + 3wt% Ni. The values of Mr, Ms and Hc increased from the zero in a pure polyester resins to (1.23 emu/g), (12.19 emu/g) and (99.7 Oe) for 20wt% (UPR/Fe_2O_3 + Ni) nanocomposites.

5. REFERENCES

1. T. Sun, H. Fan, Z. Wang, X. Liu, and Z. Wu, "Modified nano Fe_2O_3-epoxy composite with enhanced mechanical properties", *Materials & Design,* Vol. 87, (2015), 10-16, doi: 10.1016/j.matdes.2015.07.177

2. S. A. Abbas, I. F. Ali, A. A. Abdulridha "Behavior and Strength of Steel Fiber Reinforced Self-Compacting Concrete Columns Wrapped by Carbon Fiber Reinforced Polymers Strips", *International Journal of Engineering, Transactions B: Applications*, Vol. 34, No. 2, (2021), 382-392, doi: 10.5829/ije.2021.34.02b.10.

3. Hossain, M., Mobarak, M. B., Rony, F. K., Sultana, S., Mahmud, M., & Ahmed, S, "Fabrication and Characterization of Banana Fiber Reinforced Unsaturated Polyester Resin Based Composites", *In Nano Hybrids and Composites,* Vol. 29, (2020), 84-92, doi: 10.4028 /www.scientific.net /NHC.29.84

4. A. Badawi, "Characterization of the optical and mechanical properties of CdSe QDs/PMMA nanocomposite films", *Journal of Materials Science, Materials in Electronics*, Vol. 26, No.6, (2015), 3450-3457, doi.: 10.1007/s10854-015-2854-1.

5. H. M. Naguib, M. A. Ahmed, Z. L. Abo-Shanab, "Studying the loading impact of silane grafted Fe_2O_3 nanoparticles on mechanical characteristics of epoxy matrix", *Egyptian Journal of Petroleum*, Vol. 28, No. 1, (2019), 27-34, doi: 10.1016/j.ejpe.2018.10.001.

6. C. M. C. Pereira, M. Herrero, F. M. Labajos, A. T. Marques, and V. Rives, V. "Preparation and properties of new flame retardant unsaturated polyester nanocomposites based on layered double hydroxides", *Polymer Degradation and Stability*, Vol. 94, No. 6, (2009), 939-946, doi: 10.1016/j.polymdegradstab.2009.03.009.

7. D. Hazarika, K. Gupta, M. Mandal, and N. Karak, "High-performing biodegradable waterborne polyester/functionalized graphene oxide nanocomposites as an eco-friendly material", *ACS Omega*, Vol. 3, No. 2, (2018), 2292-2303, doi: 10.1021/acsomega.7b01551.

8. A.L. Gershon, D. P. Cole, A. K. Kota, and H. A. Bruck, "Nanomechanical characterization of dispersion and its effects in nano-enhanced polymers and polymer composites," *Journal of Materials Science,* Vol. 45, No. 23, (2010), 6353-6364, doi: 10.1007/s10853-010-4597-y.

9. Samaneh Katebi Koushali, Masood Hamadanian, Ahmed Reza Ghasemi and Mahdi Ashrafi," Investigation of Mechanical Properties of Polyester/polyethylene Glycol/TiO_2 Nanocomposites", *Journal of Nanostructures*, Vol. 11, No.1, (2021), 38-47, doi: 10.22052/JNS.2021.01.005.

10. Hadia Noor, Muhammad Waqas Hanif, Sobia Latif, Zubair Ahmad, Saira Riaz and Shahad Naseem, "Dielectric and Magnetic response of iron oxide nanoparticles embedded in unsaturated polyester resin", *Physica B: Physics of Condensed Matter*, (2021), 1-5, doi: 10.1016/j.physb.2020.412554.

11. Grazielle de Silva Maradini, Michel Picanco Oliveira, "Impact and Tensile Properties of Polyester Nanocomposites Reinforced with Conifer Fiber Cellulose Nanocrystal:A Previous Study Extension", *Polymers,* Vol. 13, (2021), 1-11, doi: 10.3390/polym13111878.

12. M. T. Rahman, Md. Asadul Hoque, G. T. Rahman, M. N. Azmi, M. A. Gafur, Ruhul A. Khan and M. Khalid Hossain, "Fe_2O_3 nanoparticles dispersed unsaturated polyester resin-based nanocomposites: effect of gamma radiation on mechanical properties"., *Radiation Effects and Defects in Solids,* Vol. 174, No. 5-6, (2019), 480-493, doi: 10.1080/10420150.2019.1606809.

13. M. T. Rahman, Md. Asadul Hoque, G. T. Rahman, M. A. Gafur, Ruhul A. Khan, and M. Khalid Hossain, "Study on the mechanical, electrical and optical properties of metal-oxide nanoparticles dispersed unsaturated polyester resin nanocomposites" *Results in Physics*, Vol. 13, (2019), doi: 10.1016/j.rinp.2019.102264.

14. A. T. Seyhan, F. H. Gojny, M. Tanoğlu, and K. Schulte, "Critical aspects related to processing of carbon nanotube/unsaturated thermoset polyester nanocomposites, *"European Polymer Journal*, Vol. 43, No. 2, (2007), 374-379, doi: 10.1016/j.eurpolymj.2006.11.018.

15. A. Sanida, S. G. Stavropoulos, T. Speliotis, and G. C. Psarras, "Probing the magnetoelectric response and energy efficiency in Fe_3O_4/epoxy nanocomposites," *Polymer Testing*, Vol. 88, (2020), doi: 10.1016/j.polymertesting.2020.106560.

16. A. Sanida, S. G. Stavropoulos, and G. C. Psarras, "A comparative thermomechanical study of ferrite/polymer nanocomposites," *Procedia Structural Integrity*, Vol. 10, (2018), 257-263, doi: 10.1016/j.prostr.2018.09.036

17. K. Kumar, P. K. Ghosh, A. Kumar, and O. Singh, "Enhanced Thermomechanical Properties of ZrO_2 Particle Reinforced Epoxy Nanocomposite," *Journal of Materials Engineering and Performance*, Vol. 30, No. 1, (2021), 145-153, doi: 10.1007/s11665-020-05350-3.

18. T. K. Bindu Sharmila, J. V. Antony, M. P. Jayakrishnan, P. M. Sabura Beegum, and E. T. Thachil, "Mechanical, thermal and dielectric properties of hybrid composites of epoxy and reduced graphene oxide/iron oxide," *Materials Design*, Vol. 90, 66-75, (2016), doi: 10.1016/j.matdes.2015.10.055.

19. J. Huang, Y. Cao, X. Zhang, Y. Li, J. Guo, S. Wei, and Z. Guo, "Magnetic epoxy nanocomposites with superparamagnetic $MnFe_2O_4$ nanoparticles," *AIP Advances*, Vol. 5, No. 9, (2015), doi: 10.1063/1.4932381.

20. Lu C., and Mai Y-W, "Permability modeling of polymer-layered silicate nanocomposites", *Composite Science Technology*, Vol. 67, 2895-2902, (2007), doi: 10.1016/j.compscitech.2007.05.008.

21. O. M. Amin, A. Triki, M. B. Hassen, M.R. Sanjoy, M. Arous and Kallel Ali," Effect of alfa fiber mechanical separation on dielectric properties of hybrid unsaturated polyester comopsites", *Polymer Composites*, 40, (2019), 1774-1785, doi: 10.1002/pc.24934.

22. Y. J, Kim, Y. D. Liu, Y- SeO, and H. J. Chio," Pickering-emulsion-polymerized polystyrene/ Fe_2O_3 composite particles and their magneto responsive characteristics*",* *Langmuri*, Vol. 29, (2013), 4959-4965, doi: 10.1021/la400523w.

Persian Abstract

چکیده

این تحقیق با هدف بررسی تأثیر نانوذرات Ni, Fe_2O_3 به عنوان یک ماده تقویت کننده بر خواص مکانیکی پلی استر غیراشباع (UPR) به عنوان یک ماتریس برای تولید یک ماده نانوکامپوزیت با استفاده از یک مسیر ریخته گری انجام شده است. آزمایشات مختلفی برای تعیین ویژگیهای نانوکامپوزیت تولید شده انجام شد ، مانند میکروسکوپ الکترونی روبشی انتشار میدان (FESEM)، طیف سنجی پراکندگی انرژی (EDS) و طیف سنج مادون قرمز تبدیل فوریه (FTIR). آزمایشات مکانیکی شامل کشش ، خمش و سختی بر روی نمونه ها در دمای اتاق مطابق با استانداردهای ASTM انجام شد ، در حالی که ویژگی های مغناطیسی توسط مغناطیس سنج نمونه ارتعاشی (VSM) تعیین شد. نانوذرات Fe_2O_3 با درصدهای وزنی مختلف که از ۰ تا٪ وزنی تا ۲۰ درصد وزنی و غلظت ثابت ۳ درصد وزنی از نانوذرات نیکل در رزین پلی استر غیر اشباع گنجانیده شد. تصاویر FESEM و EDS یکنواختی نانوذرات Ni, Fe_2O_3 را به رزین پلی استر غیر اشباع خالص (UPR) نشان داد. در حالی که ، بهبود مدول یانگ ، مقاومت کششی ، مقاومت خمشی و سختی با موارد UPR مقایسه شد. بهبود در مدول جوان ۱۰.۰۲، ، در مقاومت کششی ۴۴.۰۸، ، در مقاومت خمشی ۱۳.۵۵ and و در سختی مقاومت بود. همچنین ، خواص مغناطیسی ، از جمله مغناطیس شدن اشباع مغناطیس شدن باقی مانده و نیروی اجباری افزایش غلظت نانوذرات افزایش می یابد. درصد مطلوب برای بهبود خواص مکانیکی در٪ ۱۵ درصد وزنی Fe_2O_3 یافت شد و سپس از این غلظت بیشتر شد ، در حالی که افزایش سختی در٪ ۲۰٪ وزنی Fe_2O_3 به دست آمده است.

International Journal of Engineering

Experimental and Numerical Study on a New Double-walled Tuned Liquid Damper

V. R. Meshkat Rouhani, G. Zamani Ahari*, H. Saeed Monir

Department of Civil Engineering, Faculty of Engineering, Urmia University, Urmia, Iran

P A P E R   I N F O

A B S T R A C T

To endure strong ground motions in large earthquakes, structures need to be equipped with tools to damp the huge amounts of energy induced by these excitations. In conventional buildings, seismic energy is often handled by a combination of rigidity-ductility measures and energy dissipation solutions. Since these buildings often have very low damping capability, the amount of energy dissipated within their elastic behavior phase tends to be negligible. Passive dampers are vibration control systems that can serve as valuable tools for controlling strong forces and reducing the probability of structural failure under seismic loads. In Tuned Liquid Dampers (TLDs), energy is dissipated by exploiting the behavior and characteristics of the liquid contained in the damper's tank. When the structure is subjected to external stimuli, the force transferred to the damper starts moving the liquid that lies stationary in the damper's tank, getting dissipated in the process. There are various classes of TLDs with different tank shapes, aspect ratios, and mechanisms of action, each with its properties and features. Another cause of energy dissipation in TLDs, in addition to the viscosity of the liquid, is the base shear force that is applied to the damper's intersection with the main structure with a phase difference relative to the external excitation, because of the difference between hydrostatic forces exerted on the walls at the two ends of the tank. Therefore, the level of liquid interaction with the damper's walls is also a determinant of the damping of external forces and thus the seismic response of the structure. The study investigated a new type of TLD with a double-walled cylindrical tank. To examine the effect of this TLD on the seismic response, a series of models were built with different liquid heights in the tank's inner and outer walls and subjected to several seismic excitations on a shaking table. The results showed that using this type of damper reduced the seismic response of the structures. Also, the reduction in seismic response was found to change significantly with the amount of liquid in the damper.

doi: 10.5829/ije.2022.35.01a.04

NOMENCLATURE

Ms	Surface wave magnitude	PGV	Peak ground velocity
D	Focal depth	PGA	Peak ground acceleration
PGD	Peak ground displacement		

1. INTRODUCTION

To endure strong ground motions in large earthquakes, structures need to be equipped with tools to damp the huge amount of energy induced by these motions. This can be done through methods such as increasing the damping capability of the structure, which will allow it to absorb, damp, and reflect some portion of the input energy, thus reducing the amount of energy transferred to the structure and therefore the level of energy dissipation required for structural members, which allows the structure to be constructed with less ductility. One of the common methods of vibration control in large structures is to use tuned liquid dampers (TLDs). The most common form of TLD is the one consisting of a half-filled water tank that is rigidly mounted on the top floors of the main structure (usually the last floor) of the building. The tanks of TLDs can be built with a variety of geometries, including rectangular and circular shapes (rectangular tanks tend to be somewhat heavier than circular tanks).

*Corresponding Author Institutional Email: g.zamani@urmia.ac.ir
(G. Zamani Ahari)

One of the main causes of energy dissipation in TLDs is the viscosity of the water moving inside the tank in steady and turbulent states, which can be strengthened mechanically by placing mesh screens inside the tank compartment. Another important cause of energy dissipation in these dampers is the base shear force that is applied to the place where the damper is attached to the main structure with a phase difference relative to the external excitation because of the difference in hydrostatic force on the walls at the two ends of the tank. Instead of water tanks, TLDs can be built with interconnected tube-shaped containers with columns of liquid moving inside. This modified version of TLD is called the Tuned Liquid Column Damper (TLCD). Since TLDs fall in the category of passive dampers, another group of TLDs called the Active Tuned Liquid Column Damper (ATLCD) have also been designed by combining TLCD with an active mechanism, which offers higher effectiveness in controlling the oscillation amplitude and acceleration response of the structure.

In [1], it was stated that in Japan, where earthquakes are common and strong seismic activities can cause catastrophic damages every 2 or 3 years, structures of a refinery, petrochemical, chemical, and other such plants have to be designed and constructed to endure such seismic loads. In these plants, the equipment called pressure vessels, which must work under high pressures and temperatures, are often designed to endure these operating loads rather than seismic loads. However, in cylindrical tanks where the integrity is determined by the seismic loads, the structure may be designed with thin walls and the contained liquid can more easily interact with the structure. Thus, during an earthquake, the motion of the contained liquid can damage the wall or roof of the cylindrical tank or cause the liquid to spill out of the tank, causing fire [1].

TLD is a passive vibration control device consisting of a rigid tank filled with water that relies on the movement of water inside it to dissipate energy. Research has shown that TLD is more effective when it has a larger base acceleration amplitude because this allows it to dissipate more energy through increased fluid movement. This feature has been emphasized in some TLD configurations. In one of such configurations, the damper is rigidly connected to a secondary mass, which itself is connected to the main structure through a spring system. This alternative configuration is known as the Hybrid Mass Liquid Damper (HMLD). It should be noted that when the secondary spring is stiff, the alternative and standard TLD configurations will be similar. It has been observed that for a given structure with HMLD, there is an optimal secondary spring stiffness at which the effectiveness of HMLD will be maximal [2].

In [3], researchers studied the effect of various components of the earthquake on the motion response of liquid storage tanks. Firstly, they reviewed the theories that are commonly used for the unidirectional analysis of liquid behavior in cylindrical tanks. Then they used the Finite Element Modeling (FEM) method to simulate the dynamic response of the liquid tank system. To validate the FEM method, they applied it to a set of experimental data available in the literature. They then conducted a parametric study on a series of vertical cylindrical tanks with different aspect ratios under various earthquake acceleration time series, where each tank was subjected to unidirectional and bidirectional excitations. They also examined the suggestions of some seismic codes for the estimation of Maximum Sloshing Wave Height (MSWH) and evaluated the accuracy of the proposed prediction methods numerically. In the end, the simple equation available for estimating MSWH under unidirectional excitation was extended for bidirectional excitation [3].

As structures become taller and thinner, their vibrational response and weight become increasingly challenging design considerations. TLDs are cost-effective vibration dampers that can be used to suppress structural vibrations. In TLDs, energy is dissipated through the friction of the liquid boundary layer and wave breaking. The potential behaviors of TLDs and their interaction with structures could be very complex. In [4], an advanced experimental method called the Real-Time Hybrid Simulation (RTHS) was used to conduct a comprehensive parametric study to evaluate the effectiveness of TLDs. In RTHS, the effect of TLD is determined experimentally while the structure is modeled and analyzed, and this allows the TLD structure interactions to be determined in real-time. By treating the structure as an analytical model, RTHS offers a unique level of flexibility in the analysis. In this study, researchers considered a wide range of values for parameters including TLD/structure mass ratio, TLD/structure frequency ratio, and structural damping. They also experimentally evaluated the accuracy of FVM/FEM, which combines the finite element method (FEM) with finite volume method (FVM), in the modeling of liquid and solid domains to capture the TLD-structure interactions. The results of this study provided a better understanding of TLDs and their interaction with structures and also contributed to the advanced design of these devices [4].

In another study, researchers investigated the application of TLDs in reducing wind-induced vibrations of base-isolated structures. They modeled TLD as an equivalent linearized mechanical system where natural frequency and damping of the fluid motion are amplitude-dependent. These researchers also modeled the base-isolated structure as a modified version of the linearized Bouc-Wen model, so that the behavior of Stable Unbonded Fiber Reinforced Elastomeric Isolators (SU-FREIs) could be described. They combined TLD and base-isolated structures to form a system of coupled ordinary differential equations. They also presented a preliminary TLD design

method for determining the proper tank dimensions and screen properties. The equivalent linearized mechanical model was validated through time simulations of the nonlinear behavior of the structure and fluid. This study reported that TLD can serve as an effective means to control wind-induced vibrations of base-isolated structures [5].

Crowley and Porter studied the effect of screens on the natural frequency and performance of TLDs. The experimental investigations of these researchers showed that the screen's solidity ratio is usually determined for using TLD as a means of frequency shift [6, 7]. When a TLD is subjected to large amplitude excitations, because of the horizontal velocity component in the wave motion, the wave threshold decreases as the amplitude increases. This is known as wave breaking. At this stage, simple linear models can no longer describe the behavior of the liquid, and the wave breaking changes the motion frequency of the liquid [8]. Furthermore, this complex nonlinear phenomenon affects the shear force generated due to TLD and the motion of the structure, an effect that is difficult to model accurately. Various numerical and experimental studies have been carried out on the use of other configurations of TLDs, including TLCDs, in suppressing the structural vibrations induced by seismic and wind loads [9, 10]. In [11], researchers studied the seismic interaction of tall buildings and TLDs with internal screens by replacing TLDs with equivalent amplitude-dependent tuned mass dampers (TMDs). In these models, parameters of equivalent TMDs were applied to the equation of motion of structures with the assumption that TLD is of the single degree of freedom type [11]. The majority of previous experimental studies and nonlinear modeling efforts have been focused on understanding the behavior of rectangular or circular TLDs. However, Love and Tait [12] developed a nonlinear multivariate model to describe the behavior of liquid inside a flat tank with arbitrary geometry. They also used a modal expansion technique for the nonlinear simulation of TLDs with damping screens [13]. Recently, Malekghasemi et al. [14] presented a new analytical method using the finite volume and finite element methods (FVM and FEM) for modeling the liquid and solid domains of TLDs. In this FVM/FEM model, the fluid and solid domains are discretized independently, and the interaction between the two domains is represented by alternating iterations at the interface.

A tuned liquid damper (TLD) is a passive vibration control device consisting of a rigid tank filled with water that relies on the motion of water inside it for energy dissipation. In a TLD with a standard configuration, the damper is rigidly connected to the top of the building structure. Research has shown that TLD is more effective when the base acceleration amplitude is larger, as increased liquid motion results in more energy dissipation. This feature has been used in alternative TLD configurations. In one alternative configuration, the damper is rigidly connected to a secondary mass, which itself is connected to the main structure through a spring system. This alternative configuration is known as the Hybrid Mass Liquid Damper (HMLD). For a secondary spring with a given stiffness, the TLD base is subjected to a large amplitude acceleration that increases its effect. It should be noted that when the secondary spring is stiff, the alternative and standard TLD configurations will be similar. It has been reported that for a given structure with HMLD, there is an optimal secondary spring stiffness at which the effectiveness of HMLD will be maximal. The optimized HMLD configuration has shown to be a more effective control device than the standard TLD configuration for both harmonic and large earthquake motions [2]. As structures become taller and thinner, their vibrational response and weight become increasingly challenging design considerations. TLDs are cost-effective vibration dampers that can be used to suppress structural vibrations. In TLDs, energy is dissipated through the friction of the liquid boundary layer, free surface interactions, and wave breaking. The dynamic features of TLD and its interaction with the structure are quite complex. In a study, an advanced experimental method called the Real-Time Hybrid Simulation (RTHS) has been used to conduct a comprehensive parametric study to evaluate the effectiveness of TLDs. In RTHS, the effect of TLD is determined experimentally while the structure is modeled by a computer, and this allows the TLD structure interactions to be determined in real-time. By treating the structure as an analytical model, RTHS offers unique flexibility that allows a wide range of parameters to be tested without changing the experimental setting. In this study, a wide range of values for parameters including TLD/structure mass ratio, TLD/structure frequency ratio, and structural damping have been considered. Also, the accuracy of FVM/FEM, which combines finite element method (FEM) with finite volume method (FVM), in the modeling of liquid and solid domains to capture the TLD-structure interactions have been experimentally investigated. The results of this study offer a better understanding of TLDs and their interaction with structures and also contributes to the advanced design of TLDs, which in turn may result in wider use of these devices [4].

An important cause of energy dissipation in TLDs, in addition to the viscosity of the liquid, is the difference between hydrostatic forces on the walls at the two ends of the tank and the phase difference relative to the external excitation. Therefore, it can be stated that the level of liquid interaction with the damper's walls is a determinant of the damping of forces applied to the structure. Thus, the more the liquid collides with the tank wall, or in other words the higher the contact level between the liquid and the walls, the greater will be the capacity for energy dissipation.

In an experiment, the TLD-adjusted fluid on a reduced shear frame under harmonic loads was also investigated. In this research, a seismic table test is applied to 3-layer shear frame models with TLD under harmonic loading. In the first stage, free vibration tests are performed on the structure, and first, the free vibration frequency of the structure is determined. Displacement and acceleration are measured in different classes of structures. A container in the form of a rectangular prism is then created as a TLD model. The liquid is poured into a container and the same experiments are repeated at different heights of the liquid. The effect of the TLD program on structural models concerning displacement and acceleration of structures has been investigated. As a result of the experiments performed, most TLD models are determined by changing behavior and acceleration. The results show that all damping models significantly reduce the level of seismic behavior of the structure under harmonic loading [4].

In another experiment, instead of using TLD, TLCD was used under the same conditions as before. As a result of the experiments performed, the most convenient TLCD models are determined according to the displacement behavior. The results show that all damping models significantly reduce damping in the seismic behavior of structures under harmonic loading. Experimental results show that all TLCD models effectively reduce the response of the structure in terms of displacement [4].

Also, series of experimental studies were performed on tuned liquid column damper as an effective device for seismic control in structures [17].

In this study, through series of shaking table tests and statistical analysis, the efficiency of Uniform Tuned Liquid Column Damper (UTLCD) in structures resting on loose soils, considering soil-structure interaction was investigated. Through statistical analysis of the experimental tests was demonstrated that the mentioned factors are effective in response to the structure. Using Response Surface Methodology (RSM), the optimum values of the factors to minimize the top story displacement have been found. [4].

The tuned liquid column damper (TLCD) having a uniform cross-sectional tube of U-shaped, occupied with liquid is used as a vibrational response mitigation device. Different studies on the unconstrained optimization performance of TLCBD subjected to the stochastic earthquake have been performed where limitations on the maximum amplitude of liquid present in the vertical portion of the tube were not imposed. The present investigation considers the optimum performance of the structure with TLCBD for mitigating the vibrational response with limited liquid movement in the vertical portion of the tube. A numerical study has been carried out to demonstrate the difference between constrained and unconstrained optimization of the structure-TLCBD system. Numerical results show the influence of constraining cases on optimum parameters and performance behavior of the structure-TLCBD system[4].

The innovation of the proposed TLD model in the current study versus TLDs with a similar mechanism is that, by doubling the water reservoir, the behavior of water movement in the outer and the inner tank becomes different. There are two relaxation conditions at the bottom of the reservoirs. The internal wall network controls the water movement, and in this way an appropriate damping behavior is created.

The present study investigated the behavior of a TLD with a double-walled cylindrical tank, where using the double-walled design is intended to increase the interaction of the liquid with walls and thus the capability of better damping. For this investigation, the following objectives were pursued:

1. Investigating the optimal liquid height, which depends on the optimal weight of the liquid relative to the total weight of the structure

2. Investigating the effect of liquid type on the effect of dampers on the seismic response of the structure

In the damper considered in this research, the interaction between the liquid and tank walls has been increased by using two walls with placing fins between them.

2. EXPERIMENTAL INVESTIGATION

The TLD considered in this research is a cylindrical damper with two walls, an inner wall and an outer wall, with a diameter of 30 and 50 cm, respectively. The walls are interconnected with fins at two different levels, which control the interaction of the liquid with the tank. The diagram of this TLD is shown in Figure 1.

For this investigation, several laboratory specimens with and without this TLD were constructed and subjected to several seismic records on the shaking table. The liquid used in this study was water. The height of the water column in the inner and outer wall was considered as a variable. To investigate the effects of the damper on the seismic response of the structure on the shaking table, the displacement and acceleration history of the specimens with the damper was studied and compared with that of the specimens without the damper.

The shaking table of the laboratory is 3×2 meters in size, has a weight capacity of 6 tons, and can produce a maximum acceleration of 1g and displacement of ±10 cm at frequencies of up to 50 Hz. This table provides one-dimensional movements. The constructed structure was restrained against lateral movements by four roller supports and was free to move only in the longitudinal direction of the shaking table. The measurements were

made with four acceleration sensors and two displacement sensors. One acceleration sensor was mounted on the table floor, another was installed on the foundation, and the other two were placed on the floors in the middle of the floor beam. The test setup and details are shown in Figures 2 to 7. The dimensions of the damper and the specifications of the studied models are mentioned in Table 1 and Table 2, respectively.

A good level of consistency was observed between the accelerations recorded on the table and the foundation, indicating the suitable rigidity of the table. Since the goal was to measure the relative displacement of the foundation and the structure itself, a vertical 4×8 cm rectangular steel hollow section was installed on the foundation and the
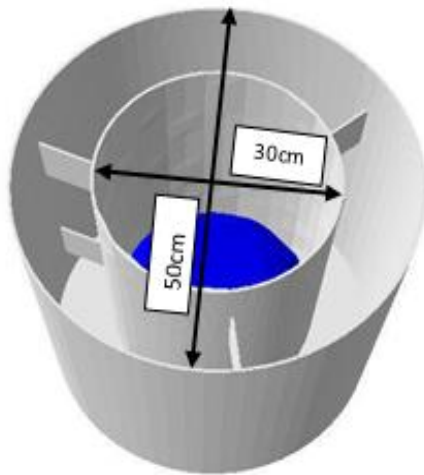
Figure 1. Three-dimensional diagram of the double-walle TLD
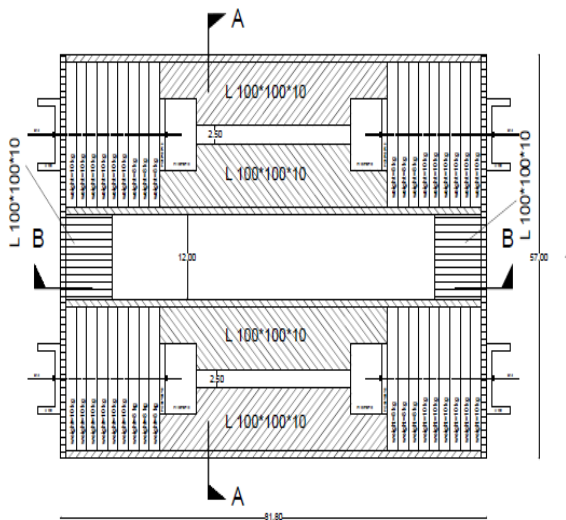
Figure 2. Plan of the structure with weights
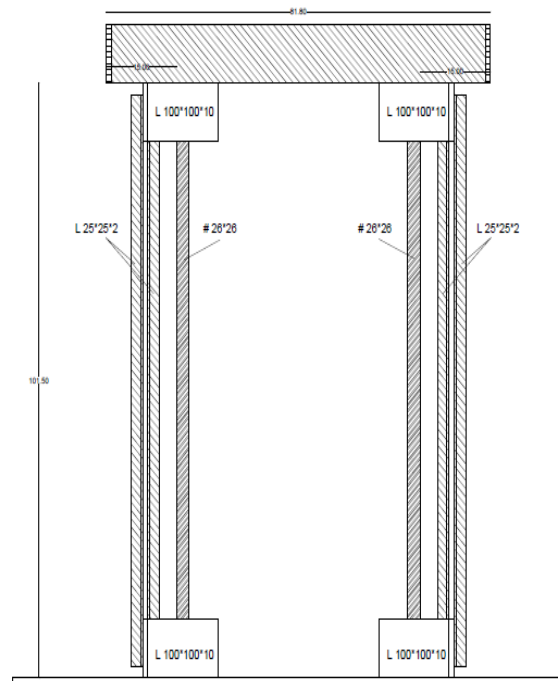
Figure 3. Transverse cross-section
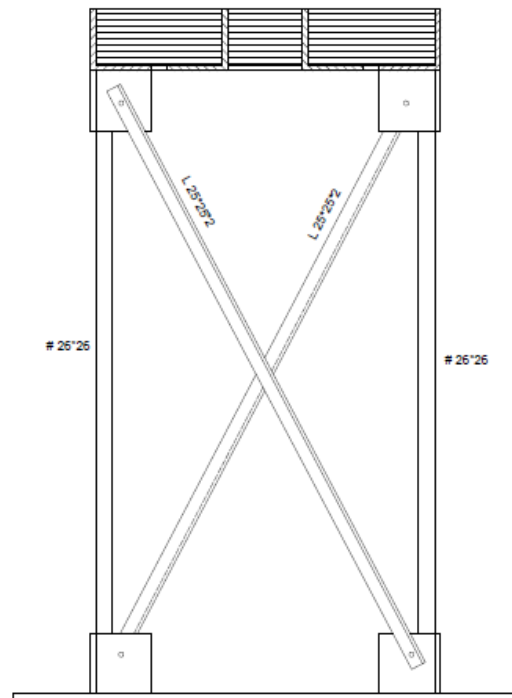
Figure 4. Longitudinal cross-section

displacement sensors were mounted on this member in the middle of each floor. Thus, being connected to the foundation on one side and the structure on the other side, the displacement sensors were measuring the relative displacement during vibration.

Figure 5. Installation of the structure and the damper on   th   shaking table

Figure 6. Position of the strain gauge (LVDT) on the   shakin   table

Figure 7. The shaking table used in the experiments

TABLE 1. Dimensions of the used damper

Dimension	Outer tank	Inner tank
Diameter	50 cm	30 cm
Height	60 cm	50 cm
Thickness	0.5 mm	0.5 mm

TABLE 2. Specifications of the studied models

Specimen	Liquid height in the inner tank (cm)	Liquid height in the outer tank (cm)
I0-O0	0	0
I0-O20	0	20
I0-O40	0	40
I15-O0	15	0
I15-O20	15	20
I15-O40	15	40
I30-O0	30	0
I30-O20	30	20
I30-O40	30	40

3. CHARACTERISTICS OF ACCELERATION RECORDS

Three earthquake records were used to investigate the effects of the double-walled TLD on the seismic response on the shaking table. The characteristics of these records are given in Table 3.

4. RESULTS

4. 1. Displacement Results   This section presents and discusses the displacement history of the models with and without the considered TLD under different seismic excitations. In this section, the comparisons are made to the results of model I0-O0, where the outer and inner tanks are empty. The displacement history diagrams of the models for the El Centro, Tabas, and Kobe records are illustrated in Figures 8 to 15, Figures 16 to 23, and Figures 24 to 31, respectively. In the following, these results are also tabulated for better and more accurate comparisons. To obtain these results, first, the height of the water in the inner tank was assumed to be variable while keeping the height of the liquid in the outer tank constant. Then, the height of the water in the outer tank was taken as a variable while keeping the height of the liquid in the inner tank constant. Finally, the height of the water in both inner and outer tanks was assumed as a variable. It should be noted that all the results presented in the following tables are relative to the I0-O0 model.

TABLE 3. Characteristics of acceleration records used in the shaking table experiment

Record	Symbol	Ms	d (km)	PGA (cm/s²)	PGV (cm/s)	PGD (cm)
El Centro 1940	El Centro	6.95	6.1	312.7	36.1	21.3
Kobe 1995	Kakogawa	6.9	22.5	317.8	26.8	8.8
Tabas 1978	Tabas	7.35	1.79	837.8	98.8	37.5
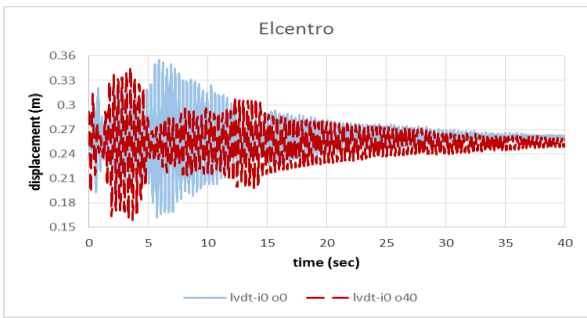
Figure 8. Comparison of the displacement history diagram of the I0-O40 model under the El Centro record
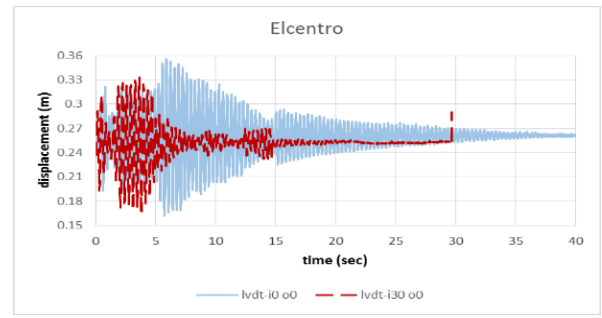
Figure 12. Comparison of the displacement history diagram of the I30-O0 model under the El Centro record
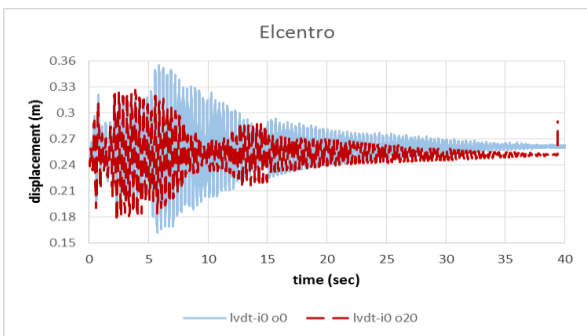
Figure 9. Comparison of the displacement history diagram of the I0-O20 model under the El Centro record
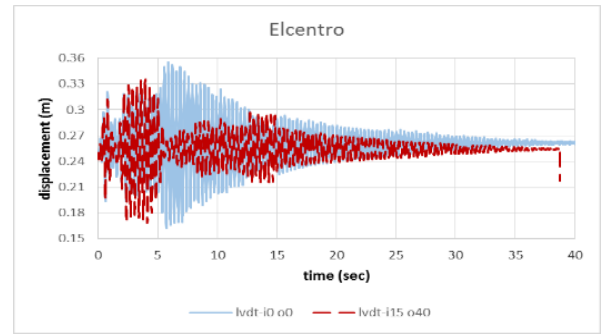
Figure 13. Comparison of the displacement history diagram of the I15-O40 model under the El Centro record
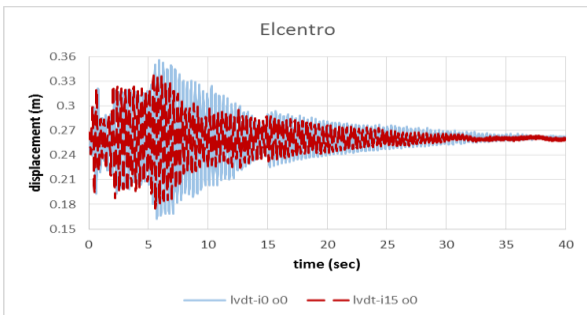
Figure 10. Comparison of the displacement history diagram of the I15-O0 model under the El Centro record
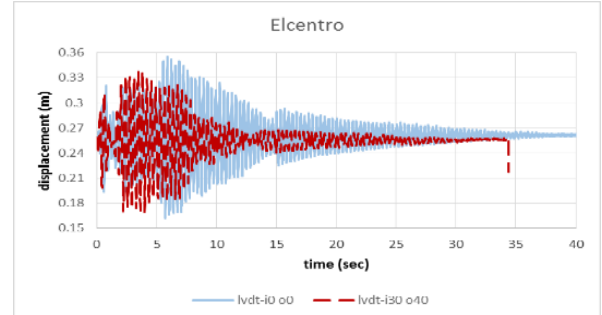
Figure 14. Comparison of the displacement history diagram of the I30-O40 model under the El Centro record
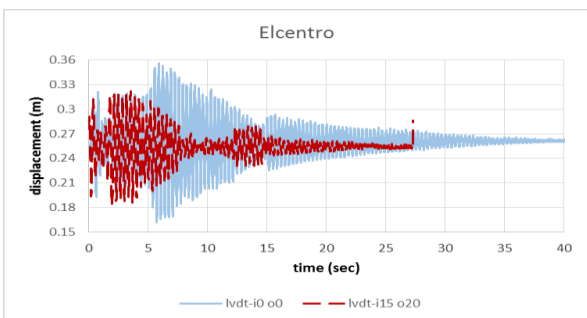
Figure 11. Comparison of the displacement history diagram of the I15-O20 model under the El Centro record
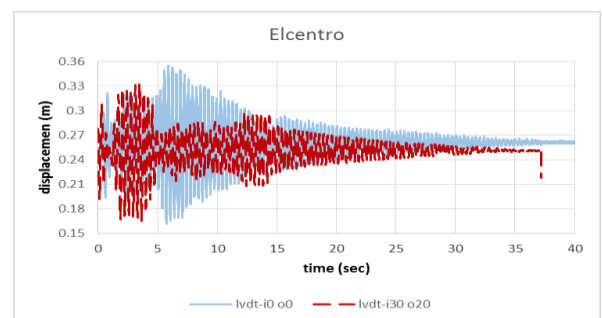
Figure 15. Comparison of the displacement history diagram of the I30-O20 model under the El Centro record

As the above diagrams demonstrate, the displacement history diagram under the El Centro record shows greater variation in the I0-O0 model than in others. Regarding the effect of liquid, the results suggest that the presence of liquid in the tank has reduced the displacement. The best possible result, i.e., the lowest displacement, under this excitation has occurred when the liquid height in the

inner and outer tanks has been 15 cm and 20 cm, respectively.

The maximum displacement of all models under the El Centro record and their displacement reduction ratios relative to I0-O0 are provided in Tables 4 and 5, respectively.

TABLE 4. Effect of the liquid in the inner and outer tanks of the considered TLD on the displacement response under the El Centro record

Effect of the liquid in the outer tank on the displacement response under the El Centro record								
Specimen	I0-O0	I0-O20	I0-O40	I15-O0	I15-O20	I15-O40	I30-O0	I30-O20	I30-O40
Max. Disp. (m)	0.35	0.326	0.344	0.340	0.322	0.336	0.332	0.332.	0.339
Effect of the liquid in the inner tank on the displacement response under the El Centro record								
Specimen	I0-O0	I15-O0	I30-O0	I0-O20	I15-O20	I30-O20	I0-O40	I15-O40	I30-O40
Max. Disp. (m)	0.35	0.340	0.332	0.326	0.322	0.332	0.344	0.336	0.339

TABLE 5. Displacement reduction ratio relative to I0-O0 under the El Centro record

Specimen	I0-O0	I0-O20	I0-O40	I1-O0	I15-O20	I15-O40	I30-O0	I30-O20	I30-O40
%	—	8%	3%	4.20%	9.20%	5.30%	6.40%	6.30%	4.50%
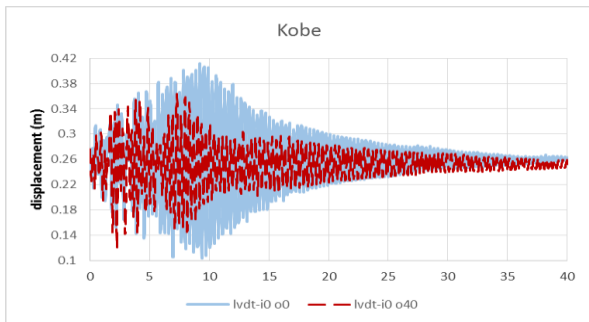
Figure 16. Comparison of the displacement history diagram of the I0-O40 model under the Kobe record
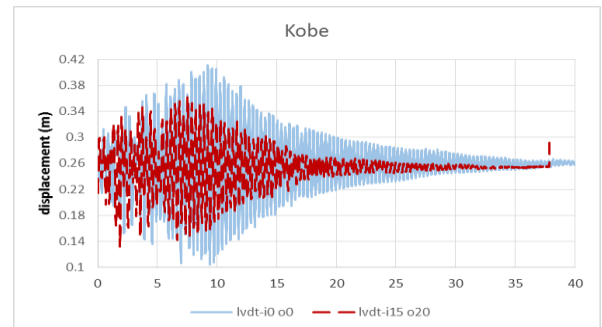
Figure 18. Comparison of the displacement history diagram of the I15-O20 model under the Kobe record
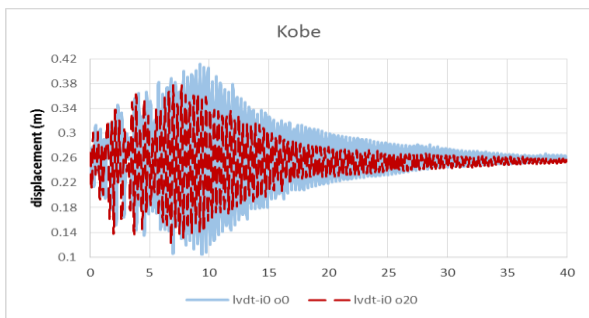
Figure 17. Comparison of the displacement history diagram of the I0-O20 model under the Kobe record
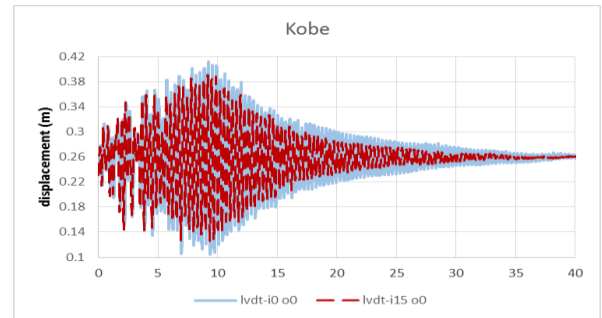
Figure 19. Comparison of the displacement history diagram of the I15-O0 model under the Kobe record
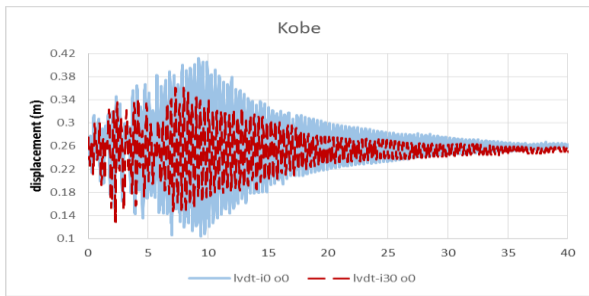
Figure 20. Comparison of the displacement history diagram of the I30-O0 model under the Kobe record
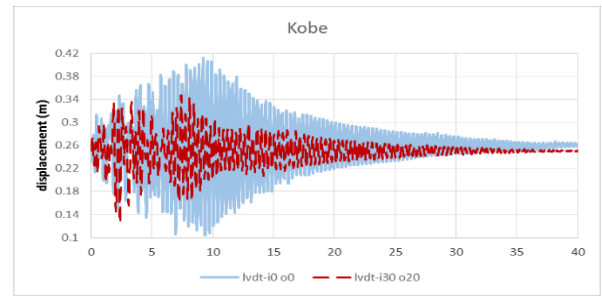
Figure 21. Comparison of the displacement history diagram of the I15-O40 model under the Kobe record

Figure 22. Comparison of the displacement history diagram of the I30-O40 model under the Kobe record

Figure 23. Comparison of the displacement history diagram of the I30-O20 model under the Kobe record
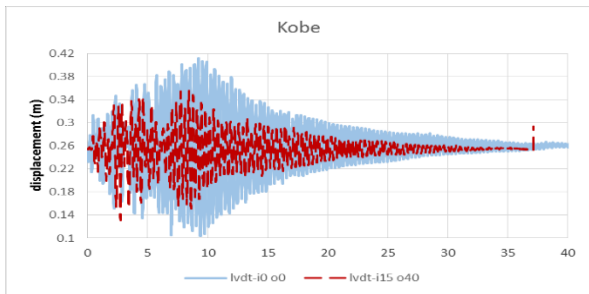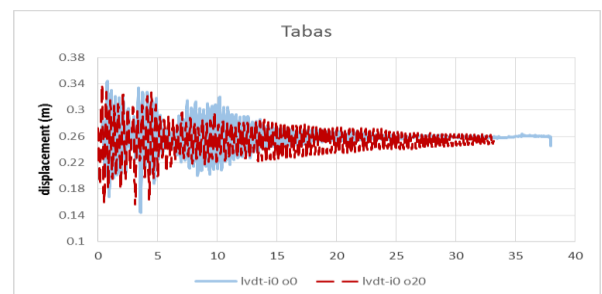
Figure 24. Comparison of the displacement history diagram of the I0-O20 model under the Tabas record
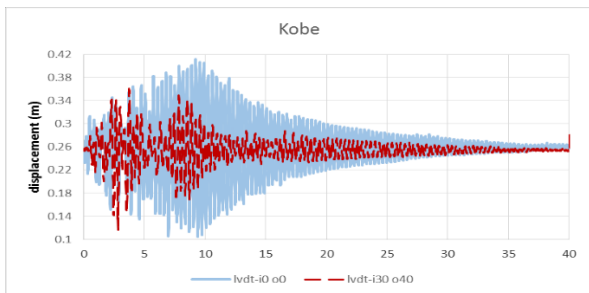
In the above diagrams, it can be seen that under the Kobe record, the displacement history diagram of the I0-O0 model has greater variation than that of other models. These results also show that the presence of liquid in the tank has resulted in reduced displacement. The lowest displacement under the Kobe record has occurred when the liquid height in the inner and outer tanks has been 30 cm and 20 cm, respectively.

Tables 6 and 7 show the maximum displacement of all models under the Kobe record and their displacement reduction ratios relative to I0-O0.

TABLE 6. Effect of the liquid in the inner and outer tanks of the considered TLD on the displacement response under the Kobe record

Effect of the liquid in the outer tank on the displacement response under the El Centro record								
Specimen	I0-O0	I0-O20	I0-O40	I15-O0	I15-O20	I15-O40	I30-O0	I30-O20	I30-O40
Max. Disp. (m)	0.411	0.377	0.363	0.390	0.363	0.355	0.36	0.347	0.361
Effect of the liquid in the inner tank on the displacement response under the El Centro record								
Specimen	I0-O0	I15-O0	I30-O0	I0-O20	I15-O20	I30-O20	I0-O40	I15-O40	I30-O40
Max. Disp. (m)	0.411	0.390	0.36	0.377	0.363	0.347	0.363	0.355	0.361

TABLE 7. Displacement reduction ratio relative to I0-O0 under the Kobe record

Specimen	I0-O0	I0-O20	I0-O40	I1-O0	I15-O20	I15-O40	I30-O0	I30-O20	I30-O40
%	__	8.20%	11.70%	5.10%	11.67%	13.70%	12.40%	15.50%	12.16%
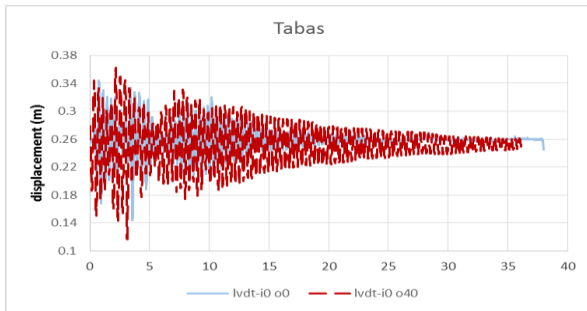
Figure 25. Comparison of the displacement history diagram of the I0-O40 model under the Tabas record
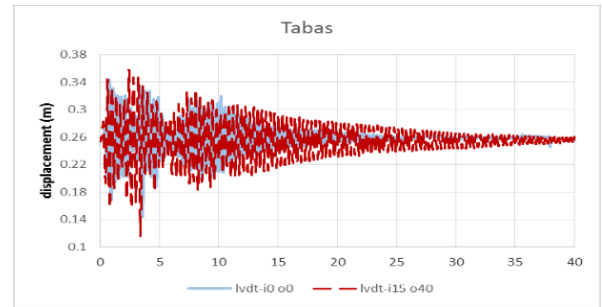
Figure 29. Comparison of the displacement history diagram of the I15-O40 model under the Tabas record
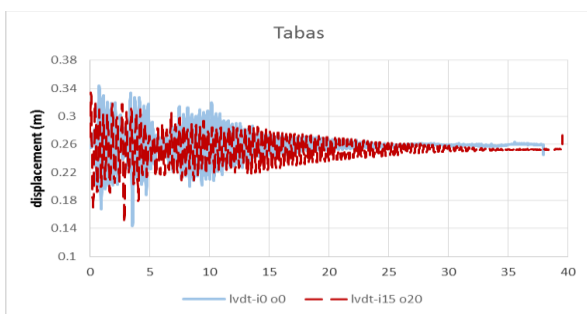
Figure 26. Comparison of the displacement history diagram of the I15-O20 model under the Tabas record
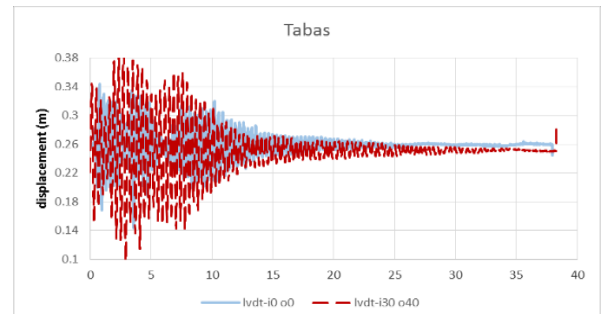
Figure 30. Comparison of the displacement history diagram of the I30-O40 model under the Tabas record
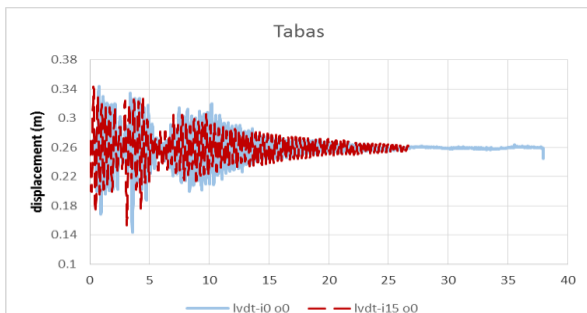
**Figure 27.** Comparison of the displacement history diagram of the I15-O0 model under the Tabas record
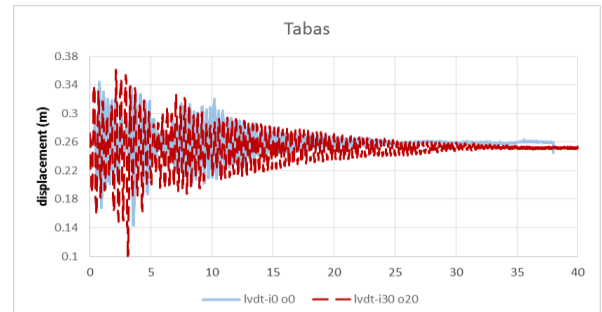
Figure 31. Comparison of the displacement history diagram of the I30-O20 model under the Tabas record
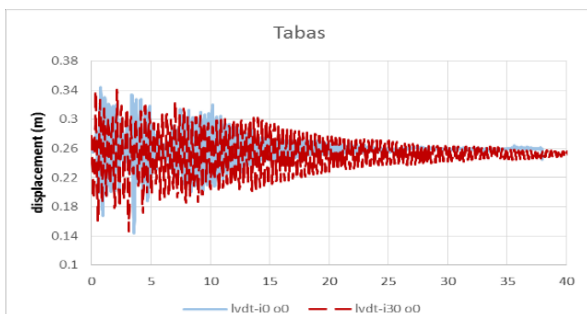
Figure 28. Comparison of the displacement history diagram of the I30-O0 model under the Tabas record

In the above diagrams, it can be seen that unlike under Kobe and El Centro records, the displacement history diagram with the greatest variation under the Tabas record is the one belonging to the I30-O40 model. This means that under the Tabas record, the considered TLD not only does not have a positive effect but increases the displacement. Regarding the effect of liquid, the results suggest under the Tabas record, the presence of liquid in the tank has reduced the displacement in some cases and increased it in others. Under this record, the lowest displacement has occurred when the liquid height in the inner and outer tanks has been 15 cm and 20 cm, respectively.

The maximum displacement values of all models under the Tabas record are given in Table 8 and the displacement reduction ratios of these models relative to I0-O0 are provided in Table 9.

4. 2. Acceleration Results   This section presents the acceleration history of the models with and without the considered TLD under the seismic excitations of El Centro, Tabas, and Kobe records. As before, all comparisons made in this section are relative to the results obtained with I0-O0. The acceleration history diagrams of the models for the El Centro, Tabas, and Kobe records are presented in Figures 32 to 39, Figures 40 to 47, and Figures 48 to 55, respectively. For a more accurate comparison, these results are also presented in more detail in the following tables. Again, to obtain these results, first, the height of the water in the inner tank was assumed to be variable and the height of the liquid in the outer tank was kept constant. Then, the height of the water in the outer tank was considered to be variable and the height of the liquid in the inner tank was kept constant. And finally, the height of the water in both inner and outer tanks was assumed to be variable. As mentioned, all the results presented in the tables are relative to the results of the I0-O0 model.

As can be seen, the greatest variation in the acceleration history diagram under the El Centro record belongs to the I0-O40 model. Regarding the effect of liquid, the results show that the presence of liquid in the tank has reduced the acceleration in some cases and increased it in others. The best possible result or in other words the lowest acceleration under this excitation has occurred when the liquid height in the inner and outer tanks has been 30 cm and 40 cm, respectively.

The maximum acceleration of all models under the El Centro record and their acceleration reduction ratios relative to I0-O0 are given in Tables 10 and 11, respectively.
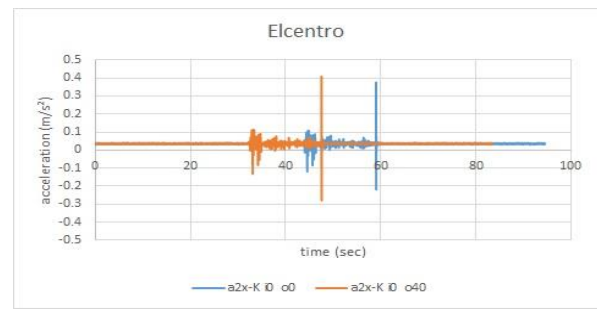
Figure 32. Comparison of the acceleration history diagram of the I0-O40 model under the El Centro record
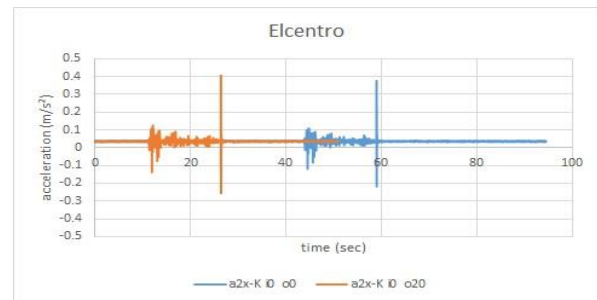
Figure 33. Comparison of the acceleration history diagram of the I0-O20 model under the El Centro record
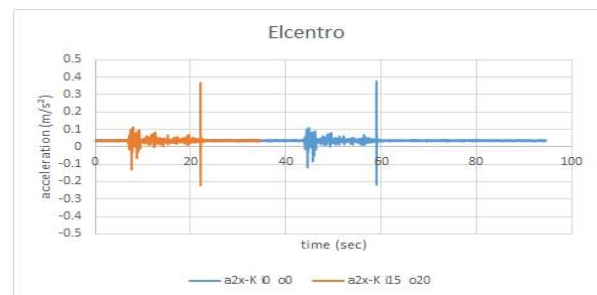

Figure 34. Comparison of the acceleration history diagram of the I15-O20 model under the El Centro record

TABLE 8. Effect of the liquid in the inner and outer tanks of the considered TLD on the displacement response under the Tabas record

Effect of the liquid in the outer tank on the displacement response under the El Centro record								
Specimen	I0-O0	I0-O20	I0-O40	I15-O0	I15-O20	I15-O40	I30-O0	I30-O20	I30-O40
Max. Disp. (m)	0.343	0.339	0.362	0.342	0.334	0.358	0.340	0.360	0.400

Effect of the liquid in the inner tank on the displacement response under the El Centro record								
Specimen	I0-O0	I15-O0	I30-O0	I0-O20	I15-O20	I30-O20	I0-O40	I15-O40	I30-O40
Max. Disp. (m)	0.343	0.342	0.340	0.339	0.334	0.360	0.362	0.358	0.400

TABLE 9. Displacement reduction ratio relative to I0-O0 under the Tabas record

Specimen	I0-O0	I0-O20	I0-O40	I1-O0	I15-O20	I15-O40	I30-O0	I30-O20	I30-O40
%	__	1%	5%	0.20%	2.60%	4.30%	0.80%	4.90%	16.60%
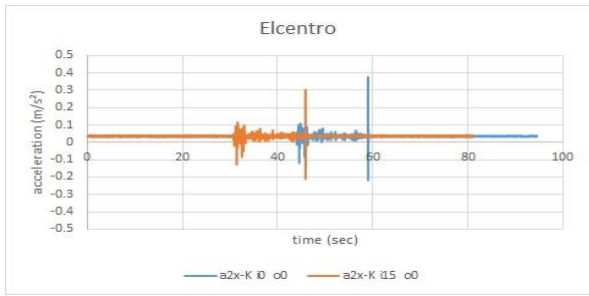
Figure 35. Comparison of the acceleration history diagram of the I15-O0 model under the El Centro record


Figure 36. Comparison of the acceleration history diagram of the I30-O0 model under the El Centro record

Figure 37. Comparison of the acceleration history diagram of the I15-O40 model under the El Centro record
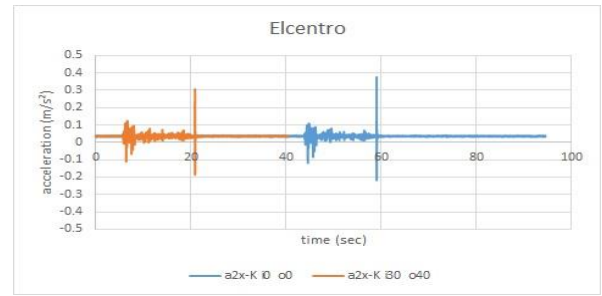
Figure 38. Comparison of the acceleration history diagram of the I30-O40 model under the El Centro record
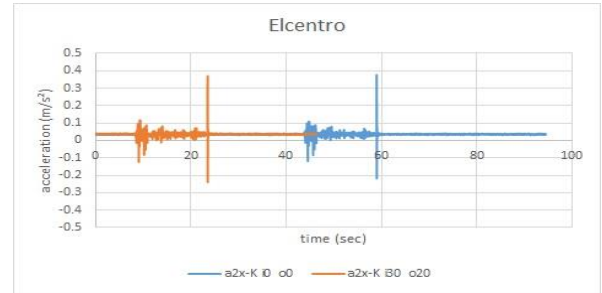
Figure 39. Comparison of the acceleration history diagram of the I30-O20 model under the El Centro record
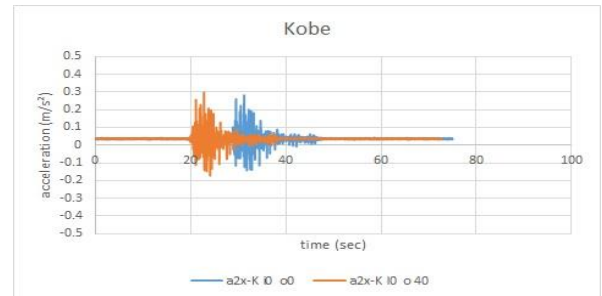
Figure 40. Comparison of the acceleration history diagram of the I0-O40 model under the Kobe record

TABLE 10. Effect of the liquid in the inner and outer tanks of the considered TLD on the acceleration response under the El Centro record

Effect of the liquid in the outer tank on the acceleration response under the El Centro record								
Specimen	I0-O0	I0-O20	I0-O40	I15-O0	I15-O20	I15-O40	I30-O0	I30-O20	I30-O40
Max. Acc.(m/s²)	0.376	0.406	0.406	0.301	0.365	0.356	0.310	0.369	0.296
Effect of the liquid in the inner tank on the acceleration response under the El Centro record								
Specimen	I0-O0	I15-O0	I30-O0	I0-O20	I15-O20	I30-O20	I0-O40	I15-O40	I30-O40
Max. Acc.(m/s²)	0.376	0.301	0.310	0.406	0.365	0.369	0.406	0.356	0.296

TABLE 11. Acceleration reduction ratio relative to I0-O0 under the El Centro record

Specimen	I0-O0	I0-O20	I0-O40	I1-O0	I15-O20	I15-O40	I30-O0	I30-O20	I30-O40
%	__	7.90%	8%	19.40%	2.90%	5.30%	18%	1.80%	21.20%
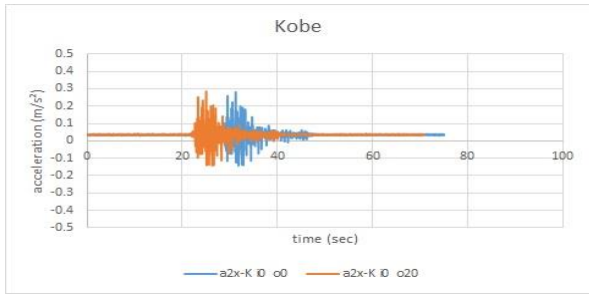
Figure 41. Comparison of the acceleration history diagram of the I0-O20 model under the Kobe record

Figure 42. Comparison of the acceleration history diagram of the I15-O20 model under the Kobe record


Figure 43. Comparison of the acceleration history diagram of the I15-O0 model under the Kobe record

**Figure 44.** Comparison of the acceleration history diagram of the I30-O0 model under the Kobe record

Figure 45. Comparison of the acceleration history diagram of the I15-O40 model under the Kobe record

4. 3. Numerical Investigation   In this part of the study, the finite element software ABAQUS was used for modeling. The structure, tank, and water inside the tank were all modeled with the C3D8R elements as shown in Figures 56 to 58.

The C3D8 element is an eight-node three-dimensional solid linear element with reduced integration.

4. 4. Modelling Verification   All laboratory experiments were modeled in ABAQUS software and the analytical models were verified in comparison to the

TABLE 14. Effect of the liquid in the inner and outer tanks of the considered TLD on the acceleration response under the Tabas record

Effect of the liquid in the outer tank on the acceleration response under the Tabas record								
Specimen	I0-O0	I0-O20	I0-O40	I15-O0	I15-O20	I15-O40	I30-O0	I30-O20	I30-O40
Max. Acc.(m/s²)	0.179	0.182	0.180	0.194	0.178	0.176	0.184	0.190	0.173
Effect of the liquid in the inner tank on the acceleration response under the Tabas record								
Specimen	I0-O0	I15-O0	I30-O0	I0-O20	I15-O20	I30-O20	I0-O40	I15-O40	I30-O40
Max. Acc.(m/s²)	0.179	0.194	0.184	0.182	0.178	0.190	0.180	0.176	0.173

TABLE 15. Acceleration reduction ratio relative to I0-O0 under the Tabas record

Specimen	I0-O0	I0-O20	I0-O40	I1-O0	I15-O20	I15-O40	I30-O0	I30-O20	I30-O40
%	__	1.60%	1%	8.30%	0.50%	1.60%	2.70%	6.10%	3.30%
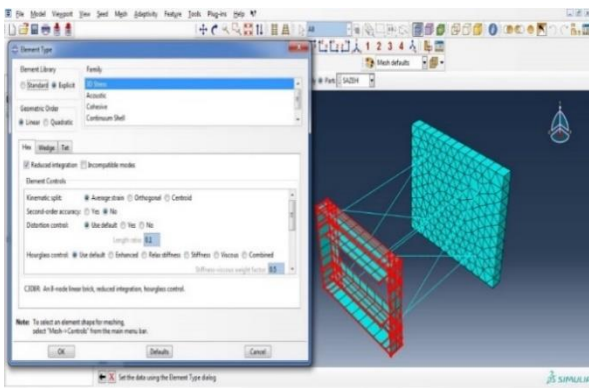
Figure 56. Modeling of the structure in ABAQUS
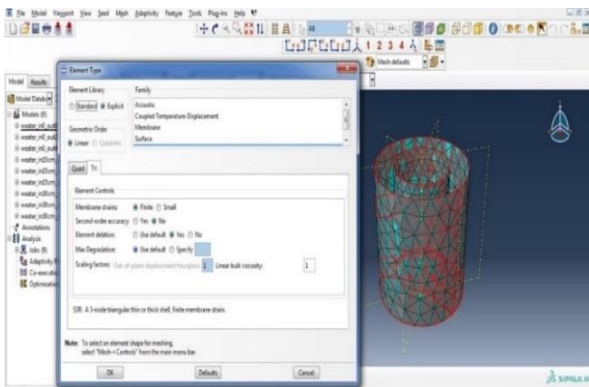
Figure 57. Modeling of the tank in ABAQUS
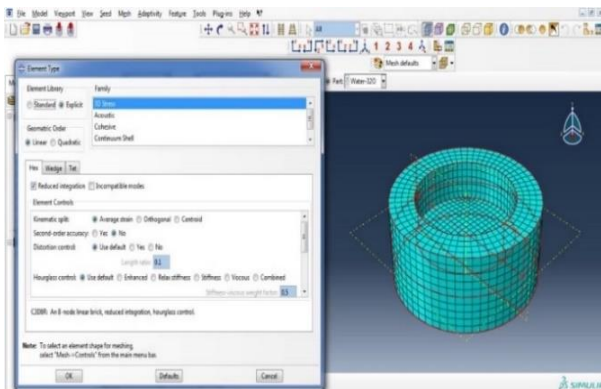
Figure 58. Modeling of the water inside the tank in ABAQUS

experiment results. Displacement and acceleration responses were used for model verification in various conditions. As an example, the verification of acceleration response of specimen I30-O40 subjected to the El Centro earthquake is shown in Figure 59.

4. 5. Numerical Results   As the numerical investigation of the effect of the considered TLD, the height of water in the inner and outer tanks was considered as 130 and 320 mm, respectively. The results were obtained once without any water in the damper, another time by water only in the
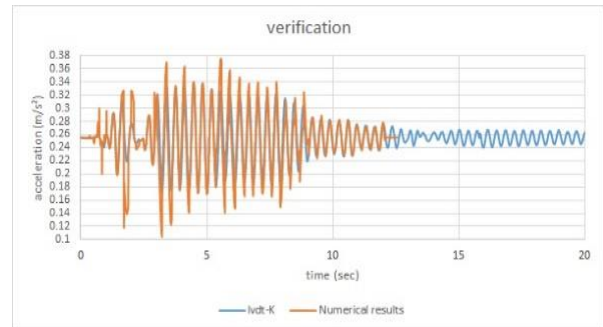
Figure 59. Comparison of analytical and experimental acceleration responses, El Centro I30-O40

inner tank, and the third time by water only in the outer tank. The seismic record used in this investigation was that of the Varzeqan earthquake. The acceleration records of this earthquake are shown in Table 16.

To evaluate the performance of the proposed damper, the effect of water level on the outer and inner walls of the reservoir in reducing the response of the structure was numerically investigated. For this purpose, the results were studied in three scenarios; without water inside the damper, water inside the inner tank, and water inside the outer tank. The response parameters employed for this evaluation are lateral displacement, acceleration, and energy which some of which are shown in Figures 60 to 63.

The results of the study on the displacement history show that the amount of lateral displacement of the structure in the case of damping has been significantly reduced. It can also be observed that the amount of lateral displacement in the case where the fluid is located in the inner or outer wall of the damper is reduced by 50% compared to the waterless state.

TABLE 16. Characteristics of acceleration records of Varzeqan earthquake

Record	Symbol	d (km)	PGA (cm/s²)	PGV (cm/s)	PGD (cm)
Varzeqan 2012	Varzeqan	9	478	41.23	9.45
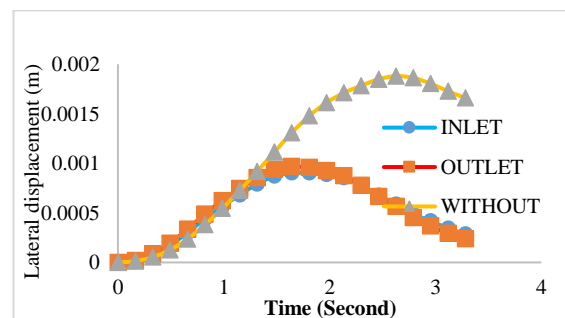
Figure 60. Numerical comparison of displacement history

From the experimental displacement and acceleration diagrams of the considered TLD modeling and analysis performed in this study, the following can be concluded:

- The models showed different displacement history results under different seismic excitations. Under El Centro and Kobe records, the I0-O0 model (the model without liquid) had a higher displacement than all liquid-containing models. This is indicative of the positive effect of the liquid on the displacement. Under the Tabas record, however, the highest displacement was observed in the model where the liquid height in the inner and outer tanks was 30 cm and 40 cm, respectively. This discrepancy can be attributed to different frequency characteristics of different records. Examining the amount of energy exerting the structure, it is observed that the damper greatly reduces the input energy, and the amount of this reduction in both types of dampers, whether the fluid is placed in the outer or inner wall, is approximately equal and reduced by 53%.

Moreover, the results of acceleration analysis show that the use of the damper also greatly reduces the amount of acceleration response.
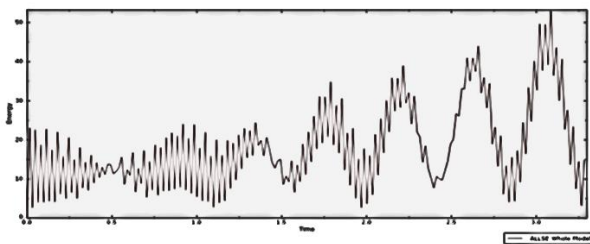
Figure 61. Numerical history of energy input when water was placed in the inner tank of the damper
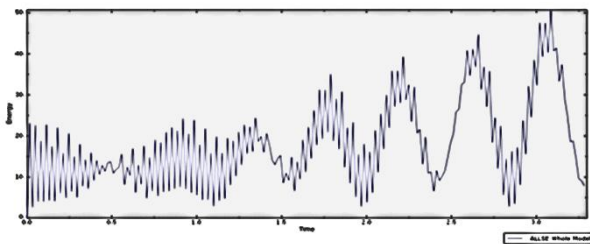
Figure 62. Numerical history of energy input when water was placed in the outer tank of the damper
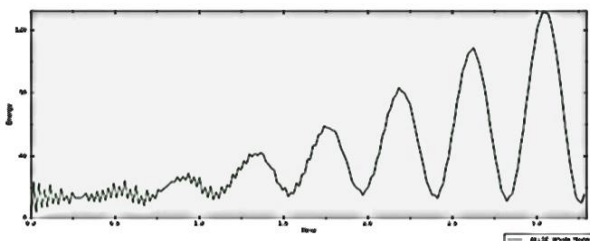
Figure 63. Numerical history of energy input in the absence of water in the damper

As an extension of the current study, the optimal state of the water amount in the modeling has been evaluated and a reduction of 16 to 33% has been achieved.

5. CONCLUSION

From the experimental displacement and acceleration diagrams of the considered TLD modeling and analysis performed in this study, the following can be concluded:
1. The models showed different displacement history results under different seismic excitations. Under El Centro and Kobe records, the I0-O0 model (the model without liquid) had a higher displacement than all liquid-containing models. This is indicative of the positive effect of the liquid on the displacement. Under the Tabas record, however, the highest displacement was observed in the model where the liquid height in the inner and outer tanks was 30 cm and 40 cm, respectively. This discrepancy can be attributed to different frequency characteristics of different records.
2. The lowest displacement was also found to somewhat vary depending on the applied seismic excitation.

For example, under the El Centro record, the lowest displacement (relative to I0-O0) was related to the model where the liquid height in the inner and outer tanks was 15 cm and 20 cm, respectively. But under the Kobe record, the lowest displacement belonged to the model I30-O20. Finally, under the Tabas record, the lowest displacement was again related to the model I15-O20.
3. Regarding the acceleration history, the results suggest that in certain cases the presence of liquid in the considered TLD significantly increases the acceleration instead of decreasing it. The highest acceleration under the El Centro and Kobe records occurred in the model I0-O40. Under the Tabas record, the highest acceleration was observed in the model I15-O0.
4. The lowest acceleration was also found to be dependent on the applied seismic excitation. Under the El Centro record, the lowest acceleration belonged to the model where the inner and outer tanks contained 30 cm and 40 cm of liquid respectively, which had a lower acceleration than I0-O0. The lowest acceleration under the Kobe record occurred in the model I30-O40. Finally, under the Tabas record, the lowest acceleration was observed in the model I30-O40.

6. REFERENCES

1.   Shoji, Y. and Munakata, H., "Sloshing of cylindrical tank due to seismic acceleration", in Abaqus Users Conference, Newport, Rhode Island., (2008).

2.   Banerji, P. and Samanta, A., "Earthquake vibration control of structures using hybrid mass liquid damper", *Engineering Structures*, Vol. 33, No. 4, (2011), 1291-1301. doi:10.1016/j.engstruct.2011.01.006.

3.   Goudarzi, M. and Sabbagh-Yazdi, S., "Evaluating 3d earthquake effects on sloshing wave height of liquid storage tanks using finite element method", *Journal of Seismology and Earthquake Engineering*, Vol. 10, No. 3, (2020), 123-136.

4.   Ashasi-Sorkhabi, A., Malekghasemi, H., Ghaemmaghami, A. and Mercan, O., "Experimental investigations of tuned liquid damper-structure interactions in resonance considering multiple parameters", *Journal of Sound and Vibration*, Vol. 388, (2017), 141-153. doi:10.1016/j.jsv.2016.10.036.

5.   Love, J., Tait, M. and Toopchi-Nezhad, H., "A hybrid structural control system using a tuned liquid damper to reduce the wind induced motion of a base isolated structure", *Engineering Structures*, Vol. 33, No. 3, (2011), 738-746. doi:10.1016/j.engstruct.2010.11.027.

6.   Crowley, S. and Porter, R., "An analysis of screen arrangements for a tuned liquid damper", *Journal of Fluids and Structures*, Vol. 34, (2012), 291-309. doi:10.1016/j.jfluidstructs.2012.06.001.

7.   Crowley, S. and Porter, R., "The effect of slatted screens on waves", *Journal of Engineering Mathematics*, Vol. 76, No. 1, (2012), 33-57.

8.   Reed, D., Yu, J., Yeh, H. and Gardarsson, S., "Investigation of tuned liquid dampers under large amplitude excitation", *Journal of Engineering Mechanics*, Vol. 124, No. 4, (1998), 405-413. doi:10.1061/(ASCE)0733-9399(1998)124:4(405).

9.   Gao, H., Kwok, K. and Samali, B., "Optimization of tuned liquid column dampers", *Engineering Structures*, Vol. 19, No. 6, (1997), 476-486. doi://10.1016/S0141-0296(96)00099-5.

10.   Zhu, F., Wang, J.-T., Jin, F., Altay, O. and Hara, T., "Real-time hybrid simulation of single and multiple tuned liquid column dampers for controlling seismic-induced response", in Proceedings of the 6th International Conference on Advances in Experimental Structural Engineering., (2015).

11.   Halabian, A. and Torki, M., "Numerical studies on the application of tuned liquid dampers with screens to control seismic response of structures", *The Structural Design of Tall and Special Buildings*, Vol. 20, No. 2, (2011), 121-150. doi:10.1002/tal.515.

12.   Love, J. and Tait, M., "Non-linear multimodal model for tuned liquid dampers of arbitrary tank geometry", *International Journal of Non-Linear Mechanics*, Vol. 46, No. 8, (2011), 1065-1075. doi:10.1016/j.ijnonlinmec.2011.04.028.

13.   Love, J. and Tait, M., "Nonlinear simulation of a tuned liquid damper with damping screens using a modal expansion technique", *Journal of Fluids and Structures*, Vol. 26, No. 7-8, (2010), 1058-1077. doi:10.1016/j.jfluidstructs.2010.07.004.

14.   Malekghasemi, H., Ashasi-Sorkhabi, A., Ghaemmaghami, A.R. and Mercan, O., "Experimental and numerical investigations of the dynamic interaction of tuned liquid damper–structure systems", *Journal of Vibration and Control*, Vol. 21, No. 14, (2015), 2707-2720. doi:10.1177/1077546313514759.

15.   Ersin, Aydin. Baki, Ozturk. Maciej, Dutkiewicz. Huseyin, Cetin. "Experiments of tuned liquid damper (TLD) on the reduced shear frame model under harmonic loads." In EPJ web of conferences (2017), Vol. 143, 02001.

16.   Ersin, Aydin. Baki, Ozturk. "Experiments of tuned liquid column damper (TLCD) on the reduced shear frames under harmonic loads. "(2018) 16th European Conference on Earthquake Engineering (16ECEE), Thessaloniki, Greece.

17.   Aydın, E., ÖZTÜRK, B., Batı, M., Kavaz, Y. and Kılıç, B., "Effects of tuned liquid column damper properties on the dynamic response of structures", ASCE-EMI 2019 International Conference, Lyon, France.

18.   A. Sarlak, H. Saeedmonir, C. Gheyratmand. "Experimental Study on Using Uniform Tuned Liquid Column Damper for Structural Control of Buildings Resting on Loose Soil." *International Journal of Engineering, Transactions A: Basics,* Vol. 31, No. 7, (2018) 1028-1037. doi: 10.5829/ije.2018.31.07a.04.

19.   S. Pal, B. K. Roy, S. Choudhury "Comparative Performance Study of Tuned Liquid Column Ball Damper for Excessive Liquid Displacement on Response Reduction of Structure" *International Journal of Engineering, Transactions B: Applications,* Vol. 33, No. 5, (2020) 753-759. doi:10.5829/ije.2020.33.05b.06.

Persian Abstract

چکیده

برای تحمل حرکات قوی زمین در زمین لرزه‌های بزرگ، سازه‌ها باید به ابزارهایی مجهز شوند تا مقادیر عظیم انرژی ناشی از این تحریکات را خنثی کنند. از آنجایی که این ساختمان‌ها اغلب قابلیت میرایی بسیار پایینی دارند، مقدار انرژی تلف شده در فاز رفتار الاستیک آنها ناچیز است. کلاس‌های مختلفی از TLDها با اشکال مخزن، نسبت ابعاد و مکانیسم‌های عمل متفاوت وجود دارد که هر کدام دارای خواص و ویژگی‌های خاص خود هستند. یکی دیگر از علل اتلاف انرژی در TLDها، علاوه بر ویسکوزیته مایع، نیروی برشی پایه است که به دلیل تفاوت بین نیروهای هیدرواستاتیکی، به تقاطع دمپر با ساختار اصلی با اختلاف فاز نسبت به تحریک خارجی وارد می‌شود. بر روی دیواره‌های دو سر مخزن اعمال می‌شود. بنابراین، سطح برهمکنش مایع با دیواره‌های میراگر نیز تعیین‌کننده میرایی نیروهای خارجی و در نتیجه پاسخ لرزه‌ای سازه است. این مطالعه نوع جدیدی از TLD را با یک مخزن استوانه‌ای دو جداره بررسی کرد. برای بررسی تأثیر این TLD بر پاسخ لرزه‌ای، یک سری مدل با ارتفاع‌های مایع مختلف در دیواره‌های داخلی و خارجی مخزن ساخته شد و تحت چندین تحریک لرزه‌ای بر روی میز لرزان قرار گرفت. نتایج نشان داد که استفاده از این نوع میراگر باعث کاهش پاسخ لرزه‌ای سازه‌ها می‌شود. همچنین، کاهش پاسخ لرزه‌ای به طور قابل توجهی با مقدار مایع در دمپر تغییر می‌کند.

International Journal of Engineering

Modal Frequencies Based Human Action Recognition Using Silhouettes and Simplicial Elements

O. Mishra[a], P. S. Kavimandan*[b], R. Kapoor[a]

[a] Delhi Technological University, Department of Electronics & Communication, Bawana Road, Delhi, India
[b] IGDTUW, Department of Information Technology, Kashmere Gate, Delhi, India

A B S T R A C T

Human action recognition has been a pioneer research problem among researchers. This paper proposed a new local feature descriptor in terms of modal frequency using silhouette and simplicial elements of a silhouette with the help of Finite Element Analysis (FEA). This local descriptor represents the distinctive human poses in the form of modal frequency. These modal frequencies reduce the feature dimension and represent a wide range of poses of human action. These modal frequencies are subject to the stiffness matrix of the body that is associated with the displacement. The silhouettes of the human body are used for the analysis. These silhouettes are represented into simplicial elements. The modal frequencies of silhouettes are calculated using simplicial elements. These modal frequencies of the silhouette are used as the feature vectors that are given to the Radial Basis Function-Support Vector Machine (RBF-SVM) classifier. The challenging datasets Weizmann, KTH and IXMAS are used for validation of the proposed methodology.

1. INTRODUCTION

Videos have become a very essential part of our life these days. We create, store and share these videos. The increasing number of accessible videos has also created the need to understand them. Several methods have been developed by researchers for human action recognition. These methodologies can be sectioned into two groups: global feature descriptors and local feature descriptors. Global features require the extraction of the human body whose action is to be recognized. The two-dimensional (2D) template matching technique is used [1-3]. In this technique, 2D silhouettes of the human body are extracted. These silhouettes are also used as space-time volumes [4, 5]. The main disadvantage of this methodology is that they require accurate background subtraction and motion of the pixels. Further global feature descriptors have major disadvantages that they give shape information but not motion information. That makes it weak in recognizing

similar types of actions such as running and jogging where motion is involved. To avoid these problems researchers developed local feature descriptors. This methodology does not require background subtraction as they are established on the spatio-temporal points. Methods reported in literature [6-14] have used famous bag-of-words models. The main disadvantage of these methodologies is that they give only motion information but no information about the structure. Methodologies reported in literature [15-22] based on silhouette analysis have a major contribution to human action recognition. Kapoor et al. [15] have used average energy silhouette images whereas a hybrid classifier is used for action recognition by Mishra et al. [16]. Wu and Shao [17] used hybrid features which include both global and local features. The pose correlogram is used as a local feature and extended MHI is used as global feature. The three-dimensional histogram of the oriented gradient is used to represent the action video [18, 19]. Silhouette-based methodologies are also used in a human pose-based action recognition [23, 24].

The silhouette-based analysis is also used in deep learning-based methodologies [25-27] but these

*Corresponding Author Institutional Email:
pronita012phd0115@igdtuw.ac.in (P. S. Kavimandan)

methodologies require large datasets. The methods based on global feature descriptors cannot give the motion information and the methodologies that are based on local descriptors cannot give shape information. Even methodology that used hybrid descriptors having both global and local descriptors require fusion problems. A feature descriptor based on the stiffness matrix discussed in literature [21] is capable of representing both shape as well as motion features. The main limitation of this methodology was that it increases the feature dimensionality and also requires large memory space. The proposed method overcomes these limitations and offers a new local feature descriptor embedding the information of both shape and motion with the help of modal frequency. Modal frequency plays an important role in the analysis of the shape of the structure against the deformation that occurred in the shape. The proposed methodology improved these issues in the following manner:

1. Modal frequencies of the human body silhouette reduce the feature dimensionality drastically when the reduced number of the mode of the frequency of the structure is selected. And thus, it takes less runtime as compared to literature [21].

2. Moreover different modes of frequencies of an action shape cover the wide range of the poses of human action. This increases the accuracy as compared to our previous work.

3. Every deformation in the shape has its unique modal frequency that represents the shape change because of motion. Therefore modal frequency is capable of representing shape and motion information. This makes the proposed method unique and more reliable as compared to other existing methods because it contains structural as well as motion information.

2. METHODOLOGY OF PROPOSED FRAMEWORK

The workflow diagram of the proposed methodology is shown in Figure 1. The first step for action recognition is to extract the silhouette from the action video. Then these silhouettes are represented in the form of simplicial elements using FEA. The displacement matrices of these simplicial elements are then found. The modal frequencies are extracted with the use of displacement matrices. Later on, feature vectors are formed in form of modal frequencies that are fed to the RBF-SVM classifier to recognize the action.
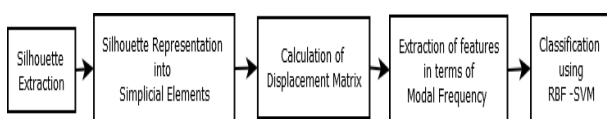
Figure 1. Workflow diagram of the proposed method

2. 1. Representation of Silhouette in Terms of Simplicial Elements   The silhouette extraction from the action video is a crucial step. Limitations such as background cluttering create a hurdle for background subtraction. The proposed methodology used the Gaussian mixture model-based background subtraction to extract the silhouette used in literature [28]. The advantage of this method is that it can deal with the problem occurring because of dynamic background and shadow. Figure 2 shows the frame of the action 'walk' and the background-subtracted image. The boundary of the silhouette is then found.

These Silhouettes are divided into different simplicial triangular elements using the Finite Element Method (Figure 3). We adopted the following steps for the representation of the simplicial elements: 1. The prominent points on the silhouette have been reported by Laptev and Lindeberg [29]. 2. These prominent points are used as the node vertices of the simplicial triangular elements.

When an actor performs actions, the prominent points (vertices of the simplicial elements) also get displaced in a unique pattern. The simplicial elements are represented by displacement matrices. The simplicial triangular element has three nodes $A(x_1,y_1)$, $B(x_2,y_2)$ and $C(x_3,y_3)$. The displacement vectors of the simplicial triangular elements given by $D = \{d_1, d_2, d_3, d_4, d_5, d_6\}^T$. Every node has a displacement in X-direction and Y-direction. Node A has displacement in X-direction is d_1 and in Y-direction is d_2, node B has displacement in X-direction is d_3 and in Y-direction is d_4 and for node C displacement in X-direction is d_5 and in Y-direction is d_6. The complete object with n elements can be represented globally by $G = \{D_1, D_2, D_3, \ldots, D_n\}^T$. Every movement of the silhouette results in the displacements of the vertices of the triangle. Figure 5 shows the small element having displacements a in X-direction and b in Y-direction.
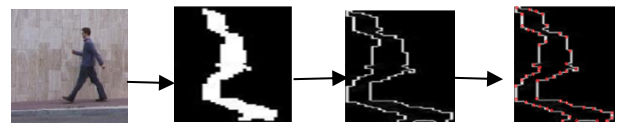
Figure 2. A frame of 'walk', background-subtracted image, external silhouette and the prominent points on the extracted silhouette
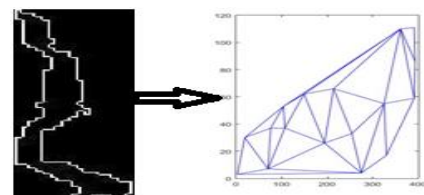
Figure 3. Representation of silhouette into simplicial elements
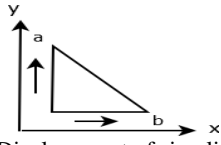
Figure 4. Displacement of simplicial element

Due to this displacement, a strain $\phi = \begin{bmatrix} \frac{\partial a}{\partial x} \\ \frac{\partial b}{\partial y} \\ \frac{\partial a}{\partial y} + \frac{\partial b}{\partial x} \end{bmatrix}$ is developed in X-direction, Y-direction and shear direction.

2. 2. Feature Extraction in Terms of Modal Frequency

We can deduce the stiffness matrix of the single triangle with the use of displacement matrices. We call this stiffness matrix as a local stiffness matrix and it can be represented by Equation (1).

$$k_l = D^T D t_e S_e \qquad (1)$$

where D is displacement matrix subject to strain, t_e is the thickness and S_e is the area of the triangle and both are assumed constant. D is also called the strain displacement matrix which can be calculated by shape functions [21]. All the local stiffness matrices of triangle elements are united systematically to form the global stiffness matrix. We first set the degree of freedom of the structure. The value of the degree of freedom will start from one to D where D is the total degree of freedom. Following steps are involved in the formation of the global stiffness matrix:

The size of the global stiffness matrix K_g will be the total number of degree of freedom and it is initialized to zero.

We computed the local stiffness matrix k_l for every triangular element.

We added the local stiffness matrix k_l to the global stiffness matrix K_g by placing it properly.

Procedures 2 and 3 are repeated until the complete global stiffness matrix is constructed.

Once we get the global stiffness matrix we can calculate the modal frequency of the complete silhouette by calculating the Eigen values of the global stiffness matrix. The Eigen value of matrix K_g can be calculated by Equation (2).

$$\left| det[K_g - \lambda_i I] \right| = 0 \qquad (2)$$

where λ_i is Eigenvalue and I is an identity matrix.

The values of the λ_i give the information the how much variance in global stiffness matrix in their directions. The highest value of Eigen value will be the principal component. In the proposed methodology, we selected three principal components.

The corresponding modal frequency can be found in Equation (3).

$$F = \sqrt{\lambda_i}/(2\pi) \qquad (3)$$

With the help of the Eigen values, modal frequencies of the silhouette of the human body are extracted by Equation (3). These principal component based modal frequencies reduce the feature dimensionality drastically. We have selected the reduced number of the mode of the frequency of the structure i.e.3. The result of three modes of frequencies (mode 1, 16.61×10^{-5}Hz, mode 2, 28.58×10^{-5}Hz and mode 3, 36.80×10^{-5}Hz) applied on Weizmann datasets for action "Clapping" are given in Figure 5.

The silhouette extracted from the sequence of frames in a video is discretized into a number of simplicial elements. The global stiffness matrix that represents the local feature of the frame has the dimension depending upon the degree of freedom. For example, if the total number of nodes/vertices of a silhouette is n and if these nodes can move in X and Y directions, the degree of freedom of complete silhouette structure will be 2n. Thus, the dimension of the global stiffness matrix will be 2n x 2n. Since we are using Eigen values, the dimension of this structure will reduce to 2n. Thus, corresponding to the dimension of 2n, we will get 2n modal frequencies, out of which we have selected the most suitable number through cross-validation. These feature vectors are fed to the RBF-SVM classifier [21, 30] to recognize the action.
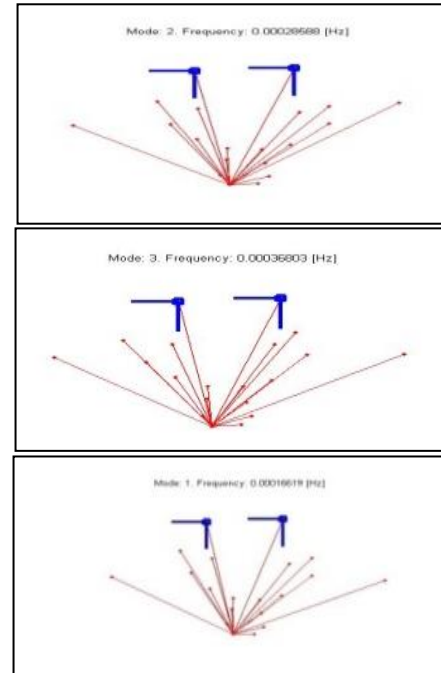
Figure 5. Three modal frequencies for action 'Clapping' of Weizmann dataset

3. EXPERIMENTAL RESULTS

To establish the authenticity of the proposed methodology, standard datasets like Weizmann, KTH and IXMAS are used. The experimentation on these datasets will also prove the robustness of the proposed methodology against background cluttering, execution rate and both inter and intra-class similarity. The proposed methodology has been developed on the following set-up:

Software: MATLAB R2015A
Hardware: Intel(R) Core (TM) i5-6200 CPU @2.30 GHz, 8 GB RAM, 64 bit Operating System

Accuracy is used as a performance evaluation parameter of the proposed methodology. For cross-validation, we used the Leave-One-Out strategy. The description of datasets is as follows:

Weizmann Dataset has 10 action classes; KTH Dataset has 6 action classes whereas IXMAS has 13 action classes. Sample frames of all three datasets are shown in Figure 6(a-c). Table 1 shows that when the total number of simplicial triangle elements in the silhouette is considered to be more than 20, it gives a superior result.

Figure 6(a). Weizmann dataset frames

Figure 6(b). KTH dataset frames

Figure 6(c). IXMAS dataset frames

TABLE 1. Parameter setting for no. of simplicial elements

Total no. of nodes	5	10	15	20	22	25
Accuracy (%)	0.67	0.83	0.89	0.93	0.94	0.94

TABLE 2. Parameter setting for no. of modes of frequency

No. of modes of frequency	1	2	3	5	7
Accuracy (%)	0.70	0.88	0.94	0.94	0.95

Moreover, any number higher than 22 do not yield significantly different results. Thus, we have selected 22 elements. We selected the reduced number of modes of frequency so that the feature vector dimension also gets reduced. Table 2 shows the result of different modes of frequency. It is clear from table 2 that three modes of frequencies gives good result and further increment in the number of modes do not show significant change. Thus, we have selected three modes of frequency for our proposed method. The graphs of modal frequencies versus the silhouettes in the frames are shown in Figure 7(a-f) where the X-axis represents the frames and the Y-axis represents a change in modal frequencies with the change in frames for different activities such as 'clapping', 'jumping', 'hand waving', 'hand waving (both hands)', 'skipping' and 'hopping'. Figure 7(a) shows 3 modes of frequency changes for the action 'clapping'.
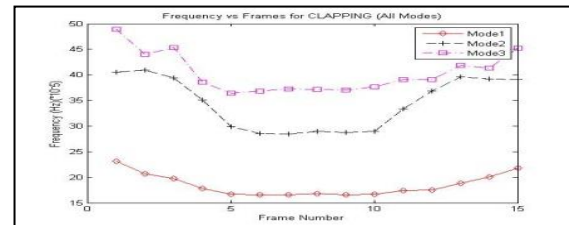
Figure 7(a). Modal Frequency for 'clapping'
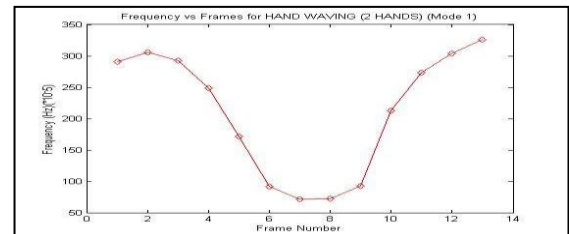
Figure 7(b). Modal Frequency for 'hand waving (both hands)'
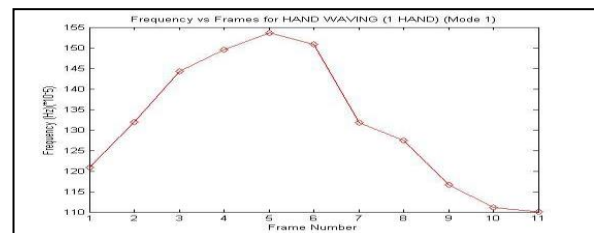
Figure 7(c). Modal Frequency for 'hand waving'
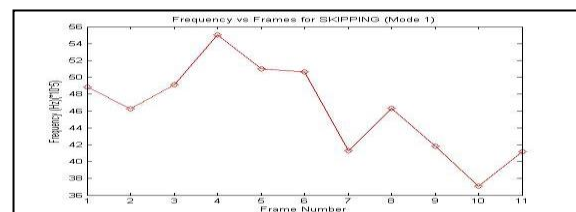
Figure 7(d). Modal Frequency for 'skipping'
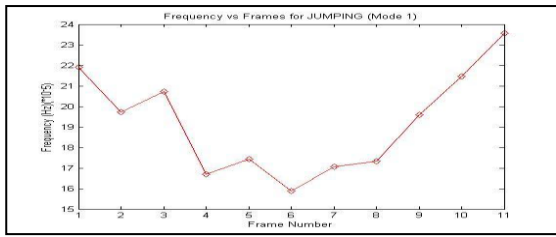
Figure 7(e). Modal Frequency for 'jumping'
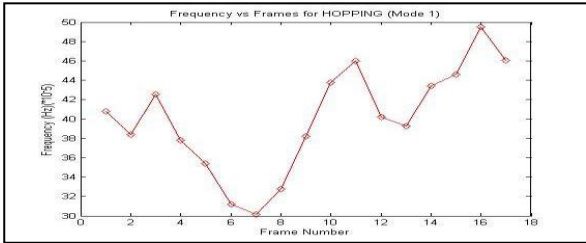
Figure 7(f). Modal Frequency for 'hopping'

3. 1. Comparison of the Proposed Algorithm with Different Methods on Standard Datasets

Weizmann dataset: Similar methodologies have been compared with the proposed methodology for the Weizmann dataset [12, 16, 17, 25, 26, 31] and the results are shown in Figure 8(a). The proposed method achieved an accuracy of 97.9%. All the methods mentioned in Figure 8(a) either retained shape information or motion information. The reason we achieved higher accuracy is that the proposed methodology has retained both shape and motion information through the modal frequencies of the silhouette structure.

KTH dataset: Figure 8(b) shows the comparison of the proposed methodology with other recent methodologies on KTH dataset [3, 12, 16, 18, 24, 25, 27, 31]. The proposed method achieved an accuracy of 96.2% for the KTH dataset.

IXMAS dataset: Figure 8(c) shows a comparison of the proposed methodology with other methodologies for IXMAS dataset [11, 16, 33]. The accuracy of the proposed method is 89.7% for IXMAS.
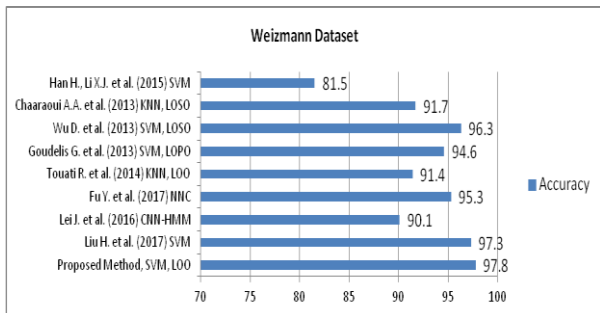
Figure 8(a). Comparison of the proposed methodology with other methods for Weizmann Dataset
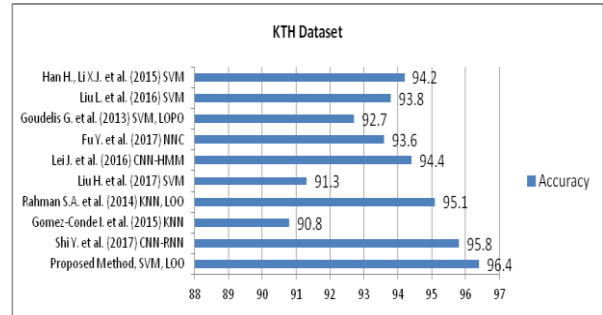
Figure 8(b). Comparison of the proposed methodology with other methods for KTH Dataset
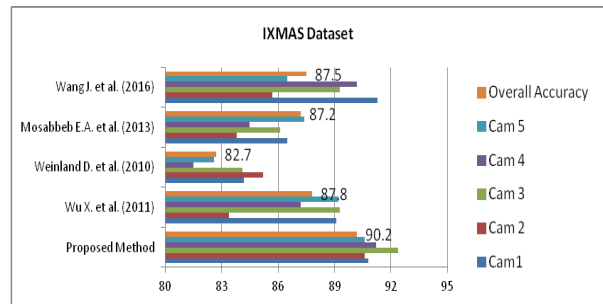
Figure 8(c). Comparison of the proposed methodology with other methods for IXMAS Data

Figure 9(a-c) show the confusion matrices of the proposed methodology applied on the Weizmann datasets, KTH dataset, Ballet dataset and IXMAS dataset, respectively. For Weizmann dataset, A1: running action is 6% confused with the action A2: walking, whereas walking action is recognized without any confusion. Similarly, A5: skipping action is 3% confused with A6: Jumping at a place whereas, action jumping at a place is 1% confused with skipping. All other actions are recognized correctly. For KTH dataset action A3: boxing is 4% confused with action A2: waving and actions A5: jogging and A6: running is 3% confused with each other. Actions such as applauding, waving and walking are correctly classified. Similarly, the confusion matrix on IXMAS datasets also shows good classification results.

	A₁	**A₂**	**A₃**	**A₄**	**A₅**	**A₆**	**A₇**	**A₈**	**A₉**	**A₁₀**
A₁	0.94	0.06	0.00	0.00	0.00	0.00	0.00	0.00	0.00	0.00
A₂	0.00	1.00	0.00	0.00	0.00	0.00	0.00	0.00	0.00	0.00
A₃	0.00	0.00	1.00	0.00	0.00	0.00	0.00	0.00	0.00	0.00
A₄	0.00	0.00	0.00	1.00	0.00	0.00	0.00	0.00	0.00	0.00
A₅	0.00	0.00	0.00	0.00	0.97	0.03	0.00	0.00	0.00	0.00
A₆	0.00	0.00	0.00	0.00	0.01	0.99	0.00	0.00	0.00	0.00
A₇	0.00	0.00	0.00	0.00	0.00	0.00	1.00	0.00	0.00	0.00
A₈	0.00	0.00	0.00	0.00	0.00	0.00	0.00	1.00	0.00	0.00
A₉	0.00	0.00	0.00	0.00	0.00	0.00	0.00	0.00	1.00	0.00
A₁₀	0.00	0.00	0.00	0.00	0.00	0.00	0.00	0.00	0.00	1.00

Figure 9(a). Confusion matrix for Weizmann Dataset (A1-Running, A2-Walking, A3-Jumping, A4-Jumping Jack, A5-Skipping, A6-Jumping at a place, A7-Side Jumping, A8-Bending, A9-Waving with one hand, A10-Waving with both hands)

	A_1	A_2	A_3	A_4	A_5	A_6
A_1	1.00	0.00	0.00	0.00	0.00	0.00
A_2	0.00	1.00	0.00	0.00	0.00	0.00
A_3	0.00	0.04	0.96	0.00	0.00	0.00
A_4	0.00	0.00	0.00	1.00	0.00	0.00
A_5	0.00	0.00	0.00	0.00	0.97	0.03
A_6	0.00	0.00	0.00	0.00	0.03	0.97

Figure 9(b). Confusion matrix for KTH Dataset (A1-Applauding, A2- Waving, A3- Boxing, A4- Walking, A5-Jogging, A6- Running)

	A_1	A_2	A_3	A_4	A_5	A_6	A_7	A_8	A_9	A_{10}	A_{11}	A_{12}	A_{13}
A_1	1.00	0.00	0.00	0.00	0.00	0.00	0.00	0.00	0.00	0.00	0.00	0.00	0.00
A_2	0.00	0.93	0.07	0.00	0.00	0.00	0.00	0.00	0.00	0.00	0.00	0.00	0.00
A_3	0.00	0.00	0.96	0.00	0.04	0.00	0.00	0.00	0.00	0.00	0.00	0.00	0.00
A_4	0.00	0.00	0.00	1.00	0.00	0.00	0.00	0.00	0.00	0.00	0.00	0.00	0.00
A_5	0.00	0.00	0.03	0.00	0.95	0.02	0.00	0.00	0.00	0.00	0.00	0.00	0.00
A_6	0.00	0.00	0.00	0.00	0.02	0.98	0.00	0.00	0.00	0.00	0.00	0.00	0.00
A_7	0.00	0.00	0.00	0.00	0.00	0.00	0.96	0.04	0.00	0.00	0.00	0.00	0.00
A_8	0.00	0.00	0.00	0.00	0.00	0.00	0.09	0.91	0.00	0.00	0.00	0.00	0.00
A_9	0.00	0.00	0.00	0.00	0.00	0.00	0.00	0.00	1.00	0.00	0.00	0.00	0.00
A_{10}	0.00	0.00	0.00	0.00	0.00	0.00	0.00	0.00	0.00	1.00	0.00	0.00	0.00
A_{11}	0.00	0.00	0.00	0.00	0.00	0.00	0.00	0.00	0.00	0.00	0.98	0.02	0.00
A_{12}	0.00	0.00	0.00	0.00	0.00	0.00	0.00	0.00	0.00	0.00	0.05	0.95	0.00
A_{13}	0.00	0.00	0.00	0.00	0.00	0.00	0.00	0.00	0.00	0.00	0.00	0.00	1.00

Figure 9(c). Confusion matrix for IXMAS Dataset (A1-Walking, A2- Waving, A3- Punching, A4- Kicking, A5-Throwing, A6- Pointing, A7- Picking Up, A8- Getting Up, A9- Sitting Down, A10-Turning Around, A11-Folding arms, A12-Checking Watch, A13-Scratching Head)

In the proposed methodology, different modes of frequencies of an action shape cover the wide range of the pose of human action. It increases the accuracy also as compared to literature [21]. Table 3 shows the comparison between these two methodologies where the accuracy of the both is comparable for Weizmann and KTH dataset but the accuracy of the proposed methodology (93.2%) is clearly superior to the IXMAS dataset where the variation in the action pose is large.

To analyze the runtime of both methodologies, NVIDIA GPU with Parallel computing Toolbox is used. The total time taken by Kapoor et al. [21] is 2.92 s, whereas the proposed methodology having 3 modes of frequency of silhouette pose takes considerably less time 1.78 s.

TABLE 3. Comparison of the proposed methodology with similar methodologies

Datasets	Methodology applied by Kapoor et al. [15]	Proposed Method
Weizmann	97.8	98.1
KTH	96.4	97.2
IXMAS	90.2	93.2

4. CONCLUSION

This is a new method to recognize human action through finite element analysis. Local features are expressed in terms of the modal frequency of the action silhouette. This offers the uniqueness of this method as it can extract both shapes as well as motion information. It overcomes the drawback of other existing state-of-the-art methods based on local features, since they are not capable of extracting both shape and motion information together. Validation of the proposed method has been performed on different datasets of challenging environments. The proposed method demonstrates its supremacy over other existing methods for both less complex datasets like Weizmann and KTH as well as complex datasets like IXMAS. The feature descriptor used in the proposed method has demonstrated very good results, but the limitation of the proposed method is that it requires a sophisticated silhouette extraction technique.

5. REFERENCES

1. Bobick, F., Davis.J. W. "The recognition of human movement using temporal templates." *IEEE Transactions on Pattern Analysis and Machine Intelligence (PAMI),* Vol. 33, No. 6, (2001), 257-267[doi: 10.1109/34.910878].

2. SouvenirR., Babbs J. "Learning the viewpoint manifold for action recognition."IEEE International Conference on Computer Vision and Pattern Recognition (CVPR'08),(2008), 1-7, doi: 10.1109/CVPR.2008.4587552.

3. Rahman S.A., Song I., Leung M.H.K., Lee I., Lee K. "Fast action recognition using negative space features." *Expert Systems Applications,* Vol. 41. No. 2, (2014), 574-587, https://doi.org/10.1016/j.eswa.2013.07.082

4. Gorelick L., Blank M., Shechtman E., Irani M., Basri R. "Action as space-time shapes." *IEEE Transaction on Pattern Analysis and Machine Intelligence,* Vol. 29, No. 12, (2017), 2247-2253, doi:10.1109/TPAMI.2007.70711

5. Grundmann M, Meier F., Essa I. "3D shape context and distance transform for action recognition."19thInternational Conference on Pattern Recognition (ICPR'08), Tampa, FL, (2008), 1-4[doi:10.1109/ICPR.2008.4761435]

6. Laptev I., Marszalek M., Schmid C., Rozenfeld B. "Learning realistic human actions from movies." IEEE Conference on Computer Vision and Pattern Recognition, Anchorage, AK, 2008, 1-8, doi: 10.1109/CVPR.2008.4587756

7. Wang Y., Mori G. "Human action recognition using semi-latent topic models." *IEEE Transactions on Pattern Analysis and Machine Intelligence,* Vol. 31, No. 10, (2009), 1762-1764, doi: 10.1109/TPAMI.2009.43

8. Wu X., Xu D., Duan L.,Luo J. "Action recognition using context and appearance distribution features." IEEE Conference on Computer Vision and Pattern Recognition (CVPR), Providence, RI, 2011, 489-496, doi:10.1109/CVPR.2011.5995624

9. Iosifidis A., Tefas A., Pitas I. "Discriminant bag of wordsbased representation for human action recognition." *Pattern Recognition Letters,* Vol. 49, No. 1, (2014), 185-192, https://doi.org/10.1016/j.patrec.2014.07.011

10. Liu L., Shao L., Li X., Lu K. "Learning spatio-temporal representations for action recognition: A genetic programming approach." *IEEE Transactions on Cybernetics,* Vol. 46, No. 1, (2016), 158-170, doi: 10.1109/TCYB.2015.2399172

11. Wang J., Zheng H., Gao J., Cen J. "Cross-view action recognition based on a statistical translation framework." *IEEE Transactions on Circuits and Systems for Video Technology,* Vol. 26, No. 8, (2016), 1461-1475, doi: 10.1109/TCSVT.2014.2382984.

12. Fu Y., Zhang T., Wang W. "Sparse coding-based space-time video representation for action recognition." *Multimedia Tools and Applications,* Vol. 76, No. 10, (2017), 12645-12658 https://doi.org/10.1007/s11042-016-3630-9

13. Gomez-Conde I., Olivieri D.N. A KPCA spatio-temporal differential geometric trajectory cloud classifier for recognizing human actions in a CBVR system," *Expert Systems Applications,* Vol. 42, No. 13, (2015), 5472-5490 https://doi.org/10.1016/j.eswa.2015.03.010.

14. Mishra O., Kapoor R., Tripathi M.M. "Human Action Recognition Using Modified Bag of Visual Word based on Spectral Perception." *International Journal of Image, Graphics and Signal Processing,* Vol. 11, No. 9, (2019), 34-43 https://doi.org/10.5815/ijigsp.2019.09.04.

15. Kapoor, R., Mishra, O. & Tripathi, M.M. "Anomaly detection in group activities based on fuzzy lattices using Schrödinger equation." *Iran Journal of Computer Science,* Vol. 3, No. 2, (2020), 103-114. https://doi.org/10.1007/s42044-019-00045-y.

16. Mishra O., Kavimandan P.S., Tripathi M.M., Kapoor R., Yadav K. "Human Action Recognition Using a New Hybrid Descriptor."In: Harvey D., Kar H., Verma S., Bhadauria V. (eds) Advances in VLSI, Communication, and Signal Processing. Lecture Notes in Electrical Engineering, Vol 683, (2021) Springer, Singapore. https://doi.org/10.1007/978-981-15-6840-4_43

17. Wu D., Shao L. "Silhouette analysis-based action recognition via exploiting human poses." *IEEE Transactions on Circuits and Systems for Video Technology,* Vol. 23, No. 2, (2013), 236-243, doi: 10.1109/TCSVT.2012.2203731.

18. Touati R., Mignotte M. "MDS-based multi-axial dimensionality reduction model for human action recognition."Canadian Conference on Computer and Robot Vision, 2014, 262-267, doi: 10.1109/CRV.2014.42.

19. Weinland D., Özuysal M., Fua P. "Making action recognition robust to occlusions and viewpoint changes"In: Daniilidis K., Maragos P., Paragios N. (eds) Computer Vision - ECCV 2010, Lecture Notes in Computer Science, (2010), 6313, 635-648 https://doi.org/10.1007/978-3-642-15558-1_46.

20. Xia L.M., Huang J.X., Tan L.Z. "Human action recognition based on chaotic invariants", *Journal of Central University,* Vol. 20, No. 11, (2013), 3171-3179, https://doi.org/10.1007/s11771-013-1841-z

21. Kapoor R., Mishra O., Tripathi M.M. "Human action recognition using descriptor based on selective finite element analysis.", *Journal of Electrical Engineering,* Vol. 70, No. 6, 2019, 443-453, doi: https://doi.org/10.2478/jee-2019-0077.

22. Kavimandan, P.S., Kapoor R., Yadav K."Human Action Recognition using Prominent Camera," *International Journal of Engineering, B: Applications,* Vol. 34, No. 02, (2021), 427-432. doi: https://dx.doi.org/10.5829/ije.2021.34.02b.14

23. Chaaraoui A.A., Pérez P.C., Florez-Revuelta F."Silhouette-based human action recognition using sequences of key poses," *Pattern Recognition Letters,* Vol. 34, No. 15, (2013), 1799-1807. https://doi.org/10.1016/j.patrec.2013.01.021.

24. Goudelis G., Karpouzis K., Kollias S. "Exploring trace transform for robust human action recognition." *Pattern Recognition,* Vol. 46, No. 12, (2013), 3238-3248 https://doi.org/10.1016/j.patcog.2013.06.006.

25. Lei J., Li G., Zhang J.,Guo Q., Tu D. "Continuous action segmentation and recognition using hybrid convolutional neural network-hidden Markov model." *IET Computer Vision*, Vol. 10, No. 6, (2016), 537-544, http://dx.doi.org/10.1049/iet-cvi.2015.0408.

26. Liu H., Shu N., Tang Q., Zhang W. "Computational model based on the neural network of visual cortex for human action recognition." *IEEE Transactions on Neural Networks and Learning Systems,* Vol. 29, No. 5, (2018), 1427-1440, doi: 10.1109/TNNLS.2017.2669522.

27. Shi Y., Tian Y.,Wang Y., Huang T. "Sequential deep trajectory descriptor for action recognition with three-stream CNN." *IEEE Transactions on Multimedia,* Vol. 19, No. 7, (2017), 1510-1520, doi: 10.1109/TMM.2017.2666540.

28. Dou J., Li J. "Robust human action recognition based on spatiotemporal descriptors and motion temporal templates." *Optik*, Vol. 125, No. 7, (2014), 1891-1896, https://doi.org/10.1016/j.ijleo.2013.10.022.

29. Laptev I., Lindeberg T. "Space-time interest points." Proceedings Ninth IEEE International Conference on Computer Vision, Nice, France, (2003), 432-439, doi: 10.1109/ICCV.2003.1238378.

30. Chittora A., Mishra O., "Face Recognition Using RBF Kernel Based Support Vector Machine," *International Journal of Future Computer and Communication,* Vol. 1, No. 3, (2012), 280-283, doi: 10.7763/IJFCC.2012.V1.75

31. Han H., Li X.J. "Human action recognition with sparse geometric features."*The Imaging Science Journal,* Vol. 63, No. 1, (2015), 45-53, doi: 10.1179/1743131X14Y.0000000091.

32. Liu L., Shao L., Li X. "Learning spatio-temporal representations for action recognition: A genetic programming approach." *IEEE Transactions on Cybernetics,* Vol. 46, No. 1, (2016), 158-170 [https://doi.org/10.1016/B978-0-12-818597-1.50072-2].

33. Mosabbeb E.A., RaahemifarK., Fathy M. "Multi-view human activity recognition in distributed camera sensor networks." *Sensors,* Vol. 13, No. 7, (2013), 8750-8770. https://dx.doi.org/10.3390%2Fs130708750

34. Hosseini M.S.,Ghaderi F., "A hybrid deep learning Architecture Using 3-D CNNs and CRUs for Human Action Recognition." *International Journal of Engineering, B: Applications, Transactions B: Applications,* Vol. 33, No. 5, (2020), 959-965. doi: 10.5829/IJE.2020.33.05B.29

Persian Abstract

چکیده

به رسمیت شناختن عملکرد انسان یک مشکل تحقیقاتی پیشگام در بین محققان بوده است. این مقاله یک توصیف کننده ویژه بومی جدید از نظر فرکانس مد با استفاده ازسایه و عناصر ساده یک شبه با کمک تجزیه و تحلیل عناصر محدود ارائه کرده است. این توصیف کننده بومی نشان دهنده حالت های متمایز انسان در قالب فرکانس مودال است. این فرکانس های مد بعد ویژگی را کاهش می دهد و طیف وسیعی از حالت های عملکرد انسان را نشان می دهد. این فرکانس های مودال تابع ماتریس سختی بدن است که با جابجایی همراه است. برای تجزیه و تحلیل از سایه های بدن انسان استفاده می شود. این سایه ها در عناصر ساده نشان داده شده اند. فرکانس مودال سایه ها با استفاده از عناصر ساده محاسبه می شود. این فرکانس های مد سایه به عنوان بردارهای ویژگی استفاده می شود که به طبقه بندی شعاع تابع پشتیبانی ماشین بردار (RBF-SVM) داده می شود. مجموعه های چالش برانگیز Weizmann، KTH و IXMAS برای اعتباربخشی روش پیشنهادی استفاده می شوند.

International Journal of Engineering

Retrofitting and Rehabilitation in Steel Moment-resisting Frame with Prestressed Concrete Slab against Progressive Collapse Potential

A. Shokoohfar*, P. Kaafi Siyahestalkhi

Department of Civil Engineering, Qazvin Branch, Islamic Azad University, Qazvin, Iran

PAPER INFO	ABSTRACT
	Diaphragms are a fundamental part of the earthquake-resistant system, and in terms of rigidity, it is essential to transmit dynamic loads on a base of the structure. Also, floor openings on the response of buildings against progressive collapse are issues that have received less attention. In this study, floor opening surfaces and their positions on the progressive collapse potential of steel moment-resisting frame (SMRF) buildings were investigated according to the alternate load path method. Moreover, to retrofit and rehabilitate the two-way reinforced concrete (RC) slabs against a progressive collapse, two strategies, prestressed concrete slabs and installing carbon fiber reinforced polymer sheets on the surface of the old concrete slab, were proposed and six-story SMRF buildings were simulated using the finite element method. The maximum axial force around the removal column is 20% greater than the corresponding values on the floor opening is in the corner of the plan and the appropriate performance of the prestressed concrete slab leads to the load distribution in the ceiling diaphragm.

1. INTRODUCTION

Progressive collapse is a phenomenon in which one or several main members of a structure suddenly fail, and a total or a large part of it undergoes failure [1-3]. The mentioned initial damage in the above definition can occur in different members such as beams, columns, floors, load-bearing walls, etc. Although, the probability of these accidents occurring in ordinary buildings is not significant, this phenomenon becomes a critical and important issue when it may be with many humans, economic, and security losses.

Airplane impact, design or construction errors, fire, gas explosions, accidental overload, hazardous materials, vehicle collisions, bomb blasts, etc., are some of the unusual loads that can lead to the progressive collapse of buildings [4-6]. Because the probability occurrence of these hazards is low; they are not considered in the structural design or indirectly investigated by the passive defense protection measures. Most of these loads happen in a short period and lead to dynamic responses [7, 8].

Many buildings have suffered a progressive collapse in recent decades. Figure 1 demonstrates a timeline of the most important progressive collapse events all over the world. Mark's Campanile collapse [9], the University of Aberdeen Zoology building demolition in Scotland [10], the partial destruction of the Ronan Point tower in England [11], the destruction of the U.S. Embassy in Beirut in Lebanon [12], L'Ambiance Plaza progressive collapsed in the United States [13], Murrah building explosion in the USA [14], demolition of Sampoong department store in South Korea [15], progressive collapse of Khobar Towers in Saudi Arabia [16], airstrikes on world trade center tower in the USA [17], demolition part of the Tropicana Parking Garage in the USA [18], demolition part of Saadatabad building in Iran [19], demolition of Margalla towers in Pakistan [20], demolition of Plasco building in Iran [6] and demolition part of Beirut buildings in Lebanon [21] are the progressive collapse events that can be mention. The above-mentioned events have resulted in deaths and injuries of significant number of human beings. A review

Corresponding Author Email: ahmadshookoohfar@gmail.com (A. Shookoohfar)

of other similar accidents worldwide showed that the progressive collapse potential of buildings could be decrease by safety improvement, repairing, and strengthening damaged structures. The timeline of the most important progressive collapse events all over the world is shown in Figure 1.

Numerous studies have been performed on progressive collapse. Each study evaluated part of this phenomenon. Many studies have been performed to investigate the contribution of structural members such as beams and columns in the vicinity of the removed column and the effect of different lateral bearing systems against progressive collapse [22-30]. In other studies, different types of progressive collapse analysis methods were investigated [31-38]. Several researchers investigated different types of beam-column connections on the response of concrete and steel structures against progressive collapse [39-43]. On the other hand, various studies were conducted to evaluate the vulnerability of masonry buildings, and the importance of rehabilitation of these structures was raised [44-46].

Ozturk et al. [47] studied the retrofit methodology by adopted fiber reinforced polymers (FRP) material on the existing building, analysis results showed that there are improvements in stable maximum drift due to apply of FRP as compared with the control building. Ozturk. [48, 49] studied the focuses on a displacement-based approach for analyzing the seismic behavior of two monumental buildings located in the historical

Cappadocia region of Turkey. Modal, response spectrum, and dynamic analyses for different ground motions were applied to these building models. It is observed that slab discontinuities on the gallery floor constitute a major element in the structural damage expected for the building.

Various studies were performed on the response of steel moment-resisting frames (SMRFs) against progressive collapse. The response of SMRFs against various scenarios of progressive collapse due to fire was investigated. Dynamic analysis was used for this purpose. A method was proposed to consider the heat caused by a fire in the progressive collapse process [50]. The progressive collapse behavior of steel frames with different beam-column connections was investigated. The results showed that welded flange plate (WFP) connections have higher flexural strength than bolted [51]. Beam-column connections with reduced cross-section against progressive collapse were investigated. The results showed that in connections with reduced cross-sections, the diameter and distance of the web openings are among the important parameters that affect structure response against progressive collapse [52]. Progressive collapse due to a fire in the Plasco building in Tehran (Iran) was investigated. The results showed that the building vulnerability was due to insufficient ductility and structural continuity, which led to the spread of damage to the entire structure [6]. The vulnerability of
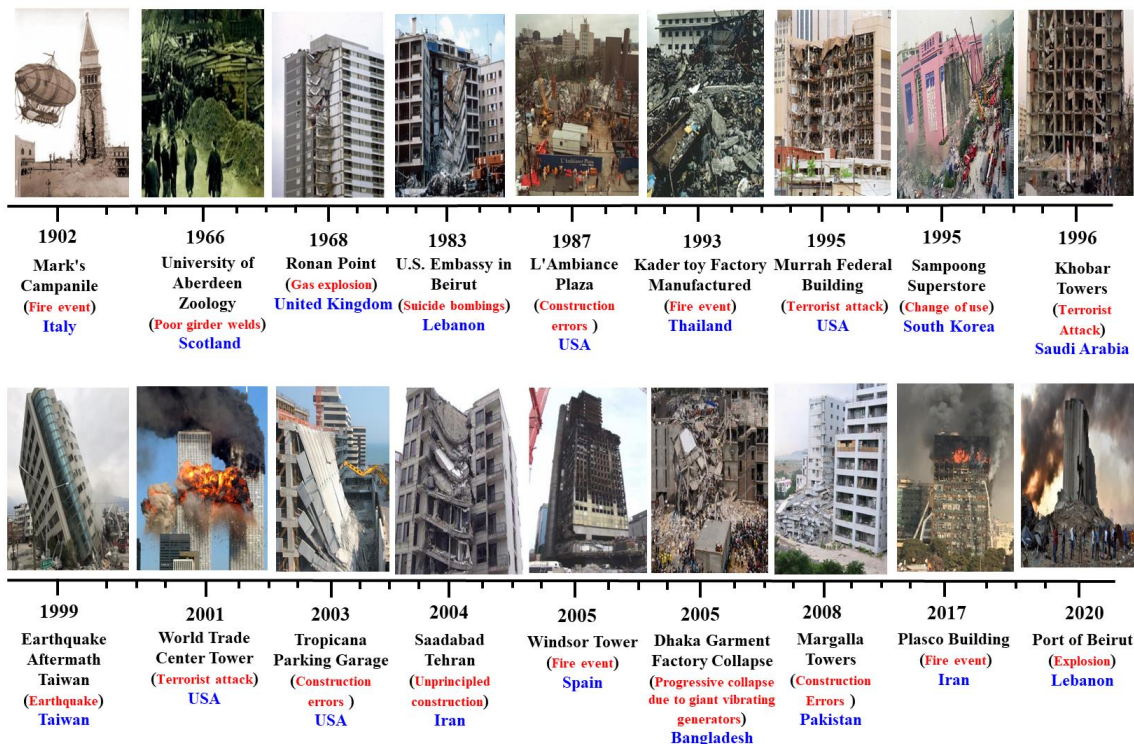
Figure 1. Timeline of the most important progressive collapse events all over the world

buildings with irregular voided located in seismic areas was investigated. The results showed that the structures situated in high seismic zones could pass progressive collapse analyses. The seismicity level of the site is more important than another parameter, such as the height or irregularity of the structure [45].

One of the important members of the structure that has been less studied than other members is the effect of the floor contribution on the strength of the structure to progressive collapse. The floor system is one of the elements that resist progressive collapse due to removing the column.

The roof system of many old steel buildings must be retrofit. The seismic performance of the old steel structures depends on the quality of the welding procedure and the tensile strength of the steel used. With proper welding quality and proper material specifications, there are several major disadvantages in older steel buildings that cause severe earthquake damages. The brick arch panels are generally used as floor systems in the old steel buildings of Iran. These floors were composed of steel beams and compression bricks. The brick arches are not well in earthquakes due to the lack of integration and high weight. An example of these buildings is shown in Figure 2. Flexural forces redistribution and the shear response, interaction with columns for increasing frame performance, and membrane performance are factors that can affect the redistribution of gravitational forces in the damaged buildings. Immediately after the column's destruction, the column bends, bending cracks, rebar yielding of the slab occur, and the beam forces increase [54]. These axial compressive forces can have a major effect on the flexural behavior and changes in the vertical load-bearing capacity of the beams. The forces created inside the roof diaphragm help reduce the vertical displacement of the top point of the removed column and thus help to improve the behavior of the structure against progressive collapse.

In fact, today, openings are created in the building floors in many buildings due to architectural considerations. Since in the studies of progressive collapse, little attention has been paid to the effect of opening on the floors with reinforced concrete (RC) slabs, in the present study, this issue is investigated. On the other hand, the slab opening leads to a change in the structural response of progressive collapse. Thus, in the present study, by simulating the opening in RC slabs and changing the dimensions and position of these openings in SMRF buildings, the effect of size and opening position on the resistance of the SMRF buildings against progressive collapse will be investigated.

Most modeling to progressive collapse using software analysis was investigated. Engineers' familiarity with this software doubles the need to clarify vague angles of modeling this phenomenon in such software. ABAQUS [55] software has a more prominent position among this software due to its suitable capabilities. However, little research has been done on floor modeling in this software in the face of progressive collapse. In most modeling, the effects of the floor simulation on progressive collapse have been ignored. In this study, the effect of definable characteristics of floor diaphragm in ABAQUS software was applied for progressive collapse analysis of SMRF buildings. Two strategies of retrofitting and improvement of floor diaphragm were proposed.

Prestressed concrete slabs were used for rehabilitation, and their performance was compared with conventional reinforced concrete (RC) slabs. Prestressing is a method of reinforcing concrete or other materials with high-strength steel strands or rebars. Concrete slabs based on prestressing methods have significant architectural, structural, and economic advantages. Thus, one of the most important objectives of the present study is to investigate the effect of slab prestressing on the progressive collapse of steel buildings. Carbon Fiber Reinforced Polymers (CFRP) can increase the load-bearing capacity of the structure, improve the building performance in bearing live loads or restore the lost strength of the floor and slab due to steel corrosion. The results of previous studies have shown that the strength of the floor and slab significantly improves after retrofitting with CFRP, and they can be easily glued over concrete floors and slabs due to low thickness and easy installation. Retrofitting of floor and slab with CFRP can also act as insulation and increase the structure's load-

Figure 2. Demolition of the brick arch panel in a steel building to strengthen in Iran

bearing capacity and achieve the desired performance in the structure. Strengthening the floor and slab with CFRP increases the shear and flexural strength, and It retrofits the structure against corrosion, vibration, and abrasion and ultimately improves the performance level of the structure against earthquakes [56-62]. Due to the mentioned advantages in the present study and several cases, CFRP sheets are used to increase the resistance of the floor slab against progressive collapse. The flowchart of the study process is shown in Figure 3. Details and variables are presented in the next section.

2. INTRODUCING THE STUDIED BUILDINGS

Variables include floor opening position (corner and middle of plan), floor opening dimensions (4000×10000 and 6000×12000 mm), and floor slab condition (two-way RC slab, prestressed reinforced concrete slab, retrofitting two-way RC slab with CFRP). For this purpose, six-story SMRF buildings were modeled and analyzed in Figure 3.

All modes are summarized in Table 1. All the buildings have the same plan, and the height of each story was considered 3200 mm. The building lateral load-bearing system is an intermediate moment-resisting frame in both x and y directions. The plan dimensions of the studied buildings and the location of the openings are shown in Figure 4. The steel used is St37 building steel with 370 MPa ultimate strength and 240 MPa yielding strength. Etabs [63] software and load-resistance factor design were used for modeling and analysis. The importance level of buildings concerning residential use is medium importance. Two-way RC slabs were considered as floors in the initial design. The thickness of

the concrete slab was 250 mm, and reinforcing bars with a diameter of 14 mm was used at intervals of 150 mm.

The dimensions and specifications of the designed sections are presented in Table 2. The beam cross-sections of the first to the third floor, fourth to the fifth floor, and sixth floor were considered IPE550, IPE500, and IPE450, respectively. Also, the cross-sections of the columns for the first to second levels Box400×400×30, for the third to fourth levels Box400× 400×20 and the fifth and sixth levels Box400×400×14 were considered. After determining the beams and columns sections, all the buildings were simulated in three dimensions using ABAQUS software. Etabs is an advanced software in building modeling. Still, due to some limitations, such as the inability to simulate concrete slab cracks and very low outputs, the phenomenon of progressive collapse cannot be simulated using this software. Nonlinear dynamic analysis by direct integration method was used to evaluate the progressive collapse. Details of finite element simulation are provided below. The results of studies on progressive collapse show that the corner columns removal on the ground floor leads to far more critical responses [64-66]. Thus, in all cases, A1 and B1 columns on the ground floor were removed.

3. FINITE ELEMENT SIMULATION

The structural elements considered in this research include beams, columns, two-way RC slab, prestressed slabs, and CFRP. The beam and column sections were defined using the Beam element, and steel rebar was used wire. Also, concrete slab and CFRP sheets were defined using shell elements. In this study, the concrete damage plasticity model (CDPM) was used to define concrete.
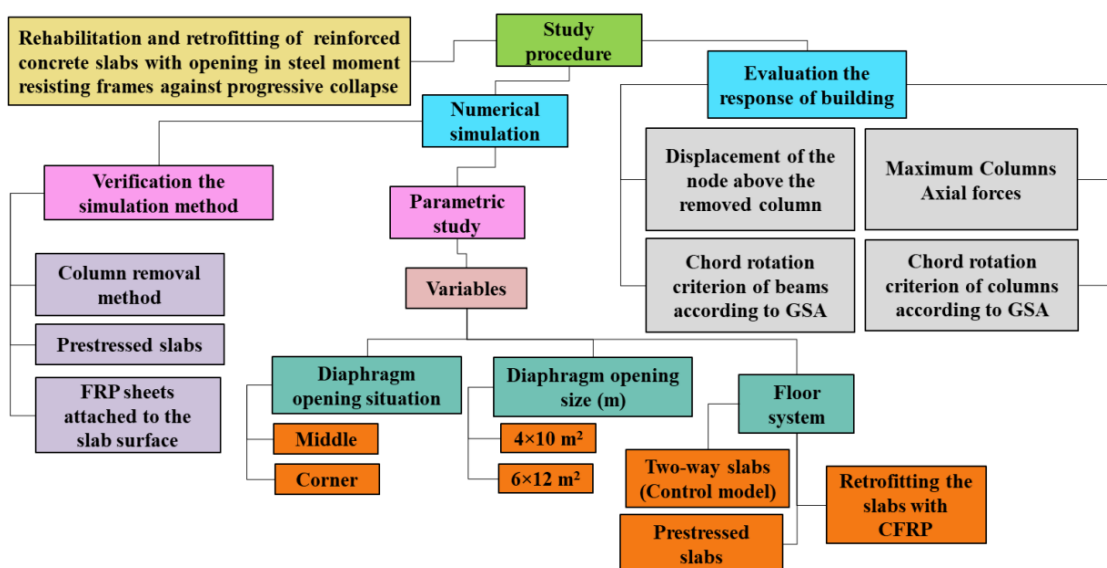
Figure 3. Research process

TABLE 1. Introducing the investigated cases

Case	Floor opening situation	Floor opening size (m)	Concrete slab type	Columns removed at ground floor
1	Corner	4×10	Two-way RC slabs	A1 & B1
2	Middle	4×10	Two-way RC slabs	A1 & B1
3	Corner	6×12	Two-way RC slabs	A1 & B1
4	Middle	6×12	Two-way RC slabs	A1 & B1
5	Corner	4×10	Prestressed RC slabs	A1 & B1
6	Middle	4×10	Prestressed RC slabs	A1 & B1
7	Corner	6×12	Prestressed RC slabs	A1 & B1
8	Middle	6×12	Prestressed RC slabs	A1 & B1
9	Corner	4×10	Retrofitting RC slabs with CFRP	A1 & B1
10	Middle	4×10	Retrofitting RC slabs with CFRP	A1 & B1
11	Corner	6×12	Retrofitting RC slabs with CFRP	A1 & B1
12	Middle	6×12	Retrofitting RC slabs with CFRP	A1 & B1

TABLE 2. Column and beam sections

Case	Designation	Flange thickness (mm)	Web thickness (mm)	Width (mm)	Depth (mm)	Mass/meter (kg/m)
	IPE400	13.5	8.6	180	400	66.3
Beam sections	IPE450	14.6	9.4	190	450	77.6
	IPE550	17.2	11.1	210	550	106
	Designation	**Thickness (mm)**		**Width (mm)**	**Mass/meter (kg/m)**	
	Box450×450×30	30		450	200.2	
Column sections	Box350×350×30	30		350	157.8	
	Box300×300×30	30		300	134.2	
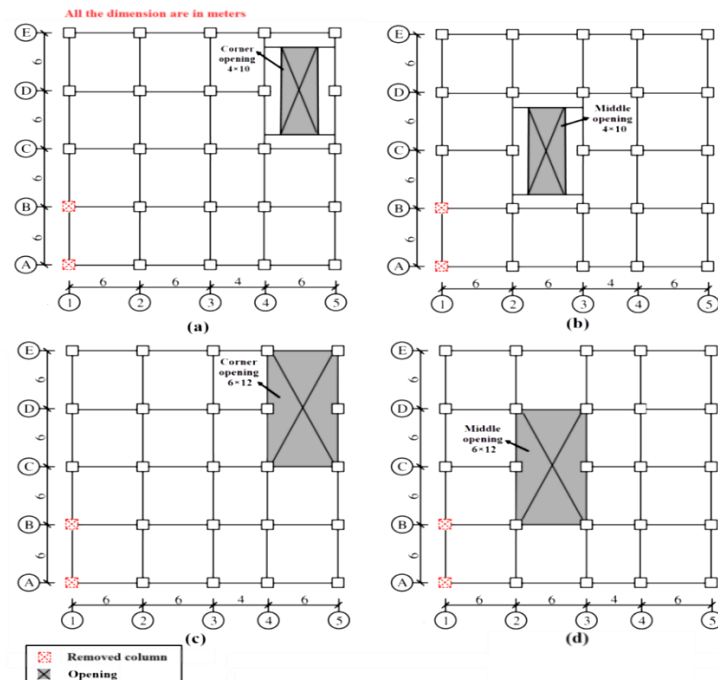
Figure 4. Typical plan layout of the model with different floor opening situation (a) Corner opening (4×10 m) (b) Middle opening (4×10 m) (c) Corner opening (6×12 m) (d) Middle opening (6×12 m)

This section considered the characteristics of damage index in compression (dc) and tension (dt). The parameters are shown in Figure 5.

The CDPM is based on similar damaged and is designed for concrete under ideal loadings. The effect of reducing elastic hardness resulting from plastic strains under both tension and pressure is considered in this model. The development of stiffness recovery effects during loads is also considered. Due to the fact that in the concrete damaged plasticity model, the concrete properties are defined both under tension and pressure for the program, and this model can consider the effect of reducing concrete hardness affected by hysteresis loading. Therefore, the concrete damaged plasticity model is the most suitable option for beam modeling in this project. The detailed analysis of this model and its parameters are discussed in Equations (1-3).

$$\varepsilon_t^{cr} = \varepsilon_t - \varepsilon_t^{el} \tag{1}$$

$$\varepsilon_t^{el} = \frac{\sigma_t}{E_0} \tag{2}$$

$$\varepsilon_t^{\sim pl} = \varepsilon_t^{\sim ck} - \frac{d_t}{(1-d_t)} \frac{\sigma_t}{E_0} \tag{3}$$

To define the elastic behavior of rebar, it is necessary to define the elastic modulus and the Poisson's ratio, equal to 210000 MPa and 0.3, respectively. The density of steel was considered 7850 kg/m³. However, this behavioral phase is responsible for small applied loads. To determine the exact behavior of materials at large applied loads, it is necessary to define the yield and ultimate point. The used steel is St37 building steel. For steel components, the strength such as the yield point is 240 MPa, and the strength such as the failure point is 370 MPa. The characteristics of the materials used in the present study are given in Table 3. The model's damping coefficient was 5%—used Riley's method to define the
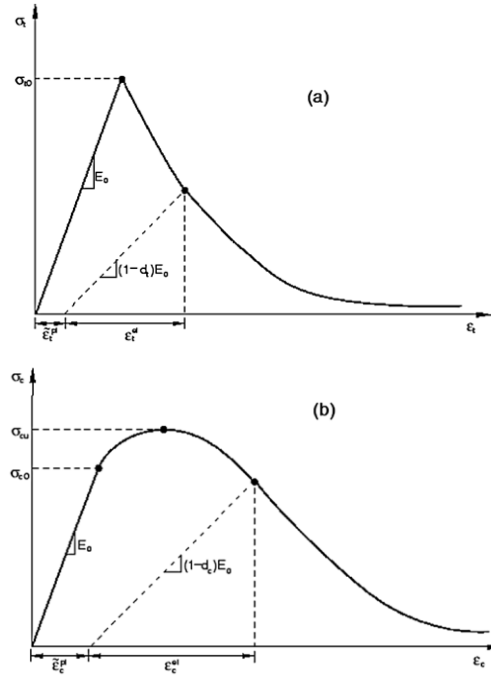
Figure 5. CDPM parameter, (a) tension (b) compression

damping of the structure. By extracting the alternation times of the structure and calculating its natural frequency, the mass damping coefficient (α) and the stiffness damping coefficient (β) according to Equation (4) were obtained and defined in ABAQUS software.

$$\xi = \frac{\alpha}{2\psi_n} + \frac{\beta \psi_n}{2} \tag{4}$$

Shell and Truss's elements were used for S4R and T3D2 meshing, respectively. To determine the optimal mesh in modeling used the method of examining the convergence of the responses. According to Figure 6, the structure was analyzed, and to correct the mesh method, collected the maximum stress in beam and column in structure. The mesh in the present study is considered to be 80 mm.

TABLE 3. The mechanical properties of materials (Units: Newton, Meter)

Concrete	Young's modulus	Poisson's ratio	Plasticity parameters of concrete				
			Dilation angle (ψ)	Eccentricity (m)	F_{bo}/f_c	Kc	Viscosity parameter
	3×10^{10}	0.2	31	0.1	1.16	0.667	0.001
	Young's modulus	Poisson's ratio	Yield strength	Tension strength	Elongation (%)		Equivalent diameter
Steel	2.1×10^{13}	0.3	390×10^6	560×10^6	30		---
Prestressed Steel	1.8×10^8	0.3	16.87×10^8	18.11×10^8	3.5		13.35×10^{-3}
CFRP	Young's modulus	Poisson's ratio		Thickness	Tension strength		Elongation (%)
	10075×10^7	0.22		11×10^{-5}	4200×10^6		1.8

The distribution of the loads by the prestressed cables in each direction depends on the support distance in different directions. The prestressing force of cables was obtained according to Equation (5):

$$P = q.r \tag{5}$$

In this relation, q is the amount of external load perpendicular to the cable in width of one meter, and r is the average radius of curvature of the cable. In the case of using cables with the relatively low friction coefficient and length of 30 to 40 meters, the area of prestressed cable with a suitable approximation of Equation (6) is obtained:

$$A_P = \frac{p}{0.95 \times 0.65 \times f_{pk}} \tag{6}$$

f_{pk} is the amount of stress on the prestressed cable.

According to the used cables, the limit stresses due to friction are obtained from Equation (7):

$$P_x = P_j \times e^{-(\mu\alpha + Kx)} \tag{7}$$

where, P_x = Stress at distance x from the jacking point, P_j = stress at jacking point, μ = coefficient of angular friction, α = total angle change of the strand in radians from the stressing point to distance x (Figure 7), K= Wobble coefficient of friction expressed (rad. per meter).

The initial step is to simulate prestressed axial load and the initial tensile stress applied to the rebars. To transfer the prestressing of the rebar to the concrete slab, the stresses were applied in the initial step, and in the next steps, the applied tensile stresses cause pressure in the concrete slab (Figure 8).

Dynamic Explicit analysis was used for nonlinear dynamic analysis, and this type of analysis makes it possible to define general contact conditions and apply large deformation theory. For this purpose, two steps are defined: the first step of prestressed loading and the second step by gravity loading in structure. Tie constraints were used to define interaction and contact between all surfaces [7, 8]. This constraint allows combining two surfaces whose meshes are different from each other and is one of the most widely used constraints in civil engineering.
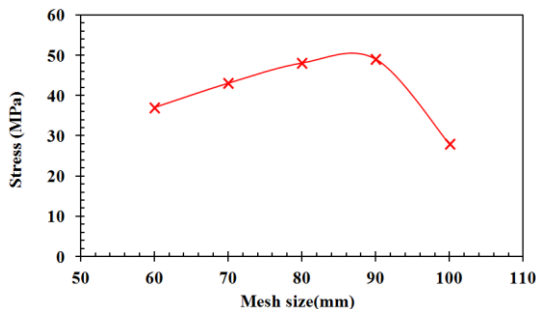
Figure 6. Mesh sensitivity analysis of the studied steel structures
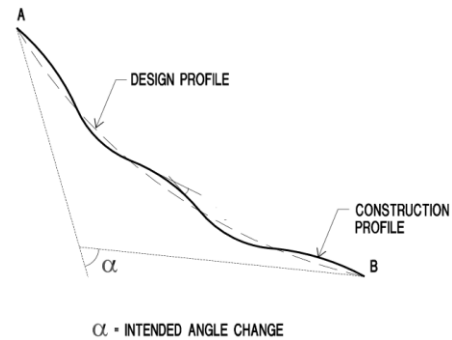
Figure 7. α parameter in prestressed cable relations
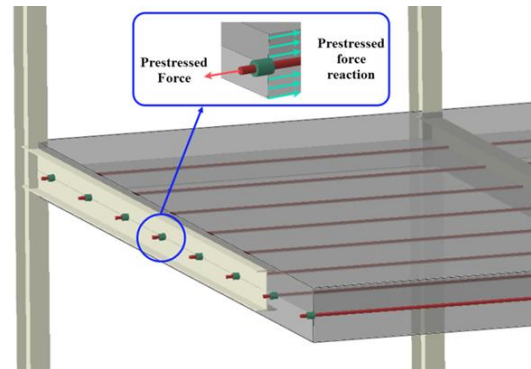
Figure 8. Simulation of prestressed slab floor in SMRF buildings

For gravitational loading of the structure, in addition to the gravitational force of the ground, a load combination related to progressive collapse was applied. In nonlinear dynamic analysis, the removal column is not modeled from scratch. Unlike nonlinear static analysis, in nonlinear dynamic analysis, the internal loads of the column removal site must be applied to the top of the removed column to be applied in one step under another impact load and zero the column load. To define the supports, the end of the columns was tied in all directions, and movement and rotation were prevented. To simulate the sudden removal of the column, columns B1 and A1 were first removed from the model. The internal forces of the column were applied in the opposite direction at the location of the column node. According to UFC2009, the removal time of these forces must be less than 0.1 vertical rotation time of the structure in the vertical movement mode above the column. In this study, to define the boundary conditions, the ends of all columns are defined as fixed. This support prevents movement and rotation. The loads applied to the structure include the weight of the structural components (beams, columns, and slabs), dead and live loads on the structure floor, and the progressive collapse potential was Evaluate by considering the alternative load path model. In this method, the structure is designed so that if a member is removed and the load transfer path is damaged, there are

other alternative paths for transferring the load to the ground. Thus, structures are designed to remove special columns or walls [2]. The assessment of progressive collapse potential was performed using the alternative load path method, independent of the collapse factor, and proposed by GSA and DOD [1]. The removal site columns in the studied models were removed for modeling in the software, and loading was done according to UFC regulations [1]. The applied loads were applied to the studied models as a combination of the following loads.

- Gravity load increased was used for the floors above the removed columns. This combination of load should be affected in the form of intensified gravity load as follows on the openings adjacent to the removed elements in all floors above these elements:

$$G_{LD} = \Omega_{LD}[(0.9 \text{ or } 1.2) D + (0.5L \text{ or } 0.2S)] \qquad (8)$$

G_{LD}= Gravitational intensified load for deformation-controlled efforts in the linear static method
D = Dead load considering the exponential load
L = Live load
S = Snow load
Ω_{LD} = increase coefficient to calculate the deformation control effort

- And the gravitational load on the other surfaces of the roof is obtained from the following equation with the G load combination:

$$G = [(0.9 \text{ or } 1.2) D + (0.5L \text{ or } 0.2S)] \qquad (9)$$

In this Equation (9), G is gravity load.

4. VALIDATION

Validation is done to ensure the output results of ABAQUS software. Because in this software, there are many options for modeling geometry, the interaction between components, loading method, etc., and changing each of them can vary the analysis results. Thus, by comparing the results of the experimental samples with the ABAQUS numerical models; it can be shown that the modeling is correct. Then, new results can be obtained by changing the parameters. Three parallel issues were investigated in the present study: progressive collapse due to removing the column in steel buildings, simulation of prestressed concrete slabs, and simulation of CFRP sheets installed on concrete surfaces. Thus, three different laboratory studies were selected and simulated using the used simulation method in the present study.

4. 1. Investigation Accuracy of the used Method for Column Removal (Alternative Load Path Method)
The accuracy of the simulation method used in column removal was evaluated by simulation of an experimental frame made in the study of Guo et al. [67]. The frame has one floor and four spans made in the laboratory with a

1:3 scale. The length and height of each frame span were considered 2 and 1.20 meters, respectively. The steel beams were completely welded to the flange of the columns as the beam-column connections have rigid. The cross-section of the beams was H 200×100×5.5×8, and the cross-section of the columns was H 200×200×8×12. (Numbers after H in order are: d: total height of section; bf: flange width; tw: web thickness; tf: flange thickness). The slab's width and depth were 800 and 100 mm, respectively. The steel percentage of reinforcement mesh was considered 0.85%. Longitudinal reinforcement bars with a diameter of 12 mm were placed in two layers at equal distances along the slab width. Also, transverse reinforcing bars were used with 8 mm diameter in the steel reinforcement mesh to prevent concrete failure. To simulate the column removal, the middle column also has no support. The column's bottom was welded to a beam attached to the ground to create fixed support. The behavior of the frame and the concrete slab was evaluated during the test. For this purpose, a linear variable differential transformer (displacement sensor or LVDT) was placed vertically in the middle of the frame at the column C location. Also, four displacement sensors were used to measure the displacement of columns A, B, D, and E. A hydraulic jack with 500 kN load capacity was used on the top of column C for applying vertical load. Also, a 1000 kN load measuring device was used to measure the vertical load. Using this method and the mentioned devices, it was easily possible to investigate the redistribution and transmission of internal force after removing the frame middle column. The load was applied according to JGJ 101-96 [68].

The load-deflection controlling method was used until the frame reached ultimate capacity. The load-deflection diagram of the laboratory sample, the models of Guo et al. [67] and the present study is shown in Figure 9. The maximum load and corresponding deflection in the laboratory study were 400 kN and 440 mm, respectively. The maximum load in the finite element study with ABAQUS software was also done by Guo et al. [67]. It is 450 kN, with a corresponding displacement of approximately 500 mm. The maximum load of the model simulated by the method used in the present study is 412 kN, with a corresponding deformation of approximately 452 mm. Thus, the maximum displacement values and ultimate load in the finite element modeling method used in this study, which was performed using ABAQUS software, have a relatively good accuracy compared to the laboratory study.

4. 2. Evaluation of the used Method Accuracy in Simulating CFRP Sheets Installed on Reinforcement Concrete Slab
This section investigated the validation of the finite element method (FEM) used to simulate CFRP sheets installed on reinforcement concrete slab. For this purpose, a reinforced concrete slab made in the laboratory study

(a)

(b)

(c)
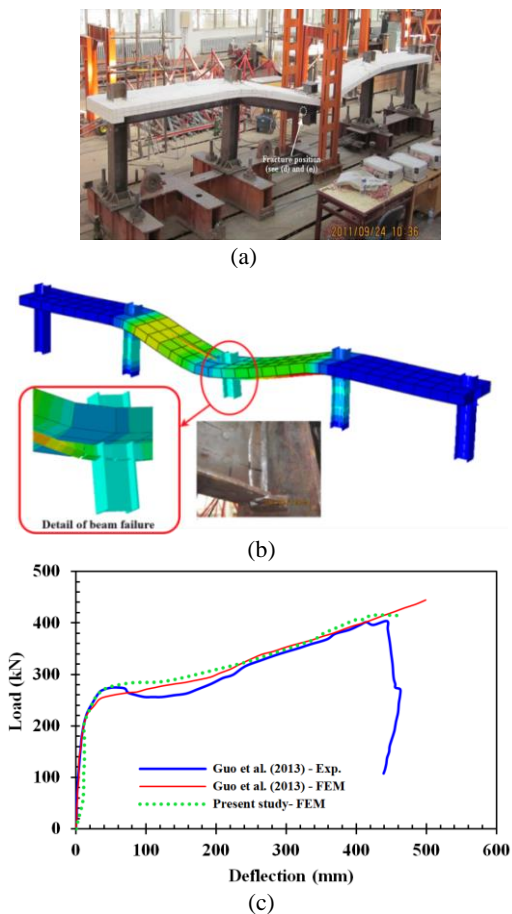
Figure 9. Verification of progressive collapse analysis using APM a: Experimental specimen [88] b: FEM in this study c: Comparison of load-displacement diagrams

of Flurat et al. [68] was simulated using the FEM and the technique used in the present study.

In the Flurat et al. [68] study, reinforcement concrete slabs were tested in 3 different modes (Figure 10). Among these models, FS-01-FRP (slab without opening and retrofitted with CFRP) and RLC-02-FRP (slab with opening and retrofitted with CFRP), and RLC-02 (slab with opening and without retrofitting) were selected for validation.

Two of the three selected specimens have CFRP sheets installed using near-surfaces mounted and externally bonded methods. The characteristic compressive strength of the concrete used in the FS-01-(CFRP) and RSC-01 (CFRP) modes was 65 and 62 MPa, respectively. The longitudinal and transverse reinforcing steel were ribbed rebar type. CFRP fibers with a near-surface mounted method have an elastic modulus of 165 GPa and a failure strain of 1.7%. Also, the thickness of the used CFRP sheets is 1.2 mm. Also, CFRP sheets in EBR method had an elastic modulus of 231 GPa and a rupture strain of 1.7%. Also, the thickness of the used CFRP sheets was 0.12 mm. The load was applied incrementally on the upper surface of the reinforcement

concrete slab (center of the slab), and the corresponding displacement was recorded.

Load and displacement values of finite element and laboratory models of FS-01-FRP slabs (slab without opening and retrofitted with CFRP), RLC-02-FRP (retrofitted slab with opening), and RLC-02 (slab with the opening without retrofitting) are shown in Figure 10. As can be seen in this diagram, the maximum load and displacement values obtained from the laboratory specimens and the finite element are close to each other; thus, can say that the finite element simulation method used in the present study can predict the behavior of reinforced concrete slabs reinforced with CFRP sheets with good accuracy. Also, by observing the cracks in slab , the values of the stresses in concrete slab are consistent with the values of the stresses created by the finite element method.

4. 3. Evaluating the Accuracy of the Method used in Simulating Prestressed Slabs
Bailey and Ellobody [69] laboratory study was used to validate the method used in simulating prestressed slabs. Four experiments under heat and two experiments at ambient temperature were performed on strips of prestressed slabs with similar discontinuous tendons. Two post-tensioned slab specimens, T1 and T2, were tested under ambient temperature to determine slab capacity under normal conditions. Four test specimens T1, T2, T3, and T4, were heated using a gas furnace. From these models, T1 model was selected for validation. Post-tensioned concrete slabs were designed by BS 8110-1. The tendons were made of a high-strength 7-strand steel rope. The slabs' length, width, and depth were 4300, 1600, and 160 mm, respectively. The span of the tested slab was 4 m. Each slab had three parabolic tendons with a diameter of 15.7 mm and an area of 150 mm^2, and average tensile strength of 1846 MPa.

According to Figure 11a, one tendon was placed in the middle of the slab and the other two on both sides at a distance of 530 mm. The two tendon ends were located exactly in the center of the slab depth at the restraint site. The distance between the lower surface of the slab and the tendon center was 37 mm. Steel seats to build the second-degree parabolic path for the tendon were used. Details of the used restraints are shown in Figure 11b. The high compressive strength from the cable to the concrete at the abutment creates tensile stress around the restraints. Other specifications are provided by Bailey and Ellobody [69].

The accuracy of modeling depends on the input data completeness and their precision. The main inputs of this problem include the material's stress-strain curve characteristics. To verify the sample, T1 specimen used. A load-deflection diagram in the middle of the span was obtained and compared with laboratory results. It is impossible to provide a model that exactly matches the experiment results; thus, changing various parameters
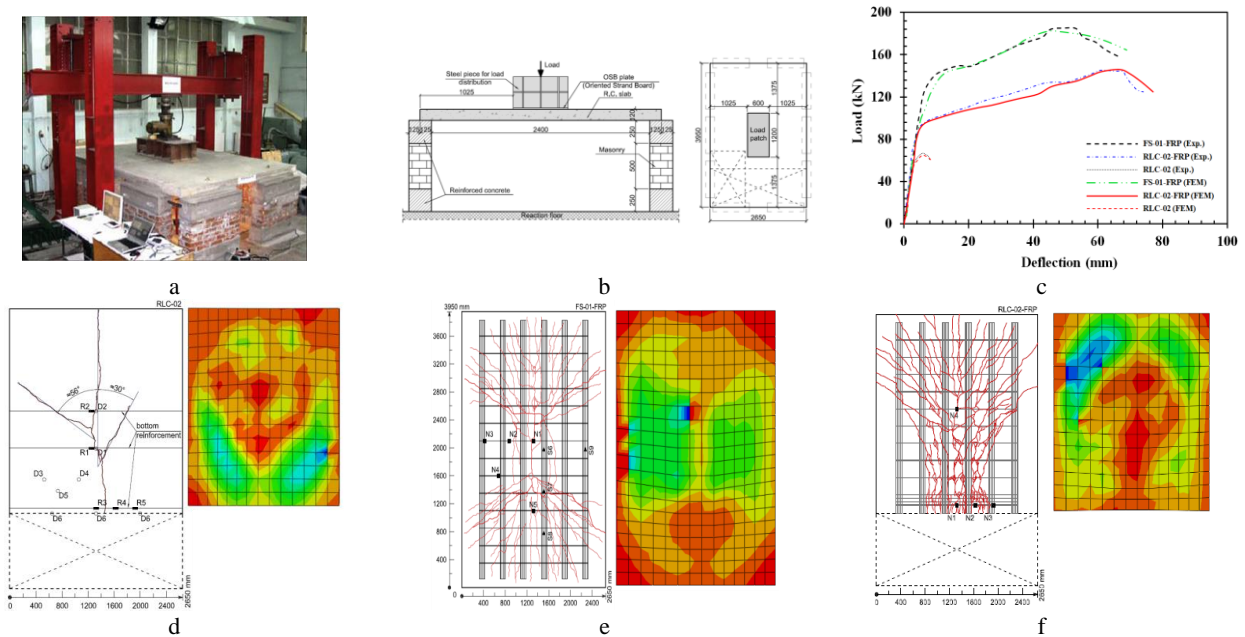
Figure 10. Verification of the finite element method used in a simulation of the CFRP sheets on the surfaces of the concrete slabs (a) The slab specimen in the experimental study of Flurat et al.[89] (b) Geometric properties (c) load-deflection curves (d) RLC-02 FEM in this study (e) FS-01-FRP FEM in this study (f) RLC-02-FRP FEM in this study

such as concrete plastic properties, mesh, constraints, boundary conditions, etc., must achieve an acceptable error. Comparison between laboratory and analytical model curves are shown in Figure 11c. The experimental and the numerical achieved ultimate loads were 156.6 kN and 157.3 kN, respectively. The ultimate load predicted by the model has an error of 0.44% compared to the laboratory model and is acceptable with a good approximation.
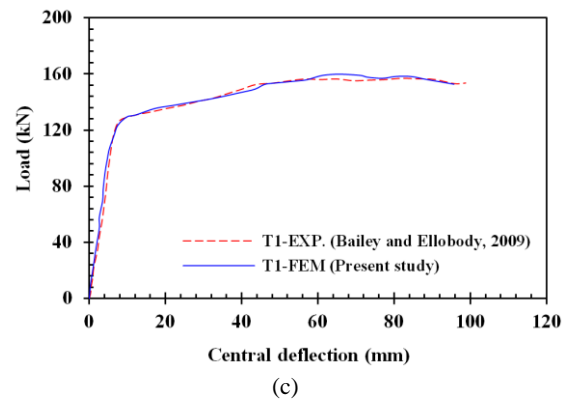
Figure 11. (a) Prestressed concrete slabs made in Bailey and Ellobody [90] laboratory study (b) Displacement contour of finite element model of T1 slab in this study (c) Comparison between the proposed model and laboratory results of load-deflection at ambient temperature
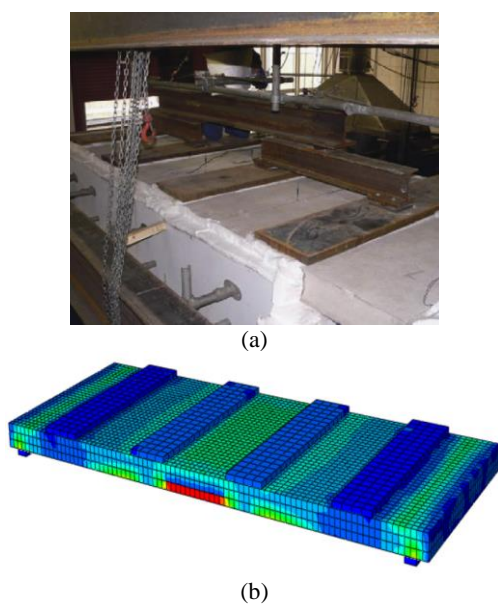
5. RESULTS OF COLUMN REMOVAL ANALYSIS

The progressive collapse trend was investigated after modeling and analyzing the buildings. Since all sections were designed to withstand earthquakes and there are no earthquake-related loads in the event of progressive collapse, it is possible that even with the removal of some main load-bearing members; other columns still have sufficient capacity to withstand incoming loads. The outputs for each of the modes are provided below.

5. 1. Use of Two-way RC Slab as a Floor System

According to Figure 12, in SMRF buildings with two-way RC slab, two corner columns on the ground floor were removed. The axial force of column B2 in the buildings with a two-way RC slab floor system is shown in Figure 13. The reason for choosing column B2 is that this column is located most adjacent to the removal columns. After the removal process, more axial force is created in it compared to other columns.

When the floor opening is located in the corner of the building plan, and the floor opening dimensions are 4×10 and 6×12 square meters, the axial force of column B2 is equal to 2700 and 2498 kN, respectively. Then over time of analysis, these loads reached 2217 and 2498 kN. The axial forces are created in column B2 when the floor opening is in the middle of the building plan and dimensions are 4×10 and 6×12 square meters, are about 2900 and 3450 kN, respectively, which over time of analysis reduces to 2489 and 2990 kN.

According to the mentioned, it can be stated that in SMRF buildings with two-way RC slab floor system, which is exposed to the removal of corner columns, opening the floor in middle compared to corner, created more axial forces around the removal place. Thus, in a SMRF building with a two-way RC slab where the floor opening is located in the middle compared to the corner, depending on the floor opening dimensions, the axial

forces created around the removed column are more than 18 to 20 percent.

On the other hand, in SMRF buildings with a two-way RC slab floor system, increasing the floor opening dimensions from 4×10 to 6×12 square meters, depending on the floor opening location, the axial force has increased 12 to 19 percent.

The vertical displacement in column removal location is another criterion used to investigate the buildings against progressive collapse. The displacement history of the node above the removed column (column B2) for states 1 to 4 is shown in Figure 14. The largest displacement is related to the case that in the two-way RC slab floor, opening with dimensions of 6×12 square meters is located in the middle of the plan, and its value is 19.3 mm.

Also, the least displacement is related to the situation in the two-way RC slab floor, an opening with dimensions of 4×10 square meters is used in the corner of the plan, and its value is 13.1 mm. According to the obtained displacement values, the choice of floor opening dimensions and location has an impact on the response of steel structures to the removal of the columns; also, the floor opening position has increased the vertical displacement of the node above the removed column by about 25 to 33%, depending on the dimensions of the opening.

Fully damage   **Undamaged**
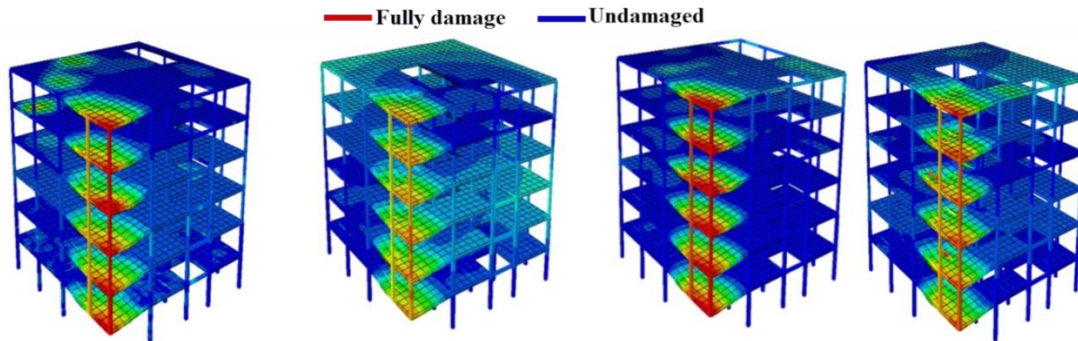
Two-way RC slabs- Cor-4×10   Two-way RC slabs-Mid-4×10   Two-way RC slabs- Cor-6×12   Two-way RC slabs-Mid-6×10

Figure 12. Deformed shape in buildings with Two-way RC slabs after removing columns
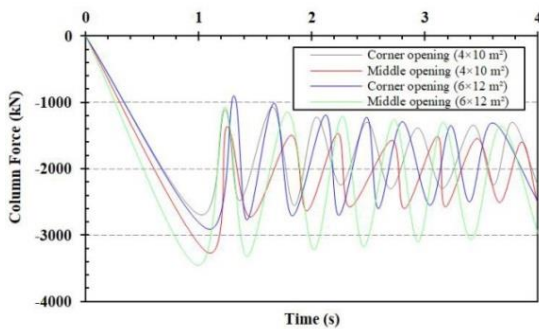
Figure 13. The axial force of the column B2 at the ground floor (Two-way RC slab cases)
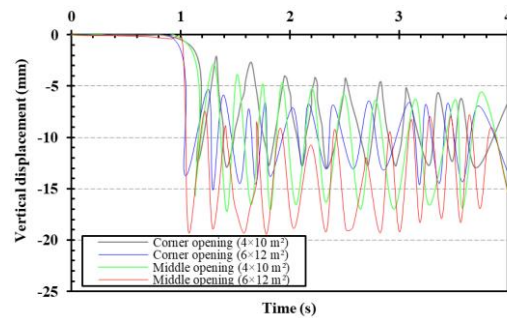
Figure 14. Displacement of the node above the removed column (Column A1) for the buildings with two-way RC slab floor systems

Figure 15. Deformed shape in buildings with Prestressed slabs after removing columns
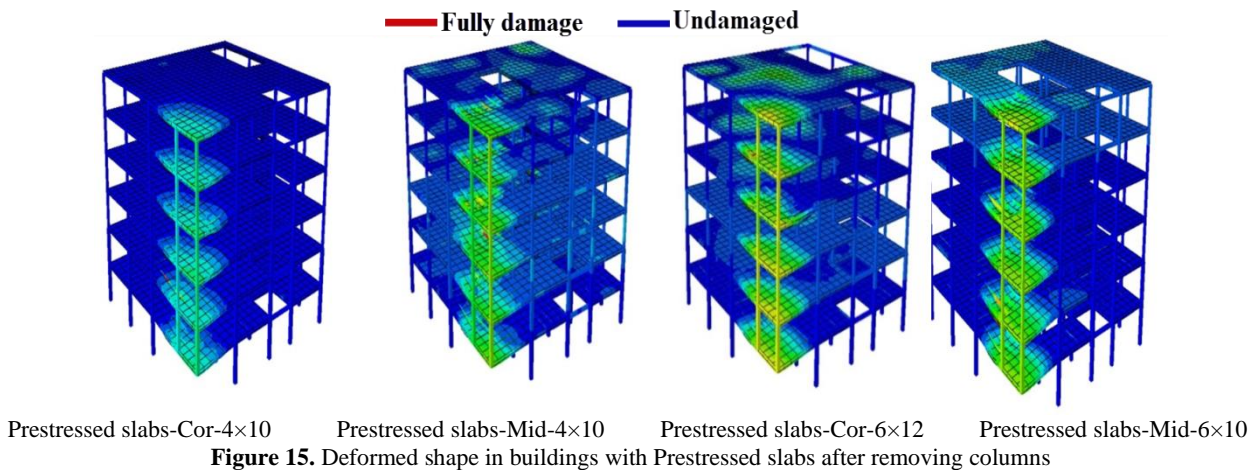
5. 2. Use of Prestressed Slab System as Floor

Prestressing is necessary to create constant compressive stress in a concrete member. Thus, tensile stresses due to dead and live loads are neutralized in this member due to compressive stress. As a result, load-bearing capacity increases. Permanent compressive stress was applied to the concrete section by completely placing the steel in the concrete part, pulling and restraining it on the member on both sides [70-72]. According to Figure 15, two corner columns on the ground floor were removed in steel buildings with a prestressed slab as the floor system., selected the axial force values of column B2 and the vertical displacement on the removal site.

The axial force of column B2 of SMRF buildings with a prestressed slab system on the floor is shown in Figure 16. The maximum axial force of column B2 for each of the modes PS-slabs-Cor-4×10, PS-Mid-4×10, PS-Cor-6×12, and PS-Mid-6×12, are 1800, 2100, 2100, and 2400 kN, respectively .Changing the floor opening position from the corner to the middle in SMRF buildings with prestressed concrete floor has increased the axial force created around the removal site by 14 to 16 percent, depending on the floor opening dimensions. On the other hand, increasing the floor opening dimensions from 4×10 to 6×12 square meters, depending on the floor opening location, has increased the column adjacent axial force to the removal site by about 15 to 17 percent. The displacement history of the node above the removed column (column B2) for modes 5 to 8 are shown in Figure 17. The maximum displacement is related to the situation that in the prestressed slab floor, an opening with dimensions of 6×12 square meters is installed in the middle of the plan, and its value is equal to 12.3 mm. Also, the least displacement is related to the situation that in the prestressed slab floor, an opening with dimensions of 4×10 square meters is used in the middle of the plan, and its value is equal to 8.1 mm. Changing the prestressed slab opening position from the corner to the middle has

increased the vertical displacement of the node above the removed column from 10 to 30%, depending on the opening dimensions. Also, an 80% increase in the steel building floor opening surface that uses a prestressed slab has increased the vertical displacement depending on opening dimensions of the node above the column by about 16 to 37%.
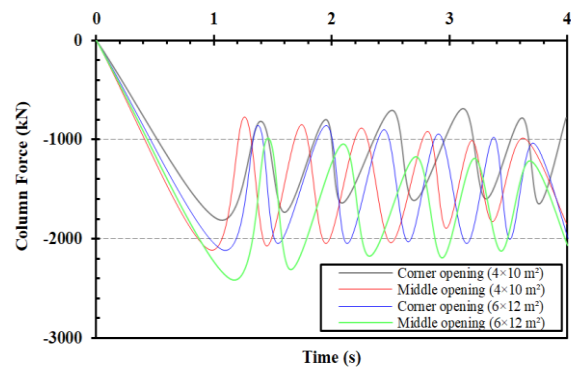
Figure 16. The axial force of the column B2 at the ground floor (Prestressed slab cases)
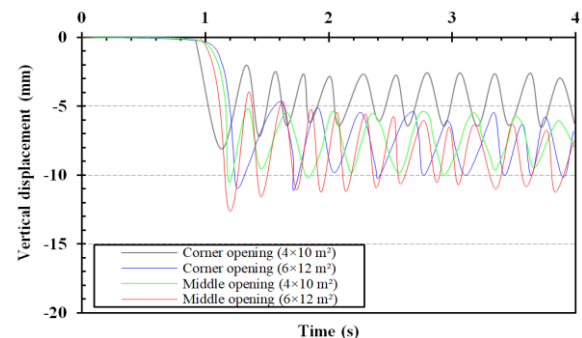
Figure 17. Displacement of the node above the removed column (Column A1) for the buildings with prestressed slab floor

5. 3. Use of Two-way RC Slab System Retrofitted with CFRP Sheets

Retrofitting concrete slab with CFRP is done locally to increase the bearing capacity of the slab, increase the slab resistance to corrosion, decrease compressive strength of concrete, increase flexural strength, shear, etc. Slabs are responsible for withstanding vertical loads, but because they also have the function of the horizontal diaphragm, they must be connected to the structure's strong lateral members and have sufficient rigidity and strength. A concrete slab retrofitted with CFRP can increase bending capacity. This method can also restore the original capacity of the slab, which has been reduced due to steel corrosion. Today, fiber-reinforced polymeric materials instead of traditional materials and existing methods are common in the world. Retrofitted slab with CFRP, while having lightweight, has high tensile strength [73-76].

Following Figure 18, in steel buildings with two-way RC slab floors retrofitted with CFRP sheets, removed two corner columns were on the ground floor. In this case, the axial force of column B2 and vertical displacement in the removal location were extracted. The axial force of column B2 in SMRF buildings with

retrofitted two-way RC slabs (CFRP sheets) is shown in Figure 19. The maximum axial force of modes CFRP-Cor-4×10, CFRP-Mid-4×10, CFRP-Cor-6×12, and CFRP-Mid-6×12 is 2580, 2750, 2700, and 2900 kN, respectively.

In SMRF buildings with retrofitted two-way RC slab using CFRP, changing the floor opening position from the corner to the middle depending on the floor opening dimensions increased the axial force created around the removal site by 6.5 up to 7%. On the other hand, increasing the floor opening dimensions from 4×10 to 6×12 square meters, depending on the floor opening location, has increased the axial force of the column adjacent to the removal site by about 4 to 7.5 percent. The displacement history of the node above the removal column (column B2) for states 9 to 12 are shown in Figure 20. An 80% increase in the floor opening dimensions located in the middle of the plan has increased the displacement of the removal site to the 14 to 46%, depending on the floor opening position. In terms of the removal column location displacement, it is better to place the floor opening in the corner of the plan than

Fully damage — **Undamaged**

| Two-way RC slabs retrofitted with CFRP-Cor-4×10 | Two-way RC slabs retrofitted with CFRP-Mid-4×10 | Two-way RC slabs retrofitted with CFRP-Cor-6×12 | Two-way RC slabs retrofitted with CFRP-Mid-6×10 |
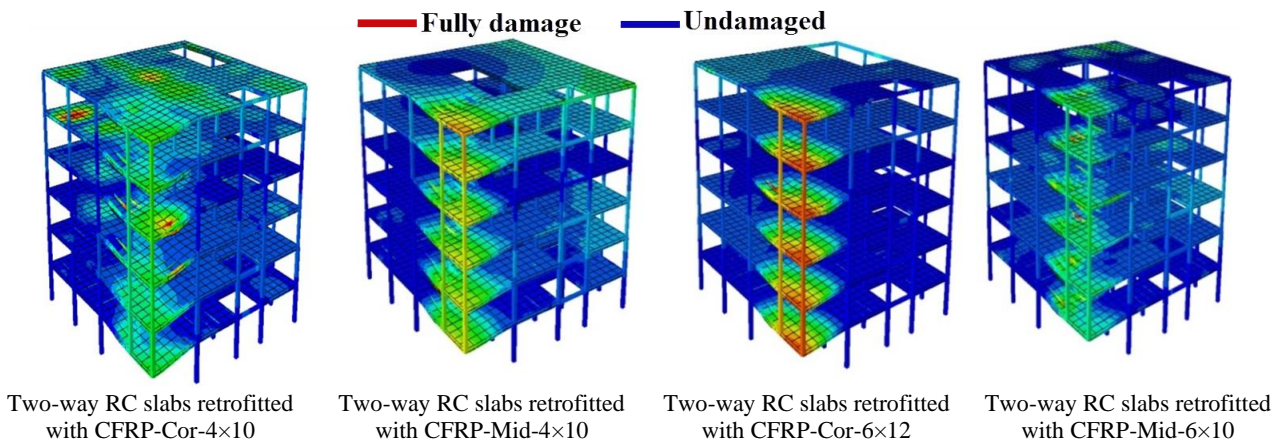
Figure 18. Deformed shape in buildings with Two-way RC slabs after removing columns
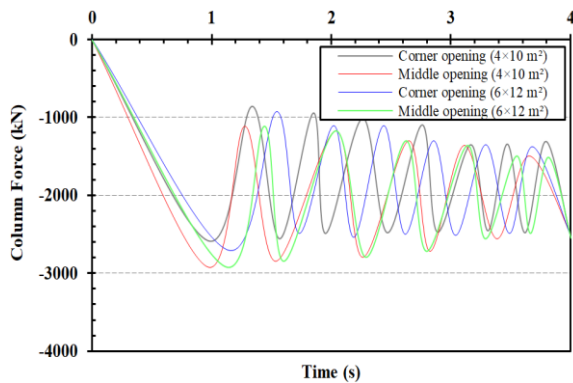
Figure 19. The axial force of the column B2 at the ground floor (two-way RC slabs retrofitted with CFRP cases)
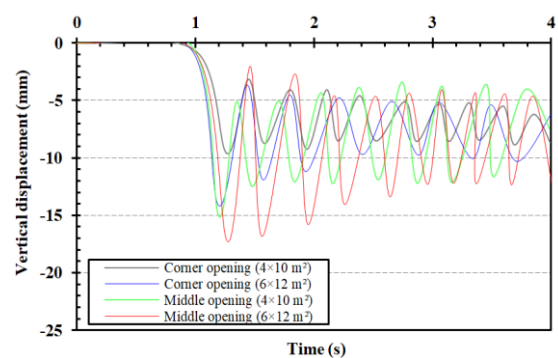
Figure 20. Displacement of the node above the removed column (Column A1) for the buildings with two-way RC slabs retrofitted with CFRP cases

to place it in the middle of the building plan; Because the displacement corresponding to the floor opening positions in the middle, depending on the floor opening dimensions, is 56 to 46 percent higher than the values corresponding to the floor opening position in the corner.

6. RESULTS

Progressive collapse analysis of buildings without considering the floor simulation can affect the engineering judgment about the strength of a structure [19]. One of the studied variable parameters is the effect of floor type on the SMRF buildings against column removal. In the present study, three types of conditions were for the building floor, including two-way RC slabs, prestressed slab, and two-way RC slab retrofitted with CFRP sheets, respectively. The maximum axial force created in the column adjacent to the removal site on the ground floor for the 12 modes is presented in Figure 21. The best performance in axial force redistribution is related to the buildings in which the prestressed slab is used as a gravity bearing system. The corresponding axial forces of the PS-Cor-4×10, PS-Mid-4×10, PS-Cor-6×12, and PS-Mid-6×12 modes are 33, 35, 27, and 30% less than corresponding values in buildings with two-way RC slab, respectively.

The low tensile strength of concrete and vulnerability are major problems in the concrete components. On the other hand, concrete is very resistant to pressure. Also, after bending due to the application of load, it remains under pressure by pre-compression of the concrete member, thus providing a more efficient design. Therefore, the present study analysis results confirm that prestressed concrete slabs have higher yield strength and over-strength due to prestressed tendons than conventional steel reinforcement. The basic design criterion of RC for both prestressed and non-prestressed types is to place steel reinforcement in the positions of the concrete that will be created by external loading. In prestressed concrete, high-strength steel rebar is used, which is pulled before applying external load. This initial tension of the steel rebar pre-compressed the adjacent concrete and created a condition in which the concrete can undergo more loads before cracking. In non-prestressed slabs, there is no stress or strain in either steel or concrete before applying loads. It requires a relatively small load for creating cracks on concrete on such a floor. The tensile stresses created in the steel rebar of the floor slab are very small before cracking.

During the failure, the moment is tolerated by creating high tensile stresses in the reinforcement bar and high compressive stresses in concrete. The action of prestressing creates a self-balancing stress system. These self-balancing stresses are high tensile stresses in prestressed steel that result in a tensile force P and cross-tensions in concrete that results in a compressive force

equal to P.

The axial force corresponding to CFRP-Cor-4×10, CFRP-Mid-4 × 10, CFRP-Cor-6 × 12, and CFRP-Mid-6×12 modes are 4, 15, 7, and 16% less than corresponding values in buildings with two-way RC slabs, respectively. The maximum vertical displacement of the column removal location for the 12 modes is shown in Figure 22.

The displacement corresponding to the buildings, in which the prestressed slab is used, depending on the location of the floor opening and the dimensions of the opening, is about 27 to 39 percent less than the values corresponding to the buildings with two-way RC slabs.

The use of prestressed cables on the floor effectively reduces the structure's potential against progressive collapse and can reduce the moment in the critical section and increase the bearing capacity. Also, the corresponding displacement of buildings that use reinforcement two-way RC slab with CFRP, depending on the floor opening location and the floor opening dimensions, is about 8 to 26 percent less than the values corresponding to buildings with two-way RC slabs. Investigating the deformation condition and stress contours in the structures after removing the two
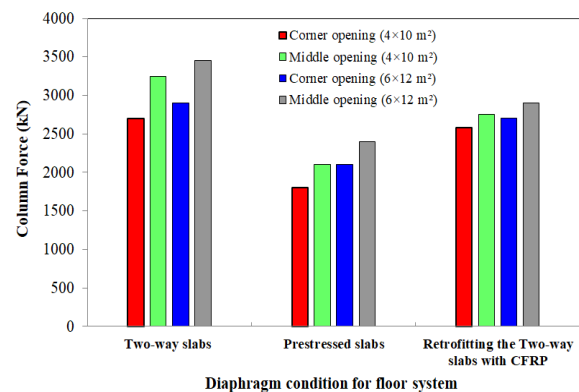
Figure 21. Comparison of the maximum Axial force of column B2 at the ground floor
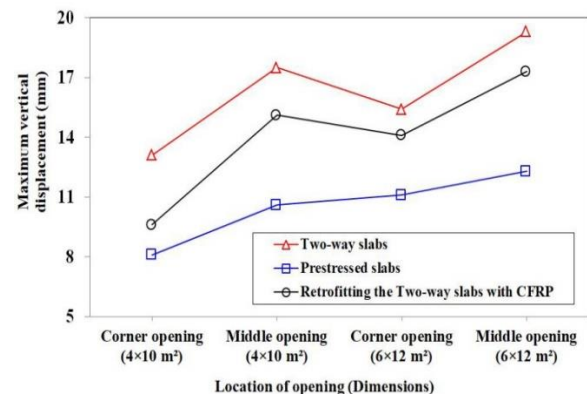
Figure 22. Comparison of the maximum vertical displacement of the node above column A1

corner columns can say that the structure's deformation occurs locally in the same corner panel. The rest of the structure remains integrated and elastic. The diagrams related to the axial force in the columns adjacent to the removal corner column in the structural model found that the most effective after removing the corner column is on column B2.

By observing the flexural condition of beams and connections in the damaged area for structures can be expressed, all beams are designed with sufficient flexural strength and stiffness; even after removing two key columns from the structure, can withstand the spread of collapse. However, in the case of flexural connections, it should be noted that connections usually have less rotational capacity than members of structures such as beams. Thus, to prevent the spread of damage in the structure after column removal, it is necessary to use bending connections with more ductility due to having more rotational capacity. If the vertical deformation of the structure increases after column removal, it can absorb and depreciate by enduring longer periods and provide more energy to the structure.

According to the displacement diagram and the flexural moment near and far from the failure point in the corner column, using prestressed slabs and CFRP sheets can reduce the amount of deflection and flexural moment.

Regarding the displacement of the top point of the removal column and flexural moment in the position near and far from the failure point in the corner column, using prestressed slabs and CFRP sheets can reduce the deflection and flexural moment. Because columns in steel-moment frames are primarily responsible for providing lateral stiffness, they usually have sufficient size and strength. Accordingly, by increasing the ductility due to the selection of sections based on compression constraints commensurate with the desired ductility, the column's performance against the spread of collapse improves. Control of member deformation criteria is one of the acceptance criteria that should be considered in evaluating the structure's behavior against progressive collapse. Deformation limits are applied to ensure a proper response to column removal.

In the structure design, the stresses created in the members are compared and controlled with the allowable stresses. But in the design against the progressive collapse the deformation, is the basis for judging the structure acceptability based on performance levels. These limits are determined based on laboratory results or experimental evidence. Because loads from accidents such as explosions, design errors, execution, impact, etc., are unpredictable, a conservative amount is considered to ensure sufficient section capacity. Limitations for deformation are determined based on safety concepts and protection criteria on the building performance levels.

One of these limitations is the rotation criterion, which makes the maximum deformation response a function of the member length and indicates the percentage of instability in the critical areas of the member. The rotation of beams and columns is calculated according to GSA [2] using Equations (7) and (8). The parameter θ is shown in Figure 23.

$$\theta = \frac{ZF_{ye}l_b}{6EI_b} \tag{7}$$

$$\theta = \frac{ZF_{ye}l_c}{6EI_c}\left(1 - \frac{P}{P_{ye}}\right) \tag{8}$$

where Z = Plastic section modulus, F_{ye} = Expected yield strength of the material, I = moment of inertia, L_b = Beam length, L_c = Column length, E = Modulus of elasticity, P = Axial force in the member, P_{ye} = Expected axial yield force of the member.

The maximum rotation angles of the beams and columns for the 12 cases are shown in Figures 24 and 25. In these figures, the allowable rotation angle according to the GSA regulations is shown. According to GSA, the maximum rotation angle of beams and columns is 0.21 radians. In the mentioned figures, the values of the maximum rotation angle with the regulations allowable value are also compared with each other. The maximum rotation angle of the beams in the cases corresponding to the concrete slabs is more than 0.21 radians. The maximum rotation angle of the beams corresponding to the modes S-C-4×10, S-C-6×10, S-M-4×10, and S-M-6×12 has been 0.26, 0.3, 0.28, and 0.31 radians, respectively.
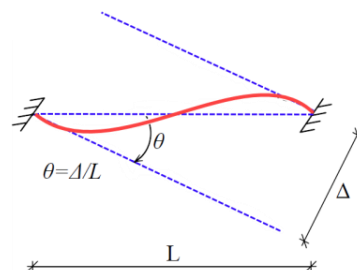
Figure 23. Definition of chord rotation [2]
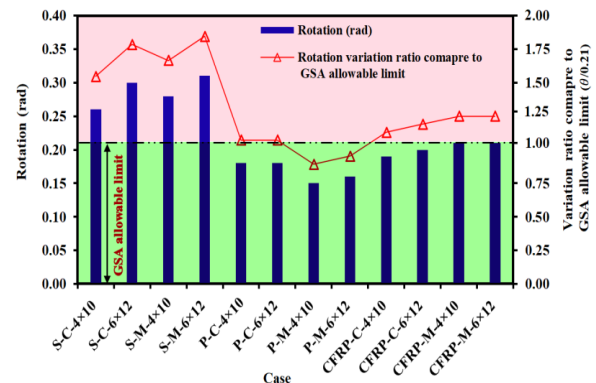
Figure 24. Maximum angle rotation of the beams and their comparison with the allowable value of GSA regulations
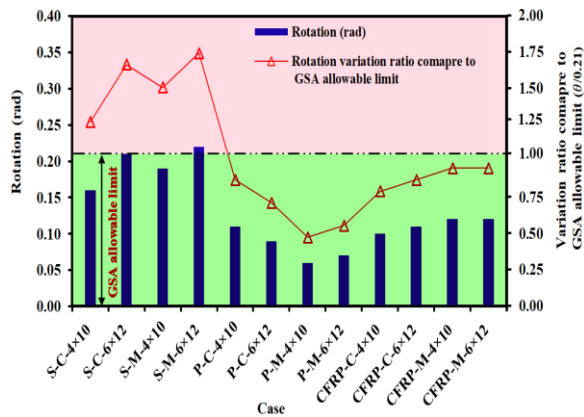
Figure 25. Maximum angle rotation of the columns and their comparison with the allowable value of GSA regulations

The use of prestressed concrete slabs has significantly reduced the beam's rotation angle. The rotation angles corresponding to the modes P-C-4×10, P-C-6×10, P-M-4×10, and P-M-6×12 have been 0.18, 0.18, 0.15, and 0.16 radians, respectively. This means that the maximum angle rotation corresponding to the retrofitted states with prestressed slabs, depending on the floor opening dimensions and position, is 31 to 48% lower than the values corresponding to two-way RC slabs mode. The cables used to prestress the concrete slabs increased the energy absorption behavior of the structure against column removal by increasing energy absorption, and the beams and columns around the removal site performed better in redistributing forces. On the other hand, the maximum beam rotation angles corresponding to CFRP-C-4×10, CFRP-C-6×10, CFRP-M-4×10, and CFRP-M-6×12 modes have been 0.19, 0.2, 0.21, and 0.21, respectively. The addition of CFRP sheets to the exterior surfaces of two-way RC slabs has reduced the maximum rotation angle of the beams adjacent to the removal location by 25 to 33%, depending on the floor opening position and dimensions.

The maximum angle rotation of the columns is shown in Figure 25 and compares with the GSA limit. The maximum angle rotation of the columns corresponding to the modes S-C-4×10, S-C-6×10, S-M-4×10, and S-M-6×12 has been 0.16, 0.21, 0.19, and 0.22, respectively.

The rotational angles corresponding to the modes P-C-4×10, P-C-6×10, P-M-4×10, and P-M-6×12 were 0.11, 0.09, 0.06, and 0.07, respectively. This means that the maximum angle rotation of the columns corresponding to the modes of use of prestressed slabs, depending on the floor opening dimensions and position, is 31 to 68% less than the values corresponding to the conventional two-way RC slabs mode. The compressive force applied to the concrete due to prestressing will neutralize the tensile stress due to the applied loads. The whole member will pressurize, and carry the compressive force by the concrete will be used optimally. On the other hand, due to the removal of tensile stress and the placement of the

entire section in compression, the need for rebar in a concrete member similar to an RC member is reduced. Also, the member's behavior in the bent position is improved, and the tensile cracks are removed, and the deformation is reduced. As a result, the main purpose of prestressing a concrete member is to limit the tensile stresses and cracks caused by the bending moment due to the loads applied to that member, and this process leads to an improvement in the response of the structure against progressive failure. On the other hand, the maximum rotation angles of the columns corresponding to CFRP-C-4×10, CFRP-C-6×10, CFRP-M-4×10, and CFRP-M-6×12 have been 0.1, 0.11, 0.12, and 0.12, respectively. The addition of CFRP sheets to the exterior surfaces of two-way RC slabs has reduced the maximum rotation angle of adjacent columns to the removal location by 36 to 47%, depending on the location and floor opening dimensions.

7. SUMMARY AND CONCLUSIONS

Due to the removal of large amounts of concrete and reinforcement bars, the ability of the structure to withstand the loads may be reduced, and there may be a need to provide a solution to increase the load-bearing capacity.

This study investigated another method to increase the bearing capacity of the structure called prestressing and evaluated the effect of the surface and position of the RC floor opening on the progressive collapse potential of SMRF buildings. Proposed two solutions to rehabilitate and retrofit two-way RC slabs against progressive collapse. To rehabilitate, prestressed RC slabs were used, and to retrofit, used the method of installing CFRP sheets on the surface of the old concrete slab. In this section, the most important results are presented:

- The use of cable systems to restore the cross-section to its original shape is suitable for repair and can reduce the flexural moment in the critical section and increase the bearing capacity. The displacement corresponding to the buildings, in which the prestressed slab is used, depending on the opening and the dimensions of the opening, is about 27% to 39% less than the values corresponding to the buildings with two-way RC slabs. The use of prestressed cables in the roof effectively reduces the potential of the structure against progressive collapse.

- In SMRF buildings with a two-way RC slab system that is exposed to the removal of corner columns, the presence of an opening in the middle of the building plan creates more axial forces around the removal site compared to the position in which the floor opening is in the corner of the plan. Also, the axial forces created around the removed column of the SMRF buildings with a two-way slab in which the opening is located in the middle of the plan, depending on the

opening dimensions, is about 18% to 20% more than the corresponding value in the presence of an opening in the corner.

- In SMRF buildings with a two-way RC slab floor system, increasing the opening ranges from 4×10 square meters to 6×12 square meters, depending on the location of the opening, has increased the axial force created around the removal site by about 12% to 19%. Changing the opening from the corner to the middle in SMRF buildings with prestressed concrete slabs has increased the axial force created around the removal site by 14% to 16 %, depending on the dimensions of the opening. On the other hand, increasing the dimensions of the opening from 4×10 to 6×12 square meters, depending on the location of the opening, has increased the axial force of the column adjacent to the removal site by about 15% to 17%. According to the obtained displacement values, it can be stated that the choice of dimensions and location of the opening has an impact on the response of SMRF buildings to column removal; an 80% increase in the floor opening surface in a steel structure using a two-way RC slab has increased the vertical displacement of the node above the column by about 10% to 17%, depending on the floor opening position.

- Retrofitting of concrete slab with CFRP is done locally to increase the bearing capacity of the slab, increase the slab resistance to corrosion, and increase flexural and shear strength. Slabs are practically responsible for withstanding vertical loads. Because they also have the function of the horizontal diaphragm, they must be connected to the strong lateral members of the structure and have sufficient rigidity and strength. This method can also restore the original capacity of the slab, which has been reduced due to corrosion of the steel.

8. REFERENCES

1. UFC 4–023-03, "Design of Buildings to Resist Progressive Collapse." Department of Defense Unified Facilities Criteria, (2016).

2. GSA, General Service Administration, Washington D.C "Alternate path analysis and design guidelines for progressive collapse resistance", (2016).

3. ASCE 7–05, "Minimum Design Loads for Buildings and Other Structures". American Society of Civil Engineers New York, (2005).

4. Kiakojouri, F., De Biagi, V., Chiaia, B., Sheidaii, M. R. (2020). "Progressive collapse of framed building structures: Current knowledge and future prospects." *Engineering Structures,* (2020), Vol. 206, 110061, DOI: 10.1016/j.engstruct.2019.110061

5. Galal, M. A., Bandyopadhyay, M., Banik, A. K. "Dual effect of axial tension force developed in catenary action during progressive collapse of 3D composite semi-rigid jointed frames." *Structures,* Vol. 19, (2019), 507-519.

6. Shakib, H., Zakersalehi, M., Jahangiri, V., Zamanian, R. "Evaluation of plasco building fire-induced progressive collapse." *Structures*, Vol. 28, (2020), 205-224, DOI: 10.1016/j.istruc.2020.08.058.

7. Bagheripourasil, M., Mohammadi, Y. "Comparison between alternative load path method and a direct applying blast loading method in assessment of the progressive collapse," *Journal of Rehabilitation in Civil Engineering*, Vol. 3, No. 2, (2015), 1-15, DOI; 10.22075/jrce.2015.367.

8. Pourasil, M.B., Mohammadi, Y. Gholizad, A. "A proposed procedure for progressive collapse analysis of common steel building structures to blast loading." *KSCE Journal of Civil Engineering*, Vol. 21, (2017), 2186-2194, DOI: 10.1007/s12205-017-0559-0

9. Abdelwahed, B. "A review on building progressive collapse, survey and discussion" *Case Studies in Construction Materials*, Vol. 11, e00264 DOI: 10.1016/j.cscm.2019.e00264

10. Fruhwald, E., Serrano, E., Toratti, T., Emilsson, A., Thelandersson, S. "Design of safe timber structures-How can we learn from failures in concrete, steel and timber?", Report TVBK-3053, 2007.

11. Russell, J. M., Sagaseta, J., Cormie, D., Jones, A. E. K. "Historical review of prescriptive design rules for robustness after the collapse of Ronan Point." *Structures*, Vol. 20, (2019), 365-373.

12. Byfield, M., Mudalige, W., Morison, C., Stoddart, E. "A review of progressive collapse research and regulations." *Proceedings of the Institution of Civil Engineers-Structures and Buildings*, Vol. 167, No. 8, (2014), 447-456, DOI: 10.1680/stbu.12.00023.

13. Martin, R., Delatte, N. J. "Another looks at the L'Ambiance Plaza collapse. *Journal of Performance of Constructed Facilities*," Vol. 14, No. 4, (2000), 160-165, DOI: 10.1061/(ASCE)0887-3828(2000)14:4(160)

14. Osteraas, J. D. "Murrah building bombing revisited: A qualitative assessment of blast damage and collapse patterns." *Journal of Performance of Constructed Facilities*, Vol. 20, No. 4, (2006), 330-335, DOI: 10.1061/(ASCE)0887-3828(2006)20:4(330).

15. Gardner, N. J., Huh, J., Chung, L. "Lessons from the Sampoong department store collapse." *Cement and Concrete Composites*, Vol. 24, No. 6, (2002), 523-529. DOI: 10.1016/S0958-9465(01)00068-3.

16. El-Tawil, S., Li, H., Kunnath, S. "Computational simulation of gravity-induced progressive collapse of steel-frame buildings: Current trends and future research needs." *Journal of Structural Engineering*, Vol. 140, No. 8, (2014), A2513001, DOI: 10.1061/(ASCE)ST.1943-541X.0000897.

17. Kotsovinos, P., Usmani, A. "The World Trade Center 9/11 disaster and progressive collapse of tall buildings." *Fire Technology*, Vol. 49, No. 3, (2013), 741-765, DOI: 10.1007/s10694-012-0283-8.

18. Bosela Jr, P., Bosela, P. "Tropicana Parking Garage Collapse." In Forensic Engineering 2018: Forging Forensic Frontiers Reston, VA: American Society of Civil Engineers. (2018), 1118-1124.

19. Kaafi, P., Ghodrati Amiri, G. "Investigation of the progressive collapse potential in steel buildings with composite floor system," World Academy of Science, Engineering and Technology, *International Journal of Civil and Environmental Engineering,* Vol.1, No. 8, (2014).

20. Maqsood, S. T., Schwarz, J. "Analysis of building damage during the 8 October 2005 earthquake in Pakistan." *Seismological Research Letters*, Vol. 79, No. 2, (2008), 163-177, DOI: 10.1785/gssrl.79.2.163

21. Rigby, S. E., Lodge, T. J., Alotaibi, S., Barr, A. D., Clarke, S. D., Langdon, G. S., Tyas, A. "Preliminary yield estimation of the 2020 Beirut explosion using video footage from social media" *Shock Waves*, (2020), 1-5.

22. Mousapoor, E., Ghiasi, V., Madandoust, R. "Macro modeling of slab-column connections in progressive collapse with post-punching effect." *Structures*, Vol. 27, (2020), 837-852, 10.1016/j.istruc.2020.06.025.

23. Shan, S., Li, S. "Fire-induced progressive collapse mechanisms of steel frames with partial infill walls", *Structures*", Vol. 25, (2020) 347-359, DOI: 10.1016/j.istruc.2020.03.023.

24. Meng, B., Hao, J., Zhong, W., Tan, Z., Duan, S. "Improving collapse-resistance performance of steel frame with openings in beam web." *Structures,* Vol. 27, 2156-2169, 10.1016/j.istruc.2020.08.009.

25. Rezvani, F. H., Yousefi, A. M., Ronagh, H. R. "Effect of span length on progressive collapse behaviour of steel moment resisting frames." *Structures,* Vol. 3, 81-89. 10.1016/j.istruc.2015.03.004.

26. Kong, D. Y., Yang, Y., Yang, B., Zhou, X. H. "Experimental Study on Progressive Collapse of 3D Steel Frames under Concentrated and Uniformly Distributed Loading Conditions." *Journal of Structural Engineering*, Vol. 146, No. 4, (2020), 04020017.

27. Wang, J., Wang, W., Bao, Y., Lehman, D. "Numerical investigation on progressive collapse resistance of steel-concrete composite floor systems." *Structure and Infrastructure Engineering,* (2020), Vol. 18, No. 2, 1-15, DOI: 10.1080/15732479.2020.1733622

28. Tavakoli, H. R., Alashti, A. R. "Evaluation of progressive collapse potential of multi-story moment resisting steel frame buildings under lateral loading", *Scientia Iranica*, Vol. 20, No. 1, (2013), 77-86.

29. Wang, W. M., Li, H. N., Tian, L. "Progressive collapse analysis of transmission tower-line system under earthquake." *Advanced Steel Construction*, Vol. 9, No. 2, (2013), 161-172.

30. Salmasi, A. C., Sheidaii, M. R. "Assessment of eccentrically braced frames strength against progressive collapse." *International Journal of Steel Structures*, Vol. 17, No. 2, 543-551.

31. Qiao, H., Luo, C., Wei, J., Chen, Y. "Progressive Collapse Analysis for Steel-Braced Frames Considering Vierendeel Action." *Journal of Performance of Constructed Facilities*, Vol. 34, No. 4, (2020), 04020069.

32. Elsanadedy, H. M., Al-Salloum, Y. A., Alrubaidi, M. A., Almusallam, T. H., Abbas, H. "Finite element analysis for progressive collapse potential of precast concrete beam-to-column connections strengthened with steel plates, *Journal of Building Engineering*, Vol. 34, No. 11, (2020), 101875, DOI: 10.1016/j.jobe.2020.101875

33. Sun, R., Huang, Z., Burgess, I. W. "Progressive collapse analysis of steel structures under fire conditions." *Engineering Structures*, Vol. 34, (2012), 400-413, DOI: 10.1016/j.engstruct.2011.10.009.

34. Gerasimidis, S., Sideri, J. "A new partial-distributed damage method for progressive collapse analysis of steel frames." *Journal of Constructional Steel Research*, Vol. 119, (2016), 233-245. DOI: 10.1016/j.jcsr.2015.12.012

35. Pordel Maragheh, B., Jalali, A., Mirhoseini Hezaveh, S. M. (2020). "Effect of Initial Local Failure Type on Steel Braced Frame Buildings against Progressive Collapse." *International Journal of Engineering*, *Transactions A: Basics*, Vol. 33, No. 1, (2020), 34-46. doi: 10.5829/ije.2020.33.01a.05

36. Fu, F., "3-D nonlinear dynamic progressive collapse analysis of multi-story steel composite frame buildings—Parametric study." *Engineering Structures*, Vol. 32, No. 12, (2010), 3974-3980, DOI: 10.1016/j.engstruct.2010.09.008.

37. Naji, A., Irani, F. "Progressive collapse analysis of steel frames: Simplified procedure and explicit expression for dynamic increase factor." *International Journal of Steel Structures*, Vol. 12, No. 4, (2012), 537-549.

38. Karimian, A., Armaghani, A., Behravesh, A. "Performance of Low-yield Strength Plates in Beam-column Connections against Progressive Collapse." *KSCE Journal of Civil Engineering*, Vol. 23, No. 1, (2019), 335-345, DOI: 10.1007/s12205-018-0653-y

39. Zahrai, S. M., Zeighami, E. "Cyclic Behavior of Variously Drilled Flange Beam Connected to Box Column." *AUT Journal of Civil Engineering*. DOI: 10.22060/ajce.2020.17448.5633

40. Liu, C., Fung, T. C., Tan, K. H. "Dynamic performance of flush end-plate beam-column connections and design applications in progressive collapse." *Journal of Structural Engineering*, Vol. 142, No. 1, (2016), 04015074, DOI: 10.1061/(ASCE)ST.1943-541X.0001329

41. Yang, B., Tan, K. H. "Robustness of bolted-angle connections against progressive collapse: Experimental tests of beam-column joints and development of component-based models." *Journal of Structural Engineering*, Vol. 13, No. 9, (2013) 1498-1514, DOI: 10.1061/(ASCE)ST.1943-541X.0000749

42. Wang, F., Yang, J., Pan, Z. "Progressive collapse behaviour of steel framed substructures with various beam-column connections." *Engineering Failure Analysis*, Vo. 109, (2020), 104399, DOI: 10.1016/j.engfailanal.2020.104399

43. Chen, Y., Huo, J., Chen, W., Hao, H., Elghazouli, A. Y. "Experimental and numerical assessment of welded steel beam-column connections under impact loading." *Journal of Constructional Steel Research*, Vol. 175, (2020), 106368, DOI: 10.1016/j.jcsr.2020.106368.

44. Li, S. Q., Yu, T. L., Jia, J. F. "Empirical seismic vulnerability and damage of bottom frame seismic wall masonry structure: A case study in Dujiangyan (China) region", *International Journal of Engineering, Transactions C: Aspects*, Vol. 32, No. 9, (2019), 1260-1268. DOI: 10.5829/ije.2019.32.09c.05.

45. Li, S. Q., Yu, T. L., Jia, J. F. "Investigation and analysis of empirical field seismic damage to bottom frame seismic wall masonry structure", *International Journal of Engineering, Transactions B: Applications*, Vol. 32, No. 8, (2019), 1082-1089. DOI: 10.5829/ije.2019.32.08b.04

46. Li, S. Q., Yu, T. L., Chen, Y. S. "Comparison of macroseismic intensity scales by considering empirical observations of structural seismic damage", *Earthquake Spectra*, Vol. 37, No. 1, (2021), 449-485. DOI: 10.1177/8755293020944174

47. Ozturk, B., Yilmaz, C., Şentürk, T. "Effect of FRP retrofitting application on seismic behavior of a historical building at Niğde", 14th European Conference on Earthquake Engineering 2010: Ohrid, Republic of Macedonia, (2010).

48. Ozturk, B. "Seismic behavior of two monumental buildings in historical Cappadocia region of Turkey." *Bulletin of Earthquake Engineering*, Vol. 15, No. 7, (2017), 3103-3123.

49. Oztürk, B., Şentürk, T., Yilmaz, C. "Analytical Investigation of Effect of Retrofit Application using FRP on Seismic Behavior of a Monumental Building at Historical Cappadocia Region of Turkey."

50. Zhu, Y. F., Chen, C. H., Huang, Y., Huang, Z. H., Yao, Y., Keer, L. M. "Dynamic progressive collapse of steel moment frames under different fire scenarios." *Journal of Constructional Steel Research*, Vol. 173, (2020), 106256.

51. Wang, F., Yang, J., Pan, Z. "Progressive collapse behaviour of steel framed substructures with various beam-column connections." *Engineering Failure Analysis*, Vol. 109, (2020), 104399, DOI: 10.1016/j.engfailanal.2020.104399.

52. Qiao, H., Chen, Y., Wang, J., Chen, C. "Experimental study on beam-to-column connections with reduced beam section against progressive collapse." *Journal of Constructional Steel Research*, Vol. 175, (2020), 106358, DOI: 10.1016/j.jcsr.2020.106358.

53. Mousapoor, E., Ghiasi, V., Madandoust, R. "Macro modeling of slab-column connections in progressive collapse with post-punching effect." *Structures*, Vol. 27, 837-852, DOI: 10.1016/j.istruc.2020.06.025.

54. Livingston, E., Sasani, M., Bazan, M., Sagiroglu, S. "Progressive collapse resistance of RC beams." *Engineering Structures*, Vol. 95, (2015), 61-70, DOI: 10.1016/j.engstruct.2015.03.044

55. Abaqus theory manual. Version, Hibbitt. (2016). Pawtucket (RI): Karlsson and Sorensen, Inc.

56. Torabian, A., Isufi, B., Mostofinejad, D., Ramos, A. P. "Flexural strengthening of flat slabs with FRP composites using EBR and EBROG methods." *Engineering Structures*, Vol. 211, (2020), 110483.

57. Sharif, A., Al-Sulaimani, G. J., Basunbul, I. A., Baluch, M. H., Ghaleb, B. N. "Strengthening of initially loaded reinforced concrete beams using FRP plates." *Structural Journal,* Vol. 91, No. 2, (1994), 160-168.

58. Mostofinejad, D., Hajrasouliha, M. "Shear retrofitting of corner 3D-reinforced concrete beam-column joints using externally bonded CFRP reinforcement on grooves." *Journal of Composites for Construction*, Vol. 22, No. 5, (2018), 04018037, DOI: 10.1061/(ASCE)CC.1943-5614.0000862.

59. Jafarian, N., Mostofinejad, D., Naderi, A. "Effects of FRP grids on punching shear behavior of reinforced concrete slabs." *Structures*, Vol. 28, 2523-2536, DOI: 10.1016/j.istruc.2020.10.061

60. Gao, D., Fang, D., You, P., Chen, G., Tang, J. "Flexural behavior of reinforced concrete one-way slabs strengthened via external post-tensioned FRP tendons." *Engineering Structures*, Vol. 216, (2020), 110718, DOI: 10.1016/j.engstruct.2020.110718.

61. Chen, W., Pham, T. M., Elchalakani, M., Li, H., Hao, H., Chen, L. "Experimental and Numerical Study of Basalt FRP Strip Strengthened RC Slabs under Impact Loads." *International Journal of Structural Stability and Dynamics*, Vol. 20, No. 6, (2020), 2040001, DOI: 10.1142/S0219455420400015.

62. Tao, Y., Wang, W. "Flexural performance of Reinforced Concrete One-way Slabs Strengthened by FRP Grid." *In IOP Conference Series: Earth and Environmental Science,* Vol. 560, No. 1, 012092, IOP Publishing.

63. ETABS, C. (2015). 15.0. Berkeley. CA: Computers and Structures Inc.

64. Feng Fu. "Response of a multi-storey steel composite building with concentric bracing under consecutive column removal scenarios." *Journal of Constructional Steel Research*, Vol. 70, (2012), 115–126. DOI: org/10.1016/j.jcsr.2011.10.012.

65. Hosseini, S. M., Amiri, G. G. "Successive collapse potential of eccentric braced frames in comparison with buckling-restrained braces in eccentric configurations" *International Journal of Steel Structures*, Vol. 17, No. 2, (2017), 481-489. DOI: org/10.1007/s13296-017-6008-6.

66. Mohammadi, Y, Bagheripourasil, M, "Investigation of steel buildings response equipped with buckling-restrained braces against progressive collapse", *Journal of Structural and Construction Engineering (JSCE)*, Vol. 8, No. 2, (2019), 119-140, DOI: 10.22065/jsce.2019.153064.1688.

67. Guo, L., Gao, S., Fu, F., Wang, Y. "Experimental study and numerical analysis of progressive collapse resistance of composite frames." *Journal of Constructional Steel Research*, Vol. 89, (2013), 236-251.

68. Floruț, S. C., Sas, G., Popescu, C., Stoian, V. "Tests on reinforced concrete slabs with cut-out openings strengthened with fiber-reinforced polymers." *Composites Part B: Engineering*, Vol. 66, 484-493, DOI: 10.1016/j.compositesb.2014.06.008.

69. Ellobody, E., Bailey, C. G. "Modeling of unbonded post-tensioned concrete slabs under fire conditions." *Fire Safety Journal*, Vol. 44, No. 2, (2009), 159-167.

70. Nawy, E. G. (1996). Prestressed concrete. A fundamental approach (No. Second Edition).

71. Kong, F. K., Evans, R. H. "Reinforced and prestressed concrete.", (2013), DOI: 10.1017/CBO9781107282223.

72. Ma, G., Du, Q. "Structural health evaluation of the prestressed concrete using advanced acoustic emission (AE) parameters." *Construction and Building Materials*, Vol. 250, (2020), 118860, DOI: 10.1016/j.conbuildmat.2020.118860.

73. Wu, C., Oehlers, D. J., Rebentrost, M., Leach, J., Whittaker, A. S. "Blast testing of ultra-high-performance fiber and FRP-retrofitted concrete slabs." *Engineering Structures*," Vol. 31, No. 9, (2009), 2060-2069.

74. Mosallam, A. S., Mosalam, K. M. "Strengthening of two-way concrete slabs with FRP composite laminates." *Construction and building materials*, Vol. 17, No. 1, (2003), 43-54.

75. Hassan, T., Rizkalla, S. "Flexural strengthening of prestressed bridge slabs with FRP systems." *PCI Journal*, Vol. 47, No. 1.

76. Abdulrahman, B. Q., Aziz, O. Q. "Strengthening RC flat slab-column connections with FRP composites: A review and comparative study." *Journal of King Saud University-Engineering Sciences*, Vol. 33, No. 7, (2021), 471-481. DOI: 10.1016/j.jksues.2020.07.005.

Persian Abstract

چکیده

یکی از موضوعاتی که در زمینه خرابی پیش‌رونده‌ی ساختمان‌های فولادی، توجه‌ی کمتری به آن شده است، بررسی اثر وجود بازشوی سقف بر پاسخ این ساختمان‌ها در برابر احتمال وقوع خرابی پیش‌رونده می‌باشد. در این مطالعه به بررسی تحلیلی اثر سطح و موقعیت بازشوی سقف بتن مسلح بر پتانسیل خرابی پیش‌رونده ساختمان‌های فولادی پرداخته شد. همچنین دو راهکار جهت بهسازی و مقاوم سازی دال‌های دو طرفه بتنی در برابر خرابی پیش‌رونده پیشنهاد شد. به منظور بهسازی از دال‌های بتنی پیش‌تنیده استفاده شد و به منظور مقاوم سازی، روش نصب ورق‌های CFRP برروی سطح دال بتنی قدیمی بکار برده شد. مدلسازی با استفاده از روش اجزاء محدود و نرم افزار ABAQUS انجام شد. صحت روش شبیه‌سازی مورد استفاده با مدلسازی مطالعات آزمایشگاهی مختلف ارزیابی شد و تطابق مناسبی بین نتایج آزمایشگاهی و شبیه‌سازی اجزاء محدود مشاهده شد. ابعاد بازشوهای سقف به ترتیب ۴×۱۰ و ۶×۱۲ متر مربع و موقعیت آنها در گوشه و وسط پلان در نظرگرفته شد. نتایج حاصل از تحلیل خرابی پیش رونده نشان داد در ساختمان‌های فولادی با سیستم قاب خمشی، هنگامی که ستون‌های گوشه حذف می‌شوند و بازشوها در وسط پلان سازه قرار دارند، نیروهای محوری ستون‌های اطراف محل حذف، بسته به نوع سقف در نظر گرفته شده ۱۸ تا ۲۰ درصد بیشتر از مقادیر متناظر با حالت‌های وجود بازشو در گوشه پلان می‌باشند. همچنین افزایش ابعاد بازشو از ۴×۱۰ مترمربع به ۶×۱۲ متر مربع، بسته به موقعیت قرارگیری بازشو و نوع سقف در نظر گرفته شده، نیروی محوری ایجاد شده در اطراف محل حذف را حدوداً ۱۲ تا ۱۹ درصد افزایش داد. از بین دال‌دو طرفه بتن مسلح، دال بتن مسلح پیش تنیده و دال دو طرفه بتن مسلح مقاوم سازی شده با CFRP، دال‌های پیش تنیده بهترین عملکرد را داشتند؛ بطوریکه نیروهای محوری اطراف محل حذف متناظر با آنها بسته به موقعیت و ابعاد بازشو در حدود ۲۷ تا ۳۵ درصد کمتر از مقادیر متناظر با دال‌های دو طرفه شد. در دال‌های بتنی پیش‌تنیده تاندون‌های با مقاومت کششی بالا بجای آرماتورهای معمولی قرار می‌گیرند و در دو انتها توسط گره‌های مخصوص به تیر تثبیت می‌شوند. این کابل‌ها تحت کشش زیادی قرار می‌گیرند و پس از رها شدن از کشش، تمایل به جمع شدن و رسیدن به حالت اولیه دارند. بنابراین نیروی فشاری زیادی در قسمت زیرین تار خنثی در بتن ایجاد می‌شود. این نیروهای فشاری در مقابل نیروهای کششی که به واسطه بارهای ثقلی در بتن ایجاد می‌شود، قرار می‌گیرند و مقداری از نیروهای ناشی از بارهای ثقلی را خنثی می‌نمایند و بدین ترتیب پتانسیل سازه در برابر خرابی پیش‌رونده کاهش می‌یابد.

International Journal of Engineering

Strengthening of RC Beams using Steel Plate-fiber Concrete Composite Jackets: Finite Element Simulation and Experimental Investigation

M. Shadmand, A. Hedayatnasab*, O. Kohnehpooshi

Department of Civil Engineering, Sanandaj Branch, Islamic Azad University, Sanandaj, Iran

P A P E R I N F O	*A B S T R A C T*
	In this research, steel plate-fiber concrete composite jackets (SPFCJ) was used to strengthen the RC beams. The accuracy of the analysis method was evaluated by modeling RC beams fabricated in the laboratory, and a good agreement was observed. Variables in the finite element method (FEM) analysis include the strength class of concrete used in the main beam (15, 20, and 25 MPa), the beam length (1.4 and 2.8 m), the type of jackets (RC jacket, SPFCJ, and CFRP sheet), and jacket thickness (40, 60 and 80 mm). SPFCJ is effective for all three concrete grades and increased the energy absorption capacity by 1.88, 2.07, and 2.25 times, respectively. The bearing capacity of the strengthened beam with 60 mm composite jackets increased by 79 and 20% more than the values corresponding to jackets with 40 and 80 mm thickness. The jacket thickness parameter significantly influences the response of strengthened beams with the proposed composite jackets. Depending on the dimensions and geometric characteristics of the beam, the appropriate thickness for the jacket should be considered, and increasing the thickness can not always improve the beam bearing capacity.

1. INTRODUCTION

Failure of reinforced concrete (RC) beams in the event of severe earthquakes may be due to insufficient steel reinforcement or non-compliance with new regulations [1-3]. Strengthening the beams and historical buildings in seismic design for RC structures is an important issue [4-8].

Researchers have considered the strengthening of RC beams in recent years [9-12]. Attar et al. [13] investigated the strengthened RC beams with self-compacting concrete (SCC) jackets containing fibers. The variables included the percentage of steel fibers (SFs), the effect of GFRP rebars, different ratios of longitudinal rebars, and the impact of shear rebars. The proposed concrete jackets improved the bearing capacity and the mid-span deflection of the beams by 44 and 25%, respectively [13]. Kim et al. [14] investigated the strengthened RC beams using modularized steel plates. The steel plates were

bolted to the beam surfaces. The dimensions of the plates were obtained using the finite element method (FEM). The proposed steel plates increased the bearing capacity by 7 times [14]. Rahimi et al. [15] investigated the effect of aramid fiber reinforcement polymer (AFRP) and glass fiber reinforcement polymer (GFRP) on the strengthened deep RC beams and compared their response with the performance of CFRP sheets. The number of FRP layers was 1, 2, and 3. Depending on the number of sheets, the addition of AFRP, CFRP, and GFRP sheets increased the bearing capacity by 65 to 94%, 87 to 130%, and 96 to 133%, respectively [15]. Artiningsih et al. [16] strengthened RC beams using the glass fiber jacketing system. Two different failure levels were considered for the beams. Depending on the failure level, the maximum load increased by about 52 to 115% [16].

Faez et al. [11] investigated the strengthened RC beams using concrete jackets containing aluminum oxide nanoparticles and silica fume. The results showed that

*Corresponding Author Email: Hedayatnasab_arastoo@yahoo.com (A. Hedayatnasab)

RC jackets containing aluminum nanoparticles, depending on the thickness jacket, the number of rebars used in the jackets, and the length of the beam span, have increased the flexural strength by 155 to 447% [11]. Mohsenzadeh et al. [12] investigated the strengthened RC beams using SCC jacket containing glass fiber and fibrous silica fume gel (FSFG). Concrete jackets containing glass fiber and FSCG, depending on the amount of glass fiber, have increased the energy absorption capacity of the beams by about 89 to 463%. Concrete jackets containing FSFG and glass fiber delay forming the concrete's first cracks and increase the energy absorption capacity [12].

On the other hand, steel fiber reinforced concrete (SFRC) has been considered due to many advantages [17-19]. According to previous studies, strengthened RC beams using steel plate-fiber concrete composite jackets (SPFCJ) were investigated in the present study. For this purpose, studies were performed in both laboratory and numerical sections. The experimental results of the proposed method were presented entirely by Shadmand et al. [20]. The results can be used in many RC buildings that have been damaged due to lack of adequate supervision, incorrect design, and executive errors. A new method has been introduced to strengthen RC beams. SFRC and steel jackets are used next to each other. In previous studies, the entire surrounding surfaces of the beams are strengthened using reinforcing elements; but in this research about 75% of the peripheral surfaces of the beams was retrofitted.

The mechanical properties of SFRC are evaluated by considering two variables: the amount of SFs (0, 0.5, 1, 1.5, and 2% of the concrete volume) and the category of concrete (40, 50, and 60 MPa). In the second part, the flexural load test of the beams was performed in the strengthening and without strengthening modes. The studied variables include the SFs (0, 1, and 2% of concrete volume) and the type of strengthening method (RC jacket, SPFCJ, CFRP sheet). In order to strengthen the beams with jackets, the dimensions of the beams were increased from the bottom and sides. At the end of laboratory studies, the beams' behavior was compared using load-displacement diagrams. After laboratory studies, several beams prepared in the laboratory were simulated using the FEM using ABAQUS software [21].

2. THE STUDY PROCEDURE

The flowchart of the study is presented in Figure 1. As can be seen, the present study was conducted in three sections: preliminary, laboratory, and numerical studies. The laboratory study was performed in two separate sections. In the first part, the mechanical properties of SFRC are evaluated by considering two variables: the amount of SFs (0, 0.5, 1, 1.5, and 2% of concrete volume)

and the strength category of concrete (40, 50, and 60 MPa). The experiments are presented in Table 1. The failure age of the samples was considered to be 28 days.

In the second part, the four-point flexural test of the beams was performed in the strengthened and non-strengthened modes. The studied variables include the amount of SFs (0, 1, and 2% of concrete volume) and the type of strengthening method (Table 2). Table 3 summarized the types of modes studied in the laboratory strengthening section.

Details of the proposed method are provided in the literature [20]. The loading device is shown in Figure 2.

3. LABORATORY PROGRAM

3. 1. Materials　　　　The materials include coarse and fine aggregates, cement, water, superplasticizers, and
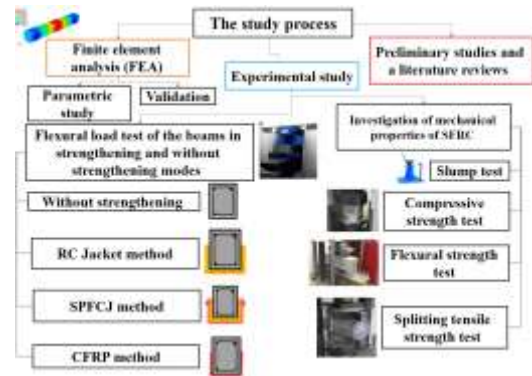
Figure 1. Flowchart of the study process

TABLE 1. Variables studied in laboratory study (Mechanical properties of SFRC)

Category of concrete	C40, C50, and C60
The amount of SFs	0, 0.5, 1, 1.5, and 2% volume of concrete

Description: Slump, splitting tensile strength, compressive strength, and flexural strength tests were conducted.

TABLE 2. Variables studied in laboratory study (Laboratory strengthening) [20]

Name	Strengthening method	Steel fiber (%)
NR	-	-
J-F0		0
J-F1	RC jacket	1
J-F2		2
CJ-F0		0
CJ-F1	SPFCJ	1
CJ-F2		2
CFRP	CFRP	--

TABLE 3. The mixing scheme used in the study of the properties of SFRC

Name	Strength grade (MPa)	Cement (kg)	Gravel (kg/m³)	Sand (kg/m³)	Water (lit)	Steel fiber (%)	SP (%)
C40F0	40	400	839	801	180	0	1
C40F0.5	40	400	839	801	180	0.5	1
C40F1	40	400	839	801	180	1	1
C40F1.5	40	400	839	801	180	1.5	1
C40F2	40	400	839	801	180	2	1
C50F0	50	500	785	710	225	0	1
C50F0.5	50	500	785	710	225	0.5	1
C50F1	50	500	785	710	225	1	1
C50F1.5	50	500	785	710	225	1.5	1
C50F2	50	500	785	710	225	2	1
C60F0	60	600	678	672	270	0	1
C60F0.5	60	600	678	672	270	0.5	1
C60F1	60	600	678	672	270	1	1
C60F1.5	60	600	678	672	270	1.5	1
C60F2	60	600	678	672	270	2	1

C: Concrete grade (Strength)   F: Steel fiber   SP: Superplasticizer

SFs. Coarse and fine aggregates grading test is conducted. The apparent density of the sand in saturated state with dry surface is 2.6 ton/m³. The apparent density of gravel in saturated state with dry surface is 2.65 t/m³.

Portland cement type II was used. The density and specific surface area of cement were 3.16 g/cm³ and 3350 cm²/g, respectively. The superplasticizer is liquid and its color is brown. Its density is 1.1 g/cm³. The steel fibers are simple with hooked ends. Detailed specifications of materials are provided in the literature [20].

3. 2. Experimental Tests   Figure 3 shows the experiments. The fresh concrete properties were evaluated using the slump test following ASTM C143 [22]. The compressive strength test was performed following ASTM C39 [23]. The flexural strength of concrete was performed following ASTM C293 [24]. The splitting tensile strength test was conducted following ASTM C496 [25]. For this purpose, cylindrical specimens with dimensions of 15×30 cm were prepared and tested.

Geometric dimensions of the beams and steel reinforcement characteristics were selected based on laboratory facilities and studies in retrofitting the RC beams. The main beams' length, width, and height were considered as 1600, 150, and 200 mm, respectively (Figure 4) [20].

3. 3. Mixing Design   The standard mixing design

method of ACI-211 [26] regulation is used. The mixing plan of concrete samples prepared in the technology section, main beams, and concrete jackets presented in Tables 3 and 4. During concreting, sand, gravel, cement, and water were mixed with a mixer for two minutes, and then the SFs, which were clean and free of any waste and

(a)

(b)
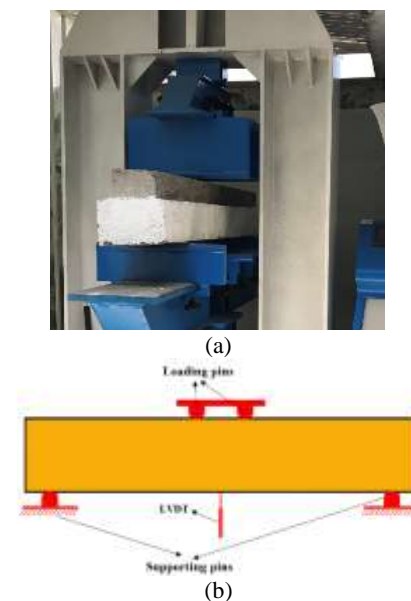
Figure 2. Four-point flexural test a: Loading frame b: LVDT, Supports, and the loading pins of the beams [18]

Figure 3. Experimental tests a: Slump test (b) Cubic specimens (c) Mixing concrete (d) Compressive strength (e) Splitting tensile strength f: Flexural strength
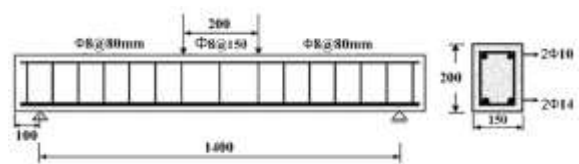
Figure 4. Geometric properties [20]

oil, were gradually poured into the mixer. After adding the fibers, the mixer was allowed to run for another three minutes until the fibers were spread throughout the concrete and the mixture was completely uniform.

TABLE 4. Mixing design used to make beams and jackets [18]

Member	Mix code	$\dfrac{W}{C}$	C (kg/m^3)	G (kg/m^3)	S (kg/m^3)	F (%)	SP (%)
Original Beam	NR	0.45	350	955	885	-	-
RC Jacket	J-F0	0.45	500	785	710	0	1
	J-F1	0.45	500	785	710	1	1
	J-F2	0.45	500	785	710	2	1
	CJ-F0	0.45	500	785	710	0	1
	CJ-F1	0.45	500	785	710	1	1
	CJ-F2	0.45	500	785	710	2	1

W: Water   C: Cement   G: Gravel   S: Sand   F: Steel fiber SP: Superplasticizer

4. TEST RESULTS

4. 1. Workibilty and Mechanical Properties   The properties of fresh concrete were investigated using the slump test. According to ACI 211.1-91 [26-28], the allowable range slump is 25 to 100 mm for reinforced concrete beams. The slump values for 15 typical concrete samples are shown in Figure 5. The slump values of all 15 samples are within the allowable limits of the regulations. The increase in compressive strength under the influence of fibers can be explained by the fact that the presence of fibers delays the growth of fine cracks in concrete, which in turn increases the resistance and strain under maximum load (Table 5) [29-31]. The fibers prevent microcrack spread, leading to greater compressive strength. While at the macro scale, it increases energy absorption [32, 33].

It is observed that the addition of SFs to concrete samples, can increase the tensile strength of concrete samples from 1.5 to 50.1%.

Special attention is paid to the shape of the fibers used (hooked), which leads to an increase in their elongation resistance as a result of improving the matrix-fiber continuity [32-34]. Also, it is observed that the addition of SFs to ordinary concrete samples, depending on the

amount of fibers and concrete category, can increase the flexural strength of concrete samples from 3.1 to 50.1 %.

4. 2. Results of Four-point Bending Test   The four-point bending test and crack distribution results are presented in the literature [20]. The crack distribution of the beams is illustrated in Figure 6. Load-deflection curves are presented in Figure 7. Also, crack load (P_{cr}), yield load (P_y), maximum load (P_u), crack deflection (Δ_{cr}), yield deflection (Δ_y) and ultimate deflection (Δ_u), ductility, stiffness, and adsorption capacity, the energy absorption are presented in Table 6. Each of the parameters is stated in Figure 8.
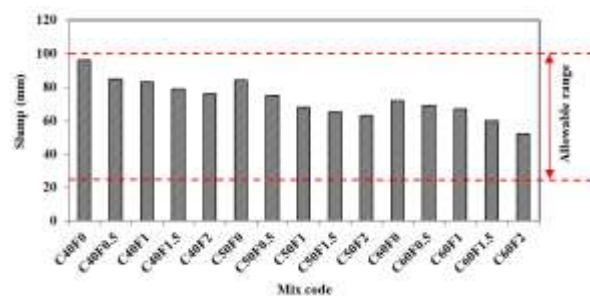
Figure 5. Slump values of samples in different mix proportions

TABLE 5. The test results (Mechanical properties)

Name	Compressive strength (MPa)	Variation (%)	Splitting tensile strength (MPa)	Variation (%)	Flexural strength (MPa)	Variation (%)
C40F0	36.9	–	3.12	–	4.21	–
C40F0.5	37	0.3	3.28	5.1	4.34	3.10
C40F1	37.1	0.5	3.89	24.7	4.5	6.90
C40F1.5	37.4	1.4	3.91	25.3	5.39	28
C40F2	37.6	1.9	3.98	27.6	6.32	50.10
C50F0	44.1	–	3.41	–	4.81	–
C50F0.5	44.2	0.3	3.9	14.4	5.1	6
C50F1	44.5	0.9	4.30	26.3	5.62	16.80
C50F1.5	45.1	2.3	4.80	40.8	5.93	23.30
C50F2	45.3	2.7	5.10	49.6	7.10	47.60
C60F0	52.1	–	3.85	–	5.10	–
C60F0.5	52.6	1	4.23	9.9	5.81	13.90
C60F1	53.2	2.1	4.61	19.8	5.91	15.90
C60F1.5	53.8	3.3	5.20	35	6.15	20.60
C60F2	54.1	3.8	5.80	50.1	6.41	45.30

NR

J-F0

J-F1

J-F2

CJ-F0

CJ-F1

CJ-F2

CFRP

Figure 6. Crack distribution [18]

4. 3. Comparative Study with Other Studies To compare the performance of the method proposed in this section, a comparative study of this method with similar studies has been conducted.

In the study of Ying et al. [35], the method of steel plates and rebar planting was used to strengthen RC beams, and the highest rate of increase in bearing capacity was reported to be 1.47. In the study of Abdulla [36], jackets containing cement mortars reinforced with glass fibers and carbon fibers were used to strengthen the beams, and the bearing capacity of the beams was increased by 1.33 times in the maximum case. Abdullah et al. [37] investigated the strengthening beams using CFRP rebars buried in the surface. The maximum increase in bearing capacity compared to the reference samples was 1.59 [37].

(a)

(b)
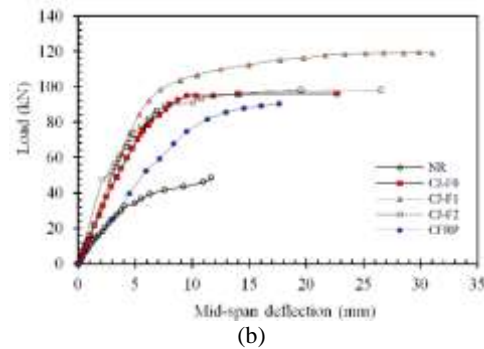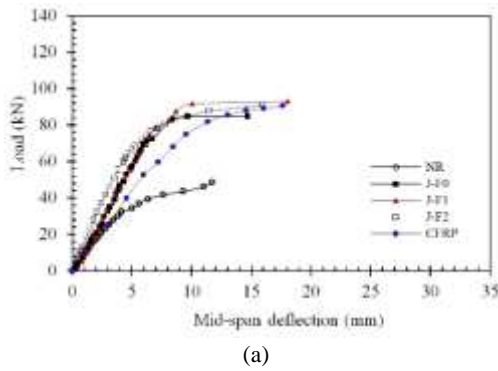
Figure 7. Load-deflection a: RC jackets b: SPFCJ [18]

TABLE 6. Crack, yield, and maximum point values

Code	Load (kN)			Mid-Span deflection (mm)			Ductility index	Stiffness (N/mm)	3
	Crack point	Yield point	Max. point	Crack point	Yield point	Max. point			
NR	4.1	34.2	52	0.5	5	11.7	2.34	8228.6	382
J-F0	7.2	66.3	85	1	5.7	14.7	2.58	8605.7	916
J-F1	9.3	68.9	93	1.30	6.16	17.9	2.69	922.2	1097
J-F2	9.0	68.7	91	1.20	5.9	15.9	2.91	8948.6	1266
CJ-F0	11.1	87.2	96.1	1.80	7.7	22.7	2.95	185085.7	1822
CJ-F1	12.9	101	119	2.4	8.95	31.8	3.55	16457.1	3119
CJ-F2	13.6	89.3	98.1	2.1	7.73	26.6	3.44	16525.7	2259
CFRP	5.1	62.3	90.8	0.89	7.3	17.5	2.40	8537.1	1074
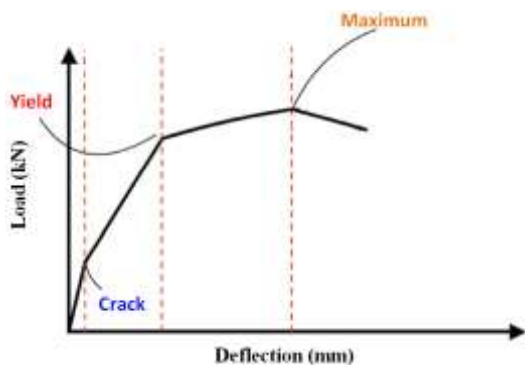
Figure 8. Hypothetical load-displacement diagram

Faez et al. [11] investigated the reinforcement of reinforced concrete beams using concrete jackets containing aluminum oxide nanoparticles. In this study, the highest rate of increase in bearing capacity was 2.75. Nanda and Bahra [38] used the method of gluing GFRP sheets in beam reinforcement. The results showed that this method could increase the bearing capacity by 1.34 times. Yu et al. [39] investigated the strengthening of severely damaged concrete beams using CFRP sheets. They showed that installing CFRP sheets can increase the maximum beam load by about 2.13 times. Zhang et al. [40] used concrete layers to strengthening RC beams and showed that this method could improve the bearing capacity by about 2.2 times. The present study results also showed that using SPFCJ containing SFs can increase the bearing capacity of beams by about 2.28 times.

5. FINITE ELEMENT ANALYSIS

The high cost of experimental experiments in civil engineering has necessitated the evaluation of software simulation methods. Due to the wide range of parameters involved in beam strengthening, decisions about design strategies and components are virtually impossible without simulation tools. In order to use the simulation tools correctly in the design and evaluation process, it is necessary to check their validity through scientific methods because the validity and accuracy of such devices are affected by various factors and require appropriate software depending on the type of parameters and data. In this research, the validity of simulation software (ABAQUS) has been investigated by experimental method.

This section describes the simulation method used. The simulated components include the main beam, the main beam longitudinal rebars, the transverse rebars in the main beam, the concrete jacket, steel reinforcement of the jacket steel plate for SPFCJs, the CFRP sheets and the distributed steel plates. The behavior of these models was defined in the Part section of the software. The main beams, concrete jacket, and load-bearing steel plates were determined using the solid element. Solid elements have a special place in terms of being the most used among the types of elements.

Longitudinal rebars of the main beam, transverse rebars in the main beam, and steel reinforcement rebars of the jackets were defined using the Wire element. CFRP sheets and steel plates were defined for use in SPFCJ using the shell element. Concrete, steel, and CFRP sheets are among the materials defined in the modeling of the beams understudy in different states. The properties of these materials are applied in the property section. Poisson's coefficient of concrete was considered 0.2. Also, the resistance classes of the main beams were considered C15, C20, and C25, respectively. Compressive and tensile strengths of the mentioned categories were performed by performing compressive and tensile strength tests. Table 7 lists the specifications for these concretes.

Also, from the mixing designs considered for reinforced concrete with SFs, a design was selected in which one percent of SFs was used. This choice is because this mixing design had better results in compressive, tensile, and flexural strengths than other designs. The compressive strength and tensile strength of this design were 37.1 MPa and 3.89 MPa, respectively. Steel rebars are ribbed and A3. Figure 9 shows the stress-strain diagram of the rebars.

The concrete structure was defined using the concrete damage plasticity (CDP). This model can show the nonlinear behavior and failure characteristics of brittle materials such as concrete. The CDP model in ABAQUS software is based on the model presented by Lulliner et al. [41]. The main priority of the damaged concrete plastic model is to provide the ability to analyze

Figure 9. Stress-strain diagram of simulated rebars

concrete structures under cyclic or dynamic loads. The behavior of concrete under low confinement pressure is generally brittle, which means that the main mechanism of failure is to create cracks in tension and crushing in pressure. If the confinement pressure is large enough to prevent cracks from spreading, then the brittle behavior of the concrete becomes ductile. This model assumes that the two main factors in concrete failure are cracking due to tension and crushing under pressure [42-44]. This model assumes that the strain rate is obtained from the sum of the elastic and plastic strain rates. In general, it can be said that the inelastic response of models in ABAQUS is divided into two separate parts: elastic response with reversible and inelastic with irreversible (permanent). This assumption is the primary basis of the following relation:

$$\varepsilon = \varepsilon^{el} + \varepsilon^{pl} \tag{1}$$

The concrete structure was defined using the CDP model. This model can show the nonlinear behavior and failure characteristics of brittle materials such as concrete. The strain rate of the elastic and plastic part and the strain rate of the plastic part. Two stiffness variables control changes in the yield procedure (or failure procedure) ε_t^{pl} and ε_c^{pl} which depend on the failure mechanism under tensile and compressive loads, respectively.

Figures 10 and 11 show concrete's tensile stress and axial response defined under the plastic damage parameter. It is assumed that under uniaxial stress; The stress-strain response of concrete is linear up to the yield stress phase σ_0^t (Figure 10), the flow stress occurs at the same time as the formation of fine cracks in concrete materials. After yield tension; The response to softening stress and the appearance of fine cracks is macroscopically visible and causes strain accumulation (permanent deformation) in concrete materials. On the other hand, under uniaxial pressure, it is assumed that the response is linear up to the initial yield stress stage (Figure 11). After initial yield, the strain stress response is typically defined by the stress hardening behavior

TABLE 7. Specifications of concretes used in main beams and proposed jackets

Member	Concrete grade	Steel fiber (%)	Compressive strength (MPa)	Spilitting tensile strength (MPa)
Main beam	C15	0	15.6	1.58
	C20	0	20.5	2.1
	C25	0	27.3	2.26
RC jacket	C40	1	37.1	3.89
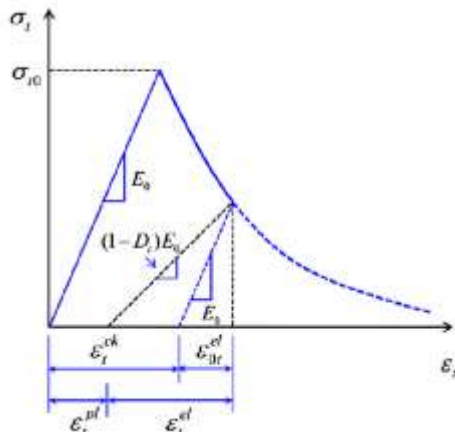
Figure 10. Definition of tensile properties of concrete in CDP model [21]
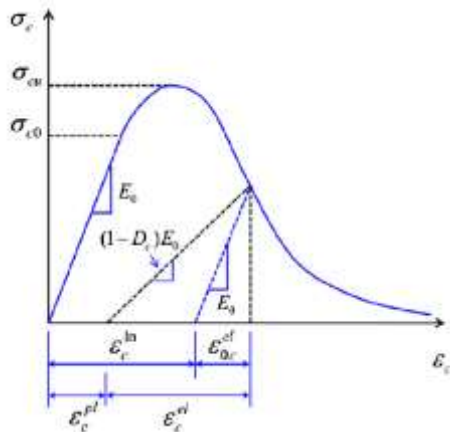
Figure 11. Definition of compressive properties of concrete in CDP model [21]

followed by strain-softening until the ultimate stress stage σ_{cu}. These hypotheses, despite their simplicity, cover the main capabilities of the concrete response. In this case, the strain stress relationship can be written according to the scalar variable of concrete damage as Equations (3) and (4) [21]:

$$\varepsilon_t^{\sim pl} = \varepsilon_t^{\sim ck} - \frac{d_t}{(1-d_t)}\frac{\sigma_t}{E_0} \quad (3)$$

$$\varepsilon_c^{\sim pl} = \varepsilon_c^{\sim in} - \frac{d_c}{(1-d_c)}\frac{\sigma_c}{E_0} \quad (4)$$

In this regard, E_0 is the initial elastic modulus (undamaged concrete) which, after multiplication in the damage parameters $(1-d_t)$ and $(1-d_c)$ becomes the variable of concrete damage. In other words, if the concrete is loaded in this state, it will respond with a gentler slope than the initial state in the strain stress curve. This is due

to the damage done to it in the previous loading. In practice, the hardness of the current damaged condition is less than the hardness of the original undamaged state of the concrete sample. The value of the damage variables d_t and d_c can range from zero, which represents no damage; If we ignore the elastic part with linear curves, in this case, the plastic strain curve of plastic stress is obtained. This means that the values of elastic stress and strain must be removed from the program input values. It is worth mentioning that the program can find the yield strain by dividing the yield stress by the elastic modulus of concrete and, therefore, practically the elastic part of the strain stress curve, which is linear. It is necessary to define the dilation angle values, eccentricity, K coefficient, and Poisson's coefficient. The dilation angle expresses the relationship between volumetric strain and shear strain. The expansion angle is considered to be greater than the internal friction angle of the concrete. The eccentricity potential of plastic is a small positive number equal to the tensile strength ratio to compressive strength of concrete. K is the coefficient that is considered 0.667 for concrete by default. The viscosity parameter is a parameter that is regarded as 0.00 by default. Table 8 presents the values of the parameters required to use the "concrete with damaged plasticity" model.

The thickness of CFRP fibers used is equal to 1 mm, and its unit mass of surface area is similar to 1536 N/m^2, and its Poisson coefficient is equal to 0.25, and its modulus of elasticity is equal to 2.4×10^5 MPa. Defining interactions between different members in ABAQUS simulation is one of the steps that must be done with great precision. The Embedded region was used to determine the interaction between steel rebars and concrete. Using the interaction module and clicking on constraint, the constraints were selected, and first, the buried area (reinforcements) was established, then the concrete area was selected for the host.

Definition of interaction between RC jackets and main beam, Definition of interaction between composite steel jackets and main beam, the interaction between steel plates and concrete jacket, and interaction between FRP and the main beam was done using tie element. The advantage of using the tie constraint is that it facilitates

TABLE 8. Specifications of concrete materials introduced to the software [45]

Parameter	
Dilation angle	$36°$
Eccentricity parameter	0.1
K	0.667
Viscosity	0
Poisson coefficient	0.2

the meshwork, and two pieces can have completely different mesh. At the point of contact, the two pieces should have the same mesh; depending on the complexity of the model, geometry may be a little difficult.

At ABAQUS, there are two different types of meshing methodologies called top-down and bottom-up. Of course, sometimes, the two meshing methodologies refer to automatic meshing and manual meshing, respectively, which refers to using and implementing each of these methods. Four different meshing techniques can be used Structured, sweep, accessible and Bottom-up. The first three techniques use the top-down methodology, and the last technique uses the bottom-up method to generate the mesh. It should be noted that not every piece of geometry can be meshed using any of the above methods. This parameter is entirely qualitative and is limited only to compare the degree of simplicity in meshing two different pieces. The Meshability of a piece can always be increased by partitioning it into a mesh module and dividing it into simpler sections, reducing the complexity. The structured sweep technique was used. In this case, there is the most control over the elements. Figure 12 shows the types of simple patterns for meshing more complex parts.

The basis of the solution in finite element software is the meshing and division of the main model into a limited number (limited means a definite number and does not imply the limit on the number) of smaller components. But the main question is: how many of these small members are needed to have a reliable solution? This question does not have a unique answer, but a criterion must be set to reach a reasonable response in choosing the number of elements. One of the most important parameters in solving finite elements is discussing the time and cost of solving. This parameter directly depends on the number of elements created. If 100 elements are selected for networking a problem, it will take less time to solve the same problem than solving the same problem with 200 elements. The number of elements and the elements' geometry and appearance are effective parameters in the discussion of convergence. First, a reasonable number of elements must be used. One of the essential points in determining the initial number of elements is the discussion of geometry and meshing order.

The optimal mesh size in the studied beams was calculated using the trial and error method. Based on this, the mesh dimensions considered to be 35 mm. Figure 12 shows an example of modeling.

6. VALIDATION

One of the essential parts of software simulations is to check the accuracy of the simulation method used. Validation is the process of evaluating a simulation

Figure 12. A picture of the meshing of several models

method to check whether the software used is properly accurate or not. In the present study, four beams prepared in the laboratory were simulated using the modeling method. Their responses were compared with each other in the form of load-displacement diagrams. The names and specifications of the selected beams are presented in Table 9. Among the beams prepared in the laboratory, beams named NR, J-F1, CJ-F1, and CFRP were simulated. The NR beam is the same as the control beam or non-strengthened beam. CJ-F1 is a beam whose peripheral surfaces are reinforced with SPFCJ containing 1% SFs.

Figures 13a to 13c show the crack distribution and load-displacement diagrams of the finite element model and the laboratory sample of the NR beam. Crack, yield and maximum loads, and energy absorption capacity of the NR beam finite element model are 3.8, 34.9, and 44.3 kN and 378 kJ, respectively. Crack loads, yield, and maximum laboratory samples of NR beam were 4.1, 34.2, and 48.5 kN and 382 kJ, respectively.

TABLE 9. The variables studied in the present study

Beam name	Strengthening method	Fibers used in the jacket (%)
NR	Control beam (C20)	–
J-F1	RC Jacket	1
CJ-F1	Steel Plate-Fiber Concrete Composite Jackets	1
CFRP	CFRP	–

(a)

(b)

(c)
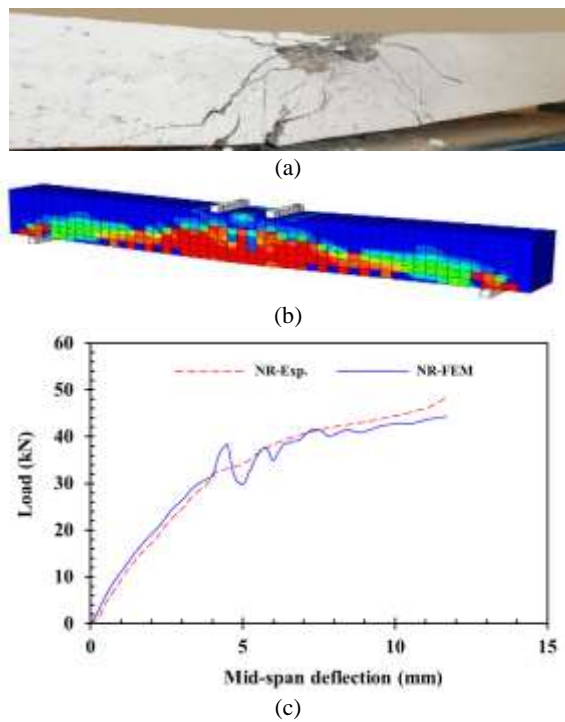
Figure 13. (a) Crack distribution in NR beam laboratory samples (b) Crack distribution in the finite element model of NR beam (c) Comparison of load-deflection diagrams of NR beam

Figures 14a to 14c show the crack distribution and load-displacement diagrams of the finite element model and the laboratory sample of the J-F1 beam. Crack, yield, maximum loads, and energy absorption capacity of the J-F1 finite element model are 9.6, 72.6 and 87.8 kN, and 1319 kJ. Crack loads, yield, and maximum laboratory sample of J-F1 beam are 9.3, 68.9, and 93 kN, and 1097 kJ, respectively.

Figures 15a to 15c show the crack distribution and load-displacement diagrams of the finite element model and the laboratory specimen of the CJ-F1 beam. Crack, yield and maximum loads, and energy absorption capacity of the CJ-F1 finite element beam model are 13.1, 99, and 121 kN and 2983 kJ, respectively. Crack loads, yield, and maximum laboratory samples of CJ-F1 beam are 12.9, 101, and 119 kN and 3119 kJ, respectively.

(a)

(b)

(c)
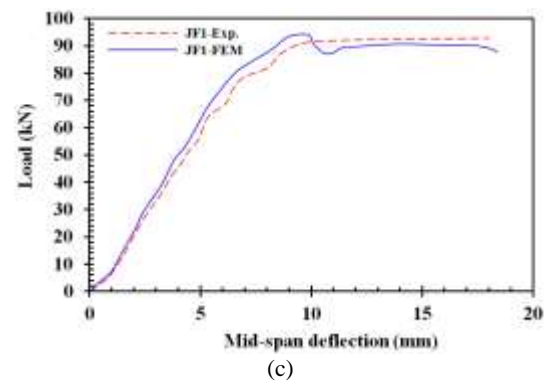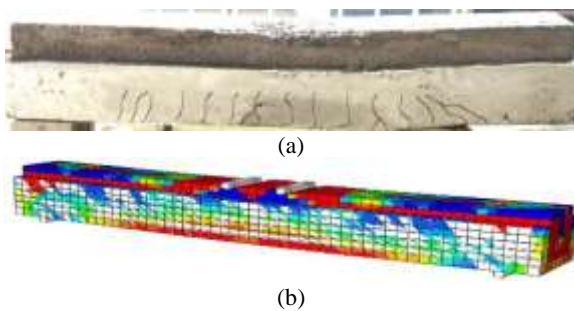
Figure 14. (a) Crack distribution in J-F1beam laboratory samples b: Crack distribution in the finite element model of NR beam c: Comparison of load-deflection diagrams of J-F1 beam

Figures 16a to 16c show crack distribution and load-displacement diagrams of the finite element model and the laboratory sample of CFRP beams. Crack, yield and maximum loads, and energy absorption capacity of the CFRP finite element model are 5.4, 68.4, and 92.6 kN and 1145 kJ, respectively. Crack, yield, and maximum laboratory loads of CFRP beam are 5.1, 62.3, and 90.8 kN and 1074 kJ, respectively.

Table 10 shows the percentage of load differences related to laboratory samples and finite element models. In the NR beam, the difference of crack load is about 7.9%, the difference of yield load is about 2%, and the maximum load difference is about 8.6%.

(a)

(b)

(c)
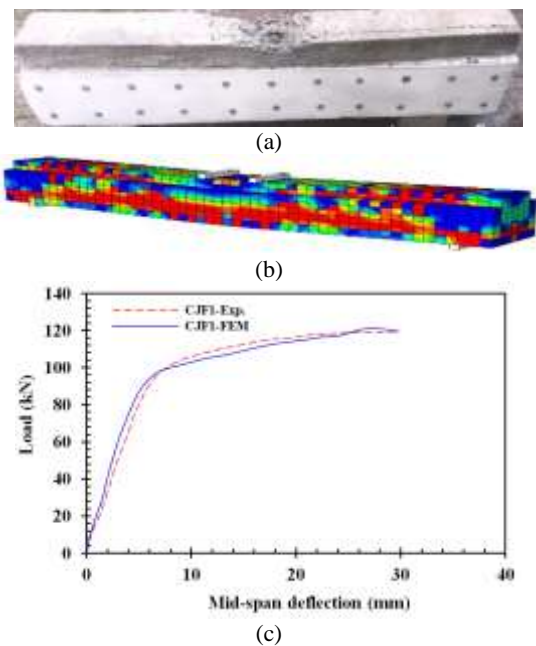
Figure 15. a: Crack distribution in CJ-F1beam laboratory samples b: Crack distribution in the finite element model of CJ-F1beam c: Comparison of load-deflection diagrams of CJ-F1 beam

(a)

(b)

(c)
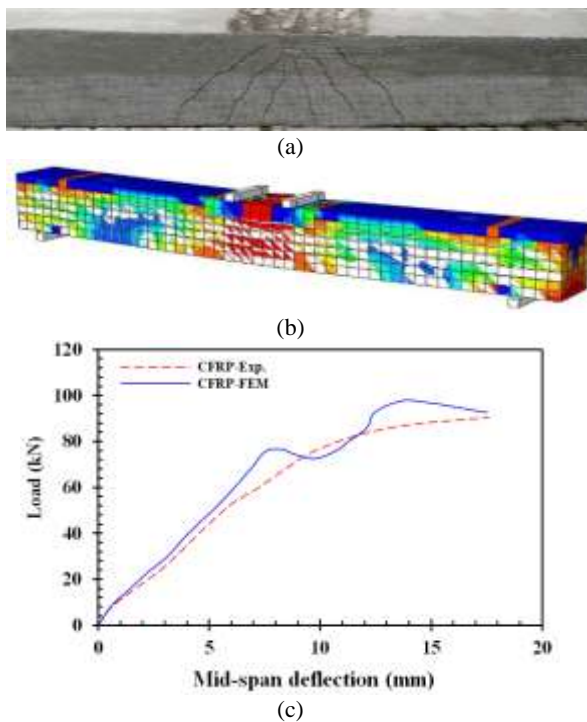
Figure 16. (a) Crack distribution in CFRP beam laboratory samples (b) Crack distribution in the finite element model of CFRP beam (c) Comparison of load-deflection diagrams of CFRP beam

In the J-F1 beam, the difference between crack load is about 1.3 percent, yield load difference is about 5.1 percent, and maximum load difference is about 5.9 percent. In the CJ-F1 beam, the difference between crack load is about 1.5 percent, yield load difference is about 2 percent, and maximum load difference is about 1.7 percent. In CFRP beam, the difference of crack load is about 5.6%, the difference of yield load is about 8.9%, and the maximum load difference is about 1.9%. According to the obtained values, it can be stated that the method used in simulating reinforced beams with concrete jacket, SPFCJ, and CFRP techniques has good accuracy, and this method can have an acceptable prediction.

7. FEA RESULTS

After examining the accuracy of the simulation method used, the results of FEA are presented in this section. For this purpose, first, the variable parameters are introduced, and then the outputs of the FEA of the models are shown for each of the states. Finally, the effect of each of the variable parameters on the behavior of the beams is evaluated. As observed in the laboratory strengthening section, variables such as the type of jacket (RC jacket, SPFCJ, CFRP) and the amount of SFs used in the jacket

TABLE 10. Percentage difference between laboratory samples and finite element models

Name	Crack load (kN)			Yield load (kN)			Maximum load (kN)		
	EXP.	FEM	Variation (%)	EXP.	FEM	Variation (%)	EXP	FEM	Variation (%)
NR	4.1	3.8	7.9	34.2	34.9	2	52	47.9	8.6
J-F1	9.3	9.6	3.1	68.9	72.6	5.1	93	87.8	5.9
CJ-F1	12.9	13.1	1.5	101	99	2	119	121	1.7
CFRP	5.1	5.4	5.6	62.3	68.4	8.9	90.8	92.6	1.9

(0, 1, and 2% by volume of concrete). Variable parameters in FEA include the strength class of concrete used in the main beam (C15, C20, and C25), the length of the beams (1.4 and 2.8 m), the type of jacket (RC jacket, SPFCJ, CFRP), and jacket thickness (40, 60 and 80 mm). The main beam's compressive strength is considered as a variable because in many RC buildings, the compressive strength of the concrete is not following the designer's purpose (compressive strength characteristic of concrete during design) is significantly different. Therefore, according to the tests provided by reputable concrete laboratories, three common concrete grades in the finite element section were considered for beams. The efficiency of the strengthening method in beams with different compressive strengths can be measured. Also, beam span length was evaluated as one

of the variables in FEA. For this purpose, the span length was doubled so that the performance of the proposed reinforcement methods in longer beams could be evaluated. The thickness of the proposed concrete jackets is also one of the parameters that can affect the results. For this purpose, three thicknesses of 40, 60, and 80 mm were considered for the cover. Thus, at first, the thickness of the jackets was considered to be 40 mm for the initial 24 cases, and then the optimal condition was selected, and the thickness of the jacket was increased by 1.5 and 2 times. The thickness of the steel sheet used in SPFCJs, the thickness of CFRP sheets, the geometrical and mechanical characteristics of longitudinal and transverse steel beams of the main beams, the geometrical and mechanical characteristics of the veneer rebar network, the geometric cross-section of the main beams and the

abutment conditions are fixed in all cases. Table 11 introduces the desired parameters. In this table, the letter C indicates the category of concrete used, and the number after it shows the concrete strength of the main beam in megapascals. The letter L also shows the length of the beam span, and the number after it indicates the length of the beam in megapascals. Also, each of the terms CJ, J, and FRP refer to reinforced beams with concrete-steel composite jackets, concrete jackets, and FRP. Figure 17 presents the geometric characteristics of the beams understudy in the finite element study.

TABLE 11. Introduces the studied parameters in FEA

No.	Name	Main beam concrete category (MPa)	Beam span (mm)	Jacket thickness (mm)	Jacket type
1	C15-L1.4	15			
2	C20-L1.4	20	1400		
3	C25-L1.4	25			-----
4	C15-L2.8	15			
5	C20-L2.8	20	2800		
6	C25-L2.8	25			
7	C15-L1.4-CJ	15			
8	C20-L1.4-CJ	20	1400		
9	C25-L1.4-CJ	25			SPFCJ
10	C15-L2.8-CJ	15			
11	C20-L2.8-CJ	20	2800		
12	C25-L2.8-CJ	25			
13	C15-L1.4-J	15			
14	C20-L1.4-J	20	1400	40	
15	C25-L1.4-J	25			RC Jacket
16	C15-L2.8-J	15			
17	C20-L2.8-J	20	2800		
18	C25-L2.8-J	25			
19	C15-L1.4-CFRP	15			
20	C20-L1.4-CFRP	20	1400		
21	C25-L1.4-CFRP	25			FRP
22	C15-L2.8-CFRP	15			
23	C20-L2.8-CFRP	20	2800		
24	C25-L2.8-CFRP	25			
25	Optimal mode with 60 mm jacket thickness				
26	Optimal mode with 80 mm jacket thickness				

The load was applied in four points similar to the laboratory conditions, and the displacement corresponding to the middle of the span was measured. Figure 18 illustrates how the load is applied to the beams. The details of the beam were presented in the literature [20].

The results of the FEA of beams are presented in four different groups (Figures 19-22). In the first group, outputs related to control beams (without strengthening), in the second group, outputs related to beams strengthened with RC jackets, in the third group, outputs related to beams strengthened with SPFCJ, the fourth group, outputs related to beams strengthened with CFRP sheets are presented. Figure 8 provides a hypothetical load-displacement diagram to introduce the points corresponding to crack, yield, and the maximum bearing load of the beam.

(a)

(b)
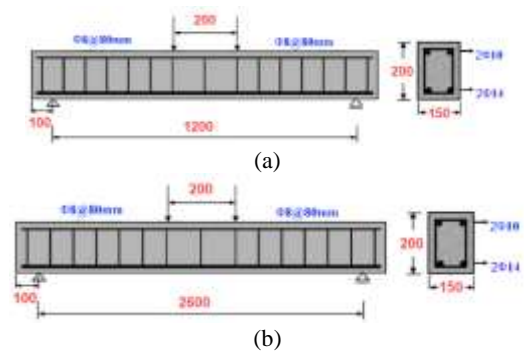
Figure 17. Geometric characteristics of finite element model of concrete beams understudy (a) 1.4-meter beam (b) 2.8-meter beam
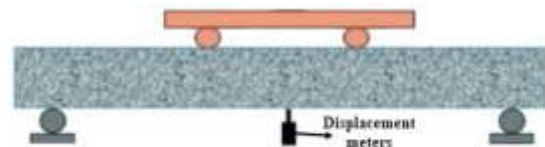
Figure 18. Loading
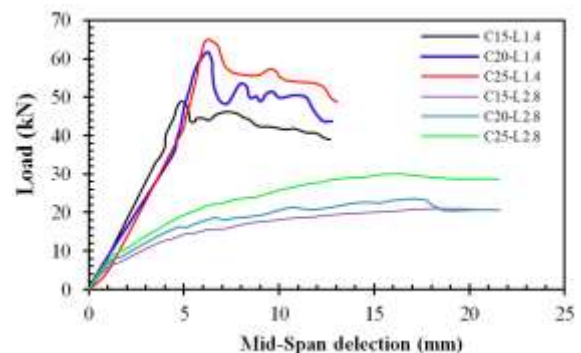
Figure 19. Load-mid span deflection curves of control beams (without reinforcement)
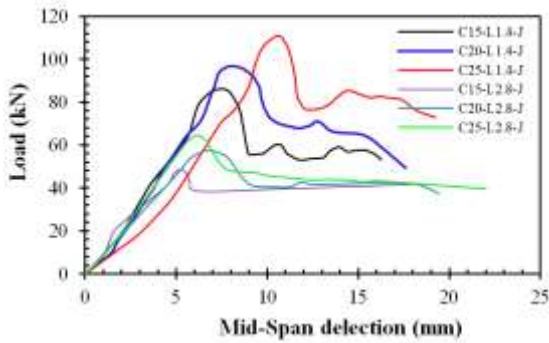
Figure 20. Load-mid span deflection curves of strengthened beams with SPFCJ
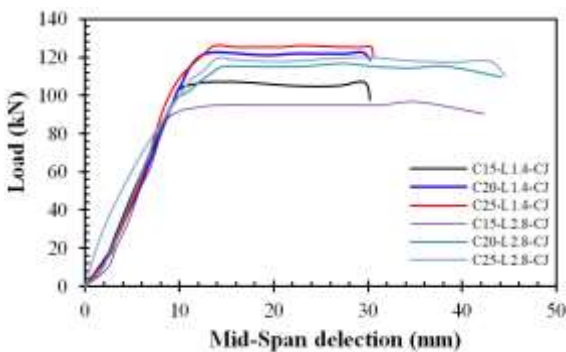
Figure 21. Load-mid span deflection curves of strengthened beams with RC jacket
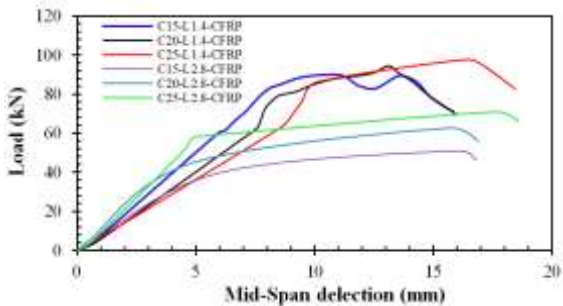
Figure 22. Load-mid span deflection curves of strengthened beams with CFRP sheets

7. 1. Energy Absorption Capacity   In Figures 23 and 24, the energy absorption capacity of beams with a span length of 1.40 m and 2.8 m are compared with each other. The addition of SPFCJ containing SFs to the beams is effective for all three categories of concrete used. It has increased the energy absorption capacity by 5.83, 5.83, and 5.63 times, respectively. Also, the addition of RC jackets with SFs to the beams is effective for all three categories of concrete used. It has increased the energy absorption capacity by 1.87, 2.7, and 2.25 times, respectively. The performance of CFRP sheets was almost similar to that of RC jackets. The addition of

CFRP sheets of C15, C20, and C25 beams increased the energy absorption capacity by 2.19, 1.87, and 2.12 times compared to the control sample, respectively.

In Figures 25 and 26, the energy absorption capacity of beams with a span length of 1.4 m and 2.80 m are compared with each other. The addition of SPFCJ to beams with a span length of 2.8 m is effective for all three categories of concrete used. It has increased the energy absorption capacity by 9.72, 11.03, and 9.16 times, respectively. Also, the addition of RC jackets with SFs to the beams is effective for all three categories of concrete used. It has increased the energy absorption capacity by 1.82, 1.91, and 1.8 times, respectively. The addition of CFRP sheets of C15, C20, and C25 grade beams increased the energy absorption capacity by 1.71, 1.93, and 2.02 times compared to the control sample, respectively.

Strength classes of C20 and C25 are classes that are used in many common construction projects, and class C15 is a class that represents the strength of a weak beam. According to Figures 23 to 26, it can be stated that in all three strengthened methods used, the change in the concrete category of the main beam did not significantly change the performance of the methods.
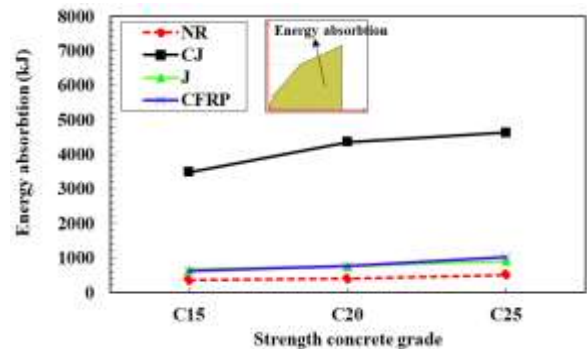
Figure 23. Comparison of energy absorption capacity of beams with a span length of 1.4 m
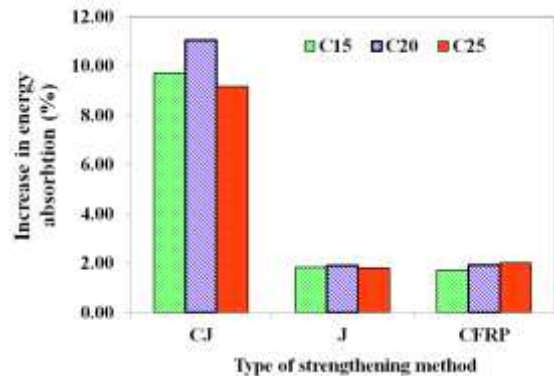
Figure 24. Increase in energy absorption capacity of RC beams compared to non-strengthened beams (control) with a span length of 1.4 m

TABLE 12. FEA results

Name	Load			Deflection			Energy absorption (kJ)	Ductility (μ)
	Crack (kN)	Yield (kN)	Max. (kN)	Crack (kN)	Yield (kN)	Max. (kN)		
C15-L1.4	3.9	33.4	48	0.5	4.8	12.5	450	2.6
C20-L1.4	4.5	35.6	61	0.6	4.9	12.9	499	2.63
C25-L1.4	4.9	39.1	65	1.4	5.8	13	540	2.24
C15-L2.8	3.4	17	24	1.5	8	21.5	358	2.68
C20-L2.8	3.8	18	26	1.6	8.5	21.3	395	2.5
C25-L2.8	4.1	24	30	1.7	10	21.5	505	2.15
C15-L1.4-CJ	8.5	98	116	2.5	9.1	30.3	2624	3.33
C20-L1.4-CJ	10.8	104	121	2.7	9.6	31.6	2909	3.29
C25-L1.4-CJ	11.1	110	127	2.9	10	32.6	3041	3.26
C15-L2.8-CJ	8.1	86	97	2.2	8.9	42.3	3480	4.75
C20-L2.8-CJ	8.9	91	114	2.3	9.1	44.5	4357	4.89
C25-L2.8-CJ	10.3	96	119	2.4	9.6	45.8	4624	4.77
C15-L1.4-J	8.9	67.5	88	1.1	5.9	16.3	848	2.36
C20-L1.4-J	9.1	69.3	95	1.4	6.25	17.5	1032	2.41
C25-L1.4-J	10.3	70.6	110	1.6	7	19	1214	2.38
C15-L2.8-J	7.9	40.6	48	0.8	4.5	18	653	2.95
C20-L2.8-J	8.3	45.9	55	0.9	5	19	754	3.02
C25-L2.8-J	8.9	58.3	63	1	5.3	22	910	3.28
C15-L1.4-FRP	4	59	88	0.7	6	15	987	2.50
C20-L1.4-FRP	5	61	99.3	0.8	7	16	932	2.29
C25-L1.4-FRP	6.3	63.3	95	0.9	8.5	18.5	1143	2.18
C15-L2.8-FRP	3.5	39	51	0.5	5.9	16.3	612	2.76
C20-L2.8-FRP	4.5	45	63	0.5	4.9	16.9	763	3.45
C25-L2.8-FRP	4.9	51	71	0.6	4.9	18.9	1018	3.86
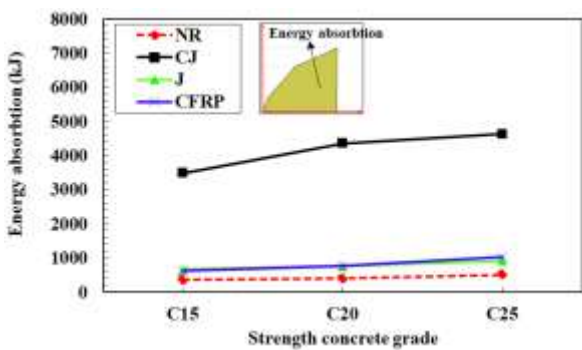
Figure 25. Comparison of energy absorption capacity of beams with span length of 2.8 m
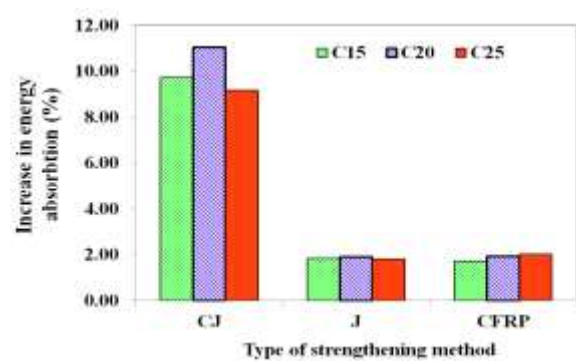
Figure 26. Values of percentage increase in energy absorption capacity of RC beams compared to non-reinforced beams (control) with a span length of 2.8 meters

Figure 27 compares the values of percentage increase in energy absorption capacity of RC beams compared to control beams. According to this diagram, the proposed

method has been more effective in longer beams; the SPFCJ in beams with a span length of 2.8 meters has

increased the energy absorption capacity depending on the strength class of the main beam from 9 to 11 times. However, in beams with a span length of 1.4 m, the use of the proposed composite jackets has increased the energy absorption capacity by about 5 to 6 times.

The performance of RC jackets containing SFs and the CFRP method on increasing the bearing capacity of beams for both considered span lengths are almost similar. Depending on the length of the spans and the concrete category of the main beam, the energy absorption capacity is in between 1.8 to 2.5 times.

7. 2. Comparison of Crack Load Values

The crack load in the studied beams is presented in Figure 28. SPFCJ in all cases has increased the crack resistance of the beams. The crack load of the strengthened beams with the proposed jackets has increased by 2.2 to 2.5 times depending on the strength class of the main beam and the span length. The CFRP method had less effect on increasing the crack load than the other two methods such that using this method, the load on the beams increased by only about 10 to 20%.

7. 3. Comparison of Yield Load

The point of the load-displacement curve at which the curve fails locally is considered as the yield point. Accordingly, the yield load of the 24 finite element models simulated is presented in Figure 28. The addition of SPFCJ jackets containing SFs increased the yield load of beams with strength classes C15, C20, and C25 and a span of 1.4 m by 2.9, 2.9, and 2.8 times, respectively. The SPFCJ increased the yield load of beams with strength classes C15, C20, and C25 and with a span of 2.8 meters by 1.5, 1.5, and 4 times, respectively.

The effectiveness of reinforced concrete jacket methods containing SFs and CFRP sheets had less effect on improving the yield load of beams compared to the proposed method. The use of concrete jackets containing SFs increased the yield load of beams with resistance classes C15, C20, and C25 and with a span of 1.4 meters by 2, 1.9, and 1.8 times, respectively. The RC jackets

Figure 28. Load values corresponding to the first crack in the beams and their increase ratios compared to the control samples

containing SFs increased the yield load of beams with resistance classes C15, C20, and C25 and with a span of 2.8 meters by 2.4, 2.6, and 2.4 times, respectively.

7. 4. Comparison of Bearing Capacity of Beams (Maximum Load)

The maximum load that the beam can withstand is called the bearing capacity or maximum load. The load capacity of beams with a span length of 1.4 m, which strengthened using SPFCJ, in which concrete with grades C15, C20, and C25 have been used, increased by 2.4, 2, and 2 times, respectively. Bearing capacity of beams with a span length of 2.8 m, which have been strengthened using SPFCJ in which concrete with grades C15, C20, and C25 have been used, increased by 4, 4.4, and 4 times, respectively (Figure 30). From these values, it can be concluded that the proposed method has a good performance for the three strength classes. Also, the effectiveness of SPFCJ is more effective in beams with longer span lengths.

RC jackets containing SFs increased the maximum load of beams with strength classes C15, C20, and C25 and with a span of 1.4 meters by 1.8, 1.6, and 1.7 times,

Figure 27. Comparison of the energy absorption capacity increase compared to non-strengthened beams (control) to investigate the effect of change along the span
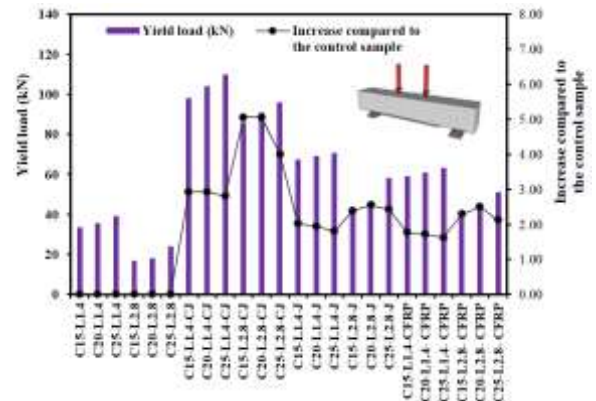
Figure 29. The yield values of the beams and their increase ratios in comparison with the control samples
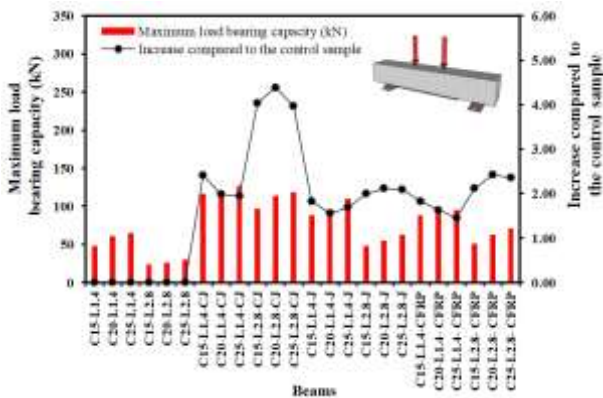
Figure 30. Maximum beam load values and their increase ratios compared to control specimens

respectively. RC jackets containing SFs caused the maximum load of beams with strength class C15, C20, and C25 and with a span of 2.8 meters to increase by 2, 1.2, and 1.2 times, respectively. The use of CFRP sheets increased the maximum load of beams with strength classes C15, C20, and C25 and with a span of 1.4 meters by 1.8, 1.6, and 1.5 times, respectively. The use of CFRP sheets increased the maximum load of beams with strength classes C15, C20, and C25 and with a span of 2.8 meters by 2.1, 2.1, and 2.4 times, respectively.

7. 5. Ductility Figure 31 compares the ductility coefficient of the studied beams. SPFCJ has increased the ductility of the specimens. SPFCJ makes the beams to withstand larger forces with more ductility. These jackets perform better than concrete fibers strengthened with SFs and CFRP sheets. The ductility of strengthened beams with SPFCJ increases by 22 to 96%, depending on the category of concrete used and span length.

7. 6. Investigation of the Effect of Change in the Thickness of the Proposed Concrete Jackets The thickness of the proposed jackets containing SFs is one of the parameters whose amount can affect the response of the beam. This section examines this parameter. The C25-L1.4-CJ beam performed better than
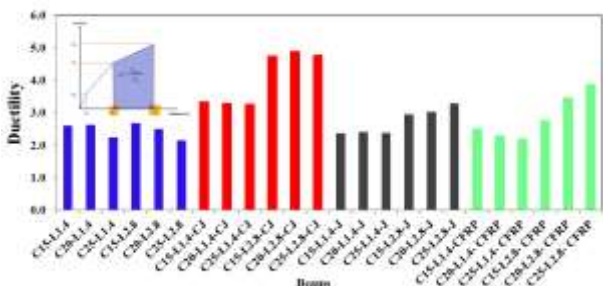
Figure 31. Comparison of ductility coefficients of beams in different states

other modes of energy absorption capacity, bearing capacity, crack and yield loads and ductility. The thickness of the cover of this beam was 40 mm. The mentioned beam was simulated again with two different jacket thicknesses (60 and 80 mm), and the results of its analysis were presented in Figures 32 and 33.

In the beam that was strengthened using the C25-L1.4-CJ-t60 jacket, the crack, yield, and maximum beam loads were 46, 196, and 228 kN, respectively. Also, the corresponding displacements with crack and yield loads were equal to 0.3 and 6.47 mm, respectively. The ultimate displacement of this beam was 32 mm.

According to Figure 33 in the beam that was strengthened using the C25-L1.4-CJ-t80 jacket, the crack loads, yield, and maximum loads were 32, 147, and 190 kN, respectively. Also, the corresponding displacements to crack and yield loads were equal to 0.49 and 5.8 mm, respectively.

Figure 34 and Table 13 compare the load-deflection curves of strengthened beams with SPFCJ to investigate changes in the thickness of the jacket. Among the three thicknesses considered for jackets, 60 mm thick has the best performance in terms of energy absorption capacity compared to the other two thicknesses. Energy absorption capacity corresponding to the C25-L1.4-CJ-t60 mode is approximately two times that of the C25-L1.4-CJ-t40 mode and 18% higher than the C25-L1.4-CJ-t80 mode. In terms of load-bearing capacity or maximum load-bearing capacity, jackets with a thickness of 60 mm had a relatively better performance; So that the bearing capacity of the strengthened beam with 60 mm composite jacket has been increased by 79 and 20% more than the values corresponding to 40 and 80 mm jackets.

(a)

(b)
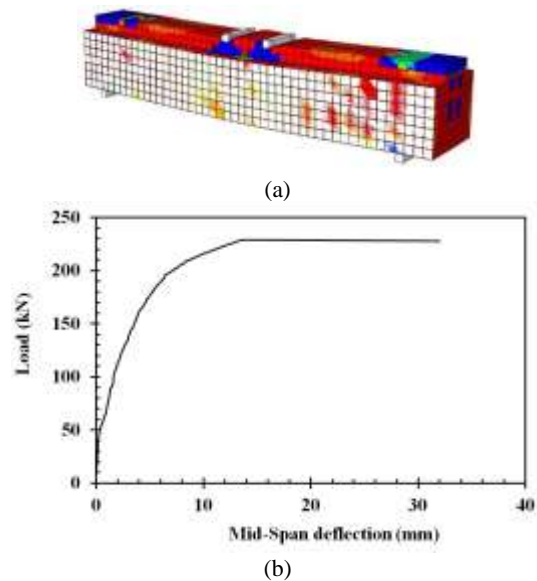
Figure 32. Results of analysis of C25-L1.4-CJ beam with 60 mm jacket thickness a: Crack distribution and deformable shape b: Load-deflection curve

(a)

(b)
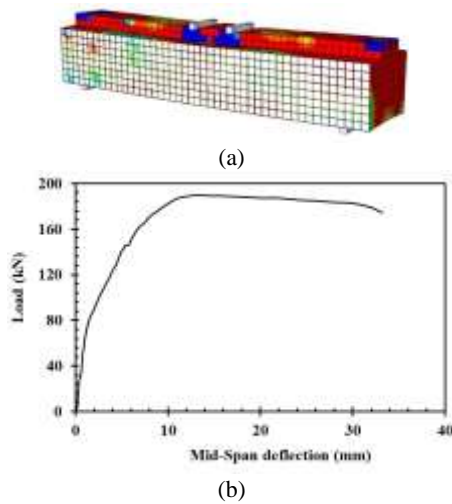
Figure 33. Results of C25-L1.4-CJ beam analysis with 80 mm jacket thickness (a) Crack distribution and modified shape (b) load-displacement curve
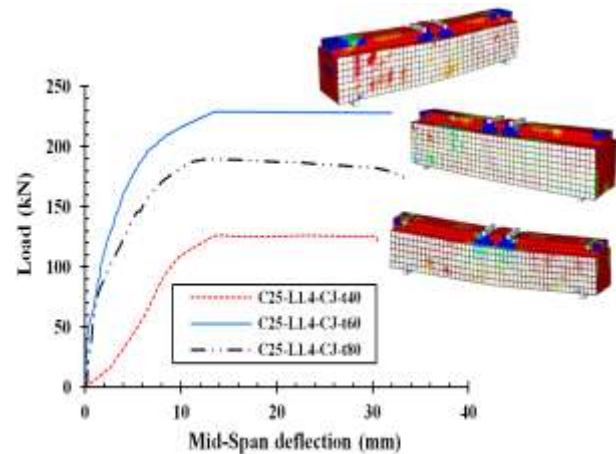
Figure 34. Comparison of load-deflection curves of strengthened beams with SPFCJ to investigate changes in jacket thickness

TABLE 13. Comparison of strengthened beams to investigate the effect of change in the thickness of the proposed composite jacket

Name	Load (kN)			Deflection (mm)			Ductility	Energy absorption (J)
	Crack	Yield	Max.	Crack	Yield	Max.		
C25-L1.4-CJ-t40	11.1	110	127	2.9	10	32.6	3.26	3041
C25-L1.4-CJ-t60	46	196	228	0.3	6.47	32	4.94	6597
C25-L1.4-CJ-t80	32	147	190	0.49	5.8	33.9	5.84	5585

It can be said that the jacket thickness parameter has a significant role in the response of strengthened beams with the proposed composite jackets, and depending on the dimensions and geometric characteristics of the beam, a suitable thickness should be considered for the jacket.

8. CONCLUSIONS

In this study, the strengthening of RC beams using SPFCJ jackets was investigated. For this purpose, the effect of parameters such as compressive strength of the main concrete beam jacket thickness and span length using FEA, was evaluated. The accuracy of the FEA method was evaluated by modeling a number of laboratory beams prepared by Shadmand et al. [20], and it was shown that the method used can provide an accurate prediction of the beam response. This section summarizes some of the most important results:
- The ductility of strengthened beams with SPFCJ jackets containing SFs has increased from 26 to 52%, depending on the amount of fibers compared to the control sample. As the concrete jacket contains fibers, the beams can withstand more forces with more ductility.

- Strength classes C20 and C25 are classes that are used in many common construction projects, and class C15 is a class that represents the resistance of a weak beam. In all three reinforcement methods used, the change in the concrete category of the main beam did not significantly change the performance of the proposed method.
- The proposed method has been more effective in longer beams. The SPFCJ in beams with a span length of 2.8 meters has increased the energy absorption capacity depending on the strength class of the main beam from 9 to 11 times. In beams with a span length of 1.4 m, the proposed composite jackets have increased the energy absorption capacity by about 5 to 6 times.
- SPFCJ in all cases has increased the crack resistance of the beams; So that the crack load of the reinforced beams with the proposed jackets has increased 2.2 to 2.5 times depending on the resistance class of the main beam and the span length. The CFRP method had less effect on increasing the crack load than the other two methods. Using this method, the load on the beams increased by only about 10 to 20%.
- The bearing capacity of beams with a span length of 2.8 m, which have been strengthened using SPFCJ with grades C15, C20, and C25, increased 4, 4.4, and

4 times, respectively. From these values, it can be concluded that the proposed method has a good performance for the three strength. Also, the effectiveness of SPFCJ is more effective in beams with longer span lengths.

The strengthened beams with SPFCJ can depend on several factors. Therefore, to develop the present study, the following suggestions are presented:

- Investigating the effect of changing the percentage of steel reinforcement used in the main beams on the present study results.
- Investigating the use of other fibers such as basalt and polypropylene in RC jackets to strengthen concrete beams.
- Combined use of nanoparticles and types of fibers such as basalt, glass, and polypropylene in RC jackets to strengthen these beams.
- Investigation of strengthening of RC beams with composite jackets strengthened with SFs against cyclic loading.

9. REFERENCES

1. Khan, MA., "Toward Key Research Gaps in Design Recommendations on Flexurally Plated RC Beams Susceptible to Premature Failures." *Journal of Bridge Engineering*, Vol. 26, No. 9, (2021), 04021067. Doi: doi.org/10.1061/(ASCE)BE.1943-5592.0001772

2. Deng, Y., Ma, F., Zhang, H., Wong, S. H., Pankaj, P., Zhu, L., & Bahadori-Jahromi, A., "Experimental study on shear performance of RC beams strengthened with NSM CFRP prestressed concrete prisms." *Engineering Structures*, Vol. 235, (2021), 112004. Doi: doi.org/10.1016/j.engstruct.2021.112004

3. Yuan, P., Xiao, L., Wang, X., & Xu, G., "Failure mechanism of corroded RC beams strengthened at shear and bending positions." *Engineering Structures*, Vol. 240, (2021), 112382. Doi: doi.org/10.1016/j.engstruct.2021.112382

4. Liu, X., Gernay, T., Li, L. Z., & Lu, ZD., "Seismic performance of post-fire reinforced concrete beam-column joints strengthened with steel haunch system." *Engineering Structures*, Vol. 234, (2021), 111978. Doi: doi.org/10.1016/j.engstruct.2021.111978

5. Ozturk, B., Yilmaz, C., Şentürk, T. "Effect of FRP retrofitting application on seismic behavior of a historical building at Nigde, Turkey", 14th European Conference on Earthquake Engineering. (2010), Ohrid, Republic of Macedonia.

6. Ozturk, B. A. K. İ., Senturk, T., Yilmaz, C. "Analytical investigation of effect of retrofit application using CFRP on seismic behavior of a monumental building at historical Cappadocia region of Turkey", (2010), In 9th US National and 10th Canadian Conference on Earthquake Engineering, Toronto, Canada.

7. Shen, D., Li, M., Kang, J., Liu, C., Li, C., "Experimental studies on the seismic behavior of reinforced concrete beam-column joints strengthened with basalt fiber-reinforced polymer sheets." *Construction and Building Materials*, Vol. 287, (2021), 122901. Doi: doi.org/10.1016/j.conbuildmat.2021.122901

8. Nie, XF., Zhang, SS., Yu, T., "On the FE modelling of RC beams with a fibre-reinforced polymer (FRP)-strengthened web opening." *Composite Structures*, Vol. 271, (2021), 114161. Doi: doi.org/10.1016/j.compstruct.2021.114161

9. Rahmani, I., Maleki, A., Lotfollahi-Yaghin, MA., "A laboratory study on the flexural and shear behavior of rc beams retrofitted with steel fiber-reinforced self-compacting concrete jacket". *Iranian Journal of Science and Technology*, (2020), 1-17. Doi: doi:org/10.1007/s40996-020-00547-x

10. Maraq, MA., Tayeh, BA., Ziara, MM., Alyousef, R., "Flexural behavior of RC beams strengthened with steel wire mesh and self-compacting concrete jacketing—experimental investigation and test results." *Journal of Materials Research and Technology*, Vol. 10, (2021), 1002-1019. Doi: doi.org/10.1016/j.jmrt.2020.12.069

11. Faez, A., Sayari, A., & Manei, S., "Retrofitting of RC beams using reinforced self-compacting concrete jackets containing aluminum oxide nanoparticles." *International Journal of Engineering, Transactions B: Applications*, Vol. 34, No. 5, (2021), 1195-1212. Doi: 10.5829/ije.2021.34.05b.13

12. Mohsenzadeh, S., Maleki, A, Lotfollahi-Yaghin, MA., "Strengthening of RC beams using SCC jacket consisting of glass fiber and fiber-silica fume composite gel", *International Journal of Engineering, Transactions B: Applications,* Vol. 34, No. 8, (2021), 1923-1939. Doi: 10.5829/ije.2021.34.08b.14

13. Attar, H. S., Esfahani, M. R., Ramezani, A. "Experimental investigation of flexural and shear strengthening of RC beams using fiber-reinforced self-consolidating concrete jackets." *In Structures*, Vol. 27, (2020), 46-53. Doi: doi.org/10.1016/j.istruc.2020.05.032

14. Kim, MS., Lee, YH., "Flexural Behavior of Reinforced Concrete Beams Retrofitted with Modularized Steel Plates" *Applied Sciences*, Vol. 11, No. 5, (2021), 2348. Doi: doi.org/10.3390/app11052348

15. Rahimi, SB., Jalali, A., Mirhoseini, SM, Zeighami, E., "Experimental Comparison of Different Types of FRP Wrapping in Repairing of RC Deep Beams with Circular Openings". *International Journal of Engineering, Transactions B: Applications,* Vol. 34, No. 8, (2021), 1961-1973. doi: 10.5829/ije.2021.34.08b.17

16. Artiningsih, T. P., Lirawati, L., Helmi, N., "Retrofitting of Reinforced Concrete Beams Using a Fiberglass Jacketing System." *Journal of Advanced Civil and Environmental Engineering*, Vol. 4, No. 1, (2021), 44-50. Doi: doi.org/10.30659/jacee.4.1.44-50

17. Do Thi, MD., Lam, TQK., "Design parameters of steel fiber concrete beams." *Magazine of Civil Engineering,* Vol. 2, (2021), 10207-10207. Doi: 10.1007/978-981-33-6208-6_30

18. Kang, MC., Yoo, DY., Gupta, R., "Machine learning-based prediction for compressive and flexural strengths of steel fiber-reinforced concrete." *Construction and Building Materials*, Vol. 266, (2021), 121117. Doi: doi.org/10.1016/j.conbuildmat.2020.121117

19. Awolusi, TF., Oke, OL., Atoyebi, OD., Akinkurolere, O., Sojobi, AO., "Waste tires steel fiber in concrete: A review." *Innovative Infrastructure Solutions*, Vol. 6, Vol. 1, (2021)., 1-12. Doi: doi.org/10.1007/s41062-020-00393-w

20. Shadmand, M., Hedayatnasab, A., Kohnehpooshi, O., "Retrofitting of reinforced concrete beams with steel fiber reinforced composite jackets". *International Journal of Engineering, Transactions B: Applications,* Vol. 33, No. 5, (2020), 770-783. Doi: 10.5829/ije.2020.33.05b.08

21. Hibbitt, H., Karlsson, B., and Sorensen, E., "ABAQUS user's manual." Providence, RI: Dassaulat Systems Simulia Corp, (2016).

22. ASTM C143 / C143M-20, Standard Test Method for Slump of Hydraulic-Cement Concrete, ASTM International, West Conshohocken, PA, (2020).

23. ASTM Standard C39/C39M-18, Standard test method for compressive strength of cylindrical concrete specimens, ASTM International, West Conshohocken PA, (2018).

24. ASTM C293/ C293M-16, Standard Test Method for Flexural Strength of Concrete (Using Simple Beam With Center-Point Loading), ASTM International, West Conshohocken, PA, (2016).

25. ASTM Standard C496/C496M-17 Standard test method for splitting tensile strength of cylindrical concrete specimens, ASTM International, West Conshohocken PA, (2017).

26. Standard practice for selecting proportions for normal, heavyweight, andmass concrete, ACI 211.1-91 (1991), ACI Committee 211, Farmington Hills, MI, USA.

27. Soon, Poh Yap., Kuan Ren Khaw, U., Johnson Alengaram, Mohd Zamin Jumaat., "Effect of fiber aspect ratio on the torsional behavior of steel fiber-reinforced normal weight concrete and lightweight concrete." *Engineering Structures* Vol. 101, (2015), 24– 33. Doi: 10.1016/j.engstruct.2015.07.007

28. Han, J., Zhao, M., Chen, J., Lan, X. "Effects of steel fiber length and coarse aggregate maximum size on mechanical properties of steel fiber reinforced concrete." *Construction and Building Materials*, Vol. 209, (2019), 577-591. Doi: 10.1016/j.conbuildmat.2019.03.086

29. Wu, Z., Shi, C., He, W., Wu, L., "Effects of steel fiber content and shape on mechanical properties of ultra high performance concrete." *Construction and Building Materials*, Vol. 103, (2016), 8-14. Doi: doi.org/10.1016/j.conbuildmat.2015.11.028

30. Song, PS., Hwang, S., "Mechanical properties of high-strength steel fiber-reinforced concrete," *Construction and Building Materials* Vol. 18 (2004). Doi: doi.org/10.1016/j.conbuildmat.2004.04.027

31. Abbass, W., Khan, MI., Mourad, S., "Evaluation of mechanical properties of steel fiber reinforced concrete with different strengths of concrete." *Construction and Building Materials*, Vol. 168, (2018), 556-569. Doi: doi.org/10.1016/j.conbuildmat.2018.02.164

32. Madandoust, R., Ranjbar, MM., Ghavidel, R., Shahabi, SF., "Assessment of factors influencing mechanical properties of steel fiber reinforced self-compacting concrete." *Materials & Design*, Vol. 83, (2015), 284-294. Doi: 10.1016/j.matdes.2015.06.024

33. Neves, Rui D., J. C. O, Fernandes de Almeida., "Compressive behaviour of steel fibre reinforced concrete." *Structural Concrete,* Vol. 6, No.1, (2005), 1-8.

34. Cardoso, DC., Pereira, GB., Silva, FA., Silva Filho, JJ., Pereira, EV., "Influence of SFs on the Flexural Behavior of RC Beams with Low Reinforcing Ratios: Analytical and Experimental Investigation" *Composite Structures,* (2019). 110926. Doi: doi.org/10.1016/j.compstruct.2019.110926

35. Ying, H., Huawei, P., Xueyou, Q., Jun, P., Xiancun, L., Qiyun, P., Bao, L., "Performance of Reinforced Concrete Beams Retrofitted by a Direct-Shear Anchorage Retrofitting System." *Procedia Engineering*, Vol. 210, (2017), 132-140.

36. Abdulla, Jabr., "Flexural Strengthening of RC beams using Fiber Reinforced Cementitious Matrix." FRCM, University of Windsor Scholarship at UWindsor, (2017). Doi: 10.1061/(ASCE)CC.1943-5614.0000473

37. Abdallah, M., Al Mahmoud, F., Boissiere, R., Khelil, A., Mercier, J., "Experimental study on strengthening of RC beams with Side Near Surface Mounted technique-CFRP bars." *Composite Structures*, Vol. 234, (2020), 111716. Doi: doi.org/10.1016/j.compstruct.2019.111716

38. Nanda, RP., Behera, B., "Experimental study of shear-deficient RC beam wrapped with GFRP." *International Journal of Civil Engineering*, Vol. 18, No. 6, (2020), 655-664. Doi: doi.org/10.1007/s40999-020-00498-4

39. Yu, F., Zhou, H., Jiang, N., Fang, Y., Song, J., Feng, C., Guan, Y., "Flexural experiment and capacity investigation of CFRP repaired RC beams under heavy pre-damaged level." *Construction and Building Materials*, Vol. 230, (2020) 117030. Doi: 10.1016/j.conbuildmat.2019.117030

40. Zhang, Y., Li, X., Zhu, Y., Shao, X., "Experimental study on flexural behavior of damaged reinforced concrete (RC) beam strengthened by toughness-improved ultra-high performance concrete (UHPC) layer." *Composites Part B: Engineering*, Vol. 186, (2020), 107834. Doi: doi.org/10.1016/j.compositesb.2020.107834

41. Lubliner, J., Oliver, J., Oller, S., Onate, E. "A plastic-damage model for concrete" *International Journal of Solids and Structures,* Vol. 25, No. 3, (1989), 299-326.

42. Shoja, E., Alielahi, H. (2020). An Investigation of the Seismic Interaction of Surface Foundations and Underground Cavities Using Finite Element Method. *International Journal of Engineering, Transactions C: Aspects,* Vol. 33, No. 9, 1721-1730. doi: 10.5829/ije.2020.33.09c.04

43. Bagheripourasil, M., Mohammadi, Y., Gholizad, A. "Progressive Collapse Analysis Methods Due to Blast Loading in Steel Moment Frames." *Journal of Modeling in Engineering*, Vol. 15, No. 51, (2017), 51-65. DOI: 10.22075/jme.2017.2688

44. Kaafi, P., Ghodrati Amiri, G."Investigation of the Progressive Collapse Potential in Steel Buildings with Composite Floor System." *Journal of Structural Engineering and Geo-Techniques*, Vol. 10, No. 2, (2020), 1-8.

45. Kmiecik, P., Kamiński, M., "Modelling of reinforced concrete structures and composite structures with concrete strength degradation taken into consideration." *Archives of Civil and Mechanical Engineering*, Vol. 11, No. 3, (2011), 623-636. Doi: doi.org/10.1016/S1644-9665(12)60105-8

Persian Abstract

چکیده

در مطالعه حاضر رفتار تیرهای بتنی مسلح مقاوم سازی شده با ژاکت‌های کامپوزیتی فولادی – بتنی مسلح به الیاف فولادی با استفاده از تحلیل اجزاء محدود ارزیابی شده است. همچنین صحت روش تحلیل با مدل‌سازی تعدادی تیر بتن مسلح که در آزمایشگاه ساخته شد، ارزیابی گردید و تطابق مناسبی مشاهده گردید. پارامترهای متغیر در تحلیل اجزاء محدود به ترتیب شامل رده مقاومتی بتن مورد استفاده در تیر اصلی (۱۵، ۲۰ و ۲۵ مگاپاسکال)، طول دهانه تیرها (۱.۴ و ۲.۸ متر)، نوع روکش (روکش بتنی مسلح، روکش بتنی مسلح حاوی الیاف فولادی، روکش کامپوزیت فولادی – بتنی حاوی الیاف فولادی، ورق CFRP) و ضخامت روکش (۴۰، ۶۰ و ۸۰ میلیمتر) می‌باشند. دلیل اینکه مقاومت فشاری تیر اصلی به عنوان متغیر در نظر گرفته شده است آن است که در بسیاری از ساختمان‌های بتن مسلح، مقاومت فشاری بتن مورد نظر مطابق با اهداف طراح (مقاومت فشاری مشخصه بتن در هنگام طراحی) نمی باشد و تفاوت قابل توجهی دارد. نتایج تحلیل اجزاء محدود نشان داد که افزودن روکش‌های بتنی مسلح به الیاف فولادی به تیرها برای هر سه رده بتن مصرفی موثر می‌باشد و توانسته ظرفیت جذب انرژی را به ترتیب ۱.۸۸، ۲.۰۷و ۲.۲۵ برابر افزایش دهد. از بین سه ضخامت در نظر گرفته شده برای روکش‌ها، از جنبه ظرفیت باربری روکش‌های با ضخامت ۶۰ میلیمتر عملکرد نسبتاً بهتری داشتند؛ بطوریکه ظرفیت باربری تیر مقاوم سازی شده با روکش کامپوزیتی ۶۰ میلیمتری به مقدار ۷۹ و ۲۰ درصد بیشتر از مقادیر متناظر با روکش‌های ۴۰ و ۸۰ میلیمتری شده است. پارامتر ضخامت روکش نقش قابل توجهی بر پاسخ تیرهای مقاوم سازی با روکش‌های کامپوزیتی پیشنهادی دارد و بسته به ابعاد و مشخصات هندسی تیر می‌بایست، ضخامت مناسبی را برای روکش در نظر گرفت و افزایش ضخامت همواره نمی‌تواند منجر به بهبود پاسخ تیر شود.

International Journal of Engineering

Coded Thermal Wave Imaging Based Defect Detection in Composites using Neural Networks

M. Parvez M.*[a], J. Shanmugam[a], M. Sangeetha[a], V. S. Ghali[b]

[a] Department of Electronics and Communication Engineering, Bharath Institute of Higher Education and Research, Chennai, TN, India
[b] Department of Electronics and Communication Engineering, Koneru Lakshmaiah Education Foundation, Vaddeswaram, AP, India

P A P E R I N F O	*A B S T R A C T*
	Industry 4.0 focuses on the deployment of artificial intelligence in various fields for automation of variety of industrial applications like aerospace, defence, material manufacturing, etc. Application of these principles to active thermography, facilitates automatic defect detection without human intervention and helps in automation in assessing the integrity and product quality. This paper employs artificial neural network (ANN) based classification post-processing modality for exploring subsurface anomalies with improved resolution and enhanced detectability. A modified bi-phase seven-bit barker coded thermal wave imaging is used to simulate the specimens. Experimentation has been carried over carbon fiber reinforced plastic (CFRP) and glass fiber reinforced plastic (GFRP) specimens using artificially made flat bottom holes of various sizes and depths. A phase based theoretical model also developed for quantitative assessment of depth of the anomaly and experimentally cross verified with a maximum depth error of 3%. Additionally, subsurface anomalies are compared based on probability of detection (POD) and signal to noise ratio (SNR). ANN provides better visualization of defects with 96% probability of detection even for small aspect ratio in contrast to conventional post processing modalities.

1. INTRODUCTION

There is a growing demand for applications in load-bearing structures such as transportation instruments, aerospace equipment, wind turbines, and medical devices. Therefore, to minimize the essential security concerns and maintenance cost, a robust and consistent non-destructive testing (NDT) is necessary for testing of composite materials [1]. In general, NDT consists of various non-invasive inspection techniques [2-3] to assess the material properties and structural characteristics of the components, or entire processing units. The demand for material defect detection increases various challenges in NDT [4-6]. Compared to traditional NDT methods, infrared thermography is a new NDT technology that has evolved rapidly in the recent years.

Active infrared thermography grabs the attention as

a reason of fast, complete field, non-invasive and non-contact defect detection characteristics. Several categories of active infrared thermography, based on the input stimulus are pulse thermography (PT), pulse phased thermography (PPT), lock-in thermography (LT), and Non-Stationary Thermal Wave Imaging (NSTWI). Pulse thermography uses an external heat stimulus of high power for a small duration to energize the test specimen [7]. The requirement in extreme power and effects associated to non-uniform are significant limitations for the case of pulse thermography. Subsequently, to surmount constraints of pulse thermography with a continuous sinusoidal input stimulus of low power, the lock-in thermography is introduced. In pulse phased thermography phase based analysis is performed to explore the subsurface details. The investigation is similar to pulse thermography, in pulse phased thermography a phase-based analysis is performed as like lock-in thermography [8-9]. Since the sinusoidal stimulus consists of mono frequency, it can probe into a particular depth only. However, in realistic

scenario anomalies may occur at different locations. To test the realistic scenarios, it is required to perform repetitive experiments with altered frequencies which is a major constraint for its applicability [10]. Moreover, the requirement of high power is the major drawback of pulse phased thermography [11].

However, to examine an object in single experimentation for a small duration of time, non-stationary thermal wave imaging is used [12]. Linear frequency modulated thermography uses frequency modulated chirp stimulus of low power through lower frequency band towards the test of entire sample during a particular investigation. Since the low frequency probes deep into the object, it explores the subsurface characteristics [13]. Later, quadratic frequency modulated thermography uses quadratic chirp. The quadratic chirp signal probes more deeply into the object than its linear counterpart, and it gives the visualization, in-depth details with better contrast [14].

In recent years, an evolving non-stationary thermal wave imaging system with its unique depth resolution and defect detection characteristics is Barker coded thermal wave imaging (BCTWI). The present work uses BCTWI followed by artificial neural network (ANN) based on post-processing technique to explore the subsurface details. Employing various signal processing algorithms, the processing of recorded thermal response is handled to obtain the qualitative and quantitative subsurface details. The obtained results are compared with the metrics via full width at half maxima (FWHM), probability of detection (POD), and signal to noise ratio (SNR).

Barker coded thermal wave imaging system is implemented in this work to facilitate high depth resolution and sensitivity, by suppressing the limited resolution and by increasing the depth probing capabilities. It was found that detection performance and depth resolution can be enhanced by decrease in the size of side lobes than main lobe due to concentration of greater energy. This can be achieved through the system of barker coded thermal wave imaging. In brief, for detecting the defects and estimating its relative sizes, the neural network basis classification framework was implemented. Furthermore, by the way of backscatter signals from the concept of BCTWI the quantitative depth estimation has been carried out. ANN based analysis is ensured to have experimentally enhanced reliability, defect detection of artificially created bottom holes in the materials of GFRP and CFRP, quantitative estimation of depths using BCTWI.

Organization of manuscript is as follows: section I introduces thermography with the necessity for barker coded thermal wave imaging and section 2 provides theory of barker coded thermal wave imaging technique followed by experimentation and processing techniques in section 3. Later, section 4 discusses a brief note about the results.

2. CONCEPT OF THERMAL BARKER CODED THERMAL WAVES

A model associated with thermal wave propagation based on heat equations involves the backscatter of the waves for evaluating the subsurface anomalies and validation as well. In BCTWI a code-based stimulus is emitted near to test object surface that relatively provokes thermal waves close to the surface propagating into the interiors of the object [15, 16]. Resulting thermal waves that are propagated signifies towards the back as of the boundary leading to temperature rise above object surface. Also, the response of temperature is quantified in resolving a 1D heat equation assuming coordinate system to be rectangular and is shown in Equation (1).

$$\frac{\partial^2 T}{\partial x^2} = \frac{1}{\alpha} \frac{\partial T}{\partial t} \tag{1}$$

Here diffusion coefficient is symbolized as 'α', T (x, t) denotes instant temperature at a given time instance 't' with equivalent value of depth as 'x', coded flux having peak power is signified as Q_0. With the consideration of delayed step responses in combination, the excited stimulation is given as in Equation (2).

$$Q(t) = Q_0 \sum_{i=1}^{4} (-1)^{n_i} u(t - a_i \tau) \tag{2}$$

where n_i=0,1,2,3 and a_i =0,3,5,6
Under the adiabatic boundary condition, the equation for heat diffusion is solved, i.e., exchange of heat flux by backward portion stands at insignificant rate, as followed in Equation (3).

$$-k \frac{\partial T}{\partial x}\bigg|_{x=L} = 0 \tag{3}$$

The test object surface is stimulated using BCTWI. Over the surface sample, the obtained incident energy will be attenuated in a thin layer, further a related heat flux is produced on the sample upper surface as in Equation (4).

$$-k \frac{\partial T}{\partial x}\bigg|_{x=0} = \sum_{i=1}^{4} (-1)^{n_i} u(t - a_i \tau) \tag{4}$$

where 'k' indicates thermal conductivity of material, presumed not a dependable quantity of temperature and finite thickness of the sample is denoted with 'L'. By

solving Equation (1) with the above conditions, the specimen's thermal response is obtained in the Laplacian domain is shown by Equation (5).

$$T(x,s) = \frac{Q(s)e^{-\sigma x}}{k\sigma} \tag{5}$$

The corresponding radiation of the received thermal response with the help of an IR sensor with a sampling rate of 'fs' is captured. Further, it can be determined by using the following equations.

$$R(x,w) = \mu_r \int_0^d T(x,w)e^{-\mu x}dx$$

$$R(d,w) = \frac{-\mu_r\sqrt{\alpha}Q(jw)}{k\sqrt{jw}}\left(\frac{1}{\left(\sqrt{\frac{jw}{\alpha}}+\mu\right)} - \frac{e^{\left(\sqrt{\frac{w}{2\alpha}}+\mu\right)d}e^{j\sqrt{\frac{w}{2\alpha}}d}}{\left(\sqrt{\frac{jw}{\alpha}}+\mu\right)}\right)$$

where 'μ_r' is infrared absorption coefficient and

$$Q(jw) = \frac{1}{jw}\left[1 - e^{-3jw} - e^{-5jw} - e^{-6jw}\right]$$

$$R(d,w) = \frac{\mu\sqrt{\alpha}\left[1-e^{-3jw}-e^{-5jw}-e^{-6jw}\right]}{kjw\sqrt{jw}}\left(\frac{1-e^{-\left(\sqrt{\frac{jw}{\alpha}}+\mu\right)d}}{\left(\sqrt{\frac{jw}{\alpha}}+\mu\right)}\right) \tag{6}$$

Put $jw = \dfrac{\log\left(re^{j\theta}\right)}{t}$ and extract the phase component in Equation (6),

$$\phi_{CZT} = \frac{\pi}{4} - \frac{\theta}{2t} - \sqrt{\frac{\theta}{2t\alpha}}d - \phi_1 + \tan^{-1}\left(-\frac{\frac{\theta}{\sqrt{2t\alpha}}}{\mu_a + \frac{1}{\sqrt{2t\alpha}}}\right) \tag{7}$$

$$\phi_1 = \tan^{-1}\left(\frac{\sin\left(\frac{7\theta}{2t}\right)\sin\left(\frac{\theta}{2t}\right)+\sin\left(\frac{3\theta}{2t}\right)\sin\left(\frac{\theta}{2t}\right)}{\cos\left(\frac{7\theta}{2t}\right)\cos\left(\frac{\theta}{2t}\right)+\cos\left(\frac{3\theta}{2t}\right)\cos\left(\frac{\theta}{2t}\right)}\right)$$

From Equation (7), the extracted phase proportionally changes with respect to depth associated with defect, which is further applied to estimate the depth of defects.

3. EXPERIMENTATION AND PROCESSING

The active thermal wave imaging scheme illustration is depicted through Figure 1. In present experimental setup, the sample is kept opposite to a pair of halogen lights, which are of 1KW power each. The sample is stimulated by an optical stimulus with a sweep frequency rate of 0.01-0.1Hz for duration of 100 s with 25Hz frame rate. However, Infrared (IR) camera is positioned at one meter opposite to test sample, to record the reflected thermal response. The halogen lamps were placed to facilitate a uniform illumination.

The 7-bit barker-coded optical stimulus is enacted uniformly on the surface of test sample, then its corresponding temperature contrast over the test sample will be captured by IR camera [15]. Initially, the captured thermal response is processed by using a suitable linear fitting procedure to remove the static response and to retain the dynamic part of the response. The dynamic part of captured thermal response will undergo further post processing using suitable signal processing techniques and ANN based algorithm to analyze the subsurface features.

3. 1. Pre-processing   To minimize the non-uniformity in the emission, the radiation issues and to visualize the subsurface anomalies accurately, signal processing algorithms are employed over the dynamic part of the recorded response. With the help of appropriate linear fitting technique on the recorded infrared data, the dynamic part is retained by eradicating of static part from the response.

3. 2. Post-processing
3. 2. 1. FFT Phase   For separation of frequency, the FFT phase employs a fast Fourier transform (FFT). In the current investigation, over the thermal profile at each pixel value the FFT is employed [17]. At each frequency component the phase values are determined, thereby assigning corresponding phase values of frequency components to the respective pixel positions in a systematic manner for developing the phase grams. Moreover, the phase image constructed exhibits contrast phase because of the phase delay associated from anomalies of thermal waves at various depths [18]. Accordingly, the frequency consistent to the phase image demonstrating the determination of defects as stated in Equation (8).

$$f = \frac{F_s n}{N} \tag{8}$$

where Fs is rate of capture or sampling frequency, n is
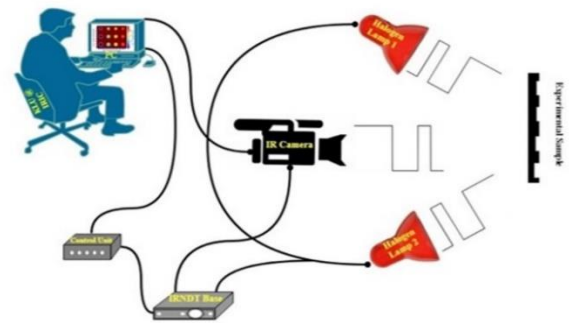
Figure 1. Pictorial Representation of the active thermal wave imaging scheme

quantity of the phase image, and N is quantity of the samples in thermal profile.

3. 2. 2. Hilbert Phase
In this method a time domain phase is used to discriminate the defective locations from its counter parts. In the first stage, Hilbert transform based pulse compression is performed by using Equation (9). In the next stage, the ordinary pulse compression value is determined using Equation (10). Further, the time-domain phase of a particular pixel is obtained by using Equation (11) [19].

$$Q_1 = IFFT\left[\left\{FFT\left(Hilb\left(T_r\right)\right)\right\} * \left\{FFT\left(T\right)\right\}\right] \tag{9}$$

Furthermore, in the next phase procedure, the normal cross-correlation can be performed among the thermal profile as reference and temporal for individual pixels as shown in Equation (10).

$$Q_2 = IFFT\left[\left\{FFT\left(T_r\right)\right\} * \left\{FFT\left(T\right)\right\}\right] \tag{10}$$

Finally, the time domain phase will be obtained using

$$\theta = \tan^{-1}\left(\frac{Q_1}{Q_2}\right) \tag{11}$$

by re-arranging the outcome phase values into corresponding positions, the time-domain phase images are obtained.

3. 2. 3. Pulse Compression
As per the methodology, the attenuation and delay possessed through correlated thermal waves are used to discriminate the defective locations from its counterparts [20]. Initially during the period of stage 1, a thermal profile as a reference point is carefully chosen as of the exact location of the region that is non-defective. Later, with the help of reference point the interrelationship for the two points said to be the cross-correlation is conducted, which results a correlation coefficient sequence between 0 to 1 using Equation (12). These obtained normalized correlation coefficients are rearranged into their corresponding pixel locations to form correlation images for that delayed instant. The correlation contrast in constructed images is helpful to visualize the defects. This coefficient contrast obtained can be utilized for subsurface feature extraction [21].

$$g\left(\tau\right) = \int_{-\infty}^{\infty} s\left(t\right)h\left(\tau+t\right)dt \tag{12}$$

Figure 2 shows the block diagram representation of various signal processing methods [21]. Figures 2a and 2b show the processing approaches steps for obtaining the frequency domain-based results whereas Figure 2c shows the processing steps to obtain time-domain phase results.
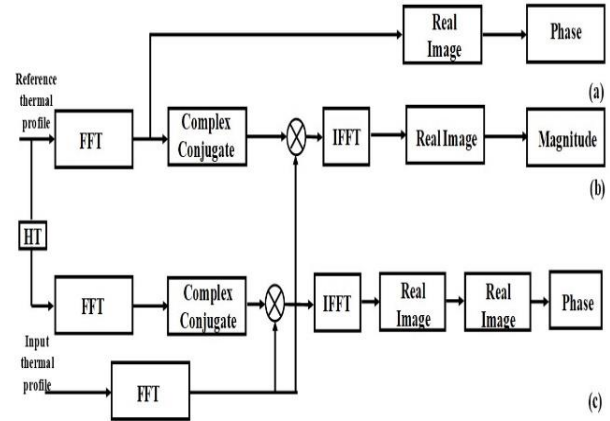
Figure 2. Block diagram representation of various singnal processing approaches

3. 2. 4. Artificial Neural Network
Based on the research undertaken in the area of Inverse Heat Transfer Problem (IHTP), this study aims for quantitative and qualitative detection of defects through ANN based model, which is further validated experimentally [22].

The Artificial Neural Networks (ANN) have been widely used to classify the information regarding subsurface characteristics qualitatively and quantitatively. This contribution focuses on qualitatively assessing the subsurface anomalies using classification-based modality using ANN and quantitatively visualizing the depth of anomalies using phase-based depth assessment using BCTWI. Generally, ANNs comprise of units that are interconnected which are termed as artificial neurons as depicted in Figure 3. Input layer (Input) is considered as temporal thermal profile information and associated parameters (neurons) offer over the output (output layer), correspondingly the other neurons from the view are hidden (hidden layers). Based on the interconnection between neurons, the network membership function is determined, in which the connections are not simple, merely particular non-linear functions [23-25]. The network utilizes multilayer perceptron NN using 250 input nodes. The network employs successive hidden layers which has nodes about 50 and 25, respectively. These nodes were used for training and analysis partitioning as two targets carrying single output node which is signified as targeted areas of defective and non-defective regions. For detection and quantification assessment, a tan-sigmoid activation function is utilized in combination with the back propagation neural network (BPNN). Through the classification based supervised learning, the detection and quantification of irregularity characteristics including depth and location is conducted in the range of two successive actions. The temporal

sequence of the thermograms is first recorded, later training vectors are formed correspondingly to the data acquisition. In a sequence, input count is equivalent to the thermogram count using which training vectors are formed. After the adjustment of weights through back propagation, the outputs offered are defected and non-defected region.

3. 2. 4. 1. Clasiification Mode for Anomaly Detection
To model and detect the features of subsurface of inverse thermography problem, the classification employs the phases of training and testing phase. The temporal thermal response of defect spots resembles the unique characteristics of subsurface anomalies in the terms of delay and attenuation, but non-defective points retain similar properties that employs in classifying defect points for particular methodology. In the phase of training, the removal of mean thermal profile at some defect-free spots (100 intended for the case) were down sampled further utilized for network training. In which the network has achieved 100 times targeting "0" over such period of 150 s with the system configuration of Intel 7 processor with specifications of 16 GB RAM, 512 GB SSD.

For recognition, the data provided during the test phase should be classified into defective and non-defective points. Each down converted pixel in the case of temporal thermal can be given as input i.e., input layer, then propagates additional to the hidden layer besides eventually stretched to the output layer, which produces whichever a defective or a non-defective class. It uses a backpropagation algorithm to set weights and generate binary values based on the state of the output. The Backpropagation (BP) algorithm uses the method of gradient descent to seek the minimum of the error function by optimal weight nodes [17]. Consider a Neural Network (NN) with k inputs and l outputs, in which, w_{ij} is the weight associated with the interconnection between the node of one layer and the node of the next layer. Besides, are denoted by the input and target of the dataset respectively; is the outputs of neural networks with the inputs. The minimized error function of the network is described as Equation (13).

$$E = \frac{1}{n}\sum_{i=1}^{n}\left\|o_i - y_i\right\|^2 \tag{13}$$

The BPNN aims to look for a local point that represents a minimum of the error function. The initial weights are selected stochastically by the BP algorithm. In the next stage, to correct initial weight, using an iterative process of gradient descent, the error function computes repeatedly [23] using Equation (14).

$$\nabla E = \frac{\partial E1}{\partial w_{ij}} \tag{14}$$

Each weight is updated with the following Equation (15).

$$\nabla w_{ij} = -\gamma \frac{\partial E}{\partial w_{ij}} \tag{15}$$

The weight's updating of BPNN can be obtained by using Equation (16).

$$w_{ij}(t+1) = w_{ij}(t) + \Delta w_{ij}(t)$$

$$w_{ij}(t+1) = w_{ij}(t) - \gamma \frac{\partial E}{\partial w_{ij}} + \xi(t) \tag{16}$$

where, γ is the constant or learning rate of NN, and $\xi(t)$ is a stochastic term. Defective areas can be characterized with "1" and non-defective areas can be characterized by "0". Consequently, with the detection outcome, all pixels exist under thermogram can be further categorized as non-defective or defective areas of the test sample [22-23].

3. 2. 4. 2. Estimation of Depth
In order to estimate and visualize the depths quantitatively, Fast Fourier transform is applied over each and every thermal profile pertaining to each pixel location in view and corresponding phase images were developed. Chirp z transform is applied over selected range of frequencies [26] about the frequency corresponding to the best phase image possessing all the subsurface details. Further, this phase value is converted to the corresponding depth value using Equation (7) and phase value of each pixel in view is represented with this corresponding value quantitatively in Figure 10; thus, the subsurface features will be represented in terms of their corresponding depths for ease of further analysis.
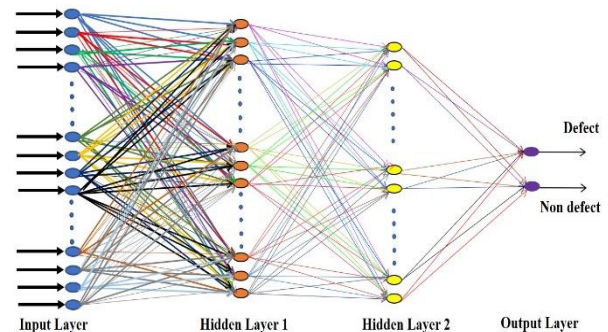
Figure 3. Block diagram of neural network used for classification of defects

4. RESULTS AND DISCUSSIONS

With the two samples of Glass fiber reinforced plastic (GFRP) and Carbon fiber reinforced plastic (CFRP), the experimentation has been undertaken to assess the proposed approach. The GFRP sample consists of 10 Teflon patches with different size variations at two different depth value. Whereas the CFRP sample comprises of 12 artificially made flat bottom holes with size variations at variety of depth rates as depicted in Figure 4.

By means of 7-bit barker coded optical stimulus, the sample to be tested has been energized for a time period of 100s. The pair of halogen lamps, which are of 1 kW power each one is focused on the test sample. With the help of camera that is maintained at 1m distance to the test sample holding specifics of FLIR SC 655A IR with spectral range of 7.5-14µm and 25 fps, the temporal thermal response has been captured from the surface region of test sample. Figure 5 depicts the set up for experimentation for active infrared thermography.
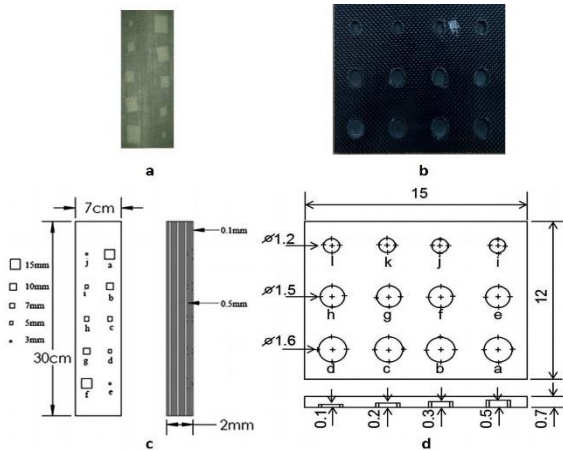
Figure 4. Experimental a. GFRP and b. CFRP specimen & Layout of c. GFRP and d. CFRP specimen

Figure 5. Active infrared tehrmography experimental setup

To obtain subsurface features using a suitable post-processing method, the mean from thermal profiles is removed to extract the dynamic response of each pixel. In comparison with conventional methods for processing such as PC, FFT phase, Hilbert phase and ANN based method is also implemented against detrended (detached mean) contour profile for extracting the details of subsurface. Figure 6 represents the processed results to visualize the subsurface details by using different post processing methods and proposed ANN method for experimental specimen of GFRP. Figure 7 illustrates the subsurface details of CFRP sample by means of different post processing methods and proposed ANN methodology.

Figures 6d and 7d show the artificial neural network-based classification modality exhibits all the defects with good contrast and better visualization. Among several processing approaches, the artificial neural network offers superior detectability with good contrast.

Eventually, the detectability of several processing methods can be measured by the help of signal to noise ratios (SNR). The calculation of SNR of individual pixel is done by means Equation (17) for which the mean of the defective and non-defective area along with standard deviation of the non-defective region are
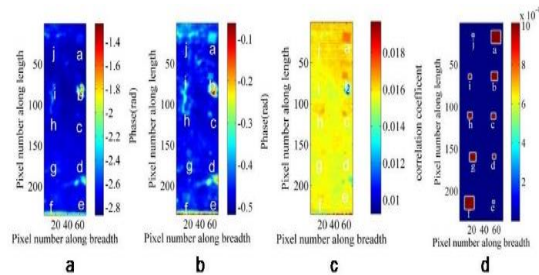
Figure 6. Outputs of a. FFT Phase b. Hilbert phase c. Pulse compression d. Aritificial neural networks for GFRP sample
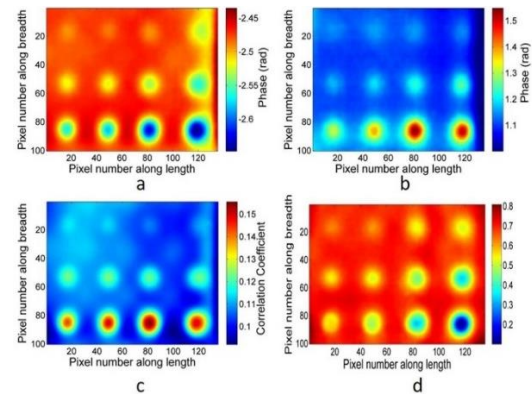
Figure 7. Outputs of a. FFT Phase b. Hilbert phase c. Pulse compression d. Aritificial neural networks for GFRP sample

calculated [27]. The SNR's of CFRP and GFRP samples for various processing methods and proposed ANN method is represented in Figures 8 and 9, respectively.

It is clear from the Figures 8 and 9; the artificial neural network-based methodology provides us better results compared to that of other processing methodologies.

$$SNR(dB) = \frac{\text{mean of defective area-mean of non defective area}}{\text{standard deviation of non defective area}} \quad (17)$$

4. 1. Analysis for Quantitative Depth   FFT is applied over thermal profile and corresponding phase images were generated among them phase gram at 0.01hz is presenting all the subsurface details hence, the frequency band 0.005-0.015hz is zoomed with 8192 samples and observing corresponding phase values the phase gram at 0.01056hz is presented the defects very clearly. Hence corresponding phase values of the defects were taken for quantification leading to the depth estimation as shown in Figure10 of CFRP.

4. 2. Defect Sizing   The full width at half maxima (FWHM) method has utilized for calculation of defect sizing [27]. The sizing of defects at different depths of the GFRP sample for different processing methods has been computed, and the obtained values are shown in Table 1. The size estimated from the artificial neural network nearly resembles that of the actual defect size.

4. 3. Probability of Detection (POD)   As per the industrial requirements processing method mush possess the high reliability in terms of defect detection even for small aspect ratios, reliability of the proposed modality is evaluated through POD [27-28].

Figure 11 depicts about the estimate of POD as well as aspect ratio of a variety of post-processing techniques such as artificial neural networks (ANN), pulse compression (PC), Hilbert phase (HP), and phase analysis (FFT). From the above figure, the ANN has the highest Probability of detection even for small aspect ratios as compared to the other post-processing methodologies.

TABLE 1. Comparison of processed data for full width half maxima

Sample	Defect	Actual Size (mm)	FFT Phase	HP	PC	ANN
	a	15	14.11	14.22	14.32	**15.12**
	b	10	9.21	9.13	9.7	**10.12**
GFRP	c	7	6.12	7.62	6.48	**7.01**
	d	5	4.63	4.31	4.82	**5.11**
	e	3	2.68	2.64	2.83	**3.03**
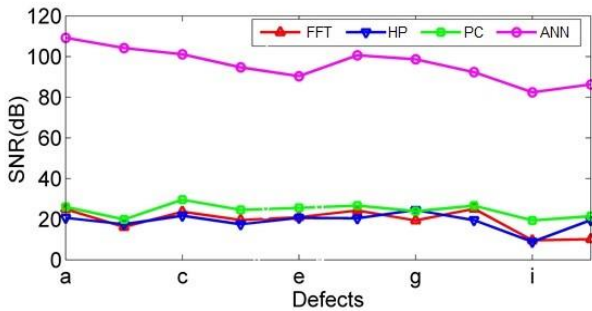
Figure 8. SNR for processed results of GFRP data

Figure 10. Defects involved for CFRP samples in respective to depth verses phase constrast

Figure 9. SNR for processed results of CFRP data
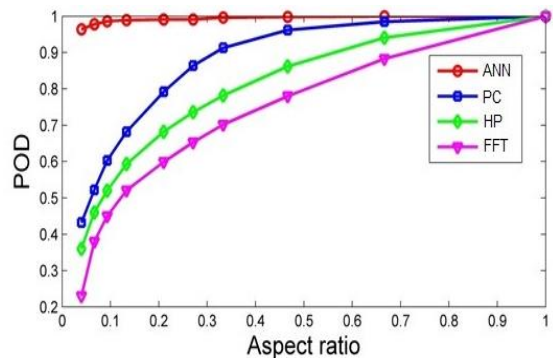
Figure 11. Curve of POD for various post-processing methods

5. CONCLUSION

To detect and differentiate subsurface anomalies in the experimentation of GFRP and CFRP specimens, the artificial neural network-based classification technique is employed using BCTWI. By exerting the experimental validation, the capability of the proposed ANN-based approach has been demonstrated. A phase based theoretical model was developed with a maximum depth error of 3%. The obtained results evident for the estimation of sizing by applying full width at half maxima with an average error percentage of 4.2 including the reliability at the combined analysis of POD based assessment. SNR is also considered to further validate the potentiality of detecting the defects. Based on the above validation parameters the analysis dependent on ANN technique holds by experimentation is achieved with enhanced reliability, detection of depth and evaluation of the subsurface anomalies quantitatively by employing BCTWI.

6. REFERENCES

1. X. Maldague, Theory and practice of infrared thermography for non-destructive testing. New York, US: Wiley, 2001.

2. J. González-Durán, M. Zamora-Antuñano, L. Lira-Cortés, J. Rodríguez-Reséndiz, J. Olivares-Ramírez and N. Lozano, "Numerical Simulation for the Combustion Chamber of a Reference Calorimeter", *Processes*, Vol. 8, No. 5, (2020), 575. doi: 10.3390/pr8050575.

3. J. González-Durán, J. Rodríguez-Reséndiz, J. Ramirez, M. Zamora-Antuñano and L. Lira-Cortes, "Finite-Element Simulation for Thermal Modeling of a Cell in an Adiabatic Calorimeter", *Energies*, Vol. 13, No. 9, (2020), 2300, doi: 10.3390/en13092300.

4. T. Yektaniroumand, M. Niaz Azari and M. Gholami, "Optimal Rotor Fault Detection in Induction Motor Using Particle-Swarm Optimization Optimized Neural Network", *International Journal of Engineering, Transactions B: Applications*, Vol. 31, No. 11, (2018), 1876-1882. doi: 10.5829/ije.2018.31.11b.11.

5. H. Bui et al., "Characterization of Electrical Conductivity of Anisotropic CFRP Materials by Means of Induction Thermography Technique", *IEEE Transactions on Magnetics*, Vol. 54, No. 3, (2018), 1-4, doi: 10.1109/tmag.2017.2742979.

6. H. Kim, "FPGA-based of Thermogram Enhancement Algorithm for Non-destructive Thermal Characterization", *International Journal of Engineering, Transactions A: Basics*, Vol. 31, No. 10, (2018), 1675-1681, doi:10.5829/ije.2018.31.10a.09.

7. X. Guo and V. Vavilov, "Pulsed thermographic evaluation of disbonds in the insulation of solid rocket motors made of elastomers", *Polymer Testing*, Vol. 45, (2015), 31-40, doi: 10.1016/j.polymertesting.2015.04.015

8. H. Song, H. Lim, S. Lee, H. Sohn, W. Yun and E. Song, "Automated detection and quantification of hidden voids in triplex bonding layers using active lock-in thermography*", NDT & E International*, Vol. 74, (2015), 94-105, doi 10.1016/j.ndteint.2015.05.004

9. C. Wallbrink, S. Wade and R. Jones, "The effect of size on the quantitative estimation of defect depth in steel structures using lock-in thermography", *Journal of Applied Physics*, Vol. 101, (2007). doi: 10, 104907, 2007.

10. C. Ibarra Castanedo, N. Avdelidis and X. Maldague, "Qualitative and quantitative assessment of steel plates using pulsed phase thermography", *Materials Evaluation*, Vol. 63, No. 11, (2005), 1128-1133, doi: 10.1117/12.602360

11. X. Maldague and S. Marinetti, "Pulse phase infrared thermography", *Journal of Applied Physics* 79, No. 5, (1996), 2694-2698, doi: 10.1063/1.362662.

12. G. Dua, V. Arora and R. Mulaveesala, "Defect Detection Capabilities of Pulse Compression Based Infrared Non-Destructive Testing and Evaluation", *IEEE Sensors Journal*, Vol. 21, No. 6, (2021), 7940-7947. doi: 10.1109/jsen.2020.3046320.

13. J. Ahmad, A. Akula, R. Mulaveesala, and H. K. Sardana, "Barker coded thermal wave imaging for non-destructive testing and evaluation of steel material", *IEEE Sensors Journal*., Vol. 19, No. 2, (2019), 735-742. doi: 10.1109/JSEN.2018.2877726

14. G. Chandra Sekhar Yadav, V. Ghali and N. Baloji, "A Time Frequency-Based Approach for Defect Detection in Composites Using Nonstationary Thermal Wave Imaging", *Russian Journal of Non-destructive Testing*, Vol. 57, No. 6, 486-499, (2021). doi: 10.1134/s1061830921060061.

15. M. Parvez M, J. Shanmugam and V. Ghali, "Decision tree-based subsurface analysis using Barker coded thermal wave imaging", *Infrared Physics & Technology*, Vol. 109, (2020), 103380. doi: 10.1016/j.infrared.2020.103380.

16. M. Parvez, J. Shanmugam and V. Ghali, "Fuzzy C-based Automatic Defect Detection using Barker Coded Thermal Wave Imaging", *International Journal of Performability Engineering*, Vol. 17, No. 5, (2021), 484. doi: 10.23940/ijpe.21.05. 8.484490.

17. M. Mahani and M. Besanjideh, "Nonlinear and Non-stationary Vibration Analysis for Mechanical Fault Detection Using EMD-FFT Method", *International Journal of Engineering, Transactions C: Aspecls*, Vol. 25, No. 4, (2012), 363-372, doi: 10.5829/idosi.ije.2012.25.04c.11.

18. N. Tabatabaei and A. Mandelis, "Thermal-wave radar: a novel subsurface imaging modality with extended depth-resolution dynamic range", *The Review of Scientific Instruments*, 80 (2009) 034902. doi: 10.1063/1.3095560

19. J. A. Siddiqui, S. Patil, S. S. Chouhan, S. Wuriti, V. Arora, and R. Mulaveesala, "An efficient pulse compression favourable thermal excitation scheme for non-destructive testing using infrared thermography", *Electron Letters*, Vol. 56, No. 19, 1003-1005, (2020). doi: 10.1049/el.2020.0914

20. A. Vijaya Lakshmi, V. Gopitilak, M. Parvez, S. Subhani and V. Ghali, "Artificial neural networks based quantitative evaluation of subsurface anomalies in quadratic frequency modulated thermal wave imaging", *Infrared Physics & Technology*, Vol. 97, (2019), 108-115, doi:10.1016/j.infrared.2018.12.013.

21. N.Saeed, M. A.Omar, Y.A.Rahman, "A neural network approach for quantifying defects depth, for non-destructive testing thermograms", *Infrared Physics & Technology* 94 (2018), 55-64, doi: 10.1016/j.infrared.2018.08.022

22. S. Dudzik, "Investigations of a heat exchanger using infrared thermography and artificial neural networks", *Sensors and Actuators A: Physical,* Vol. 166, No. 1, (2011), 149-156. doi: 10.1016/j.sna.2010.12.001

23. O. Rodriguez-Abreo, J. Rodriguez-Resendiz, C. Fuentes-Silva, R. Hernandez-Alvarado and M. Falcon "Self-Tuning Neural Network PID With Dynamic Response Control*", IEEE Access*, Vol. 9, (2021), 65206-65215, doi: 10.1109/access.2021.3075452.

24.   E. Cruz-Miguel, J. García-Martínez, J. Rodríguez-Reséndiz and R. Carrillo-Serrano, "A New Methodology for a Retrofitted Self-tuned Controller with Open-Source FPGA", *Sensors*, Vol. 20, No. 21, (2020), 6155. doi: 10.3390/s20216155.

25.   D. Siddharth, D. K. J. Saini, P. Singh"An Efficient Approach for Edge Detection Technique Using Kalman Filter with Artificial Neural Network", *International Journal of Engineering, Transactions C: Aspects*, Vol. 34, No. 12, (2021), 1-7, doi: 10.5829/IJE.2021.34.12C.04

26.   V. Arora, J.A. Siddiqui, R. Mulaveesala, A. Muniyappa, "Pulse compression approach to non-stationary infrared thermal wave imaging for non-destructive testing of carbon fibre reinforced polymers", *IEEE Sensors Journal*, Vol. 15, No. 2, (2015), 663-664. doi: 10.1109/JSEN.2014.2361391

27.   M. F. Beemer and S. M. Shepard, "Aspect ratio considerations for flat bottom hole defects in active thermography", *Quantitative InfraRed Thermography*, Vol. 15, No. 1, (2018), 1-16. doi: 10.1080/17686733.2017.1328642

28.   M. Keller, Popelin, A. L. Bousquet, N. Bousquet, E. Remy "Nonparametric estimation of the probability of detection of flaws in an industrial component, from destructive and non-destructive testing data, using approximate Bayesian computation", *Risk Analysis*, Vol. 35, (2015), 1595-1610. doi: 10.1111/risa.12484

Persian Abstract

چکیده

صنعت ۴.۰ بر استقرار هوش مصنوعی در زمینه های مختلف برای اتوماسیون انواع کاربردهای صنعتی مانند هوافضا ، دفاع ، تولید مواد و غیره تمرکز دارد. کاربرد این اصول در ترموگرافی فعال ، تشخیص خودکار نقص را بدون دخالت انسان تسهیل می کند و در ارزیابی. یکپارچگی و کیفیت اتوماسیون کمک می کند محصول این مقاله از روش طبقه بندی مبتنی بر شبکه عصبی مصنوعی (ANN) برای بررسی ناهنجاری های زیر سطحی با وضوح بهتر و قابلیت تشخیص بیشتر استفاده می کند. برای شبیه سازی نمونه ها از یک تصویربرداری موج حرارتی هفت مرحله ای اصلاح شده با پارکر استفاده می شود. آزمایش بر روی نمونه های پلاستیکی تقویت شده با الیاف کربن (CFRP)و پلاستیک تقویت شده با الیاف شیشه (GFRP)با استفاده از سوراخ های ته صاف مصنوعی در اندازه ها و اعماق مختلف انجام شده است. یک مدل نظری مبتنی بر فاز نیز برای ارزیابی کمی عمق ناهنجاری توسعه یافته و به صورت تجربی با حداکثر خطای عمق ۳ cross تأیید شده است. علاوه بر این ، ناهنجاری های زیر سطحی بر اساس احتمال تشخیص (POD)و نسبت سیگنال به نویز (SNR) مقایسه می شوند. ANN تجسم بهتری از نقایص با ۹۶٪ احتمال تشخیص حتی در نسبت ابعاد کوچک در مقایسه با روشهای معمول پردازش پست فراهم می کند.

International Journal of Engineering

Precast Concrete Column Beam Connection Using Dowels Due to Cyclic Load

H. A. Tumengkol*, R. Irmawaty, H. Parung, A. Amiruddin

Department of Civil engineering, Universitas Hasanuddin Indonesia

	A B S T R A C T The beam-column connection plays an important role in the building structure, especially when the load is cyclic. The main problem that must be solved is the beam and column connection panels. The purpose of this study was to analyze the characteristics of the hysteresis loop of the displacement load relationship with the control displacement of the precast beam-column connection due to cyclic loading. The research method used is the experimental method with a measurable object design test and a special testing method. The results of this study indicate that normal concrete has a compressive strength of 26.43 MPa, while grouted concrete has a compressive strength of 36.97 MPa. The findings of this study also show that the bond stress grouted concrete increases by 102.4% from normal concrete for D13 diameter screw reinforcement, while for D16 diameter, the adhesive stress increases by 51.63%. The findings of this study also show that in the ultimate condition, the load obtained in the tensile load is 13.58 kN with a displacement of 87.58 mm, while the compressive load is 12.62 kN with a displacement of 88.30 mm. This study concludes that the behavior of precast beam-column joints with dowels is stronger in resisting cyclic loads. *doi*: 10.5829/ije.2022.35.01a.09

NOMENCLATURE

BR	v	U	Horizontal components of velocity (m/s)
C_c	Cunningham correction factor	V	Vertical components of velocity (m/s)
c_k	Discrete lattice velocity in direction (k)	U_i, U_j	Random numbers between 0 and 1
c_S	Speed of sound in Lattice scale	**Greek Symbols**	
d^p	Particle diameter (µm)	ρ	Density (kg/m^3)
f_k^{eq}	Equilibrium distribution function	τ	Lattice relaxation time
g	Gravity (m/s^2)	$\tau_p = \dfrac{\rho^p c_c (d^p)^2}{18\mu}$	Particle relaxation time (s)
$\emptyset y = \Delta y$	Displacement at melting L (test object height)	Δt	Lattice time step
$\emptyset u = \Delta u$	Ultimate current shift L (test object height)	v	Kinematic viscosity (m^2/s)
Pu	Beban ultimate	λ	Gas mean free path (µm)
Py	Tegangan leleh baja	**Subscripts**	
$\emptyset y$	Perpindahan t	p	Particle
$S = \rho^p / \rho^g$	Particle Specific density	g	Gas

1. INTRODUCTION

Structural design is very important to pay attention to the column beam connection elements as the main point to withstand cyclic loads. Cyclic loads can be caused by earthquakes. The part of the building structure that is susceptible to cyclic loading is at the connection of the beam and column panels [1]. This is due to the specific nature of the radiated energy and the occurrence of very large shear forces, especially at the beam-column connection. These shear forces can frustrate the joint panel core either because the shear capacity is exceeded

*Corresponding Author Email: tumengkolherman@yahoo.co.id (H. A. Tumengkol)

or because the reinforcement bonds in the joint are damaged.

The beam-column connection is a vital component in a building structure. This section is very important because it has a major role in transferring the forces in one element to other elements in the structure [2-3]. Due to the influence of lateral forces such as cyclic loads, these beam-column joints experience greater shear and horizontal forces than adjacent beam and column elements [4-6]. The flow of force through the beam-column joint can be disrupted if this connection is not able to provide adequate shear strength. If the shear capacity at this interface is insufficient, cracks can occur, and eventually, structural failure occurs.

The connection of precast concrete beam-columns is one solution to anticipate the failure of the building structure. Precast concrete is a component or structural element that is not cast at the place where the element is installed, but is cast in a place where the casting process and maintenance are carried out properly according to existing methods [7-8]. Precast concrete has many advantages compared to conventional concrete, including being able to speed up project execution time [5]. The many advantages of precast concrete make its use increased in recent years.

Hysteresis characteristics of load-displacement relationship loop with control displacement of precast beam-column joints due to cyclic loading [9-11]. The problem that arises is the difficulty of mapping the load-displacement characteristics of the beam of building precast column beams due to cyclic loading [12-14]. Precast beam-column joints, which are specific to the area of connection of precast parts. The construction will then be given a cyclic loading. The purpose of this study was to analyze the hysteresis characteristics of the load-displacement relationship with the controlled displacement of the precast beam-column connection due to cyclic loading. This study is intended to examine the behavior of beam-column joints for each model made. The results of this study can be a recommendation or input to construction implements regarding the behavior and concept of connection planning in precast concrete.

2. SPECIMENS AND TESTING METHOD

2. 1. Test Object Design   For the beam-column connection specimen, there are 3 models, namely monolith beam and column, grout connection with 2 pegs and grout connection with 4 pegs. (Figures 1, 2 and 3).

For columns measuring 30 cm x 30 cm with a length (ln) of 295 cm. As for the beam measuring 20 cm x 30 cm with a length of 145 cm.

The test was carried out at the Structure and Materials Laboratory, Faculty of Engineering, Hasanuddin University. Cyclic testing equipment used with an
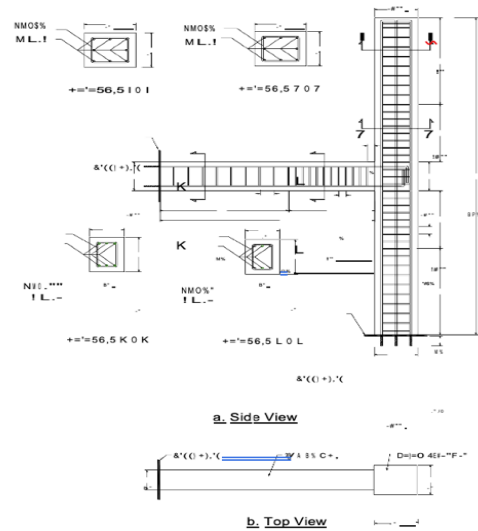
Figure 1. Monolith column beam test object (BN)
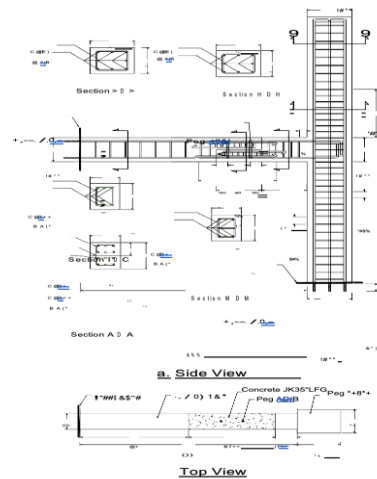
Figure 2. Test object for connection of 2 pegs(BG-1)
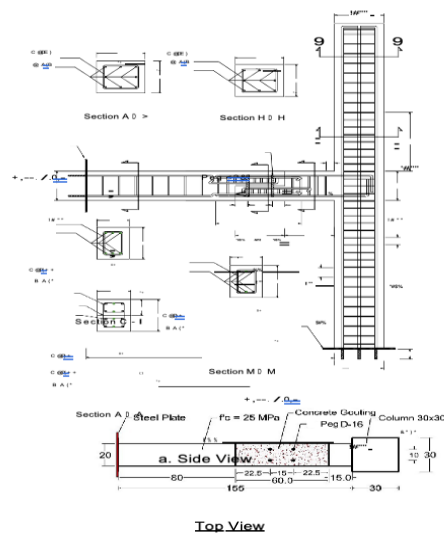
Figure 3. Test object 4 stake connection (BG-2)

actuator capable of 1500 kN with a maximum displacement of ± 20 cm.

The setup for testing the BN, BG-1, and BG-2 specimens is shown in Figure 4.

In addition, at the bottom, a plate with a thickness of 2 cm is installed and mounted on a strong floor with a thickness of 1.5 m through a rod measuring 1.5" (38 mm).

2. 2. Testing Method
1. Strain Gauge in Reinforcement and Concrete

For the strain gauge installed on steel reinforcement to determine whether the reinforcement has experienced yielding and on the concrete to determine whether the concrete has reached its ultimate condition.

For strain gauge reinforcement type FLK-6-11-5L installed on horizontal reinforcement and transverse reinforcement (see Figure 5).

2. LVDT

To measure the displacement of the beam-column joint test object, a linear variable displacement transducer (LVDT) was installed.

Equipment setup

BN

BG-1

BG-2
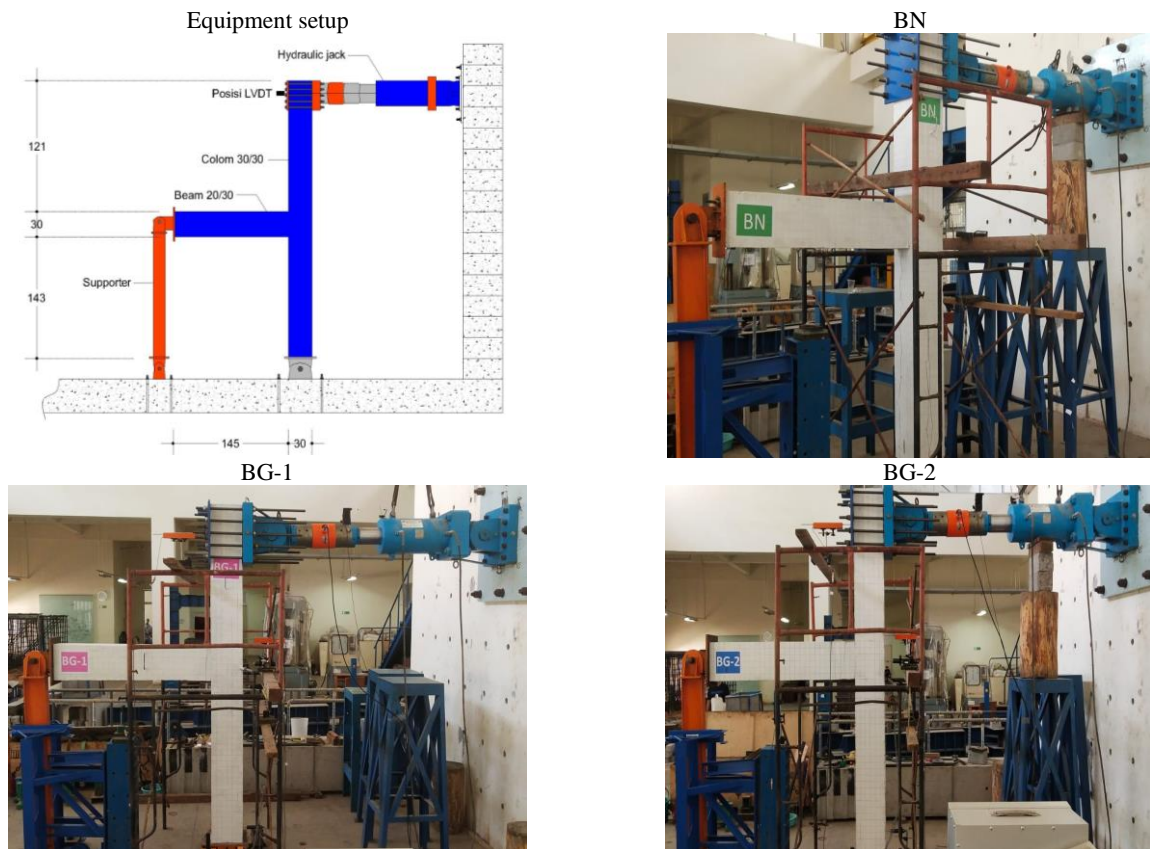
Figure 4. Cyclic testing equipment setup

Strain Gauge Installation Photos

Monolithic Concrete (BN)

B 2 Post Precast Concrete Joints (BG-1)
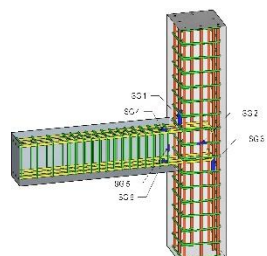
4 Stake Precast Joint Concrete (BG-2)
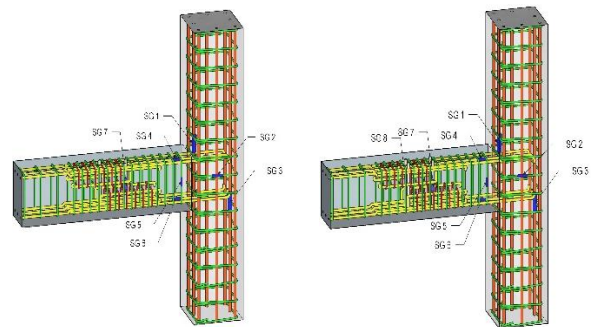
Figure 5. Strain gauge on steel

There are 6 LVDTs installed with capacities of 100 mm and 50 mm. For LVDT with a capacity of 100 mm, it is installed to measure the horizontal displacement at the top of the column and the center of the column, while LVDT with a capacity of 50 mm is installed at the bottom of the column and in the middle of the beam span (see Figure 6.)

2. 3. Cyclic Testing Procedure   For testing with cyclic loads refer to SNI 7834:2013 regarding test methods and criteria for acceptance of precast reinforced concrete moment-bearing frame structures for buildings referring to ACI 374.1-05 concerning Acceptance Criteria for Moment Frames based on Structural Testing.

The conditions are explained as follows:
1. The specimen shall be loaded by a sequence of displacement control cycles that represent the expected displacement between floors at the joint during an earthquake;
2. Three full cycles must be applied to each deviation ratio;
3. The initial deviation ratio must be within the range of the linear elastic behavior of the specimen. The next deviation ratio must be not less than 5/4 times and not more than 3/2 times the previous deviation ratio.
4. The test must be continued by increasing the deviation ratio gradually to the minimum deviation ratio value is 0.035. (See Figure 7).

3. RESULT AND DISSCUSION

3. 1. Hysteretic Behavior of Beam-column Joints
3. 1. 1. Load–Displacement Relationship   This section discusses the load-displacement relationship

Figure 6. LVDT on test pieces and installation photos
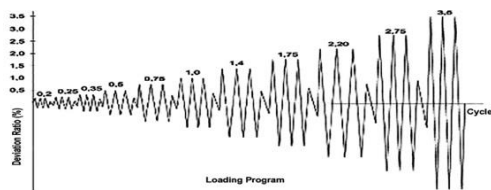
Figure 7. Loading program according to SNI 7834:2012

due to cyclic loading for specimens for monolith beam-column joints, precast beam-column joints of 2 and 4 posts. Table 1 summarizes the value of displacement loads for the three types of beam-column connections.
Monolith (BN) Beam-Column Joint Test Objects

Figure 8 Shows the results of cyclic testing for monolithic beam-column (BN) connections. In the ultimate condition, the load obtained in the tensile load is 13.58 kN with a displacement of 87.58 mm. Meanwhile, when the compressive load is 12.62 kN with a displacement of 88.30 mm. The load that occurs at the first yield is 11 kN with a displacement of 37.44 mm. For the first crack, the load is 3.5 kN and the displacement is 7.08 mm.
Precast Beam-Column Joint Test Objects 2 Posts (BG-1)

Figure 9 Shows the load and displacement relationship for the BG-1 test specimen due to cyclic loading. In the first crack condition, the load is 3.90 kN with a deviation of 9.15 mm. While for the first yield condition, the load value is 12.89 kN with a deviation of 42.66 mm. In the ultimate condition at the time of tensile load, the load value is 18.54 kN with a deviation of 94.42 mm. At the time of compressive load, the value of the load is 14.01 kN with a deviation of 96.88 mm.
Precast Beam-Column Joint Test Objects 4 Posts (BG-2)

The load obtained at the ultimate tensile load is 20.80 kN and the displacement is 96.80 mm. Meanwhile, when

TABLE 1. Load–displacement of BN, BG1, and BG2 test specimens

Test Object	First crack		First Yield		Ultimate			
					Press		Pull	
	P_{cr}	Δ_{cr}	P_y	Δ_y	P_u^+	Δ_u^+	P_u^-	Δ_u^-
	(kN)	(mm)	(kN)	(mm)	(kN)	(mm)	(kN)	(mm)
BN	3.5	7.08	11.00	37.44	12.62	88.30	13.58	87.58
BG-1	3.90	9.15	12.89	42.66	14.01	96.88	18.54	94.42
BG-2	4.30	9.91	13.11	47	16.41	98.90	20.80	96.80
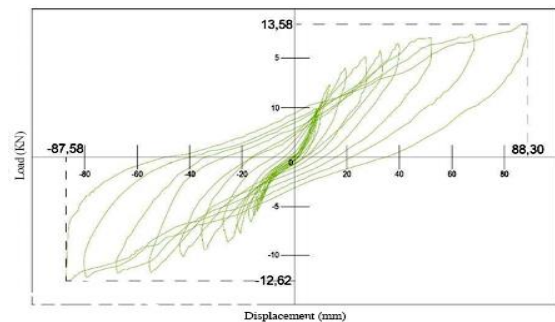
Figure 8. The load-displacement relationship due to cyclic loads on the BN test object
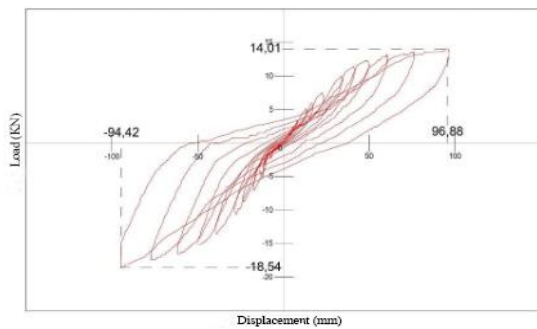
Figure 9. Relationship of load – displacement due to cyclic load on the test object BG-1

the ultimate compressive load is 16.41 kN with a displacement of 98.90 mm. The load at the first yield is 13.11 kN with a displacement of 47 mm. For the first crack, the load is 4.30 kN and the displacement is 9.91 mm (see Figure 10).

Load Capacity of Monolith Beam-Column Joints and Precast Beam-Column Joints with Pegs

From Table 1, it can be concluded that the load capacity at the time of the first crack for precast beam-column joints is greater than the load capacity of monolith beam-column joints. The load capacity of precast 4-post beam-column joints is greater than the load capacity of 2-post precast joints.

The same applies to load capacity at the time of the first yield. For the load capacity of the precast beam-column connection of 4 pegs more than the precast beam-column connection of 2 pegs and monolith. Figure 10 and Table 2 show the ultimate load capacity for monolithic and precast beam-column connections using dowels.

In the ultimate condition, the load capacity of precast beam-column joints with dowels is more than the load capacity of monolith beam-column connections. At the compression load, the load capacity of the precast beam-column connection with 2 posts increased by 13.9% and for the precast beam-column connection with 4 posts increased by 30% compared to the load capacity of the
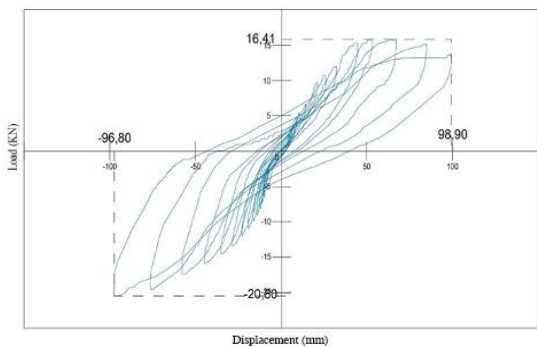
Figure 10. Load-displacement relationship due to cyclic load on the BG-2 test object
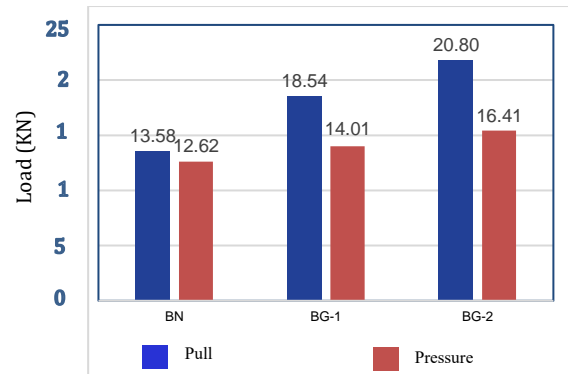
Figure 11. Ultimate load of SBK BN, BG-1, and BG-2 specimens

TABLE 2. The increase in the Pu value of precast SBK against monolithic SBK

Load	BG – 1	BG – 2
Pressure	13.9 %	30 %
Pull	36,5 %	53,2 %

monolith beam-column connection. At the tensile load, the load capacity for the precast beam-column connection with 2 posts increased by 36.5% and for the precast beam-column connection with 4 posts, it increased by 53.2% compared to the load capacity of the monolith beam-column connection.

In general, the increase in load capacity at the precast beam-column connection is due to the area being grouted with a strength of 36.97 Mpa, which is greater than the compressive strength of the concrete used in these elements. The greatest strength in the area causes the connection to become stiffer so that the load capacity increases [15-18].

3. 2. Crack Pattern   Figures 12(a), 13(a), and 14(a) are images of the initial crack pattern at a drift of 0.5% for monolithic connections and precast 2 (two) and 4 (four) posts. More cracks occurred in monolith joints compared to BG-2 precast (4 pegs) and BG-1 precast (2 pegs) joints. For cracks as a whole occur in the beam area. Figures 5(b), 6(b), and 7(b) are images of the fracture pattern of monolith joints and precast joints at a drift of 0.75%. For cracks that occur more tightly in the beam area for monolithic connections (BN) when compared to 2-post precast connections (BG-1) and 4-post precast connections (BG-2). In the column, especially the lower column, the cracks that occur are more for the BG-1 and BG-2 precast joints when compared to the monolith (BN) connection [19-22].

Figures 12€, 13€, and 14€ are crack patterns for monolithic and precast beam-column joints at 1% drift. In this condition, the crack pattern is almost the same as
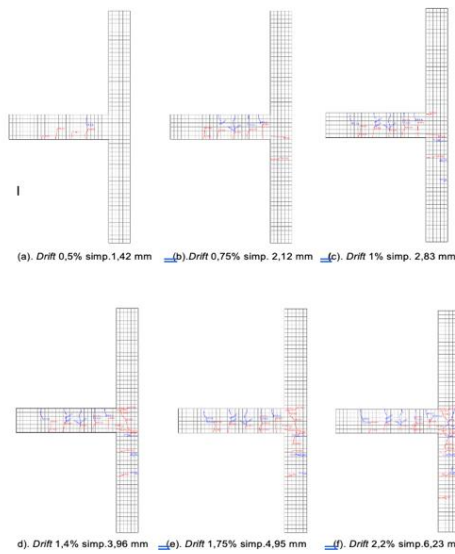
Figure 12. Pattern of monolithic beam-column (BN) joint cracks

Figure 13. Crack pattern of 2-post precast beam-column connection (BG-1)

Figure 14. Crack pattern of 4-post precast beam-column connection (BG-2)

Figures 12€, 13€, and 13€ show the crack pattern for beam-column joints with a drift of 1.75%. The crack pattern was almost the same with a 1.4% drift and an increasing number of cracks. In this condition, cracks have occurred in the area where the beam-column meets for the precast connection of 2 pegs (BG-1) and 4 posts (BG-2).

Figures 12(f), 13(f), and 14(f) are crack pattern images for joints at 2.2% drift. The crack pattern model is the same as the crack pattern at 1.75% drift with more cracks.

3. 3. Ductility of Beam-column Joints   This section discusses the behavior of beam-column joints in relation to ductility. Ductility is related to the displacement that occurs in the ultimate condition, namely the condition when the structure collapses and the displacement that occurs in the first yield condition of the reinforcement.

The displacement at the ultimate condition and yielding condition in the reinforcement is obtained from the load hysteretic curve – displacement when given a cyclic load [23]. Parameters related to ductility are displacements, especially in the first yield condition of the reinforcement (Δy) and in the ultimate condition, namely structural failure (Δu). To calculate displacement ductility, displacement parameters are used, while curvature ductility uses curvature value parameters or cross-sectional curvature and load values due to cyclic loads.

3. 4. Displacement Ductility   Table 3 shows the displacement values at the first yield condition of the

the crack pattern that occurs at a drift of 0.75% with an increase in the number of cracks.

Figures 10(d), 11(d), and 12(d) show the crack patterns for beam-column joints at 1.4% drift. Cracks are more common in the beam area for monolithic beam-column (BN) connections and precast beam-column joints BG-1 and BG-2.

In the column, cracks have started to increase but only occur at the bottom of the column. Especially in the monolith beam-column connection, cracks have occurred at the beam-column meeting area.

reinforcement and at the ultimate condition. The values of Δy and Δu can be seen in the Backbone curve.

In yield conditions, the displacements that occur at the monolithic beam-column connection (BN), the precast 2-pin beam-column connection (BG-1), and the 4-post precast beam-column connection (BG-2) are 37.44 mm, 42.66 mm, and 47 mm, respectively. The ductility value is calculated based on the ratio of the displacement value in the ultimate condition to the yield condition. From Table 3, the ductility values for the BN, BG-1, and BG-2 specimens are obtained, 2.34, 2.21 and 2.06, respectively.

From Figure 15, it can be seen that the ductility value of the BN test object is 2.34, while the BG-1 test object is 2.21 and the BG-2 test object is 2.06. Based on this value, it can be concluded that the monolithic beam-column connection (BN) has a higher ductility value than the precast beam-column connection using dowels (BG-1 and BG-2).

For the ductility value of the precast beam-column connection of 2 pegs, it is 0.94 times the ductility value of the monolith beam-column connection or reduced by 5.56%. Meanwhile, in the precast beam-column connection with 4 pegs, the ductility value is 0.88 times or reduced by 12%. For the precast beam-column connection with 2 pegs, the ductility value is greater than the precast beam-column connection with 4 posts.

The ductility of precast beam-column joints using dowels is smaller than the ductility of monolithic beam-column joints due to the presence of grouting in the beam connection area which makes the cross-section stiffer due to the greater compressive strength of the concrete in that area [24-25].

TABLE 3. Displacement in yield and ultimate conditions

SBK Test Object	First Yield	Ultimate	Ductility
	Δ_y (mm)	Δ_u (mm)	
BN	37.44	87.58	2.34
BG-1	42.66	94.42	2.21
BG-2	47	96.80	2.06
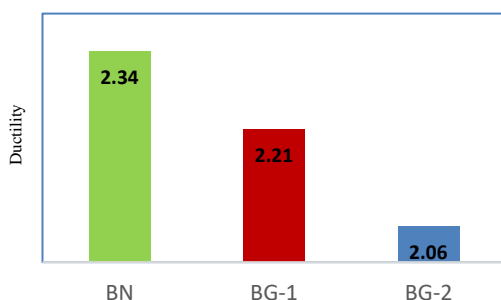
Figure 15. Ductility values for BN, BG-1, BG-2. Specimens

3. 1. 2. Classification of Ductility of Beam-column Joints   Table 4 shows the classification of ductility according to ASCE 41-17.

ASCE 41-17 divides ductility according to 3 categories, namely low ductility, moderate ductility, and high ductility. For low ductility, it has a value of less than 2, while medium ductility has a value between 2 to 4. For high ductility, it has a value of more than 4 [26-27].

From Table 4, for monolithic beam-column connection (BN) and precast beam-column connection (BG-1 and BG-2), the ductility values are 2.34, 2.21, and 2.06, respectively. Based on these values, it can be concluded that the specimens for monolithic and precast beam-column joints are categorized as structural elements with moderate ductility values.

3. 5. Curvature   The curvature ductility is calculated based on the load and displacement relationship (drift). Generally, the load is normalized to the load at yielding conditions, while the displacement can be converted to the value of curvature (curvature), drift (in units of %), or chord rotation (rotation).

Normalized load and curvature values for BN, BG-1, and BG-2 specimens are presented in Table 5.
Note:

$$* \ \emptyset y = \frac{\Delta y \ (Displacement \ at \ melting)}{L \ (test \ object \ height)}$$

$$** \ \emptyset u = \frac{\Delta u \ (Ultimate \ current \ shift)}{L \ (test \ object \ height)}$$

For BN specimens, the curvature value of the melting condition is 0.013 and in the ultimate condition is 0.031. In the BG-1 test object, the curvature value is 0.015 for

TABLE 4. Classification of test object ductility according to ASCE 41-17

Test Object	Ductility	Category	ASCE 41-17
BN	2.34	Moderate ductility	
			< 2, low ductility
BG-1	2.21	Moderate ductilty	2 to 4, moderate ductilty
			> 4, high ductility
BG-2	2.06	Moderate ductility	

TABLE 5. Load and curvature for BN, BG-1, BG-2 . specimens

SBK Test Object	P_y (kN)	P_u (kN)	P_U/P_y	Δ_y (mm)	$\emptyset_y$*	Δ_u (mm)	$\emptyset_u$**
BN	11.00	13.58	1.23	37.44	0.013	87.58	0.031
BG-1	12.89	18.54	1.43	42.66	0.015	94.42	0.033
BG-2	13.11	20.80	1.59	47	0.016	96.80	0.034

the melting condition and 0.033 for the ultimate condition. While in BG-2, the curvature value of the melting condition is 0.016 and in the ultimate condition is 0.034.

Figure 16, shows the curvature ductility for the specimens BN, BG-1, BG-2.

In the melting condition, the curvature ductility for the specimens BN, BG-1, and BG-2 were 0.013, 0.015, and 0.016, respectively. From this value, it can be seen that the curvature ductility value for precast beam-column joints using dowels is more than the curvature ductility value for monolith beam-column connections or an increase of 15.38% (BG-1 against BN) and 20% (BG-2). Against BN).

Based on ASCE 41-17 (Tables 10-11), the required ductility value under life safety (LS) conditions is 0.01. The curvature ductility values for the specimens BN, BG-1, and BG-2 are more than the values required in ASCE 41-17. This means that beam-column connections, both monolithic and precast using dowels, have good performance in carrying earthquake loads under moderate seismic conditions (medium earthquakes).

In the collapse prevention (CP) condition, the curvature ductility value required in ASCE 41-17 is 0.015, while the curvature ductility value for BN, BG-1, and BG-2 is more than the required value. It can be concluded that beam-column connections, both monolithic and precast, have excellent performance in carrying earthquake loads under severe seismic conditions (strong earthquakes).

From the results of the discussion in the previous section, it can be explained that the empirical findings are as follows:

Precast beam-column joints with dowels have a greater load capacity than monolithic beam-column joints. For precast SBK 2 pegs increased 11.01% - 36.52% and SBK 4 pegs increased 30.03% - 53.2% due to compressive and tensile loads.

The ductility value for monolithic SBK is greater than that of precast SBK with pegs, but the curvature ductility of precast SBK is still higher than normal SBK. SBK monolith and precast have good performance at moderate and strong earthquake levels, according to ASCE 41-17.
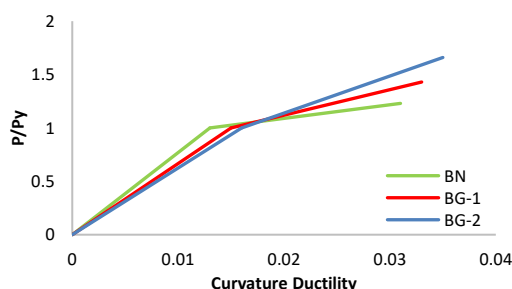
Figure 16. Bending ductility of BN, BG-1, BG-2

The stiffness degradation for precast SBK with 2 pins (5.23%) and 4 posts (4.90%) is smaller than monolith SBK (5.36%), stating that precast SBK with pegs is stiffer compared to SBK monolith.

Precast beam-column joints using dowels have a higher energy dissipation value than monolith beam-column joints, an increase of 3.42% for SBK 2 pegs and 7.97% for SBK 4 pegs.

For the connection of precast concrete column beams with dowels, it has good performance in terms of strength, ductility, stiffness, and energy dissipation. The connection of precast concrete column beams using 2 pegs is good enough to be applied at work, this is also to facilitate implementation in the field.

4. CONCLUSION

This study concludes that the hysteresis characteristics of the load-displacement relationship with displacement control of precast beam-column joints are very good for cyclic loads. The fact that the results of laboratory tests have shown that the capacity of monolithic beam-column (BN) connections is at a compressive load of 12.62 kN, while the load for 2 precast SBK increases by 11.01%-36.52% to a load value of 18.54 kN with a deviation. of 94.42 mm, and for 4 post precast, SBK increased by 30.03% - 53.2% of ultimate tensile load is 20.80 kN and the displacement is 96.80 mm compared to the load capacity of SBK monolith. This study concludes that by using 2 and 4 pins in the beam-column connection, the results are better. This study also concluded that the ductility value of SBK precast 2 pegs was 2.21 smaller than the actual SBK monolith ductility value of 2.34 or decreased by 5.56%. Meanwhile, in precast SBK 4 pegs the ductility value was 2.06 or decreased by 8.55%. Thus, this study concludes that the use of posts with 2 and 4 posts can reduce the ductility value.

5. REFERENCES

1. Breccolotti, M., Gentile, S., Tommasini, M., Materazzi, A.L., Bonfigli. MF, Pasqualini. B, Colone. V, Gianesini. M., "Beam-column joints in continuous RC frames: Comparison between cast-in-situ and precast solutions," *Engineering Structures,* Vol. 127, (2016), 129-144. doi: 10.1016/j.engstruct.2016.08.018.

2. Ma, F., Deng, M., Yang, Y., "Experimental study on internal precast beam-column ultra-high-performance concrete connection and shear capacity of its joint," *Journal of Building Engineering*, (2021), 103204. doi: https://doi.org/10.1016/j.jobe.2021.103204.

3. Wu, B., Peng, C.W., Zhao, X.Y., "Cyclic loading tests of semi-precast circular steel tubular columns incorporating precast segments containing demolished concrete lumps," *Engineering Structures*, Vol. 211, (2020), 110438. doi: https://doi.org/10.1016/j.engstruct.2020.110438.

4. Xie, L., Wu, J., Zhang, J., Liu, C., "Experimental study of mechanical properties of beam-column joint of a replaceable energy-dissipation connector-precast concrete frame," *Journal of Building Engineering*, Vol. 43, (2021), 102588. doi: https://doi.org/10.1016/j.jobe.2021.102588.

5. Yan, Q., Chen, T., Xie, Z., "Seismic experimental study on a precast concrete beam-column connection with grout sleeves," *Engineering Structures*, Vol. 155, (2018), 330-344. doi: https://doi.org/10.1016/j.engstruct.2017.09.027

6. Cai, X., Pan, Z., Zhu, Y., Gong N., Wang, Y., "Experimental and numerical investigations of self-centering post-tensioned precast beam-to-column connections with steel top and seat angles," *Engineering Structures*., Vol. 226, (2021), 111397. doi: https://doi.org/10.1016/j.engstruct.2020.111397.

7. Kataoka, M.N., Ferreira, M.A., de Cresce E.D., Ana, L.H., "Nonlinear FE analysis of slab-beam-column connection in precast concrete structures," *Engineering Structures*, Vol. 143, (2017), 306-315. doi: https://doi.org/10.1016/j.engstruct.2017.04.028.

8. Zhang, J., Ding, C., Rong, X., Yang, H., Li, Y., "Development and experimental investigation of hybrid precast concrete beam-column joints" *Engineering Structures*, Vol. 219, (2020), 110922. doi: https://doi.org/10.1016/j.engstruct.2020.110922.

9. Li, Z, Qi, Y, Teng. J., "Experimental investigation of prefabricated beam-to-column steel joints for precast concrete structures under cyclic loading," *Engineering Structures*, Vol. 209, (2020), 110217. doi: https://doi.org/10.1016/j.engstruct.2020.110217.

10. Wang. H, Marino. EM, Pan. P, Liu. H, Nie. X., "Experimental study of a novel precast prestressed reinforced concrete beam-to-column joint," *Engineering Structures*, Vol. 156, (2018), 68-81. doi: https://doi.org/10.1016/j.engstruct.2017.11.011.

11. Kang, SB, Tan, KH., "Behaviour of precast concrete beam-column sub-assemblages subject to column removal," *Engineering Structures*, Vol. 93, (2015), 85-96. doi: https://doi.org/10.1016/j.engstruct.2015.03.027.

12. Hu, G., Huang, W., Xie, H., "Mechanical behavior of a replaceable energy dissipation device for precast concrete beam-column connections," *Journal of Constructional Steel Researchs*, Vol. 164, (2020), 105816. doi: https://doi.org/10.1016/j.jcsr.2019.105816.

13. Singhal, S., Chourasia, A., Kajale, Y., "Cyclic behaviour of precast reinforced concrete beam-columns connected with headed bars," *Journal of Building Engineering*, Vol. 42, (2021), 103078. doi: https://doi.org/10.1016/j.jobe.2021.103078.

14. Yang, J., Guo, T., Chai, S., "Experimental and numerical investigation on seismic behaviours of beam-column joints of precast prestressed concrete frame under given corrosion levels," *Structures*, Vol. 27, (2020), 1209-1221. doi: https://doi.org/10.1016/j.istruc.2020.07.007.

15. Ghayeb, H.H., Razak, H.A., Sulong, N.H.R., "Development and testing of hybrid precast concrete beam-to-column connections

under cyclic loading," *Construction and Building Materials*, Vol. 151, (2017), 258-278. doi: https://doi.org/10.1016/j.conbuildmat.2017.06.073.

16. Do, T. A., Chen, H. L., Leon. G., Nguyen, T.H., "A combined finite difference and finite element model for temperature and stress predictions of cast-in-place cap beam on precast columns," *Construction and Building Materials*, Vol. 217, (2019), 172-184. doi: https://doi.org/10.1016/j.conbuildmat.2019.05.019.

17. Li, D., Wu, C., Zhou, Y., Luo, W., Lie, W., "A precast beam-column connection using metallic damper as connector: Experiment and application," *Journal of Constructional Steel Researchs*, Vol. 181, (2021), 106628, doi: https://doi.org/10.1016/j.jcsr.2021.106628.

18. Nzabonimpa, J.D., Hong, W.K., Kim, J., "Experimental and non-linear numerical investigation of the novel detachable mechanical joints with laminated plates for composite precast beam-column joint," *Composite Structures*, Vol. 185, (2018), 286-303, doi: https://doi.org/10.1016/j.compstruct.2017.11.024.

19. Wang, H., Marino, E.M., Pan, P., "Design, testing and finite element analysis of an improved precast prestressed beam-to-column joint," *Engineering Structures*, Vol. 199, (2019), 109661, doi: https://doi.org/10.1016/j.engstruct.2019.109661.

20. Gou, S., Ding, R., Fan, J., Nie, X., Zhang., J., "Seismic performance of a novel precast concrete beam-column connection using low-shrinkage engineered cementitious composites," *Construction and Building Materials*, Vol. 192, (2018), 643-656, doi: https://doi.org/10.1016/j.conbuildmat.2018.10.103.

21. Guerrero, H., Rodriguez, V., Escobar, J.A., Alcocer, S.M., Bennetts, F, Suarez, M., "Experimental tests of precast reinforced concrete beam-column connections," *Soil Dynamics and Earthquake Engineering*, Vol. 125, (2019), 105743, doi: https://doi.org/10.1016/j.soildyn.2019.105743.

22. L Li, S. Q., Yu, T. L., Chen, Y. S. "Comparison of macroseismic intensity scales by considering empirical observations of structural seismic damage", *Earthquak Spectra*, Vol. 37, No. 1, (2021), 449-485. DOI: 10.1177/8755293020944174.

23. Li, S. Q., Yu, T. L., Jia, J. F. "Empirical seismic vulnerability and damage of bottom frame seismic wall masonry structure: A case study in Dujiangyan (China) region", *International Journal of Engineering, Transactions C: Aspects*, Vol. 32, No. 9, (2019), 1260-1268. DOI: 10.5829/ije.2019.32.09c.05

24. ACI Committee 318-89, "Building Code Requirements for Reinforce Concrete (ACI 318-89)," Illionis, (1989)

25. Li, S. Q., Yu, T. L., Jia, J. F. "Investigation and analysis of empirical field seismic damage to bottom frame seismic wall masonry structure", *International Journal of Engineering, Transactions B: Applications*, Vol. 32, No. 8, (2019), 1082-1089. DOI: 10.5829/ije.2019.32.08b.04.

26. ACI, "Recommendations for Design of Beam-Column Connections in Monolithic Reinforced Concrete Structures," ACI 352R-02, American Concret Institute, Farmington Hills, Ml., (2002).

27. ASTM, "Concrete and Material, Annual Book of ASTM Standart," Vol. 04 No.02, (1993) Philadelpia

Persian Abstract

چکیده

اتصال تیر و ستون نقش مهمی در ساختار ساختمان ایفا می کند ، به ویژه هنگامی که بار چرخه ای است. مشکل اصلی که باید حل شود ، پانل های اتصال تیر و ستون است. هدف از این مطالعه تجزیه و تحلیل ویژگی های حلقه پسماند رابطه بار جابجایی کنترل اتصال تیر و ستون پیش ساخته به دلیل بارگذاری چرخه ای بود. روش تحقیق مورد استفاده روش آزمایشی با آزمون طراحی شیء قابل اندازه گیری و روش آزمایش ویژه است. نتایج این مطالعه نشان می دهد که بتن معمولی دارای مقاومت فشاری ۲۶.۴۳ مگاپاسکال است ، در حالی که بتن دوغابدار دارای مقاومت فشاری ۳۶.۹۷ مگاپاسکال است. یافته های این مطالعه همچنین نشان می دهد که بتن دوغاب تنش پیوند ۱۰۲.۴ درصد از بتن معمولی برای تقویت پیچ با قطر D13 افزایش می یابد ، در حالی که برای قطر D16 ، تنش چسبندگی به میزان ۵۱.۶۳ درصد افزایش می یابد. یافته های این مطالعه همچنین نشان می دهد که در شرایط نهایی ، بار به دست آمده در بار کششی ۱۳۸/۵۸ کیلو نیوتن با جابجایی ۵۸/۸۷ میلی متر است ، در حالی که بار فشاری ۱۲/۶۲ کیلو نیوتن با جابجایی ۸۸/۳۰ میلی متر است. این مطالعه نتیجه می گیرد که رفتار اتصالات تیر و ستون پیش ساخته با رولپلاک در مقاومت در برابر بارهای چرخه ای قوی تر است.

International Journal of Engineering

An Experimental Investigation of Parabolic Trough Collector using Industrial-grade Multiwall Carbon Nanotube- H$_2$O Based Nanofluid

P. M. Gautam*, M. K.Chudasama

Mechanical Engineering Department, Government Engineering College, Dahod, India

A B S T R A C T

Solar thermal systems for heating have a high level of reliability. The usage of parabolic trough collectors (PTC) for domestic applications is still quite limited; furthermore, commercial utilization of nanofluids in these applications is rare. The influence of MWCNT nanofluid as a heat transfer fluid on the efficiency of a locally developed parabolic trough collector was experimentally examined. The effect of surfactant on nanofluid stability was also investigated, and it was revealed that nanoparticles could be evenly suspended in base fluid for at least 10 days and less than one month using Triton X-100. Experiments were also conducted to determine the optimal quantity of Triton X-100 surfactant; it is possible to make nanoparticles stable for 28 days in base fluid with the ratio of Triton X-100 to MWCNT as 0.5:1. At 2.0, 3.0, and 4.0 L/min flow rates, MWCNT/H$_2$O is used at three-particle concentrations of 0.1, 0.2, and 0.3% by weight. The experiment is carried out under outdoor operating conditions. With 3 L/min at 0.2 wt.%, MWCNT nanofluid achieves a maximum thermal efficiency that is 22% greater than the water. The findings provide important information about the commercialization of a locally developed PTC.

doi: 10.5829/ije.2022.35.01a.10

1. INTRODUCTION

Researchers have been emphasized using sustainable and renewable energy these days. Over the past few years, renewable energy has been widely used, including wind energy, hydrogen energy, and solar energy. Solar energy is the most favorable type of renewable source of energy that can, directly and indirectly, be transformed into various forms of energy. One of the strongest sources of renewable energy with limited environmental effects is solar energy. A well-established technology is the solar parabolic trough collector and it has been proposed for several applications, such as power generation and water heating, but the performance of these collectors is restricted by the working fluid's absorption properties. This technology has recently been combined with the evolving nanofluids and liquid-nanoparticle suspension technologies to create a new class of solar collectors

based on nanofluids. The performance increase was seen in the use of nanofluids as the absorption media in solar thermal collectors. In India, over 90% of the country during the summer season a large amount of solar radiation is received in the order of 3.0–6.5 (10.8–23.4 MJ/m^2-day) kWh/m^2-day [1]. Rehan et al. [2] assessed the maximum efficiencies for Al$_2$O$_3$ and Fe$_2$O$_3$ nano-fluids at 2 L/min and found 13 and 11% increment, respectively compared to water under the same operating conditions. In improving the performance of PTC compared to Fe$_2$O$_3$ for domestic applications, Al$_2$O$_3$ nanofluids seemed more favorable. Chaudhari et al. [3] found that solar thermal efficiency can be increased by approximately 7% by Al$_2$O$_3$ nanofluid and the heat transfer coefficient can be increased by 32 %. Sunil et al. [4] investigated SiO$_2$-H$_2$O-based nanofluid is comparatively more efficient at higher volume flow rates and concentrations. Ebrazeh et al. [5] has examined that due to its high energy content, the use of nanofluids increases thermal efficiency. In a wide range of studies, Al$_2$O$_3$ nanoparticle has been used because of its lower price. Also, the collector's thermal

Corresponding Author Institutional Email: gautampapil@gmail.com (P. M. Gautam)

efficiency can be improved by raising the working fluid inlet temperature. Among all forms of nanofluids, the use of MWCNTs has the best thermal performance. Verma et al. [6] assessed multiwalled carbon nanotube/water and reported the highest increase in a collector's energy efficiency, which is 23.47%, followed by 16.97, 12.64, 8.28, 5.09, and 4.08%, respectively for graphene/water, Copper oxide/water, aluminium oxide/water, titanium oxide /water, and silicon oxide/water compare to water as the base fluid. The percentage decrease in the area observed in various nanofluids was given as 19.01% as the optimum in MWCNTs/water followed by 14.66, 10.66, 8.78, 4.83 and 3.99%, respectively in graphene, copper, aluminium, titanium, and silicon oxide-based nanofluids. Verma et al. [7] evaluated the use of MgO nanofluid improves the solar collector efficiency by 9.34% for 0.75% of particle volume fraction and volume flow rate at 1.5 L/min compared to water as working fluid. Yousefi et al. [8] found a large improvement in efficiency due to increasing the weight fraction from 0.2 to 0.4%. Using the surfactant also results in an improvement in efficiency. The optimum sonication time was selected to be 30 min. Rastogi et al. [9] proved that Triton X-100 was the best dispersing agent for suspending MWCNTs as a non-ionic surfactant. Maximum dispersion was given by the Triton X-100 among many surfactants like Tween 80, Tween 20, and sodium dodecyl sulfate (SDS). The optimum amount of surfactant required in the case of Triton X-100 is also lower than that of other surfactants. The optimal ratio of Triton X-100-to-CNT was selected to be 1:350. Mishra et al. [10] scrutinized MWCNT nanofluid 0.02 wt% with 160 L/h showed better results for overall thermal efficiency and the use of surfactant Triton X-100 with MWCNT nanofluid was also used to increase the amount of base fluid heat absorption power. Bernard et al. [11] studied that with a mass flow rate of 0.0069 kg/s, 0.0138 kg/s, and 0.0207 kg/s, the heat energy obtained by the MWCNT fluid has increased by 5.2 %, 7.3 %, and 7.2 % compared to water. Hachicha et al. [12] evaluated MWCNT nanoparticles in water results in a 12, 16, and 21% raised in Nusselt number for nanoparticle concentrations of 0.05, 0.1, and 0.3%. The use of low concentrations of nanofluid could improve thermo-hydraulic performance at flow rates below 0.2 L/s, Khanafer et al. [13] surveyed available studies in the literature of solar systems and concluded an increase in thermal conductivity of nanofluid is an important factor for improving the efficiency of nanofluid. Higher volume fractions of nanoparticles do not increase performance regularly. Due to the addition of nanoparticles, the rise in nanofluid viscosity is a major drawback since it is associated with increasing pumping capacity. Thus, the use of low viscosity and high thermal conductivity nanofluids is favorable.

Borode et al. [14] described carbon nanomaterials as the most promising for the preparation of nanofluids and the application of heat transfer. This research result showed that carbon-based nanofluids increased the collector performance of flat-plate, evacuated-tube, parabolic trough, and hybrid photovoltaic thermal solar collectors by up to 95.12, 93.43, 74.7, and 97.3%, respectively, with a low concentration of about 0.3 vol.%. Bindu et al. [21] proved improvement in thermophysical characteristics and thermal conductivity of the HTF by nanoparticles such as CuO, Ag, TiO_2, Al_2O_3, SiO_2, MWCNT, CNT, and mixture of the particles forming hybrid nanofluid. The use of nanofluid in PTC improves the system's thermal efficiency. Hussein et al. [15] explained the challenges and difficulties that arise during nanofluid preparation and in an application, (i) A long time is required for the nanofluid to be stable with base fluids. (ii) The toxicity of the nanofluid is high, so it needs to be taken care of during its preparation. (iii) Preparation and testing of the nanofluid are extremely expensive. (iv) The high viscosity of the nanofluid contributes to an increase in the pressure drops and also increases the necessary pumping power. (v) The presence of nanoparticles in the nanofluid can lead to long-term solar collector corrosion and erosion. Olia et al. [16] examined the use of copper nanoparticles led to improve thermal efficiency in metallic nanofluids, followed by CuO, TiO_2, and Al_2O_3, among all the nanoparticles examined, the MWCNT nanoparticle can lead to the highest increase in thermal efficiency for non-metallic nanofluids. Mirabootalebi et al. [20] altering the effective variables, such as increasing milling time, selecting the suitable temperature, utilizing different sizes of balls, and using a special vial, can increase the quality and quantity of MWCNTs. Three essential components of the experiments conducted and described in this article are innovative. (1) With thorough research of such systems, rare relevant literature or experimental data is found for climatic conditions of underdeveloped countries, particularly in South Asia, such as India. Furthermore, different types of nanoparticles are utilized in different climates; however, the experimental examination of industrial-grade MWCNT-H2O is only found in a numerical study. Furthermore, the vast bulk of nano-fluids research is focused on high-temperature applications, particularly for power production, whereas the current effort is mostly focused on low-temperature domestic uses. As a result, the provided findings provide a valuable dataset for the future feasibility of independent PTC applications in off-grid settings. (2) The developed system reported here made use of comprehensive local fabrication capabilities and materials that were readily available locally. The performance rating of entirely local PTC under various atmospheric and operating conditions, as well as nanoparticle amounts, adds great

value to these findings, particularly for regional growth. (3) The complete replacement of the PTC's expensive conventional receiver tube with a two-sided open evacuated tube. Finally, parametric variations in nanoparticle weight fractions and flow rates are investigated and reported hereunder local climatic conditions. The provided findings provide insight into the performance of the linear PTC system in terms of product commercialization in similar climatic locations.

2. EXPERIMENTAL SETUP AND PROCEDURE

2. 1. Material   The nanoparticles employed in the experimental study were MWCNT of industrial grade. The Nanoparticles with 99% purity were purchased from ''adnano Technologies India''. To disperse MWCNT nanopowder, laboratory-grade Triton X-100 was utilized as a surfactant. The properties of the nanoparticles used are listed in Table 1, for the manufacture of water-based nanofluids; distilled water was employed as the based fluid. Figure 1 shows the TEM images of industrial-grade MWCNT.

2. 2. Requirement of Surfactant   Based on the collected data and the comprehensive survey carried out, Triton X-100 is the best dispersing agent for suspending MWCNT as a non-ionic surfactant. The Triton X-100 is confirmed among different surfactants since the optimum amount of Triton X-100 surfactant
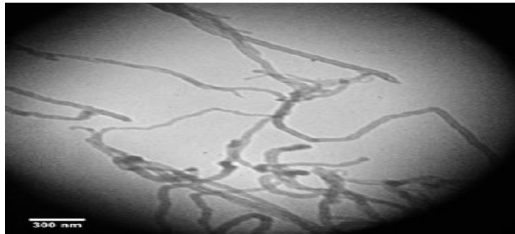
Figure 1. TEM micrograph image of MWCNT nanoparticles at 300 nm [17]

TABLE 1. Properties of Nanoparticles[17]

Multi-Walled Carbon Nanotubes	Description
Purity	~99 %
Outer Diameter	10-30 nm
Inner Diameter	5-10 nm
Length	>10 μm
Surface Area	110 - 350 m^2/g
CNT content	~95-99 %
Bulk Density	0.14 g/cm^3
Color	Black Powder

required is also lower than that of other surfactants [9]. It is also used to increase the amount of base fluid heat absorption power; Triton X-100 is a colorless viscous fluid. Beaker A represents the Nanofluid without surfactant and Beaker B represents the Nanofluid with surfactant. To avoid agglomeration of nanoparticles magnetic stirrer and sonication were done for 2 and 3 h, respectively with both samples.

The above Figure 2A depicts that agglomeration of nanoparticles in nanofluid without surfactant would start after 1h and afterward sedimentation of nanoparticles will be observed. Figures 2B, 2C, 2D and 2E show process of agglomeration is quite significant after 2, 3, and 4h. Complete sedimentation can be observed after 5h in Figure 2E.

Figure 2A. Condition of Nanofluids after 1h. of preparation
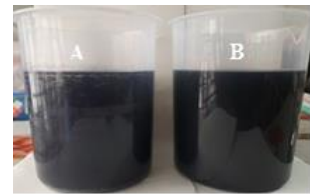
Figure 2B. Condition of Nanofluids after 2h of preparation
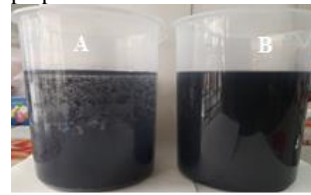
Figure 2C. Condition of Nanofluids after 3h of preparation
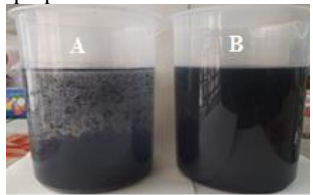
Figure 2D. Condition of Nanofluids after 4h of preparation
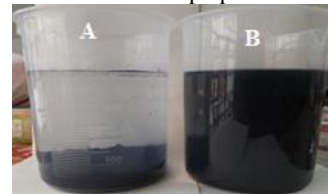
Figure 2E. Condition of Nanofluids after 5h of preparation

While in the case of nanofluid with the surfactant, nanoparticles can be evenly suspended in base fluid for at least 10 days and less than 1 month for Triton.

2. 3. Required Optimum Quantity of Surfactant Based on the extensive literature survey one question need to be addressed, what should be the optimal quantity of surfactant in the particular experimentation. There are different ratios of Triton X-100: MWCNT available in the literature. As far as present research is concern following ratios of Triton X-100: MWCNT have been selected (i) 0.1:1 (ii) 0.25:1 (iii) 0.5:1 [18].
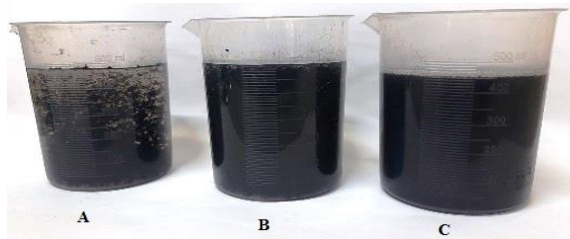
Figure 3. Surfactant: MWCNT ratio, (A) 0.1:1 (B) 0.25:1 (C) 0.5:1

Pilot experimentation was carried out to check the period of stability of nanoparticles in the base fluid. In Figure 3 beakers A, B and C represent the different nanofluids with Triton X-100: MWCNT followed by 0.1:1, 0.25:1, and 0.5:1 ratio. A continuous observation was done for 1 month to observe the sedimentation time taken by the different nanofluid. After 11 days agglomeration was started in nanofluid having surfactant: MWCNT ratio 0.1:1, which can be identified from Beaker A. In the case of Beaker B agglomeration time was 18 days and Beaker C shows maximum stability time for nanoparticles in base fluid as 28 days. To conclude this pilot experiment, one conclusion can be made that Triton X-100 with 0.5 % of MWCNT by weight gives quite enough stability in suspension for a considerable time.

2. 4. Nanofluids Preparation Method
MWCNT water-based nanofluids i.e. MWCNT/H$_2$O is used at three particles concentrations of 0.10, 0.20, and 0.30 % by weight at 2.0, 3.0 and 4.0 L/min flow rates.

To make stable nanofluids, a weighted amount of nanoparticles was first dispersed in a base fluid containing a surfactant. Then, using a 40 kHz ultrasonic vibrator, sonication was used to obtain homogenized dispersed nanofluids, as shown in Figure 4. To avoid agglomeration, researchers employed a two-step approach of sonication and magnetic stirrer to prepare MWCNT/H$_2$O nanofluids [18]. In this experiment, distilled water was mixed with a weighted amount of MWCNT nanopowder and the surfactant Triton X-100. To avoid nanoparticle aggregation, a magnetic stirrer was employed to disperse nanoparticles in distilled water for 2 hours, as illustrated in Figure 5. And then

Figure 4. Ultrasonic vibrator

Figure 5. Magnetic stirrer with a hot plate

sonication for 3 hours was done to stabilize the nanofluids.

2. 5. Experimental Line Layout   Under actual conditions in Surat, Gujarat, India (21°10'45.8"N, 72°48'47.6"E), the thermal performance of a parabolic trough collector with water and MWCNT/H$_2$O was compared. The nanofluids were formed utilizing a two-step method in distilled water with the inclusion of Triton X-100 as a surfactant, as well as a sonicator at various nanoparticle mass fractions. In addition to the effects of three different concentrations; 0.1, 0.2 and 0.3 %, by weight, three flow rates; 2, 3 and 4 L/min were also studied. In March near to equinox i.e. 8th to 19th March, experiments were conducted daily from 10:30 a.m. to 2:00 p.m. The experimental setup is depicted in Figure 6. The nanofluid would be re-circulated at any point during the close cycle. The supply pump draws the working fluid from a single nanofluid storage tank and sends it to the parabolic trough receiver. A mechanical stirrer is offered for optimal fluid mixing and equal temperature distribution. The rotameter's control knob can be used to change the working fluid mass flow rate. In addition to controlling the working fluid's mass flow rate, a by-pass arrangement valve is also given. Two temperature sensors are positioned at the intake and outlet sections of the working fluid, respectively, to measure the inlet and outlet temperatures.

Two different sensors will monitor the skin temperature of the receiving tube and the skin temperature of the reflecting sheet, while one individual sensor will measure the ambient temperature. All of these temperature sensors are calibrated with PT-100 kinds before being linked to a computer for analysis.

3. DESIGN OF PTC SYSTEM

Parabolic profile curves, MS pipe struts, and a two-sided evacuated tube with supporting coupling are all
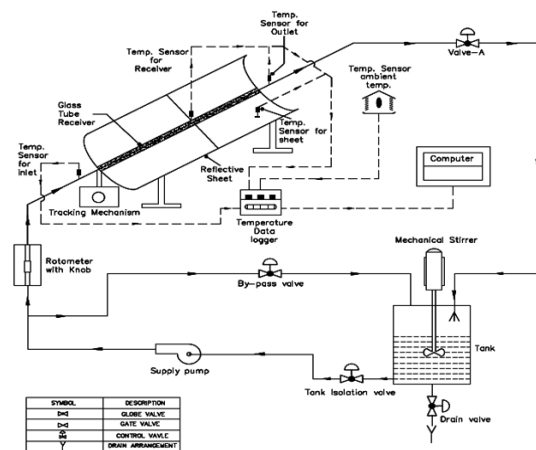
Figure 6. Schematic line layout of the PTC test setup

part of the experimental setup. When incident radiation strikes the PTC's aperture, it forms an angle with the PTC's central plane. The rim angle determines the curvature of a parabola. Equation (1) is the general equation of a parabola in a coordinate system [19]. where f = parabola focal distance (m). W_a = parabolic aperture.

$$y^2 = 4fx \qquad (1)$$

The collector concentration ratio C, which is defined as the ratio of the aperture area A_{ap} to the receiver area A_r and is represented by Equation (2), is another significant parameter in PTC. D = Diameter required to intercept the entire solar image.

$$C = \frac{W_a}{\pi D} \qquad (2)$$

Equation (3) can be used to calculate the parabolic aperture, where φ_r = Rim angle (°)

$$W_a = 4f \tan\left[\frac{\varphi_r}{2}\right] \qquad (3)$$

The acrylic material required for parabolic surface construction is determined by the amount of the rim angle. Equation 4 can be used to compute the length of a reflective surface curve[19].

$$S = \frac{H_p}{2}\left\{\sec\left(\frac{\varphi_r}{2}\right)\tan\left(\frac{\varphi_r}{2}\right) + \ln\left[\sec\left(\frac{\varphi_r}{2}\right) + \tan\left(\frac{\varphi_r}{2}\right)\right]\right\} \qquad (4)$$

H_p = Latus rectum of the parabola (m) = 1. In the case of 90° rim angle, it is equal to aperture. S = 1.147 m, Now the total reflective sheet area required for fabrication is, A = 2.0 m^2. Table 2 provides a summary of PTC's important characteristics.

The current research work is depicted in Figure 7.

3. 1. Thermal Analysis   Equation (5) indicates the available sun irradiation (Q_s) at the aperture can be used to compute the input energy [2]. Where G_b = Direct solar irradiation (W/m^2). $\dot{m}$ = Mass flow rate (kg/s), C_p= Specific heat (Kj/Kg °C), T_i = Inlet water temperature (°C), T_o= Outlet water temperature (°C).

$$Q_s = A_{ap} \times G_b \qquad (5)$$

The amount of useful heat gained by the collector's working fluid is determined by Equation (6) [2].

$$Q_u = \dot{m}c_p(T_o - T_i) \qquad (6)$$

Equation (7) is used to compute the collector's experimental thermal efficiency.

TABLE 2. The summary of the PTC key features.

PTC key feature	
Collector dimensions	1.00 m ×1.70 m
C	5.5
W_a[m]	1
H_p[m]	1
f[m]	0.250
D[mm]	58
φ_r[deg]	90°
A_{ap}[m^2]	1.70

Figure 7. Experimental setup of PTC with two-sided open evacuated tube receiver

$$\eta_t = \frac{\dot{m}c_p(T_o - T_i)}{A_{ap}G_b} \qquad (7)$$

3. 2. The Volume Fraction of Nanoparticles in the Base Fluid   The current study's analysis is based on different amounts of nanoparticles presented as a percentage by weight fraction, which can be converted to volume fraction using the Equation (8) [2] relationship, as shown in Table 3.

$$\varphi \times 100 = \frac{\left[\dfrac{w_{MWCNT}}{\rho_{MWCNT}}\right]}{\left[\dfrac{w_{MWCNT}}{\rho_{MWCNT}}\right] + \left[\dfrac{w_{Base\ fluid}}{\rho_{Base\ fluid}}\right]} \qquad (8)$$

4. RESULTS AND DISCUSSION

The thermal efficiency of PTC using water and water-based MWCNT nanofluids was experimentally studied under the actual outdoor operating parameters. The

TABLE 3. Volume fractions of nanoparticles

Sr. No.	Mass fraction of Nanoparticles by weight (%)	Density of nanoparticles ρ_{MWCNT} (kg/m^3)	Mass of Base fluid $W_{base\ fluid}$ (kg)	Density of Base fluid $\rho_{base\ fluid}$ (kg/m^3)	Volume Fraction (%)
1	0.1	140	0.998	999.972	0.007
2	0.2	140	0.998	999.972	0.014
3	0.3	140	0.998	999.972	0.021

influence of varied mass flow rates on the thermal efficiency of water and water-based MWCNT nanofluids with different concentrations by weight is shown. Figure 8 shows the variation in thermal efficiency at 2 L/min distilled water and compared with the nanofluid having different fractions i.e. 0.1, 0.2, and 0.3% by weight of MWCNT. The maximum efficiency achieves by the water is 33.43%. With the same flow rate and at 0.1, 0.2, and 0.3 wt.% obtained maximum efficiencies are 37.81, 39.65, and 38.48%, respectively. It should be mentioned that the thermal efficiency of MWCNT nanofluids is at 0.20 wt.% is higher than water and other nanofluids of various fractions at the same flow rate. Figure 8A depicts the change in thermal efficiency at 3 L/min distilled water when compared to nanofluids containing various fractions of MWCNT, viz. 0.1, 0.2, and 0.3 wt.%. The water achieves an efficiency of 37.09%. The efficiencies were obtained with the same flow rate and at 0.1, 0.2, and 0.3 wt.% are 37.81, 39.65, and 38.48%, respectively. It's worth noting that at 0.20 wt.%, MWCNT nanofluids have greater thermal efficiency than water and the nanofluids of various fractions at the same flow rate. Thermal efficiency at 4 L/min of distilled water and the different fraction of nanoparticles are shown in Figure 8B. The 35.61, 41.04, 42.93, and 41.56% are the maximum efficiencies achieved by the distilled water, 0.1, 0.2 and 0.3 wt %, respectively. It can be noted that again 0.20 wt %, MWCNT nanofluids have better thermal efficiency than water and other nanofluids at the tested flow rate.

Figure 8A. Variation of efficiency with distilled water and different weight concentration at 3 L/min
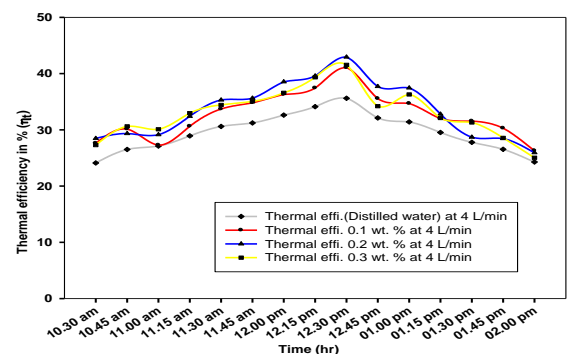
Figure 8B. Variation of efficiency with distilled water and different weight concentration at 4 L/min

It was observed that maximum efficiency conditions occur near solar noontime. Figure 9 shows the percentage gain in thermal efficiency at 2 L/min. The maximum gain was observed at 0.2 wt.% followed by a 19 % increment compared to base fluid efficiency, and the all-over average gain was 14.0%. In the case of 0.1 wt.% fraction average and maximum improvement were 8 and 13% respectively. 11 and 15 % were the values of average and maximum efficiency gain with 0.3 wt. %. Figure 9A depicts the percentage gain in thermal efficiency at 3.0 L/min with different concentrations of Nanoparticles. The highest gain was observed at 0.2 wt.% as 22% and average improvement was 19%. This was the highest efficiency achieved during the complete experimentation. 14 and 19% were the averages and maximum efficiency increment noted at 0.1 wt.%. The maximum gain was 20% and the average gain was 16% at 0.3 wt.%. The percentage gain in thermal efficiency at 4.0 L/min with different concentrations of Nanoparticles was shown in Figure 9B. The performance of fraction 0.2 wt.% was highest at 21% and the average value of efficiency gain was 13%. The maximum and average gains of efficiencies were 15 and 11% at 0.1 wt.% respectively. The performance at 0.3 wt.% is worthy as compared to 0.1 wt.% but it is less than 0.2 wt. %.17 and 12% are the values of maximum

Figure 8. Variation of efficiency with distilled water and different weight concentration at 2 L/min
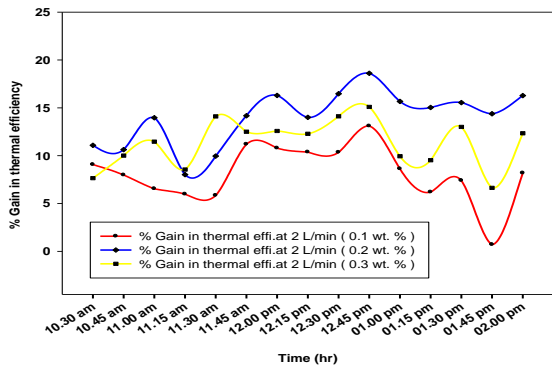
Figure 9. Percentage gain in efficiency w.r.t distilled water at 2 L/min
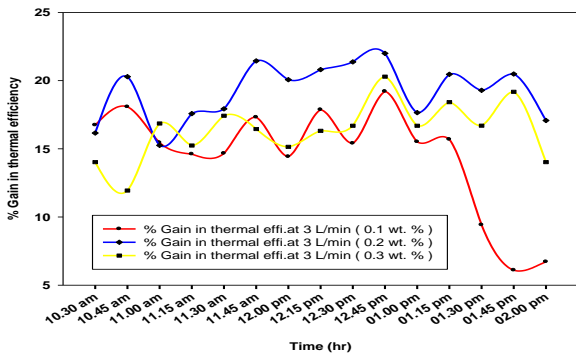
Figure 9A. Percentage gain in efficiency w.r.t distilled water at 3 L/min.

and average efficiency gain respectively. Variation in the efficiency of PTC using MWCNT/H$_2$O with 0.1 wt. % at different flow rates are plotted in Figure 10. It can be observed that nanofluids with 3 L/min and 0.1 wt. % sustain its maximum value during the whole experimentation period. The maximum efficiency was 44.22% observed with 3 L/min at 12.45 pm. The efficiency of PTC utilizing water-based MWCNT with 0.2 concentrations by weight at varied flow rates is depicted in Figure 10A. When comparing the efficiency of MWCNT/H$_2$O nanofluids with 3 L/min and 0.2 wt.% to other flow rates at the same concentration, it is worth noting that the efficiency of MWCNT/H$_2$O nanofluids with 3 L/min and 0.2 wt.% is the highest at 45.25%. Figure 10B shows the efficiency of PTC using water-based MWCNT with 0.3 wt.% at various flow rates. When comparing the efficiency of MWCNT/H$_2$O nanofluids with 3 L/min and 0.3 wt.% to other flow rates at the same concentration, the efficiency of nanofluids with 3 L/min and 0.3 wt.% comes highest as 44.62%. The highest thermal efficiency for PTC was achieved at a 3 L/min flow rate with 0.2 wt.% across the whole experiment. Figure 11 shows the average values of direct normal irradiation on that particular day. Direct

solar radiations were recorded using a handy Solarimeter (MECO-936) with 20 reading storing facilities.

The variations in ambient temperature and wind speed of the environment data for 3 L/min with 0.2 wt. % during the test day is given in Figure 12. Data were measured and recorded by using PT-100 type thermometer and digital AVM-03 anemometer, respectively.
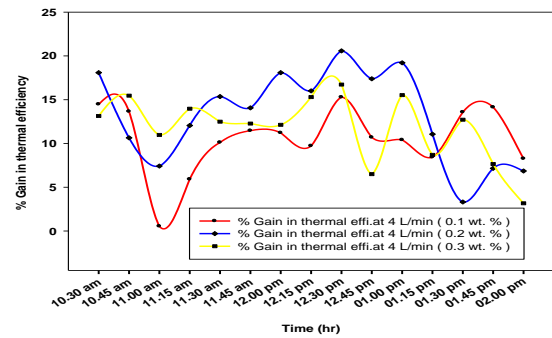
Figure 9B. Percentage gain in efficiency w.r.t distilled water at 4 L/min
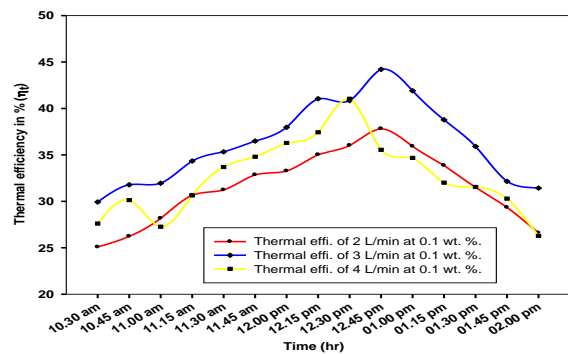
Figure 10. Variation in efficiency with 0.1 wt.% with different flow rates (L/min)
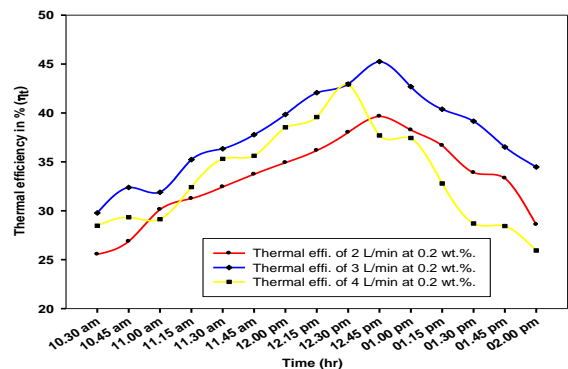
Figure 10A. Variation in efficiency with 0.2 wt.% with different flow rates (L/min)
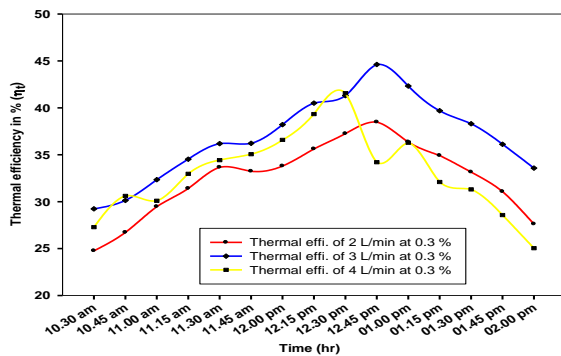
Figure 10B. Variation in efficiency with 0.3 wt.% with different flow rates (L/min)
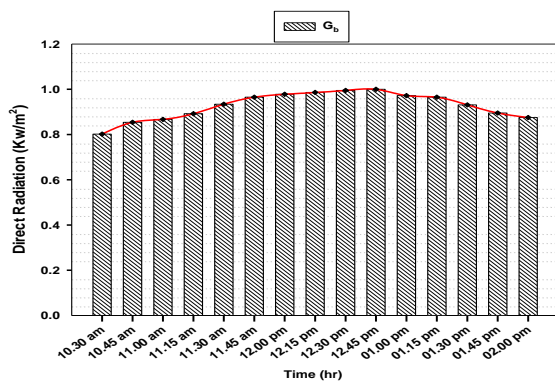
Figure 11. The average value of G_b for 3 L/min with 0.2 wt.%
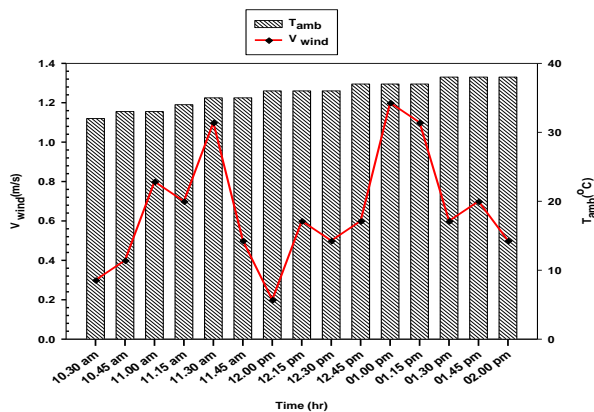
Figure 12. The ambient temperature and wind speed for 3 L/min with 0.2 wt.%

5. CONCLUSION

(i) In the present work, the impact of surfactant on nanofluid stability was experimentally studied and found that for Triton X-100, nanoparticles can be evenly suspended in base fluid for at least 10 days and less than one month. Surfactant is the safest and most environmentally friendly way to obtain nanofluid stability.

(ii) The optimal quantity of Triton X-100 surfactant was also evaluated experimentally, there were three ratios of Triton X-100: MWCNT selected i.e. (i) 0.1:1 (ii) 0.25:1 and (iii) 0.5:1. Based on the stability of the nanoparticles in nanofluid 0.5:1 has been selected, it can make nanoparticles stable for 28 days in the base fluid.

(iii) The effect of mass flow rate and particle weight fraction on the PTC's efficiency is investigated in this study. The results show that using MWCNT nanofluid as a working fluid boosts solar collector efficiency. The optical and heat transfer properties of HTF are improved by suspending nanoparticles in a base fluid with a higher relative surface area.

(iv) The maximum thermal efficiency achieved by MWCNT nanofluid with 3 L/min at 0.2 wt. % is 22 % higher than the base fluid.

(v) The higher concentration of nanoparticles in the base fluid may lead to deterioration of thermal properties and a rise in viscosity value, which would increase the power consumption of the working fluid supply pump.

(vi) Demonstrating that the use of nanofluids makes a solar collector system more compact and efficient at converting available solar energy into various forms of energy for beneficial use. Making a solar collector more compact and using MWCNT/H_2O nanofluid instead of traditional fluid water can make it more cost-effective.

(vii) There are still several stumbling barriers that need to be removed before commercializing the applications of nanofluid, i.e. Cost of mass production, instability, agglomeration, increased pump power, and corrosion.

6. REFERENCES

1. B. Jamil, A.T. Siddiqui, N. Akhtar, "Estimation of solar radiation and Optimum tilt angles for south-facing surfaces in Humid Subtropical Climatic Region of India", *Engineering Science and Technology, an International Journal,* Vol. 19, (2016), 1826-1835. https://doi.org/10.1016/j.jestch.2016.10.004.

2. M.A. Rehan, M. Ali, N.A. Sheikh, M.S. Khalil, G.Q. Chaudhary, T. ur Rashid, M. Shehryar, "Experimental performance analysis of low concentration ratio solar parabolic trough collectors with nanofluids in winter conditions", *Renewable Energy* 118, (2018), 742-751. https://doi.org/10.1016/j.renene.2017.11.062.

3. K. Chaudhari, P. Walke, U. Wankhede, R. Shelke, "An Experimental Investigation of a Nanofluid (Al₂O₃+H2O) Based Parabolic Trough Solar Collectors", *British Journal of Applied Science & Technology* Vol. 9, (2015), 551-557. https://doi.org/10.9734/bjast/2015/11946.

4. K. Sunil, L.A.L. Kundan, S. Sumeet, "Performance Evaluation of a Nanofluid Based Parabolic Solar Collector–an Experimental Study", Proc. Twelveth IRF International Conference 31st August 2014, Chennai, India, ISBN 978-93-84209-48-3. (2014) 29-35.

5.   S. Ebrazeh, M. Sheikholeslami, "Applications of nanomaterial for Parabolic trough collector", *Powder Technology* 375, (2020), 472-492. https://doi.org/10.1016/j.powtec.2020.08.005.

6.   S. K. Verma, A. K. Tiwari, D.S. Chauhan, "Experimental evaluation of flat plate solar collector using nanofluids", *Energy Conversion and Management* Vol. 134, (2017), 103-115. https://doi.org/10.1016/j.enconman.2016.12.037.

7.   S.K. Verma, A.K. Tiwari, D.S. Chauhan, "Performance augmentation in flat plate solar collectorusing MgO/water nanofluid", *Energy Conversion and. Management* 124, (2016), 607-617. j.enconman.2016.07.007.

8.   T. Yousefi, F. Veisy, E. Shojaeizadeh, S. Zinadini, "An experimental investigation on the effect of MWCNT-H_2O nanofluid on the efficiency of flat-plate solar collectors", *Experimental Thermal and Fluid Science*, Vol. 39, (2012), 207-212. https://doi.org/10.1016/j.expthermflusci.2012.01.025.

9.   R. Rastogi, R. Kaushal, S.K. Tripathi, A.L. Sharma, I. Kaur, L.M. Bharadwaj, "Comparative study of carbon nanotube dispersion using surfactants", *Journal of Colloid and Interface Sience,* Vol. 328, (2008), 421-428. https://doi.org/10.1016/j.jcis.2008.09.015.

10. R.S. Mishra, H. Singh, "Comparative study of parabolic trough collector through MWCNT/ H_2O nanofluid and water", *International Journal of Research in Engineering and Innovation,* (2017), 64-70.

11. S. S. Bernard, G. Suresh, M. D. J. Ahmed, G. Mageshwaran, V. Madanagopal, J. Karthikeyan, "Performance analysis of MWCNT fluid parabolic trough collector for whole year", *Materials Today: Proceedings* Vol. 45, (2021), 1308-1311. https://doi.org/10.1016/j.matpr.2020.05.289.

12. A.A. Hachicha, Z. Said, S.M.A. Rahman, E. Al- Sarairah, "On the thermal and thermodynamic analysis of parabolic trough collector technology using industrial-grade MWCNT based nanofluid", *Renewable Energy,* Vol. 161, (2020), 1303-1317. https://doi.org/10.1016/j.matpr.2020.05.289

13. K. Khanafer, K. Vafai, "A review on the applications of nanofluids in solar energy field", *Renewable Energy* 123, (2018), 398-406. https://doi.org/10.1016/j.renene.2018.01.097.

14. A. Borode, N. Ahmed, P. Olubambi, "A review of solar collectors using carbon–based nanofluids", *Journal of Cleaner Production,* Vol. 241, (2019), 118311. https://doi.org/10.1016/j.jclepro.2019.118311.

15. A.K.Hussein, "Applications of nanotechnology to improve the performance of solar collectors- Recent advances and overview", *Renewable and Sustainable Energy Reviews* 62, (2016), 767-792. https://doi.org/10.1016/j.rser.2016.04.050.

16. H. Olia, M. Torabi, M. Bahiraei, M.H. Ahmadi, M. Goodarzi, M.R. Safaei, "Application of nanofluids in thermal performance Enhancement of parabolic trough solar collector: State-of-the-art", *Applied Sciences* 9, (2019). https://doi.org/10.3390/app9030463.

17. Adnano Technologies India, "MWCNT Nanopowder", Available at: https://ad-nanotech.com/, accessed on 13/10/2020, (2020).

18. A.O. Borode, N.A. Ahmed, P.A. Olubambi, "Surfactant–aided dispersion of carbon nanomaterials in aqueous solution", *Physics of Fluids,* Vol. 31, No. 7, (2019), 071301. https://doi.org/10.1063/1.5105380.

19. Kalogirou S. "Solar energy engineering: processes and systems". USA: Academic Press; 2009.

20. S.O. Mirabootalebi, G.H. Akbari, R.M. Babaheydari, "Mass Production and Growth Mechanism of Carbon Nanotubes in Optimized Mechanothermal Method" *International Journal of Engineering, Transactions A: Basics*, 34, (2021), 2332-2340. https://doi: 10.5829/ije.2021.34.10a.14.

21. M.V. Bindu, G.M. Joselin Herbert, "A review on application of nanomaterials in heat transfer fluid for parabolic trough concentrator", *Materials Today Proceedings,* Vol. 46, (2021), 7651-7660. https://doi.org/10.1016/j.matpr.2021.01.957.

Persian Abstract

چکیده

سیستم های حرارتی خورشیدی برای گرمایش دارای قابلیت اطمینان بالایی هستند. استفاده از کولکتورهای سهمی (PTC) برای کاربردهای داخلی هنوز کاملاً محدود است. علاوه بر این ، استفاده تجاری از نانوسیالات در این برنامه ها نادر است. تاثیر نانوسیال MWCNT به عنوان یک سیال انتقال حرارت بر بازده یک کولکتور سهموی محلی توسعه یافته به صورت تجربی مورد بررسی قرار گرفت. تأثیر سورفاکتانت بر پایداری نانوسیالات نیز مورد بررسی قرار گرفت و مشخص شد که نانوذرات را می توان با استفاده از تریتون X-100 به مدت ۱۰ روز و کمتر از یک ماه به طور همگن در مایع پایه معلق کرد. آزمایشاتی نیز برای تعیین مقدار بهینه سورفکتانت تریتون X-100 انجام شد. می توان نانوذرات را به مدت ۲۸ روز در سیال پایه با نسبت Triton X-100 به MWCNT 0.5: 1 پایدار کرد. در سرعت جریان ۲.۰ ، ۳.۰ و ۴.۰ لیتر در دقیقه ، MWCNT/H2O در سه غلظت های ذره ای ۰.۱ درصد ، ۰.۲ درصد و ۰.۳ درصد وزنی استفاده می شود. این آزمایش در شرایط عملیاتی در فضای باز انجام می شود. با ۳ لیتر در دقیقه در ۰.۲ وزنی. ٪ ، نانوسیال MWCNT حداکثر بازده حرارتی را بدست می آورد که ۲۲ درصد بیشتر از آب است. یافته ها اطلاعات مهمی در مورد تجاری سازی PTC توسعه یافته محلی ارائه می دهد.

International Journal of Engineering

A Genetic Algorithm Based on Optimization for Doubly Fed Induction Generator

A. Guediri*, A. Guediri, S. Touil

University of El Oued, VTRS Laboratory, Fac. Technology, El Oued, Algeria

PAPER INFO

ABSTRACT

In this paper, we will be interested in studying a system consisting of a wind turbine operating at variable wind speed, and a two-feed asynchronous machine (DFIG) connected to the grid by the stator and fed by a transducer at the side of the rotor. The conductors are separately controlled for active and reactive power flow between the stator (DFIG) and the grid. The proposed controllers generate reference voltages for the rotor to ensure that the active and reactive power reaches the required reference values, to ensure effective tracking of the optimum operating point and obtaining the maximum electrical power output. Dynamic analysis of the system is performed under the variable wind speed. This analysis is based on active and reactive energy control. The new work in this paper is to introduce theories of genetic algorithms into the control strategy used in the switching chain of wind turbines, to improve performance and efficiency. Simulation results applied to genetic algorithms give greater efficiency, impressive results, and stability to wind turbine systems compared to classic PI regulators. Then, artificial intelligent controls, such as genetic algorithms control, are applied. Results obtained, in Matlab/Simulink environment, show the efficiency of this proposed unit.

doi: 10.5829/ije.2022.35.01a.11

NOMENCLATURE

θ_{sl}	Angle between the phase axis of the first stator winding and the rotor axis (rad)	Caer-estimated	Estimated aerodynamic torque (N.m)
θ_s	Angle between the axis of the first phase of the stator winding and the d axis (rad)	Qs-ref	The reactive power at the reference stator (VAR)
θ_r	Angle between the axis of the first phase of the rotor and the d axis (rad)	Ps-ref	The active power at the reference stator (W)
w_s	Electric stator pulse (rad/s)	Qs-meas	The reactive power at the measured stator (VAR)
Caer	Wind turbine aerodynamic torque (N.m)	Ps-meas	The active power at the measured stator (W)
Cp	Wind turbine power coefficient	Cem-ref	Electromagnetic torque reference (N.m)
$\Omega_{turbine\_estimated}$	Estimated mechanical speed of the turbine (rad/s)	Vestimated	Estimated wind speed (m/s)
B(BITA)	Turbine blade pitch angle (rad)	λ	Relative wind speed (m/s)
g	Slip	S	Area swept by the wind turbine rotor (m2)
Ω_{mec}	Mechanical speed (rad/s)	PL	Active line power (W)
R	Turbine radius (m)	QL	Line reactive power (VAR)
Vdc	DC bus voltage (V)	Tt	The turbine torque (N.m)
λ_{opt}	Optimal speed ratio (m/s)	fr	Rotor feed frequency (Hz)
G	Multiplier gain	**Greek Symbols**	
wr	Electric rotor pulsation (rad/s)	ρ	Air density at 15 ° C (kg/m³)
Ird , Irq	Rotor current along the d axis, q (A)	**Abbreviations**	
φ_s	stator flux (Wb)	MPPT	Maximum Power Point Tracking
Ps	Active stator power (W)	DFIG	Doubly-fed induction generator
Q_s	Reactive stator power (VAR)	PWM	Acronyme Pulse with modulation
Sr	Apparent rotor power (VA)	RSC	Rotor side converter

*Corresponding Author Email: abdelhafid-guediri@univ-eloued.dz (A. Guediri)

Cem	Electromagnetic torque (N.m)	LSC	Line side converter
Ss	Apparent stator power (VA)	PI	Proportional Integral
wt	Turbine speed (rad/s)	ref	Index indicating the reference (the setpoint)
Pr	Active rotor power (W)	DC/AC	Direct Current/Alternative Current
Qr	Reactive rotor power (VAR)	THD	Total Harmonic Distortion
Vs	Stator voltage vector (V)	GA	Genetic algorithm

1. INTRODUCTION

Wind energy is one of the most promising sources of renewable energies in the world, and this is mainly due to the reduction of environmental pollution resulting from classical power plants, as well as the dependence on fossil fuels with limited reserves [1]. Electric power generated from wind power plants is the fastest developing and most promising renewable energy source. The environmental degradation of air is one of the major problems that prompted authorities around the world to take a set of measures to reduce emissions of pollutants. To adapt to these new restrictions, environmentally friendly energy such as wind energy has been promoted, as many wind plants have been established in the world and are the only inexpensive and capable of mass production.

The optimization procedure is a technique of great importance for dealing with decision-making problems. It has grown significantly with the great development of computer systems technologies in terms of processing capacity and speed [2]. In fact, optimization seeks to improve performance by approaching one (or more) ideal point among many possible points or solutions based on criteria dictated by the specifications of the systems considered. It is one of the most important branches of modern applied mathematics, and a lot of practical and theoretical research has been devoted to it. Parvane et al. [3] investigated on theory includes the quantitative study of optimzation methods by genetic algorithm. The solution to an optimization problem involves exploring the search space in order to maximize (or reduce) a particular function. The relative complexities (in size or structure) of the search space and functionality to be optimized lead to the use of radically different accuracy methods [4]. Optimization methods can be categorized in different ways; Deterministic and non-deterministic methods (also called stochastic or stochastic research methods), the choice of this or that method depends on the system to be studied and its complexity [5]. Deterministic methods are characterized by their simplicity and speed. They used in the case when the system to be improved has a simple structure. But the main drawback of these methods is that this simplicity decreases as the number of variables to be optimized increases and the system becomes complex.

Under these conditions, the solution can converge towards local solutions [6]. While stochastic methods are more efficient and effective methods, they use stochastic processes based on stochastic exploration of the space of possible solutions [7]. Among the latter, we found the genetic algorithm, which represents a rather rich and interesting family of stochastic optimization algorithms. It was inspired by the concepts of evolution and natural selection. Thanks to probabilistic research based on the mechanism of natural selection and genetics, genetic algorithms are highly effective and powerful in a general set of problems. The genetic algorithm maintains a set of encoded solutions, and guides this set towards the optimal solution [8]. In fact, to find an optimal solution to a problem in a complex space, it is necessary to find a compromise between two goals: exploring better solutions and powerful exploitation of the search space. Analytical studies have shown that genetic algorithms optimally manage this trade-off [9]. This article aims to present the theoretical foundations of genetic algorithms. Next, we will discuss their request to improve the parameters of the two regulators that were previously used for DFIG speed modulation.

The main contribution of this paper has been summarized as follows:

- Study of a system consisting of a variable wind speed wind turbine and an asynchronous du-al-feed machine (DFIG) connected to the grid by a stator and fed by a transducer.
- The response of the system was verified by applying the proposed regulator in terms of its effectiveness towards the active and reactive power.
- Improvement in the results obtained through previous published works, in terms of response time, accuracy, low error, and stability.

2. MAXIMIZATION OF POWER WITHOUT SPEED CONTROL

The control model is based on the assumption that the wind speed is slightly different at a steady state. In this case, we get [10]:

$$C_{aer} = C_p \frac{1}{2} \rho S \frac{1}{\Omega_{turbine\_estimated}} v^3_{estimated} \tag{1}$$

With:

$$v_{estimated} = \frac{\Omega_{turbine\_estimated} \cdot R}{\lambda} \tag{2}$$

where w_t represents the rotational speed of the wind turbine. Figure 1 Shows a typical relationship between

the power coefficient *Cp* and the tip-speed ratio. It should be noted that there is a value of λ to ensure a maximum of *Cp*. Thus, it can be stated that, for a specified wind velocity, there is a turbine rotational speed value that allows capturing the maximum mechanical power attainable from the wind, and this is, precisely, the turbine speed to be followed [11].

We set the speed ratio to the value $\lambda_{Cp\,max}$ which corresponds to the maximum power factor $C_{p\,max}$ and by adding the above equations, we will obtain the reference torque that is directly proportional to the square of the generator speed [12].

$$C_{em\_ref} = \frac{\rho \pi R^5}{2G^3} \frac{C_p}{\lambda^3_{C_{p\,max}}} \Omega^2_{mec} \tag{3}$$

Figure 2 represents the diagram and the model of maximization of the power extracted without speed control.

By neglecting losses of electrical origin, the electrical power becomes equal to the electromagnetic power defined by $(\Omega_{mec}.C_{em})$. This power (reference power) will be counted negatively because it is opposed to the aerodynamic power to respect the receiver convention of the assembly [13]. When these two powers are equal, the wind turbine rotates at a constant speed.
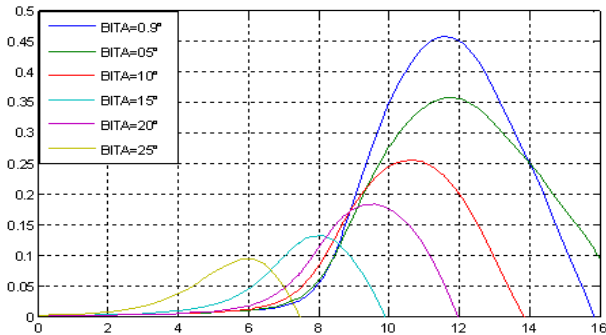
Figure 1. Typical power coefficient versus tip-speed-ratio curve
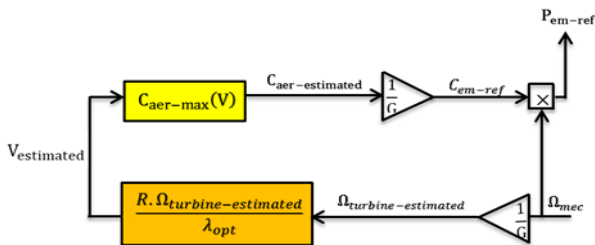
Figure 2. Power maximization block diagram extracted without speed control
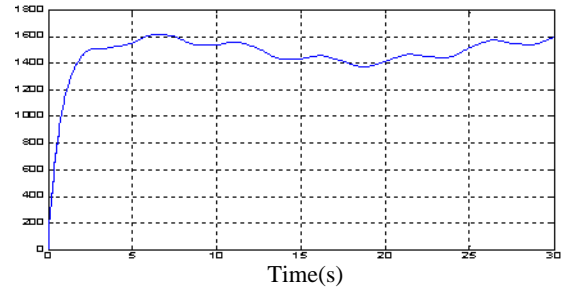
Figure 3. Mechanical speed (tr/min)
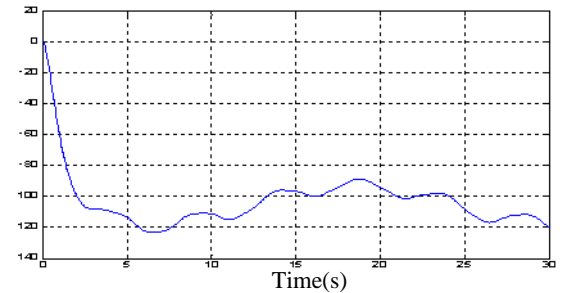
Figure 4. Electric power (N.m)

3. ACTIVE AND REACTIVE POWER CONTROL OF DFIG

The active and reactive power at grid terminals or the voltage is controlled by the reactive current flowing in the rotor converter. When the wind turbine is operated in vary regulation mode the reactive power at grid terminals is kept constant by a vary regulator. The output of the voltage regulator or varied regulator is the referenced-axis current that must be injected into the rotor by the rotor converter. The same current regulator as for the power control is used to regulate the actual direct rotor current of positive-sequence current to its reference value [14].
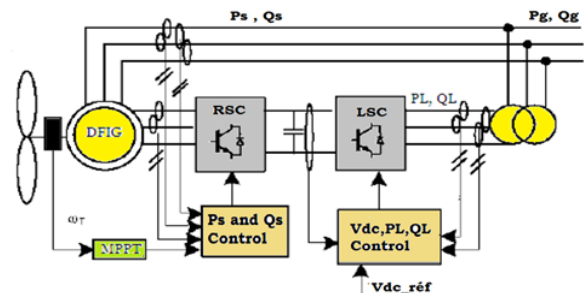
Figure 5. Powers exchange between DFIG, Converters and grid

The rotor side converter ensures a decoupled active and reactive stator power control, Ps and Qs, according to the reference torque delivered by the Maximum Power Point Tracking control (MPPT). The grid side converter controls the power flow exchange with the grid via the rotor, by maintaining the DC bus at a constant voltage level and by imposing the reactive power [15]. The active and reactive power control equations are given below [16]:

$$\begin{aligned} S_s &= P_s + jQ_s \\ S_r &= P_r + jQ_r \end{aligned} \tag{4}$$

The active and reactive forces are shown using the following equations [17]:

$$\begin{cases} Ps = -\bar{V}_s \frac{M}{L_s}.I_{rq} \\ Q_s = \frac{V_s.\varphi_s}{L_s} - \frac{V_sM}{L_s}I_{rd} \\ P_r = gV_s\frac{M}{L_s}.I_{rq} \\ Q_r = gV_s\frac{M}{L_s}.I_{rd} \end{cases} \tag{5}$$

4. ARITHMETIC CROSSING (BARYCENTRIC)

This technique was developed by "Michalewicz". For this type of crossing, we choose exchange positions randomly, then arithmetic means weighted by a coefficient a. When this operation is applied to two parents C_1 (i) and C_2 (i), two children (offspring) E_1 (i) and E_2 (i) are generated, such as [18]:

$$\begin{aligned} E_1(i) &= a\,C_1(i) + (1-a)C_2(i) \\ E_2(i) &= (1-a)C_1(i) + aC_2(i) \end{aligned} \tag{6}$$

In the case of a uniform arithmetic crossing, the value of a is a constant chosen by the user, on the other hand, if the value of a is generated randomly in the interval of [-0.5; 1.5], then we are in the case of a non-uniform arithmetic crossing. The following figure illustrates an example of the application of this type of crossing [19]: According to this figure, the two new third genes were born by:

$$\begin{cases} E_1^3(i) = a\,C_1^3 + (1-a)C_2^3 \\ E_2^3(i) = (1-a)C_1^3 + aC_2^3 \end{cases} \tag{7}$$

5. UNIFORM MUTATION

For each gene that mutates, we take two numbers τ and r. The first can take the values +1 for a positive change and -1 for a negative change. The second is a generated number randomly in the interval [0 1]. It determines the magnitude of the change. In these conditions, the gene C_i ′ which replaces the mutated gene C_i is calculated from one of the two following relationships [20]:

$$\begin{cases} C_i' = C_i + (C_{max} - C_i)\left(1 - r^{\left(1-\frac{G_F}{G_T}\right)^5}\right) & if\ \tau = +1 \\ C_i' = C_i - (C_i - C_{min})\left(1 - r^{\left(1-\frac{G_F}{G_T}\right)^5}\right) & if\ \tau = -1 \end{cases} \tag{8}$$

here C_{max}, C_{min} denote the lower and higher limits of the price of the parameter C_i, respectively; and $G_F \leq G_T$ represents the era for which the amplitude of the mutation cancels out.

6. OPTIMIZATION PROCEDURE FOR THE TWO REGULATORS

The optimization method is a hybrid algorithm that consists of a genetic set of rules blended with a local search method (Gradient or Simplex) and which acts at the parameters of the regulator [21]. The following Figure illustrates the diagram of this method.

The procedure for optimizing regulator parameters summarized by using the following steps [22]:

- An initial offspring was born randomly.
- Evaluate this offspring.
- Apply genetic operators (selection, crossing, mutation).
- Evaluate the sort of the new offspring created through genetic operators.
- Repeat the process for a given variety of offsprings.
- Choose the best character from the new offspring.
- Use a nearby seek approach (gradient or simplex) to finalize the optimization operation achieved by using the genetic algorithm.

Figure 6. The arithmetic crossover
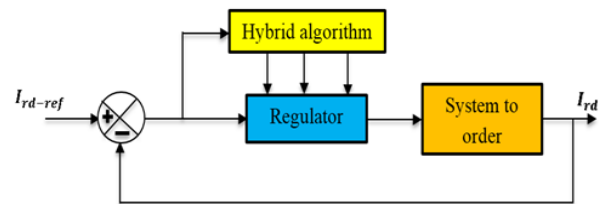
Figure 7. Principle of optimization using a genetic gradient or simplex algorithm

7. OPTIMIZATION OF THE CLASSIC PI REGULATOR

The optimization of this regulator is executed with the aid of a hybrid genetic set of the simplex rules by using the method of ″Gatool″ window which has been evolved by Matlab. Here are the parameters of the algorithm used [23]:

- Size of the offspring T = 20
- Selection using roulette.
- Multiple crossing with a chance $pc = 0.8$.
- Uniform mutation with opportunity $pm = 0.01$.
- Number of offspring N = 49.
- Hybridization technique: simplex.

8. SIMULATION RESULTS

To be able to show the usefulness of the optimization of classical PI gains through the genetic algorithm mixed with the simplex method, we executed out the same simulation steps supplied in this paper. From the simulation results obtained, we can observe the improvement in dynamic overall performance. The consequences of the simulation mentioned in the genetic algorithm manipulating the wind electric machine depend mainly on DFIG to supply the grid with electricity in Figure 8; where we observed a marked improvement on the dynamic level compared to the PI regulators:

Figure 9 represents the evolution of the continuous vector voltage, which shows the following:

- The DC bus voltage reaches the set point, which is 514.6 V in a shorter response time, with no overshoot.
- The shape of the DC vector voltage is smoother, which has the advantage of changing the wind speed.
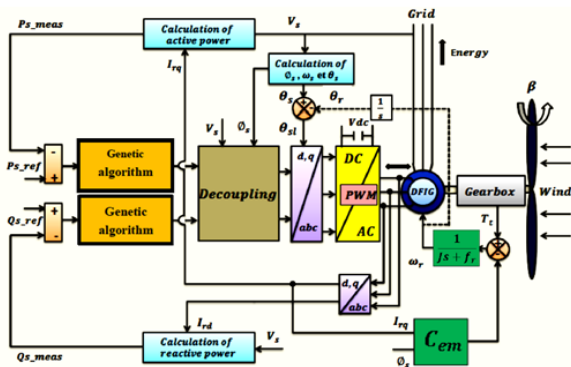
Figure 8. Global block diagram of the command of the genetic algorithm based on DFIG
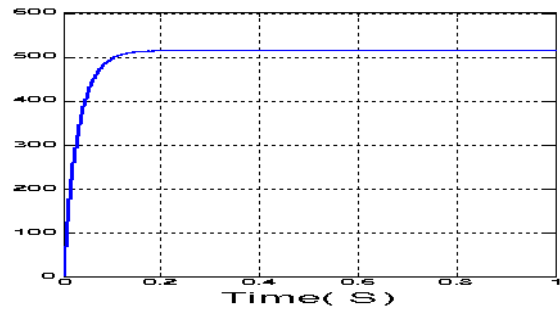
Figure 9. DC bus voltage (V)

For the robustness tests of the control by genetic algorithm regulator, we studied the influence of the variation of the rotor resistance, own inductance and mutual on the performance of the control. The simulation results of our wind power system (Turbine + DFIG) controlled by genetic algorithm regulator.

The starting is no-load then a reference active power is applied:

- Between t = 0.2s and t = 0.6 s negative scale (Pref = -20000W).
- Between t = 0.6s and t = 1s (Pref = - 10000W);

Reactive power: between t = 0 s and t = 1 s step (Qref = 0 var).

The figures below show the performance of the reactive and active stator power PI- genetic algorithm control applied to the DFIG.

Figures10 and 11 illustrate the responses of the system with the genetic algorithm controller. In general, it can be seen that the power steps are followed by the generator for both active and reactive power. However, we observe that the effect of the coupling appears on one of the two powers when changing the setpoint of the other power.

We can demonstrate the performance of these regulator in both transient and steady state using the following criteria:

- Maximum error (overshoot).
- The recovery or stabilization time (the response time).
- The residual error (the static error).

The forward and quadratic components of the rotor current are shown in Figure 12 illustrate the control error of ird and irq. From these curves, we see that: - PI regulator maintain rotor currents at their respective references imposed by stator voltage regulation; - a reduction in the load induces a reduction in the rotor current; - the error in checking ird and irq is practically zero. The result obtained are illustrated in Figure 13 shows that the electromagnetic coulpe perfectly followed its benchmark with good dynamic performance, less oscillation and overshoot.

Moreover, the result in Figures 14 and15 illustrate the simulation results of the stator currents along the d and q axis and the three-phase stator currents generated by al DFIG are proportional to the active power supplied. The waveform of the current is almost sinusoidal for both stator current, which means good quality of power supplied to the grid. Figures 16 and 17 illustrate the simulation results of the stator current voltages at the terminals of the DFIG and the control voltages of the rotor, the latter were obtained by a voltage inverter controlled by the genetic algorithm and which uses MLI technique. This approach shows the waveform of the stator voltage and current. We can notice that the stator voltage is equal to that of the grid, while the waveform of the current is related to that of the active power and the reactive power.

The genetic algorithm regulator do not generate any overshoot, particularly at transient. For the other
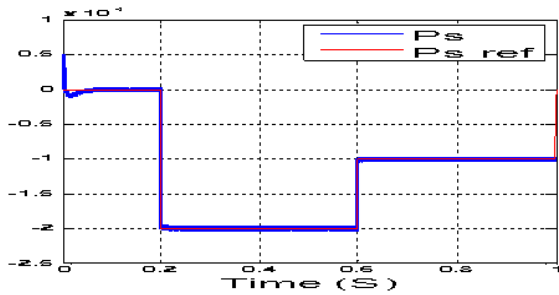
Figure 10. Active power stator (W)
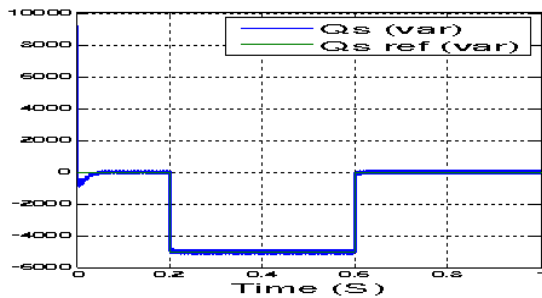
Figure 11. Reactive power stator (VAR)
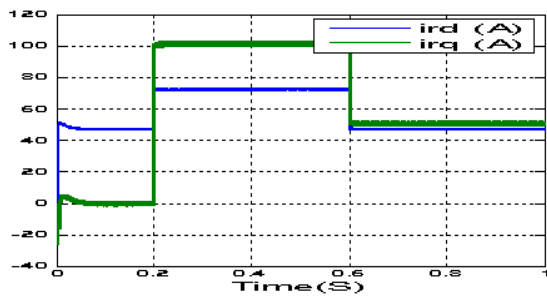
Figure 12. Direct currents and rotor quadrature(A)
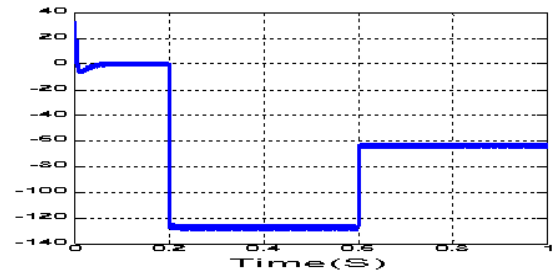
Figure 13. Electromagnetic torque (N.m)
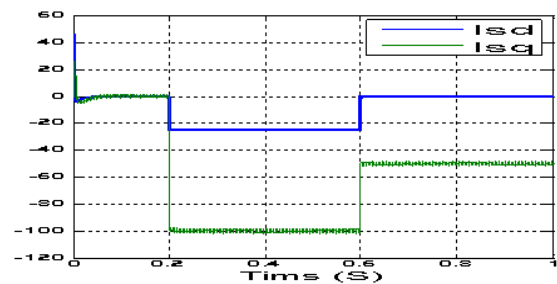
Figure 14. Direct currents and stator quadrature(A)
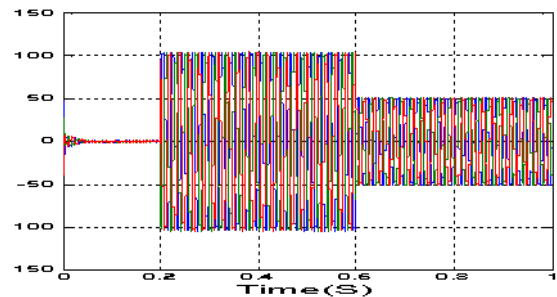
Figure 15. Rotary three-phase current (A)
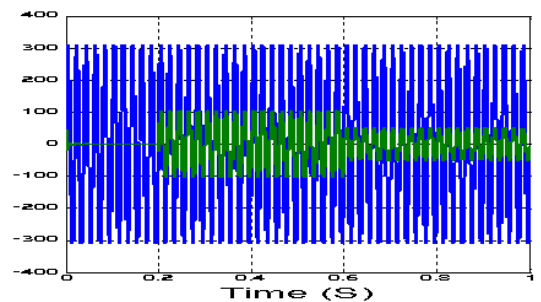
Figure 16. The stator current and voltage (V)

performances, they are almost similar to that of the PI regulator.

The regulation by genetic algorithm control shows excellence through the effective rejection of the effects of the disturbances from which the authorities trace their references completely.
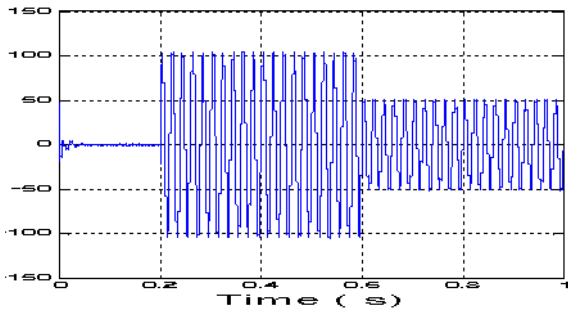
Figure 17. The stator current (A)

9.   COMPARE   SEARCH   RESULTS   WITH GRAPHICALLY RELEVANT REFERENCES

In order to measure the performance of the synthesized genetic algorithm controller and compare them with those of the conventional regulator, evaluation criteria must be defined . These criteria must take into account both the maximum amplitude of the regulator error and the time required for the system to return to the setpoint after a disturbance or to reach a new reference.

Tuning by genetic algorithm may override tuning by (PI) with respect to the quality of the dynamic response of the system. Indeed, the latter further reduces the response time by producing a limited overshoot accompanied by weak oscillations around the setpoint in steady state, the precision is not as good as that of a regulator (PI) where the integral action eliminates the static error, this then suggests the combination of the two types of regulators .

- A genetic algorithm regulator: for the transient regime.
- A regulator (PI): for the steady state.

The major drawback of genetic algorithms regulators is the matching of gains ensuring system stability. In addition, the order is calculated only from the two values: the error and the variation of the error.

The genetic algorithm applied in this article has been proven to be very effective compared to the results published in Indonesia Journal of Electrical Engineering and Computer Science under the title Optimization of PI Controller Using Genetic Algorithm for Wind Turbine Application as well as in the International Journal of System Assurance engineering and Management under the title of fuzzy modeling and control of a wind power system based on a dual-feed asynchronous machine to supply power to the electric grid. The following points are stated as:

- Response time
- Precision
- The error
- Quality
- Stability

- Exceeding
- Total Harmonic Distortion (THD)
- Sinusoidal.
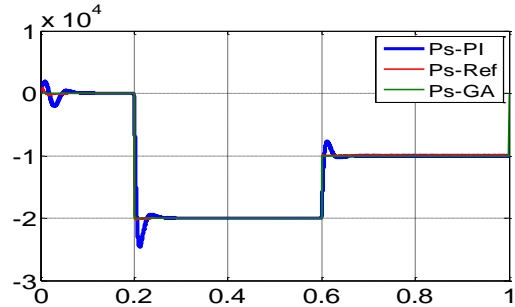
Figure 18. Active power stator (W)
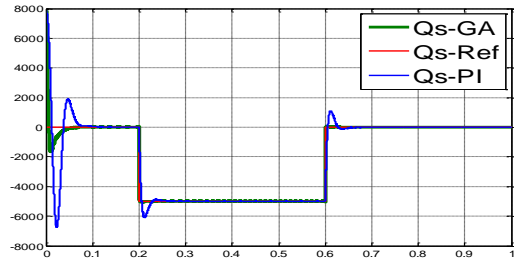
Figure 19. Reactive power stator (VAR)
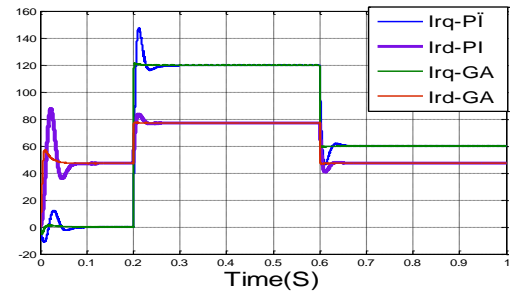
Figure 20. Direct currents and rotor quadrature(A)
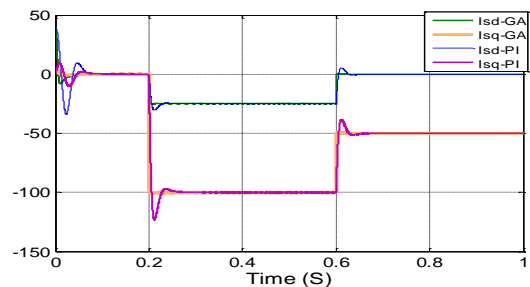
Figure 21. Direct currents and stator quadrature(A)

10. CONCLUSION

In this paper, we proposed a fuzzy logic controller and an active and reactive gene algorithm connected to a stator network (DFIG). Genetic algorithm efficacy tested under different operating conditions, demonstrating optimization and efficiency in terms of duns against changing rotor resistance, insensitivity to torque disturbance, re-reducing response time, accuracy, speed or overtaking, large overrun reduction at start-up, and avoiding peak activity power, reduced power ripples and improved THD, as well as faster dynamics with little stability error in all dynamic operating conditions. The simulation results showed good control behavior oriented towards better performance of the proposed controller.

11. APPENDIX

TABLE 1. Parameters of 1.5 MW DFIG

Symbol	Parameters	Value
R	Blade radius	35.25m
N	Number of blades	3
G	Gearbox ratio	90
J	Moment of inertia	1000 Kg.m^2
fv	Viscous friction coefficient	0.0024 N.m.s^{-1}
V	Nominal wind speed	16 m/s
Vd	Cut-in wind speed	4 m/s
Vm	Cut-out wind speed	25 m/s

TABLE 2. Parameters of Turbine

Symbol	Parameters	Value
Pn	Rated Power	1.5 MW
Vs	Stator Voltage	300 V
Fs	Stator Frequency	50 Hz
Rs	Stator Resistance	0.012 Ω
Ls	Stator Leakage Inductance	0.0205H
Rr	Rotor Resistance	0.021Ω
Lr	Rotor Leakage Inductance	0.0204H
M	Mutual Inductance	0.0169H
P	Pairs of poles number	2
J	Rotor inertia	1000 Kg.m^2

12. REFERENCES

1. Sockeel, N., Shi, J., Shahverdi, M. and Mazzola, M., "Sensitivity analysis of the battery model for model predictive control implemented into a plug-in hybrid electric vehicle", in Transportation Electrification Conference and Expo (ITEC), 2017 IEEE, (2017), 493-500, doi: 10.1109/ITEC.2017.7993320

2. Suthar, B. and Patel, A., "Design optimization of axial flux surface mounted permanent magnet brushless dc motor for electrical vehicle based on genetic algorithm'', *International Journal of Engineering, Transactions A Basics*, Vol. 31, No. 7, (2018), 1050-1056, doi: 10.5829/ije.2018.31.07a.07

3. Parvane, M., Rahimi, E. and Jafarinejad, F., "Optimization of quantum cellular automata circuits by genetic algorithm", *International Journal of Engineering, Transactions B Applications*, Vol. 33, No. 2, (2020), 229-236, doi: 10.5829/IJE.2020.33.02B.07

4. Guediri, A.K., Ben Attous, D. "Modeling and fuzzy control of a wind energy system based on double-fed asynchronous machine for supply of power to the electrical network". *International Journal of System Assurance Engineering and Management*. Vol. 8, No. 1, (2017), 353-360. doi :10.1007/s13198-015-0367-1

5. Mohammed Taoussi, Mohammed Karim, Dalila Hammoumi, Chakib El Bekkali, Badre Bossoufi, Najib El Ouanjli. "Comparative study between backstepping adaptive and fieldoriented control of the DFIG applied to wind turbines", International Conference on Advanced Technologies for Signal and Image Processing (ATSIP), 2017, doi: 10.1109/ATSIP.2017.8075592

6. Yamina Belgaid, M'hamed Helaimi, Rachid Taleb, Mohammed Benali Youcef " Optimal tuning of PI controller using genetic algorithm for wind turbine application ", *Indonesian Journal of Electrical Engineering and Computer Science* Vol. 18, No. 1, (2020), 167-178, doi:10.11591/ijeecs.v18.i1.

7. Azari, M.N., Samami, M. and Pahnehkolaei, S.A., "Optimal design of a brushless dc motor, by cuckoo optimization algorithm (research note)", *International Journal of Engineering-Transactions B: Applications*, Vol. 30, No. 5, (2017), 668-677, doi: 10.5829/idosi.ije.2017.30.05b.06

8. Patel, A. N., and B. N. Suthar. "Design optimization of axial flux surface mounted permanent magnet brushless dc motor for electrical vehicle based on genetic algorithm." *International Journal of Engineering, Transactions A Basics*, Vol. 31, No. 7 (2018), 1050-1056. doi: 10.5829/ije.2018.31.07a.07

9. Hai-Hui Huang, Yong Liang. "An integrative analysis system of gene expression using self-paced learning and SCAD-Net", *Expert Systems with Applications*, Vol. 135, (2019), 102-112. doi: 10.1016/J.ESWA.2019.06.016

10. Siraj K, Siraj H, and Nasir M, "Modeling and control of a doubly fed induction generator for grid integrated wind turbine," 16th International Power Electronics and Motion Control Conference and Exposition, (2014), 901-906, doi: 10.1109/EPEPEMC.2014.6980613

11. Kharoubi, S. and El Menzhi, L. Wind turbine doubly-fed induction generator defects diagnosis using rotor currents lissajous curves. *International Journal of Power Electronics and Drive Systems*, Vol. 11, No. 4, (2020), 2083. doi: 10.11591/ijpeds.v11.i4.pp2083-2090

12. K. S. Al-Najdi and J. Mantere, "Localized rotor overheating of large Direct on Line (DOL) motors," Petroleum and Chemical Industry ConferenceEurope, (2014), 1-11. doi: 10.1109/PCICEurope.2014.6900055

13. S. Gao, H. Zhao, Y. Gui, D. Zhou and F. Blaabjerg, "An Improved Direct Power Control for Doubly Fed Induction Generator," in *IEEE Transactions on Power Electronics*, vol. 36, No. 4, (2021), 4672-4685, doi: 10.1109/TPEL.2020.3024620.

14. Karad, Shivaji, and Ritula Thakur. "Recent trends of control strategies for doubly fed induction generator-based wind turbine systems: A comparative review." *Archives of Computational Methods in Engineering* 28.1 (2021), 15-29, doi:10.1007/s11831-019-09367-3

15. Hala Alami Aroussi, ElMostafa Ziani, Manale Bouderbala, Badre Bossoufi. "Elaborated Direct Power Control Applied to Wind Power System under Variable Speed", 7th International Renewable and Sustainable Energy Conference (IRSEC), (2019). doi: 10.1109/IRSEC48032.2019.9078307

16. Abdoune, Fateh, Djamal Aouzellag, and Kaci Ghedamsi. "Terminal voltage build-up and control of a DFIG based stand-alone wind energy conversion system." *Renewable Energy* 97 (2016), 468-480, doi: 10.1016/j.renene.2016.06.005

17. Han, Yang. "Reactive power capabilities of DFIG-based wind park for low-voltage ride through (LVRT) performance", International Conference on Quality Reliability Risk Maintenance and Safety Engineering (QR2MSE), (2013), doi: 10.1109/QR2MSE.2013.6625971

18. Huang Hai Hui, LiangYong "An integrative analysis system of gene expression using self-paced learning and SCAD-Net", *Expert Systems with Applications,* Vol. 135, (2019), 102-112, doi: 10.1016/J.ESWA.2019.06.016

19. N. Jabbour, E. Tsioumas, C. Mademlis and E. Solomin, "A Highly Effective Fault-Ride-Through Strategy for a Wind Energy Conversion System with a Doubly Fed Induction Generator," in *IEEE Transactions on Power Electronics*, Vol. 35, No. 8, (2020), 8154-8164, doi: 10.1109/TPEL.2020.2967971.

20. Delima, Allemar Jhone P., Ariel M. Sison, and Ruji P. Medina, "A Modified Genetic Algorithm with a New Crossover Mating Scheme," *Indonesian Journal of Electrical engineering and informatics*, Vol. 7, (2019), 165-181, doi: 10.11591/ijeei.v7i2.1047

21. Tan, A., Tang, Z., Sun, X. et al. Genetic Algorithm-Based Analysis of the Effects of an Additional Damping Controller for a Doubly Fed Induction Generator. *Journal of Electrical Engineering & Technology,* Vol. 15, No. 4, (2020), 1585-1593, doi :10.1007/s42835-020-00440-7

22. U. Javed, M. A. Arshad, M. Jawad, N. Shabbir, L. Kütt and A. Rassõlkin, "Active and Reactive Power Control of DFIG using Optimized Fractional Order-PI Controller,"2021IEEE International Power Electronics and Motion Control Conference (PEMC), (2021), 398-404, doi: 10.1109/PEMC48073.2021.9432608.

23. Spiegel, Jacob O., and Jacob D. Durrant. "AutoGrow4: an open-source genetic algorithm for de novo drug design and lead optimization." *Journal of Cheminformatics* 12.1 (2020), 1-16, doi: 10.1186/s13321-020-00429-4

Persian Abstract

چکیده

در این مقاله ، ما به مطالعه یک سیستم متشکل از یک توربین بادی با سرعت متغیر باد و یک ماشین ناهمزمان دو تغذیه (DFIG) علاقه مند خواهیم بود که توسط استاتور به شبکه متصل شده و توسط یک مبدل در کنار آن تغذیه می شود. روتور هادی ها به طور جداگانه برای جریان قدرت فعال و راکتیو بین استاتور (DFIG) و شبکه کنترل می شوند. کنترل کننده های پیشنهادی ولتاژهای مرجع را برای روتور ایجاد می کنند تا اطمینان حاصل شود که قدرت فعال و راکتیو به مقادیر مرجع مورد نیاز می رسد ، برای اطمینان از ردیابی موثر نقطه بهینه عملکرد و دستیابی به حداکثر توان خروجی الکتریکی. تحلیل دینامیکی سیستم تحت سرعت متغیر باد انجام می شود. این تجزیه و تحلیل بر اساس کنترل انرژی فعال و واکنش پذیر است. کار جدید در این مقاله معرفی نظریه های الگوریتم های ژنتیک در استراتژی کنترل مورد استفاده در زنجیره سوئیچ توربین های بادی ، برای بهبود عملکرد و کارایی مناسب است. نتایج شبیه سازی اعمال شده بر روی الگوریتم های ژنتیک در مقایسه با تنظیم کننده های کلاسیک PI ، کارآیی ، نتایج چشمگیر و پایداری سیستم های توربین بادی را نشان می دهد. سپس ، کنترل های مصنوعی هوشمند ، مانند کنترل الگوریتم های ژنتیک ، اعمال می شوند. به نتایج به دست آمده ، در محیط Matlab/Simulink، نشان می دهد که الگوریتم ژنتیکی راندمان موثر دارد.

International Journal of Engineering

Fuzzy Centralized Coordinate Learning and Hybrid Loss for Human Activity Recognition

M. Bourjandi, M. Yadollahzadeh Tabari*, M. Golsorkhtabaramiri

Department of Computer Engineering, Babol Branch, Islamic Azad University, Babol, Iran

P A P E R I N F O	*A B S T R A C T*
	Human activity recognition has been a popular research topic in recent years. The rapid development of deep learning techniques has greatly helped researchers to achieve success in this field. But the researchers usually over look the distribution of features in the coordinate space despite its significant effect on the convergence status of network and classification of activities. This paper proposes a combined method based on fuzzy centralized coordinate learning (FCCL) and a hybrid loss function to overcome the explained constraint. The FCCL induces features to be dispersedly spanned across all quadrants of the coordinate space. For this reason, the angle between the feature vectors of the activity classes increases significantly. Furthermore, a hybrid loss function is presented to increase the discriminative power of the proposed method. Our experiments were carried out on the opportunity and the PAMAP2 datasets. The proposed method has been compared with six machine learning and three deep learning methods for activity recognition. Experimental results showed that the proposed method outperformed all of the comparative methods due to identifying discriminative features. The proposed method successfully enhanced the average accuracy by 17.01% and 3.96% on the PAMAP2 and opportunity datasets, respectively, compared to the deep learning methods.

NOMENCLATURE

P_k	predicted posterior probability(k-th class)	$S_o(x_1.x_2)$	cosine similarity of the two feature vectors
μ_u	mean of u	$\theta_{y_i.i}$	intersection angle between $\frac{w}{||w||}$ and $\vartheta(x)$
σ_u^2	variance of u	β	Balance parameter
$\Gamma()$	gamma function	τ	adaptive parameter
D	degree of freedom	$L_{softmax}$	Soft-Max loss function
γ_1, γ_2	fuzzy decay factors	L_{SAAM}	Simple adaptive angular margin loss function
o_b	mean vector produced by the current mini batch	ΔO	difference between the old mean vector and o_b
σ_b	standard deviation vector produced by the current mini batch	$\Delta\sigma$	difference between the old standard deviation vector and σ_b

1. INTRODUCTION

Human activity recognition (HAR) is a field of study to identify and analyze the activities performed by a person (or persons). Today, the HAR methods are widely used in various areas, including the healthcare [1-2], smart cities [3], and affordable mobile devices [4]. Machine learning algorithms and deep learning methods are the most common and popular methods widely used in HAR.

HAR still faces two issues: 1) How to extract discriminative features from raw data, and 2) How to apply discriminative loss functions in feature classification.

The top well-known methods in the machine learning algorithms include the k-Nearest Neighbor (k-NN) algorithm [5], Artificial Neural Networks (ANN), Support Vector Machine (SVM) [6], the Random Forest (RF) [7], Decision Tree (DT), and Naive Bayes (NB) [8].

* Corresponding Author Institutional Email: *m_tabari@baboliau.ac.ir* (M. Yadollahzadeh Tabari)

Bustoni *et al.* [9] compared the recognition performance of SVM, k-NN, and Random Forest machine learning algorithms on HAR. Their results showed that the highest accuracy and recall were achieved by the SVM method with Support Vector Classifier (SVC) and Radial Basis Function (RBF) kernels, which are 87 and 85%, respectively. The drawback of these methods is that they use hand-crafted features that rely heavily on human experience or knowledge.

In contrast to machine learning algorithms with shallow statistical features, deep learning methods include high-level and meaningful features and have achieved good performance in HAR [10-14]. Various deep learning-based techniques, such as AutoEncoders (AEs), convolutional neural networks (CNNs), recurrent neural networks (RNNs), have successfully been used in HAR [1, 11-12]. Panwar et al. [15] designed a CNN model to recognize three fundamental movements of the human forearm using a single wrist-worn accelerometer sensor. Their results showed that the CNN model outperformed SVM and K-means because it automatically extracts the high-level features. The limitation of the CNN model is that it ignores the temporal dependencies within the data [11, 16].

In recent articles, researchers have extensively employed hybrid networks that benefit from the advantages of different networks [1]. Javier et al. [17] proposed a hybrid method for HAR based on convolutional and Long Short-Term Memory recurrent (LSTM) networks called Deep ConvLSTM. The Deep ConvLSTM method consists of convolutional, recurrent, and Soft-Max layers. This method achieved an F1-score 69% performance using only signals obtained from accelerometers on the OPPORTUNITY dataset. This value was improved by 20% using signals acquired from accelerometers, gyroscopes, and magnetic sensors. The low efficiency of this method is due to the Soft-Max Loss which cannot obtain discriminative features for activity recognition [18]. In litertaure [19], a hybrid method, called CNN-LSTM-ELM, was proposed, which used ELM in the last layer for classification purposes. This method achieved an F1-score of 90.8% on the OPPORTUNITY dataset. The limitation of this method is the high sensitivity to hidden nodes [20].

Recently, the combination of the margin-based loss with deep learning methods has led to acquiring discriminative features and successful results in face recognition [21-22]. Zhang et al. [23] proposed a new learning method called centralized coordinate learning (CCL) to identify differential features in facial recognition. They conducted experiments on six datasets: LFW [24], CACD [25], SLLFW [26], CALFW [27], YouTube Face [28], and MegaFace [29]. The accuracy level reached 99.4% accuracy on the LFW dataset.

A combined method is presented in this paper to solve the limits mentioned in the recent HAR methods. This combined method is based on fuzzy centralized coordinate learning (FCCL) and a hybrid loss function.

The proposed FCCL method dispersedly spans the features in the coordinate space to increase the angle between different activity classes. The hybrid loss function classifies the obtained discriminative features with high accuracy, and its contributions are as follows:
1. we present the FCCL to learn the discriminative features, which increase intra-class compactness and inter-class diversity in activity classes.
2. Using a new loss function called the hybrid loss for enhancing the separability of different activity classes.

This article is organized as follows: in Section 2, the architecture of the proposed method has been expressed for the accurate identification of human activity. Two used datasets, the performance metrics, and experimental settings are introduced in Section 3. Finally, in Section 4, the experiments and results are discussed.

2. PROPOSED METHOD

This research has attempted to overcome the limitations mentioned in the previous section by presenting a combined method based on the FCCL and a hybrid loss function. Figure 1 presents a workflow of the proposed method. According to this figure, the first step in the proposed method is to receive raw data from wearable sensors. Many HAR methods [10-11, 30] have used statistical features such as symbolic representation [31], statistics of raw data, and transform coding [32]; however, they have overlooked the short-term and long-term temporal dependencies between the features. To solve this problem, we use a combination of the CNN and LSTM networks to extract the features, shown in Figure 2. In the second step, we presented the FCCL to learn discriminative features which improve intra-class compactness and inter-class diversity. Finally, according to Figure 2, a hybrid loss function is proposed to improve the separability of different activity classes. In the following, the proposed method is described in detail.

2. 1. Feature Extraction Using the Hybrid Deep Learning Method   An essential step in HAR is to extract high-level features from time-series data. Deep neural networks (DNNs) can be proposed to extract meaningful features. Most researchers use CNN to recognize human activities with wearable sensors [33]. The main layers used in deep convolution networks are the convolution, the max-pooling, and the fully connected layers. In the convolution layer, filters are used to represent an abstract of the input data [34]. CNNs automatically learn the local and short-term features of time series data but ignore temporal dependencies within data [11]. The LSTM is a type of DNNs that extracts temporal dependencies within data and widely combines with CCNs. The advantage of LSTM is the ability to learn
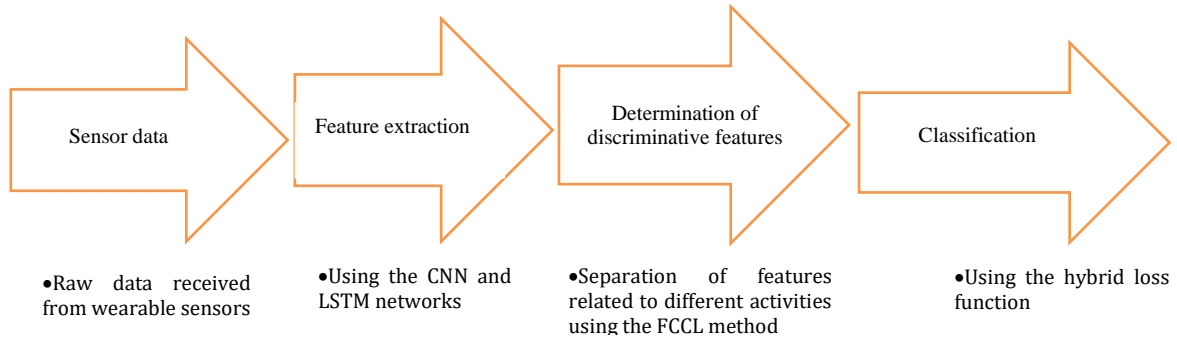
Figure 1. Basic block diagram of the work in this research
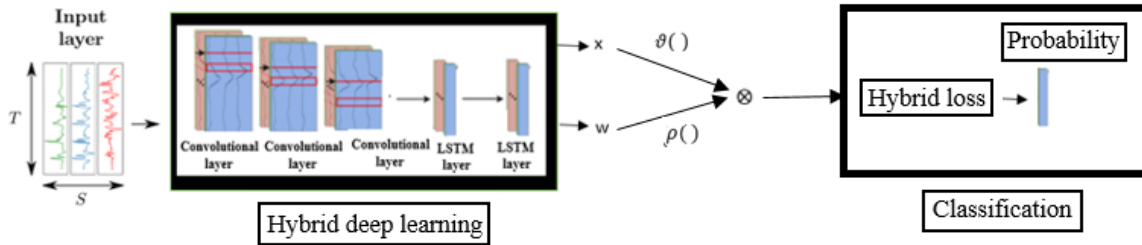
Figure 2. The architecture of the proposed method; x and w are the feature and classification vectors, respectively. $\rho(\ )$ and $\vartheta(\ )$ are transformation functions on parameters w and x, respectively

long-term dependency, which is not possible by recurrent neural networks [35]. The present study uses a hybrid deep learning method based on CNN and LSTM networks to take advantage of both, in which the output of the last convolutional layer feeds into the LSTM layer. According to Figure 2, three convolutional layers and two LSTM layers are used for feature extraction.

2. 2. Fuzzy Centrolized Coordinate Learning Soft-Max loss [18] is a standard multiclass classification loss function in DNN. Soft-Max loss projects an input feature into a probability distribution [39]. The Soft-Max loss is defined as:

$$P_k = \frac{\exp(Z_k)}{\sum_{j=1}^{K} \exp(Z_j)} \tag{1}$$

$$Z_j = w_j^T x + b_j \tag{2}$$

where P_k is the predicted posterior probability for the k-th class, x is the extracted feature at the last layer of the hybrid deep learning method, w_j and b_j are classification vector, and the bias belonging to j-th class, respectively. According to Equation (2), the features x and the classification vectors w_j are parameters learned in the training step. Proper formulation of features x and the classification vectors w greatly affects the network convergence [23]. An appropriate formulation of w

reduces the classification gap between the training and test steps. The efficient formulation of x can increase the angle between feature vectors related to different classes. For that reason, two functions $\rho(\ )$ and $\vartheta(\ )$ on parameters w and x, respectively, are used during the CCL for more effective network training [23]. In addition, we set b_j to 0 for simplicity. With considering the two functions $\rho(\ )$ and $\vartheta(\ )$, Equation (2) is rewritten as follows:

$$Z = \rho(w)^T \vartheta(x) \tag{3}$$

Based on the previous research [23], $\rho(w)$ is set to $\frac{w}{\|w\|}$. According to Equations (1) and (2), $\vartheta(x)$ will significantly affect the predicted posterior probability of a class (P_k) and the final output of the deep network. If $\|\vartheta(x)\|$ is small, the predicted posterior probability of all samples will be similar so that the loss function will be less discriminative between activities of different classes. Once $\|\vartheta(x)\|$ is large, the probabilities may vary much and cause instability in the learning of the deep network. Hence, this function should be formulated to separate the feature vectors of different classes by large angles. Therefore, in this article, the extracted features are spanned across all quadrants of the coordinate space using the FCCL method. For each dimension i of the feature vector x, $\vartheta(x_i)$ is defined as follows [23]:

$$\vartheta(x_i) = \frac{x(i) - o(i)}{\sigma(i)} \tag{4}$$

where $o = E[x]$ is the mean vector of x, and $\sigma(i)$ is the standard deviation of $x(i)$. To simplify the analysis, we use the L_2 norm of $\vartheta(x_i)$, i.e., $||\vartheta(x)||$.

$$u = ||\vartheta(x)|| = \sqrt{\sum_{j=1}^{D} \left(\vartheta(x(j)) \right)^2} \tag{5}$$

The mean and variance of u are formulated as follows:

$$\mu_u = E[u] = \sqrt{2} \, \frac{\Gamma(\frac{D+1}{2})}{\Gamma(\frac{D}{2})} \tag{6}$$

$$\sigma_u^2 = D - \mu_u^2 \tag{7}$$

The $\Gamma(\ )$ is a Gamma function and the values of μ_u and σ_u^2 are determined according to the degree of freedom D. According to the experiments performed by Zhang et al., the best rational choice for D is 374 [23]. The origin vector (o) and the standard deviation (σ), which are two key factors in the function $\vartheta(x)$, are learned during deep neural network training. In the following, an example is given to illustrate how o affects the function $\vartheta(x)$. The cosine similarity of the two feature vectors x_1 and x_2 is formulated in Equation (8), by taking o as the coordinate origin.

$$S_o(x_1.x_2) = \frac{(x_1 - o)^T (x_2 - o)}{||x_1 - o|| \, ||x_2 - o||} \tag{8}$$

According to Equation (8), o affects the similarity between x_1 and x_2. For example, if $x_1 = [0.1,\ 0.1,\ 0.1]$, $x_2 = [0.1, 0.2, 0.1]$, and $o = [0, 0, 0]$, the intersection angle between x_1 and x_2 is 19.6º and $S_o(x_1, x_2) = 0.942$. If the origin vector shifts to [-0.03, -0.03, -0.03], then the intersection angle is 16.26 º and $S_o(x_1.x_2) = 0.96$. According to the example above, if the origin vector o moves a little, the angle and similarity between the feature vectors are greatly affected. Therefore, the values of o and σ in each update should not change much during DNN training. For that reason, in this article, the fuzzy decay factors of γ_1 and γ_2 are proposed to determine the appropriate balance between the new and old values of o and σ, respectively. The parameters $\sigma \ and \ o$ are updated with decay factors as follows:

$$o_{new} = \gamma_1 \, o_{old} + (1 - \gamma_1) o_b \tag{9}$$

$$\sigma_{new} = \gamma_2 \, \sigma_{old} + (1 - \gamma_2) \sigma_b \tag{10}$$

where o_b and σ_b are the mean and standard deviation vectors produced by the current mini batch. In   the previously conducted research [23], γ_1 and γ_2 were set to 0.99, but in the present article, the exact value of these variables is determined in a fuzzy way. For this purpose, we used the variables ΔO and $\Delta \sigma$. Equations (11) and (12) show the values of ΔO and $\Delta \sigma$.

$$\Delta O = ||o_{old} - o_b|| \tag{11}$$

$$\Delta \sigma = ||\sigma_{old} - \sigma_b|| \tag{12}$$

In the following, a fuzzy system is presented to determine the fuzzy value of γ_1 based on the variable ΔO. In a similar way, the value of γ_2 in Equation (10) is determined by a fuzzy system based on variable $\Delta \sigma$. Figure 3 shows the structure of the fuzzy system to find the appropriate value of γ_1 . As can be seen in this figure, the input of this system is the fuzzy values corresponding to the variable ΔO. The fuzzy sets of input variable ΔO are illustrated in Figure 4. These fuzzy sets are based on the Gaussian membership function.

The fuzzy sets of input and the competitive fuzzy rules in Table 1 are obtained by performing different experiments on the PAMAP2 and OPPORTUNITY datasets. As shown in Figure 4, we use five fuzzy sets for the variable ΔO. The value of γ_1 is set based on the membership value of ΔO to each of the fuzzy sets. When maximum membership value of ΔO is related to very low or low fuzzy sets, we can increase the effectiveness of o_b more reliably for updating parameter o_{new}. For this reason, γ_1 is set by a small value. The range of γ_1 is [0,0.55] or(0.55,0.67) according to $\mu_{very\ low}(\Delta O)$ in rule1 or $\mu_{low}(\Delta O)$ in rules 2 and 3, respectively. Similarly, when maximum membership value of ΔO is related to very high or high fuzzy sets, the fuzzy value of γ_1 is increased to prevent creating an unstable state in the network and increase the effect of the parameter o_{old} . Therefore, the range of γ_1 is [0.82,0.96) or 0.99 according to $\mu_{high}(\Delta O)$ in rules 6 and 7 or $\mu_{very\ high}(\Delta O)$ in rule 8, respectively. The value of γ_2 in Equation (10) is determined similarly based on the fuzzy
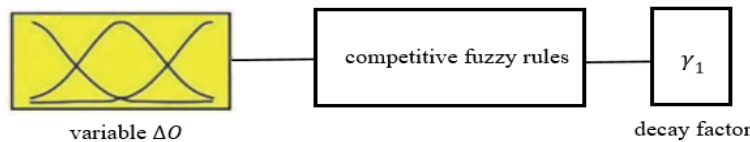
Figure 3. The structure of the fuzzy system to find the appropriate value of γ_1
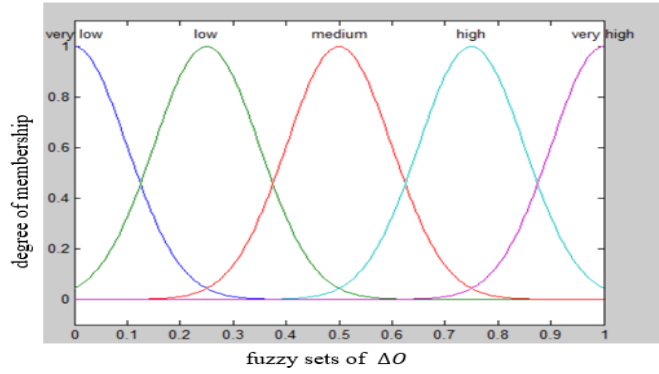
Figure 4. The fuzzy sets of input variable ΔO

TABLE 1. Competitive fuzzy rules

1-	If $(0.45 \leq \mu_{very\ low}(\Delta O) \leq 1)$ then $(\gamma_1 = 1 - \mu_{very\ low}(\Delta O))$
2-	If $(0.45 < \mu_{low}(\Delta O) \leq 1)$ and $(\mu_{very\ low}(\Delta O) < 0.45)$ then $(\gamma_1 = 0.51 + \frac{\mu_{low}(\Delta O)}{10})$
3-	If $(0.45 < \mu_{low}(\Delta O) < 1)$ and $(\mu_{medium}(\Delta O) < 0.45)$ then $(\gamma_1 = 0.61 + \frac{1 - \mu_{low}(\Delta O)}{10})$
4-	If $(0.45 \leq \mu_{medium}(\Delta O) \leq 1)$ and $(\mu_{low}(\Delta O) < 0.45)$ then $(\gamma_1 = 0.6 + \frac{\mu_{medium}(\Delta O)}{7})$
5-	If $(0.45 < \mu_{medium}(\Delta O) < 1)$ and $(\mu_{high}(\Delta O) < 0.45)$ then $(\gamma_1 = 0.74 + \frac{1 - \mu_{medium}(\Delta O)}{7})$
6-	If $(0.45 \leq \mu_{high}(\Delta O) < 1)$ and $(\mu_{medium}(\Delta O) < 0.45)$ then $(\gamma_1 = 0.73 + \frac{\mu_{high}(\Delta O)}{5})$
7-	If $(0.8 < \mu_{high}(\Delta O) \leq 1)$ and $(\mu_{very\ high}(\Delta O) < 0.2)$ then $(\gamma_1 = 0.91 + \frac{1 - \mu_{high}(\Delta O)}{5})$
8-	If $(0.2 \leq \mu_{veryhigh}(\Delta O))$ then $(\gamma_1 = 0.99)$

sets of input variable $\triangle\sigma$. Therefore, these fuzzy values (γ_1 and γ_2) effectively determine variables o_{new} and σ_{new} at each step.

2. 3. Hybrid Loss   Various classification functions are used to determine the final output in the last layer of deep neural networks. In literature, different classification functions have been proposed, but all of them have some drawbacks. To provide a more compact classification boundary for accurate user activities identification for HAR, we presented a combination of Soft-Max loss and Simple Adaptive Angular Margin (SAAM) loss, called hybrid loss. According to the definition of cosine similarity, the Soft-Max and SAAM loss functions are formulated as Equations (13) and (14), respectively, as follows:

$$L_{Soft-max} = \sum_i^N -\log \left(\frac{\exp\left(\|\vartheta(x_i)\| \cos\left(\theta_{y_i.i}\right)\right)}{\sum_{k=1}^K \exp\left(\|\vartheta(x_i)\| \cos(\theta_{k.i})\right)}\right) \tag{13}$$

$$L_{SAAM} = \sum_i^N -\log \left(\frac{\exp\left(\|\vartheta(x_i)\| \cos\left(\tau\theta_{y_i.i}\right)\right)}{\exp\left(\|\vartheta(x_i)\| \cos\left(\tau\theta_{y_i.i}\right)+\sum_{k \neq y_i}\exp\left(\|\vartheta(x_i)\| \cos(\theta_{k.i})\right)\right)}\right) \tag{14}$$

(a) original data distribution   (b) Soft-Max loss   (c) Hybrid loss
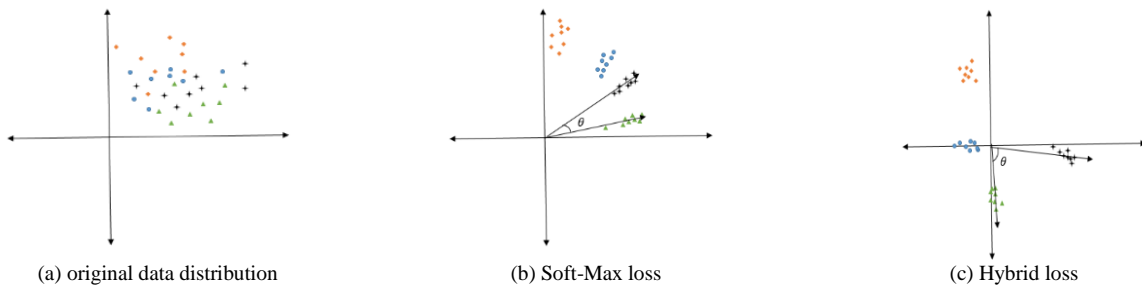
Figure 5. Illustration of the effects of various loss functions. The "orange rhombuses", "blue dots", "black stars" and "green triangles" represent the samples of four activities classes. (a) Original data distribution. (b) Converged features by using the Soft-Max loss. (c) Converged features by using the hybrid loss

where $\theta_{y_i.i}$ is the intersection angle between $\frac{w}{||w||}$ and $\vartheta(x)$ and range of $\theta_{y_i.i}$ is $[0. \pi]$. The adaptive parameter τ is set based on the range of $\theta_{y_i.i}$ [23].

According to Equations (13) and (14), $||\vartheta(x_i)||$ and $\cos(\theta_{y_i.i})$ will affect the loss functions and, both depend on the form of $\vartheta(x_i)$. In Sub-section 2.2, we formulated $\vartheta(x)$ well. The hybrid loss function is shown in Equation (15) based on $L_{Soft-max}$ and L_{SAAM}.

$$L_{hybrid\ loss} = \frac{\beta\ L_{softmax} + L_{SAAM}}{\beta + 1} \qquad (15)$$

Parameter β is a value to balance between the Soft-Max loss and the SAAM loss. The value of β is determined based on the value of $\theta_{y_i.i}$ as follows:

$$\beta = \begin{cases} 3. & \frac{\pi}{3} < \theta_{y_i.i} \leq \pi; \\ 2. & \frac{\pi}{30} < \theta_{y_i.i} \leq \frac{\pi}{3}; \\ 2 \times \cos(\theta_{y_i.i}). & \theta_{y_i.i} \leq \pi/30 \end{cases} \qquad (16)$$

According to Equation (16), the range of $\theta_{y_i.i}$ is partition into three distances, based on which β is set. When $\frac{\pi}{3} < \theta_{y_i.i} \leq \pi$, the angle is big enough to supply enough gradient information for training. thus, the Soft-Max loss function can classify the activities accurately, and we fix the parameter β =3. When $\frac{\pi}{30} < \theta_{y_i.i} \leq \frac{\pi}{3}$, the ability of Soft-Max loss to extract discriminative features decreases, so we try to reduce its effect on the proposed hybrid loss, and β is set to 2. As the angle decreases, the SAAM loss function can enhance the separability of neighboring classes by using parameter τ. Thus, when $\theta_{y_i.i} \leq \pi/30$, the effect of Soft-Max loss decreases slowly based on $\theta_{y_i.i}$, and we set β =$2 \times \cos(\theta_{y_i.i})$. In Figure 5, we show the differences of the two loss functions on the classification of features, including the Soft-Max loss in Equation (13) and the hybrid loss in Equation (15). According to Figure 5(b), the centers of activity classes are placed in a unit hypersphere and are very close to each other. Therefore, the angle θ between the features of two different classes is small. The hybrid loss causes the extracted features to span across all quadrants of the coordinate space. As shown in Figure 5(c), the dispersed distribution of features increases the angle between neighboring classes and improves the separability.

3. EXPERIMENTAL EVALUATION

Several experiments were performed to determine the effectiveness of the proposed method. To this end, two benchmark datasets were used, which contain the human activity of daily living. These data were recorded using a combination of environmental sensors and body-

connected sensors in the environment. The experiments were performed using the Keras framework in Python 3 on a system with Windows 10. The system uses a quad-core processor with 2.30 GHz speed and a GeForce GTX 950M graphics card. Section 3.1 provides a brief overview of the datasets used for the evaluation, and Section 3.2 describes the evaluation method. Finally, the settings of the deep learning methods are presented in Section 3.3.

3. 1. Datasets   The proposed method was evaluated on two benchmark datasets widely used in literature. These datasets include data streams received from the sensors embedded in different positions of the participants' bodies. The activity recognition datasets usually include various activities such as walking, cycling, and goal-oriented activities. In the experiments performed in this article, the OPPORTUNITY [36] and PAMAP2 [37] datasets were used. The OPPORTUNITY dataset has an unbalanced class distribution such that most of the samples belong to the NULL class. In contrast, the PAMAP2 dataset contains a balanced distribution of human activities. These datasets are available at the

UCI Machine learning repository ^{2}.

• **OPPORTUNITY**

The OPPORTUNITY dataset [36] includes annotated recordings from four subjects performing 17 different daily activities in a kitchen scenario. A NULL class also exists that is not associated with any of the daily activities. The data were collected using body-worn sensors. These sensors contain five commercial RS485-networked XSense inertial measurement units, 12 Bluetooth acceleration sensors, and commercial InertiaCube3 inertial sensors. They were placed on a custom-made motion jacket, the limbs, and each foot, respectively. These sensors perform sampling with a frequency of 30 Hz. During the recordings, for each subject, six different runs were recorded. Five runs were termed Activity of Daily Life (ADL), and one run was termed drill run (Drill). In ADL1 to ADL5, the subjects performed all of the different scripted activities, and in the Drill, they replicated each activity 20 times. To deal with the problem of missing data, 38 sensor channels (including accelerometer recordings) were removed and the remaining 107-dimensional data were used for our experiments. We selected the ADL1-3 and Drill runs as the training set and the ADL4-5 runs as the testing set. For the segmentation phase, a fixed-length sliding window was applied to slicing the data. Based on the previous research, a sliding window of 2 s and a sliding stride of 3 were used in this article [1].

• **PAMAP2**

The PAMAP2 Physical Activity Monitoring dataset consists of 12 daily living activities, i.e., lie, sit, stand,

---

^{2} http://archive.ics.uci.edu/ml

walk, run, cycle, Nordic walk, iron, vacuum, jump rope, ascend, and descend stairs, which are performed by nine subjects. The data were recorded by three inertial measurement units (accelerometer, gyroscope, and magnetometer) and a heart rate monitor attached to the participant's hands, chest, and ankles [37]. These sensors performed sampling with a frequency of 33 Hz. Data were collected in more than 10 hours, and the obtained dataset had 52 dimensions. For the segmentation phase, sliding windows of 5.12 s were used with 1 s stepping between adjacent windows (78% overlap). Runs 1 and 2 for subject5 were used in the validation set and runs 1 and 2 for subject6 in the test set. The remaining data were used in the train set.

3. 2. Model Evaluation It is now necessary to examine the effectiveness of the proposed method in human activity recognition. Since the recognition rate of the majority class greatly affects the performance statistics in the minority classes and the OPPORTUNITY dataset is highly unbalanced (the NULL class includes more than 75% of the total data). Thus, in addition to the accuracy criterion, the weighted F1-score and the average F1-score were used, which were independent of the class distribution. The weighted F1-score is formulated by Equation (17) as follows:

$$\text{weighted F1} - \text{score } (\text{F1}_W) = \sum_i 2 \times w_i \frac{precision_i \times recall_i}{precision_i + recall_i} \tag{17}$$

$$precision = \frac{TP}{TP+FP} \tag{18}$$

$$recall = \frac{TP}{TP+FN} \tag{19}$$

$$w_i = \frac{m_i}{M} \tag{20}$$

where TP refers to the number of samples correctly recognized in the positive class, FP refers to the number of samples incorrectly identified in the negative class. TN refers to the number of samples correctly recognized in the negative class, and FN refers to the number of samples incorrectly identified in the positive class. In Equation (20), parameter i is the class index, w_i is the ratio of data in class i, m_i is the number of samples in class i, and M is the total number of samples considered. The average F1-score is not dependent on the class distribution and is formulated by Equation (21) as follows:

$$\text{average F1} - \text{score } (\text{F1}_A) = \frac{2}{m_i} \sum_i \frac{precision_i \times recall_i}{precision_i + recall_i} \tag{21}$$

TABLE 2. Settings of hyperparameters related to the deep learning methods

Model	Layer	Parameter	Value	Classifier
CNN-LSTM-ELM [19]	2-5	Convolutional(Kernel Size)	(5,1)	ELM
		Convolutional (sliding stride)	(1,1)	
		Convolutional(Kernels)	$50^2,40^3,30^4,40^5$	
	6-7	LSTM (number of neurons)	128	
Hybrid [1]	2	Convolutional(Kernel Size)	(11,1)	Soft-Max
		Convolutional (sliding stride)	(1,1)	
		Convolutional(Kernels)	50	
		Convolutional (Pooling Size)	(2,1)	
	3-4	LSTM(cells)	27	
		Output of LSTM cells	600	
	5	Fully connected	512	
Deep ConvLSTM [17]	2-5	Convolutional(Kernel Size)	(5,1)	Soft-Max
		Convolutional (sliding stride)	(1,1)	
		Convolutional(Kernels)	64	
	6	LSTM (number of neurons)	128	
	7	Fully connected	n_c	
Proposed method	2-4	Convolutional(Kernel Size)	(11,1)	Hybrid Loss
		Convolutional (sliding stride)	(1,1)	
		Convolutional(Kernels)	60	
	5-6	LSTM(cells)	27	
		Output of LSTM cells	600	

3. 3. Model Setting   Table 2 shows the settings of the hyperparameters related to the four deep learning methods used in this article. The network parameters are optimized by minimizing the cross-entropy loss function. This optimization is done using mini-batch gradient descent with the RMSProp update rule. In Table 2, the fully connected layers were followed by a Rectified Linear Unit (ReLU) activation layer to prepare the non-linear presentation. Each of the convolution blocks in Table 2 includes convolution layers and ReLU, and in the hybrid method, in addition to them, it consists of the max-pooling layer. The size of the sliding window defined the number of cells in the LSTM layers. In the LSTM cells, sigmoid and hyperbolic functions are used for gate and other activations, respectively. After the last fully connected layer is used, a classifier layer is employed to provide predictions for each class. All parameters of the deep learning methods were randomly initialized and trained using the ADADELTA optimizer [38] with default parameters (initial learning rate of 1) for 50 epochs. The batch size is set to 100. In this article, the sliding time window size (T) and the number of sensor channels (n) were fixed at 64 and 107, respectively.

4. EXPERIMENTAL RESULTS

In this section, the performance of the proposed method is evaluated and analyzed on two benchmark datasets. This section is organized as follows: the analysis of the results obtained from the proposed method and its comparison with other known methods are presented in Sub-section 4.1; a comparison between the proposed method and three machine learning algorithms is provided in Sub-section 4.2. Finally, the performance of the Soft-Max and hybrid loss functions are examined in Sub-section 4.3.

4. 1. Performance Comparison   A comparison between the deep learning methods and the proposed method based on the performance parameters is shown in Table 3. The performance parameters include the accuracy (ACC), weighted F1-score ($F1_W$), and average F1-score ($F1_A$). According to Table 3, the proposed method has the highest score in terms of overall performance on the two defined datasets.

Specifically, the accuracy, weighted F1-score, and average F1-score of the proposed method increased to 93.13% and 93.28% and 78.12%, respectively, on the OPPORTUNITY dataset. The OPPORTUNITY data set is imbalanced [36]; this leads to insufficient training in all tested methods. Thus, the average F1- score has improved less compared to the other performance parameters. There is a significant difference between the average F1-score in CNN-LSTM-ELM [19] and hybrid method [1] with the Deep ConvLSTM method [17], which is due to the use of a suitable classifier in the last

layer and the appropriate number of LSTM layers. One of the drawbacks of the CNN-LSTM-ELM method, which has led to its low efficiency compared to the proposed method, is its strong dependence on the number of hidden nodes. According to Table 3, the proposed method has increased the average accuracy by 6.75% compared to the hybrid method on the two datasets. This improvement is due to the extracted discriminative features, which significantly enhance intra-class compression and inter-class diversity. For a more detailed analysis, the results of different deep learning methods were compared on each class of the PAMAP2 dataset. Figure 6(a) illustrates the F1-score of each class for our proposed method and the deep learning methods. According to Figure 6(a), the lowest efficiency is attributed to the "standing" activity. The values of F1-score in "standing" activity with the Deep ConvLSTM, CNN-LSTM-ELM, hybrid, and proposed methods are 38%, 48%, 54%, and 86%, respectively. Thus, the value of the F1-score achieves an increase of 48% by the proposed method, compared with the Deep ConvLSTM. The highest difference of F1-score between the hybrid and proposed methods is related to the "standing" and "vacuum cleaning" activities. This significant increase in F1-score (related to the "standing" and "vacuum cleaning" activities) indicates the high ability of the proposed method to determine discriminative features because it is a key parameter in identifying activities. The proposed method reached an F1-score of 84% in "rope jumping"; thus, the F1-score increased by 9% compared with the hybrid method. Figure 6(b) illustrates the confusion matrixes of all deep learning methods on the PAMAP2 dataset. Confusion matrixes contain detailed information about the actual and predicted classifications conducted by the system; therefore, it determines the nature of the classification error. According to Figure 6(b), the number of classes correctly predicted by the proposed method was more than other deep methods. The Deep ConvLSTM method only recognized the activities of 3 classes correctly, and the most errors in the CNN-LSTM-ELM and hybrid methods were related to classes 4, 11, and 1.

4. 2. Comparison with Machine Learning Algorithms   In order to show the effectiveness of the proposed method, a comparison has been made between it and machine learning algorithms on the OPPORTUNITY dataset. Table 4 shows the results of this comparison. A total of 18 hand-crafted features were used, including 15 simple statistical values and three frequency values, which were calculated on each sensor channel independently [1]. In addition, we trained machine learning algorithms with extracted features from the first layer fully connected to the LSTM network.

TABLE 3. Classification performance results (in percent) of the various deep learning methods on the OPPORTUNITY and the PAMAP2 datasets

Method	OPPORTUNITY			PAMAP2		
	ACC	F1$_W$	F1$_A$	ACC	F1$_W$	F1$_A$
Deep ConvLSTM [17]	87.47	87.23	55.49	67.54	66.12	58.76
CNN-LSTM-ELM [19]	91.34	90.85	70.38	85	83.12	76
Hybrid [1]	91.76	91.56	70.86	85.12	83.73	76.10
Proposed method	**94.15**	**94.05**	**79.12**	**96.23**	**96.11**	**95.78**
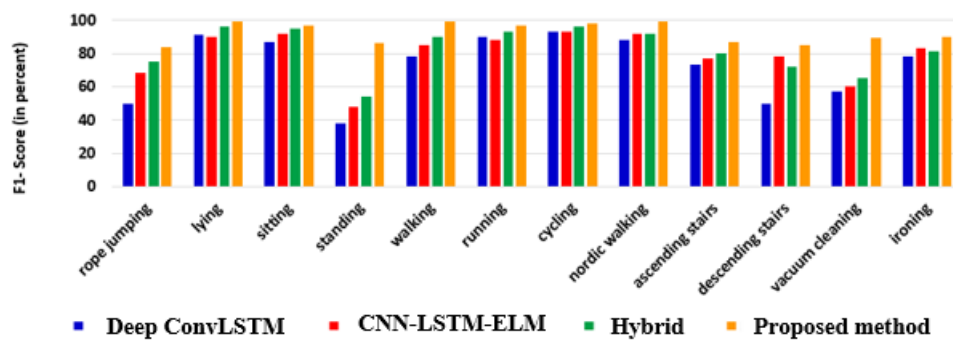
(a)
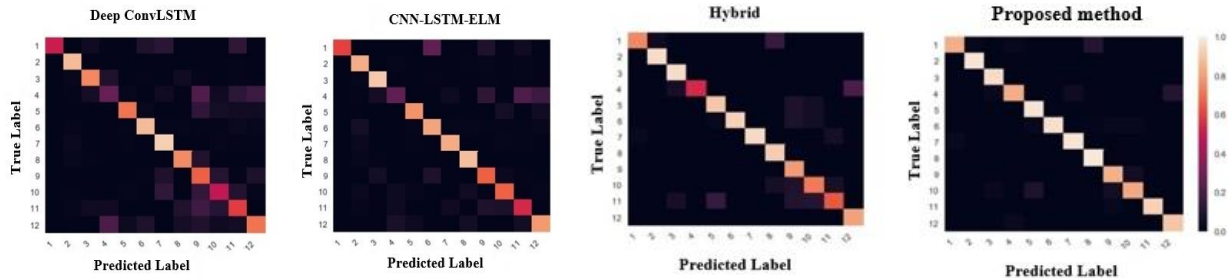
(b)

Figure 6. (a) The F1-score of each class of various deep learning methods on the PAMAP2 dataset. (b) Confusion matrix of the deep learning methods on the PAMAP2 dataset: 1: rope jumping; 2: lying; 3: sitting; 4: standing; 5: walking; 6: running; 7: cycling; 8: Nordic walking; 9: ascending stairs; 10: descending stairs; 11: vacuum cleaning and 12: ironing.

TABLE 4. Classification performance results (in percent) of proposed method and three machine learning classifiers on the OPPORTUNITY dataset

Method	ACC	F1$_W$	F1$_A$
SVM	89.96	89.53	63.76
Random Forest	89.21	87.08	52.45
Naive Bayes	44.79	52.61	32.81
LSTM-SVM	91.81	91.62	70.24
LSTM- Random Forest	91.84	91.63	70.24
LSTM- Naive Bayes	91.15	91.29	69.03
Proposed method	**94.13**	**94.28**	**79.12**
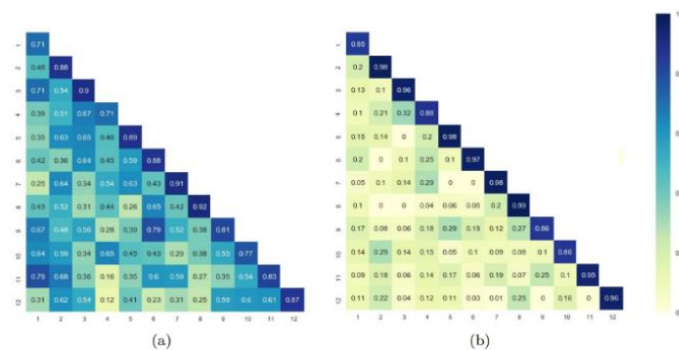
Figure 7. Heatmaps of cosine similarity of all classes using different loss functions on the PAMAP2 testing dataset: (a) Soft-Max loss; (b) hybrid loss

There was a significant efficiency improvement for the three machine learning algorithms, especially Naive Bayes. The highest efficiency was related to the proposed method; its average F1-score reached up to 79.12%. This high efficiency indicates the ability of the proposed method to improve the discrimination capability of extracted features.

4. 3. Comparison Between Soft-max and Hybrid Losses

The effectiveness of the hybrid loss was assessed by comparing its performance with the Soft-Max loss function. This evaluation was done by calculating the cosine similarity (i.e., intra-class and inter-class). The heatmap of these similarities on the PAMAP2 dataset is presented in Figure 7. The proposed method, which has the highest performance on the PAMAP2 dataset, is used in this experiment. Features are extracted by the hybrid deep learning method for these two loss functions. Figure 7(a) and 7(b) show the heatmaps of cosine similarity related to the proposed method with Soft-Max and hybrid loss functions, respectively. As shown in Figure 7(a) the Soft-Max function resulted in the least intra-class similarity. Based on the results obtained, the hybrid loss can capture more discriminative features than the Soft-Max loss function. The hybrid loss effectively improved intra-class compactness and inter-class variety.

5. CONCLUSIONS

This research work applied the combined method based on the fuzzy centralized coordinate learning (FCCL) and hybrid loss function to deal with two well-known issues in sensor-based HAR. The first one is to extract discriminative features. For this reason, the extracted features are dispersed in the coordinate space by using the FCCL. In this case, intra-class diversity and inter-class similarity are significantly decreased. The second problem is the separability of different user activities by using the appropriate classifier. We have used the hybrid

loss function as the classifier. Two benchmark datasets, OPPORTUNITY, and PAMAP2 were used to evaluate the performance and compare the proposed method with three deep learning methods, i.e., CNN-LSTM-ELM, Deep ConvLstm, and hybrid methods. The results showed that the proposed method outperformed all the three deep learning methods. In addition, a comparison was made between the proposed method and the three machine learning algorithms on the OPPORTUNITY dataset. The proposed method can improve the classification performance compared to the machine learning algorithms. Performance was significantly improved when the LSTM network was used in the machine learning algorithms for feature extraction. However, the proposed method could increase the discrimination capability of extracted features compared with machine learning algorithms. For future research, we aim to study the effectiveness of the proposed method on the open-set human activity recognition and the use of methods to enhance the sequential learning adaptive capability. A potential working direction could be using of a transfer learning approach (which reuses learned previous knowledge) to identify the activities carried out by various types of users in different environmental situations.

6. REFERENCES

1. Li, Frédéric, Kimiaki Shirahama, Muhammad Adeel Nisar, Lukas Köping, and Marcin Grzegorzek. "Comparison of feature learning methods for human activity recognition using wearable sensors." *Sensors* 18, No. 2, (2018), 679, DOI: 10.3390/s18020679 .

2. Ogbuabor, Godwin, and Robert La. "Human activity recognition for healthcare using smartphones." Proceedings of the 2018 10th International Conference on Machine Learning and Computing. (2018), https://doi.org/10.1145/3195106.3195157.

3. Khan, Adil Mehmood, Y-K. Lee, Seok-Yong Lee, and T-S. Kim. "Human activity recognition via an accelerometer-enabled-smartphone using kernel discriminant analysis." In 2010 5th international conference on future information technology, IEEE, (2010), 1-6. DOI: 10.1109/FUTURETECH.2010.5482729.

4. Shoaib, Muhammad, Stephan Bosch, Ozlem Durmaz Incel, Hans Scholten, and Paul JM Havinga. "A survey of online activity recognition using mobile phones." *Sensors* 15, No. 1, (2015), 2059-2085, https://doi.org/10.3390/s150102059.

5. Mobark, Mohammed, Suriayati Chuprat, and Teddy Mantoro. "Improving the accuracy of complex activities recognition using accelerometer-embedded mobile phone classifiers." In 2017 Second International Conference on Informatics and Computing (ICIC), IEEE, (2017), 1-5. DOI: 10.1109/IAC.2017.8280606.

6. Chen, Zhenghua, Qingchang Zhu, Yeng Chai Soh, and Le Zhang. "Robust human activity recognition using smartphone sensors via CT-PCA and online SVM." IEEE Transactions on Industrial Informatics 13, No. 6, (2017), 3070-3080, DOI: 10.1109/TII.2017.2712746.

7. Uddin, Md Taufeeq, Md Muttaleb Billah, and Md Faisal Hossain. "Random forests based recognition of human activities and postural transitions on smartphone." In 2016 5th International Conference on Informatics, Electronics and Vision (ICIEV), pp. 250-255. IEEE, (2016), DOI: 10.1109/ICIEV.2016.7760005.

8. Fan, Liwei, Kim-Leng Poh, and Peng Zhou. "A sequential feature extraction approach for naïve bayes classification of microarray data." *Expert Systems with Applications* 36, No. 6, (2009), 9919-9923.

9. Bustoni, I. A., I. Hidayatulloh, A. M. Ningtyas, A. Purwaningsih, and S. N. Azhari. "Classification methods performance on human activity recognition." In Journal of Physics: Conference Series, vol. 1456, No. 1, p. 012027. IOP Publishing, (2020).

10. Georgiou, Theodoros, Yu Liu, Wei Chen, and Michael Lew. "A survey of traditional and deep learning-based feature descriptors for high dimensional data in computer vision." *International Journal of Multimedia Information Retrieval* 9, No. 3, (2020), 135-170.

11. Dargan, Shaveta, Munish Kumar, Maruthi Rohit Ayyagari, and Gulshan Kumar. "A survey of deep learning and its applications: a new paradigm to machine learning." *Archives of Computational Methods in Engineering* 27, No. 4, (2020), 1071-1092.

12. Feizi, A. "Convolutional gating network for object tracking." *International Journal of Engineering, Transactions A: Basics* 32, No. 7, (2019), 931-939, DOI: 10.5829/ije.2019.32.07a.05.

13. Hassanpour, M., and H. Malek. "Learning Document Image Features With SqueezeNet Convolutional Neural Network." *International Journal of Engineering* 33, No. 7, (2020), 1201-1207, DOI: 10.5829/ije.2020.33.07a.05.

14. Chikhaoui, Belkacem, and Frank Gouineau. "Towards automatic feature extraction for activity recognition from wearable sensors: a deep learning approach." In 2017 IEEE International Conference on Data Mining Workshops (ICDMW), 693-702. IEEE, (2017), DOI: 10.1109/ICDMW.2017.97.

15. Panwar, Madhuri, S. Ram Dyuthi, K. Chandra Prakash, Dwaipayan Biswas, Amit Acharyya, Koushik Maharatna, Arvind Gautam, and Ganesh R. Naik. "CNN based approach for activity recognition using a wrist-worn accelerometer." In 2017 39th Annual International Conference of the IEEE Engineering in Medicine and Biology Society (EMBC), 2438-2441. IEEE, (2017), DOI: 10.1109/EMBC.2017.8037349.

16. Cruciani, Federico, Anastasios Vafeiadis, Chris Nugent, Ian Cleland, Paul McCullagh, Konstantinos Votis, Dimitrios Giakoumis, Dimitrios Tzovaras, Liming Chen, and Raouf Hamzaoui. "Feature learning for human activity recognition using convolutional neural networks." *CCF Transactions on Pervasive Computing and Interaction* 2, No. 1, (2020), 18-32.

17. Ordóñez, Francisco Javier, and Daniel Roggen. "Deep convolutional and lstm recurrent neural networks for multimodal wearable activity recognition." *Sensors* 16, No. 1, (2016), 115, https://doi.org/10.3390/s16010115.

18. Goodfellow, Ian, Yoshua Bengio, and Aaron Courville. "Softmax units for multinoulli output distributions. Deep Learning." (2018), 180-184.

19. Sun, Jian, Yongling Fu, Shengguang Li, Jie He, Cheng Xu, and Lin Tan. "Sequential human activity recognition based on deep convolutional network and extreme learning machine using wearable sensors." *Journal of Sensors,* (2018), https://doi.org/10.1155/2018/8580959.

20. Huang, Guang-Bin, Hongming Zhou, Xiaojian Ding, and Rui Zhang. "Extreme learning machine for regression and multiclass classification." *IEEE Transactions on Systems, Man, and Cybernetics, Part B (Cybernetics)* 42, No. 2, (2011), 513-529, DOI: 10.1109/TSMCB.2011.2168604.

21. Liu, Weiyang, Yandong Wen, Zhiding Yu, and Meng Yang. "Large-margin softmax loss for convolutional neural networks." In International Conference on Machine Learning, vol. 2, No. 3, p. 7. (2016).

22. Liu, Weiyang, Yandong Wen, Zhiding Yu, Ming Li, Bhiksha Raj, and Le Song. "Sphereface: Deep hypersphere embedding for face recognition." In Proceedings of the IEEE conference on computer vision and pattern recognition, pp. 212-220. (2017).

23. Qi, Xianbiao, and Lei Zhang. "Face recognition via centralized coordinate learning." arXiv preprint arXiv$:1801.05678$ (2018).

24. Huang, Gary B., Marwan Mattar, Tamara Berg, and Eric Learned-Miller. "Labeled faces in the wild: A database forstudying face recognition in unconstrained environments." In Workshop on faces in'Real-Life'Images: detection, alignment, and recognition. (2008).

25. Chen, Bor-Chun, Chu-Song Chen, and Winston H. Hsu. "Cross-age reference coding for age-invariant face recognition and retrieval." In European conference on computer vision, pp. 768-783. Springer, Cham, (2014).

26. Deng, Weihong, Jiani Hu, Nanhai Zhang, Binghui Chen, and Jun Guo. "Fine-grained face verification: FGLFW database, baselines, and human-DCMN partnership." *Pattern Recognition* 66 (2017), 63-73, https://doi.org/10.1016/j.patcog.2016.11.023.

27. Zheng, Tianyue, Weihong Deng, and Jiani Hu. "Cross-age lfw: A database for studying cross-age face recognition in unconstrained environments." arXiv preprint arXiv:1708.08197 (2017).

28. Wolf, Lior, Tal Hassner, and Itay Maoz. "Face recognition in unconstrained videos with matched background similarity." In in Computer Vision and Pattern Recognition (CVPR) 2011, pp. 529-534. IEEE, (2011), DOI: 10.1109/CVPR.2011.5995566

29. Kemelmacher-Shlizerman, Ira, Steven M. Seitz, Daniel Miller, and Evan Brossard. "The megaface benchmark: 1 million faces for recognition at scale." In Proceedings of the IEEE conference on computer vision and pattern recognition, pp. 4873-4882. (2016).

30. Lara, Oscar D., and Miguel A. Labrador. "A survey on human activity recognition using wearable sensors." *IEEE Communications Surveys & Tutorials* 15, No. 3, (2012), 1192-1209, DOI: 10.1109/SURV.2012.110112.00192.

31. Lin J, Keogh E, Lonardi S, Chiu B. "A symbolic representation of time series, with implications for streaming algorithms". InProceedings of the 8th ACM SIGMOD workshop on Research issues in data mining and knowledge discovery 2003; 2-11, https://doi.org/10.1145/882082.882086.

32. Cook, Diane J., and Narayanan C. Krishnan. "Activity learning: discovering, recognizing, and predicting human behavior from sensor data". *John Wiley & Sons*, (2015).

33. Lawal, Isah A., and Sophia Bano. "Deep human activity recognition with localisation of wearable sensors." *IEEE Access* 8, (2020), 155060-155070, DOI: 10.1109ACCESS.2020.3017681.

34. Zohrevand, A., Imani, Z. and Ezoji, M.. "Deep Convolutional Neural Network for Finger-knuckle-print Recognition". *International Journal of Engineering, Transactions A: Basics*,

2021, Vol. 34, No. 7, 1684-1693, DOI: 10.5829/ije.2021.34.07a.12.

35. Gers, Felix A., Nicol N. Schraudolph, and Jürgen Schmidhuber. "Learning precise timing with LSTM recurrent networks." *Journal of Machine Learning Research* 3, (2002), 115-143.

36. Chavarriaga, Ricardo, Hesam Sagha, Alberto Calatroni, Sundara Tejaswi Digumarti, Gerhard Tröster, José del R. Millán, and Daniel Roggen. "The Opportunity challenge: A benchmark database for on-body sensor-based activity recognition**."** *Pattern Recognition Letters* 34, No. 15, (2013), 2033-2042, https://doi.org/10.1016/j.patrec.2012.12.014.

37. Reiss, Attila, and Didier Stricker. "Introducing a new benchmarked dataset for activity monitoring." In 2012 16th international symposium on wearable computers, IEEE, (2012), 108-109. DOI: 10.1109/ISWC.2012.13.

38. Zeiler, Matthew D. "Adadelta: an adaptive learning rate method." arXiv preprint arXiv:1212.5701 (2012).

39. Krizhevsky, Alex, Ilya Sutskever, and Geoffrey E. Hinton. "Imagenet classification with deep convolutional neural networks." Advances in neural information processing systems 25 (2012), 1097-1105.

Persian Abstract

چکیده

تشخیص فعالیتهای انسان، یکی از موضوعات تحقیقاتی رایج در سالهای اخیر بوده است. توسعه سریع تکنیک های یادگیری عمیق به محققان در دستیابی موفقیت در این زمینه بسیار کمک کرده است. اما محققان معمولاً از توزیع ویژگی ها در فضای مختصات با وجود تأثیر قابل توجه آن بر وضعیت همگرایی شبکه و طبقه بندی فعالیت ها چشم پوشی می کنند. این مقاله یک روش ترکیبی مبتنی بر یادگیری متمرکز مختصات فازی و تابع هزینه ترکیبی، برای غلبه بر محدودیت توضیح داده شده پیشنهاد می کند. یادگیری مختصات متمرکز فازی باعث می شود که ویژگی ها به صورت پراکنده در تمام چهاربخش از فضای مختصات پخش شوند. به همین دلیل، زاویه بین بردارهای ویژگی کلاسهای فعالیت توجهی افزایش می یابد. علاوه بر این ، یک تابع هزینه ترکیبی برای افزایش قدرت تشخیص در روش پیشنهادی، ارائه شده است. آزمایشات ما بر روی مجموعه داده های OPPORTUNITY و PAMAP 2 انجام شده است. روش پیشنهادی با شش روش یادگیری ماشین و سه روش یادگیری عمیق برای تشخیص فعالیت مقایسه شده است. نتایج تجربی نشان داده است که روش پیشنهادی به دلیل شناسایی ویژگی های تبعیض آمیز بهتراز تمامی روش های مقایسه ای عمل می کند. روش پیشنهادی با موفقیت میانگین دقت را تا ۱۷.۰۱ درصد و ۳.۹۶ درصد درمقایسه با روشهای یادگیری عمیق، به ترتیب بر روی مجموعه داده های PAMAP2 و OPPORTUNITY بهبود بخشیده است.

International Journal of Engineering

Effects of Drilling Mud Properties on Hydrate Dissociation Around Wellbore during Drilling Operation in Hydrate Reservoir

Q. Li[a], Q. Li*[b]

[a] *School of Energy Science and Engineering, Henan Polytechnic University, Jiaozuo, China*
[b] *College of Science, Heilongjiang Bayi agriculture University, Daqing, China*

A B S T R A C T

Natural gas hydrate is a potential energy source in the near future, and its commercial development can alleviate the global energy crisis. Disturbance of drilling mud invasion on hydrate reservoir can lead to hydrate dissociation, affecting wellbore stability while drilling in clayey silt hydrate reservoirs. In this work, the coupled thermo-hydro-chemical finite element model was developed, and influences of drilling mud properties on hydrate dissociation were investigated. The obtained results show that the hydrate dissociation range around wellbore widens as the mud temperature increases. The final dissociation range caused by drilling mud invasion nonlinearly increases from 3.83cm to 10.57cm when the mud temperature has increased from 17.25℃ to 21.25℃. Therefore, the drilling mud needs to be cooled during preparation in platform. In addition, dissociation range narrows as the bottom-hole pressure increases. Dissociation range decreases from 12.18cm to 7.46cm when the bottom-hole pressure is increased from 14.50MPa to 17.00MPa. Thus, the overbalanced/near-balanced drilling operation is preferred during drilling in hydrate reservoirs, and the underbalanced drilling operation is not recommended. Moreover, the increase of mud salinity exacerbates hydrate dissociation in the near-wellbore region. In view of the prevention of hydrate dissociation in the near-wellbore, it is necessary to confect the drilling mud that with appropriate salinity while drilling in hydrate-bearing sediments.

doi: 10.5829/ije.2022.35.01a.13

1. INTRODUCTION

Natural gas hydrates are ice-like crystalline that is formed by water and gas molecules at low temperature and high pressure [1-3]. Some investigations found that organic carbon stored in gas hydrates is about twice as much that in conventional fossil energy sources [2, 4-6]. Moreover, it is estimated that natural gas hydrates discovered in the South China Sea are about 64 billion tons of oil equivalent [4], which is only about 80% of China's total proved reserves. Natural gas hydrates are bound to be an important potential replacement energy source in China in the near future. Therefore, it is of great significance to carry out numerical and/or experimental investigations related to gas hydrates to ensure energy supply and energy security.

Four strategies are usually used for gas production from hydrate reservoir: (1) Depressurization [7], to decrease the reservoir pressure below the phase equilibrium pressure; (2) Thermal stimulation [8], to heat the reservoir above the phase equilibrium temperature with injection of hot water, hot brine or steam; (3) Thermodynamic inhibitor injection, to inject chemicals [9]; and (4) combination of these above strategies [10]. Among them, the last one appears to be the most efficient. In the past two decades, several field trials have been conducted [11], but most have failed for different reasons. Even so, current research on hydrate development is generally in the stage of theoretical investigation and laboratory exploration, its commercial development still has a long way to go.

Up to now, investigations related to hydrate development mainly focus on the optimization of

Corresponding Author Institutional Email: B16020083@s.upc.edu.cn
(Q. Li)

production strategies. Li et al. [12] explored the production behavior when horizontal wellbore are used to develop hydrate deposits in the northern South China Sea. The investigation found that current production methods are unable to achieve the goal of commercial development of natural gas hydrates. Wang et al. [13] evaluated the gas production potential of hydrate reservoir in the South China Sea by depressurization. The investigation results showed that the maximum gas production rate was only 9500m³/d, which was far lower than the goal of commercial development offshore. Feng et al. [14] evaluated the effect of well configuration on hydrate dissociation behaviors when depressurization and thermal stimulation methods were simultaneously used. The simulation results indicated that the horizontal wellbore was more efficient for development of hydrate reservoirs. Overall, these studies are beneficial to understand the gas production behavior during development with different strategies. However, almost all studies have proved that no matter which production strategy is adopted, it is difficult to realize its large-scale exploitation. Therefore, if the old development ideas were not broken through, the road to commercial development must be long and difficult.

Accelerating dissociation of gas hydrates in reservoir is the focus for development of natural gas hydrates. However, hydrate dissociation around wellbore while drilling in hydrate reservoirs will worsen the borehole collapse, affecting drilling safety [15]. Therefore, inhibiting excessive hydrate dissociation in the near-wellbore region is an important idea for ensuring wellbore integrity during drilling in hydrate reservoir. However, the reality is that most studies related to hydrate dissociation kinetics concentrate on the effect of inhibitors in drilling fluid on phase equilibrium conditions. Sensitivity analysis of dissociation status of hydrate around wellbore during the drilling operation is scarce now. Fereidounpour and Vatani [16] developed the polyacrylate drilling fluid to prevent hydrate dissociation and wellbore instability caused by disturbance of drilling mud during drilling operation. The experimental results show that the designed drilling fluids can effectively reduce the possibility of hydrate dissociation in the near-wellbore region. Zhao et al. [17] investigated the effect of inhibitors in water-based drilling fluid on hydrate dissociation during drilling operation. They found that all of thermodynamic hydrate inhibitors can affect hydrate dissociation. Moreover, the investigation showed that the combination of 0.1wt% polyvinyl pyrrolidone and 0.5wt% soybean lecithin exhibited the best inhibition effect. Therefore, it is of great engineering significance to carry out investigation on hydrate dissociation around wellbore during drilling in hydrate reservoirs. Moreover, conduction of relevant scientific research can provide theoretical premise for the

design and optimization of the corresponding drilling operation.

In the present work, a numerical simulation model for investigating hydrate dissociation around wellbore during drilling operation is developed. Based on this, influences of mud properties (such as mud density and temperature) on hydrate dissociation caused by drilling mud disturbance are then investigated. The aim of this work is to provide reference for in-depth understanding the mechanism of wellbore instability in hydrate reservoirs.

2. FUNDAMENTAL THEORY

During drilling in hydrate reservoir, mud temperature is usually higher than the initial reservoir temperature. Besides, mud pressure is generally close to the initial pore pressure. In this case, disturbance of drilling mud is detrimental to stability of natural gas hydrates around wellbore, resulting in serious hydrate dissociation. Moreover, the dissociation products of hydrates enter the wellbore and change the bottom-hole pressure, affecting drilling safety [18]. Considering the fact that hydrate dissociation caused by drilling mud disturbance around wellbore is a complex process involving seepage, heat transfer and phase change [19], relevant fundamental theories should be clarified.

2. 1. Mass Conservation Equations   The continuity equations for methane gas, water and hydrate in hydrate reservoir can be expressed by Equations (1), (2) and (3), respectively.

$$-\nabla \cdot \left(\varphi \rho_g S_g v_g \right) + m_g + q_g = \frac{\partial (\varphi \rho_g S_g)}{\partial t} \qquad (1)$$

$$-\nabla \cdot \left(\varphi \rho_w S_w v_w \right) + m_w + q_w = \frac{\partial (\varphi \rho_w S_w)}{\partial t} \qquad (2)$$

$$-\nabla \cdot \left(\varphi \rho_h S_h v_s \right) - m_h = \frac{\partial (\varphi \rho_h S_h)}{\partial t} \qquad (3)$$

where φ, S and ρ indicate porosity (%), saturation (%) and density (kg/m³), respectively; m is the formation rate of hydrate or production rate of dissociation products (kg/s); q represents the source/sink terms of dissociation products (unitless); v is the velocity (m/s); t is time (s). In addition, the subscripts g, w and h represent methane gas, water and hydrate, respectively.

2. 2. Filtration Equations   The seepage of all fluids in the pores follows Darcy's law, which can be expressed as:

$$Q = -\frac{KA\nabla P}{\mu L} \tag{4}$$

where Q is the flow rate (m³/s); K is the permeability (m^2); P is the pressure (Pa); μ represents the fluid viscosity in reservoir (Ps·s); A is the cross-sectional area of the reservoir (m²); L is the length of reservoir (m).

Therefore, filtration equations of methane gas and water in hydrate reservoir can be written as the following equations, respectively:

$$\varphi S_g v_{rg} = -\frac{K_{rg}}{\mu_g}\left(\nabla P_g + \rho_g g\right) \tag{5}$$

$$\varphi S_w v_{rw} = -\frac{K_{rw}}{\mu_w}\left(\nabla P_w + \rho_w g\right) \tag{6}$$

where g is the gravitational acceleration (m/s²). The subscripts rw and rg represent the relative value of water and methane gas, respectively.

2. 3 Energy Conservation Equation   Hydrate dissociation is an endothermic reaction [20], which can affect the reservoir temperature. Besides, heat transfer and thermal convection occurred in the near-wellbore region during drilling operation are also two important factors affecting reservoir temperature. Therefore, the energy conservation equation can be written as

$$\nabla \cdot \left(\lambda_c \nabla T\right) - \nabla \cdot \left(\rho_g v_g H_g + \rho_w v_w H_w\right) + Q_{in} = \frac{\partial}{\partial t}$$
$$\left[(1-\varphi)\rho_r H_r + \varphi S_h \rho_h H_h + \varphi S_g \rho_g H_g + \varphi S_w \rho_w H_w\right] \tag{7}$$

where λ_c is the thermal conductivity of reservoir (W/(m·K)); H is the enthalpy (J/mol); T is the reservoir temperature (K); Q_{in} is external energy supplement (J).

2. 4. Stability of Methane Hydrate   Phase equilibrium equation of methane hydrate in Equation (8) is commonly preferred to determine hydrate dissociation or not in fresh water [21].

$$Log_{10}P_{eq} = 0.034T_{eq} + 0.0005T_{eq}^2 + 6.4804 \tag{8}$$

where P_{eq} and T_{eq} are the equilibrium pressure (Pa) and the equilibrium temperature (K), respectively.

The mud salinity is an important factor affecting the stability of natural gas hydrates [22]. Effect of drilling fluid salinity on the equilibrium temperature of methane hydrate can be determined by Equation (9).

$$\Delta T_{eq} = 2335 \cdot Con / M\left(100 - Con\right) \tag{9}$$

where Con is the mud salinity (wt%); M is the relative molecular weight of inhibitor (unitless).

3. NUMERICAL SIMULATION

3. 1. Simulation Model   As we all know, drilling operation in hydrate reservoir generally only lasts for a very short time. Hydrate dissociation during drilling in hydrate reservoirs only occurs in the near-wellbore region, so the model size does not need to be particularly large. Figure 1 shows the location and geometry of the investigation model. As shown in Figure 1, the simulation model is a long rectangular cuboid stratum. The cross section of the simulation model in the Y-Z coordinate plane is a square with a side length of 1.0m, the lateral (X-direction) model length is 20.0m; which is sufficient to simulate the hydrate dissociation in the near-wellbore region during drilling operation. In addition, the borehole size is approximately 0.1988m.

During drilling operation, one side (i.e., side A in Figure 1) of the simulation model directly contacts and interacts with the drilling fluid. On the other side (i.e., side B in Figure 1) of the model is the hydrate-bearing sediments far away from the borehole. The simulation model has been divided into 200 elements along its X direction. However, there is only one element in the Y direction and the Z direction, respectively.

3. 2 Boundary Conditions   As mentioned earlier, reservoir temperature and pore pressure are the two most important factors affecting the stability of natural gas hydrates. Therefore, two boundary conditions of mud temperature and bottom-hole pressure are defined on the left side of the simulation model (i.e., side A in Figure 1). Apart from this, no other boundary conditions are defined for the model.

3. 3 Reservoir Properties   Generally speaking, reservoir properties can be obtained by the logging data. The reservoir properties at site SH2 of the GMGS-1
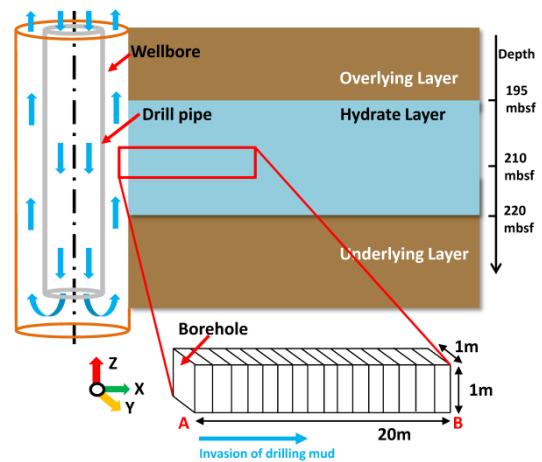
Figure 1. Location and geometry of the investigation model

project have been investigated by some experts. Figure 2 shows some reservoir properties required for investigation herein at site SH2 of the GMGS-1 project.

The exploration results indicate that hydrate reservoir at site SH2 of the GMGS-1 project is located in the depth range of 195mbsf (meaning "meters below the seafloor") to 220mbsf. Herein, the reservoir properties within the investigation model are intended to be represented by that at 210mbsf. Therefore, as can be seen from Figure 2, the reservoir porosity is 55.06%, the thermal conductivity is 1.308 W/(m·K), the hydrate saturation is 40.42%, and the reservoir temperature is 15.25℃. Besides, some other reservoir properties required to conduct the investigation are displayed in Tables 1, and 2 summarized some properties of drilling mud.

TABLE 1. Other hydrate reservoir properties required for investigation

Property	Value	Unit
Water depth	1232	m
Permeability	4.0	mD
Matrix density	2650	kg/m³
Pore pressure	15.50	MPa
Water saturations	59.58	%
Capillary pressure parameters：Van-Genuchten model	S_{ar}=0.24, n=1.84, a=10.0	
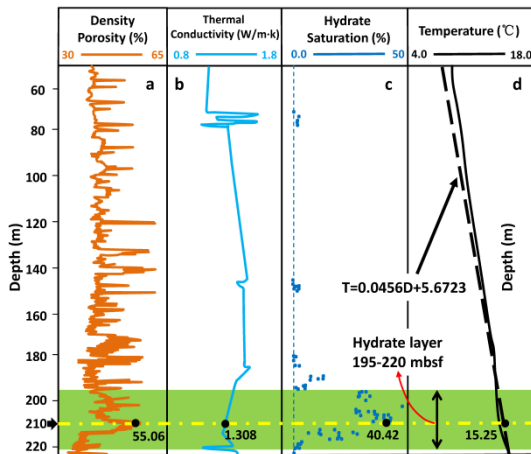
Figure 2. Some reservoir properties at site SH2

TABLE 2. Properties of drilling mud

Property	Value	Unit
Mud temperature	17.25-21.25	℃
Bottom-hole pressure	14.50-17.00	MPa
Mud salinity	0, 15 and 30	wt‰
Total drilling time	10800	S

4. RESULTS AND DISCUSSION

4. 1. Disturbance of Drilling Mud on Hydrate Reservoir   Figure 3 shows the reservoir conditions at site SH2 of GMGS-1 project and the phase equilibrium conditions of methane hydrate. As can be seen from Figure 3, natural gas hydrates under reservoir conditions are stable, but changes of reservoir temperature and reservoir pressure caused by mud invasion can result in hydrate dissociation. In other words, changes of reservoir temperature and reservoir pressure in the near-wellbore region are the premise for investigation of hydrate dissociation. Therefore, variation of temperature distribution around wellbore caused by drilling mud invasion is firstly analyzed.

Figure 4 shows the evolution of temperature distribution around wellbore when the drilling mud temperature is 17.25℃. We can see from Figure 4 that the temperature disturbance range in the near-wellbore region gradually widens during drilling operation, but the disturbance effect gradually weakens. When the drilling operation lasted for 1h (i.e., 60min), the temperature disturbance front reached the position with a distance of 14.50cm from the borehole. However, the temperature
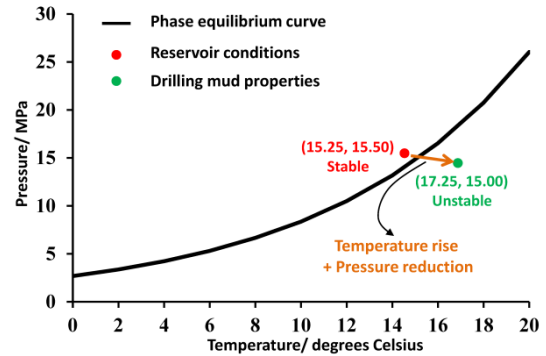
Figure 3. Reservoir conditions at site SH2 of the GMGS-1 project and the phase equilibrium condition
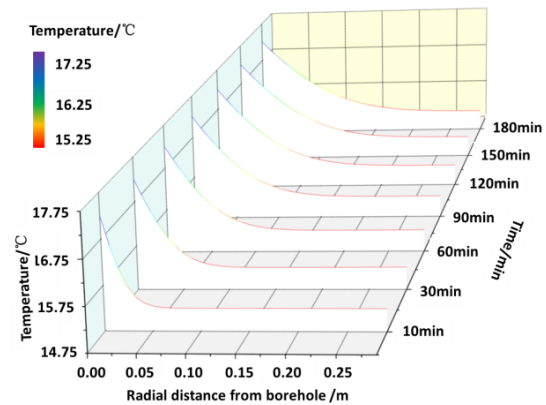
Figure 4. Evolution of temperature distribution in the near-wellbore region when the mud temperature is 17.25℃

disturbance range is only 22.35cm at the end of drilling operation. The temperature disturbance range during the first third of the drilling operation accounted for 64.88% of that for the entire drilling operation. Therefore, we can infer that if the drilling operation continues, the temperature disturbance range will continue to increase at a gradually decreasing rate.

Figure 5 shows the evolution of pore pressure within the near-wellbore region when the bottom-hole pressure is 15.00MPa. From Figure 5, one can see that the drilling mud invasion disturbs the pore pressure in the near-wellbore region severely. When the drilling operation started less than 2.0h, the pore pressure in almost the entire model had been disturbed by drilling fluid invasion. In this work, we define the situation when mud temperature is higher than the reservoir temperature as the positive temperature difference. In addition, due to mud circulation in wellbore, the mud temperature is usually higher than that of hydrate reservoir. Therefore, only the cases of positive temperature difference are investigated in this work. Figure 6 shows the dissociation range of natural gas hydrate when mud temperature is different.

4. 2 Effect of Mud Temperature on Hydrate Dissociation   Firstly, the basic characteristics of hydrate dissociation around wellbore during drilling operation are analyzed in this section. From Figure 6, one can see that hydrate dissociation range around wellbore gradually widens at a decreasing rate at any mud temperature, which can be clearly illustrated by the decreasing curve slope. Taking the mud temperature of 21.25℃ as an example, dissociation front reached the position of 6.47cm away from wellbore axis after 1 hour of drilling operation. However, the final dissociation front only reached the position of 10.93cm from the wellbore axis. Therefore, it can be inferred that the dissociation range will also continuously widen if the drilling operation continues, but the dissociation rate will
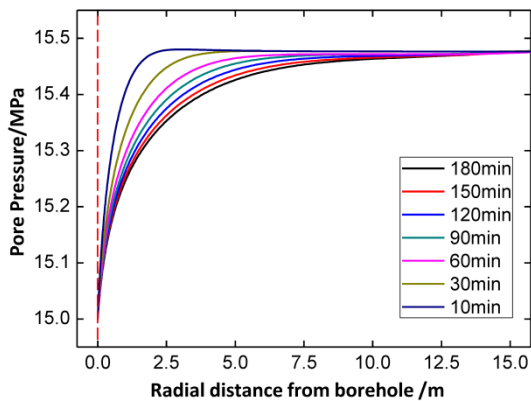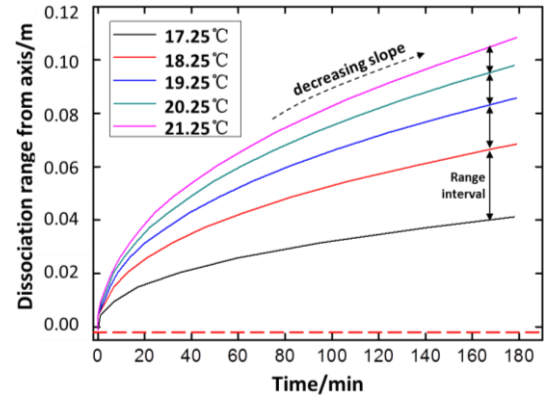
Figure 6. Effect of mud temperature on hydrate dissociation when mud pressure is 15.00MPa

gradually slow down as usual. This is mainly because that hydrate dissociation is an endothermic reaction, and hydrate dissociation can lead to the decrease of reservoir temperature near the dissociation front, hindering the further dissociation. In addition, the dissociation products (i.e., methane gas and water) can increase the pore pressure, which is another important factor hindering the further hydrate dissociation in pores.

Then, effect of mud temperature on hydrate dissociation around wellbore was analyzed. It can be seen from Figure 6 that mud temperature influences hydrate dissociation seriously while drilling in hydrate reservoir, hydrate dissociation range increases with an increase in mud temperature. When the mud temperature is 21.25℃, the final dissociation range is 10.93cm after drilling operation starts for 3 hours. However, when the mud temperatures are 20.25℃, 19.25℃, 18.25℃ and 17.25℃, the final dissociation ranges are 10.93cm, 10.02cm, 8.81cm, 7.07cm and 3.83cm, respectively. The hydrate dissociation range of the case when the mud temperature is 21.25 ℃ is 2.76 times the size when the mud temperature is 17.25℃. The main reason for this is that high positive temperature difference can result in severe heat transfer between the drilling mud and reservoir, and then reservoir temperature within the near-wellbore region will be severely disturbed. The severe disturbance of drilling mud to reservoir temperature results in a wide dissociation range of natural gas hydrate when mud temperature is high. Therefore, the drilling mud should be cooled when it is prepared on the platform, so as to avoid massive dissociation of natural gas hydrates around wellbore.

Moreover, we can also draw the conclusion from Figure 6 that with an increase in mud temperature, the difference in final dissociation range will gradually decrease for the same temperature difference (i.e., 1℃ herein). This can be clearly seen by the decreasing intervals between each curve in Figure 6. The decreasing intervals show the decreasing effect of mud temperature

Figure 5. Evolution of pore pressure within the near-wellbore region when the bottom-hole pressure is 15.00MPa

on an increase in hydrate dissociation range. In the future, effect of mud temperature on borehole collapse can be investigated. Besides, based on investigation of borehole collapse in hydrate reservoir, engineering measures for reducing the drilling risk can be proposed for mud temperature.

4. 3. Effect of Mud Density on Hydrate Dissociation
As we all know, the bottom-hole pressure can be directly simplified as the value obtained by multiplying mud density by reservoir depth. Therefore, in this section, drilling mud density is directly replaced by bottom-hole pressure, and its influence on hydrate dissociation around wellbore is discussed. Figure 7 displays the effect of bottom-hole pressure (drilling mud density) on hydrate dissociation within the near-wellbore region. As can be seen from Figure 7, hydrate dissociation around wellbore will gradually weaken with an increase in bottom-hole pressure (drilling mud density). When the bottom-hole pressure is 14.50MPa, the final dissociation range is 12.18cm. Such violent hydrate dissociation can pose a great threat to the strength of reservoir around wellbore, which is not conducive to maintaining the stability of borehole. However, when the bottom-hole pressure increases to 17.00MPa, the final dissociation range is only 7.46cm, which is only about 61.25% of that when bottom-hole pressure is 14.50MPa. According to investigation conducted by Li et al. [22], this is mainly because when the mud density is small, the pore pressure at the same location in the near-wellbore region around wellbore is relatively low. For the same ambient temperature (i.e., reservoir temperature), lower ambient pressure (i.e., pore pressure) is not conducive to the stability of natural gas hydrates in pores.

In order to prevent uncontrolled hydrate dissociation, the research results can provide the reasonable suggestion for the design of drilling fluid density used in hydrate reservoir. It can be seen from the investigation results that high-density drilling mud is preferred for
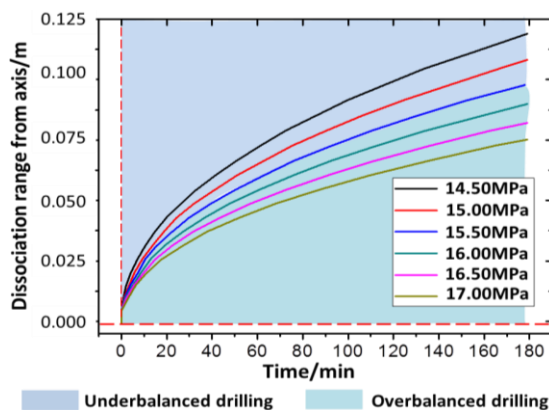
maintaining wellbore stability while drilling in the hydrate reservoirs. That is to say, in order to prevent serious borehole collapse caused by hydrate dissociation, the overbalanced drilling technology or near-balance drilling technology are recommended during drilling in hydrate reservoir. However, the underbalanced drilling operation can result in serious hydrate dissociation in clayey silt hydrate reservoirs, which may lead to the borehole collapse with the near-wellbore region. Therefore, the underbalanced drilling technology is not recommended during drilling hydrate reservoirs. Furthermore, in the future, method for determination of the safe mud weight window with considering hydrate dissociation can be explored by mechanical experiment.

4. 4. Effect of iInhibitor Concentration on Hydrate Dissociation
Hydrate inhibitors are usually used to control hydrate formation in borehole annulus or submarine pipeline for flow safety. Herein, we want to investigate the influence of inhibitor on hydrate dissociation, not on hydrate formation. NaCl is one of the most commonly mentioned inhibitors. The influence of NaCl solution concentration on hydrate dissociation around wellbore is investigated in this section. Therefore, inhibitor concentration can be considered as the mud salinity here. The effect of inhibitor on hydrate dissociation is essentially achieved by affecting its dissociation kinetic conditions. However, it is sometimes difficult to directly determine the phase equilibrium conditions for any inhibitor concentrations. Just as Figure 8 shows, a method for quantitatively determining the effect of inhibitor on phase equilibrium conditions of methane hydrate is presented. First of all, it is necessary to determine the decrease in phase equilibrium temperature caused by inhibitor addition according to Equation (7). Then, the phase equilibrium pressure can be determined by combining the calculated phase equilibrium temperature by Equation (8) through


Figure 7. Effect of mud density on hydrate dissociation when the mud temperature is 21.25℃
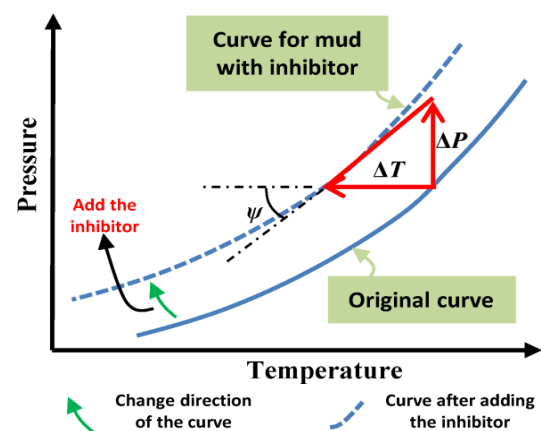
Figure 8. Method for determining effect of inhibitor (NaCl) on phase equilibrium conditions

trigonometric function. By this method, the phase equilibrium conditions for any inhibitor concentrations can be determined rapidly.

Figure 9 displays the effect of inhibitor concentration on hydrate dissociation during drilling in hydrate reservoir. As can be seen from Figure 9, hydrate dissociation occurs more and more violently with an increase in inhibitor concentration. The final hydrate dissociation range is only about 3.83cm when the inhibitor concentration is 0wt% (i.e., fresh water is used as the drilling mud). However, the dissociation range reaches 8.72cm when the inhibitor concentration has increased to 30wt%, which is 2.28 times the dissociation range when fresh water is used as the drilling mud. The influence mechanism of inhibitor concentration on hydrate dissociation around wellbore in drilling operation has been revealed in literature [21]. According to Zhao et al. [21], we know that the main reason for this is that inhibitors can reduce the range of the stable area (i.e., the upper left part of Figure 3) in the hydrate phase diagram, making the formation of naturals gas hydrates more difficult. On the contrary, addition of inhibitor can expand the range of unstable area, which makes the hydrate dissociation occurs more easily.

In spite of the fact that proper increase in inhibitors in the drilling mud can inhibit the formation of natural gas hydrates within the wellbore, which is beneficial to well control during the drilling operation. However, excessive concentrations of inhibitors can not only lead to violent hydrate dissociation and severe borehole collapse, but also may cause malignant corrosion of the casing string and affect subsequent operations. Therefore, a reasonable inhibitor concentration should be proposed according to the requirements of drilling operation, rather than an arbitrary concentration. In addition, in the future, effect mechanism of different hydrate inhibitor can be experimentally explored to facilitate the optimization of inhibitor concentration.
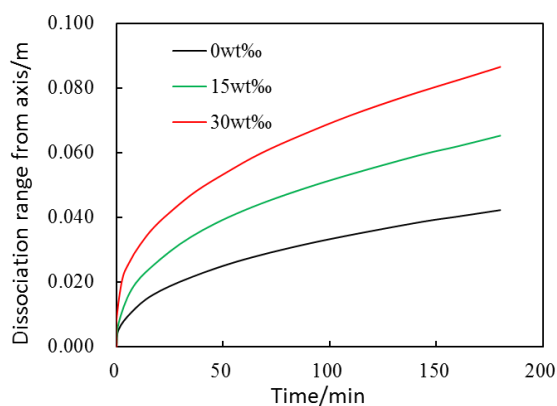
Figure 9. Effect of inhibitor concentration in drilling mud on hydrate dissociation when the mud temperature and bottom-hole pressure are 17.25°C and 15.00MPa respectively

5. CONCLUSIONS

Borehole collapse caused by hydrate dissociation in drilling operation endangers drilling safety. In this study, dissociation characteristics of natural gas hydrates around wellbore in drilling operation was explored with finite element model, and the influence of various factors on hydrate dissociation was also investigated. The obtained results demonstrate that stability of gas hydrates in near-wellbore region can be affected by drilling mud invasion through disturbing reservoir temperature and pore pressure. In drilling operation, hydrate dissociation weakens with an increase in mud density. However, an increase in drilling fluid temperature and inhibitor concentration in drilling fluid will aggravate the dissociation of gas hydrates around wellbore. Therefore, in order to weaken the influence of uncontrollable hydrate dissociation on borehole stability during drilling operation, it is effective to cool the drilling fluid or increase the drilling mud density. Besides, adding hydrate stabilizer to drilling fluid or reducing the inhibitor concentration in drilling fluid is also a desired method.

6. ACKNOWLEDGEMENTS

7. REFERENCES

1. Dvoynikov, M. V., Nutskova, M. V., Blinov, P. A. "Developments Made in the Field of Drilling Fluids by Saint Petersburg Mining University" *International Journal of Engineering, Transactions A: Basics,* Vol. 33, No. 4, (2020), 702-711. DOI: 10.5829/IJE.2020.33.04A.22

2. Klar, A., Soga, K., Ng, M. Y. A. "Coupled deformation-flow analysis for methane hydrate extraction" *Géotechnique,* Vol. 60, No. 10, (2010), 765-776. DOI: 10.1680/geot.9.P.079-3799

3. Shankar, U., Sain, K., Riedel, M. "Assessment of gas hydrate stability zone and geothermal modeling of bsr in the Andaman Sea" *Journal of Asian Earth Sciences,* Vol. 79, (2014), 358-365. DOI: 10.1016/j.jseaes.2013.10.021

4. Lu, S. M. "A global survey of gas hydrate development and reserves: Specifically in the marine field" *Renewable & Sustainable Energy Reviews,* Vol. 41, No. 4, (2015), 884-900. DOI： 10.1016/j.rser.2014.08.063

5. Gai, X. R., Sánchez, M. "A geomechanical model for gas hydrate-bearing sediments" *Environmental Geotechnics,* Vol. 4, No. 2, (2017), 143-156. DOI: 10.1680/jenge.15.00050

6. Yan, C., Cheng, Y., Li, M., Han, Z., Zhang, H., Li, Q., Teng, F., Ding, J. "Mechanical experiments and constitutive model of natural gas hydrate reservoirs" *International Journal of Hydrogen Energy,* Vol. 42, No. 31, (2017), 19810-19818. DOI: 10.1016/j.ijhydene.2017.06.135

7. Ahmadi, G., Ji, C. A., Smith, D. H. "Production of natural gas from methane hydrate by a constant downhole pressure well" *Energy Conversion and Management*, Vol. 48, No. 7, (2007), 2053-2068. DOI: 10.1016/j.enconman.2007.01.015

8. Yao, Y., Wei, M., Kang, W. "A review of wettability alteration using surfactants in carbonate reservoirs" *Advances in Colloid and Interface Science,* Vol. 294, (2021), 102477. DOI: 10.1016/j.cis.2021.102477

9. Liu, X., Jiang, R., Li, J., Huang, W. "Characteristics of Shale Gas Reservoir in Jiyang Depression and its Significance in Drilling and Exploitation" *International Journal of Engineering, Transactions B: Applications,* Vol. 33, No. 8, (2020), 1677-1686. DOI: 10.5829/IJE.2020.33.08B.27

10. Poplygin, V. V., Pavlovskaia E. E. "Investigation of the Influence of Pressures and Proppant Mass on the Well Parameters after Hydraulic Fracturing" *International Journal of Engineering, Transactions A: Basics,* Vol. 34, No. 4, (2021), 1066-1073. DOI: 10.5829/IJE.2021.34.04A.33

11. Wang, Y., Lang, X., Fan, S., Wang, S., Yu, C., Li, G. "Review on enhanced technology of natural gas hydrate recovery by carbon dioxide replacement" *Energy&Fuels,* Vol. 35, No. 5, (2021), 3659-3674. DOI:10.1021/acs.energyfuels.0c04138

12. Li, G., Moridis, G. J., Zhang, K., Li, X. S. "Evaluation of gas production potential from marine gas hydrate deposits in shenhu area of south china sea" *Energy & Fuels,* Vol. 24, No. 11, (2010), 6018-6033. DOI: 10.1021/ef100930m

13. Wang, Y., Feng, J, Li, X., Zhang, Y., Li, G. "Evaluation of gas production from marine hydrate deposits at the GMGS2-site 8, pearl river mouth basin, South China Sea" *Energies,* Vol. 9, No. 3, (2016), 222. DOI: 10.3390/en9030222

14. Su, Z., Li, H., Wu, N., Yang, S. "Effect of thermal stimulation on gas production from hydrate deposits in shenhu area of the south china sea" *Science China Earth Sciences,* Vol. 56, No. 4, (2013), 601-610. DOI: 10.1007/s11430-013-4587-4

15. Zhao, X., Qiu, Z., Gao, J., Ren, R., Li, J., Huang, W. "Mechanism and effect of nanoparticles on controlling fines migration in unconsolidated sandstone formations" *SPE Journal,* Vol. 26, No. 1, (2021), 1-13. DOI: 10.2118/204474-PA

16. Fereidounpour, A., Vatani, A. "Designing a Polyacrylate Drilling Fluid System to Improve Wellbore Stability in Hydrate Bearing Sediments" *Journal of Natural Gas Science and Engineering,* Vol. 26, (2015), 921-926. DOI: 10.1016/j.jngse.2015.06.038

17. Zhao, X., Qiu, Z., Zhao, C., Xu, J., Zhang, Y. "Inhibitory effect of water-based drilling fluid on methane hydrate dissociation" *Chemical Engineering Science*, Vol. 199, No. 18, (2019), 113-122. DOI: 10.1016/j.ces.2018.12.057

18. Tabatabaee Moradi, S.S., Nikolaev, N. I. "Study of Bonding Strength at Salt-cement Interface During Cementation of Salt Layers" *International Journal of Engineering, Transactions B: Applications,* Vol. 34, No. 2, (2021), 581-586. DOI: 10.5829/IJE.2021.34.02B.32

19. Chen, D. C., Yao, Y., Fu, G., Meng, H. X., Xie, S. X. "A new model for predicting liquid loading in deviated gas wells" *Journal of Natural Gas Science and Engineering,* Vol. 34, (2016), 178-184. DOI: 10.1016/j.jngse.2016.06.063

20. Leusheva, E., Morenov, V., Tabatabaee Moradi S. "Effect of Carbonate Additives on Dynamic Filtration Index of Drilling Mud" *International Journal of Engineering, Transactions B: Applications,* Vol. 33, No. 5, (2020), 934-939. DOI: 10.5829/IJE.2020.33.05B.26

21. Zhao, X., Qiu, Z., Zhao, C., Xu, J., Zhang, Y. "Inhibitory effect of water-based drilling fluid on methane hydrate dissociation" *Chemical Engineering Science,* (2019) Vol. 199, 113-1232. DOI: 10.1016/j.ces.2018.12.057

22. Li, Q., Liu, L., Yu, B., Guo, L., Shi, S., Miao, L. "Borehole enlargement rate as a measure of borehole instability in hydrate reservoir and its relationship with drilling mud density". *Journal of Petroleum Exploration and Production,* Vol. 11, No. 3, (2021), 1185-1198. DOI: 10.1007/s13202-021-01097-2

Persian Abstract

چکیده

هیدرات گاز طبیعی یک منبع انرژی بالقوه در آینده نزدیک است و توسعه تجاری آن می تواند بحران جهانی انرژی را کاهش دهد. اختلال در تهاجم گل حفاری به مخزن هیدرات می تواند منجر به تفکیک هیدرات شود که بر پایداری چاه در حین حفاری در مخازن هیدرات سیلت رسی تأثیر می گذارد. در این کار، مدل المان محدود حرارتی-هیدروشیمیایی جفت شده توسعه داده شد و تأثیرات خواص گل حفاری بر تفکیک هیدرات مورد بررسی قرار گرفت. نتایج بدست آمده نشان می دهد که با افزایش دمای گل، محدوده تفکیک هیدرات در اطراف چاه حفاری گسترش می یابد. محدوده تفکیک نهایی ناشی از تهاجم گل حفاری به طور غیرخطی از 3.83 سانتی متر به 10.57 سانتی متر افزایش می یابد زمانی که دمای گل از 17.25 درجه سانتیگراد به 21.25 درجه سانتیگراد افزایش می یابد. بنابراین، گل حفاری باید در حین آماده سازی در سکو خنک شود. علاوه بر این، با افزایش فشار سوراخ پایین، محدوده تفکیک باریک می شود. هنگامی که فشار سوراخ پایین از 14.50 مگاپاسکال به 17.00 مگاپاسکال افزایش می یابد، محدوده تفکیک از 12.18 سانتی متر به 7.46 سانتی متر کاهش می یابد. بنابراین، عملیات حفاری بیش از حد متعادل/تقریباً متعادل در حین حفاری در مخازن هیدرات ترجیح داده می شود و عملیات حفاری متعادل توصیه نمی شود. علاوه بر این، افزایش شوری گل باعث تشدید تفکیک هیدرات در منطقه نزدیک به چاه می شود. به منظور جلوگیری از تفکیک هیدرات در حفره نزدیک چاه، لازم است هنگام حفاری در رسوبات هیدرات دار، گل حفاری را با شوری مناسب مخلوط کرد.

International Journal of Engineering

A New Multi-valued Logic Buffer and Inverter using Metal Oxide Semiconductor Field Effect Transistor Based Differential Amplifier

A. Mokhtari, P. Kabiri*

School of Computer Engineering, Iran University of Science and Technology, Tehran, Iran

P A P E R   I N F O

A B S T R A C T

The aim of this work is to assist the design of decenary Multi-Valued Logic (MVL) circuits. This paper reports a work, in which, analog voltage-based circuitry is used to design MVL circuits. In this paper, some analog circuits are reported as elements that can be used in Multi-Valued Logic (MVL) circuitry. This article reported a Metal Oxide Semiconductor Field Effect Transistor (MOSFET)-Based Differential Amplifier (MBDA) as a key element in designing decenary MVL arithmetic unit. Operating voltage range and linearity of the gain are two important characteristics of this element. The operating voltage range for the MBDA is 0V to 5.5V as a output voltage.The achieved linear gain is within the range of 0.1V to 5.3V. Analog inverter and correction buffer circuits are reported based on MBDA. Analog inverter will be used in computational and logical decenary MVL circuits. The correction buffer is designed as an element to eliminate noises and signal drift at the output of the MVL gates and throughout data transfer.

doi: 10.5829/ije.2022.35.01a.14

1. INTRODUCTION

Silicon is now almost at its maximum speed and efforts are underway to find a suitable way to increase its speed even further. Some researchers believe in speeding up the technology by means of increasing number of processing cores and parallel processing. Other researchers are trying to use other materials, such as GaNi, to speed up digital circuits. However, one of the best ways to increase speed use of multi-valued logic circuits can be a desired solution. Using this method, more each digit can hold more data and, the trope of the circuit and consequently the speed of the circuit is increased. Additionally, increased data density can reduce the area of the circuit, and dependent on the type of design, it is possible to reduce the power consumption of the circuit as well. In other words, by using multi-value circuits, in addition to increasing the circuit speed, it is possible to reduce the area and power consumption simultaneously.

This research is a part of a larger project aimed to build arithmetic and logic units based on decenary Multi-

Valued Logic (MVL). Since arithmetic circuitry was designed using voltage-based analog circuits, a differential amplifier with linear gain was required in the design. Linearity of the gain within the maximum possible voltage range was important for the design to be able to provide uniform voltage levels within the most part of the power supply voltage range.

Initially, reported work on similar technologies as the one used in the reported work, i.e., TSMC 180nm, was studied. Hence, a number of reported amplifier designs using 180nm technology were studied. Since none of the reported designs matched the required specifications needed, it was decided to design a new differential amplifier to satisfy the decenary MVL circuits design requirements.

Based on this differential amplifier, an analog inverter was designed to support designed for the decenary MVL arithmetic and logic circuitry, as well as in designing a correction buffer to eliminate noises and signal drift at the output of the MVL gates and throughout data transfer.

In this paper, a MOSFET-Based Differential Amplifier

*Corresponding Author Institutional Email: peyman.kabiri@iust.ac.ir (P. Kabiri)

(MBDA) circuit with a new composition is presented. MVL circuits are also provided using analog instead of logic switches. This method reduces the complexity of the circuit, the number of transistors and the number of power supplies required in the circuit design. The reported circuits that are presented operate in 10 levels and are designed with uniform levels in terms of voltage. The goal is to design an amplifier with the following specifications:

1. Operating range 0V to 4.5V (decenary levels with 0.5V distance between two levels).
2. Linear gain close to the voltage range between 0V to 4.5V.
3. Amplifier with the lowest number of transistors (9 transistors are used in the reported design)
4. Amplifier with the minimum delay (higher than 100MHz)

The reported inverter and correction buffer are designed based on MBDA.

It is era of rapid change for the computing technology. Digital circuits, such as other parts of the computing technology, need fundamental changes.

2. RELATED WORKS

Many researchers are trying to make these changes in a variety of ways. Multi-Valued Logic (MVL) is an attractive research method in this area. In recent years, many researches were engaged in the field of MVL circuit design. Researchers have used various methods and technologies to implement MVL circuits. However, the main point in the reported researches demonstrated the use of switch logic. In the following, some of these articles and reported methods will be discussed. The reported works are presented in 5 categories.

1. Organic material
2. CNTFET
3. 180nm CMOS
4. Single electron transistor
5. Other technologies

In a reported work by Kim et al. [1], a ternary inverter based on a p-n lateral hetero structure is proposed. In this research, the logical values attributed to the inverter include $(0, ^1/_2, 1)$. Length of this inverter is 550µm and the power supply voltage is 10V. Having unequal input/output voltages is a disadvantage for this inverter. As an advantage, the designed circuit uses different silicon layer arrangements to produce a 3-level inverter. In this research, 2D finite-element numerical simulator software was used to simulate the gate. As an example for a new technology, Jeon et al. [2], reported ternary logic circuit based on organic material. In this paper, negative differential resistance/transconductance is the

key to the circuit design. Introduced circuits are based on Ambipolar Organic FET (AOFET). The main drawback of this design is the difference between the input and output voltage ranges of the circuit. The input voltage variation is between 0 and 200V while the output voltage variation is between 0 and 50V. Davari Shalamzari et al. [3], reported new quaternary multiplexer, half adder and multiplier using CNTFET. In this paper, designed circuits are compared against similar technologies in terms of power consumption and latency. Results show improvement in terms of circuit delay but power consumption has increased instead. The simulation was performed using HSPICE software and 32nm CNTFET library. In a reported work by Hosseini and Etezadi [4], a novel ternary MVL comparator was introduced that is expandable to a quaternary one. Using CNTFET, the reported MVL comparator was designed and simulated in both ternary and quaternary modes. Later on, Uternary function was extended in to a quaternary function using only 4 transistors. This design was simulated using Stanford 32nm CNTFET library in HSPICE. In a reported work by Jaber et al. [5], a ternary half adder and multiplexer was introduced. These circuits were designed based on 32nm CNTFET and they were simulated in HSPICE simulator. In the reported work, the ternary multiplexer's output current was supplied by one of the inputs. The cascaded number of gates would cause problems such as false voltage levels. Jaber et al. [5], proposed a half-adder where designed based on these multiplexers.

In a reported work by Hosseini and Roosta [6], ternary buffer, inverter, STNOR and STNAND circuits are introduced. In this paper, using HSPICE's CNTFET Stanford 32nm model and 0.9V power supply; they have reached to an operational frequency of 500MHz. In addition, Hosseini and Roosta [6] have compared reported results against similar reported works showing that power and latency were reduced. Chowdhury et al. [7], reported voltage mode NOR and MAX operators. The Max operator was designed using only 3 transistors. Using 2 more transistors, Chowdhury et al. [7] built a NOR operator. Designed circuits were simulated in HSPICE using 180nm library.

In other reported work by Saha and Pal [8], a circuit is proposed to convert ternary logic to binary logic. This circuit consists of 3 parts: Trit-to-Unary Decoder (TUD), Complete Unary Decoder (CUD) and Unary-to-Binary Converter (UBC). These 3 sections are arranged in series; therefore, the circuit delay is equal to the total delay of these sections. The proposed circuit was designed using TSMC 180nm model. Layout design and simulation is done using T-Spice. Simulation results showed that the circuit delay is 0.72ns and the power consumption of the

circuit at 500MTPS was 177.74µW. The circuit area was $13.77 \times 10^2 \mu m^2$ and 280 transistors were used in designing this circuit.

The Single Electron Transistor (SET) has low power consumption [9-11]. As an example, in a work reported by Gope et al. [12] a ternary Flip-Flop (FF) was designed. In this work, a completely different set of FF models were reported where the only problem was the use of large number of transistors in the design.

Sandhie et al. [13], reported ternary logic circuits based on GNRFET. In this reported work, the supply voltage was 1V and the distance between the 2 levels was 0.5V. Simulation is performed using HSPICE-GNRFET 16nm where STI and PTI gate circuits were built. STI and PTI gates were designed using 6 transistors and 2 transistors respectively. The STI gate was compared against a similar CNTFET model in terms of power consumption and latency. In both cases the proposed circuit showed improvement.

Other methods have been used to design and implement multi-valued circuits. For example, in the paper presented by Karmakar [14], a ternary inverter is built using quantum dot gate. The circuit model is designed based on Barkley Short Channel IGFET Model (BSIM) in VHDL. This paper presents 3 standard inverters Negative Ternary Inverter (NTI), Positive Ternary Inverter (PTI) and Standard Ternary Inverter (STI). Charjee et al. [15], reported a novel Random Access Memory (RAM) using MVL and fuzzy logic operators. In this paper, fuzzy interface system used with a limited number of logical steps and a 1x3 memristive crossbar array to develop a MVL-based RAM (MVLRAM). In the paper presented by Sharma and Kumre [16], a ternary arithmetic logic unit is presented. HSPICE's Stanford 32nm CNTFET model is used to design the circuits. The proposed operators include MUX, Adder, Subtractor, Multiplier and comparator. This article presents one of the most complete sets for logic and calculus operations.

Since the most important part of the article is about differential amplifiers, a number of the amplifiers provided will be also reviewed. An important feature of the amplifier in this paper is the linearity of the Voltage Transfer Characteristics (VTC).

In a reported work by Dvornikov et al. [17], a novel operational amplifier (Op-Amp) is reported. Reported Op-Amp designed based on 2 technological routes, "Inch-R/NJFET" and "Inch-P/PJFET" and simulated in LT spice CAD.

The simulation results at -197°C indicate the Op-Amp operates perfectly. Circuit power supply was 5V and current consumption was about 360µA. VTC simulated at -197°C and the linear part of graph is between -3V to 3V at the output.

In another work reported by Kuzmicz [18], a simple ultra-low power Op-Amp described. The reported Op-Amp designed in 22nm CMOS FDSOI technology with very low current consumption about 1.1µA at 0.8V power supply. In this research, 49 prototype chips tested at 0.8V supply and room temperature. Test results show the VTC graph is linear in whole power supply (0V to 0.8V).

In a research reported by Alam et al. [19], a capacitance to voltage converter is presented. This circuit was simulated using PSPICE model parameters based on standard 0.13µm CMOS process. Circuit power supply was 1.2V and the circuit combined capacitor network to the Op-Amp. VTC graph show the linear response from about -1V to 0.8V at the output.

In the paper presented by Raut et al. [20], a two-stage Op-Amp is designed using 180nm CMOS technology. The proposed Op-Amp gain is about 74.9dB and its bandwidth is 7.26 MHz. The reported Op-Amp has a classic design structure.

In another work presented by Dash et al. [21], an Op-Amp with 180nm CMOS technology is presented. One of the positive points of this Op-Amp is the low number of transistors used in this design. This Op-Amp is designed using only 8 transistors. The power supply of the circuit is 1.8V and the gain of the circuit is about 60dB.

Circuits and results presented in this paper are part of the design and results of a larger project. The main project consists of 3 main parts.

1. Designing a complete decenary (10-valued) logic with related circuits
2. Decenary memory circuit design
3. Decenary arithmetic circuits

The logic and memory sections are currently completed. For the computational part, it is necessary to design 3 basic circuits that are introduced in this article. This article is a continuation of previous research where novel decenary logic was presented. In the proposed logic, the voltage distance between 2 logic levels is considered to be 0.5V.

This paper presents elements for designing decenary MVL circuits. The reported elements designed and implemented using Metal Oxide Semiconductor Field Effect Transistor (MOSFET) transistors. In section 2, general characteristics of the proposed circuits will be explained. In section 3, the MBDA circuit will be presented which is a simplified differential amplifier design suitable for use in decenary MVL circuits. Later on, the introduction of the proposed analog inverter will be reported in section 4. In section 5, correction buffer circuit will be followed. The inverter is designed to be

analog and based on decenary MVL. Correction buffer is designed and provided to correct noise and drift errors in analog circuits within the designed circuitry. In the final section, conclusions and future work conclude the paper.

3. CIRCUIT SPECIFICATIONS

The proposed circuits are designed and simulated using the PSPICE's TSMC 180nm model [22]. The circuits have 2 supply voltages of 5.5V and -0.5V. These supply voltages are far from the transistor breakdown voltage.

For 180nm transistors, the breakdown voltage is approximately equal to 10V [23-25]. All the proposed circuits operate in analog mode and only the correction buffer circuit has a switching logic at its output. The voltage distance between the 2 levels is 0.5V. Logic level 0 is indicated by 0V and logic level 9 is indicated by 4.5V.

4. MOSFET BASED DIFFERENTIAL AMPLIFIER

A differential amplifier is a requirement for many analog operations. A number of reported differential amplifier designs with 180nm technology were tested; however, none of them satisfied specifications needed in the required decenary MVL circuit design [26-28].

Satisfying needed design requirements, a suitable amplifier had to have two necessary characteristics. Firstly, it should be able to operate in the whole range of 0V to 4.5V. Secondly, within this interval, the gain should be linear. In this application, the size of the gain is not as important as its linearity.

The reported works in this area either did not cover the voltage range required in the reported decenary MVL circuit designs [20, 21], or their gain was not linear enough [17-19].

For example, in an article submitted by Raut et al. [20], the gain circuit is excellent in terms of linearity, However, in terms of operating voltage range, the required voltage range is not provided. The operating voltage range in the provided amplifier is from -1.8V to 1.75V. In another reported work by Alam et al. [19], linear interval size of the amplifier gain is not enough. The reported linear interval is a little over 1.5V.

In decenary MVL circuits, linear gain ensures equal distances between logical levels at the output of the circuit.

Several logical conditions are required to define a differential amplifier behavior. The proposed circuit must have 2 inputs and 1 output. One of the inputs will be named positive and the other negative. Dealing with special operational conditions, operation of the proposed MBDA is set to the following special conditions. If the positive input voltage is greater than the negative input voltage, the output will be equal to the positive supply voltage. If the negative input voltage is greater than the positive input voltage, the output will be equal to the negative supply voltage. In other words, the output voltage is limited by the power supply.

The proposed MBDA circuit consists of 2 stages. Figure 1 shows the MBDA input stage, i.e., stage 1. The input stage is quite similar to other differential amplifiers. This stage is designed based on the current mirror circuit. Since gates Q1 and Q2 have the same voltages, the current passing through both transistors is the same. A small difference between the voltages of gates Q3 and Q4 causes the output voltage of the circuit to be switched high or low. These high and low signals are not strong enough and similar to the other differential amplifiers, there is a need for another circuitry stage to amplify weak high and low. In digital circuitry, weak signal is defined as a signal that is not a full swing. The same thing happens at the output of this circuit.

The easiest way to amplify these weak signals is to use a binary inverter. Stage 2 of the circuit is shown in Figure 2. The stage 2 of the circuit consists of 2 inverters and a capacitor. There are 2 reasons for using 2 inverters. First, an inverter is incapable of sharply switching to power supply voltage or ground. Second, increasing the W/L ratio requires a 2 layered circuit (to increase amplifier output current). Finally, the reason for the presence of capacitor C in the circuit is due to the destructive effect of the feedback. Differential amplifiers are usually biased with feedback. A feedback resistor is usually used to connect the output to the input. Due to the resistance path of the feedback and gate capacitor at the input, there is a delay in applying the feedback loop. This delay will cause the output of the Differential amplifier to oscillate. Capacitor C on the second stage of the circuit suffocates this oscillation. Figure 3 shows the complete MBDA circuit.
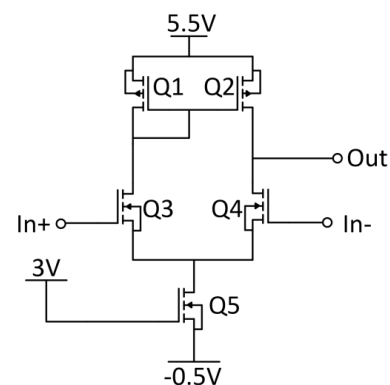
Figure 1. First stage of MBDA
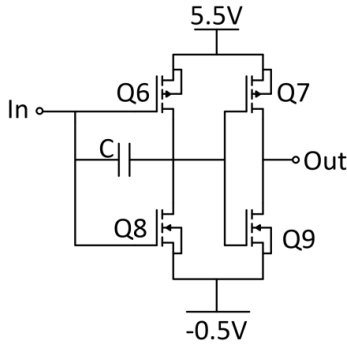
Figure 2. Second stage of MBDA
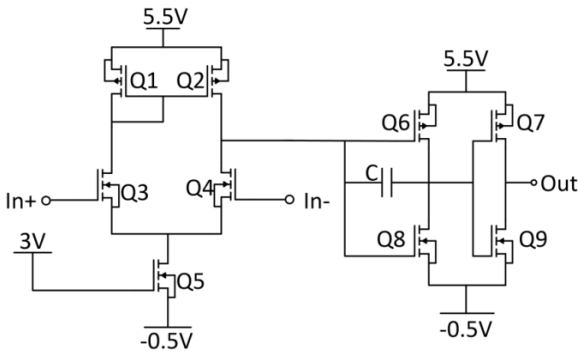
Figure 3. MBDA complete circuit

Validating functionality of the proposed MBDA, the MBDA circuit was simulated using 2 different input signals, i.e., non-inverting amplifier, Figure 4 and non-inverting summing amplifier Figure 5. In the non-inverting amplifier circuit, the circuit gain is 1. The simulation for the circuit is performed using 2 types of sinusoidal and stepped signal inputs.

Figure 6 shows the simulation results for these 2 types of input signals. In Figure 6 part (a) MVL signal sample is applied to the MBDA. In Figure 6 part (b), the sinusoidal signal is applied to the MBDA at 300 MHz (as its maximum frequency, the phase shift in it is quite

clear). Figure 6 part (c), a sinusoidal signal, with an appropriate frequency (30 MHz) for the design is applied to the MBDA.

Figure 5 is an extended version of Figure 4 with 2 inputs. The algebraic sum of the 2 input voltages will appear at the output of the circuit. Simulation results for these 2 types of inputs are presented in Figure 7. Simulation results show that the pseudo MBDA circuit behaves close to the performance of a normal MBDA. The output of a normal differential amplifier circuit with non-inverting amplifier bias is obtained using Equation (1).

The open-loop gain is also calculated from Equations (2) to (5).

$$V_{in} = \frac{R_2}{R_2 + R_F} \times V_{out} \tag{1}$$

$$V_o = \frac{-jX_c}{R_o - jX_c} AV_{id} \tag{2}$$

$$-jX_c = \frac{1}{j2\pi fc} \tag{3}$$

$$V_o = \frac{AV_{id}}{1 + j2\pi f R_o c} \tag{4}$$

$$A_{ol} = \frac{V_o}{V_{id}} \tag{5}$$

In the reported work, the open-loop gain is measured by means of simulation.

Simulation results closely follow Equation (1). Table 1 shows the W/L ratio of each transistor.

The static power consumption of a MBDA is 38.32μW and the MBDA latency at its worst is 3.28ns. MBDA Voltage Transfer Characteristics (VTC) open-loop is given in Figure 8. VTC graph is given in -40°C, 25°C and 80°C temperature.

4. 1. MBDA Specifications Since the reported MBDA circuit cannot be considered a normal differential amplifier, it cannot be easily compared against other

Figure 4. Non-inverting amplifier schematic
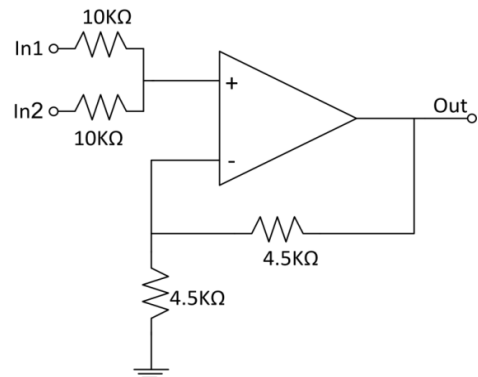
Figure 5. Non-inverting summing amplifier schematic
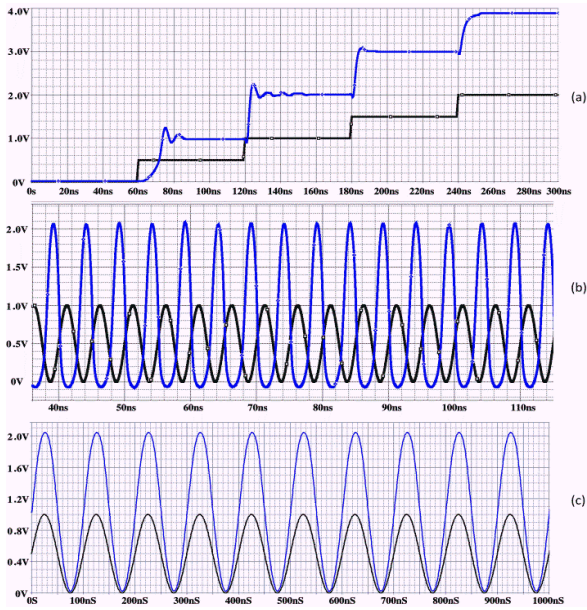
Figure 6. Non-inverting amplifier results (black: input, blue: output)
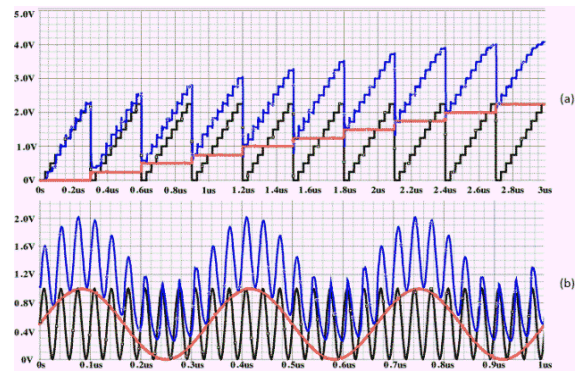
Figure 7. Non-inverting summing amplifier results (red & black: inputs, blue: output)

TABLE 1. Value of the W/L ratio of MBDA circuit transistors

	Q1	Q2	Q3	Q4	Q5	Q6	Q7	Q8	Q9
W/L	1.5	1.5	1.5	1.5	1.5	6	6	6	4.5

differential amplifiers. Difference between this MBDA and other similar differential amplifiers lays in the main purpose of its design. This element was not designed to produce power gain or for any other typical uses of a differential amplifier. The reported MBDA circuit specially designed for use in multi-valued circuits. However, as for comparison its analog specifications can be addressed.

The analog characteristics obtained from the simulation are presented in Table 2. Slew Rate (SR) and Unity Gain Bandwidth (UGB) values are reported in Table 2.

Although it will be very difficult to compare the reported MBDA against other reported ones, some of its specifications have been compared against 2 regular differential amps. Table 3 summarized the Open-loop characteristics of proposed MBDA. The comparison at 25 °C is given in Table 4 [17-20].

According to the linear gain of the MBDA, in Table 4, a series of comparisons with similar circuits are also provided. Table 4 compares variouus characteristics of the MBDA circuit provided against the other 4 differential amplifier designs. The proposed MBDA circuit performs better than other compared differential amplifiers in terms of UGB characteristics and linearity ratio along with linearity amplitude. In this research, amplitude and linearity ratio are very important for designing MVL circuits.
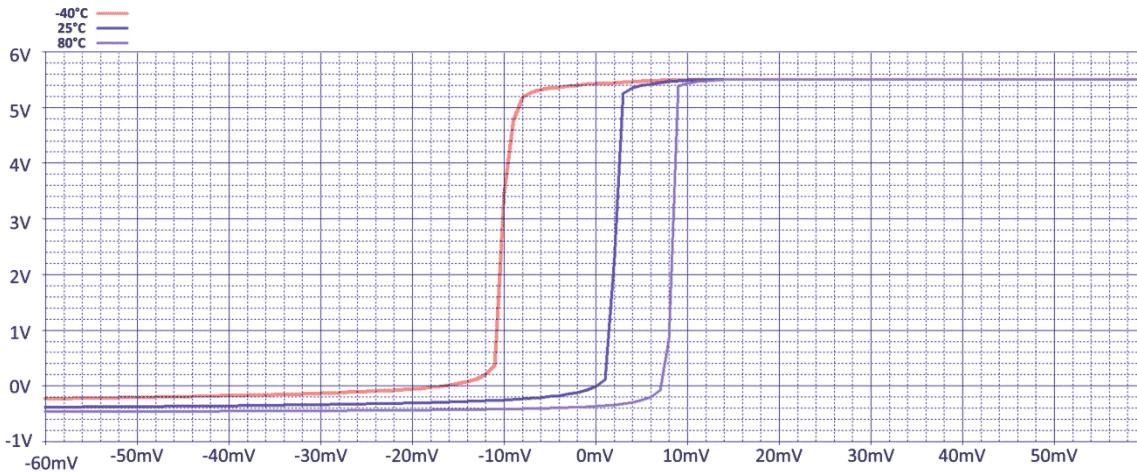
Figure 8. MBDA's open-loop VTC chart

TABLE 2. MBDA specifications

Temperature (°C)	Voltage (V)	Power Gain (dB)	SR (V/ns)	Settling time (ns)	Output swing (V)	UGB (MHz)
	2	40.53	0.33	5.9	1.96	330
-40	1.2	43.22	0.15	8	1.201	230
	1	45.38	0.1	9.9	1.01	200
	2	40.2	0.22	9	1.95	220
25	1.2	43.28	0.09	12.9	1.199	151
	1	44.68	0.07	14.95	1.02	140
	2	40.07	0.2	9	1.96	202
80	1.2	43.01	0.09	13.1	1.203	148
	1	44.17	0.06	16.15ns	1.01	121

TABLE 3. Open-loop characteristics of proposed MBDA

Supply Voltage (V)	5.5
Current Consumption (μA)	44
Power Consumption (μW)	242
Open-Loop Gain ratio – (dB)	423 – (52.528)
Process	TSMC 180 nm

4. 2. Experimental Results   Designing the differential amplifier started with 4 aforementioned goals in section 4. The first objective was to have the MBDA to operate within the range of 0V to 4.5V. Given the ability to produce output from about -0.5V to 5.5V, the first goal has been achieved.

The second goal was to have a linear gain within the range of 0V to 4.5V. This goal has also been met by

TABLE 4. Comparing the proposed MBDA against two other reported differential amplifier designs

	Gain (dB)	UGB (MHz)	Technology (nm)	Linearity Gain Region (LGR)	Power Supply	Linearity Ratio (LR)	Number of Transistors
Reported MBDA	52.528	220	180 (CMOS)	0.1V to 5.3V	-0.5V to 5.5V	%86.66	9
[20]	40	0.114	180 (CMOS)	Not specified.	-1.8V to 1.8V	Not specified.	8
[17]	97.1	Not specified.	6 (JFET)	-2.79V to 2.79V	-5V to 5V	%55.8	20
[18]	73.8	0.14	22 (CMOS)	0V to 0.8V	0V to 0.8V	%100	9
[19]	29.948	1.8	130 (CMOS)	-1V to 0.8V	-1.2V to 1.2V	%75	18

achieving a linear gain of about 0.1V to 5.3V. Two measurements were used to compare Gain's linearity in amplifiers. The first measurement is called the Linearity Gain Region (LGR). LGR is the area between start and end voltage points of the linear gain region of the open-loop VTC curve. LG measured in this circuit from is between 0.1V to 5.3V. This means that the voltage ranges for the linearity of the gain in the reported differential amplifier covers %86.66 of the power supply's voltage, i.e. Linearity Ratio or LR. The second measurement is the Maximum Difference (MD) from the straight line connecting the two LG points (Figure 9). In the reported MDBA, measured MD is about 400μV.

The third measurement is the number of transistors used in the circuit. Compared versus other reported circuits for the differential amplifier, the reported work uses 9 transistors are suitable.

Finally, the circuit delay is given in detail in Table 2. The delay is greater than expected, but does not rule out circuit design and delay is within acceptable limits, i.e., less than 100ns.

5. ANALOG INVERTER

Having built a MBDA circuit, design of an analog multi-valued inverter would be simplified. It is enough to implement the circuit in Figure 10, which is very similar to an inverting amplifier with a gain of 1. Inversion to the positive input voltage is done in MBDA. Figure 11 shows simulation results for the inverter with 3 input types. A decenary low-frequency input signal simulation result is presented in Figure 11 (a). Figure 11 (b) shows simulation results for the same input at 100 MHz (as high
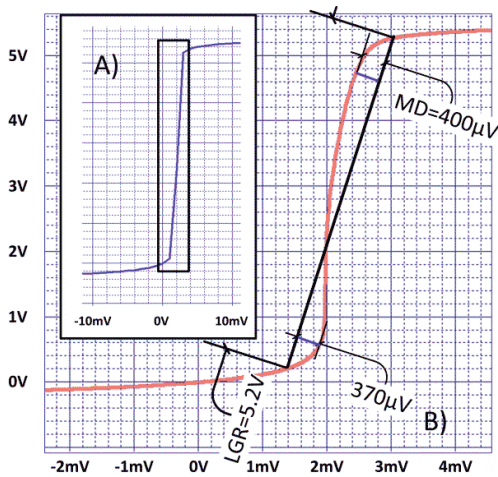
Figure 9. Gain linearity comparison A) zoom out, B) zoom in
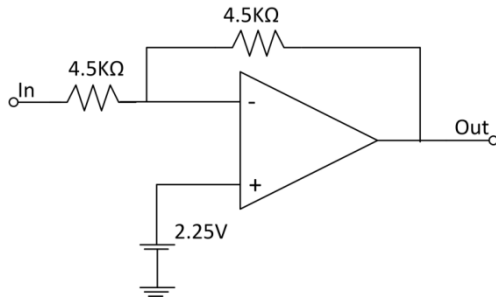
Figure 10. Analog inverter
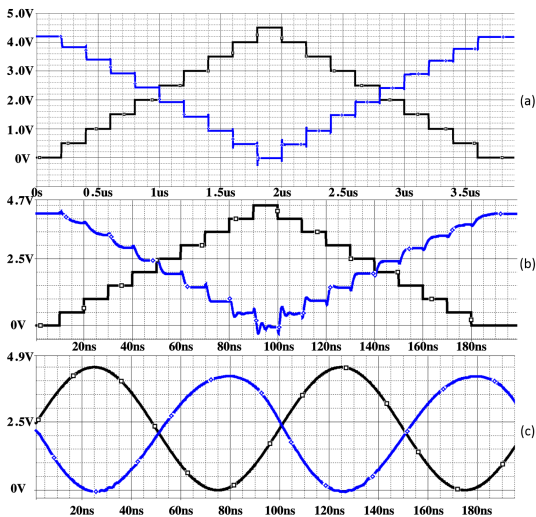
Figure 11. Analog inverter simulation results (black: input, blue: output)

frequency). Finally, Figure 11 (c) shows simulation results for a sinusoidal input signal, at 10 MHz (as low frequency). It should be noted that analog input is provided only to show its performance as an analog

circuitry.

The proposed analog inverter, with decenary logic input, is equivalent to a standard inverter in ternary logic. The proposed inverter will be used in computational circuits in a similar way to a differential amplifier. In the proposed circuit, the power consumption is greater than 70µW, and it is dependent on the circuit bias. The worst case delay is 10ns.

6. CORRECTION BUFFER

In the reported circuits, since the circuits are analog, effects of noise and drift are major drawbacks in the design. It is not possible to cascade the circuits due to the noise and drift effects. Noise effect occurs due to the absence of marginal noise and with high sensitivity. Drift means the displacement of the circuit's output voltage from the desired voltage. Inaccuracy of the physical values that determine circuit operation, such as, values of the resistors is the main reason for the drift. Correcting this problem, a correction buffer is required at the output of the circuit.

By means of this correction buffer, the possible voltage drift can be removed from the output. The correction buffer circuitry is designed based on the proposed MBDA. In the MBDA used for the correction buffer, the dumping C capacitor in Figure 2 is removed. Since these comparators do not have feedbacks and their outputs will not fluctuate due to capacitance-resistance delay. Figure 12 shows the correction buffer circuit in general.

On the output stage, the proposed correction buffer circuit behaves similar to an analog buffer. However, output of the circuit cannot reach -0.5V or 5.5V. This is due to the threshold voltage of the transistors that can vary in the maximum range of 0V to 5V. Threshold voltage is not an issue for the output of the proposed decenary circuitry, because the voltage range of the decenary circuit is 0 to 4.5V. Different types of input signals were applied to the circuit to demonstrate its performance. 3 types of input signals were applied to the proposed correction buffer circuit and simulation results are reported in Figure 13.

A Triangular signal, 2 sinusoidal signals and a decenary logic signal with a drift are applied to the circuit. The simulation results are reported. The output of each comparator is either 0V or 4.5V (dependent on the comparison situation sometimes it will be 4.5V and sometimes 0V).

Similar to a resistor ladder, due to the wired summing voltage resistance, each 4.5V adds 0.5V to the main output of the circuit. For every 0.5V increase in input voltage, the output of the comparator will change from
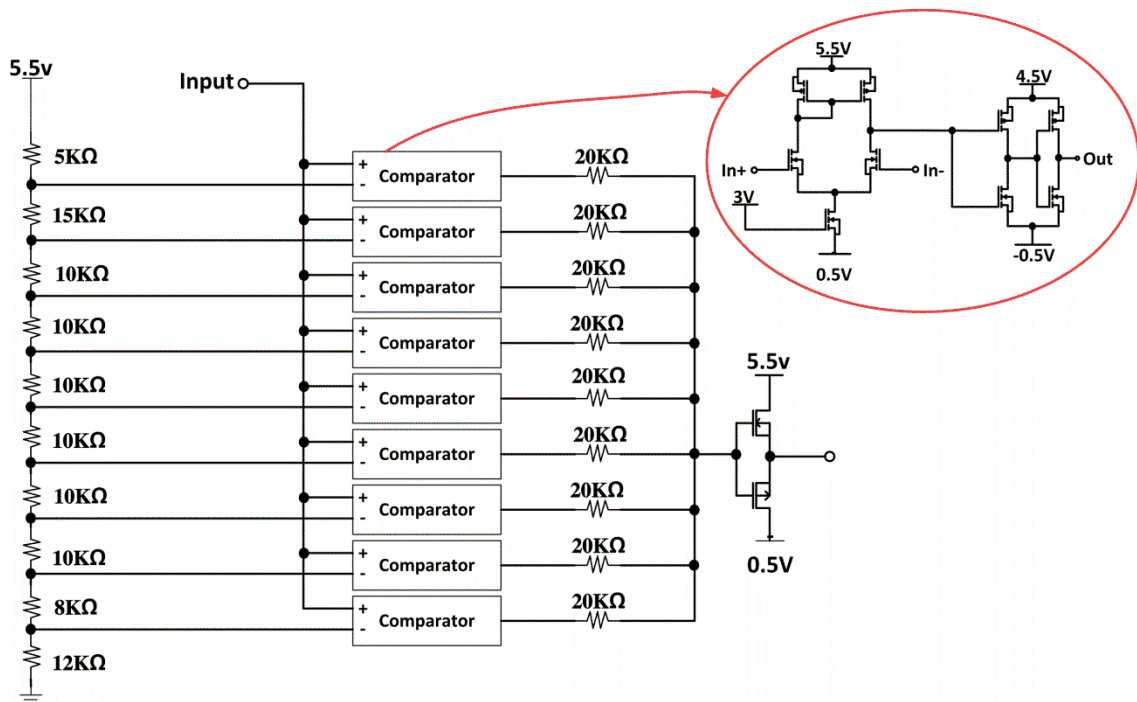
Figure 12. Correction buffer
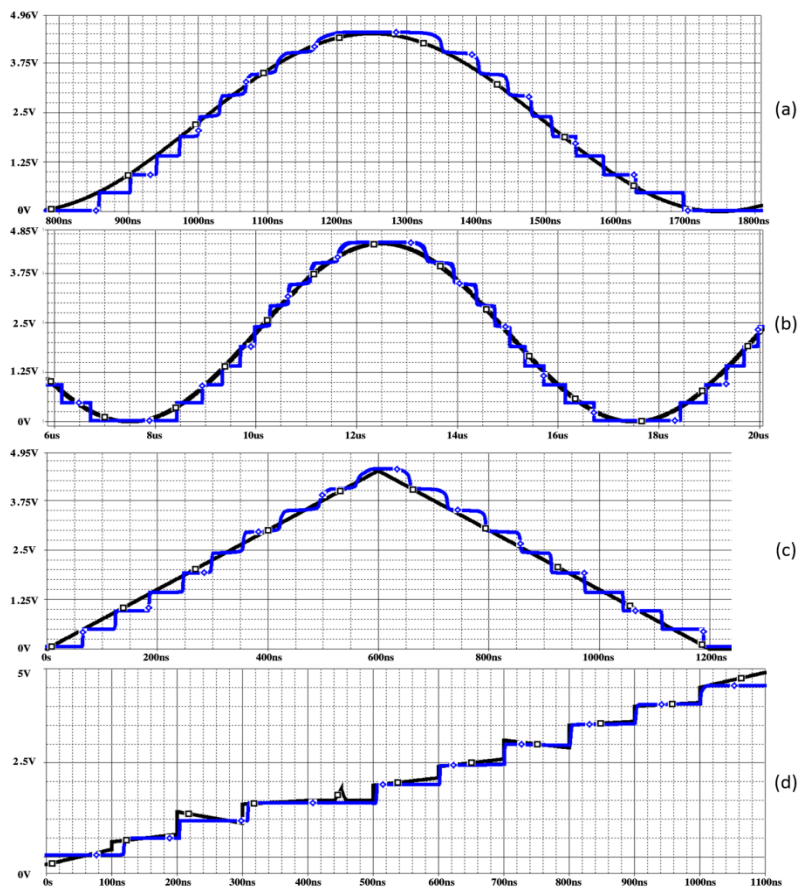


Figure 13. (a) High frequency sinusoidal signal (b) Low frequency sinusoidal signal (c) Triangular signal (d) Decenary signal results (black: input, blue: output)

0V to 4.5V. According to the simulations performed, this circuit functions as a quantizer in ADCs. The static power consumption of the circuit is about 272μW and is dependent on the resistors used in the circuit. Delay of the circuit is 20ns at its worst.

7. CONCLUSION AND FUTURE WORK

This article reports an ongoing work on the design of decenary logic circuits based on analog circuits. The goal of this research is to provide the elements needed to design MVL computational circuits. A MBDA was introduced in this paper. Contributions in MBDA circuit include the operational voltage range suitable for the application of a decenary circuit, and a differential amplifier with linear gain, i.e., MBDA.

Since the voltage distance between each level and the next level is 0.5v, the MBDA should be able to operate from 0V to 4.5V (Input voltage range and output voltage range). The proposed MBDA is capable of operating from 0V to 5.5V.

In MDBA, the linearity of the gain in the whole range of the operating voltage helps to ensure that the voltage value of each level is correct (without the need to change the MBDA resistance configuration). The proposed MBDA Gain is linear within the voltage range of 0.1V to 5.3V.

MBDA is the element by which other elements will be designed. This paper reports a decenary inverting circuit as well. Finally, a correction buffer is designed and simulated to control the error caused by noise and drift.

The analog circuits used in MVL will reduce number of the transistors and thus reduces complexity of the circuit. However, use of analog circuits will not be without its drawbacks, e.g., sensitivity to noise and drift of the output circuit that are due to the tolerance of the components. This problem has been completely fixed with the design of the corrective buffer. Correction buffer should be used at output of the chip or the feedback sections.

In other words, additional circuitry will be required to fix the noise and drift effects. Simulation results confirm correctness of the operation of the proposed circuits.

In future work, intention to complete the arithmetic circuits section using analog logic. The reported circuits have the same specifications (levels voltage distance, number of levels, manufacturing technology, voltage of power supplies) as with the decenary MVL family circuitry as discussed earlier in section 1. The most important of these drawbacks are the higher sensitivity to noise and drift of the output circuit that are due to the

tolerance of the components. This problem is fixed with the design of the corrective buffer. Correction buffer should be used at the output of the chip or the feedback sections. In other words, additional circuitry will be required to fix the noise and drift effects.

Simulation results confirm correctness of the operation of the proposed circuits. In future work, circuits with the same specifications will be introduced. These circuits include decenary logic circuitries and a decenary memory circuit.

8. REFERENCES

1. Kim, C.-H., Hayakawa, R. and Wakayama, Y., "Fundamentals of organic anti-ambipolar ternary inverters", *Advanced Electronic Materials*, Vol. 6, (2020). DOI: 10.1002/aelm.201901200.

2. Jeon, J., Kim, M.J., Shin, G., Lee, M., Kim, Y.J., Kim, B., Lee, Y., Cho, J.H. and Lee, S., "Functionalized organic material platform for realization of ternary logic circuit", *ACS Applied Materials & Interfaces*, Vol. 12, No. 5, (2020), 6119-6126. DOI: 10.1021/acsami.9b18772.

3. Davari Shalamzari, Z., Zarandi, A. and Reshadinezhad, M., "Newly multiplexer-based quaternary half-adder and multiplier using cntfets", *AEU - International Journal of Electronics and Communications*, Vol. 117, (2020), 153128. DOI: 10.1016/j.aeue.2020.153128.

4. Hosseini, S.A. and Etezadi, S., "A novel very low-complexity multi-valued logic comparator in nanoelectronics", *Circuits, Systems, and Signal Processing*, Vol. 39, No. 1, (2019), 223-244. DOI: 10.1007/s00034-019-01158-2.

5. Jaber, R.A., El-Hajj, A.M., Kassem, A., Nimri, L.A. and Haidar, A.M., "Cnfet-based designs of ternary half-adder using a novel "decoder-less" ternary multiplexer based on unary operators", *Microelectronics Journal*, Vol. 96, (2020), 104698. DOI: 10.1016/j.mejo.2019.104698.

6. Hosseini, S.A. and Roosta, E., "A novel technique to produce logic '1' in multi-threshold ternary circuits design", *Circuits, Systems, and Signal Processing*, (2020). DOI: 10.1007/s00034-020-01535-2.

7. Chowdhury, A.K., Raj, N. and Singh, A.K., "Design of low power max operator for multi-valued logic system", *Procedia Computer Science*, Vol. 70, (2015), 428-433. DOI: 10.1016/j.procs.2015.10.067.

8. Saha, A. and Pal, D., "Dpl-based novel time equalized cmos ternary-to-binary converter", *International Journal of Electronics*, Vol. 107, No. 3, (2020), 12. DOI: 10.1080/00207217.2019.1661026.

9. Durrani, Z.A.K., "Single-electron devices and circuits in silicon, Published by Imperial College press and distributed by world scientific publishing co., (2009), 300, DOI: 10.1142/p650.

10. Mahapatra, S. and Ionescu, A.M., "Hybrid cmos single-electron-transistor device and circuit design, Artech House, (2006).

11. Chaudhry, A., "Fundamentals of nanoscaled field effect transistors, Springer New York, (2013), DOI: 10.1007/978-1-4614-6822-6.

12. Gope, J., Bhadra, S., Chanda, S., Sarkar, M., Pal, S. and Rai, A., "Modelling of single electron ternary flip-flop using simon", in IEEE 7th Annual Ubiquitous Computing, Electronics & Mobile Communication Conference (UEMCON). (2016), 1-9 DOI: 10.1109/UEMCON.2016.7777931.

13. Sandhie, Z.T., Ahmed, F.U. and Chowdhury, M., "Gnrfet based ternary logic – prospects and potential implementation", in IEEE 11th Latin American Symposium on Circuits & Systems (LASCAS). (2020), 1-4 DOI: 10.1109/LASCAS45839.2020.9069028.

14. Karmakar, S., "Design of ternary logic inverter using quantum dot gate nonvolatile memory (qdnvm)", in IEEE 63rd International Midwest Symposium on Circuits and Systems (MWSCAS). (2020), 558-561 DOI: 10.1109/MWSCAS48704.2020.9184652.

15. Bhattacharjee, D., Kim, W., Chattopadhyay, A., Waser, R. and Rana, V., "Multi-valued and fuzzy logic realization using taox memristive devices", *Scientific Reports*, Vol. 8, No. 1, (2018), 8. DOI: 10.1038/s41598-017-18329-3.

16. Sharma, T. and Kumre, L., "Energy-efficient ternary arithmetic logic unit design in cntfet technology", *Circuits, Systems, and Signal Processing*, Vol. 39, No. 7, (2020), 3265-3288. DOI: 10.1007/s00034-019-01318-4.

17. Dvornikov, O.V., Prokopenko, N.N., Bugakova, A.V., Tchekhovski, V.A. and Maliy, I.V., "Cryogenic operational amplifier on complementary jfets", in 2018 IEEE East-West Design & Test Symposium (EWDTS). (2018), 1-5 DOI: 10.1109/EWDTS.2018.8524640.

18. Kuzmicz, W., "A simple ultra-low power opamp in 22 nm fdsoi", in 2019 MIXDES - 26th International Conference "Mixed Design of Integrated Circuits and Systems". (2019), 167-170 DOI: 10.23919/MIXDES.2019.8787017.

19. Alam, A.Z., Arfah, N., Khan, S. and Islam, M., "Design of capacitance to voltage converter for capacitive sensor transducer", *American Journal of Applied Sciences*, Vol. 7, (2010), 1353-1357. DOI: 10.3844/ajassp.2010.1353.1357.

20. Raut, K.J., Kshirsagar, R.V. and Bhagali, A.C., "A 180 nm low power cmos operational amplifier", in 2014 Innovative Applications of Computational Intelligence on Power, Energy and Controls with their impact on Humanity (CIPECH). (2014), 341-344 DOI: 10.1109/CIPECH.2014.7019049.

21. Dash, A., Mandal, S.K., Patro, B.S. and Anand, A., "A low offset fast settling rail-to-rail stable operational amplifier in 180 nm

technology", in 2013 IEEE Conference on Information & Communication Technologies. (2013), 793-797 DOI: 10.1109/CICT.2013.6558202.

22. Newcomb, R.W. *Tsmc180nmcmos.Lib*. 2010 [cited 2019 Nov.]; Available from: https://user.eng.umd.edu/~newcomb/courses/spring2010/303/tsmc180nmcmos.lib.

23. Hsu, F.-Z., Wu, J.-Y. and Lin, S.-D., "Low-noise single-photon avalanche diodes in 0.25 μm high-voltage cmos technology", *Optics Letters*, Vol. 38, No. 1, (2013), 2. DOI: 10.1364/OL.38.000055.

24. Marwick, M.A. and Andreou, A.G., "Fabrication and testing of single photon avalanche detectors in the tsmc 0.18μm cmos technology", in 41st Annual Conference on Information Sciences and Systems. (2007), 741-744 DOI: 10.1109/CISS.2007.4298405.

25. Rhim, J., Zeng, X., Huang, Z., Chalamalasetti, S.R., Fiorentino, M., Beausoleil, R. and Lee, M.-J., "Monolithically-integrated single-photon avalanche diode in a zero-change standard cmos process for low-cost and low-voltage lidar application", *Instruments*, Vol. 3, No. 2, (2019). DOI: 10.3390/instruments3020033.

26. Padma, S., Das, S., Sen, S. and Parikh, C.D., "High performance operational amplifier with 90db gain in scl 180nm technology", in 24th International Symposium on VLSI Design and Test (VDAT). (2020), 1-5 DOI: 10.1109/VDAT50263.2020.9190288.

27. Jose, B., Jose, L., Kiruba, R.S., Ekka, P.M. and Priya, S.S.S., "Two stage class ab op-amp for video applications", in 3rd International Conference on Trends in Electronics and Informatics (ICOEI). (2019), 224-229 DOI: 10.1109/ICOEI.2019.8862513.

28. Gupta, A. and Singh, S., "Design of two stage cmos op-amp with high slew rate and high gain in 180nm", in International Conference on I-SMAC (IoT in Social, Mobile, Analytics and Cloud) (I-SMAC). (2018), 341-345 DOI: 10.1109/I-SMAC.2018.8653750.

Persian Abstract

چکیده

هدف از کار ارائه شده، کمک به طراحی مدارهای ۱۰ ارزشی است. مدارهای مد ولتاژ آنالوگ که در منطق چندارزشی بکار گرفته شده‌اند در این مقاله ارائه شده است. تقویت کننده دیفرانسیلی بر پایه (MBDA) MOSFET ارائه شده، المان اساسی بکارگرفته شده در مدارهای ۱۰ ارزشی است. ویژگی‌های‌اساسی این المان بازه ولتاژی و خطی بودن گین آن است. بازه ولتاژی MBDA از ۰ تا ۵.۵ ولت است و بازه خطی بودن مدار از ۰.۱ ولت تا ۵.۳ ولت است. همچنین دو مدار معکوس کننده آنالوگ و بافر تصحیح کننده برپایه MBDA طراحی شده است. کاربرد مدار معکوس کننده آنالوگ در مدارهای محاسباتی و منطقی ۱۰ ارزشی خواهد بود. بافر تصحیح کننده نیز به عنوان ابزاری برای حذف نویز و لغزش سیگنال در خروجی گیت‌های چند ارزشی و در زمان انتقال داده بکار گرفته خواهد شد.

International Journal of Engineering

Lateral Load Carrying Capacity of Concrete-filled Cold-formed Steel Shear Wall

G. Sijwal[a], P. Man Pradhan[b,c], K. Phuvoravan*[a]

[a] Department of Civil Engineering, Faculty of Engineering, Kasetsart University, Bangkok, Thailand
[b] Department of Civil Engineering, School of Engineering, Kathmandu University, Dhulikhel, Nepal
[c] School of Engineering, Manmohan Technical University, Morang, Nepal

P A P E R   I N F O

A B S T R A C T

A new type of innovative composite shear wall, concrete-filled cold-formed steel shear wall (CFCSW) is proposed, composed of cold-formed channel sections arc-welded together by 20 mm length of welds and filled with concrete. The main study of CFCSW focuses on the overall behavior, ultimate load capacity, stiffness and ductility. Three specimens of CFCSW with an aspect ratio of 1.0 are tested under lateral monotonic load. Three-dimensional finite element models are developed and benchmarked with the experimental results. The validated models are used to carry out parametric studies to determine the influence of the parameters on the performance of the CFCSW. The parameters are the height, steel plate thickness, weld spacing and concrete thickness of the CFCSW. The experimental and finite element modeling results indicate that increasing the weld spacing from 105 mm to 211 mm improves the stiffness, ductility and load carrying capacity, and similarly, providing holes inside the wall increases the stiffness, ductility and peak strength of the CFCSW. The ultimate capacity of the CFCSW is the most influenced by changing the height of the wall and least influenced by varying the concrete thickness of the wall.

doi: 10.5829/ije.2022.35.01a.15

1. INTRODUCTION

Generally, reinforced concrete shear walls are used in high-rise buildings. However, they present construction difficulties, which result in delays during construction and they have limitations when more strength and more ductility are required in shear walls [1-3]. Therefore, innovation in shear wall is necessary. Four types of wall have been suggested by past researchers as alternatives to the traditional reinforced concrete shear wall. The first is the steel plate shear wall, which can withstand large inelastic deformations [4-7]; however, local buckling in the compression zone of the steel plate greatly reduces the stiffness and strength capacity of the shear wall [8]. Using stiffeners and increasing the steel plate thickness can avoid the buckling problem, but it is considered uneconomical. The second type of shear wall is the composite wall, which consists of steel frame boundaries and a steel plate inside the concrete [9-12]. The third form consists of a steel plate embedded in the reinforced

concrete shear wall [13-16]. The fourth form is a concrete wall sandwiched by two steel plates, called a double-skin composite shear wall [1, 17].

A considerable amount of research has been done on the double-skin plate composite wall. Initially, the in-plane shear behavior of a double-skin plate composite wall with boundary elements was discussed by Ozaki et al. [18]. Varma et al. [19] proposed and verified the simple mechanics-based model (MBM) for the walls with boundary elements. Furthermore, Booth et al. [20] investigated the ultimate in-plane shear strength of the steel-plate composite wall with boundary elements and found that it mainly depends on the yield strength of steel face plate and the diagonal compression capacity of the cracked infilled concrete. Epackachi et al. [21] tested four specimens, named steel-plate composite wall piers, consisting of studs and tie rods, and determined that the failure pattern of the wall is governed by flexure rather than by shear. Luo et al. [17] and Zhang et al. [2] examined the in-plane seismic behavior of the wall with

*Corresponding Author Institutional Email: fengkpp@ku.ac.th (K. Phuvoravan)

vertical stiffeners and connectors under reversed cyclic lateral load and axial compressive load. Luo et al. [17] ex-perimentally studied the behavior of the shear wall by varying the aspect ratio (height to length), concrete strength, axial compression ratio and plate thickness and found that the arrangement of the wall best utilizes the steel and concrete strength. Zhang et al. [1], through experiments, concluded that the ductility of the wall is greatly influenced by the thickness of the shear wall and the number of channels in the wall [17].

The above-mentioned researches mainly focused on cyclic behavior of the walls with the use of connectors like studs and tie rods. Therefore, a new type of composite wall (CFCSW) was put forward for ease of construction without the connectors and composed of cold-formed lipped C-sections connected by flare V-groove welds and filled concrete. Only the in-plane monotonic load was considered. The behavior of the proposed wall was investigated through the experimental tests with regards to the stiffness, ductility, ultimate capacity and failure mechanism. Finite element analysis was conducted to predict the peak strength of the wall and validated using the test results. Finally, sensitivity analysis was carried out to investigate the influence of the height, steel plate thickness, weld spacing and concrete thickness.

2. EXPERIMENTAL PROGRAM

2. 1. Specimen Description   In general, the shear walls used in the high-rise building have the thickness ranging from 300 mm to 1800 mm and the steel plate reinforcement ratio, described as $2t_p/T$, varying from 1.5%-5%, where t_p is the thickness of steel plate and T is the thickness of wall [1]. This experiment was to study the shear wall system in a high-rise building. Three 1:5 scale down CFCSW specimens were designed to represent the wall, which has the height, length and thickness of 4320 mm, 3570 mm and 510 mm, respectively. All three specimens had an aspect ratio of 1.0, where the aspect ratio is the ratio of the clear height (overall height minus loading steel plate height) to the length of the wall [1, 17]. The configurations of the three tested specimens are listed in Table 1. The details for the cross-section, elevation, and inner channel of the spec-imens are shown in Figures 1 to 5.

Initially, fourteen cold-formed steel channels were arranged as shown in Figure 1 and connected by the welds. The hollow steel wall thus formed was fillet-welded to the steel base plate of thickness 38 mm. Furthermore, shear studs were installed on the baseplate so that the concrete could transfer the load sufficiently to the baseplate. Overall, the strength of the connection between the baseplate and the wall was designed to resist the estimated ultimate load. Then, ready-mix concrete

was used to cast the wall to make the concrete-filled cold-formed steel shear wall (CFCSW). Flare V-groove welds with a length of 20 mm were used for welding, which is the minimum length of weld according to American Structural Welding code [22]. Similarly, the weld spacing of 105 mm (one eighth of overall height, Figure 2) was chosen for CFCSW1 as per the AISI code [23], whereas the weld spacings for CFCSW2 and CFCSW3 were approximately double that of CFCSW1 (Figure 3). Additionally, square holes with the size of 80 mm x 80 mm were made in the web of the inner channel sections for CFCSW1 and CFCSW2 (Figure 4) based on the AISC guideline for castellated and cellular beam [24]. Therefore, the weld spacings and the holes in the inner webs are the fundamental parameters that were investigated in this experiment regarding their effect on the structural behavior of the wall.

TABLE 1. Configurations of test specimen

Specimen	Cross-section (mm x mm)	Center-center spacing of welds (mm)	Size of square holes (mm x mm)
CFCSW1	714 x 102	105	80 x 80
CFCSW2	714 x 102	211	80 x 80
CFCSW3	714 x 102	211	No holes
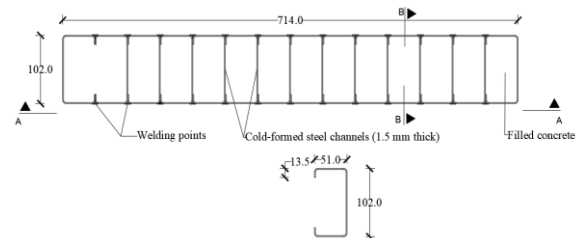
Figure 1. Typical cross-section of specimens and details of cold-formed channel section (units in mm)
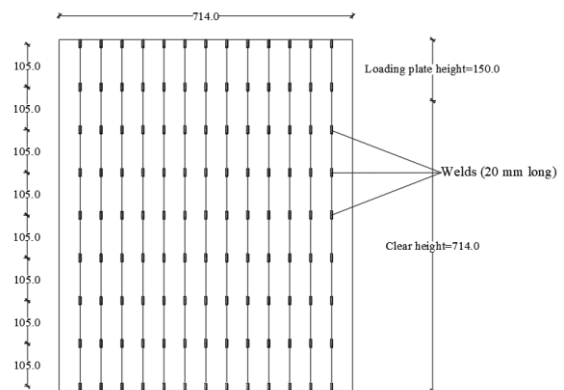
Figure 2. Elevation view A-A with welding details of CFCSW1 (units in mm)
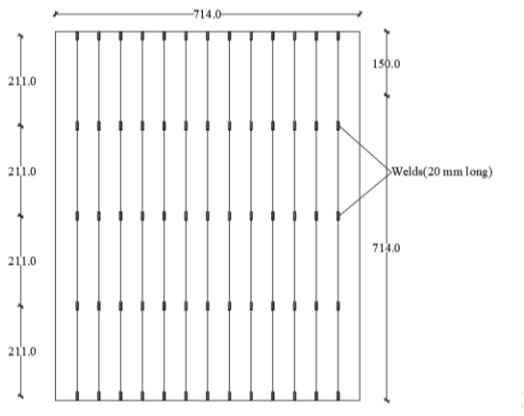
Figure 3. Elevation view A-A with welding details of CFCSW2 and CFCSW3 (units in mm)
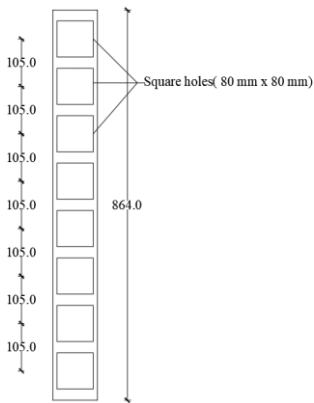
Figure 4. Details of holes in CFCSW1 and CFCSW2 (section B-B, units in mm)
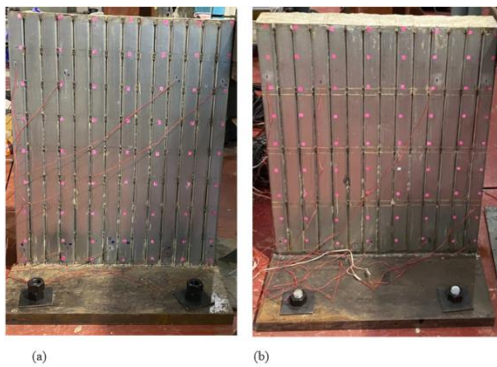
Figure 5. Specimens (a) CFCSW1 (b) CFCSW2 and CFCSW3

2. 2. Material Properties

Three tensile coupon tests were carried out to determine the mechanical properties of the cold-formed steel. Young's modulus of elasticity, the yield and ultimate strength of the cold-formed steel obtained from the tests were 197.9 GPa, 463.9 MPa and 490.9 MPa, respectively. Likewise, the compressive strength of the concrete, calculated from the concrete cylinders at 28 days, was 21.0 MPa for all three specimens.

2. 3. Test Setup and Instrumentation

The test setup used in the experiment is shown in Figures 6 and 7. The horizontal load, which was monotonic in nature, was applied using a hydraulic jack at the top of the wall via the loading plate. Eight nuts (50 mm outer diameter), four bolts (32 mm diameter) and four washer plates (25 mm thick) were used to attach the baseplate tightly to the concrete foundation block to prevent baseplate movement during the experiment. Displacement-controlled loading with a speed of approximately 0.048 mm/sec was implemented in the test. The test was terminated when the applied lateral load dropped below 75% of the ultimate strength.

The deformations in the specimens were monitored by installing strain gauges and linear variable differential transformers (LVDTs), as shown in Figure 8. Two LVDTs were used to measure the in-plane displacement at the top of the specimen and one LVDT was used to record the out-of-plane displacement of the wall. Strain gauges were attached on the top and bottom of the exterior parts of the steel channel sections at 674 mm and 60 mm above the base of the wall, respectively. The applied load was recorded using a load cell installed with the hydraulic jack during the experiment.

2. 4. Experimental Results and Discussion

The key results from the experiment are listed in Table 2. The initial stiffness, ultimate load carrying capacity, ductility, failure mode and damage to the walls were the main parameters analyzed regarding the structural behavior of the specimens during the experiment. The ductility, measured in terms of displacement, was the ratio of the yield displacement to the ultimate displacement. The ultimate displacement was taken as the displacement
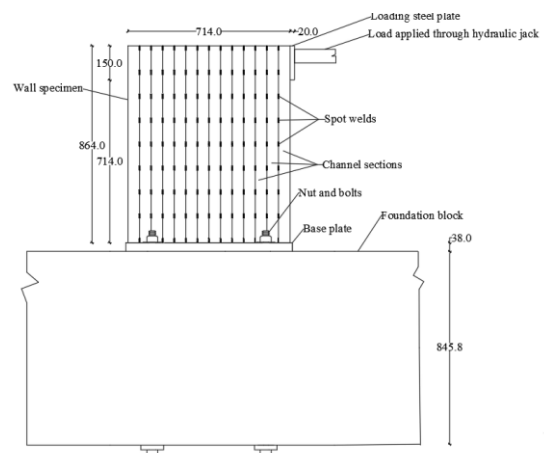
Figure 6. Experimental setup (all units in mm)
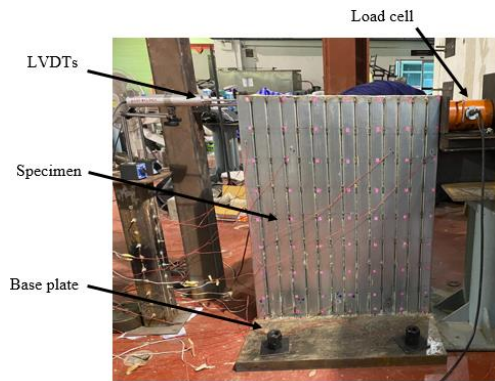
Figure 7. Actual setup in the laboratory
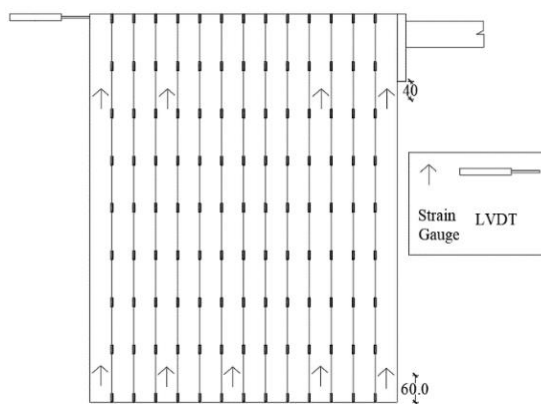
Figure 8. Instrumentation in specimen

corresponding to 85% of the ultimate load after the ultimate point [17]. As shown in Table 2, the initial stiffness of CFCSW2 was slightly higher than for CFCSW1 and CFCSW3, which was attributed to the flexibility of the foundation and base plate connection during the test.

2. 4. 1. Deformations in CFCSW1, CFCSW2 and CFCSW3   The curve shown in Figure 9 depicts that CFCSW1 failed in a brittle manner as the load dis-placement curve dropped suddenly immediately after reaching the ultimate loading stage. The first yielding of the specimen began at 227.7 kN as the steel at the bottom of the 1st channel (the 1st channel from the loading direction) started yielding in tension. Furthermore, the steel at the bottom of the 14th channel yielded at a load

TABLE 2. Summary of test results

Specimen	Initial stiffness [kN/mm]	First yield load [kN]	Ultimate load [kN]	Ductility
CFCSW1	20.62	227.7	290.7	1.65
CFCSW2	22.76	346.3	378.0	1.87
CFCSW3	19.84	230.0	250.3	1.58

of 281.5 kN in compression. On further increasing the load, fracture of the steel at the base of the 1st channel occurred at almost the ultimate load. Finally, the specimen failed by the propagation of the steel fracture to the 2nd and 3rd channels and the buckling at the base of the 14th channel, as shown in Figure 10.

While, CFCSW2 showed relatively ductile failure mechanism. CFCSW2 first started yielding at a load of 346.3 kN in the 1st channel and at a load of 356.3 kN in 14th channel. Moreover, at approximately 80% of the ultimate load after the peak point, deformations (tearing and buckling of the steel near the welds) began to occur. Eventually, fracturing and buckling of the steel channels were noticed at approximately 75 % of the peak load (Figure 11). Whereas, CFCSW3 exhibited brittle failure, as demonstrated by the load displacement curve in Figure 7. CFCSW3 yielded for the first time when the load reached 230.0 kN. In addition, the nature and characteristics of the failure of the specimen was similar to CFCSW1 (Figure 12).

2. 4. 2. Comparisions   Increasing the weld spacing shifted the failure mechanism from brittle failure, as noticed in CFCSW1, to ductile failure, as in CFCSW2.
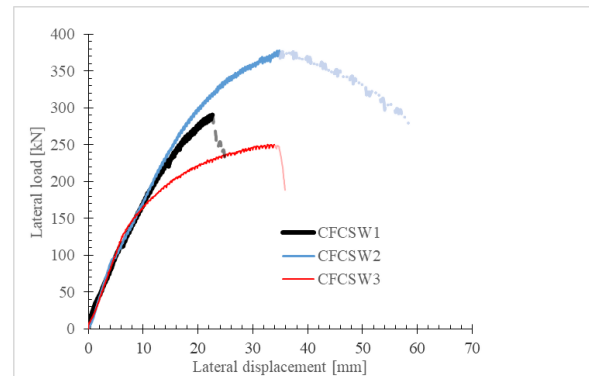
Figure 9. Lateral load displacement curve for CFCSW1, CFCSW2 and CFCSW3
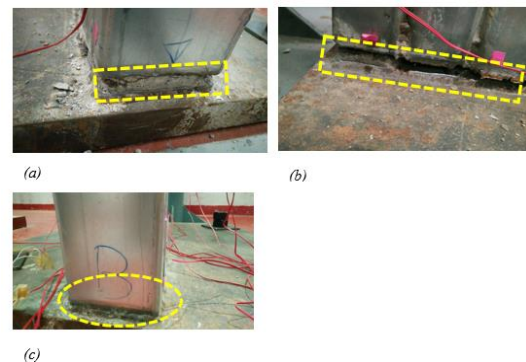
Figure 10. CFCSW1 (a) and (b), fracturing of steel and concrete cracking on tension side (c) buckling of steel on compression side
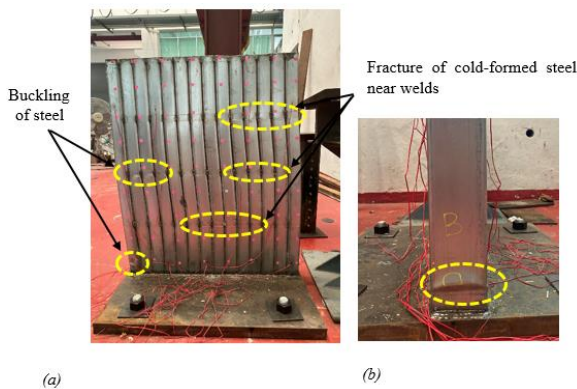
Figure 11. CFCSW2 (a) side view of damages (steel fracturing and buckling) (b) buckling of 14th channel
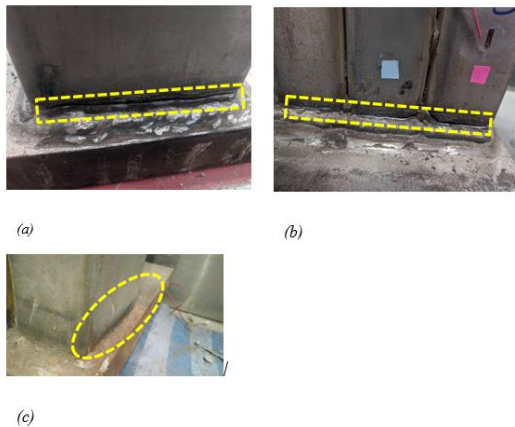
Figure 12. CFCSW3 (a) and (b), fracturing of steel at base of 1st, 2nd and 3rd channels (c) buckling of steel at base of 14th channel

The stiffness of CFCSW2 was slightly higher than for CFCSW1 prior to the first yield point, as demonstrated by curve in Figure 9. CFCSW1 and CFCSW2 yielded when the imposed loads were 227.7 kN and 325.7 kN, respectively, indicating a 52% increase in yield strength. The ultimate loads of CFCSW1 and CFCSW2 were 290.7 kN and 377.9 kN, respectively, representing a 30% improvement in ultimate capacity. The ductility ratios of CFCSW1 and CFCSW2 were 1.65 and 1.87, respectively, representing a 13% enhancement in ductility. The welds, in the form of spots, acted like rigid parts compared to the other remaining portions; consequently, column behavior was noticed between the spot welds. The heights of the column-like structures formed in CFCSW1 were about half of height of the columns in CFCSW2. Therefore, the columns in CFCSW1 behaved as short columns, which, when loaded laterally, failed by shear at the base in the experiment. In contrast, with CFCSW2, the height of the columns was sufficient to provide flexibility to the wall and thus there was ductile behavior in the experiment. Similarly,

residual stresses were generated in the channel sections due to the welding. Hence, increasing the weld spacing from 105 mm to 211 mm decreased the amount of residual stress generated in the specimen which was the another reason for such manifestation.

The failure pattern of CFCSW2, with holes, was ductile in nature, whereas CFCSW3, without holes, failed in a brittle manner, which illustrated the effect of the web holes on failure. The load displacement curve showed that CFCSW2 had high stiffness relative to CFCSW3. The yield strength of CFCSW3 was 230.0 kN, which was a 33% decrease in yield strength compared to CFCSW2. Similarly, the load corresponding to the ultimate capacity was 250.3 kN for CFCSW3, which represented a 34% decrease in ultimate capacity. For CFCSW3, the ductility ratio was about 1.58, which was 15% less than for CFCSW2. The holes in the inner webs improved the structural behavior by two means. First, it provided ductility to the wall by acting as the weakest point in the wall. Consequently, the wall utilized the strength of the concrete and steel to a greater extend. Furthermore, the holes decreased the area of contact for friction between the steel and concrete. As a result, the integrity of the composite structure was enhanced.

3. FINITE ELEMENT MODELING

3. 1. Modeling Assumptions   Non-linear finite element modeling of the specimens was conducted using the finite element software, ABAQUS. The 3-D model developed during the finite element modeling (FEM) is shown in Figure 13.

Eight-node solid elements (C3D8R) were used to model the filled concrete, base plate and loading plate. Similarly, the cold-formed channel sections were represented by four-node shell elements (S4R). Iterations with different mesh sizes were carried out to determine the optimum mesh size that did not compromise the output results, and at the same time, reduced the computation time.The filled concrete, base plate, and loading plate were meshed with a size of 20 mm x 20 mm x 20 mm. Similarly, 20 mm x 20 mm mesh was used for the steel channel sections. The welds connecting the channel sections were replicated by joining the nodes with point-based fasteners, as shown in Figure 13. Point-based fasteners are generally used to model the point-to-point connections between two or more surfaces and are independent of the mesh [25]. Surface-to-surface contact was used to represent the interaction between the concrete and steel, with hard contact attributed in the normal direction to prevent the penetration of slave nodes into the master segments, while frictional contact was assigned in a tangential direction [26]. Friction coefficient of 0.2 was used during the FEM by calibrating with the experimental results. The contact between the
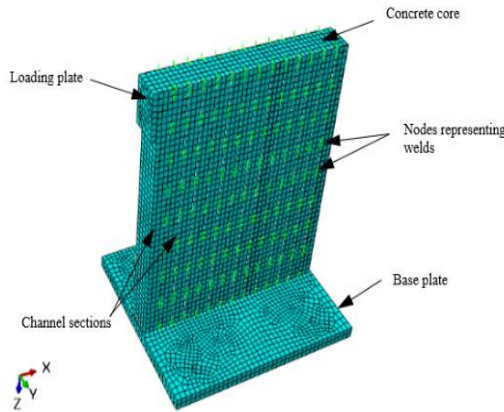
Figure 13. ABAQUS model of CFCSW

channel sections and the base plate was modeled by a surface-based shell-to-solid coupling constraint. Surface-based tie constraint was employed for simulating the contact behavior between the loading plate and the first channel section. Flexibility between the baseplate and foundation block was considered as in the experiment during the FEM. The force method was implemented for loading the steel plate.

3. 2. Material Modeling   In this research, filled concrete was modeled using the concrete-damaged plasticity (CDP) model available in ABAQUS. The CDP model can be used when concrete is subjected to monotonic, cyclic and/or dynamic loading under low confining pressures (less than four or five times the uniaxial compressive strength of concrete) [27]. This model had been deployed in similar research to simulate the behavior of concrete [28-30]. The CDP model requires the input parameters such as the uniaxial tensile and compressive behavior, damage parameters, parameters to define the flow potential and yield surface and a viscosity parameter [27]. The plasticity parameters that were determined based on trails and used in the FEM are listed in Table 3, where F_{bo}/F_{co} is the ratio of initial equibiaxial compressive yield stress to initial uniaxial compressive yield stress and K is the ratio of the second stress invariant on the tensile meridian to that on the compressive meridian.

The stress-strain curve of concrete was used to model the uniaxial compressive behavior of the concrete (Figure 14(a)), with the ascending and descending branches of the curve defined by Equation (1), which was proposed by Popovics [31] and Equation (2), which was from Sanez [32], respectively. Nguyen and Whittaker [28] demonstrated that this approach was appropriate for such types of shear wall.

$$\sigma = f_c' \frac{k\left(\frac{\varepsilon}{\varepsilon_c}\right)}{1+(k-1)\left(\frac{\varepsilon}{\varepsilon_c}\right)^r} \tag{1}$$

$$\sigma = f_c' \frac{k\left(\frac{\varepsilon}{\varepsilon_c}\right)}{1+A\left(\frac{\varepsilon}{\varepsilon_c}\right)+B\left(\frac{\varepsilon}{\varepsilon_c}\right)^2+C\left(\frac{\varepsilon}{\varepsilon_c}\right)^3} \tag{2}$$

in which:

$$k=\frac{E_o \varepsilon_c}{f_c} , \qquad k_\varepsilon=\frac{\varepsilon_f}{\varepsilon_c} , \qquad k_\sigma=\frac{f_c'}{f_f} , \qquad r=\frac{k}{k-1} ,$$

$$A=C+k-2 , \qquad B=1-2C , \qquad C=\frac{k(k_\sigma-1)}{(k_\varepsilon-1)^2} - \frac{1}{k_\varepsilon}$$

where E_o is the modulus of elasticity of concrete, f_c' is the compressive strength of concrete (21.0 MPa), ε_c is the strain corresponding to peak strength (0.002) and f_f and ε_f are stress and strain after the peak strength, which can be controlled by the user.

The concrete behavior in tension was represented by the linear stress-strain curve up to the peak strength and by the stress-crack width relationship after the peak point. Figure 14(b) shows stress-crack width relationship of concrete in tension computed as per the CEB-FIP model code 1990 [33], which includes the calculation of the tensile strength (f_t'), fracture energy (G_F), and crack width at which the tensile strength reduces to zero (w_o), using Equations (3), (4) and (5), respectively.

$$f_t'=0.95\left(\frac{f_c'}{10}\right)^{2/3} \tag{3}$$

$$G_F=0.025\left(\frac{8+f_c'}{10}\right)^{0.7} \tag{4}$$

$$w_o=2\frac{G_F}{f_t'} \tag{5}$$

(a)

(b)
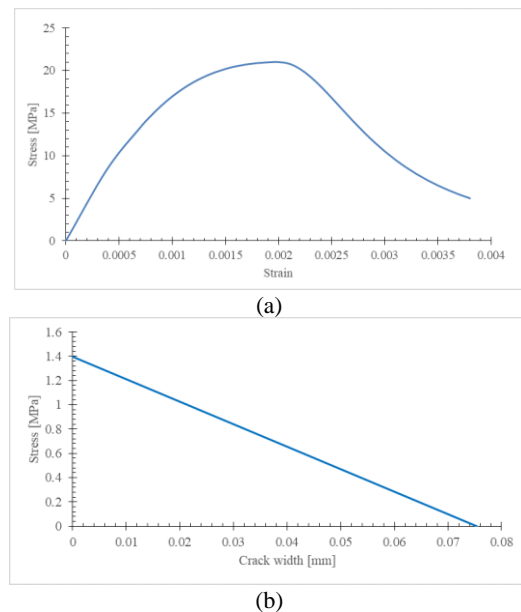
Figure 14. Stress-strain curve of concrete in: (a) Compression (b) Tension

The classical metal plasticity models in ABAQUS allows for the elastic perfectly plastic mod-eling of steel based on the Mises yield surfaces with associated plastic flow [27]. Therefore, steel during the FEM was modelled as elastic perfectly plastic, with the necessary parameters determined from the standard tensile coupon test.

3. 3. Validation of Finite Element Modeling
Figure 15 and Table 4 represent the load displacement curves and ultimate load capacities, respectively, obtained from the FEM together with the experiment results. As shown, the ultimate capacities and overall behavior of the walls were reasonably predicted by the FEMs. Furthermore, the buckling modes of 14th channel (Figure 16) verified that deformations were similar in the FEM and the experiment. The slight difference in the response between the FEM and the test could have been due to the approximations of actual materials in the FEM, selection of the material constitutive models and imperfections in the geometry.

3. 4. Parametric Study
The benchmarked FEM was further used to conduct the parametric studies to investigate the effect of different parameters on the lateral load capacity of CFCSW. CFCSW2 was selected to carry out the parametric investigation, where the variables were: the weld spacing, steel thickness, concrete thickness and the height of the wall. Table 5 presents the details of the walls with their respective

TABLE 3. Plasticity parameters

Dilation Angle	Eccentricity	F_{bo}/F_{co}	K
20	0.1	1.10	0.67
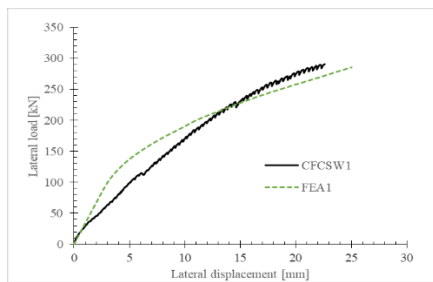
(a)
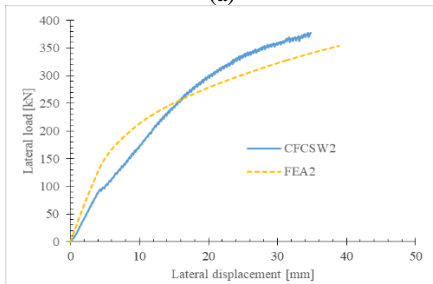
(b)
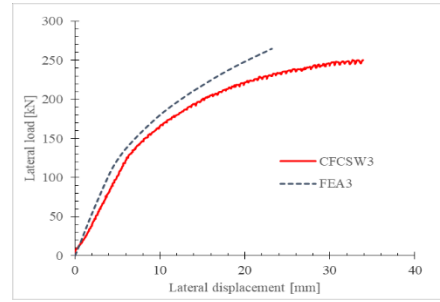
(c)

Figure 15. Comparison of load displacement curves between experiment and FEM: (a) CFCSW1 (b) CFCSW2 (c) CFCSW3

TABLE 4. Comparisions between test and FEM results

Specimen	Experimental results	FEM results	(1)/(2)
	(1) Ultimate load (kN)	(2) Ultimate load (kN)	
CFCSW1	290.6	285.4	1.02
CFCSW2	378	354.1	1.06
CFCSW3	250.3	265.1	0.95
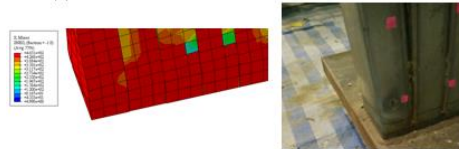
Figure 16. Buckling of last channel during FEM and in test for: (a) CFCSW1 (b) CFCSW2 (c) CFCSW3

ultimate capacities maintaining constant values for the other parameters (concrete strength, steel strength and hole size) for all analyses, except for CFCSW2 with a concrete thickness of 50 mm (CFCSW2-T50), where a hole size of 40 x 80 mm was used. Figure 17 depicts the responses of CFCSWs for different varied parameters.

3. 4. 1. Effect of Weld Spacing
Weld spacing (center to center) in the wall was varied while keeping

TABLE 5. Details of variables with obtained ultimate load

Test specimen	Clear Height (h) (mm)	Length(l) (mm)	Aspect ratio (h/l)	Weld spacing (mm)	Steel thickness (mm)	Concrete thickness (mm)	Ultimate load (kN)
CFCSW2	714	714	1	211	1.5	99	354.10
CFCSW2-WS105	714	714	1	105	1.5	99	285.44
CFCSW2-WS141	714	714	1	141	1.5	99	315.52
CFCSW2-WS281	714	714	1	281	1.5	99	311.15
CFCSW2-WS422	714	714	1	422	1.5	99	216.35
CFCSW2-t1	714	714	1	211	1	99	254.31
CFCSW2-t2	714	714	1	211	2	99	440.72
CFCSW2-t2.5	714	714	1	211	2.5	99	512.20
CFCSW2-T50	714	714	1	211	1.5	50	294.52
CFCSW2-T150	714	714	1	211	1.5	150	381.84
CFCSW2-T200	714	714	1	211	1.5	200	403.47
CFCSW2-H971	971	714	1.36	211	1.5	99	249.01
CFCSW2-H827	827	714	1.16	211	1.5	99	303.32
CFCSW2-H642	642	714	0.9	211	1.5	99	385.70

The suffix after the CFCSW2 represents the changed variables: for example, WS105, t1, T50 and H827 indicate the wall with weld spacing 105 mm, steel channel thickness 1 mm, concrete thickness 50 mm and height 827 mm, respectively.
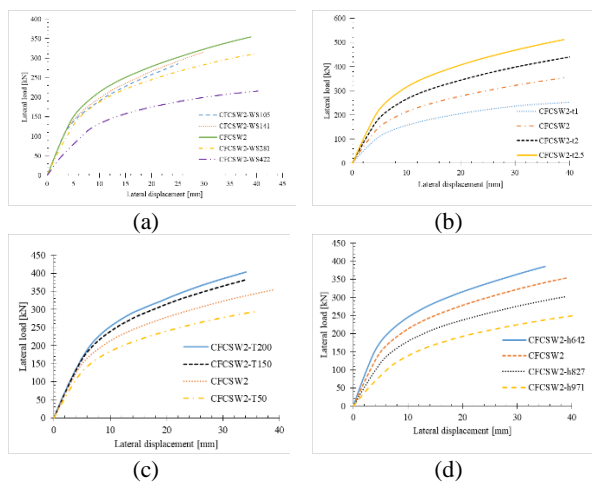
Figure 17. Load displacement curves for different parameters: (a) weld spacings (b) steel channel thicknesses (c) concrete thicknesses (d) heights

other parameters constant to determine its effect on the ultimate capacity. The load displacement curves for different weld spacings are illustrated in Figure 17(a). Figure 18 represents the deformations of the finite element models showing the yielding of steel, represented by the red color, and the cracking and crushing of concrete at the ultimate load. Decreasing the weld spacing from 211 mm to 141 mm and to 105 mm had an adverse effects on the stiffness, ductility, and ultimate load of the wall, which decreased the ultimate

load by 11 % and 19 %, respectively. Likewise, when the weld spacing was increased from 211 mm to 281 mm and to 422 mm, the ultimate capacity of the wall decreased by 12 % and 38%, respectively, and stiffness of the wall also decreased (Figure 17(a)). When the weld spacing of the wall decreased from 211 mm to 141 mm and to 105 mm, each channel section became stiffer due to its increasing unity of overall structure. However, the increase in stiffness also resulted in the concentration of stresses at specific location, and thus, the redistribution of the applied load did not happen effectively in the model till its peak load stage. This phenomenon caused the premature cracking and crushing of concrete (Figure 18(b)) and the non-uniform yielding of steel channel sections in the wall (Figure 18(a)). Similarly, increasing the weld spacing from 211 mm to 281 mm and to 422 mm loosened the integrity of the structure. So, the overall strength of materials throughout the wall was not used effectively as shown in Figures 18(e) and 18(f), where less yielded steel and smaller values of maximum principle plastic strains can be observed comparing to ones in CFCSW2 (Figures 18(c) and 18(d)). Thus, both increasing and decreasing the weld spacing from 211 mm reduced the ultimate load carrying capacity of the CFCSW.

3. 4. 2. Effect of Steel Channel Thickness   The load displacement curves with different steel thicknesses are presented in Figure 17(b). The peak strength increased by 24% and 44% with increases in the steel
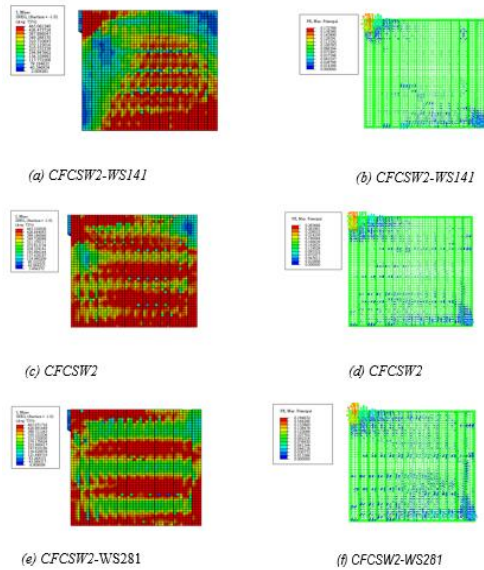
Figure 18. Yielded cold formed steel, and cracked and crushed filled concrete at ultimate load: (a) CFCSW2-WS141- steel deformation (b) CFCSW2-WS141- concrete deformation (c) CFCSW2-steel deformation (d) CFCSW2-concrete deformation (e) CFCSW2-WS281- steel deformation (f) CFCSW2-WS281-concrete deformation

thickness from 1.5 mm to 2 mm and to 2.5 mm, respectively, whereas the load capacity decreased by 28% when the steel thickness changed from 1.5 mm to 1 mm. In other words, the direct relationship between the steel thickness and ultimate capacity of CFCSW was observed.

3. 4. 3. Effect of Concrete Thickness   The filled concrete thickness, whose value is equal to the inner length of the web of the steel channel, was differed while the other parameters remained unchanged. Figure 17(c) illustrates the load displacement curves obtained from the analysis for different concrete thicknesses. Increasing the concrete thickness from 99 mm to 150 mm and to 200 mm improved the capacity by 7.8% and 20%, respectively, while decreasing concrete thickness from 99 mm to 50 mm reduced the ultimate capacity by 16 %. Therefore, the stiffness and ultimate capacity of CFCSW was proportional to the concrete thickness.

3. 4. 4. Effect of Height   The responses in terms of load displacement curves are shown in Figure 17(d). When the height of the wall was changed from 714 mm to 827 mm and to 971 mm with aspect ratio of 1.16 and 1.36, respectively, the load bearing capacity of the wall was reduced by 14% and 30%, respectively. Similarly, the stiffness of the wall decreased with an increase in height. The peak load and stiffness of the wall both increased with reduction in height from 714 mm to 642 mm. Therefore, with an increase in height, peak strength

and stiffness of the CFCSW decreased, while with a reduction in height, the strength and stiffness improved.

3. 4. 5. Sensitivity Analysis   The responses of the different CFCSW setups in terms of ultimate load capacity were analysed to determine the sensitivity of load carrying capacity of the CFCSWs to the different parameters that were altered in the parametric analysis. Figure 19 shows the sensitivity analysis of the peak strength of the CFCSWs to the parameters of weld spacing, steel plate thickness, height and concrete thickness. As depicted in Figure 17, V_u/V_u' denotes the normalized values, where V_u represents the ultimate load capacity of the CFCSWs with changed variables, while V_u' is the load capacity of CFCSW2, which was taken as mean value for comparison. Likewise, X/X' on the x-axis also indicates the normalized values of the parameters and was obtained using correlation with the parameters of CFCSW2. It can be seen in Figure 19 that the absolute change in the peak strength of the CFCSWs with the change in height was higher than for the other parameters, as the curve corresponding to the height effect was stiffer than the others. In summary, the parameters can be arranged in the following order based on maximum to minimum impact on the load carrying capacity of CFCSW: height, steel plate thickness, weld spacing and concrete thickness.
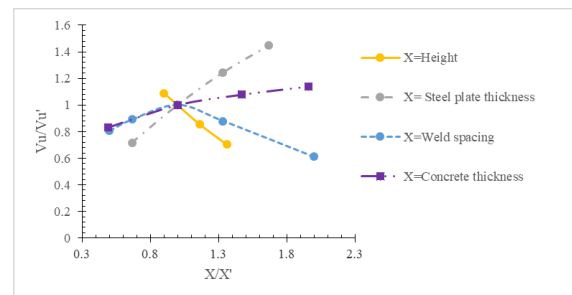
Figure 19. Sensitivity analysis of parameters on load carrying capacity of CFCSW

4. CONCLUSIONS

The following conclusions were made from this investigation:
1. Increasing the weld spacing from 105 mm to 211 mm increased the load carrying capacity by 30% and improved the stiffness and ductility of the different CFCSW types tested.
2. Providing holes inside the specimen on the web of the channel sections improved the peak strength by 50% with increase in the stiffness and ductility of the different CFCSW types tested.
3. The failure mode of the CFCSW changed from brittle mode to ductile mode with an increase in the weld

spacing from 105 mm to 211 mm as demonstrated by CFCSW1 and CFCSW2, respectively, or with the provision of holes inside the specimen as illustrated by CFCSW2 and CFCSW3, respectively.

4. Non-linear FEM was used and validated with the experimental results based on the ABAQUS modeling, and the FEMs simulated the overall behavior and satisfactorily predicted the load carrying capacity of the CFCSW.

5. Parametric studies were conducted on the benchmarked models and indicated that increasing the weld spacing from 105 mm to 211 mm increased the stiffness, ductility, and ultimate capacity, while further increasing the weld spacing from 211 mm to 422 mm decreased the stiffness and ultimate capacity of the CFCSW. Similarly, the stiffness and load carrying capacity of the CFCSW decreased with an increasing height of the wall, whereas decreasing the height improved the stiffness and capacity. Increasing the steel and concrete thickness enhanced the stiffness and peak strength of the CFCSW and vice versa.

6. The results from the sensitivity analysis illustrated that the ultimate capacity of the CFCSW was most sensitive to the effect of height, while it was least sensitive to the effect of concrete thickness.

5. REFERENCES

1. Zhang, W., Wang, K., Chen, Y., Ding, Y., "Experimental study on the seismic behaviour of composite shear walls with stiffened steel plates and infilled concrete", *Thin-Walled Structures*, Vol. 144, (2019). DOI: 10.1016/j.tws.2019.106279

2. Zhang, X., Qin, Y., Chen, Z., "Experimental seismic behavior of innovative composite shear walls", *Journal of Constructional Steel Research*, Vol. 116, (2016), 218-232. DOI: 10.1016/j.jcsr.2015.09.015

3. Pavel, F., Panfilii, P., Farangsi, E. N., "Estimation of displacement capacity of rectangular RC shear walls using experimental and analytical database", *Civil Engineering Journal*, Vol. 3, (2020). DOI: 10.14311/CEJ.2020.03.0035

4. Honarmand, S., Homami, P., Gharehbaghi, V., Farangsi, E. N., "A study on the significance of the design parameters of steel plate shear walls subjected to monotonic loading", *Civil and Environmental Engineering Reports*, Vol. 30, (2020), 0142-0154. DOI: 10.2478/ceer-2020-0056

5. Berman, J. W., "Seismic behavior of code designed steel plate shear walls", *Engineering Structures*, Vol. 33, (2011), 230-244. DOI: 10.1016/J.ENGSTRUCT.2010.10.015

6. Guo, L., Li, R., Zhang, S., Yan, G., "Hysteretic analysis of steel plate shear walls (SPSWs) and a modified strip model for SPSWs", *Advances in Structural Engineering*, Vol. 15, (2012), 1751-1764. DOI: 10.1260/1369-4332.15.10.1751

7. Nie, J., Zhu, L., Fan, J., Mo, Y., "Lateral resistance capacity of stiffened steel plate shear walls", *Thin-Walled Structures*, Vol. 67, (2013), 155-167. DOI: 10.1016/j.tws.2013.01.014

8. Chen, G., Guo Y., Fan Z., Han, Y., "Cyclic test of steel plate shear walls", *Journal of Building Structures*, Vol. 25, (2004), 19-26. http://en.cnki.com.cn/Article_en/CJFDTOTAL-JZJB200402003.htm

9. Guo, L., Li, R., Rong, Q., Zhang, S., "Cyclic behavior of SPSW and CSPSW in composite frame", *Thin-Walled Structures*, Vol. 51, (2012), 39-52. DOI: 10.1016/j.tws.2011.10.014

10. Guo, L., Rong, Q., Qu, B., Liu, J., "Testing of steel plate shear walls with composite columns and infill plates connected to beams only", *Engineering Structures*, Vol. 136, (2017), 165-179. DOI: 10.1016/j.engstruct.2017.01.027

11. Liao, F., Han, L., Tao, Z., "Seismic behaviour of circular CFST columns and RC shear wall mixed structures: Experiments", *Journal of Constructional Steel Research*, Vol. 65, (2009), 1582-1596. DOI: 10.1016/j.jcsr.2009.04.023

12. Munesi, A., Sharbatdar, M., Gholhaki, M., "An investigation into the factors influencing the cyclic behavior of the buckling-restrained steel plate shear walls", *Steel construction*, Vol. 14, (2020). DOI: 10.1002/stco.201900047

13. Dan, D., fabian, A., Stoian, V., "Theoretical and experimental study on composite steel–concrete shear walls with vertical steel encased profiles", *Journal of Constructional Steel Research*, Vol. 67, (2011), 800-813. DOI: 10.1016/j.jcsr.2010.12.013

14. Lu, X., Gan, C., Wang, W., "Study on seismic behavior of steel plate reinforced concrete shear walls", *Journal of Building Structures*, Vol. 30, (2009), 89-96. http://www.jzjgxb.com/EN/Y2009/V30/I05/89

15. Vecchio, F. J., McQuade, I., "Towards improved modeling of steel-concrete composite wall elements", *Nuclear Engineering and Design*, Vol. 241, (2011), 2629-2642. DOI: 10.1016/j.nucengdes.2011.04.006

16. Zhao, Q., Astaneh, A., "Cyclic Behavior of Traditional and Innovative Composite Shear Walls", *Journal of Structural Engineering*, Vol. 130, (2003), 271-284. DOI: 10.1061/(ASCE)0733-9445(2004)130:2(271)

17. Luo, Y., Guo, X., Li, J., Xiong, Z., Meng, L., Dong N. Zhang, J., "Experimental Research on Seismic Behaviour of the Concrete-Filled Double-Steel-Plate Composite Wall", *Advances in Structural Engineering*, Vol. 18, (2016), 1845-1858. DOI: 10.1260/1369-4332.18.11.1845

18. Ozaki, M., Akita, S., Osuga, H., Nakayama, T., Adachi, N., "Study on steel plate reinforced concrete panels subjected to cyclic in-plane shear", *Nuclear Engineering and Design*, Vol. 228, (2004), 225-244. DOI: 10.1016/j.nucengdes.2003.06.010

19. Varma, A. H., Malushte, S. R., Sener, K. C., Lia, Z., "Steel-plate composite (SC) walls for safety related nuclear facilities: Design for in-plane forces and out-of-plane moments", *Nuclear Engineering and Design*, Vol. 269, (2014), 240-249. DOI: 10.1016/j.nucengdes.2013.09.019

20. Booth, P. N., Bhardwaj, S. R., Tseng, T., Seo, J., Varma, A. H., "Ultimate shear strength of steel-plate composite (SC) walls with boundary elements", *Journal of Constructional Steel Research*, Vol. 165, (2020). DOI: 10.1016/j.jcsr.2019.105810

21. Epackachi, S., Nguyen, N. H., Kurt, E. G., Whittaker, A. S., Varma, A. H., "In-Plane Seismic Behavior of Rectangular Steel-Plate Composite Wall Piers", *Journal of Structural Engineering*, (2014). DOI: 10.1061/(ASCE) ST.1943-541X.0001148

22. AWS D1.3/D1.3M:2018, "Structural welding code- Sheet steel", (2018).

23. AISI S100-16w/S1-18, "North American specification for the design of cold-formed steel structure members", (2016).

24. AISC design guide 31, "Castellated and cellular beam design", (2016).

25. ABAQUS 6.14, "Abaqus analysis user's guide- Volume IV: Elements", (2014).

26. ABAQUS 6.14, "Abaqus analysis user's guide- Volume V: Prescribed conditions, constraints and interactions", (2014).

27. ABAQUS 6.14, "Abaqus analysis user's guide- Volume III: Materials", (2014).

28. Nguyen, N. H., Whittaker, A. S., "Numerical modelling of steel-plate concrete composite shear walls", *Engineering Structures*, Vol. 150, (2017), 1-11. DOI: 10.1016/j.engstruct.2017.06.030

29. Epackachi, S., Whittaker, A. S., "Experimental, numerical and analytical studies on the seismic response of steel-plate concrete (SC) composite shear walls", *Earthquake Engineering to Extreme Events*, (2016). http://www.buffalo.edu/mceer/catalog.host.html/content/shared/www/mceer/publications/MCEER-16-0001.detail.html

30. Rahmani, Z., Naghipour, M., Nematzadeh, M., "Flexural performance of high-strength prestressed concrete-encased concrete-filled steel tube sections", *International Journal of Engineering, Transactions C: Aspects*, Vol. 32, No. 9, (2019), 1238-1247. DOI: 10.5829/ije.2019.32.09c.03

31. Popovics, S., "A numerical approach to the complete stress-strain curve of concrete", *Cement and Concrete Research*, Vol. 3, (1973), 583-599. https://doi.org/10.1016/0008-8846(73)90096-3

32. Sanez, L. P., "Discussion of equation for the stress-strain curve of Concrete, by Desayi P. and Krishnan S", *ACI Journal*, Vol. 61, (1973), 1227-1239.

33. CEB-FIP model code 1990, "Design code", (1990).

Persian Abstract

چکیده

نوع جدیدی از دیوارهای برشی کامپوزیتی نوآورانه ، دیوار برشی فولادی شکل سرد پر شده با بتن (CFCSW)پیشنهاد شده است ، که از بخشهای کانال سرد تشکیل شده و به طول ۲۰ میلی متر جوش داده شده و با بتن پر شده است. مطالعه اصلی CFCSW بر رفتار کلی ، ظرفیت بار نهایی ، سفتی و شکل پذیری تمرکز دارد. سه نمونه از CFCSW با نسبت تصویر ۱.۰ تحت بار یکنواخت جانبی آزمایش می شوند. مدلهای اجزای محدود سه بعدی با نتایج تجربی توسعه داده شده و معیار قرار می گیرند. مدلهای معتبر برای انجام مطالعات پارامتریک برای تعیین تأثیر پارامترها بر عملکرد CFCSW استفاده می شوند. پارامترها عبارتند از ارتفاع ، ضخامت ورق فولادی ، فاصله جوش و ضخامت بتن CFCSW. نتایج مدل سازی عناصر تجربی و محدود نشان می دهد که افزایش فاصله جوش از ۱۰۵ میلی متر به ۲۱۱ میلی متر ، سخت ، شکل پذیری و ظرفیت حمل بار را بهبود می بخشد و به طور مشابه ، ایجاد سوراخ در داخل دیوار باعث افزایش سختی ، شکل پذیری و استحکام CFCSW می شود. ظرفیت نهایی CFCSW بیشترین تأثیر را بر تغییر ارتفاع دیوار می گذارد و کمترین آن را متغیر بودن ضخامت بتن دیوار می کند.

International Journal of Engineering

Stress-strain Characteristics of Reactive Powder Concrete under Cyclic Loading

A. A. Dhundasi*[a], R. B. Khadiranaikar[a], A. I. A. Momin[b]

[a] Department of Civil Engineering, Basaveshwar Engineering College, Bagalkot, Affiliated to VTU, Belagavi, Karnataka, India
[b] Department of Civil Engineering, BLDEA's Vachana Pitamaha Dr. P.G Halakatti College of Engineering and Technology Vijayapur, Affiliated to VTU, Belagavi, Karnataka, India

A B S T R A C T

Reactive powder concrete (RPC) is a type of ultra-high strength cement composite material. It has advanced mechanical properties and shows high ductility characteristics. Many researches have shown that normal and high strength concrete fails under cyclic stresses at load level below its static capacity. In the present study, the mix design guidelines to produce high strength RPC is provided. RPC with compressive strength of 120, 130 and 140MPa was produced. The mechanical properties are obtained for hardened concrete. The present study focuses on the investigation of reactive powder concrete under uniaxial compressive cyclic loading. The investigation was carried out on cubical and cylindrical specimens. The behaviour of RPC under cylic loads is studied by obtaining the stress-strain characteristics under monotonic loading and cyclic loading. Three main types of tests were performed. Stress-strain envelope curve, common point curve and stability point curves were established under repeated load cycles. The limiting stress values required for design are provided. It was concluded that peak stress of the stability point curve could be regarded as the maximum permissible stress. A nonlinear analytical expression was proposed for the normalized stresses and strain which shows a precise fit with the experimental data. The expression will assist in predicting the cyclic response of concrete required for constructional applications.

doi: 10.5829/ije.2022.35.01a.16

1. INTRODUCTION

High rise buildings, long-span bridges, tall statues of national and spiritual leaders become nation's pride, in turn creating a landmark and development of tourism. In actual operating conditions, most structures undergo variable loads. The structures are susceptible to earthquake, wind, blast and impact loads. Hence their design is mainly governed by repetitive loads rather than consideration of just gravity loads. The change with the time in the character of such loads can take a variety of forms i.e., deterministic changes, periodic and non-periodic changes which leads to complex failure mechanisms in structures. These can be expressed in terms of theory of probabilities. Thus, it is necessary to know the nature of failure, behaviour and performance of concrete under cyclic loads. Advanced analyzing

methods are required for complex structures. A realistic analysis could be possible by finite element analysis using computerized programs and it requires constitutive laws of material to be used in the construction.

1. 1. Investigation on Cyclic Loads
a. Plain Cement Concrete

The first research on compressive and tensile cyclic loads was carried out by Considere and De Joly on mortar specimens in 1898. The repeated loads were applied at a frequency of 0.07Hz. Fatigue strengths recorded were 55% of static strengths [1]. Investigations of cyclic stresses on concrete were initiated by Van Ornum in 1903, with strengths in a range of 8.4-11MPa. Subsequent experiments on low strength concrete (14-32MPa) led to develop an understating of performance under compressive cyclic loading. The fatigue strengths observed were 45-60% of static strength at a repeated loading frequency of

Corresponding Author Email: abbasdhundasi@gmail.com (A. A. Dhundasi)

6.33Hz [2]. In later years the fineness and quality of portland cement were improved which led to the production of high strength concretes. Kern and Mehmel [3] studied the effect of concrete strains under cyclic loads. Sample strengths varied from 42-60 MPa. As a result, endurance (Wohler) curves were plotted which are a function of number of cycles vs maximal prismatic stress. Khadiranaikar [4] extended the investigation with high-performance concrete. The concrete with strengths 65, 85 and 102MPa was tested under uniaxial compressive repeated loading. Curves in the forms of envelope points, common points and stability points were plotted. Analytical equations were proposed to fit the experimental data. An analytical expression was provided for normalized curves. It is shown in equation 1.

$$\sigma = \varepsilon^\beta Exp\left[\left(1 - \frac{\varepsilon}{\alpha}\right)\varepsilon\right]$$ (1)

where, σ, ε = Normalized stress and strain ratios respectively. α, β are equation parameters. The results concluded that peak stresses at common point and stability point were 0.85 and 0.75 of envelope stresses, respectively. The similar work was carried out by Aslam et al. [5] on geopolymer concrete of strengths 40-60MPa. Further equations for recycled aggregate concrete were proposed by Hu et.al [6] for numerical simulation of columns and frames subjected to cyclic loads.

b. Reinforced Cement Concrete
Study on plain concrete was insufficient for applications in recent years, where reinforced concrete was used for the construction of many structures. Hence, stress-strain models were proposed by various researchers for loading and unloading paths of confined concrete. The expressions obtained suggested that the reloading path varies in the form of cubic function [7-10]. An approach towards finite element modelling was made by Kwan and. Billington [11]. Different models were evaluated in predicting the cyclic behaviour of reinforced structural concrete. Further reinforced concrete tied columns were modelled by Lukkunaprasit and Thepmangkorn [12]. These were evaluated with experimental values by varying shapes and studying the hysteretic response under different loading cycles. Cyclic stress-strain study was done by Sadrnejad and Khosroshahi [13] with the help of simulation models for reinforced concrete (RC) under uniaxial, biaxial and triaxial compressive and tensile loads. The results indicated that the simulation models were capable of predicting the concrete behaviour under any stress path considered [13]. A theoretical analysis using various expressions was done to examine the RC bridge constructed in Iran. Azadpour and Maghsoudi [14] proposed a finite element model using ANSYS to compare the results of field analysis, which were obtained from preinstalled structural health monitoring (SHM) systems. The strains at several points on the bridge were measured using strain gauges. The strains obtained from theoretical analysis and the ANSYS model were compared with field reading. Theoretical equations provided a strain of 60-70% of field values. Whereas ANSYS model results were close to field analysis and were in the range of 80-90% of field values [14]. Research on loading history and number of cycles on fixed end RC beams and infill masonry was done. Results yielded hysteretic curves. Strut and tie models (STM) were proposed to evaluate the mode of failure and loading capacity of members [15,16]. The most recent study on RC portal frames subjected to lateral and cyclic loads was done by Gunasekaran and Choudhury [17]. The results were plotted in the form of hysteretic curves. It was observed that initiation of cracks took place at 30% of failure load. The ultimate lateral load causing failure was observed to be 62kN [17].

1. 2. Investigation on Reactive Powder Concrete
In latter part of 20th century Ultra-High-Strength Concrete (UHSC) is being employed in many important structures. Reactive-Powder-Concrete (RPC) is one, which is advanced among the group of UHSC. RPC can fulfil required characteristics of structural concrete, such as high durability, ultra-high-strength, high workability and high toughness, compared to plain concrete. RPC can take more loads, for a long-life span. Sherbroke pedestrian bridge in Canada is the first bridge constructed using RPC in 1997. It has a span of 60m. RPC of grade 200MPa was used for the construction. Seonyu footbridge in Korea with a span of 120m and Sakata Mirai bridge in Japan with a span of 50m were also constructed using RPC in 2002. RPC has also been utilized in construction of many bridges and pathways in USA, New Zealand, Australia, Austria and other parts of the world. It also has applications in the field of missile silos, energy dissipaters, airport and highway pavements and bridge piers etc.

RPC was first developed by Richard and Cheyrezy [18] using principles of homogeneity, ductility, and optimum packing. Mechanical properties of RPC were studied by Coppola et al. [19]. RPC of 200 MPa strength was produced by combinations of ambient, pressure and steam curing up to 90° – 160° C. Kumar and Gururaj [20] investigated RPC by replacing cement with metakaolin and alccofine with various proportions. They found that 51% of cement, 26% of alccofine and 15% of metakaolin will give higher strength, of up to 110MPa, among the various proportions. Elson and Sarika [21] studied many trial mixes of RPC by varying different raw materials and the highest strength of 130MPa was obtained. Optimum values of constituent materials for desired strength were obtained. The results indicated that ordinary portland cement of 1000kg/m³,

silica fume-22.25%, quartz powder-25.2%, W/B ratio-0.2 and steel fibres of 3.06%, is required to produce RPC of 130MPa Strength. Mingze et. al. [22] studied RPC under fatigue at various amplitudes. Cylindrical specimen was subjected to load (65-95% of ultimate strength) with the frequency of 3cycles/s with multi-level amplitude. They found that difference in the size of the specimen is less significant on residual strain in fatigue and relation between deformation and number of cycles was proposed. Muranal and Khadiranaikar [23] produced RPC of 180MPastrength. They studied the durability aspects of RPC under acid attacks and chloride ion permeability. The study concluded that the weight loss and reduction in strengths were very less compared to normal strength and high strength concretes. A very low to negligible amounts of chloride ions were passed through the specimens. RPC shows higher resistance under high concentrations of acids [23]. A study on mechanical properties of RPC was done by Madhkhan and Saeidian [24]. Glass fibres by volume of 1.5 - 2% were added. Normal curing yielded 90-100 MPa compressive strength. RPC with 110 - 140 MPa strengths were obtained with autoclave curing and accelerated ageing methods [24].

1. 3. Objectives   It is observed that many investigations have been carried to evaluate the behaviour of cement mortars, low - high strength plain and reinforced concretes under repeated loads. Mathematical models and analytical equations are obtained from such investigations to predict the behaviour of concrete under different stress paths. However, there is no significant data available on RPC to predict its nature under cyclic loads. Much of the investigations have been carried out to produce RPC with high strengths. But there are no standard guidelines available for mix designs. Hence an effort is made in this research to produce RPC high strengths and study its nature under cyclic loads. Following objectives have been set.
i.   To produce three grades of RPC with strengths 120MPa, 130MPa and 140MPa.
ii. To study the behaviour of RPC under monotonic load curves and cyclic load curves.
iii. To study the stresses and strains under envelope curve points, common points and stability points.
iv. To propose a single analytical equation for the normalized stress and strains.

The study will provide the optimum mix proportions to produce ultra-high strength RPC. It will also provide limiting stress values required for the designs. The analytical equation will help in predicting the behaviour of RPC under cyclic stresses. This will help the researchers and constructional engineers to use the material to its full potential.

2. MATERIALS

From the literature, it is observed that high-grade ordinary portland cement (OPC) is recommended to produce higher strengths of concrete. In present research OPC-53 grade, Ultratech cement is used. The density and fineness are 3120 kg/m^3 and 3390 cm^2/g, respectively. It confirms to IS: 4032-1985 [26]. Silica fume - 920D is obtained from ELKEM MICROSILICA$^®$ that confirms to IS: 15388-2003 [27] and ASTM C1240 [28].

In RPC, coarse aggregates are completely eliminated. Only high purity silica sand is used. It is obtained from AU(P) LTD. Mukka, Mangalore. It is yellowish-white in colour and particle size in the range of 90 μm to 600 μm. The quartz flour is brought from Raviraj Mineral Industries, Bangalore. The particle size is in the range of 10 μm to 40 μm with a specific gravity of 2.6. Quartz flour improves density and hydration process. Water to binder (w/b) ratio is very low in RPC compared to normal concrete. Hence high-range water reducing agent is used with w/b ratio of 0.2. Master Glenium product from BASF of series SKY-8233 is used as superplasticizer in the present work, which is certified from ATM C494 and IS2645-2003 [29].

3. EXPERIMENTAL PROGRAM

3. 1. Production of RPC
a. Mix Procedure and Curing:
A Pan mixture of capacity 200 litres and mixing speed of 140 – 280 RPM is used for mixing raw materials. The speed of pan mixer was set to 150 RPM. The dry mixing of cement, silica fume, sand and quartz powder was done for 2 minutes. Later, 50% by volume of water was added along with superplasticizer and mixed for 5 minutes. The remaining amount of water and superplasticizer is then added to the wet mix. The constituents are mixed for 18±2 minutes to get a wet workable mix. The mix procedure adopted was similar and improvised to the procedure recommended by Parameshwar and Subhash [25]. The flowable mix obtained is shown in Figure 1. The mix is then poured into cubical and cylindrical moulds. Cube specimens are 100×100×100mm and cylindrical specimens are of 70mm diameter and 140mm height as shown in Figure 2. The samples were allowed to set and then immersed in a tank full of clean water. Normal curing was done up to 28 days as per IS 516-1959 [30].

b. Optimum Mix proportions:
At present, there are no standard guidelines available to produce RPC. Hence many trial mixes have been carried out. Above mentioned procedure is applied and

Figure 1. Wet mix of RPC

Figure 2. Samples of RPC

optimum composition is obtained for the constituent materials. The details of mix proportions are given in Table 1.

3. 2. Monotonic Load Tests   A servo-controlled compression testing machine, of capacity 3000kN, was used to obtain compressive strengths. The load was applied at a rate of 0.5 kN/s till the complete failure of sample takes place. The loads (in kN) and deformation (in mm) are noted down. The corresponding stress and strain values are calculated. The test procedure is shown in Figure 3.

3. 3. Cyclic Load Tests   An actuator of 500 kN capacity was used to apply cyclic loads. The load was increased at the rate of 20N/s. A compressometer with a load cell was used to record load values in kN. Circumferential extensometer and LVDT's were

Figure 3. Strength Test on RPC

attached to specimens to record resultant deformation/displacement in terms of mm. The obtained data are processed in a data acquisition system. Further corresponding stress-strain values are calculated. The test setup is shown in Figure 4.

Displacement controlled cyclic load tests have been carried out in the actuator. It was possible to regulate load history by monitoring strain in each cycle. In the ascending zone of the stress-strain curve, the loads are increased gradually up to pre-established intervals of strain and then loads are released to form the descending zone. This completes one cycle. Once the material is failed at ultimate load, stress-strain curve tends to drop. Then, the releasing of load is done when the stress values are observed to decrease than the peak stress values of respective cycles. The same procedure is applied for all three grades of concrete and cyclic load curves are plotted.

The stability points test was carried out for each individual cycle obtained from cyclic load tests. The unloading was done when the reloading curve intersects with unloading curve of previous cycle. The stress values are seen to decrease and get stabilized at certain strain values. A closed hysteresis loop is formed.

TABLE 1. Mix proportions of RPC

Sl. No.	Material	M1 (120 MPa)	M2 (130 MPa)	M3 (140 MPa)	Units
1	Cement	900	900	900	Kg/m^3
2	Silica Fume	90	108	135	Kg/m^3
3	Sand	977.32	932.92	911.65	Kg/m^3
4	Quartz Powder	135	90	45	Kg/m^3
5	Sper plasticizer	22.5	18	18	Kg/m^3
6	Water	0.21	0.2	0.19	-

Figure 4. Cyclic Load Test

These values of lower bound stresses and strains are noted down. The curves are plotted by joining all the stress-strain points which forms a stability point curve.

4. RESULTS AND DISCUSSIONS

Three grades of RPC i.e., M1, M2 and M3 with compressive strengths 120 MPa, 130 MPa and 140MPa are produced for the present research. The number of loading cycles and stress levels are the major factors affecting the behaviour of RPC under cyclic loading. The effect of cyclic loading can be categorized as follows:
- High-stress levels with a low number of cycles.
- Low-stress levels with a high number of cycles.

In the former category, incremental deformations are observed which leads to formation of plastic strains and micro-cracks resulting in failure of structure. Hence present study focuses on such investigation.

4. 1. Monotonic Load Curve   Incremental uniaxial monotonic loads are applied on the cylindrical specimens until the complete failure of specimen is observed. The peak stress and strain values for each mix are noted down.

Monotonic loading curves plotted for all the mixes are shown in Figure 5. The curves are in a linear state until 85% of peak stress value. The material is in perfectly elastic state. Further, an increase in the load changes the slope of the curve. It is due to the fact that initial cracks were formed when the stress values cross 85% of the ultimate stress values. The material enters into an elasto plastic state. The specimens continue to take the loads but shows higher deformation. At ultimate load, major cracks are formed and material loses all of its elastic properties and enters into a plastic state. The effective load carrying capacity of the specimens is lost. Further increase in loading induces
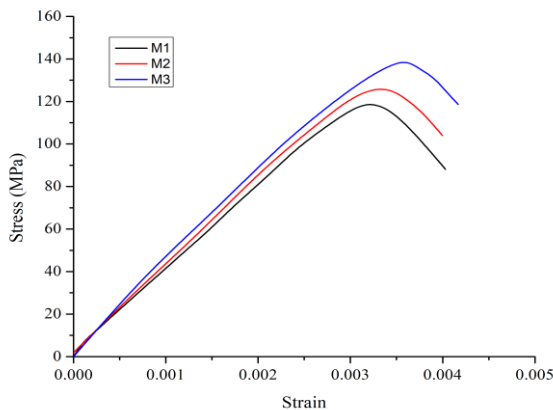
additional strains and stress values are gradually decreased until the specimen fails completely.

From Figure 5 it is observed that the curve drops steeply after peak stresses. The failure is observed to be sudden and bursting in nature. This indicates the brittle nature of RPC. The peak stress and strain value obtained by monotonic loading are shown in Table 2.

4. 2. Cyclic Load Curves   The displacement/ strain intervals are fixed. In ascending part of the curve, load values are increased up to predetermined strain interval and then the loads are released until the strain is stabilized up to certain lower bound values, which forms the descending part. This closed hysteresis loop forms one cycle. The process is repeated up to peak load/ stress values. At peak value of stress initiation of cracks takes place and the material loses its effective load carrying capacity. In proceeding cycles releasing of load is done when the reloading curve starts to descend. This process is continued until complete failure of specimen takes place. The points of strain and corresponding stress values are plotted in the form of cycles as shown in Figures 6-8 for M1, M2 and M3, respectively.

Figure 6 shows a comparison model [6] of normal strength concrete (NSC). The strength of concrete was 25MPa. From the figure, it was observed that stresses under cyclic loading are more than monotonic load stresses. The skeleton curve also known as envelope curve does not coincide with the monotonic load curve. The specimen failed after 10th cycle. The maximum strain corresponding to peak stress values was observed to be 0.002. The strain at complete failure is observed to be 0.010. It shows the ductile nature of normal concrete.

TABLE 2. Peak Monotonic Load Stress-Strains

Mix	Stress (MPa)	Strain
M1	118.19	0.003192
M2	128. 55	0.003208
M3	137.25	0.003219

Figure 5. Monotonic Load Curves
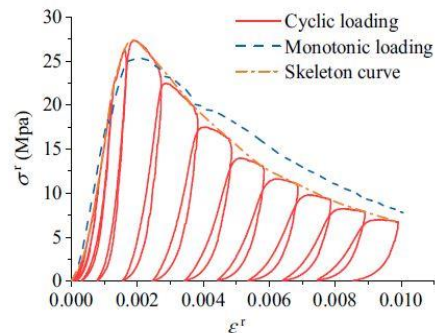
Figure 6. Comparison Model for NSC [6]
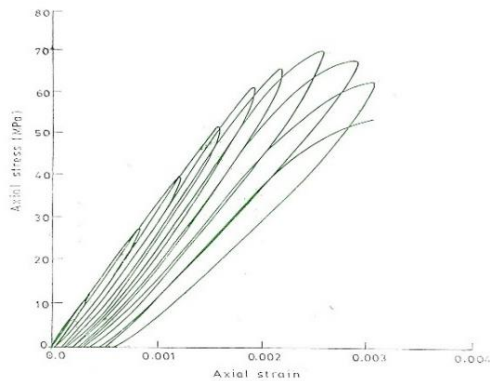
Figure 7. Comparison Model for HSC [4]
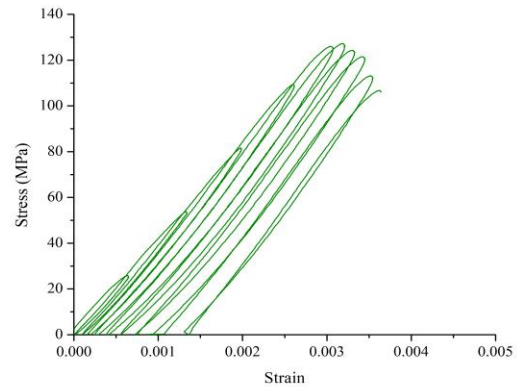
Figure 9. Cyclic Load Curves for M2
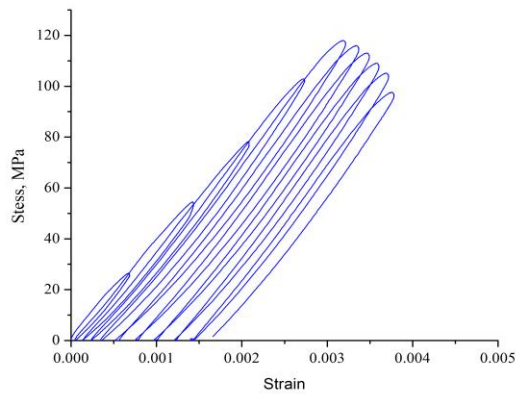
Figure 8. Cyclic Load Curves for M1
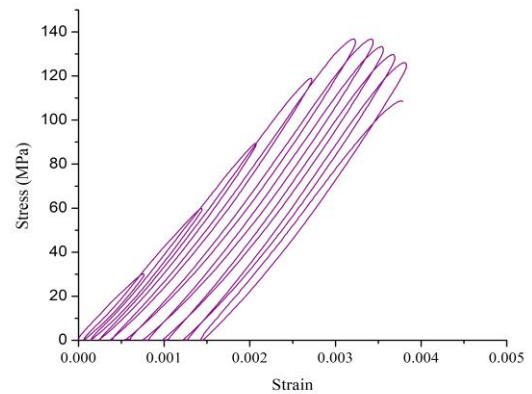
Figure 10. Cyclic Load Curves for M3

Figure 7 shows comparison models of high strength concrete (HSC). The strength of concrete was 85MPa. The results concluded that the envelope curve coincides with the monotonic load curve. The specimen failed after 11th cycle. The maximum strain corresponding to peak stress values were observed to be 0.0025. The strain at complete failure is observed to be 0.0030. It indicates that high strength concrete shows brittle nature of failure.

The results of the present study, the points of strain and corresponding stress values, are plotted in the form of cycles as shown in Figures 8-10 for M1, M2 and M3, respectively. It was observed that specimens for M1, M2 and M3 failed after 11th, 10th and 9th cycles respectively. This indicates that, as the grade of concrete increased, the resistance towards plastic stresses reduced for post-peak behaviour. The specimens tend to fail earlier than the lower grade concrete. However, RPC shows higher strain values i.e., 0.0031, at peak stress values than compared to NSC and HSC. This indicates that RPC shows better performance when subjected to higher stress values and also it can withstand more deformations. The strain at complete

failure is observed to be 0.0035 which is again more than HSC. The RPC also shows the brittle nature of failure.

4. 3. Envelope Curve   The envelope curve is plotted by superimposing the peak stress-strain points of each cycle obtained in cyclic load curves.

The envelope curve for M1 is plotted in Figure 11. It is observed that the envelope curve coincides with monotonic curve. Similar nature is observed for M2 and M3, respectively. The mean stress and strain values obtained are shown in the following Table 3.

4. 4. Common Point Curve   The common point was initially defined as a folding point by Khadiranaikar [4] as the curve started folding after the intersection of the reloading portion of curve on loading portion of previous cycle. Thus, a common point curve is obtained by joining the loci of points where reloading curve intersects with unloading curve of previous cycle. The material remains in an elasto-plastic state. The common points for M1 are shown in Figure 12.
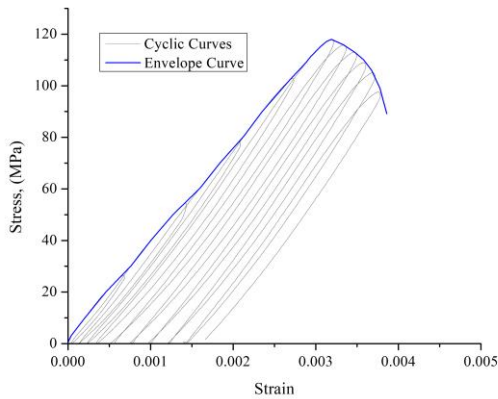
Figure 11. Envelope Curve for M1

TABLE 3. Peak Envelope Stress-Strains.

Mix	Env. Stress (MPa)	Env. Strain
M1	117.9893	0.003189
M2	127.2547	0.003197
M3	136.8497	0.003210
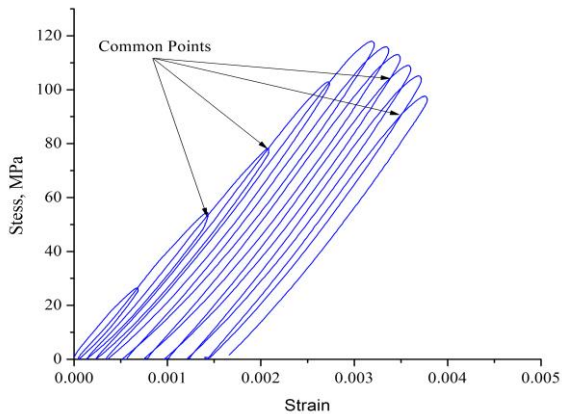
Figure 12. Common points for M1

A common point for RPC contributes much to structural design, as load beyond this limit results in remnant deformation, hence it sets an upper limit for the material to be used under cyclic loading. The mean peak stresses obtained from experiments are shown in Table 4.

TABLE 4. Peak Common Point Stress-Strains.

Mix	Stress (MPa)	Strain
M1	110.8901	0.003048
M2	119.8338	0.003137
M3	127.9705	0.003166

4. 5. Stability Point Curve   Peak stress-strain values at common points of each curve are noted down. The stresses above common points will lead to additional strains, while stresses below these values will give no additional strains and it is observed that stress-strain curve will go into a closed hysteresis loop. These points are called stability points and the loci of points as stability point curves. These points are also considered as minimum stress levels.

The stability points test curves obtained from present investigation are shown in Figures 13-15. From the figures, it is observed that the number of cycles within the loop increases with an increase in stress value to reach a stability point. When stress values reach to maximum, an initial crack is induced. The strain in the specimen is increased with the stress values being nearly the same. The slope of the curve is changed after a certain number of cycles which indicates that the specimen has failed, yet it continues to take the load and further increase in the stress levels will lead to complete failure. The factor of safety specified in IS codes is 1.5 which is suitable for normal and high strength concretes. The present investigation provides a factor of safety of 1.35**.** Maximum stability point stress observed for M1, M2 and M3 are shown in Table 5.

4. 6. Analytical Curves   The stress-strain values obtained from all the three curves are normalized with peak stress (σ_p) and peak strain (ε_p). When a linear regression model contains only one independent variable, it is referred as a simple regression model. In the present study, modelling is done between normalized stress as a dependent variable with respect to a single independent variable i.e., normalized strain. The present investigation is based on the principle of least squares. The difference between experimental observations and fitted curve in the scatter diagram are minimized, by the orthogonal regression method, to get intercepts and slope parameters. The curve is fitted by
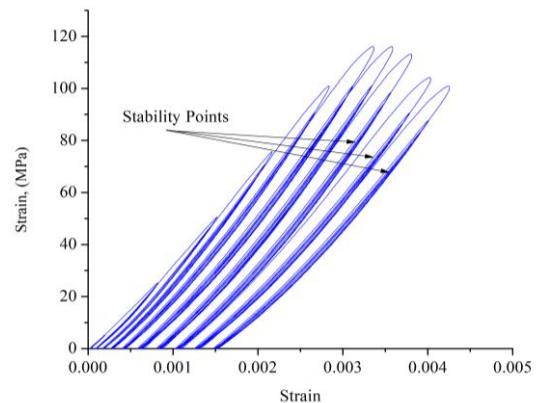
Figure 13. Stability Points test for M1
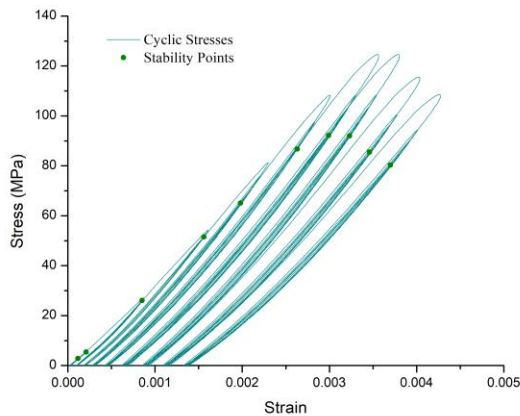
Figure 14. Stability Points test for M2
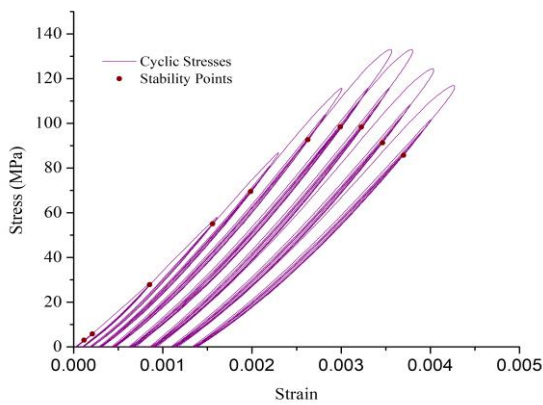
Figure 15. Stability Points test for M3

TABLE 5. Peak Stability Point Stress-Strains.

Mix	Stress (MPa)	Strain
M1	85.8386	0.002823
M2	92.1582	0.002991
M3	98.4249	0.003027

using MATLAB. The analytical expression obtained is in the Fourier form with a fitting degree of one. The proposed expression is shown below.

$$f(\sigma) = C_0 + C_1 \cos(\alpha\varepsilon) + C_2 \sin(\alpha\varepsilon) \tag{2}$$

where, σ, Ɛ are Normalized stress and strain ratios respectively, C_0 is an intercept parameter and, C_1, C_2, α are equation constants representing slope parameters.

The values of constants generated for each curve are presented in Table 6. The obtained mean values of strains are 0.003189, 0.003197 and 0.0003210 with a standard deviation of 3.41×10^{-5}, 4.62×10^{-5} and 5.91×10^{-5} for M1, M2 and M3 mixes, respectively. The obtained

mean peak stress values are 117.99 MPa, 127.26MPa and 136.85MPa with a standard deviation of 2.18MPa, 2.67MPa and 2.98MPa for M1, M2 and M3 mixes, respectively. The proportion of variance is expressed as a statistical measure R-squared (R_C) for each type of cyclic curve. It is shown in Table 6 for all the grades RPC. From the above-proposed equation, the average variance was found to be 0.981.

The normalized curves for all three mixes are shown in Figures 16-27. It is observed that the analytical curve shows a perfect fit for all the experimental points considered. From the Figures 16 to 27, it is noted that the analytical envelope curve is linear in the initial portion up to 80% of normalized stress peak. Later it is observed to be parabolic in nature. The normalized common point curve follows the same path as normalized envelope curve with lesser stress values. It exhibits curvilinear behaviour in the initial portion as shown in Figures 19 to 21. The average maximum normalized peak stress corresponding to common points

TABLE 6. Values of Equation Constants

Curves	RPC Mix	Constants				
		C0	C1	C2	α	Rc
Envelope Point	M1	0.4512	-0.4162	0.2214	2.550	0.9883
	M2	0.4594	-0.4301	0.2450	2.741	0.9864
	M3	0.4709	-0.4328	0.1961	2.560	0.9856
Common Point	M1	0.4801	-0.4020	0.0260	3.192	0.9694
	M2	0.4563	-0.4067	0.0861	2.998	0.9609
	M3	0.4851	-0.4008	0.0475	3.041	0.9745
Stability Point	M1	0.3221	-0.3125	0.1967	2.848	0.9822
	M2	0.2974	-0.2886	0.2428	2.506	0.9897
	M3	0.3018	-0.2968	0.2018	2.659	0.9905
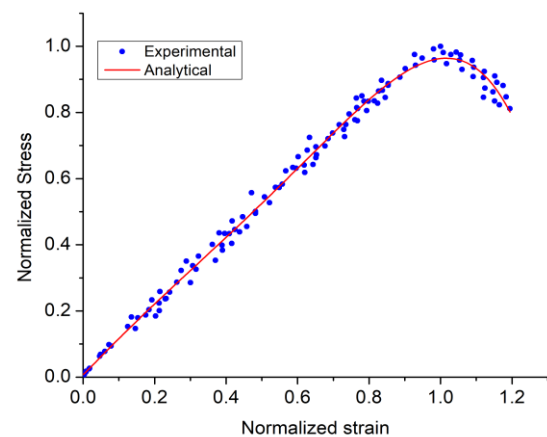
Figure 16. Normalized Envelope Curve for M1
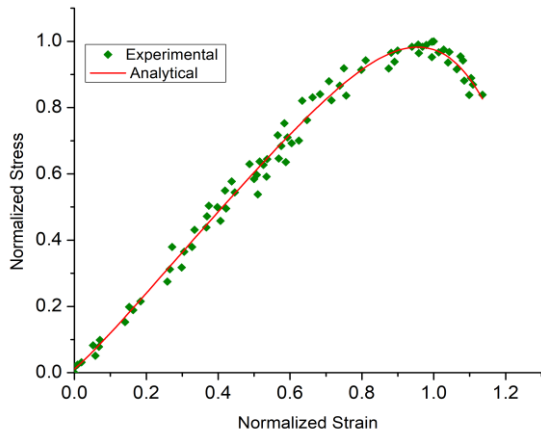
Figure 17. Normalized Envelope Curve for M2
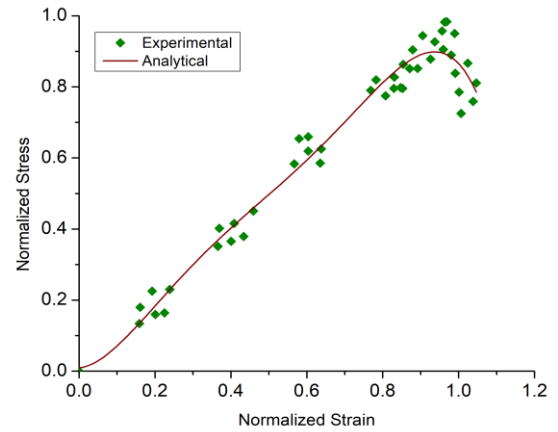
Figure 20. Normalized Common Point Curve for M2
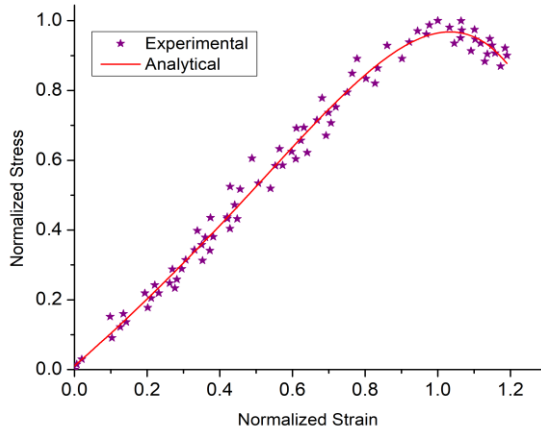
Figure 18. Normalized Envelope Curve for M3
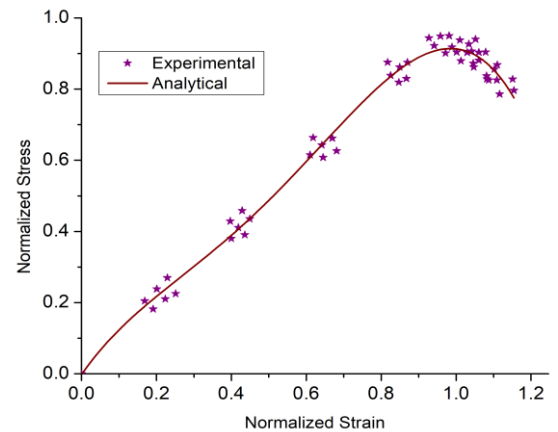
Figure 21. Normalized Common Point Curve for M3
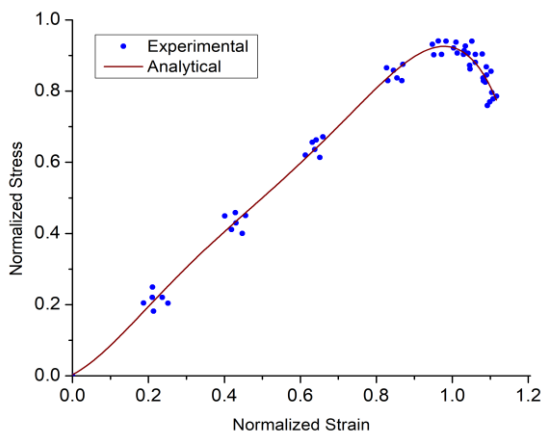
Figure 19. Normalized Common Point Curve for M1
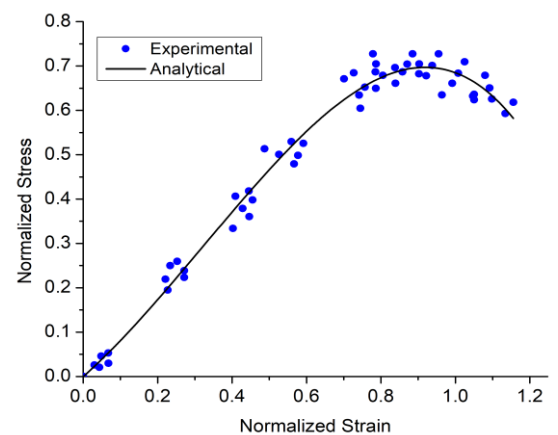
Figure 22. Normalized Stability Point Curve for M1
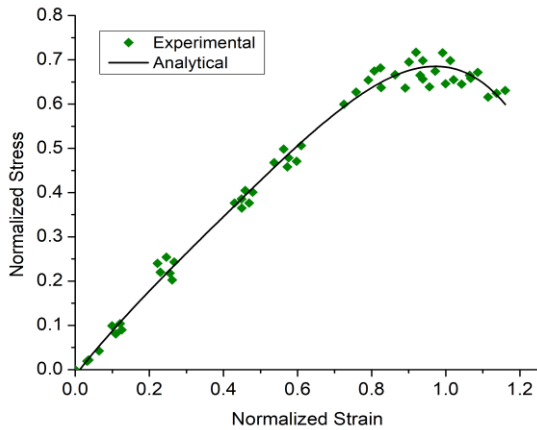
Figure 23. Normalized Stability Point Curve for M2

Figure 24. Normalized Stability Point Curve for M3

Figure 25. Combined Normalized Curves for M1

Figure 26. Combined Normalized Curves for M2

Figure 27. Combined Normalized Curves for M3

is observed to be 0.948 for all the grades of RPC. The normalized stability point curve is linear in nature as shown in Figures 22 up to 24. It provides the limits of plastic stress values beyond which failure of specimen due to plastic strain accumulation is observed. The average maximum normalized stability points stress observed is 0.728.

5. CONCLUSIONS

Reactive powder concrete is a new generation ultra-high-strength cement composite material. There are no specific guidelines available for the procedure of mix design. The present investigation aims to produce high strength RPC and to study its behaviour under cyclic loads. The conclusions drawn from the present research are as follows:

1. The procedure and mix proportions for producing ultra-high strength RPC with different constituent materials is obtained. RPC with 120MPa, 130MPa and 140MPa compressive strengths have been achieved.

2. Stress-strain characteristics of RPC under cyclic loads is compared with normal strength concrete (NSC) and high strength concrete (HSC). Higher strain values were observed at higher stress ranges.

3. The behaviour of RPC under cyclic loads is studied by plotting stress-strain monotonic curve, envelope points curve, common points curve and stability points curve.

4. It is observed that descending part of the monotonic stress-strain curve, after peak loading, falls drastically and shows the brittle nature of failure in RPC.

5. The envelope curve for all grades of concrete is similar and identical to monotonic stress-strain curve. It was also shown that envelope curve coincides with monotonic load curve at peak stresses.

6. The common point curve was established, which can be used as upper-stress limit in the design of RPC structures. It was observed that mean common point stresses are 90 - 94% of peak stress.

7. Lower strength concrete exhibited a lower stress ratio for the stability point curve. Stress values obtained in stability point curve indicate that stability point stress level is in the range of 70 - 75% of that of peak stress values before the failure of specimen.

8. The failure of specimen was initiated due to the formation of cracks at load cycles with peak stresses greater than the peak stress of stability points.

9. It was observed that both unloading and reloading curves of a cycle never intersected any other unloading and reloading curves of previous cycles respectively. It shows that in each cycle there is a residual strain. The average residual strain observed was 5×10^{-4}.

10. An analytical expression was proposed to predict the behaviour of RPC under uniaxial compressive cyclic loads. The expression exhibits a precise fit for all the grades of concrete considered.

6. REFERENCES

1. Ornum, J. L. V. "The Fatigue of Cement Products." *Transactions of the American Society of Civil Engineers*, Vol. 51, No. 2, (1903), 443-445. https://doi.org/10.1061/TACEAT.0001612.

2. J. L. Van Ornum, "Fatigue of Concrete," *Transactions, American Society of Civil Engineers*, Vol. 58, No. 1, (1907), 294-320. https://doi.org/10.1061/TACEAT.0001963.

3. Kern E, Mehmel A. "Elastische und plastische Stauchungen von Beton infolge Druckschwell- und Standbelastung. Deutscher Ausschuß K für Stahlbeton", Heft 153, W. Ernst; 1962.

4. Khadiranaikar, R. "Experimental investigation of high-performance concrete under repeated compressive loading", (2003), IIT Delhi.

5. Aslam Hutagi, R.B. Khadiranaikar, Aijaz Ahmad Zende, "Behavior of geopolymer concrete under cyclic loading", *Construction and Building Materials*, Vol. 246, (2020), 118430, https://doi.org/10.1016/j.conbuildmat.2020.118430.

6. Xiaobin Hu, Qinwang Lu, Zihao Xu, Wenliang Zhang, Shanshan Cheng, "Compressive stress-strain relation of recycled aggregate concrete under cyclic loading", *Construction and Building Materials,* Vol. 193, (2018), 72-83, ISSN 0950-0618, https://doi.org/10.1016/j.conbuildmat.2018.10.137

7. Hsu, T. T. C., "Fatigue and microcracking of concrete", *Matériaux et Construction*, Vol. 17, No. 1, (1984), 51-54. https://doi.org/10.1007/BF02474056.

8. Gosain, N. K., Jirsa, J. O., and Brown, R. H.,"Shear requirements for load reversals on RC members", *Journal of the Structural Division, ASCE*, Vol. 103, No. 7, (1977), 1461-1476, https://doi.org/10.1061/JSDEAG.0004677.

9. Hwang, T.-H., and Scribner, C. F., "R/C member cyclic response during various loadings", *Journal of Structural Engineering* 110, No. 3, (1984), 477-489, https://doi.org/10.1061/(ASCE)0733-9445(1984)110:3(477).

10. Hans W. Reinhardt, Hans A. W. Cornelissen, and Dirk A. Hordijk, "Tensile tests and failure analysis of concrete", *Journal of Structural Engineering*, Vol. 112, No. 11, (1986), 2462-2477, https://doi.org/10.1061/(ASCE)0733-9445(1986)112:11(2462).

11. W.P. Kwan1 and S. L. Billington, "Simulation of Structural Concrete Under Cyclic Load", *Journal of Structural Engineering*, Vol. 127, (2001), 1391-1401. https://doi.org/10.1061/(ASCE)0733-9445(2001)127:12(1391)

12. Panitan Lukkunaprasit and Jatupon Thepmangkorn, "Load History Effect on Cyclic Behavior of Reinforced Concrete Tied Columns", *Journal of Structural Engineering*, Vol. 130, (2004), 1629-1633. https://doi.org/10.1061/(ASCE)0733-9445(2004)130:10(1629).

13. Sadrnejad, S., Khosroshahi, A., "Substructure Model for Concrete Behavior Simulation under Cyclic Multiaxial Loading". *International Journal of Engineering, Transactions A: Basics*, Vol. 21, No. 4, (2008), 329-346.

14. Azadpour, F., Maghsoudi, A. "Stress-Strain Field and Theoretical Analysis of RC Bridge". *International Journal of Engineering, Transactions B: Applications*, Vol. 22, No. 1, (2009), 7-22.

15. Vincent Sam Jebadurai, S., Tensing, D., Freeda Christy, C. "Enhancing Performance of Infill Masonry with Skin reinforcement Subjected to Cyclic Load". *International Journal of Engineering, Transactions B: Applications,* Vol. 32, No. 2, (2019), 223-228. doi: 10.5829/ije.2019.32.02b.06.

16. Arabzadeh, A., Hizaji, R. "A Simple Approach to Predict the Shear Capacity and Failure Mode of Fix-ended Reinforced Concrete Deep Beams based on Experimental Study". *International Journal of Engineering, Transactions A: Basics*, Vol. 32, No. 4, (2019), 474-483. doi: 10.5829/ije.2019.32.04a.03

17. Gunasekaran, K., Choudhury, S. "Experimental Study on Single Bay Reinforced Coconut Shell Concrete Portal Frame under Lateral and Cyclic Load". *International Journal of*

Engineering, Transactions B: Applications, Vol. 34, No. 8 (2021), 1905-1912. doi: 10.5829/ije.2021.34.08b.12

18. Richard P and Cheyrezy M, "Composition of reactive powder concrete", *Cement and Concrete Research*, Vol. 25, No. 7 (1995), 1501-1511, http://dx.doi.org/10.1016/0008-8846(95)00144-2.

19. Coppola, L., Cerulli, T., Troli, R. and Collepardi, M. "The Influence of Raw Materials on Performance of Reactive Powder Concrete", International Conference on High-Performance Concrete and Performance and Quality of Concrete Structures, Florianopolis (1996), 502-513.

20. S. Kumar, K. Gururaj, "Reactive Powder Concrete with mineral admixtures", *Journal of Emerging Technologies and Innovative Research*, Vol. 2, No. 6, (2015). 1749-1757. doi: http://www.jetir.org/papers/JETIR1506013.pdf.

21. Elson John, Sarika S, "A Study on Properties of Reactive Powder Concrete", *International Journal of Engineering Research & Technology*, Vol. 4, (2015), 110-113. doi: 10.17577/ijertv4is110170.

22. Mingze., Yu, Zao., Sun, M., "Fatigue properties of RPC under cyclic loads of single-stage and multi-level amplitude". *Journal of Wuhan University of Technology-Mater. Sci. Ed.*, Vol. 25 (2010), 167-173. https://doi.org/10.1007/s11595-010-1167-8.

23. Santosh M Muranal and Khadiranaikar, "Study on the durability characteristics of reactive powder concrete", *International*

Journal of Structural and Civil Engineering Research, Vol. 3, No. 2, (2014), 45-56.

24. Madhkhan, M., Saeidian, P., "Mechanical Properties of Ultra-High-Performance Concrete Reinforced by Glass Fibers under Accelerated Aging", *International Journal of Engineering, Transactions B: Applications*, Vol. 34, No. 5, (2021), 1074-1084. doi: 10.5829/ije.2021.34.05b.01

25. Hiremath, Parameshwar, Yaragal, Subhash, "Influence of mixing method, speed and duration on the fresh and hardened properties of Reactive Powder Concrete", *Construction and Building Materials*, Vol. 141, (2017), 271-288. https://doi.org/10.1016/j.conbuildmat.2017.03.009

26. "Method of Chemical Analysis of Hydraulic Cement", Bureau of Indian Standards, IS-4032: 2003, New Delhi.

27. "Silica Fume - Specification", Bureau of Indian Standards, IS-15388: 1985 (Reaffirmed 2005), New Delhi.

28. "Standard Specification for Silica Fume Used in Cementitious Mixtures", ASTM, C1240-05: 2005.

29. "Integral Waterproofing Compounds for Cement Mortar and Concrete - Specification", Bureau of Indian Standards, IS-2645: 2003 (Reaffirmed 2005), New Delhi.

30. "Methods of tests for strength of concrete", Bureau of Indian Standards, IS-516:1959 (Reaffirmed 1999), New Delhi.

Persian Abstract

چکیده

بتن پودری واکنشی (RPC) نوعی ماده کامپوزیت سیمانی با مقاومت فوق العاده بالا است. خواص مکانیکی پیشرفته ای دارد و ویژگی های شکل پذیری بالایی را نشان می دهد. بسیاری از تحقیقات نشان داده اند که بتن معمولی و با مقاومت بالا تحت تنش های چرخه ای در سطح بار کمتر از ظرفیت استاتیکی خود دچار شکست می شود. در مطالعه حاضر، دستورالعمل طراحی مخلوط برای تولید RPC با مقاومت بالا ارائه شده است. RPC با مقاومت فشاری ۱۲۰، ۱۳۰ و ۱۴۰ مگاپاسکال تولید شد. خواص مکانیکی برای بتن سخت شده به دست می آید. مطالعه حاضر بر بررسی بتن پودری راکتیو تحت بارگذاری چرخه ای فشاری تک محوری تمرکز دارد. بررسی بر روی نمونه های مکعبی و استوانه ای انجام شد. رفتار RPC تحت بارهای سیلیکی با به دست آوردن ویژگی های تنش-کرنش تحت بارگذاری یکنواخت و بارگذاری چرخه ای مورد مطالعه قرار می گیرد. سه نوع اصلی آزمایش انجام شد. منحنی پوشش تنش-کرنش، منحنی نقطه مشترک و منحنی نقطه پایداری تحت سیکل های بار مکرر ایجاد شد. مقادیر تنش محدود کننده مورد نیاز برای طراحی ارائه شده است. نتیجه گیری شد که تنش اوج منحنی نقطه پایداری را می توان به عنوان حداکثر تنش مجاز در نظر گرفت. یک بیان تحلیلی غیرخطی برای تنش ها و کرنش های نرمال شده پیشنهاد شد که تناسب دقیقی با داده های تجربی نشان می دهد. این عبارت به پیش بینی پاسخ چرخه ای بتن مورد نیاز برای کاربردهای ساختمانی کمک می کند.

International Journal of Engineering

Effect of Various Microstructures Obtained from Heat Treatment on Machinability Behavior of Ti-6Al-4V Alloy

M. T. Nohgani[a], O. Bayat[*b], O. Moghadam[a], V. A. Mehrizi[c]

[a] Materials Science and Engineering Department, Imam Khomeini International University (IKIU), Qazvin, Iran
[b] Department of Material Science and Engineering, Hamedan University of Technology, Hamedan, Iran
[c] Department of Materials Engineering, Karaj Branch, Islamic Azad University, Karaj, Iran

PAPER INFO

ABSTRACT

Drilling test on cylindrical work-pieces was carried out to analysis the effect of various microstructures resulting from heat treatment on the machinability of the Ti-6Al-4V alloy. Chip morphology plays a predominant role in determining machinability and wearing of a tool during the drilling of titanium alloys. For this purpose, Ti-6Al-4V was heat treated in three variant cycles then drilled by 2mm diameter drill at 18.8 m/s speed and 0.1 mm/rev feed rate. Results show that heat treatment can affect on hardness. The SEM results showed that by changing their phase and morphology obtained from different heat treatment cycle, the machining conditions change. Increasing hardness led to increases length of spiral chips that indicate easy drilling. At a lower depth of cutting, ribbon chips are more compacted in comparison with samples which have a lower hardness. Drilling temperature was increased by increasing deep hole. Samples with lower hardness had a higher temperature in drilling.

1. INTRODUCTION

Titanium alloys are excellent candidates for high performance applications owing to their high strength to weight ratio and excellent corrosion resistance, even at high temperature [1]. However, titanium alloys are regarded as extremely difficult to cut materials. Tool wear is intense because of the high cutting temperature due to low thermal conductivity [2]. In addition, the high chemical reactivity of titanium at high temperature with most of the tool materials produces a strong adhesion of the work-piece to the tool surface, thus leading to chipping and premature tool failure [3]. Thus, the high temperature generated close to the cutting edge of the tool when machining titanium is the principal reason for the rapid wear of the tools [4].

Microstructure plays a very important role in the mechanical properties of alloys, such as strength, ductility, creep resistance, fracture toughness and crack propagation resistance [5-7]. It depends primarily on the chemical composition, processing history and thermal

treatment procedures [8-10]. The most widely used titanium alloy is Ti-6Al-4V. This alloy has an excellent combination of strength, toughness and good corrosion resistance and is useful in aerospace applications, pressure vessels, aircraft-turbine, compressor blades and discs, surgical implants and etc. [11].

Drilling is a widely used machining process and has considerable economic importance because it is usually among the final steps in the fabrication of mechanical components. The tool geometry and material deformation in drilling are complicated. In drilling, long drill life is essential to increase productivity and reduce cost [2, 3].

Titanium and titanium alloys are heat treated in order to increase strength, produce an optimum condition of ductility, machinability, and structural stability and reduce residual stresses developed during fabrication [12-14].

A large parts of Ti-6Al-4V alloy are used as machined structure and components. The machining cost of this alloy is high due to the wear of the machining tools, high

*Corresponding Author Institutional Email: obayat@hut.ac.ir (O. Bayat)

strength and work-hardening. The mentioned problems can be reduced by controlling the microstructure of alloy by heat treatment. Studies have shown that the effect of different alloy microstructures on its machining behavior is not comprehensive. In this research, different cycles of heat treatment have been used to obtain different microstructures. Then, the morphology of the chips and the wear of the drill were investigated using the drilling method.

2. MATERIALS AND METHODS

The chemical composition (alloy is 6% Al, 4% V and the balance of Ti. The primary Ti-6Al-4V alloy rods with a diameter of 22mm and 45mm of height were prepared and heat treated in three temperatures (Table 1) to achieve various hardness. All heat treatments were performed in the electro-resistance furnace. Sample (1) was no heat treated, sample (2) was heat treated at 800°C for 1 hour and quenched in air, sample (3) was heat treated at 950°C for 1 hour and quenched in water, sample (4) was heat treated at 1050°C for 1 hour and quenched in water then aged at 550°C for 4 hours and quenched in air.

Macro hardness was measured according to the ASTM E92 standard with a force of 10 kg and a time of 15 seconds. Measurements were made from 5 points of each sample and their average hardness was reported. The micro hardness measurement was performed according to ASTM E384 standard with a force of 500 g and a time of 15 seconds. In each sample, 3 measurements were performed with a distance of 1 cm. Then their average was reported.

The samples for metallographic analysis were grounded, polished and then etched in kroll's reagent with below composition 2ml HF + 6ml $(HNO)_3$+92ml H_2O. Investigation of the microstructures and chips morphology were carried out by an optical microscope and a Mira3 FESEM scanning electron microscope. Vickers hardness test was performed in kappa 100 with 15s time and 10kg force.

For machining process cutting speed and feed rate were fixed in 18.8 m/s and 0.1 mm/rev, respectively.

TABLE 1. Heat treatment cycles applied to samples

	Annealing	Aging
Sample 1	No heat treatment	-
Sample 2	800°C/1h/air	-
Sample 3	950°C/1h/water	-
Sample 4	1050°C/1h/water	550°C/4h/air

Drilling was done without lubricant and performed in Konig CNC machine. Two holes were drilled in each sample and the height of holes was 10mm.

3. RESULTS AND DISCUTION

3. 1. Heat Treatment   Heat treatment of the (α+β) titanium alloy above the β transus temperature leads to a 'lamellar' microstructural morphology, consisting of α platelets with an inter-platelet β phase. The 'lamellar' structure varies with cooling rate, ranging from colonized plate like α at a low cooling rate, a basket-weave morphology at an intermediate cooling rate and Widmanstatten at a high cooling rate, to martensite, when quenched in water [13, 14]. When processed below the β transus, Ti–6Al–4V showed an (α+β) structure with the prior α phase retained to room temperature and the β phase transformed partly [15-18]. The first sample with no heat¬ treatment, its microstructure is shown in Figure 1. Figure 1(a) shows the equiaxed microstructure consists of α and β phases, the α phase is light and β phase is dark. In SEM image (Figure 1(b)) very fine precipitated β particles in the alpha matrix is clear.

In sample (2), heat treatment at 800°C was performed stress relieving condition [19]. After heat treatment, obtained images by SEM, show β particle have further distribution in the matrix and precipitated particle is larger than sample (1) (Figures 2(a) and 2(b)). For study, drilling affects, images were taken of 10 mm depth of sample (Figures 2(c) and 2(d)). Because of the lower cooling rate in sample's core, the core had a higher
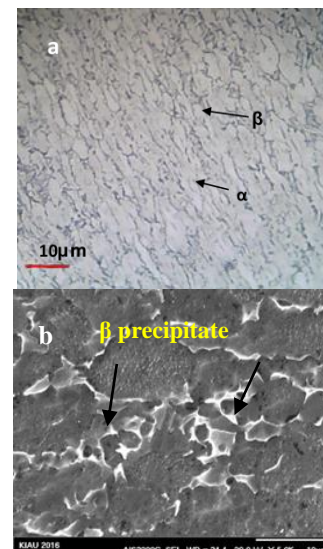
Figure 1. Received sample microstructure, a: optical microscope. and b: SEM images

temperature than the surface. More time for transformation was provided, thus, more beta phase transforms to alpha phase and lower beta phase was observed in the images.

In Ti-6Al-4V alloy, martensite starting temperature is 600°C (M_s=600°C) and β to α transformation temperature is 1000°C (M_s=1000°C). Sample 3 was annealed in 950°C and quenched in water, the expected martensitic transformation being occurred and because of the annealing temperature is below 1000°C, the primary α phase remains in the structure. In Figures 3(a) and 3(b) acicular martensite with spherical primary alpha can be seen. Move toward the depth, at distance 10 mm from the surface (Figures 3(c) and 3(d)), heat transfer is lower than the surface, additional, heat conductivity in Titanium is low also acicular structure was grown and coarsening and a widmanstatten structure was formed.
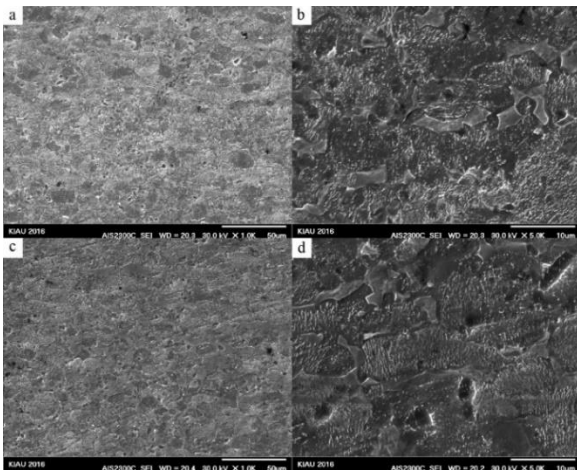
Figure 2. SEM image of the microstructure of sample 2, (a) and (b) microstructure of surface (c) and (d) microstructure of 10mm depth
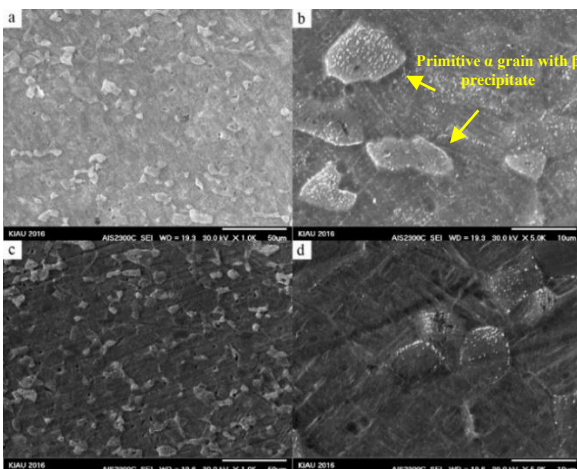
Figure 3. SEM image of the microstructure of sample 3, (a) and (b): microstructure of surface. (c) and (d): microstructure of 10mm depth

In sample 4, heat treatment at 1050°C leads to all α phase transforms to β phase and water quenching from 1050°C leads to formation ά martensite, subsequent aging in 550°C causes ά decomposition to α and β phases. In Figure 4, prior β grain is present and acicular martensite formed inside it. By aging martensite decomposes to α and β (Figures 4(b) and 4(c)), thus these precipitates particles prevent the movement of dislocations and result in hardness increasing. In the surface of the specimen due to fast cooling rate, precipitated particles are further distributed and their size are finer.

3. 2. Hardness   Average Vickers and micro Vickers hardness of samples were shown in Table 2. Sample 1 without any heat treatment with 339 Vickers hardness in the surface. Micro Vickers hardness test to compare 10 mm depth of hole and surface was done. Both surfaces had 340 micro Vickers hardness. Sample 2 was annealed at 800°C/1h and stress relieving was performed, so the hardness decreases, however, hardness is lower than sample 1. In sample 3, martensite formed and it has a high density of dislocation and twins so leads to obstacle the dislocation movement and increasing hardness. In 10mm depth, the widmansttaten structure was formed so ductility and hardness are lower than the surface that martensite observed. In sample 4, aging was led to martensite phase decomposition to alpha and beta precipitated also these precipitates phase was obstacle dislocation movement and increasing hardness.

Work material ductility is an important factor. Highly ductile materials not only permit extensive plastic deformation of the chip during cutting, which increases work, heat generation, and temperature, but also result in longer, continuous chips that remain in contact longer with the tool face, thus causing more frictional heat.
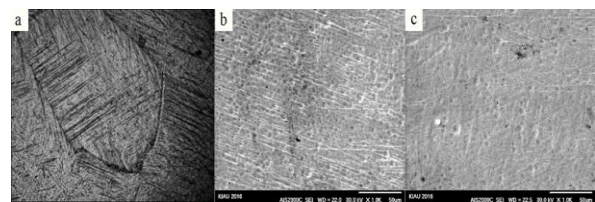
Figure 4. Microstructure of sample 4. (a): martensite structure, Optical Microscope (b): precipitated particles in surface, (c) precipitated particles in 10mm depth

TABLE 2. Hardness test results in samples 1, 2, 3 and 4

Sample No.	Surface (Vickers) (Hv)	Surface (micro Vickers) (Hv)	10mm depth (micro Vickers) (Hv)
1	339	340	340
2	320	332	301
3	393	340	328
4	500	362	336

Chips of this type are severely deformed and have a characteristic curl. On the other hand, some materials, such as gray cast iron, lack the ductility necessary for appreciable plastic chip formation. Consequently, the compressed material ahead of the tool can fail in a brittle manner anywhere ahead of the tool, producing small fragments. Such chips are termed discontinuous or segmented [20-22].

3. 3. Drilling Survey

3. 3. 1. Chips Morphology   Chips were taken to determine chips morphology. The macroscopic and SEM images of chips obtained from all samples are shown in Figures 5 and 6, respectively. Based on the chip forming mechanisms, continuous chips can be categorized to spiral chips and string chips (ribbon chip). When chips are initially generated, because the inner cutting edge moves significantly slower than the outer cutting edge, the inner chip is inherently shorter than the outer chip, this difference in length within the chip forces it flows to the drill center instead of perpendicular to the cutting edge. Furthermore, the center part of the drill flute forces the chip to curl and form a spiral shape. However, when spiral chips move in the drill flute, in order to maintain its spiral shape, they have to rotate constantly on their own axis. This rotational motion causes the spiral chips to have difficulty maintaining their shape as the hole gets deeper. If chips cannot keep up with the rotational motion, they will either break or will be forced to move along the flute without spinning, and form string chips [20]. It has been reported that the spiral cone chip is easier to be ejected so the length of spiral cone chip can be considered as a scale to evaluate the difficulty for chip evacuation in drilling [21-24]. As shown in Figures 5 and 6, in all samples both spiral and ribbon chips produced but in samples 2, 3 and 4, short and irregular chips are visible due to large resistant force, long ribbon chips will be broken into irregular short shapes.

As the hardness of the samples increases (samples 3 and 4), smaller chips are formed. Figure 5 c and d shows a reduction in chip size and the formation of small chips. This phenomenon was observed with increasing drilling depth. As explained earlier, an increase in hardness is due to the change of phases in the heat treatment cycle. Creating hard phases such as martensite changes the deformation behavior during machining. In these phases, the formation and movement of dislocations during deformation is different from soft phases such as the α phase due to the change in the crystal lattice. They have a higher coefficient of hardness and are more agile. Therefore, the chips formed during machining are broken and formed with smaller sizes.These irregular chips can block the exit way and increase force and torque in machining [23]. In Figure 5, the length of spiral and ribbon chips observed. Samples 3 and 4, have longer spiral chips rather than samples 1 and 2. These samples

have higher hardness, so can report an increase in hardness which leads easy drilling. Samples 3 and 4, have more irregular chips, these irregular chip represent friction in depth is high, high friction leads to difficulty exit and ribbon chips breaking to small and irregular chips so can report in surface heat treatment leads to ease of machining. Increasing depth and microstructure change in depth, causes machining becomes more
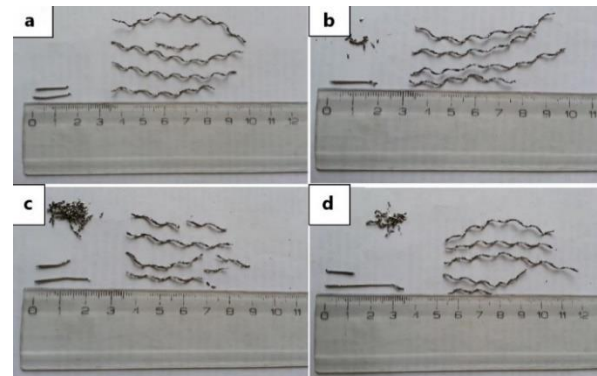
Figure 5. Macroscopic image of chip type and chip ejected from samples 1, 2, 3 and 4
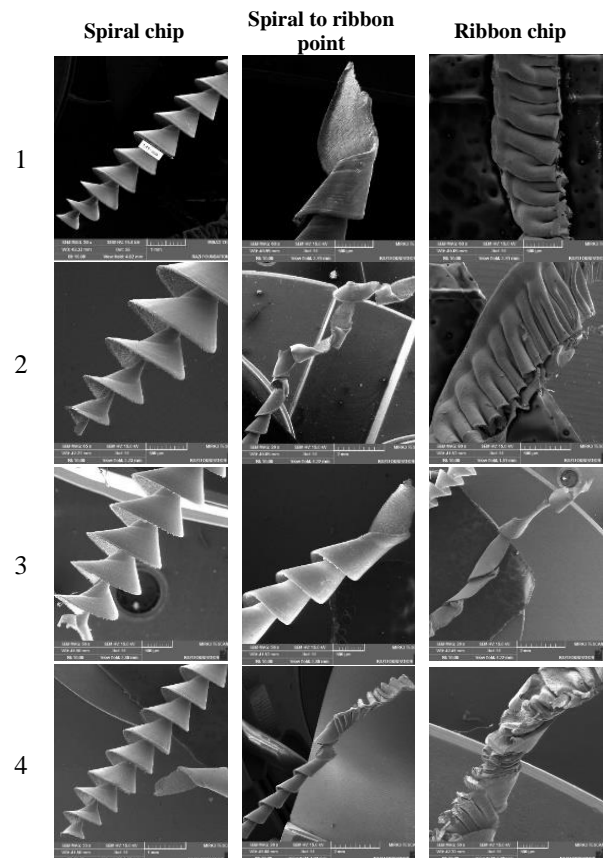
Figure 6. SEM image of chip type and chip ejected from sample 1, 2, 3 and 4

difficult. In Figures 5 and 6, spiral chips, spiral to ribbon chips point and ribbon chips observed. In all samples first spiral chips were created, then spiral chips are broken and ribbon chips produced. In sample 1, spiral chips were fractured and following ribbon chips produced. Whatever compacted ribbon chips indicated eject chips are difficult also wear in drilling hole increase and cause a decrease in tools life. In sample 2, after spiral chip, the fracture has not occurred and some spiral chips fractured after produced, this feature indicates friction is somewhat low then in the following compact ribbon chip produced. Ribbon chip in sample 2 is more compact than sample 1, can report sample 2 have difficult drilling rather than sample 1. In sample 3, after fracture, ribbon chips are not produced and morphology of chips is semi spiral and semi ribbon, because of low wear and low friction can report drilling is partly easy. Sample 4 is the only specimen which fracture has not occurred and ribbon chips following the spiral chips were formed, but as can be seen in Figure 5 the compression in ribbon chips is higher than all samples.

3. 3. 2. Drills Wear   In each work-piece 2 holes were drilled because a number of holes are limited, wear in drills is not high. Maximum wear occurred in three areas: drill point, side point and cutting edge. Figure 7 show SEM images of drills were used in drilling.

In sample 1 the morphology of drill has not been changed but abrasion wear in drill point was observed, as well as, the work-piece materials were adhered to point of drill and side edge and cutting edge nothing was observed.

In sample 2, adhered materials were more than sample 1, because, in depth of the hole, the hardness of sample 2 is lower than sample 1, so the materials adhered to the drill. At side edge and cutting edge, no wear occurred. EDS analyses of drill used in sample 2 as shown in Figure 8 (a and b) that work-piece materials were adhered to drill. In sample 3, adhered materials are low and cutting edge is very clear. In sample 4, like the previous sample adhered materials observed in EDS analyses (Figure 8 (c) and (d)), in point of a drill, the Ti, Al, and V can be observed.
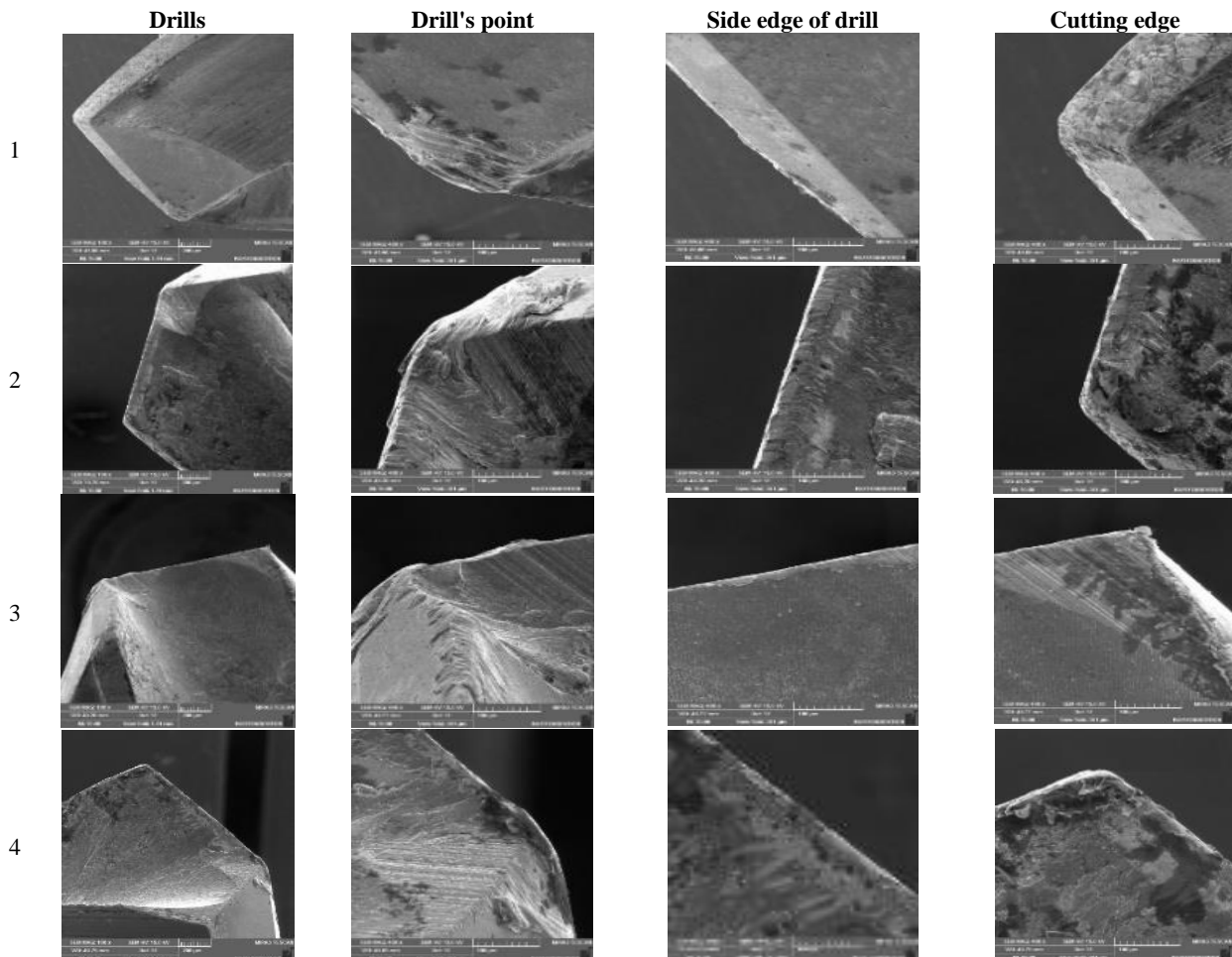
Figure 7. SEM image of different part of drills on the sample 1, 2, 3 and 4
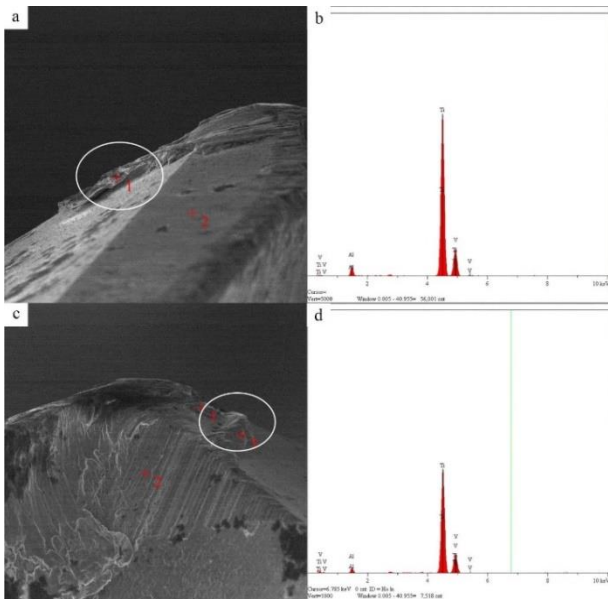
Figure 8. EDS analyses of drills point, (a) and (b): EDS analyses of sample 2 drills, adhered material are Ti, V and Al. (c) and (d): EDS analyses of sample 4: adhered material are work-piece material include Ti, V and Al..

3. 3. 3. Drilling Temperature
One of the important factor of drilling which can effect on tools wear, hole quality and chip easily exit is drilling temperature [25,26]. In Figure 9 the average temperature of 2 holes drilling was reported. In all samples with an increase in time of drilling and depth of the hole, temperature increases. These temperatures are in the range of the surface of drilling and inside the hole, where chip, drill and work material are in contact, so friction and abrasion are high. Chip exit rate was lower than produce chip so it produces more heat. Samples (3) and (4) have higher hardness and recorded the lowest temperature, in contrast, sample (2) that has the lower hardness which recorded the highest temperature.
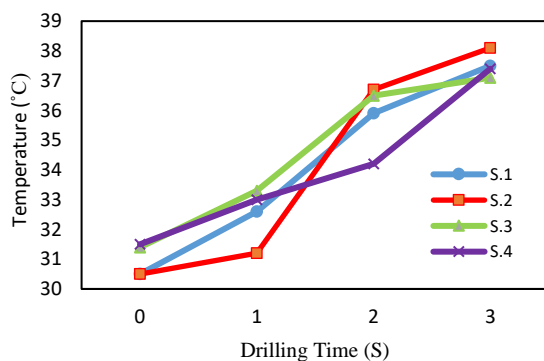
Figure 9. Drilling temperature of samples 1, 2, 3 and 4

4. CONCLUSION

Titanium has a low heat conductivity and this character affect to microstructure from surface to depth of samples in heat treatment. Hardness and microstructure of the received specimen remain with increasing depth. In other samples with an increase in depth, hardness decrease even in 10 mm far from the surface. In specimen 3, martensite was formed on the surface and moving to the depth, martensite lath was grown and widmanstatten was formed also aging lead to martensite decomposes to alpha and beta. Moving to the depth precipitated particle grew and a distance between them increased. Samples 3 and 4 had higher hardness and also had longer spiral chips, and a longer spiral chip is an evidence of easy drilling of samples. In all samples spiral chip was broken and ribbon chip produced but in sample 4 because of low wear, spiral chips were not broken and semi spiral semi ribbon chips were ejected. Also, samples 3 and 4 had a lower temperature of drilling. With an increase in hardness, temperature and drilling wear are low and by heat treatment can be provided lower-cost machining conditions.

5. REFERENCES

1. Anuj, K., Sehgal, C., Juneja, J., Singh, S., "Comparative analysis and review of materials properties used in aerospace Industries: An overview" *Materials Today*, (2021), https://doi.org/10.1016/j.matpr.2021.09.498.

2. Molinari, A., Musquar, C., Sutter, G., "Adiabatic shear banding in high-speed machining of Ti6Al4V: experiments and modeling", *International Journal of Plasticity*, Vol. 18, (2002), 443-459, https://doi.org/10.1016/S0749-6419%2801%2900003-1

3. Lia, B., Wang, Y., Li, H., You, H.,"Modelling and Numerical Simulation of Cutting Stress in End Milling of Titanium Alloy using Carbide Coated Tool", *International Journal of Engineering, Transactions A: Basics*, Vol. 28, No. 7, 1090-1098, (2015). http://dx.doi.org/10.5829/idosi.ije.2015.28.07a.16

4. Polmear, I.J., Light alloys: metallurgy of the light metals, (London Edward Arnold 1989).

5. Pengfei, G., Mingwang, F., Mei, Z., Zhenni, L., Yanxi, L., "Deformation behavior and microstructure evolution of titanium alloys with lamellar microstructure in hot working process: A review" , *Journal of Materials Science & Technology,* Vol. 39, No. 15, (2020), 56-73, https://doi.org/10.1016/j.jmst.2019.07.052

6. Lutjering, G., Albrecht, J., Ivasishin, O.M., Ankem, S., Hall, J.A., "Microstructure/Property Relationships of Titanium Alloys", *The Minerals, Metals & Materials Society*, (1994), 65-74.

7. Mykola, C., Pavlo, M., Andriy, P., Lyudmila, M., "Enhancing plasticity of high-strength titanium alloys VT 22 under impact-oscillatory loading", *Philosophical Magazine*, Vol. 97, No. 6, (2017), 389-399, https://ui.adsabs.harvard.edu/link_gateway/2017PMag.97.389C/doi:10.1080/14786435.2016.1262973

8. Semiatin, S.L., Thomas, J.F., Dadras, P., "Processing-microstructure relationships for Ti-6Al-2Sn-4Zr-2Mo-0.1 Si", *Metallurgical Transactions A*, Vol. 14, No. 11, (1983), 2363-2374. https://doi.org/10.1007/BF02663312

9. Semiatin S.L., Lahoti G.D., Oh S.I. "The Occurrence of Shear Bands in Metalworking. In: Mescall J., Weiss V. (eds) Material Behavior Under High Stress and Ultrahigh Loading Rates." Sagamore Army Materials Research Conference Proceedings, Vol. 29, (1983) Springer, Boston, MA. https://doi.org/10.1007/978-1-4613-3787-4_7

10. Jafarian, F., Mohsenia, E., Kalantarib, O.," Experimental Evaluation of Surface Alterations Induced in Machining of Ti-6Al-4V Alloy", *International Journal of Engineering, Transactions C: Aspects*, Vol. 33, No. 3, (2020), 486-493. http://dx.doi.org/10.5829/ije.2020.33.03c.13

11. Jovanovic, M.T., Tadic, S., Zec, S., Miskovic, Z., Bobic, I., "The effect of annealing temperatures and cooling rates on microstructure and mechanical properties of investment cast Ti–6Al–4V alloy", *Material and Design*, Vol. 27, (2006), 192-199. https://doi.org/10.1016/j.matdes.2004.10.017

12. Froes, F.H., Titanium: Physical Metallurgy Processing and Applications. ASM International. 2015.

13. Vassel, A., Froes, F.H., Herteman, J.P., Gazon, A., Kimura, H., Izum, O., Titanium Science and Technology. *Metallurgical Society of AIME*. (1980), 515-521.

14. Dehghani, M., Shafiei, A. R., "Influence of Water Cooling on Orthogonal Cutting Process of Ti-6Al-4V Using Smooth-Particle Hydrodynamics Method", *International Journal of Engineering, Transaction B: Applications*, Vol. 32, No. 8, 1210-1217, (2019). doi: 10.5829/ije.2019.32.08b.18

15. Punit, K., Upadrasta, R.," Microstructural optimization through heat treatment for enhancing the fracture toughness and fatigue crack growth resistance of selective laser melted Ti6Al4V alloy", *Acta Materialia*, Vol. 169, (2019), 45-59, https://doi.org/10.1016/j.actamat.2019.03.003

16. Dadras, P., J. F. Thomas, "Characterization and modeling for forging deformation of Ti-6Ai-2Sn-4Zr-2Mo-0.1 Si." *Metallurgical Transactions A*, Vol. 12, No. 11 (1981), 1867-1876.

17. Zafari A., Xia, K.," Superior titanium from hybridised microstructures–A new strategy for future alloys" *Scripta Materialia*, Vol. 173, (2019), 61-65, https://doi.org/10.1016/j.scriptamat.2019.07.031

18. Xiaoliang, L., Bing, W., "State-of-the-art of surface integrity induced by tool wear effects in machining process of titanium and nickel alloys: A review", *Measurement*, Vol. 132, (2019), 150-181, https://doi.org/10.1016/j.measurement.2018.09.045

19. Mruthunjaya, M., Yogesha,K.B., "A review on conventional and thermal assisted machining of titanium-based alloy", *Materials Today*, Vol. 46, No. 17, (2021), 8466-8472, https://doi.org/10.1016/j.matpr.2021.03.490

20. Feng, K., Jun, N., D.A. Stephenson, "continuous chip formation in drilling", *International Journal of Machine Tools & Manufacture,* Vol. 45, No. 15, (2005), 1652-1658. https://doi.org/10.1016/j.ijmachtools.2005.03.011

21. Jindal, A., "Analysis of Tool Wear Rate in Drilling Operation using Scanning Electron Microscope (SEM)", *Journal of Minerals & Materials Characterization & Engineering*, Vol. 11, (2012), 43-54, http://dx.doi.org/10.4236/jmmce.2012.111004

22. Davis, Joseph R., ed. ASM specialty handbook: tool materials. ASM international, 1995, Volum.16, Machining, 9th Edi.

23. Jinyang, X.,Mohamed, E. M, Julien,V., Ming, C., Fei, R., "On the interpretation of drilling CFRP/Ti6Al4V stacks using the orthogonal cutting method: Chip removal mode and subsurface damage formation", *Journal of Manufacturing Processes*, Vol. 44, (2019), 435-447, https://doi.org/10.1016/j.jmapro.2019.05.052

24. Okamura K, Sasahara H, Segawa T, "Low-frequency vibration drilling of titanium alloy". *JSME International Journal Series C Mechanical Systems, Machine Elements and Manufacturing*, Vol. 49, No. 1, (2006), 76-82. http://dx.doi.org/10.1299/jsmec.49.76

25. Zhu Z, Sun J, Li J, Huang P., "Investigation on the influence of tool wear upon chip morphology in end milling titanium alloy Ti6Al4V." *The International Journal of Advanced Manufacturing Technology,* Vol. 83, No. 9-12, (2016), 1477-1485. http://dx.doi.org/10.1007/s00170-015-7690-1

26. Zhu, Z., Guo, K., Sun, J., Li, J., Liu, Y., Chen, L., "Evolution of 3D chip morphology and phase transformation in dry drilling Ti6Al4V alloys evolution of 3D chip morphology and phase transformation in dry drilling Ti6Al4V alloys*". Journal of Manufacturing Processes,* Vol. 34, (2018), 531-539, https://doi.org/10.1016/j.jmapro.2018.07.001

Persian Abstract

چکیده

به منظور بررسی تاثیرریزساختارهای مختلف بر خواص ماشین¬کاری آلیاژ V4-Al6-Ti، آزمایش دریل¬کاری بر روی نمونه¬های استوانه¬ای شکل از این آلیاژ انجام شد. مورفولوژی براده نقشی اساسی بر قابلیت ماشین¬کاری و سایش ابزار را در آلیاژهای تیتانیم دارد. بدین منظور نمونه¬هایی از آلیاژ V4-Al6-Ti با سیکل¬های مخلف، عملیات حرارتی شده و سپس توسط مته به قطر ۲ میلیمتر و با سرعت ۸/۱۸ متر بر ثانیه و نرخ تغذیه¬ی ۱/۰ میلیمتر در هر دور، سوراخ¬کاری شدند. نتایج بررسی¬های میکروسکوپ الکترونی نشان داد که با تغییر فازها و مورفولوژی به دست آمده از عملیات حرارتی، شرایط ماشین¬کاری نیز تغییر می¬کند. با افزایش سختی آلیاژ، طول براده¬های مارپیچی نیز افزایش می¬یابد که بیانگر مته¬کاری آسان آن است. در این نمونه¬ها در عمق کم از ماشین¬کاری براده های روبانی شکل فشرده¬تری نیز ایجاد شد. با افزایش عمق سوراخ¬کاری، دما نیز افزایش یافت. از طرفی نمونه¬هایی که سختی پایین¬تری داشتند، دمای سوراخ-کاری پایین¬تری را ایجاد کردند.

Toward Energy-efficient Communication Protocol in Wireless Body Area Network: A Dynamic Scheduling Policy Approach

B. Vahedian[a], P. Mahmoudi-Nasr*[b]

[a] Faculty of Engineering Mazandaran Institute of Technology, Mazandaran, Iran
[b] Faculty of Engineering and Technology, University of Mazandaran, Mazandaran, Iran

PAPER INFO

ABSTRACT

Wireless body area network (WBAN) is an emerging technology that has been able to provide a better experience of mobility and flexibility for humans using tiny and low power sensors inside, outside, or around the body compared to the traditional wired monitoring systems. Due to numerous constraints in size, energy consumption, and security of implant devices in the human body, it is still a significant research challenge to design these systems in a reliable and energy-efficient fashion. To provide quality of service, timely and secure delivery of real-time data needs to be done without any loss. This paper attempts to provide a communication protocol in order to upgrade QoS levels in WBANs and reduce energy consumption in sensor nodes. To do so, the earliest deadline first (EDF) real-time scheduling algorithm and its combination with the least laxity first (LLF) scheduling algorithm were employed to prioritize sensor nodes for sending data packets. The proposed method could optimize the system performance when it is in the event of an overload and tasks miss their deadlines in a row. The OMNET++ simulation environment is used to evaluate the proposed solution's efficiency which checks packet delivery rate and mean-power consumption evaluation criteria in the sink and sensor nodes. This is done with different numbers of nodes in the network. The results show that the proposed strategy could provide an appropriate improvement in sending and receiving packets for body area networks.

doi: 10.5829/ije.2022.35.01a.18

1. INTRODUCTION

Body sensor networks (BSNs) or wireless body area networks (WBANs) are an emerging technological field for many human-centered applications, including medical monitoring, sport performance monitoring, social networking, etc. WBANs consist of low power, smart, micro- or nanotechnology sensors and actuators, which are placed on the human body or planted inside the body. Sensor nodes measure important physiological parameters such as body temperature, heart rate, body movements, blood glucose, and oxygen saturation as well as transmitting them to a local processing unit called sink node. The sink node sends information to the hospital or any health care system for diagnosis and permanent records [1]. WBANs reduce health care costs by eliminating the need for expensive monitoring of patients in hospitals. However, many social and technical challenges need to be addressed to allow for the practical acceptance of these networks [2].

Human health monitoring programs are considered critical in many cases and require low delays as well as immediate transmission of information in emergency cases. Therefore, WBANs have to provide immediate

---

* Corresponding Author Institutional Email:
P.mahmoudi@umz.ac.ir (P. Mahmoudi–Nasr)

emergency assistance to the patient in case of abnormalities in the physiological and vital signals. An important challenge of WBANs is the provision of quality of service (QoS), which must guarantee the timely and reliable delivery of real-time and non-real-time data without losing data packets [2]. Continuous patient monitoring not only requires a technological platform, but it also needs time-sensitive algorithms that prevent data packets from colliding in wireless environments and minimize energy consumption in WBANs [3].

One way to reduce energy consumption and improve the quality of service in WBANs is to prioritize data as some biological signals are more important than others. Different data collected by body sensors may differ in importance. The urgent data with the highest priority needs to be sent to the destination with the least delay. In addition, the presence of different amounts of data traffic in WBANs increases the importance of sequencing performance in coordinator nodes.

This paper attempts to offer a strategy for real-time embedded systems operating in WBANs, which includes optimizing message scheduling. Through scheduling in the transmission layer, the proposed approach not only could solve the problem of packets collision, but it could also provide a better chance of receiving higher priority data. In the proposed method, higher priority will be allocated to the nodes that are more important, for example, for the heart patient, the heart sensor has a higher priority than other sensors, so it get more priority. The proposed algorithm presents a combined EDF and LLF scheduling policy, which is used for real-time scheduling applications. The EDF scheduling algorithm is used, because the priority of information sent by nodes is not the same in WBAN.

One of the important features of EDF algorithm is its priority-orientation. This means that the algorithm schedules and prepares existing tasks based on their priority. The main advantage of EDF's strategy is that it allows the optimal utilization of the communication channel, ensures the delivery of the message within a specific time, and avoids the packet collisions. However, one of the problems with the EDF algorithm is that it is unable to manage the system in the event of an overload. This means that when one system task misses a deadline, it is likely that other subsequent tasks miss their deadlines in a row as well. In order to tackle this issue and optimize the system performance, a combination of EDF algorithm with LLF scheduling algorithm is proposed. Since the LLF scheduling algorithm is an optimal priority-based scheduling

algorithm, it could be used to solve the problems caused by the application of the EDF algorithm.

This paper attempts to show that by using the real-time scheduling algorithms and queuing the nodes based on their priority, the packet collision rate in the network is reduced and consequently the percentage of packet delivery rate in the sink node is increased. The results of the study demonstrate that the proposed method outperforms the method in which packets are sent randomly. Accordingly, the contributions of this paper is as follows:
1. Providing a method to prevent the collision of data packets sent from sensor nodes in WBANs.
2. Providing an approach to prioritize data packets before sending to enhance the QoS in WBANs.
3. Providing a solution to reduce the energy consumption of the sensor nodes in WBANs.

2. RELATED WORK

Gambhir et al. [4] proposed a protocol based on occupying the queue, along with the loss of packets to control congestion in physical sensor networks. They assumed that the nodes do not lose their functionality due to the low battery life. In this method, congestion control consisted of two phases: the fast start phase and the phase of the congestion control module. Simulation results were compared with the conventional TCP method, which indicated performance improvement in throughput and reducing the impact of congestion in the system based on the proposed method. This procedure was done after the congestion to control it in WBANs and consequently increase the throughput and networks lifetime. The current work however, aims to schedule the sending of the packets in the sensor nodes before occurrence of congestion in order to prevent it. Indumathi and Santhi [5] proposed a dynamic multilevel priority (DMP) for Wireless Sensor Networks (WSNs) where the sensor nodes were organized in a hierarchical structure. The real-time data traffic with the same priority would be processed using the shortest job first (SJF) scheduling scheme, as it is very efficient in the average waiting time of the task. It ensures the minimum end-to-end data transmission for the highest data priority while exhibiting acceptance fairness towards lowest data priority. Their experimental results showed that the proposed DMP packet scheduling scheme had better performance than the existing first come first served (FCFS) and multilevel queue scheduler in terms of the average task waiting time and end-to-end delay. Caccamo and

Zhang [6] suggested a network architecture appropriate for sensor networks along with media access control protocol based on EDF scheduling. Their main idea was to utilize the alternating feature of the sensor network traffic, so that the prioritization was used instead of control packets. As a result, they provided lower delay and more throughput. This approach was implemented through utilizing the cellular network features in the WSN network, where most of the messages are duplicate data and differ from WBANs in terms of the importance of the data sent. Facchinetti et al. [7] proposed a novel MAC layer protocol, where nodes can enter or leave the communication space while avoiding collisions caused by simultaneous transmission. The algorithm, used to access the communication channel in this protocol, was based on EDF, which not only ensured time constraints on uninterrupted messages but also provided optimal utilization of the communication channel. In this approach, the collision in the transmission of messages was prevented, because each node sent messages at different times according to the order set by EDF. In this work, however, the problem of equal deadlines (domino effect) was not considered in using EDF algorithm, which might miss other deadliness in a row with the loss of one deadline. Almeida et al. [8] proposed a MAC layer protocol for scheduling real-time communications in a network of mobile robotic units in the wireless media which used implicit EDF to guarantee the real-time network traffic. By executing and replicating the implicit EDF scheduling in parallel in all nodes, the collisions were prevented in a highly synchronized way. In this strategy, the EDF is combined with an adaptive method to support dynamic resource reservation and topology management. The simulation results showed the effectiveness of the proposed protocol, even with the transmission and mobility errors of the nodes. Here, the implicit EDF scheduling is used in MANET networks that do not have excessive physical limitations and can generally use powerful processors, radio transmitters, and batteries. WBANs, on the other hand, have many limitations in these cases. Chéour et al. [9] developed a non-exclusive multiprocessor and dynamic management policy for periodic tasks. The EDF scheduling algorithm was used to handle complex applications such as video processing. In this method, the scheduling algorithm is used as a set of rules to select the task to be executed. Moreover, it investigates deadlines, restrictions, and dependencies of each task. The EDF provides the optimal utilization of the CPU and consequently, enables energy efficiency. Additionally, the task scheduling and managing CPU

time help to improve the performance of sensor networks and predictive capabilities. Here, a real-time scheduling policy was implemented under the Linux operating system that saved significant energy. Therefore, in the proposed method, this useful feature of EDF is used to schedule the sending of packets of each sensor node in the body networks in which the energy challenge is of great importance. Wu et al. [10] proposed new techniques to limit the communication delays which were caused by collisions in the channel and sending conflicts in a wireless sensor and actuator network (WSAN). They also provided a method to reduce the disadvantages of accept control that uses the repetition of minimizing the limit of the delay for data flows with short deadlines. Their paper presented a new delay analysis for periodic streams in which transmissions are scheduled based on EDF policy. The experimental results showed that this delay analysis creates a safe limit for the real end-to-end delay. Simulation results demonstrated that EDF has a better real-time performance over static priority scheduling, and also leads to less computational cost. Ayele et al. [11] proposed a novel scheduling algorithm for hard real-time systems, reducing the amount of context switching and average waiting time, which in turn boosts the system performance. This method was a combination of EDF and LLF scheduling algorithms. The simulation results indicated that the proposed system reduces the context switching and the probability of overhead occurrence. In the current work, we used the same method to schedule the packets sending of each sensor node in physical networks. Zandvakili et al. [12] proposed a new task scheduling algorithm based on discrete pathfinder algorithm (DPFA) and modeled the objective function based on five parameters (i.e. make span, power consumption, tardiness, resource utilization and throughput). The results showed that this algorithm performs well in case of increasing the number of tasks. Yousefipour et al. [13] proposed a method for task scheduling improvement of cloud computing through an improved particle swarm optimization algorithm. In this method, selection of a proper objective function has led to balanced workload of virtual machines, decreased time of all tasks as well as maximum utilization of all resources and increased productivity in addition to dynamic placement of virtual machine on physical machine. Samal and Kabat. [14] proposed a traffic prioritized load balanced scheduling (TPLBS) algorithm for load balancing in different priority queues in WBANs. This work is to minimize packet drop in the queues to improve throughput of WBAN.

3. BASIC CONSEPTS

3. 1. WBANs   A WBAN is a wireless network that consists of tiny bio-medical nodes distributed on the body surface, underneath the skin, inside the body, or in the vicinity of the body [15]. The sensors detect physiological data and transmit it, using an access point, to the medical server. Figure 1 shows three tiers of the architecture of WBANs. When the data is received in the server, it is analyzed by medical staff to detect the patient status.

One of the most important points is to pay attention to energy consumption in sensors. Small size and, in some WBAN cases, irreplaceable batteries in the sensors must operate for multiple years. Therefore, providing a communication protocol to minimize energy consumption levels is the goal when using tiny batteries in WBAN [16]. This is while a real-time transmission protocol with guaranteed performance is required for the critical data in WBAN. In real-time WBAN applications, sensors should instantaneously sense and transmit feedback to the medical staff to process the obtained information while achieving a bounded delay latency. With the recent advances of WBAN systems, real-time applications have attracted prominent attention from researchers. In real-time WBAN applications, the criticality level of a sensor is determined based on the nature of measured data. According to the criticality level of a sensor, its priority level is determined. The priority level is used for scheduling data to minimize data collisions. Critical data should be transmitted with high priority. It means high-reliability level and minimum delay are two prerequisites for transmitting it [16].

3. 2. Real-Time Systems   A real-time system is a time-bound system that has well defined fixed time constraints. Processing must be done within the specified constraints, or the system will fail. Generally, computing systems involve one or more processes that is required to allocate a set of resources to these processes, such as computing resources, to perform user requests. These processes are divided into tasks. Tasks communicate with each other to achieve the goal of a process [17]. A task is real-time if the moments in which the results are produced are important as much as the logical accuracy of those results. A real-time system can consist of several real-time tasks. Regarding task period, real-time systems can be categorized into periodic or aperiodic tasks. In periodic tasks, a job is activated every T unit of the time where T equals its period. Aperiodic tasks are tasks in which there is no
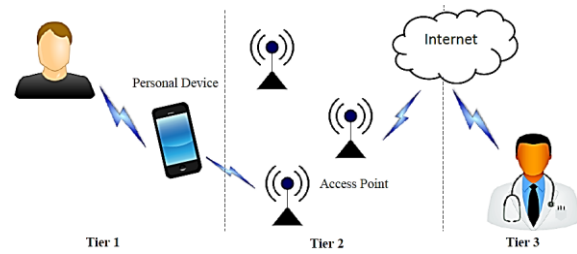
Figure 1. Three-tiers WBAN architecture

fixed time interval between consecutive activations [17].

3. 3. Task Model   In one of the simplest task models, periodic and aperiodic tasks are described by certain parameters namely execution time, deadline, and the period. The worst-case execution time (WCET) is shown as "C". It is the maximum time that a task needs a processor to finish its computation. The corresponding deadline indicated as "D" is the last moment of counting that starts from the process activation in which the calculation results are still useful. The period or the minimum time between activations is indicated by T. These features are bundled together to describe a task [18]. Equation (1) shows the model of a task, which is indicated here by the letter τ.

$$\tau = (C, T, D) \tag{1}$$

3. 4. Priority Assignment   Priority assignment of tasks in real-time systems is divided into static and dynamic modes. In static mode, the priority of tasks does not change during their execution, but in dynamic mode, this priority changes during task execution.

3. 5. Real-Time Scheduling Algorithms
3. 5. 1. RMS Scheduling Algorithm   Rate monotonic scheduling algorithm (RMS) is a static scheduling algorithm based on priority in which processes are assigned priorities as a monotonic increasing function of their rates. Equation (2) is used to determine the priority of processes in the RMS algorithm, in that the letter "τ" indicates the desired task, the letter "T" demonstrates the period of the task, and the letter "P" also shows the priority of the task. This means that for the two tasks, i and j, a higher priority is given to the task with a lower period [19].

$$\forall \tau_i, \tau_j \in \tau, T_i < T_j \Rightarrow P_i > P_j \tag{2}$$

3. 5. 2. FCFS Scheduling Algorithm   In the first come first serve (FCFS) scheduling policy, whenever a process is activated, the smallest priority is assigned to it. Over time, the age of the process and its priority increases. The process that has the highest priority is scheduled as the next process to run. A set of tasks is schedulable by FCFS if and only if all the tasks are simultaneously queued, (regardless of re-entry). Equation (3) represents this condition [20].

$$\forall_{i:\tau_i \in \tau} \sum_{j:\tau_j \in \tau} C_j \le D_i \tag{3}$$

which "τ" indicates the desired task, "C" demonstrates the worst-case execution time of the task, and "D" shows the corresponding deadline of the task.

3. 5. 3. EDF Scheduling Algorithm   The algorithm earliest deadline first (EDF) is a dynamic priority-based algorithm. It means that the priority of a request is assigned to it upon its arrival, and a higher-priority request can stop a lower priority request execution. In EDF, the higher priority is assigned to a request with the closest deadline. The utilization of this system, with the assumption that all deadlines are equal to their periods, has a limitation. Equation (4) indicates this limitation [21].

$$U = \sum_{i:\tau_i \in \tau} \frac{C_i}{T_i} \le 1 \tag{4}$$

which "τ" indicates the desired task, "T" demonstrates the period of the task, and "C" shows the worst-case execution time of the task.

In this case, EDF is an optimal scheduling policy among priority-based scheduling algorithms in which the deadlines are equal to their periods because the utilization value of no scheduling policy cannot reach above one [21].

Moreover, if EDF cannot schedule a set of tasks on a single processor, another algorithm cannot do this either [22]. The main disadvantage of the EDF scheduling algorithm is that it cannot manage the processor under overload conditions. After losing one of the deadlines, the following tasks will also miss their deadlines. This problem is known as a domino effect. It occurs when Equation (5) is valid [23].

$$\sum_{i=1}^{n} \frac{C_i}{T_i} > 1 \tag{5}$$

which "n" indicates total number of tasks, "T" demonstrates the period of the task, and "C" shows the worst-case execution time of the task.

3. 5. 4. LLF Scheduling Algorithm   Algorithm least laxity first (LLF) is another optimal scheduling algorithm based on dynamic priority assignment. The laxity of a process is the deadline of process minus the remaining execution time. Equation (6) defines the laxity of a process., which "L" indicates the laxity of a process, "D" shows the corresponding deadline of the process, and "C" shows the remaining execution time of the process.

$$L_i = D_i - C_i \tag{6}$$

In other words, it is the maximum time that the execution of a process can wait so that it does not miss its deadline. The algorithm assigns the highest priority to the process with the smallest laxity. Then, the process that has the highest priority is executed. So long as the process is running, it is possible to be stopped by another process with a smaller laxity than the running process. The problem occurs when the two processes have the same laxities. One process will be executed for a short period, and then will be preempted by another and vice versa [24].

One of the advantages of this algorithm is the fact that there is no other analysis except the schedulability test, namely the static priority assignment that should be made at the time of creation. Also, the task that is losing its deadline is detected at the same moment with the task that is not currently being performed. At that moment, the deadline is not still finished and emergency measures can be taken to cover the loss of the deadline. These advantages are associated with the issue of performing computational operations during scheduling. In addition, the LLF algorithm performs poorly when more than one task has the least laxity. In such a situation, at any unit of time, the content of the system switches from one task to another until they are finished (context switching). This behavior is referred to as the "thrashing" effect, which makes the system perform so many unnecessary switching between tasks. This high amount of context switching means loss of computing time [25].

4. PROPOSED METHOD

In this research, to support the need for real-time communication in body area networks and the energy constraints of sensor nodes in these networks, attempts are made to reduce the collision rate of packets in the network using scheduling algorithms of real-time systems and subsequently reduce energy consumption in the sensor nodes. For this purpose, the EDF scheduling algorithm and its combination with the LLF scheduling algorithm are used. In the proposed method,

it is required to assign concepts such as the period, deadline, and the worst case of execution time to the sensor nodes in order to schedule the sending of packets.

The general trend of the proposed method consists of two phases, (1) EDF prioritizing phase, (2) Correction of prioritizing phase using LLF algorithm. In this way, the EDF scheduling algorithm is executed simultaneously and in parallel on all network nodes to identify them for sending their packets. In this case, if the turn of the two nodes equals, then to refine the algorithm from the arisen problems, the laxity parameter, which is used to determine the priority in the LLF algorithm, will be used to specify the higher priority node.

4. 1. EDF Scheduling Phase

In this phase, to take advantage of the features of the EDF algorithm, it is necessary that the parameters, which are used for scheduling in real-time systems, to be allocated to the sensor nodes. For this purpose, a period, a deadline, and the worst case of execution time are determined for each node. The worst case of execution time here is the number of packets to be sent at each period. Initially, to run the EDF algorithm, nodes must send their parameters to other nodes with the broadcasting method. All nodes have a table in their memory that stores the parameters obtained from other nodes. After completing these tables, the EDF algorithm is executed on all nodes in parallel, and their turn for sending packets will be determined. Figure 2 shows the pseudo-code of the EDF algorithm.

4. 2. Correction of Prioritizing Phase Using LLF Algorithm

As previously mentioned, in the EDF algorithm, if two deadlines happen to be equal, a domino effect may occur which leads to the loss of the

next deadlines continuously. To remedy this problem, it is tried to use the laxity parameter, which is used to determine the priority in the LLF algorithm, to assign priority to the nodes to send their packets.

The correction of the scheduling phase is such that, at first, the laxity parameter is calculated for nodes with the same deadlines. Then, the sending priority is allocated to the node which has less laxity. In this case, it is determined that if the laxity value of the two nodes are equal, then the node that is currently sending packets will continue its sending. Figure 3 illustrates the complete flowchart of the proposed method.


```
Insert(q,N)  //insert the node into the EDF queue
 {
    For each node N_i in queue //i=1 to N( number of current nodes in the queue)
    {
       If ( N.deadline < N_i.deadline)
       {
          queue_insert (q,N,N_i)  //insert N before N_i
       }
    }
    If (not inserted)  //all nodes in the queue have less deadline than node N
    {
       queue_app end(queue,N)  // add N to the end of queue
    }
 }
```

**Figure 2.** EDF algorithm pseudo code
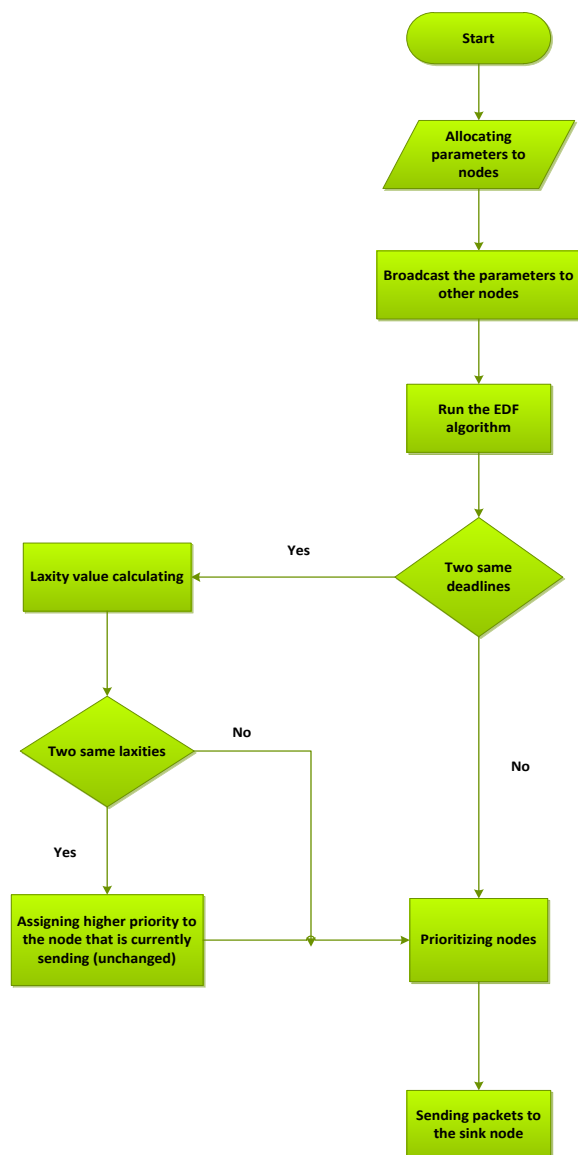
Figure 3. Complete flowchart of the proposed method

4. SIMULATION RESULTS

To simulate the proposed method, OMNET ++ simulator environment is used. Three different situations (random, EDF, proposed method) are used to simulate the body area network all of which are tested with 4, 10, 20 and 50 number of sensor nodes, and one sink node. The experimental results show that in case of dynamic scheduling, deadline based algorithms have supremacy over laxity based [26]. For this reason, the proposed method is not compared with LLF algorithm. The performance of each of the mentioned situations are evaluated in terms of two evaluation criteria; the percentage of packet delivery rate in the sink node and the average energy consumption in the sensor node. In the random scenario, whenever a node has a packet to send, it sends it to the sink node immediately without considering any time constraints. In the EDF scheduling scenario, the required parameters to execute the EDF algorithm, i.e. periodic, deadline, and the number of sent packets per period (capacity), are randomly assigned to the nodes. These parameters are stored in a table in the node's memory. Then, the nodes send their parameters to each other by broadcasting. Therefore, all nodes are aware of the parameters of the other nodes, and store this information in their table. After the tables are completed, the EDF algorithm is run simultaneously and in parallel on all nodes. According to this algorithm, the node with the smallest deadline has the highest priority. In this way, the priority and the order of the nodes to send the information packets are specified and the sending process starts.

At each period, the packet transmission at each node begins again, and this transmission must be done in a specified deadline. In this scenario, when the two nodes have the same deadlines, the algorithm randomly selects one of the two nodes.

In this case, the domino effect is likely to occur. For this reason, the algorithm is combined with the LLF scheduling algorithm in the third scenario. The hybrid scenario (EDF-LLF) behaves like the EDF scenario and the EDF scheduling algorithm runs on all the nodes in parallel and determines the nodes' turn to send packets. (EDF scheduling phase). Only when the deadlines of the two nodes are equal, it is determined that the node whose laxity parameter is less has higher priority. At this time, if the laxity of the nodes is equal, the algorithm selects the node that was sending its packets from before (unchanged). The values of characteristics assigned to each node in the EDF and EDF-LLF scenarios are randomly assigned, and attempts are

made only to establish Equation (7) between these features. In this relation, P_i is the period specified for node i and D_i, is the deadline specified for node i, and C_i, is the capacity, or the number of packets that node i sends in each period.

$$C_i \leq D_i \leq P_i \tag{7}$$

Figure 4 shows the percentage of packet delivery rate in the sink node for all three random, EDF and EDF-LLF scenarios, as a linear graph, where n = 4, and n represents the number of sensor nodes in the network and t is the simulation time.

As it can be seen, when there are 4 nodes in the network, the proposed situation works slightly better than the other two scenarios in terms of percentage of packet delivery rate in the sink node and this is due to the scheduling in packet delivery and the reduction in collisions between them.

Figures 5, 6 and 7 show that the performance of the proposed scenario, and the EDF scenario, maintain this percentage of packet delivery rate even by increasing the number of nodes in the network while the random scenario has poor performance with an increased number of nodes in the network, and its percentage of delivery rate decreases.

For a better comparison of the performance of the three scenarios in terms of the percentage of packet delivery rate in the sink node, Figure 8 shows this criterion for all three scenarios at t=150.

As it can be seen, the percentage of packet delivery rate in the sink node, for the random scenario, decreases sharply as the number of nodes increases. Because in this scenario, whenever each node has a packet to send, it sends it, which by increasing the number of nodes and consequently increasing the number of sends, the
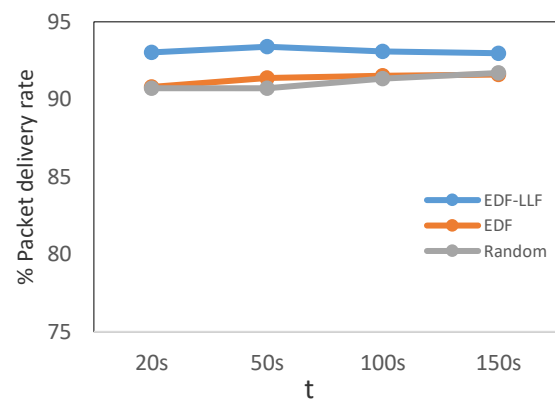
Figure 4. Packet delivery rate in the sink node, n = 4
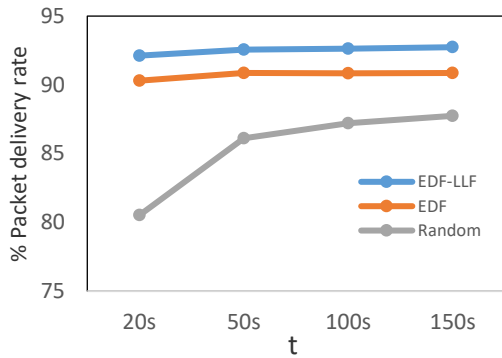
Figure 5. Packet delivery rate in the sink node, n = 10
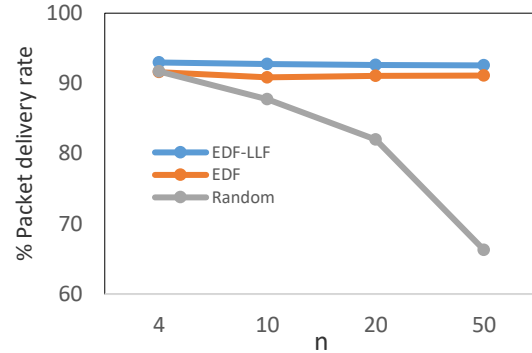
Figure 8. Packet delivery rate in the sink node at t = 150
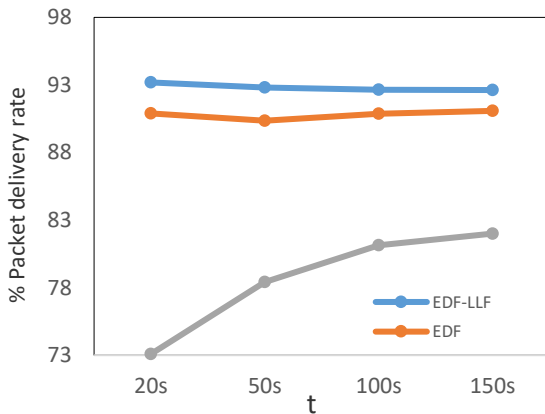
Figure 6. Packet delivery rate in the sink node, n = 20
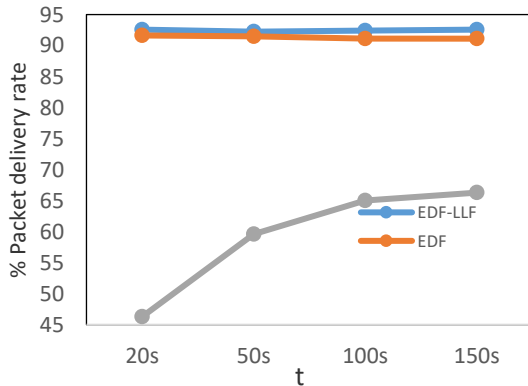
Figure 7. Packet delivery rate in the sink node, n = 50

number of collisions between sent packets also increases. This reduces the percentage of packet delivery rate in the sink node. While this case for the other two scenarios, even with increasing the number

of nodes is almost constant. As the scheduling of sending packets by real-time scheduling algorithms causes each node to send its packets in its turn, this causes the increase in the number of nodes in the network to have little effect on the percentage of packet delivery rate in the sink node. The proposed situation, by combining the two real-time scheduling algorithms and collision reduction, performs better, even compared to the EDF scenario. This is due to the better management of packet sending using the LLF algorithm. Figure 9 shows the evaluation criterion of the average energy consumption at node zero, with n= 4, for the three random, EDF, and EDF-LLF scenarios, as in linear graphs. (n represents the number of sensor nodes in the network.)

It is observed that the average energy consumption in the proposed method is higher than the random scenario in the node (0) at t=20. However, it is much less than the random scenario in continue of simulation. This is because at the beginning of the simulation, the proposed EDF-LLF algorithm has to be implemented in the nodes to specify their turn. This processing increases energy consumption at the beginning of the scenario. In continue the nodes can send their packets based on the specified order. This will reduce the average energy consumption in later times. Also, according to Figure 9, at t = 20, the average energy consumption for the EDF scenario is lower than the EDF-LLF. This is also because the EDF algorithm does not calculate the laxity parameter for prioritizing the nodes. That's why, although the energy consumption rate is low at the beginning of the scenario, it has a lower delivery rate than the EDF-LLF scenario. The same is true for the different number of sensor nodes in the network. Figure 10 shows the average power consumption at node (0) at t = 150, for all three scenarios, and all numbers of nodes. Figure 10 proves
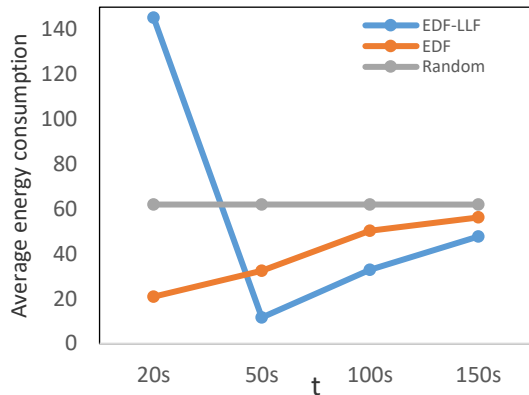
Figure 9. Average energy consumption at node zero, n = 4
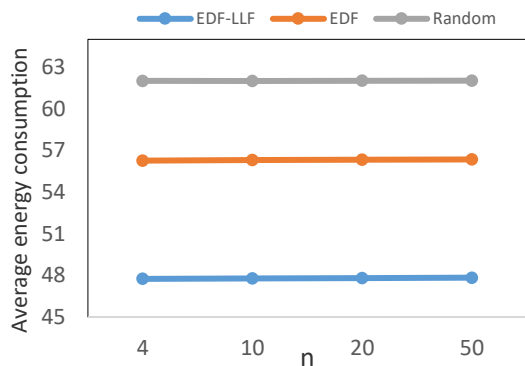
Figure 10. Average energy consumption at node zero at t = 150

that the proposed method performs better in terms of average power consumption than the other two scenarios by increasing the number of nodes.

5. CONCLUSION

This paper aims to show that using real-time scheduling algorithms and queuing nodes based on their priority could reduce the packet collision rate in the network and consequently increase the packet delivery rate in the sink node. Reduced collisions would also lead to reduced packet retransmission, which in turn reduces energy consumption in sensor nodes. This paper also shows that by combining two scheduling algorithms EDF and LLF, the problem of domino effect could be avoided and as a result, data with higher priority will have a better chance of timely reception in the sink

node. Future studies are recommended to focus on how to automatically assign priorities to the sensed data in sensor nodes.

6. ACKNOWLEDGMENTS

7. REFERENCES

1. Fortino. G, Di Fatta. G, Pathan. M and Vasilakos. A, "Cloud-assisted body area networks: State-of-the-art and future challenges", *Wireless Networks*, Vol. 20, No. 7, (2014), 1925-1938. DOI: https://doi.org/10.1007/s11276- 014-0714-1.

2. Latré, B., Braem, B., Moerman, I., Blondia, C. and Demeester, P., "A survey on wireless body area networks", *Wireless Networks*, Vol. 17, No. 1, (2011), 1-18.DOI:https://doi.org/10.1007/s11276-010-0252-4.

3. Layerle, D. and Kwasinski, A., "A power efficient pulsed mac protocol for body area networks", in 2011 IEEE 22nd International Symposium on Personal, Indoor and Mobile Radio Communications, IEEE. (2011), 2244-2248.DOI: 10.1109/PIMRC.2011.6139917.

4. Gambhir, S., Tickoo, V. and Kathuria, M., "Priority based congestion control in wban", in 2015 Eighth International Conference on Contemporary Computing (IC3), IEEE. (2015), 428-433.DOI:10.1109/IC3.2015.7346719.

5. Indumathi, M.K. and Santhi, M.M., "Efficient dynamic multilevel priority task scheduling for wireless sensor networks", *International Journal of Computer Science and Mobile Computing*, Vol. 3, No. 1, (2014), 210-217.

6. Caccamo, C. and Zhang, L.Y., "The capacity of implicit edf in wireless sensor networks", in 15th Euromicro Conference on Real-Time Systems, 2003. Proceedings., IEEE. (2003), 267-275.DOI:10.1109/EMRTS.2003.1212752.

7. Facchinetti, T., Buttazzo, G., Caccamo, M. and Almeida, L., "Wireless real-time communication protocol for cooperating mobile units", in Proceedings of the 2nd International Workshop on Real-Time LANs in the Internet Age (RTLIA 2003). (2003).

8. Almeida, L., Buttazzo, G. and Facchinetti, T., "Dynamic resource reservation and connectivity tracking to support real-time communication among mobile units", *EURASIP Journal on Wireless Communications and Networking*, Vol. 2005, No. 5, (2005), 712-730. DOI: https://doi.org/10.1155/WCN.2005.712.

9. Chéour, R., Bilavarn, S. and Abid, M., "Exploitation of the edf scheduling in the wireless sensors networks", *International Journal of Measurement Technologies and Instrumentation Engineering (IJMTIE)*, Vol. 1, No. 2, (2011), 14-27.DOI:10.4018/ijmtie.2011040102.

10. Wu, C., Sha, M., Gunatilaka, D., Saifullah, A., Lu, C. and Chen, Y., "Analysis of edf scheduling for wireless sensor-actuator networks", in 2014 IEEE 22nd International Symposium of Quality of Service (IWQoS), IEEE. (2014), 31-40.DOI:10.1109/IWQoS.2014.6914298.

11. Ayele, A.A., Rao, V.S., Dileep, K.G. and Bokka, R.K., "Combining edf and lst to enhance the performance of real-time task scheduling", in 2016 International Conference on ICT in Business Industry & Government (ICTBIG), IEEE. (2016), 1-6 DOI:10.1109/ICTBIG.2016.7892660..

12. Zandvakili, A., Mansouri, N. and Javidi, M., "Energy-aware task scheduling in cloud computing based on discrete pathfinder algorithm", *International Journal of Engineering, Transactions C: Aspects*, Vol. 34, No. 9, (2021), 2124-2136,DOI: 10.5829/ije.2021.34.09c.10.

13. Yousefipour, A., Rahmani, A. and Jahanshahi, M., "Improving the load balancing and dynamic placement of virtual machines in cloud computing using particle swarm optimization algorithm", *International Journal of Engineering, Transactions C: Aspects*, Vol. 34, No. 6, (2021), 1419-1429.DOI: 10.5829/ije.2021.34.06c.05.

14. Samal, T. and Kabat, M.R., "A prioritized traffic scheduling with load balancing in wireless body area networks", *Journal of King Saud University-Computer and Information Sciences*, (2021).DOI:https://doi.org/10.1016/j.jksuci.2020.12.023.

15. Hajar, M.S., Al-Kadri, M.O. and Kalutarage, H.K., "A survey on wireless body area networks: Architecture, security challenges and research opportunities", *Computers & Security*, (2021), 102211.DOI:https://doi.org/10.1016/j.cose.2021.102211.

16. Taleb, H., Nasser, A., Andrieux, G., Charara, N. and Motta Cruz, E., "Wireless technologies, medical applications and future challenges in wban: A survey", *Wireless Networks*, (2021), 1-25.DOI: https://doi.org/10.1007/s11276-021-02780-2.

17. Bambagini, M., Marinoni, M., Aydin, H. and Buttazzo, G., "Energy-aware scheduling for real-time systems: A survey", *ACM Transactions on Embedded Computing Systems (TECS)*, Vol. 15, No. 1, (2016), 1-34.DOI: https://doi.org/10.1145/2808231.

18. Nxumalo, M., Timm, N. and Gruner, S., "Spotlight abstraction in model checking real-time task schedulability", in International Symposium on Model Checking Software, Springer. (2021), 63-80.DOI:10.1007/978-3-030-84629-9_4:.

19. Li, Y., Liu, T., Zhu, J., Wang, X., Duan, M. and Wang, Y., "Comprehensive study of schedulability tests and optimal design for rate-monotonic scheduling", *Computer Communications*, Vol. 173, (2021), 107-119.DOI:https://doi.org/10.1016/j.comcom.2021.03.013.

20. Mondal, R.K., Nandi, E. and Sarddar, D., "Load balancing scheduling with shortest load first", *International Journal of Grid and Distributed Computing*, Vol. 8, No. 4, (2015), 171-178.DOI:http://dx.doi.org/10.14257/ijgdc.2015.8.4.17.

21. Amaro-Ortega, V., Diaz-Ramirez, A., Leticia Flores-Rios, B., Fernando Gonzalez-Navarro, F., Werner, F. and Burtseva, L., "A scheduling extension scheme of the earliest deadline first policy for hard real-time uniprocessor systems integrated on posix threads based on linux", *Computer Systems Science and Engineering*, Vol. 33, No. 1, (2018), 31-40.

22. Bhattacharyya, S., Chaki, N., Konar, D., Chakraborty, U.K. and Singh, C.T., "Advanced computational and communication paradigms" proceedings of international conference on icaccp 2017, volume 2, in Proceedings of International Conference on ICACCP, Springer. Vol. 1, No. (2017).DOI: https://doi.org/10.1007/978-981-10-8240-5.

23. Sharma, R., Nitin, N., AlShehri, M.A.R. and Dahiya, D., "Priority-based joint edf–rm scheduling algorithm for individual real-time task on distributed systems", *The Journal of Supercomputing*, Vol. 77, No. 1, (2021), 890-908.DOI: https://doi.org/10.1007/s11227-020-03306-x.

24. Shinde, V. and Biday, S.C., "Comparison of real time task scheduling algorithms", *International Journal of Computer Applications*, Vol. 158, No. 6, (2017), 37-41.

25. Selim AZ, El-Attar NE, Ghoneim ME, Awad WA. "Performance Analysis of Real-Time Scheduling Algorithms",InProceedings of the 2020 International Conference on Internet Computing for Science and Engineering (2020), 70-75. DOI:https://doi.org/10.1145/3424311.3424317.

26. Salmani, V., Naghibzadeh, M., Taherinia, A., Bahekmat, M. and Nejad, S.K., "Performance evaluation of deadline-based and laxity-based scheduling algorithms in real-time multiprocessor environments", in The 6th WSEAS International Conference on Systems Theory and Scientific Computation (ISTASC'06), Citeseer. (2006).

Persian Abstract

چکیده

شبکه‌های حسگر بدنی (WBANs) یک فناوری نوظهور هستند که با بهره‌گیری از حسگرهای کوچک و کم توان در داخل، خارج ویا اطراف بدن، توانسته‌اند تجربه‌ی بهتری از تحرک و انعطاف‌پذیری را برای انسان نسبت به سیستم‌های نظارتی سیمی سنتی فراهم کنند. به‌دلیل محدودیت زیاد در اندازه، مصرف انرژی و امنیت دستگاه‌های کاشتنی در بدن، طراحی این سیستم‌ها به‌طوری‌که قابل اطمینان و از لحاظ انرژی کارامد باشند، هنوز یک چالش تحقیقاتی بزرگ است. برای ارائه کیفیت خدمات در این شبکه‌ها، می‌بایست تحویل به موقع و مطمئن داده‌های بی‌درنگ، بدون از دست دادن بسته‌های داده، فراهم شود.در این مقاله، یک پروتکل ارتباطی به منظور ارتقای سطح کیفیت خدمات در شبکه‌های بدنی و کاهش مصرف انرژی در گره های حسگر، ارائه خواهد شد. برای انجام این‌کار، از الگوریتم زمانبندی بی‌درنگ EDF و ترکیب آن با الگوریتم زمانبندی LLF جهت نوبت‌بندی گره‌های حسگر در ارسال بسته‌های اطلاعاتی استفاده خواهد شد. به منظور بررسی کارایی راهکار پیشنهادی، از محیط شبیه‌سازی ++OMNET استفاده شده است که معیارهای ارزیابی درصد نرخ تحویل بسته در گره چاهک و میانگین مصرف انرژی در گره حسگر را با تعداد مختلف گره در شبکه بررسی می‌کند. نتایج بدست آمده، نشان می‌دهند که راهکار پیشنهادی، بهبود مناسبی در ارسال و دریافت بسته‌ها، برای شبکه‌های حسگر بدنی ایجاد می‌کند.

International Journal of Engineering

Studies on Contaminated Mine Soil and Its Remediation using Soil Washing Technique: A Case Study on Soil at Kolar Gold Fields

Sumalatha J.[a], M. Kumar C. L.[b], P. Sunagar[a], Shwetha K. G.[b], E. Noroozinejad Farsangi*[c]

[a] *Department of Civil Engineering, M S Ramaiah Institute of Technology, Bangalore, India*
[b] *Department of Civil Engineering, Nitte Meenakshi Institute of Technology, Yelahanka, Bengaluru, Karnataka, India*
[c] *Faculty of Civil and Surveying Engineering, Graduate University of Advanced Technology, Kerman, Iran*

A B S T R A C T

Uncontrolled mining and the tailings produced can cause significant environmental impacts such as water, air, and soil pollution. In the present study, a contaminated soil of gold mines located in the Karnataka state of India was studied to know the geotechnical behavior of this soil as a foundation material and to suggest a suitable soil remediation technique to avoid contamination of surrounding water bodies. The in-situ dry unit weight of soil at the selected locations varied from 15.71 to 18.75 kN/m^3. The effective shear strength parameters determined from Triaxial test results were in the range of 4.8 – 8.2 kN/m^2 and $19.4^0 – 29.8^0$, respectively, for the cohesion and angle of internal friction. The soil samples were analyzed for bearing capacity and settlement using GEO5 software tool, and the economical dimensions of the footings were estimated. It was observed that the soil has sufficient bearing capacity, and the settlements are within the allowable range. The chemical analysis of the soil samples showed that there are considerable amounts of heavy metals present in the mine soil. Though the strength of the soil is good, the contaminants in the soil may cause groundwater contamination and damages to the footings. Hence, the soil washing technique as a remediation technique was also studied through column leaching tests using different leaching solutions and found that diluted hydrochloric acid (HCl) with Ethylenediamine-tetraacetic acid (EDTA) can effectively remove the heavy metals from the soil.

doi: 10.5829/ije.2022.35.01a.19

1. INTRODUCTION

In most of the mining areas around the world, the presence of poisonous metals was observed in soil and water which caused environmental damage. The widespread metal pollution happened due to mining and smelting activities at the site may lead to multiple environmental problems [1-3]. The waste products from the mining process which are called tailings primarily consist of sand, silt, and clay sized materials with chemicals and process water. The mineralized rock from the mines is processed and reduced in size to recover the economic mineral. A significant volume of tailings produced from mining and processing is generally left as permanent features of the landscape after the mining

ceases [4]. These tailings hold minerals such as chlorite, mica, quartz, etc. and also contain micronutrients [5-6]. The ecological restoration of dumps can be made using these mill tailings containing the nutrients and the effective method of stabilization of mine wastes is by growing a vegetation cover over the dumps [7-8]. The long-term stability, aesthetic view and low maintenance are possible by using native species for the vegetation cover. To assess the suitability of different species of plants, the tailings can be mixed with the soil in different proportions and their effectiveness can be studied [7]. Apart from the metal extraction, the mining activities are also common to extract thermal water which will be used for power generation and medical spa treatments [9].

Corresponding Author Institutional Email: noroozinejad@kgut.ac.ir
(E. Noroozinejad Farsangi)

The mining activities in Kolar Gold Fields (KGF) were started around 2000 years back and has produced more than 800 tons of gold from the ore material of quantity 51 million tons. The quantity of gold yielded per ton of ore material has decreased gradually with time due to the exhaustion of the high-grade ore store. This has increased the processing costs and led to the closure of mining activities at this site for a few years. As the inferior quality of ore material was processed for yielding the gold, a huge quantity of mill tailings had generated and loaded in massive piles at KGF [10]. Around 32 million tons of tailings dumped in 15 locations along a stretch of 8 km in the mining area [11]. Effective management of these sites requires complex site characterization and selection of suitable remedial technology [12]. Rao and Reddy [5] studied the properties of the tailings at the KGF site to predict the effect of cyanide and its migration due to acid drainage. During the cyanidation process of gold extraction, there is a possibility of renaissance of cyanide in the leached solution and the factors influencing this regeneration are pH, time and temperature [13]. The concentrations of cyanide in the tailings will degrade naturally due to volatilization, leaching, and bacterial action [14].

The mining activities, which cause serious environmental threats, also cause problems to human health as the pollutants may enter directly or indirectly into human bodies through the food chain. As the industrial growth and economy of a country depend on the mining, it is very important to find the solutions to rectify the environmental problems associated with mining. Proper soil remediation techniques need to be identified and implemented at the site to avoid the problems associated with soil contamination. Soil washing with diluted chemical agents is effective in the removal of crystallized metal pollutants from the soil [15, 16]. Diluted acids such as EDTA and disodium ethylene diamine tetraacetate salt (Na$_2$-EDTA) have the capability to wash out the metal pollutants from the soil [17-20]. But, to protect the ecosystem from contamination, the efluent collected after soil washing must be treated before releasing into the environment as it contains the metal pollutants [21]. Plantation in the mining area will reduce the soil erosion and bring other ecological benefits. [5] Studied the nature of mill tailings in the study area for vegetation purpose and identified that species such as Babool, Neem, Eucalyptus and Gulmohar are apposite for the soil conditions in the study area.

In the current study, an effort is made to study the impact of dumping the mine tailings on the geotechnical characteristics of the study area. To study the geotechnical behavior of the soil at the site, four locations, namely, CN hill, Marikuppam, Champion reef and Coromandel were selected. The soil samples which were collected at the selected locations from a depth of 0.5 m were examined to know the changes in their geotechnical properties. It was found that there was not much variation in the index properties apart from the variation in specific gravity indicating the existence of heavy metals. The quality of ground water collected from the bore wells of the study area was also checked to know the level of water contamination at the site. The water tests on the samples showed that the water is slightly alkaline. To predict the suitability of these dumping areas for constructing the buildings, bearing capacity and settlement analyses were carried out with respect to each location at the study area. The geotechnical properties of the soil samples are taken as input for software to analyze its bearing capacity as well as settlement. The analyses were carried out with assumption of footing size and loads. The economical sizes of the footings at different sites were also estimated using the GEO5 software tool. It was observed that the soil is having sufficient bearing capacity and the settlements are within the allowable range. Even though the soil is having sufficient strength to take the structural loads, a contaminated soil still poses threats like water contamination when migrate into nearby water bodies. The heavy metals even enter into food chain through plants grown on this land. The soil remediation at the study area is required to remove the contaminants from the soil. Hence, the soil washing technique as a remediation technique was studied through column leaching tests. The column leaching tests were conducted with different leaching solutions and the effective leaching solution was identified. The percentage removal of metals with each solution were identified with respect to various metals presented in the soil. These results are useful to remediate the soil at the study area to remove the contaminants from the soil.

1. 1. Study Area   To study the effect of mining on soil properties, a gold mine area located at Kolar district in Karnataka state of India was selected, which is shown in Figure 1. The mining details of this area are specified in Table 1. Figure 2 shows the photographs of four locations in to study the effect of mining on soil properties, a gold mine area located at Kolar district in Karnataka state of India was selected, which is shown in Figure 1. The mining details of this area are specified in Table 1. Figure 2 shows the photographs of four locations in the study area. As the transportation of mined soil/tailings required a good infrastructure facility at the study area, it is required to conduct a survey as suggested by Ezirim and Okpoechi [22].

2. MATERIALS AND METHODS

The research methodology of the current research work is shown in the flow chart (Figure 3).

TABLE 1. Mining Details of the Study Area

Sites under consideration: CN hill, Marikuppam, Champion reef and Coromandel			
Mine starting year:	1880	Technique of gold extraction:	Cyanidation
Mine closure year:	2001	Volume of ore milled:	51.124 million tons
No. of mining shaft locations:	12	Volume of tailings generated:	32 million tons
No. of tailing dump sites:	15	Gold produced:	800.3 tons
Deepest mine: Location and shaft:	Champion reef Gifford shaft	Depth of the deepest mine:	3.2 km below ground surface
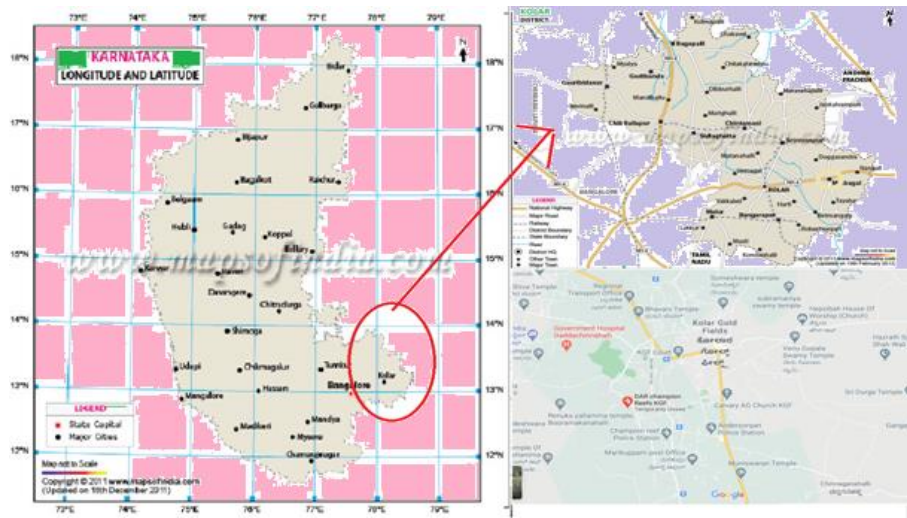
Figure 1. Study Area

(a) Marikuppam site

(b) Cyanide Hill (CN hill)

(c) Coromandel Site

(d) Champion reef- Gifford shaft dump site

Figure 2. Photographs at the Selected Locations of Study Area
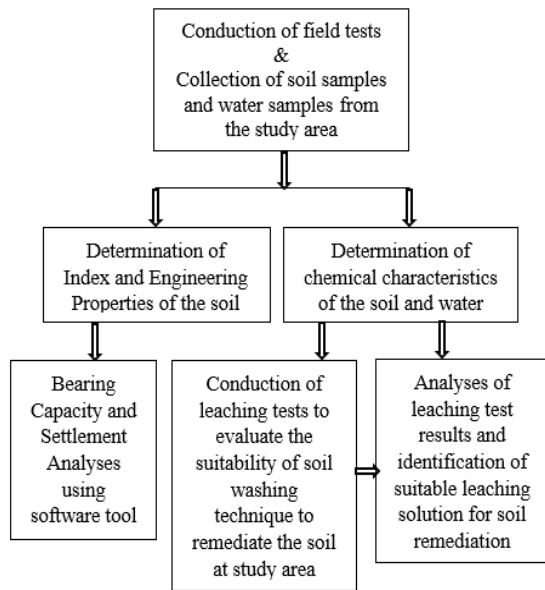
Figure 3. Flowchart of the research methodology

2. 1. Mine Soil Samples The disturbed and undisturbed samples of soil were collected from four major dump sites, i.e., Marikuppam (Residential-oldest dumpsite), Cyanide hill (CN hill), Coromandel and Champion reef- Gifford shaft. The properties of the collected soil samples such as specific gravity, plasticity characteristics, soil classification, compaction characteristics, density and permeability are determined according to the procedures given in various Indian Standard Codes [23-27] which are specified in Table 2.

TABLE 2. Index Properties of Mine Soil Samples

Location	Marik-uppam	CN hill	Coromandel	Champion reef
Specific Gravity	2.76	2.42	2.72	2.89
Liquid limit (%)	51.50	38.64	32.29	27.69
PL (%)	28.42	22.70	22.31	18.78
SL (%)	9.23	14.23	19.95	18.42
I_p (%)	23.08	15.94	9.98	8.91
% Gravel	9.7	14.85	0.75	0.7
% Sand	68.7	66.30	67.05	69.95
% Fines	21.6	18.85	32.2	29.35
Cu	10.12	3.51	4.42	2.86
Cc	1.4	0.68	1.77	1.36
Soil type as per IS classification	SW-SC	SC	SM	SM
In-situ bulk unit weight (kN/m³)	16.75	14.32	13.4	12.87

In-situ water content	21.63	10.27	2.19	1.52
In-Situ dry unit weight (kN/m³)	13.78	13	13.12	12.67
In-situ void ratio	0.965	0.83	1.03	1.24
Maximum dry unit weight from compaction test (kN/m³)	15.71	18.60	18.40	18.75
OMC (%)	20	14.8	14.2	15
Coefficient of permeability, k (cm/s)	2.04×10^{-3}	1.19×10^{-3}	2.32×10^{-4}	1.19×10^{-4}

2. 2. Water Samples at the Study Area The ground water recharge characteristics of mining areas will vary as the backfill material properties differ from the original topsoil characteristics. The quality of ground water may also get affected as the backfill material may produce leachates of chemicals after mixing with the rain water. To analyze the quality of ground water in the study area, water samples at the selected locations of the study area were collected. The test results of the water samples are given in Table 3. The pH of natural water at study area ranges between 4–9 and the majority of the water samples are slightly alkaline. The presence of carbonates and bicarbonates of calcium and magnesium ions in the water show that the water is unsuitable for domestic purposes. Hardness can be removed by adopting some of the methods such as, addition of chemicals like lime/soda, using an ion exchange process such as resin etc.

2. 3. Direct Shear Tests on Soil Samples of Study Area The direct shear tests were carried out using the guidelines given by soil testing methods (IS BIS 2720) [28] to know the shear strength parameters of test samples. To carry out the experiments, the oven dried soil

TABLE 3. Characteristics of Water Samples

Characteristics of water sample	Marikuppam	CN site	Coromandel	Champion reef
Acidity	0	0	0	0
Alkalinity (mg/l of CaCO₃)				
Phenolphthalein alkalinity	0	0	0	0
Methyl orange alkalinity	345.33	394.67	298.78	274.67
Total Hardness (mg/l of CaCO₃)	1185	1168	956	668
pH	7-7.5	6.5-7.5	6.5-7.5	6.5-7.5

sample was tamped in the shear box and the dry density was determined. The normal stress was applied through loading frame and shear stress through an electric motor. The normal stress was maintained constant and the shear load was applied till failure. The stress – strain curves were plotted to find the maximum shear stresses corresponding to the normal stresses applied. The normal and shear stresses of the samples tested were plotted on a graph and the shear strength parameters of soils were assessed. The parameters, thus estimated are as shown in Table 4.

2. 4. Triaxial Tests on Mine Soil Samples To estimate the effective shear strength properties of mine soil samples, the triaxial test procedures and soil testing methods (IS BIS 2720)[29] were adopted. The diameter and length of test samples are 3.8 cm and 7.6 cm, respectively, which were compacted to their maximum density. The soil samples were subjected to vertical and lateral pressures to find the principal stresses corresponding to failure. The shear strength parameters of soil were obtained by plotting Mohr circles using these principal stresses. The pore pressures developed in the soil samples during testing were also noted to determine the effective values of stresses and shear parameters. The shear strength parameters, thus estimated are presented in Table 4.

2. 5. Consolidation Tests on Mine Soil Samples The consolidation tests on the soil samples were carried out as per the provisions in soil testing methods (IS BIS 2720) [30]. In the current investigation, these experiments were conducted to analyze the variations in consolidation properties such as compression index (Cc) and coefficient of consolidation (Cv). The normal stress applied on the soil samples was in the range of 50 to 800 kPa. The dial gauge readings (R) corresponding to different time periods (t) and pressure increments (σ^1) were noted and their corresponding voids ratio (e) were calculated. The e-log σ^1 plot was prepared and the slope of compression curve was taken as Cc. The R vs. log t plot was also prepared and Cv was estimated. The results

of consolidation tests and the estimated properties are arranged in Table 5.

2. 5. Leaching Tests on Soil Samples The soil samples were tested with diluted chemical acids such as HCl, EDTA and combination of these two. The soil samples were subjected to a continuous supply of diluted acid solution and the effluent concentrations were measured with time. With this, the metals leached out with respect to each chemical acid were measured and the effective agent was identified [31].

3. RESULTS AND DISCUSSION

3. 1. Geotechnical Characteristics of Contaminated Soil Samples in The Study Area The physical and chemical characteristics of the soil of selected locations were studied in detail. The soil is sandy soil and the index properties are not affected much due to the contamination happened during the process of mining. The specific gravity is slightly higher than the normal soil, which indicates the existence of heavy metals in the mine soil. The shear parameters (C&Ø) are relatively not affected, indicating that the effect of contamination on shear strength is negligible. To assess the bearing capacity as well as the settlement characteristics of this soil, GEO5 software tool is used.

TABLE 4. Shear Strength Parameters of Soil Samples

Location	Marikuppam	CN hill	Coromandal	Champion reef
Direct Shear Test				
Cohesion, C (KPa)	12.8	14.6	15.4	16.8
Angle of internal friction, Ø	24.1	23.6	18.4	16.7
Triaxial Test				
Effective cohesion, C¹ (KPa)	8.2	7.7	5.9	4.8
Effective Angle of internal friction, Ø¹	29.8	26.2	21.7	19.4

TABLE 5. Consolidation Properties of the Soil in Study Area

Sample location	Bulk unit weight, kN/m³	Natural Moisture Content, %	Consolidation characteristics				
			Compression Index (Cc)	Swelling Index (Cs)	Pre-consolidation pressure (Pc), kN/m²	Coefficient of compressibility (a_v) cm²/kg	Coefficient of consolidation (Cv) m²/year
CN Site	14.32	10.27	0.12	0.009	176.52	0.12-2.48	0.69-4.87
Marikuppam	16.75	21.64	0.24	0.014	176.52	0.02-0.16	1.32-5
Champion Reef	12.87	1.52	0.21	0.015	147.1	0.08-0.51	1.27-3.05
Coromandel	13.4	2.19	0.19	0.011	98.07	0.1-1.71	2.51-9.09

3. 2. Ground Water Characteristics at The Study Area   The Acidity for all the water samples was found to be zero, which concludes that the water contains very minimal or nil hydrogen ions. Alkalinity for water samples from Marikuppam, CN site and Champion reef was found to be 345.33 mg/l of $CaCO_3$, 394.67 mg/l of $CaCO_3$ and 274.67mg/l of $CaCO_3$, respectively, which are within the permissible limit (600 mg/l of $CaCO_3$). But the lower values of alkalinity indicate that the water contains heavy metals (IS 10500-1991). Hardness of water in Marikuppam, CN site and Champion reef was found to be 1185 mg/l of $CaCO_3$, 1185 mg/l of $CaCO_3$ and 668 mg/l of $CaCO_3$ respectively, which is greater than the permissible limits (600 mg/l of $CaCO_3$). The pH of the water in the 3 selected study area is in the range of 7 to 7.5 which specifies the soil is slightly alkaline.

3. 3. Bearing Capacity Analysis of Soils in The Study Area   The The results of laboratory experiments were provided as input to the software and the bearing capacity was analyzed for a footing of size 1.6 m x 2 m placed at 1.5 m depth. The vertical load on the footing was taken as 300 kN with a service load of 214.29 kN. The footing details and soil properties are shown in Figure 4 (for Marikuppam soil). From the analysis, the bearing capacity of the Marikuppam soil was estimated as 1001.97 kPa and the factor of safety corresponding to a contact pressure of 112.89 kPa was found as 8.88 which is relatively high. Hence, to get an economical section using the inbuilt functions of the software, the footing size was revised. The revised size, thus obtained from Marikuppam soil is 0.7 x 0.7 m (Figure 5). The CN hill soil was studied in the similar
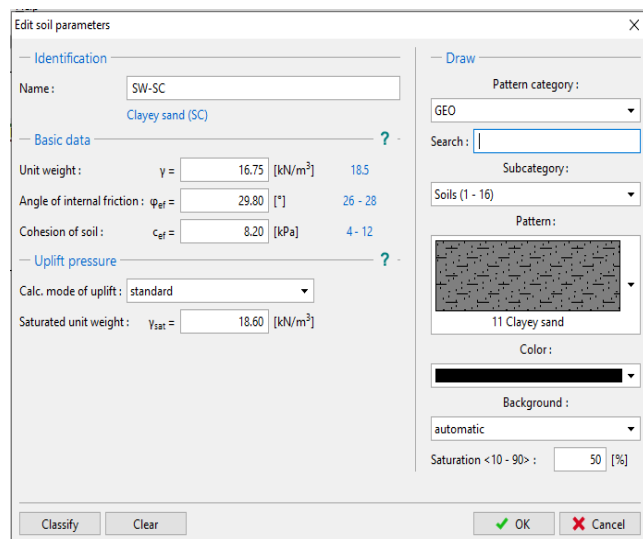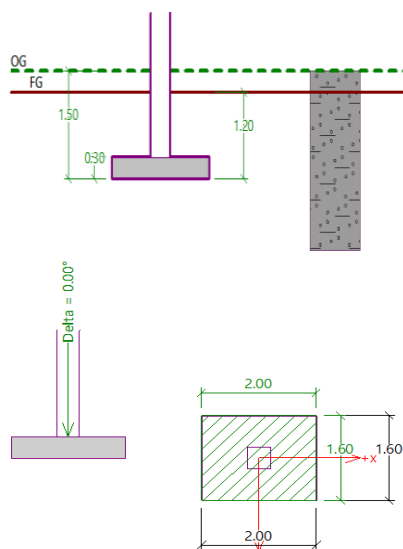
Figure 4. Foundation and Soil Details as Input to GEO5 Software (For Marikuppam Site)
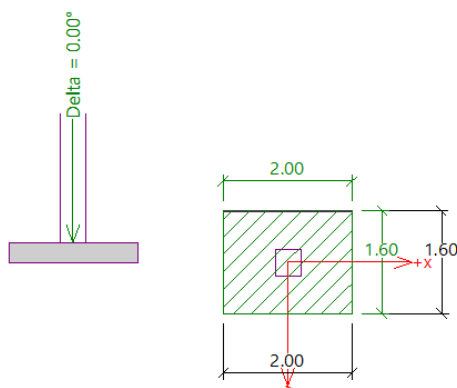
Verification of spread footing bearing capacity
Vertical bearing capacity check
Shape of contact stress : rectangle
Most unfavorable load case No. 1. (Load No. 1)
Design bearing capacity of found.soil R_d = 1001.97 kPa
Extreme contact stress σ = 112.89 kPa

Factor of safety = 8.88 > 1.50
Bearing capacity in the vertical direction is SATISFACTORY
Verification of load eccentricity
Max. eccentricity in direction of base length e_x = 0.000<0.333
Max. eccentricity in direction of base width e_y = 0.000<0.333
Max. overall eccentricity e_t = 0.000<0.333
Eccentricity of load is SATISFACTORY

Horizontal bearing capacity check
Most unfavorable load case No. 1. (Load No. 1)
Horizontal bearing capacity R_{dh} = 237.45 kN
Extreme horizontal force   H   =   0.00 kN

Factor of safety = 1000.00 > 1.50
Bearing capacity in the horizontal direction is SATISFACTORY
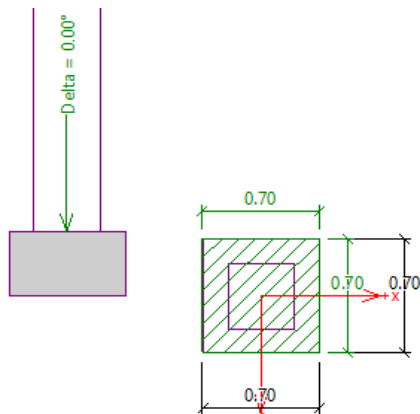
Verification of spread footing bearing capacity
Vertical bearing capacity check
Shape of contact stress : rectangle
Most unfavorable load case No. 1. (Load No. 1)
Design bearing capacity of found.soil R_d = 997.11 kPa
Extreme contact stress   σ = 630.47 kPa

Factor of safety = 1.58 > 1.50
Bearing capacity in the vertical direction is SATISFACTORY
Verification of load eccentricity
Max. eccentricity in direction of base length e_x = 0.000<0.333
Max. eccentricity in direction of base width e_y = 0.000<0.333
Max. overall eccentricity e_t = 0.000<0.333
Eccentricity of load is SATISFACTORY

Horizontal bearing capacity check
Most unfavorable load case No. 1. (Load No. 1)
Horizontal bearing capacity R_{dh} = 183.30 kN
Extreme horizontal force   H =   0.00 kN

Factor of safety = 1000.00 > 1.50
Bearing capacity in the horizontal direction is SATISFACTORY

Figure 5. Bearing Capacity Analysis of Marikuppam Soil

way and found that the footing dimension of 0.7 x 0.7 m was not sufficient (Figure 6). The revised dimension of 0.9 x 0.9 m yielded an economical design with a factor of safety of 1.55 and bearing capacity of 600.53 kPa. The economical footing dimensions obtained for Coromandel and Champion Reef soils were 1.2 x 1.3 m and 1.5 X 1.5 m, respectively (Figures 7 and 8). The bearing capacities obtained for Coromandel and Champion Reef soils corresponding to these dimensions were estimated as 327.32 kPa and 240.45 kPa, respectively.
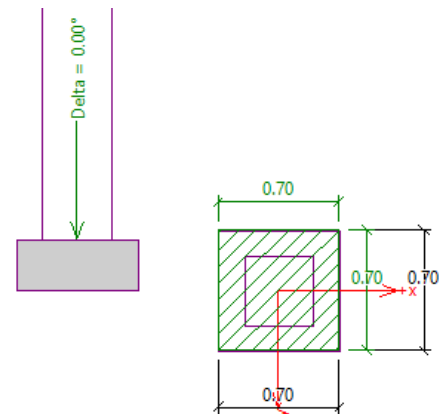
Verification of spread footing bearing capacity
Vertical bearing capacity check
Shape of contact stress : rectangle
Most unfavorable load case No. 1. (Load No. 1)
Design bearing capacity of found.soil R_d = 599.66 kPa
Extreme contact stress   σ = 627.82 kPa

Factor of safety = 0.96 < 1.50
Bearing capacity in the vertical direction is NOT SATISFACTORY
Verification of load eccentricity
Max. eccentricity in direction of base length e_x = 0.000<0.333
Max. eccentricity in direction of base width e_y = 0.000<0.333
Max. overall eccentricity e_t = 0.000<0.333
Eccentricity of load is SATISFACTORY

Horizontal bearing capacity check
Most unfavorable load case No. 1. (Load No. 1)
Horizontal bearing capacity R_{dh} = 156.91 kN
Extreme horizontal force   H =   0.00 kN

Factor of safety = 1000.00 > 1.50
Bearing capacity in the horizontal direction is SATISFACTORY

Verification of spread footing bearing capacity
Vertical bearing capacity check
Shape of contact stress : rectangle
Most unfavorable load case No. 1. (Load No. 1)
Design bearing capacity of found.soil R_d = 600.53 kPa
Extreme contact stress   σ = 387.61 kPa

Factor of safety = 1.55 > 1.50
Bearing capacity in the vertical direction is SATISFACTORY
Verification of load eccentricity
Max. eccentricity in direction of base length e_x = 0.000<0.333
Max. eccentricity in direction of base width e_y = 0.000<0.333
Max. overall eccentricity e_t = 0.000<0.333
Eccentricity of load is SATISFACTORY

Horizontal bearing capacity check
Most unfavorable load case No. 1. (Load No. 1)
Horizontal bearing capacity R_{dh} = 162.99 kN
Extreme horizontal force   H =   0.00 kN

Factor of safety = 1000.00 > 1.50
Bearing capacity in the horizontal direction is SATISFACTORY
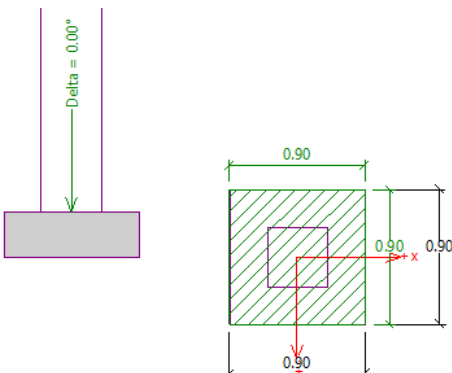
Figure 6. Bearing Capacity Analysis of CN Site Soil
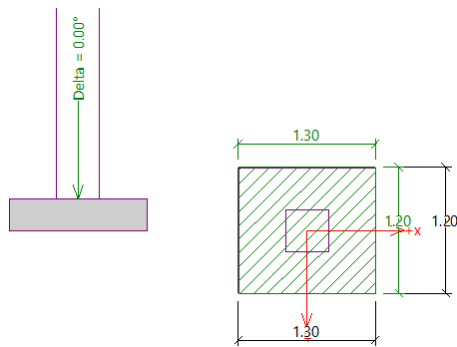
Verification of spread footing bearing capacity
Vertical bearing capacity check
Shape of contact stress : rectangle
Most unfavorable load case No. 1. (Load No. 1)
Design bearing capacity of found.soil R_d = 327.32 kPa
Extreme contact stress   σ = 210.77 kPa

Factor of safety = 1.55 > 1.50
Bearing capacity in the vertical direction is SATISFACTORY
Verification of load eccentricity
Max. eccentricity in direction of base length e_x = 0.000<0.333
Max. eccentricity in direction of base width e_y = 0.000<0.333
Max. overall eccentricity e_t = 0.000<0.333
Eccentricity of load is SATISFACTORY

Horizontal bearing capacity check
Most unfavorable load case No. 1. (Load No. 1)
Horizontal bearing capacity R_{dh} = 143.24 kN
Extreme horizontal force   H = 0.00 kN

Factor of safety = 1000.00 > 1.50
Bearing capacity in the horizontal direction is SATISFACTORY

Figure 7. Bearing Capacity Analysis of Coromandel Site Soil
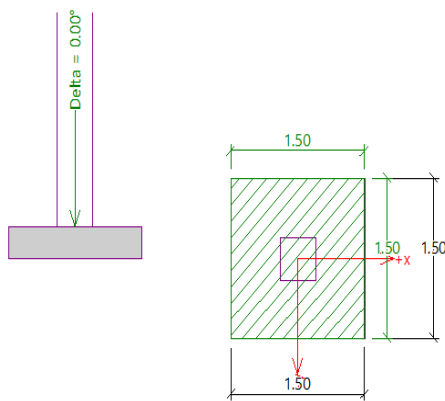
Verification of spread footing bearing capacity
Vertical bearing capacity check
Shape of contact stress : rectangle
Most unfavorable load case No. 1. (Load No. 1)
Design bearing capacity of found.soil R_d = 240.45 kPa
Extreme contact stress   σ = 152.20 kPa

Factor of safety = 1.58 > 1.50
Bearing capacity in the vertical direction is SATISFACTORY
Verification of load eccentricity
Max. eccentricity in direction of base length e_x = 0.000<0.333
Max. eccentricity in direction of base width e_y = 0.000<0.333
Max. overall eccentricity e_t = 0.000<0.333
Eccentricity of load is SATISFACTORY

Horizontal bearing capacity check
Most unfavorable load case No. 1. (Load No. 1)
Horizontal bearing capacity R_{dh} = 135.46 kN
Extreme horizontal force   H = 0.00 kN

Factor of safety = 1000.00 > 1.50
Bearing capacity in the horizontal direction is SATISFACTORY

Figure 8. Bearing Capacity Analysis of Champion Reef Site Soil

3. 4. Settlement Analysis of Soils in the Study Area
The settlements that may occur at four locations of the study area were analyzed by taking the economical dimensions that were obtained from the bearing capacity analysis. The results of settlement analyses corresponding to four locations are shown in Figures 9-12. The estimated settlements respectively, for Marikuppam soil, CN site soil, Coromandel soil and Champion Reef soil are 13.5 mm, 10.5 mm, 7.4 mm and 6.1 mm which are less than the permissible settlement (25 mm). A parametric study was conducted to know the variations in the settlement values with the applied load. The settlements corresponding to vertical loads of 300 kN, 400 kN, 500 kN, 600 kN, 700 kN, 800= kN, 900 kN and 1000 kN were estimated with respect to each location of the study area (Table 6). From this table, it can be observed that the settlements corresponding to vetical load of 600 kN and above are above 25 mm. The effective

dimensions of footings corresponding to these vertical loads to keep the settlements below 25 mm are given in Table 7.

TABLE 6. Settlements (mm) with different vertical loads

Vertical Load	Marik-uppam	CN hill	Coromandel	Champion reef
300	13.5	١٠/٧	٧/٧	۶/۵
400	18.5	١۴/۵	١٠/۴	٨/٧
500	23.4	١٨/٣	١٣/٢	١١/٠
600	28.3	22.2	١۶/٠	١٣/۴
700	33.2	26.0	١٨/٨	١۵/۶
800	38.2	٣٠/٠	٢١/٧	١٨/٠
900	43.1	٣٣/٨	٢۴/۴	٢٠/٣
١٠٠٠	۴٨/٢	٣٧/٨	٢٧/٣	٢٢/٨

TABLE 7. Effective sizes (m) of footings subjected to different vertical loads

Vertical Load	Marik-uppam	CN hill	Coromandel	Champion reef
٣٠٠	٠/٧x٠/٧	0.9x0.9	١/٢x١/٣	١/٥x١/٥
٤٠٠	٠/٧x٠/٧	0.9x0.9	١/٢x١/٣	١/٥x١/٥
٥٠٠	٠/٧x٠/٧	0.9x0.9	١/٢x١/٣	١/٥x١/٥
600	0.8x0.8	0.9x0.9	١/٢x١/٣	١/٥x١/٥
700	1.0x1.0	1.0x1.0	١/٢x١/٣	١/٥x١/٥
800	1.1x1.1	1.1x1.1	١/٢x١/٣	١/٥x١/٥
900	1.2x1.2	١/٣x١/٣	١/٢x١/٣	١/٥x١/٥
١٠٠٠	١/٥x١/٥	١/٤x١/٤	١/٤x١/٤	١/٥x١/٥

Settlement and rotation of foundation - results

Foundation stiffness:
Average modulus of deformation E_{def} = 7.79 MPa
Foundation in the longitudinal direction is rigid (k=303.21)
Foundation in the direction of width is rigid (k=303.21)

Verification of load eccentricity
Max. eccentricity in direction of base length e_x = 0.000<0.33
Max. eccentricity in direction of base width e_y = 0.000<0.33
Max. overall eccentricity e_t = 0.000<0.33
Eccentricity of load is SATISFACTORY

Overall settlement and rotation of foundation:
Foundation settlement   = 13.5 mm
Depth of influence zone = 3.02 m
Rotation in direction of x = 0.000 (tan*1000); (0.0E+00 °)
Rotation in direction of y = 0.000 (tan*1000); (0.0E+00 °)

Figure 9. The Estimated Settlement of Marikuppam Soil

Settlement and rotation of foundation - results

Foundation stiffness:
Average modulus of deformation E_{def} = 7.79 MPa
Foundation in the longitudinal direction is rigid (k=142.66)
Foundation in the direction of width is rigid (k=142.66)

Verification of load eccentricity
Max. eccentricity in direction of base length e_x = 0.000<0.333
Max. eccentricity in direction of base width e_y = 0.000<0.333
Max. overall eccentricity e_t = 0.000<0.333
Eccentricity of load is SATISFACTORY

Overall settlement and rotation of foundation:
Foundation settlement   = 10.5 mm
Depth of influence zone = 3.21 m
Rotation in direction of x = 0.000 (tan*1000); (0.0E+00 °)
Rotation in direction of y = 0.000 (tan*1000); (0.0E+00 °)

Figure 10. The Estimated Settlement of CN Site Soil

3. 5. Results of Column Leaching Tests The soil in the study area needs to be remediated to remove the contaminants and to avoid problems due to contamination. The initial concentrations of chromium, lead, nickel, copper and zinc in the soil samples, respectively, were 45.72, 27.33, 19.78, 9.49 and 6.99 mg/kg. The metal concentrations were almost same for all the four locations and hence the soil samples were mixed thoroughly and the leaching tests were conducted with different leaching solutions. The diluted acids were passed through the soil and the effluent concentrations were determined. From the effluent concentrations, the quantity of metals leaached were estimated and the percentage removal of metals were calculated. The metals leached out with respect to each leaching solution are given in Table 8. From this table it can be observed

Settlement and rotation of foundation - results

Foundation stiffness:
Average modulus of deformation E_{def} = 7.79 MPa
Foundation in the longitudinal direction is rigid (k=47.34)
Foundation in the direction of width is rigid (k=60.19)

Verification of load eccentricity
Max. eccentricity in direction of base length e_x = 0.000<0.333
Max. eccentricity in direction of base width e_y = 0.000<0.333
Max. overall eccentricity e_t = 0.000<0.333
Eccentricity of load is SATISFACTORY

Overall settlement and rotation of foundation:
Foundation settlement   =   7.4 mm
Depth of influence zone = 3.25 m
Rotation in direction of x = 0.000 (tan*1000); (0.0E+00 °)
Rotation in direction of y = 0.000 (tan*1000); (0.0E+00 °)

Figure 11. The Estimated Settlement of Coromandel Site Soil

Settlement and rotation of foundation - results

Foundation stiffness:
Average modulus of deformation E_{def} = 7.79 MPa
Foundation in the longitudinal direction is rigid (k=30.81)
Foundation in the direction of width is rigid (k=30.81)

Verification of load eccentricity
Max. eccentricity in direction of base length e_x = 0.000<0.333
Max. eccentricity in direction of base width e_y = 0.000<0.333
Max. overall eccentricity e_t = 0.000<0.333
Eccentricity of load is SATISFACTORY

Overall settlement and rotation of foundation:
Foundation settlement   =   6.1 mm
Depth of influence zone = 3.27 m
Rotation in direction of x = 0.000 (tan*1000); (0.0E+00 °)
Rotation in direction of y = 0.000 (tan*1000); (0.0E+00 °)

Figure 12. The Estimated Settlement of Champion Reef Site Soil

that the highest removal efficiency was achieved with 0.1 N HCl + EDTA. With this solution, the percentage removal of chromium, lead, nickel, copper and zinc in the soil samples were 66.17%, 77.84%, 83.74%, 88.74% and 93.44%, respectively. It was found that a combination of HCl and EDTA solution diluted to 0.1 normality has yielded the best results and it can be used as a leaching agent to implement the soil washing technique as remediation in the study area. The results are similar to the Indian reported data [31].

TABLE 8. Percentage removal of metals with different leaching solutions

Leaching Solution	Chromium	Lead	Nickel	Copper	Zinc
0.1 N HCl	23.35	33.54	50.35	62.93	57.30
0.1 N EDTA	44.72	57.51	61.33	84.47	81.58
0.1 N EDTA+HCl	66.17	77.84	83.74	88.74	93.44

4. CONCLUSIONS

The Geotechnical behaviour and remediation of soil in the mining area was studied in detail. The soil properties corresponding to four locations, namely Marikuppam, CN site, Coromandel and Champion reef were studied. It was observed that there were not much variations in the index properties The analyses of bearing capacity and settlement of soils were carried out using GEO5 software tool. From the analyses the minimum dimensions of the footings required at 1.5 m depth for Marikuppam, CN site, Coromandel and Champion reef soils were estimated to be 0.7 x 0.7 m, 0.9 x 0.9 m, 1.2 X 1.3 m and 1.5 x 1.5 m, respectively. A parametric study was also conducted to know the variations in the settlements with respect to different loading conditions. Though the soil is having sufficient strength to take the structural loads, it may cause contamination of nearby water bodies as it contains

considerable amounts of heavy metals. Hence, to remediate the soil, the soil washing technique was studied by conducting the column leaching tests with three leaching solutions. It was found that the soil washing technique can be effectively used as a remediation technique to clean up the site from heavy metals with a combination of diluted HCl and EDTA.

5. REFERENCES

1. Li, X., Thornton, I., I.," Partitioning the heavy metals in soils contaminated by past mining and smelting activities", *Environmental Geochemistry and Health*, Vol. 16, No. 2, (1994), 93-93. doi.org/10.1007/BF00209845

2. Åström, M., Nylund, K., "Impact of historical metal works on the concentrations of major and trace elements in sediments: a case study in Finland", *Applied Geochemistry*, Vol. 15, No. 6, (2000), 807-817. doi.org/10.1016/S0883-2927(99)00089-X

3. Gemici, Ü., Oyman, T. Gemici and T.Oyman, "The influence of the abandoned Kalecik Hg mine on water and stream sediments (Karaburun, Izmir, Turkey)", *Science of the Total Environment*, Vol. 312, No. 1-3, (2003), 155-166. doi.org/10.1016/S0048-9697(03)00008-1

4. Craw, D., "Geochemical changes in mine tailings during a transition to pressure–oxidation process discharge, Macraes Mine, New Zealand", *Journal of Geochemical Exploration*, Vol. 80, No. 1, (2003), 81-94. doi.org/10.1016/S0375-6742(03)00184-5

5. Rao, S. M., Reddy, B. V., "Characterization of Kolar gold field mine tailings for cyanide and acid drainage", *Geotechnical & Geological Engineering*, Vol. 24, No. 6, (2006), 1545-1559. doi.org/10.1007/s10706-005-3372-3

6. Divya, S., "Use of gold ore tailings (GOT) as a source of micronutrients to sunflower (Helianthus annuus L.) in a vertisol" (Doctoral dissertation, UAS, Dharwad) (2007).

7. Roy, S., Gupta, P., Renaldy, T. A., "Impacts of Gold Mill Tailings Dumps on Agriculture Lands and its Ecological Restoration at Kolar Gold Fields, India", *Resources and Environment*, Vol. 2, No. 1, (2012), 67-79. doi.org/10.5923/j.re.20120201.09

8. Williamson, A., Johnson, M. S., "Reclamation of metalliferous mine wastes", In Effect of heavy metal pollution on plants, Springer, Dordrecht, (1981), 185-212. doi.org/10.1007/978-94-009-8099-0_6

9. Langer, P. "Groundwater Mining in Contemporary Urban Development for European Spa Towns". *Journal of Human, Earth, and Future*, Vol. 1, No. 1, (2020), 1-9. doi.org/10.28991/HEF-2020-01-01-01

10. Chandra, R., Sathya, V., Prusty, B. A. K., Azeez, P. A., Mahimairaja, S., "The Kolar Gold Mines, India: present status and prospects for phytomining", In 2014-Sustainable Industrial Processing Summit, Vol. 1, (2014), 273-282. doi.org/10.13140/2.1.3719.9684

11. Krishna, B. R., Gejji, F. H., "The golden earth' of Karnataka", *Current Science*, Vol. 80, No. 12, (2001), 1475-1476. http://www.jstor.org/stable/24106272

12. Krishna, A. K., Mohan, K. R., Murthy, N. N.," Monitored natural attenuation as a remediation tool for heavy metal contamination in soils in an abandoned gold mine area", *Current Science*, (2010), 628-635. https://www.jstor.org/stable/24108315

13. Gönen, N., Kabasakal, O. S., Özdil, G., "Recovery of cyanide in gold leach waste solution by volatilization and absorption",

Journal of Hazardous Materials, Vol. 113, No. 1-3, (2004), 231-236. doi.org/10.1016/j.jhazmat.2004.06.029

14. Zagury, G. J., Oudjehani, K., Deschênes, L., "Characterization and availability of cyanide in solid mine tailings from gold extraction plants", *Science of the Total Environment*, Vol. 320, No. 2-3, (2004), 211-224. doi.org/10.1016/j.scitotenv.2003.08.012

15. Gebreyesus, S. T., "Heavy metals in contaminated soil: sources & washing through chemical extractants", *American Scientific Research Journal for Engineering, Technology, and Sciences (ASRJETS)*, Vol. 10, No. 1, (2014), 54-60.

16. Sumalatha J, Naveen B P, Malik R K, "Efficiency of Washing Techniques for Removal of Heavy Metals from Industrial Sludge", *Pollution*, Vol. 5, No. 1, (2019), 189-198. doi.org/10.22059/poll.2018.264574.507

17. Zou, Z., Qiu, R., Zhang, W., Dong, H., Zhao, Z., Zhang, T., Cai, X., "The study of operating variables in soil washing with EDTA", *Environmental Pollution*, Vol. 157, No. 1, (2009), 229-236. doi.org/10.1016/j.envpol.2008.07.009

18. Khalkhaliani, D. N., Mesdaghinia, A., Mahvi, A. H., Nouri, J., Vaezi, F., "An experimental study of heavy metal extraction, using various concentration of EDTA in a sandy loam soils", *Pakistan Journal of Biological Sciences*, Vol. 9, No. 5, (2006), 837-842. doi.org/10.3923/pjbs.2006.837.842

19. Mohamadi, S., Saeedi, M., Mollahosseini, A. "Desorption Kinetics of Heavy Metals (Lead, Zinc, and Nickel) Coexisted with Phenanthrene from a Natural High Buffering Soil" *International Journal of Engineering, Transactions C: Aspects*, Vol. 32, No. 12, (2019), 1716-1725.doi.org/10.5829/IJE.2019.32.12C.04

20. Habibi Davijani, A., Anbia, M. "Synthesis of ethylenediamine-modified ordered mesoporous carbon as a new nanoporous adsorbent for removal of cu (ii) and pb (ii) ions from aqueous media", *International Journal of Engineering, Transactions C: Aspects*, Vol. 27, No. 9, (2014), 1415-1422. doi.org/10.5829/idosi.ije.2014.27.09c.11

21. Ajemba, R. "Adsorption of malachite green from aqueous solution using activated ntezi clay: Optimization, isotherm and kinetic studies" *International Journal of Engineering, Transactions C: Aspects*, Vol. 27, No. 6, (2014), 839-854. doi.org/10.5829/idosi.ije.2014.27.06c.03

22. Ezirim, O. N., Okpoechi, C. U. "Community-driven Development Strategy for Sustainable Infrastructure." *Journal of Human, Earth, and Future*, Vol. 1, No. 2, (2020), 48-59. doi.org/10.28991/HEF-2020-01-02-01

23. IS BIS. 2720. Methods of Test for Soils Part 3: Determination of Specific Gravity. Bureau of Indian Standards, New Delhi, India, (1980), 1-8.

24. IS BIS. 2720. Methods of Test for Soils: Part 4 Grain Size Analysis. Bureau of Indian Standards, New Delhi, India, (1985), 1-38.

25. IS BIS. 2720. Methods of Test for Soils: Part 5 Determination of Liquid and Plastic Limit. Bureau of Indian Standards, New Delhi, India, (1985), 1-16.

26. IS BIS. 2720. Methods of Test for Soils: Part 7 Determination of Water Content-Dry Density Relation Using Light Compaction. Bureau of Indian Standards, New Delhi, India, (1980), 1-9.

27. IS BIS. 1498. Classification and Identification of Soils for General Engineering Purposes. Methods of Test for Soils. New Delhi, India, (1970), 3-23.

28. IS BIS. 2720. Methods of Test for Soils Part 13, Method of test for soils, direct shear test, New Delhi, India, (1986), 4-11.

29. IS BIS. 2720. Methods of Test for Soils Part 12: Methods of test for soils, determination of shear strength of soil by triaxial test. New Delhi, India, (1981), 4-38.

30. IS BIS. 2720. Methods of Test for Soils: Part 15: Code of practice for Determination of Consolidation properties. Bureau of Indian Standards, New Delhi, India, (1986), 1-16.

31. Sumalatha, J., Naveen, B. P., Malik, R. K., "Toxic Metals Removal from Industrial Sludge by Using Different Leaching Solution", *Journal of The Institution of Engineers (India):*

Series A, Vol. 100, No. 2, (2019), 337-345. doi.org/10.1007/s40030-019-00361-3

32. IS BIS. 1904. Indian standard code of practice for design and construction of foundations in soils: general requirements. Bureau of Indian Standards, New Delhi, India, (1986), p 19.

Persian Abstract

چکیده

معادن کنترل نشده و باطله های تولید شده می تواند اثرات زیست محیطی قابل توجهی مانند آلودگی آب، هوا و خاک داشته باشد. در مطالعه حاضر، خاک آلوده معادن طلا واقع در ایالت کارناتاکا هندوستان برای شناخت رفتار ژئوتکنیکی این خاک به عنوان ماده پی و پیشنهاد یک روش اصلاح خاک مناسب برای جلوگیری از آلودگی آب های اطراف مورد مطالعه قرار گرفته است. وزن واحد خشک خاک در مکان های انتخاب شده از ۱۵.۷۱ تا ۱۸.۷۵ کیلونیوتن بر متر مکعب متغیر بود. پارامترهای مقاومت برشی مؤثر تعیین‌شده از نتایج آزمایش سه محوری به ترتیب در محدوده ۴۸ – ۸.۲ کیلونیوتن بر متر مربع و ۱۹.۴۰ – ۲۹.۸۰ درجه برای چسبندگی و زاویه اصطکاک داخلی بوده است. نمونه‌های خاک از نظر ظرفیت باربری و نشست با استفاده از نرم‌افزار GEO5 مورد تجزیه و تحلیل قرار گرفت و پی ها به لحاظ اقتصادی مورد ارزیابی قرار گرفتند. مشاهده شد که خاک دارای ظرفیت باربری کافی بوده و نشست‌ها در محدوده مجاز قرار دارند. تجزیه شیمیایی نمونه های خاک نشان داد که مقادیر قابل توجهی فلزات سنگین در خاک معدن وجود دارد. اگرچه استحکام خاک خوب است، اما آلاینده های موجود در خاک ممکن است باعث آلودگی آب های زیرزمینی و آسیب به پی ها شده باشد. از این رو، تکنیک شستشوی خاک به عنوان یک تکنیک اصلاحی نیز از طریق آزمایش‌های آبشویی ستونی با استفاده از محلول‌های لیچینگ مختلف مورد مطالعه قرار گرفت و مشخص شد که اسید هیدروکلریک (HCl) رقیق‌شده با اتیلن دی‌آمین تتراستیک اسید (EDTA) می‌تواند به طور مؤثر فلزات سنگین را از خاک حذف نماید.

International Journal of Engineering

J o u r n a l   H o m e p a g e :   w w w . i j e . i r

Optimization of Ultrasonic-assisted Friction Stir Welded using Taguchi Approach

M. S. El-Wazery*[a,b], O. M. Mabrouk[a], A. R. El-sissy[b]

[a] Production Engineering & Mechanical Design Department, Faculty of Engineering, Menoufia University, Shebin El-Kom, Egypt
[b] Currently, Mechatronics Engineering Department, High Institute of Engineering and Technology – Elmahala Elkobra, Egypt

P A P E R I N F O	*A B S T R A C T*
	Friction stir welding process (FSW) is a solid-state welding technique which has several unique advantages. On the other hand, FSW process has some limitations such as low speed and high torque which limit the productivity and applicability of the process. To overcome these limitations, several secondary energy sources were integrated with FSW process. In the present paper, FSW was assisted by ultrasonic vibration energy in a process known as ultrasonic assisted friction stir welding (UAFSW). This paper aims to optimize the main process parameters of UAFSW process using 4 levels for each parameter with a total number of 16 experimental trials using Taguchi technique to help welders to select the proper parameters to achieve the highest efficiency of the joint in terms of the ultimate tensile strength (UTS). The parameters to be optimized are vibration amplitude (20-80 μm), traverse speed (40-160 mm/min) and tool rotational speed (630-1200 rpm). In addition, ANOVA analysis was utilized to determine the contribution percentage of each process parameter. The effect of each process parameter on the UTS was also investigated and analyzed. The results showed that the optimum condition is 20 μm, 80 mm/min, and 800 rpm. ANOVA analysis demonstrated that the rotational speed is the most significant parameter. An UTS of 290 MPa is predicted by the model, where the actual value is 297 MPa with an error percentage of 3.5%.

1. INTRODUCTION

Friction Stir Welding (FSW) is a new procedure employed to weld two metal pieces depending on the heat generated by friction between the tool and the base metal. AA 6082 is considered as one of the most promising alloys, as it has the highest strength of all 6xxx series alloys with excellent corrosion resistance, tensile strength, and hardness so; it can be used in aerospace industry and heat sink applications, bridges, beer barrels, cranes, and trusses. [1-3]. Traditional FSW depends on the frictional heat and plastic deformation. The process has some disadvantages such as the low welding speed, heavy welding loads on the tool [4]. The enhancement in the plastic material flow have been investigated [5- 8]. Mabrouk et al. [9] used a mathematical model to express the heat generation during ultrasonic vibration improved friction stir welding process. The moving heat source

technique was applied to simulate the welding process. The comparison between measured and simulated results showed acceptable accuracy of the model.

Thomä et al. [10] investigated the role of ultrasonic vibration in dissimilar FSW of aluminum to steel. The study showed that the steel particles from the base metal in the nugget zone produced by the assistance of ultrasonic vibration were less and smaller than those found in the nugget zone produced by conventional FSW. Hua et al. [11] investigated the influences of ultrasonic vibration on the mechanical properties, microstructure in terms of tensile properties, micro-hardness, weld formation, weld appearance by conducting a comparative study between conventional FSW and ultrasonic-assisted FSW. Ultrasonic vibration caused grain refinement at the stirring zone as well as its desirable role in improving the mechanical properties and eliminating some weld defects at high welding speeds. Several modeling techniques

* Corresponding Author Institutional Email:
eng_mahmoudsamir@yahoo.com (M. S. El-Wazery)

such as response surface methodology (RSM), Taguchi method, and artificial neural networks (ANN) were applied to FSW and UAFSW processes for several reasons such as: determining the contribution percentage of each process parameter, determining the optimum combination of process parameters, obtaining a mathematical model for the output in terms of the input process parameters [12-13]. Nourani et al. [14] analyzed the process variables of FSW process of AA 6061 using the Taguchi approach to minimize the heat affected zone (HAZ) distance from the weld line. Three process parameters i.e. traverse speed, rotational speed and axial force at three levels were involved in the model with a total number of 9 experiments. ANOVA analysis was also performed to evalute the significant parameter. The optimum combination of process parameters is a traverse speed of 1.9 mm/s, rotational speed of 385 rpm, and axial force of 11 kN. Effect of the welding parameters (i.e. ultrasonic power, rotational speed, traverse speed, and axial force) in UAFSW process on the tribological and mechanical properties of AA 6061 joints was studied. The experiments were carried out according to the L9Taguchi design. The objective was to maximize the formability and tensile strength as well as, minimizing the surface roughness and sliding wear rate once as a single-objective optimization problem using Taguchi technique and again as a multi-objective optimization problem using grey relational analysis [15]. Taguchi technique was applied to FSW process of AA 6082-T6 to obtain the optimum combination of process parameters to achieve the best ultimate tensile strength. The welding speed, rotational speed, pin profile, and tool shoulder diameter were the input process variables that have been used at 4 levels with a total number of 16 experiments. ANOVA analysis was also performed to determine the contribution percentage of each parameter. The optimum combination is a welding speed of 30 mm/min, rotational speed of 1200 rpm and tool with a cylindrical threaded pin, and diameter of shoulder of 16 mm [16]. Rostamiyan et al. [17] analyzed the effect of the process parameters such as ultrasonic vibration, rotational speed, tool plunge depth, and dwell time on hardness and lap shear force (LSF) by developing L_{18} Taguchi design. The contribution percentage of each parameter was also calculated using the analysis of variances. It was reported that ultrasonic vibration has a favorable effect on both LSF and hardness of welded joints and has the highest contribution percentage. The optimum condition was determined by grey relational analysis and a combination of applying ultrasonic vibration, 1200 rpm rotational speed, 6 mm tool plunge depth and 6 s dwell time was found to achieve the maximum LSF and hardness. The process parameters in FSW of AA 5083 were modeled and analyzed utilizing response surface methodology. The experiments were conducted according to the central composite design with a total number of 30 experiments.

The process parameters included in this model were traverse speed, rotational speed, tool tilt angle, and dwell time. The responses in the model are tensile strength and elongation. Empirical relationship was summarized between the responses input and process parameters. The established models have revealed that tool rotational speed and tool tilt angle have a more dominant influence on the responses as compared to other parameters [18]. It is clear from the review that there is a shortage in optimizing the UAFSW process. This study aims to analyze the effect of the process parameters such as tool rotational speed, vibration amplitude and traverse speed, in UAFSW process on the tensile properties using the Taguchi technique. In addition, determining the optimum combination of process parameters.

2. EXPERIMENTAL PROCEDURES

2. 1. Materials   In this paper, the material used is Aluminum alloy 6082-T61. T61 is the temperature designation and refers to the alloy is solution heat-treated, artificially aged, and then stress relieved by stretching. The chemical compositions and mechanical properties of AA6082-T61 as provided by the supplier are shown in Tables 1 and 2 [11,19].

The dimensions of an aluminum sheet samples are ($160 \times 100 \times 3$) mm and were cut using an abrasive water jet machine.

The ultrasonic processor was utilized to obtain the required ultrasonic vibration. A vibrating tool head (sonotrode) is considering the critical component of the processor, which evaluates the maximum amplitude and output power of the device, An ultrasonic processor processed by (Hielscher ultrasonics GmbH) was utilized to obtain the required ultrasonic vibration. Ultrasonic vibration waves of amplitude from 20 μm up to 100 μm, frequency of 20 KHz, and a power of 85 Watt were employed [9]. The ultrasonic processor is attached to the head of a milling machine through a suitable attachment as shown in Figure 1. The tool head can move along the welding line ahead of the FSW tool by a distance of 25 mm and with an inclination angle of 60° to keep it away from the tool. Therefore, the ultrasonic vibration waves can be transmitted directly into the workpiece area without any loss in the transmitted energy [11].

TABLE 1. Mechanical properties of AA6082-T61

UTS (MPa)	YS (MPa)	Elongation (%)	Hardness (HV)
320	230	9	112

TABLE 2. Chemical composition of AA6082

Si	Fe	Cu	Mn	Mg	Cr	Ni	Ti	Al
0.9	0.5	0.1	0.7	0.6	0.25	0.2	0.1	REM

Figure 1. Experimental setup including the ultrasonic processor

2. 2. Process Parameters

The experiments were carried out to study the effect of the main process parameters involved in UAFSW process (i.e. rotational speed, amplitude and traverse speed) on the joint efficiency besides determining the optimum condition to achieve the maximum joint efficiency using Taguchi technique.

3. DESIGN OF EXPERIMENTS

Taguchi technique is a powerful statistical tool that was utilized extensively in various fields. Taguchi technique is applied to investigate the impact ratio of the process parameters, in addition to, determining the optimum condition in UAFSW process. Taguchi technique with four levels and three factors was applied. The values of the three factors i.e. rotational speed, welding speed, and ultrasonic vibration amplitude are listed in Table 3.

3. 1. Tests and Measurements

A tensile test was performed for the welded joints as the ultimate tensile strenght was utilized as the output function in TAGUCHI model to express the joint efficiency and quality. The design and planning of the experiments according to TAGUCHI technique with total number of 16 experiments is given in Table 4.

4. RESULTS AND DISCUSSION

4. 1. Optimization of UAFSW

Taguchi experimental design technique L_{16} orthogonal array was

TABLE 3. Process parameters and their levels

Process parameter	Range	Level 1	Level 2	Level 3	Level 4
Rotational speed (rpm)	630:1200	630	800	1000	1200
Traverse speed (mm/min)	40:160	40	80	120	160
Amplitude (μm)	20:80	20	40	60	80

TABLE 4. Design and planning of experiments according to Taguchi

	Rot. Speed	Trav. Speed	Amplitude
1	630	40	20
2	630	80	40
3	630	120	60
4	630	160	80
5	800	40	40
6	800	80	20
7	800	120	80
8	800	160	60
9	1000	40	60
10	1000	80	80
11	1000	120	20
12	1000	160	40
13	1200	40	80
14	1200	80	60
15	1200	120	40
16	1200	160	20

to evaluate the effect of the traverse speed, tool rotational speed and vibration amplitude at four levels as control factors, on the UTS of the welded joints resulting from UAFSW process as the response (quality characteristic). As well as determining the optimum condition of process parameters to achieve the best weld quality in terms of the UTS. This is carried out using two measures, namely, signal to noise ratio (S/N ratio) and the mean, which are calculated for each experimental trial. S/N ratio is chosen according to the objective function. In this analysis, the S/N ratio is chosen according to "larger is better" criteria, as the objective function is to maximize the response. In this case, the S/N ratio is estimated from Equation (1) [20]:

$$\eta = -10 \log(n^{-1} \sum Y^{-2}) \qquad (1)$$

where, η is the S/N ratio, n is the number of experiments, and Y is the experimental value of the response. On the other hand, the mean for one level is estimated as the average of all responses that are related to that level. Minitab 18.1 software was utilized to perform this analysis. After the experiments were carried out according to Taguchi design of experiments, a tensile test was performed to measure the UTS for each sample. The values of process parameters and the corresponding UTS for each experimental trial are listed in Table 5. ANOVA was also applied to determine the contribution percentage of each process parameter.

4. 2. Taguchi Analysis After running the analysis using Minitab 18.1 software, the experimental data was transformed into S/N ratio values and average means for each control factor under different levels as shown in the response Table 6.

4. 2. 1. Optimum Condition As the better-quality characteristic i.e. UTS corresponds to the larger S/N ratio as observed from the response table. The optimal level of each process parameter can be determined based on the values of the S/N ratio which are provided in the response

TABLE 5. Design of experiment using Taguchi and the corresponding UTS

Test	Control factors			Response
	Rot. Speed (Rpm)	Trav. Speed (mm/min)	Vibr. Amplitude (μm)	UTS (MPa)
1	630	40	20	126
2	630	80	40	120
3	630	120	60	116
4	630	160	80	91
5	800	40	40	188
6	800	80	20	197
7	800	120	80	132
8	800	160	60	121
9	1000	40	60	143
10	1000	80	80	152
11	1000	120	20	137
12	1000	160	40	125
13	1200	40	80	132
14	1200	80	60	154
15	1200	120	40	118
16	1200	160	20	130

TABLE 6. S/N ratios and means for each process parameter at different levels

Level	S/N ratios (dB)			Means (MPa)		
	Rot. Speed	Trav. Speed	Vibr. Amp.	Rot. Speed	Trav. Speed	Vibr. Amp.
1	39.98	42.76	42.71	100.8	140.0	140.0
2	43.5	43.23	42.05	154.5	148.3	130.3
3	42.22	41.03	41.57	129.5	113.3	121.3
4	41.79	40.47	41.17	123.5	106.8	116.8
Delta	3.52	2.76	1.54	53.8	41.5	23.3
Rank	1	2	3	1	2	3

table. It is clear from the results that, rotational speed at level 2 (800 rpm), traverse speed at level 2 (80 mm/min), and vibration amplitude at level 1 (20 μm) are the optimum process parameters condition to obtain the largest UTS. The same result can be realized from the main effect plots for both, the S/N ratios and means as shown in Figures 2 and 3, respectively.

4. 3. Determining the Most Significant Parameter The response table can be used also to determine the most significant factor, as each factor has its rank. It is clear from the results that, the rotational speed is the most influential factor because it has a higher rank, followed by the traverse speed then followed by the vibration amplitude.

4. 4. Effects of Process Parameters on The Response The effects of the different process parameters on the response (UTS) can be investigated through discussing and explaining the main effects plots obtained from Taguchi analysis as follows.

4. 4. 1. Effect of Rotational Speed Figure 3 shows the UTS at various rotational speeds. The lowest value of UTS is at a rotational speed of 630 rpm. This may be attributed to the lower heat input due to using low rotational speed. Low heat input causes inadequate material softening, leading to improper material flow. Thus, the weld joint is incomplete and different defects such as tunnel defects are encountered. The UTS reaches its maximum value at a rotational speed of 800 rpm. On the further increase of the rotational speed, the UTS decrease. This reduction can be explained by the coarsening of grain structures at the weld zone due to the excessive heating resulting from high rotational speeds.

4. 4. 2. Effect of Traverse Speed The effect of the traverse speed on the UTS is shown in Figure 2. As
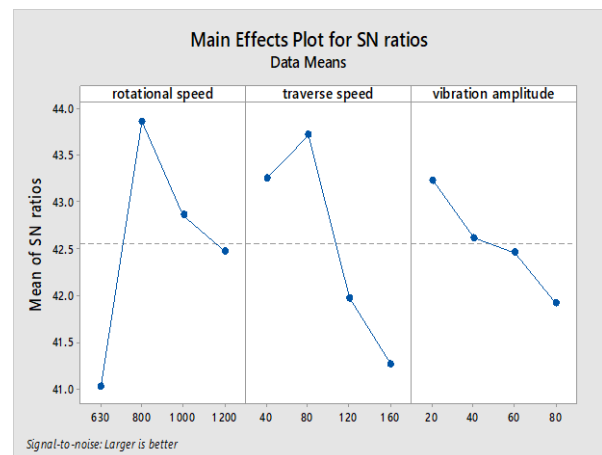
Figure 2. A plot for S/N ratios
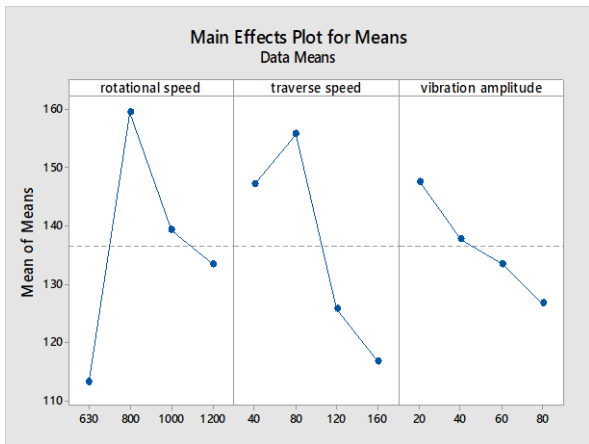
Figure 3. A plot for means

shown from the figure, the optimum value of UTS is at a traverse speed of 80 mm/min. By increasing the traverse speed to 120 mm/min a considerable reduction in the UTS is recorded due to the low heat input and insufficient material plasticization. The worst value of UTS was recorded when a traverse speed of 160 mm/min was applied, where the very low heat input causes insuffient softening leading to significant defects at the weld zone that deteriorate the mechanical properties.

4. 4. 3. Effect of Vibration Amplitude   As shown in Figure 3, the maximum value of the UTS is at a vibration amplitude of 20 μm then, the value decreases until reaches its lowest value at a vibration amplitude of 80 μm. From the previous findings, it can be stated that increasing the amplitude of the ultrasonic vibration may cause acoustic hardening leading to a negative effect on the materials flow and subsequently on the UTS of the joints.

4. 5. The Maximum Value of Response at the Optimum Condition   One of the powerful tools in Taguchi approach is the ability to predict the value of the response at any experimental condition if even it was not performed. The value of the optimum condition was predicted and a value of 290 MPa was obtained.

4. 6. ANOVA Analysis   ANOVA test was conducted using Minitab software to evelute the process parameters significance which affect the ultimate tensile strength of FSW joints by calculating the contribution percentage for each process parameter. ANOVA results are indicated in Table 7. As shown from the results, the rotational speed is the most prominent factor with a contributing factor of 41.09 % on the UTS of FSW joints, followed by the traverse speed which has a contribution percentage of 37.52 %. The lowest effective parameter is the vibration amplitude with a contribution percentage of 8.57 %. Another type of data that can be obtained from

ANOVA is the interaction plot which is used mainly to show how the relationship between a process parameter depends on the other process parameters, as shown in Figure 4. As shown from the figure, the lines are not parallel and there are intersections between them. This indicates that the relation between one process parameter and the UTS depends on the values of the other parameters. For instance, at a rotational speed of 800 rpm, the value of the UTS is highly affected by the value of the traverse speed and reaches its maximum value at a traverse speed of 80 mm/min and the vibration amplitude of 20 μm.

4. 7. Confirmation Test   The final step has to verify the predicted value of the UTS at the optimum condition. An experimental trial was performed at the optimum condition, a rotational speed at level 2 (800 rpm), a traverse speed at level 2 (80 mm/min), and a vibration amplitude at level 1 (20 μm). The tensile test was conducted on the friction stir welded joint which was welded at the optimum condition and UTS of 290 MPa was recorded. While the actual value of the experiment was 297 MPa, here an error of 3.5%, as the percentage of error was realized.

TABLE 7. ANOVA analysis

| Source	DF	SS	MS	F-Value	P-Value	% Contribution
RS	3	4344.2	1448.1	6.41	0.027	41.09%
TS	3	3966.8	1322.3	5.86	0.032	37.52%
VA	3	906.3	302.1	1.34	0.347	8.57%
Error	6	1354.5	225.7			12.81%
Total	15	10571.8				100.00%
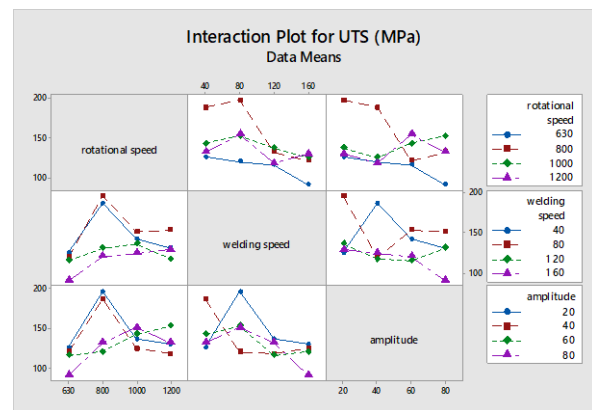
Figure 4. Interaction plots for means of UTS

5. CONCLUSIONS

The Ultrasonic-assisted FSW process was optimized using Taguchi technique to evaluate the optimum condition of process parameters and analyzing the process parameters effect on the joint quality using the UTS as the objective function. The results showd that a vibration amblitude of 20 μm, a traverse speed of 80 mm/min and a rotational speed of 800 rpm are the optimum condition to achieve the highest UTS. The predicted value of the UTS at the optimum condition is 290 MPa which is in a good agreement with the actual value of 297 MPa with 3.5% error. Rotational speed was found to be the most effective parameter. The effect of each process parameter was investigated. A reduction in the UTS value was realized by reducing the rotational speed and increasing the traverse speed and this can be attributed to the fall in the heat input which results in inadequate softening and improper material flow. Increasing the vibration amplitude larger than 20 μm can cause acoustic hardening rather than acoustic softening leading to a decrese in the UTS.

6. REFERENCES

1. K. P., Mehta, and V. J., Badheka. "A review on dissimilar friction stir welding of copper to aluminum: process, properties, and variants" *Materials and Manufacturing Processes* 31, No. 3, (2016), 233-254.

2. R. S., Mishra and Z. Y., Ma. "Friction stirs welding and processing". *Material Science Engineering* 50, (2005), 1-78.

3. N., Ethiraj, T., Sivabalan, B., Sivakumar, S., Amar, N., Vengadeswaran, K., Vetrivel. "Effect of tool rotational speed on the tensile and microstructural properties of friction stir welded different grades of stainless-steel joints" *International Journal of Engineering, Transactions A: Basics* Vol. 33, No. 1, (2020) 141-147.

4. T., DebRoy, A., De, H., Bhadeshia, "Tool durability maps for friction stir welding of an aluminium alloy" *Proceedings of the Royal Society A: Mathematical, Physical and Engineering Sciences* 468, (2012), 3552-3570. Doi.org/10.1098/rspa.2012.0270

5. M., Tiwan, and I., Kusmono. "Effect of pin geometry and tool rotational speed on microstructure and mechanical properties of friction stir spot welded joints in AA2024-O aluminum alloy Sci." *International Journal of Engineering, Transactions B: Applications* Vol. 34, No. 08, (2021), 1949-1960. Doi: 10.5829/ije.2021.34.08b.16

6. K. H., Song, T., Tsumura, K., Nakata. "Development of microstructure and mechanical properties in Laser-FSW hybrid welded inconel 600", *Materials Transactions* 50, (2009), No. 7, 1832-7. Doi.org/10.2320/materrans.M2009058

7. L., Zhou, G., Li, C., Liu, J., Wang, Y., Huang, J., Feng, and F., Meng. "Microstructural characteristics and mechanical properties of Al–Mg–Si alloy self-reacting friction stir welded joints", *Science and Technology of Welding and Joining* 22, No. 5, (2017), 438-445. Doi.10.1080/13621718.2016.1251733

8. A., lvarez, M., Garcia, G., Pena, J., Sotelo, and D Verdera. "Evaluation of an induction-assisted friction stir welding technique for super duplex stainless steels" *Surface and Interface Analysis* 46, No. 10-11, (2014), 892-896. Doi: 10.1002/sia.5442

9. O. M., Mabrouk, M. S., El-Wazery, M. A., EL-Desouky. "Simulating ultrasonic vibration enhanced FSW process of AA6082 using finite element method", IOP Conference Series: Materials Science and Engineering, Vol. 973 (2020) 012023, 1-9. Doi:10.1088/1757-899X/973/1/012023

10. M., Thomä, G., Wanger, B., Strab, B., Wolter, S., Benfer, and W., Furbeth. "Ultrasound enhanced friction stir welding of aluminum and steel: Process and properties of EN AW 6061/DC04-Joints". *Journal of Materials Science & Technology* 34, No. 1, (2018), 163-172. Doi.org/10.1016/j.jmst.017.10.002

11. Y., Hua, H., Liu, H., Fujii, H. "Improving the mechanical properties of 2219-T6 aluminum alloy joints by ultrasonic vibrations during friction stir welding", *Journal of Materials Processing Tech.* 271, (2019), 75-84. Doi.org/10.1016/j.jmatprotec.2019.03.013

12. K., Nakowong, and K., Sillapasa. "Optimized Parameter for Butt Joint in Friction Stir Welding of Semi-Solid Aluminum Alloy 5083 Using Taguchi Technique", *Journal of Manufacturing and Materials Processing,* Vol. 5, No. 3 (2021), 88. Doi.org/10.3390/jmmp5030088

13. I. A., Daniyan, K., Mpofu1, A. O., Adeodu. "Optimization of welding parameters using Taguchi and response surface methodology for rail car bracket assembly", *International Journal of Advanced Manufacturing Technology* 100, (2019), 2221-2228. Doi.org/10.1007/s00170-018-2878-9

14. M., Nourani, A., Milani, and S., Yannacopoulos. "Taguchi optimization of process parameters in friction stir welding of 6061 aluminum alloy: A review and case study", *Engineering* 3, No. 2, (2011), 144-154. Doi.10.4236/ENG.2011.32017

15. M., Ahmadnia, A., Seidanloo, R., Teimouri, Y., Rostamiyan, and G., Titrashi. "Determining influence of ultrasonic-assisted friction stir welding parameters on mechanical and tribological properties of AA6061 joints" *International Journal of Advanced Manufacturing Technology* 78, No. (9-12), (2015), 2009-2024. Doi.10.1007/s00170-015-6784-0

16. R., Mishra, and S., Jain. "Friction stir welding (FSW) process on aluminum alloy 6082-T6 using Taguchi". *International Journal of Research in Engineering and Innovation,* (2019).

17. Y., Rostamiyan, A., Seidanloo, H., Sohrabpoor and R., Teimouri. Experimental studies on ultrasonically assisted friction stir spot welding of AA6061. *Archives of Civil and Mechanical Engineering* 15, No. 2, (2015), 335-346. Doi. 10.1016/j.acme.2014.06.005

18. J., Kundu, and H., Singh. "Modelling and analysis of process parameters in friction stir welding of AA5083-H321 using response surface methodology" *Advances in Materials and Processing Technologies* 4, No. 2, (2018), 183-199. Doi. 10.1080/2374068X.2017.1411039

19. M., Fond, "Technical and physical properties Available from: www.commercialefond.it.

20. R., Roy, "Design of experiments using the Taguchi approach: 16 steps to product and process improvement" 2001: John Wiley & Sons.

Persian Abstract

چکیده

فرآیند جوشکاری اصطکاکی اغتشاشی یکی از روش های جوشکاری حالت جامد است. از سوی دیگر، فرآیند FSW دارای محدودیت هایی مانند سرعت کم و گشتاور بالا است که بهره وری و کاربرد فرآیند را محدود می کند. برای غلبه بر این محدودیت ها، چندین منبع انرژی ثانویه با فرآیند FSW ادغام شدند. در مقاله حاضر، FSW توسط انرژی ارتعاشی اولتراسونیک در فرآیندی به نام جوشکاری اغتشاشی اصطکاکی به کمک اولتراسونیک (UAFSW)عمل می‌کند. هدف این مقاله بهینه سازی پارامترهای فرآیند اصلی فرآیند UAFSW با استفاده از 4 سطح برای هر پارامتر با مجموع 16 آزمایش تجربی با استفاده از تکنیک تاگوچی است تا به جوشکاران کمک کند تا پارامترهای مناسب را برای دستیابی به بالاترین راندمان اتصال از نظر نهایی انتخاب کنند. استحکام کششی (UTS)پارامترهایی که باید بهینه شوند عبارتند از دامنه ارتعاش (80–20 میکرومتر)، سرعت تراورس (160–40 میلی متر در دقیقه) و سرعت چرخش ابزار (1200–630 دور در دقیقه). علاوه بر این، تجزیه و تحلیل ANOVA برای تعیین درصد مشارکت هر پارامتر فرآیند استفاده گردد. تأثیر هر پارامتر فرآیند بر UTS نیز مورد بررسی و تجزیه و تحلیل قرار گرفت. نتایج نشان داد که شرایط بهینه 20 میکرومتر، 80 میلی‌متر در دقیقه و 800 دور در دقیقه است. تجزیه و تحلیل ANOVA نشان داد که سرعت چرخش مهم ترین پارامتر است. UTS 290 مگاپاسکال توسط مدل پیش‌بینی می‌شود که در آن مقدار واقعی 297 مگاپاسکال با درصد خطای 3.5 درصد است.

International Journal of Engineering

Preparation of Porous Alumina/Nano-Nickel Composite by Gel Casting and Carbothermic Reduction

Z. Hosseini[a,b], S. Mollazadeh Beidokhti[b], J. Vahdati Khaki[b], M. Pourabdoli*[a]

[a] Department of Materials Engineering, Hamedan University of Technology, Hamedan, Iran
[b] Department of Materials Engineering, Faculty of Engineering, Ferdowsi University of Mashhad, Mashhad, Iran

P A P E R I N F O

A B S T R A C T

Effects of dispersant (Tri polyphosphate sodium) amount on gel viscosity, mechanical activation of raw materials, raw materials mixture composition, and reduction atmosphere on the prepared composites and NiO reduction mechanism were investigated. It was found that 2.5 wt % dispersant is an optimum amount for a gel suspension with 50 V% of solid consisting of alumina, graphite, and nickel oxide. XRD results of reduced and sintered product (at 1200-1500 °C) showed that alumina, nickel, and nickel aluminate spinel are present in the prepared composite. The porosity of the composite made with 12 h ball milled-alumina was 48%, while it was 64 % in the sample made with 20 min ball-milled alumina. The results of TG-DTA analyses showed that the reduction temperature and mechanism are dependent on the raw materials' ball milling time. Thermal analyses revealed that mechanical activation of raw materials decreases the NiO reduction temperature and increases the metallic Ni production.

doi: 10.5829/ije.2022.35.01a.21

1. INTRODUCTION

From the unique advantages of hybrid composites over conventional composites are the balanced strength and stiffness, the desired mechanical properties, cost and weight reduction [1, 2]. Porous ceramic materials with a combination of metals have emerged as a new class of materials. These materials exhibit unusual mechanical and thermal properties, including energy storage, vibration and sound absorption, and thermal insulation, leading to a wide range of applications [3, 4].

Alumina-nickel bodies are attractive due to their mechanical and magnetic properties as well as their widespread use in the catalyst industry [5, 6]. The presence of porosity in the alumina body of composite increases its surface activity and uses possibility in various applications such as absorbers, filters, and electrical sensors [7]. In the preparation of alumina-nickel bodies, instead of the direct use of nickel, nickel oxide or nickel nitrate is used to supply metallic nickel

(during the reduction process) to make the uniform distribution of small nickel particles in the final body [8]. Usually, in the methods of making alumina-nickel composites, a pre-formed body of a mixture of alumina and nickel oxide is made. The body is then placed in a furnace under the flow of hydrogen gas to reduce the nickel oxide to metallic nickel. Common methods of forming alumina-nickel composites such as pressing, sol-gel, and slurry casting methods have problems that prevent their widespread use, and except for the slurry casting method, it is not possible to make a porous product with mentioned methods [7, 9-11]. The gel casting method is a relatively simple process to produce a body with final dimensions close to the original raw body. In this method, the ceramic slurry containing the polymerizable additives is poured into a mold in the desired shape. Since the particles do not have the opportunity to settle down in the slurry, they stick together due to the gelling process and take the shape of a mold. Finally, after leaving the mold, the casting part is

Corresponding Author Institutional Email: mpourabdoli@hut.ac.ir
(M. Pourabdoli)

dried and sintered [5]. Although in the gel casting process, the slurry contains a large volume of solids (about 50% by volume or more), it still has a high fluidity [12]. The mold materials used in this method are cheap and include wax, plastic, glass, and metal [13, 14]. The amount of organic monomers in the gel casting method is very small compared to other processes, and it is easily removed during the burning of the adhesive, and the parts are strong enough to be machined [5]. The gel casting method was first used in the metals and ceramics processing group at Oak Ridge National Laboratory during the 1990s [15]. This relatively simple method was performed to solve challenges such as limitations in the production of parts with desired shape and size. This method can be used for the production of a wide range of materials including metals, ceramics, alloys and composites [16].

In recent years, the use of gel casting method for the production of various composites as well as porous products has been considered during various researches such as production of porous alumina composites containing nickel nanoparticles with nickel nitrate as a source of nickel and hydrogen gas as the reducing agent [5], porous alumina-nickel composite as a catalyst with nickel oxide as a source of supply of nickel and CO gas as a reducing agent [17], porous silicon carbide with carbon in resin as reducing agent and source of carbon and SiO as source of Si [17], alumina composite containing tungsten nanoparticles by gel casting method and tungsten in situ reduction [19], alumina-nickel composite with complex shapes by gel casting and using 3D printer technology [20], alumina-nickel composite by gel casting method and centrifugal method for fabrication of parts with high density and homogeneous properties [21], alumina-nickel layer composites by casting alumina gel between tungsten metal plates [22], making transparent alumina plates by gel casting with pressure control [23]. The study of the effect of thermal regime and atmosphere on the properties of alumina-nickel composite made of nickel powder by sol method was investigated by Zygmuntowicz et al. [24]. In addition, magnesium aluminate spinel with alumina and magnesium oxide by gel casting method [25], use of pre-sinter to improve the mechanical properties of alumina based composites made by gel casting [26], and recently, making high porosity alumina with suitable strength by gel casting method and optimizing the production process were invesitgated [27].

In this research, a porous alumina-nickel composite containing nickel nanoparticles was prepared by gel casting, in which for the first time, instead of using reducing gas, graphite particles (dispersed in the preformed body) were used as the reducing agent. The advantages of this new method are the reduction of nickel oxide by graphite instead of reducing gas removes the complex equipment from the system, the possibility of using conventional furnaces, the possibility of the composite production under air atmosphere, and creating the porosity in the composite body during the reduction process. All these advantages reduce production costs, in addition to the fact that the properties of the produced composite in terms of quality are quite competitive with the quality of the produced composite with other methods. Moreover, in this study, mechanical activation of the raw materials was used to control and change the temperature of the reduction process. Reduction with graphite compared to reduction with CO gas has the advantage such as uniform distribution of graphite particles in the composite and then removing graphite during the reduction process resulted in uniform distribution of porosity in the composite structure. Also, since graphite is an industrial lubricant and its coefficient of friction is low, so its presence in the gel casting process increases the slurry fluidity and more uniform filling of the mold and thus helps to improve the gel casting process.

2. MATERIALS AND METHODS

2. 1. Raw Materials   Raw materials, including nickel oxide, alumina, and graphite were used so that the final composite (after reduction and sintering) contained 5% V of nickel metal. The raw materials specifications used to prepare the slurry required for the gel casting process are given in Table 1.

In this research, two different methods namely Methods 1 and 2 were used to prepare the main samples of porous alumina-nickel composite and the resulting samples were named SM1 and SM2, respectively (Table 2). Also, various experiments using a mixture of the raw material without gel casting and only to investigate the NiO carbothermic reduction mechanisms were conducted according to the conditions given in Table 3.

TABLE 1. Specifications of the raw materials

Material	Purity (wt %)	Particle size (µm)	
α-Alumina	98.5	88	Iran Alumina
Nickel Oxide	99.9	2	Merck
Graphite	99	100 nm	Armina
Gelatin	98	<800	Microteb
CMC adhesive Carboxylmethyl callouses	99.5	<150	Yolung-china
Dispersant Tripolyphosphate sodium	99.8	<150	LYG-china

2. 2. Methods of Preparation and Characterization of Porous Alumina-nickel Composite
The following methods were used to prepare the porous alumina-nickel composite:

Method 1: alumina powder mixed with 15 wt % ethanol and ball milled (20 minutes, rotation speed of 230 rpm, ball to powder ratio of 12) in a planetary ball mill (M200-Retsch-Germany) equipped with a polyethylene chamber and alumina balls. Next, the milled alumina was passed through a sieve (mesh 70 equivalents to 210 µm) and dried in an oven at 110 °C for 1 h. Graphite powder and nickel oxide were weighed based on reaction 1 (section 3.3) and their purity (Table 1). Then, they were ball milled in the air for 6 h with a ball to powder weight ratio of 12, at a rotation speed of 230 rpm.

To mix graphite powder and nickel oxide with alumina powder, these powders were milled for 5 minutes with the ball to powder weight ratio of 12 in air. In a solution containing 6 wt % gelatin, the gelatin powder was dissolved in distilled water for 2 hours at 45 °C with using a heater/magnetic stirrer [28]. The amount of distilled water required to prepare the gel casting slurry was subtracted from the amount of water in which the gelatin was dissolved. For the preparation of the gel casting slurry, the gelatin solution was mixed with graphite powder, nickel oxide, alumina, and distilled water, along with sodium triphosphate as a dispersant and CMC adhesive with specified weight ratios according to Table 2 using a mixer (model MY2011-NabBei) for 10 minutes. Then, the prepared slurry was poured into a cylindrical aluminum mold with a diameter of 1.5 cm and filled to a height of 1.5 cm. To dry the piece more evenly and prevent distortion and cracking, the mold was covered with a plastic bag and placed in an environment at a temperature of 20 °C for 72 h [29]. Then, the dried piece was removed from the mold.

Reduction and sintering processes were conducted in an electric furnace (Nobertherm-Ht 40/17) in the air. To prevent the oxidation of the reduced nickel, the piece was placed in an alumina crucible filled with carbon powder [30]. Then, the process was started from ambient temperature with a heating rate of 10 °C/min and continued until the furnace temperature reached 1200 °C. The piece was kept at 1200 °C for half an hour. Then, the process was continued with a heating rate of 2.5 °C/min to 1500 °C and it was kept at this temperature for half an hour. After finishing the process, the piece was gradually cooled in the furnace to room temperature.

Method 2: The difference between the first and second methods was in the ball milling time of alumina, nickel oxide, and graphite. To reduce the particle size of alumina and have a dense piece, the ball milling time of alumina in this method was 12 h at a speed of 230 rpm and the ball to powder weight ratio of 12. The ball-milling time of graphite and nickel oxide was 10 minutes just to increase their contact.

The phase analysis of the SM1 and SM2 samples was performed by XRD (X'pert PW 3040/60-Philips) at 25 °C with a step of 0.2 degrees using Cu-kα radiation. SEM images were prepared by Scanning Electron Microscope (VP 14500-LEO) and used to observe the

TABLE 2. Coding and preparation conditions of alumina-nickel composites

Code	Composition (wt %)							Ball milling time of graphite and nickel oxide mixture	Ball milling time of alumina ball milling	Sintering
	Alumina	**Graphite**	**Nickel oxide**	**Gelatin**	**Dispersant**	**Distilled water**	**CMC adhesive**			
SM1								6 h	20 min	Half an hour at a temperature of 1200 °C then increase the temperature to 1500 °C
SM2	58.63	1.36	8.50	0.75	2.50	28.2	0.075	10 min	12 h	

Other details were described in 2-2 section.

TABLE 3. Specifications of powder samples and conditions for TG-DTA tests

Code	Powder composition (wt %)			Ball milling time (min)	Ball to powder weight ratio	Rotation speed (rpm)	Atmosphere	Heating rate (°C/min)	TG-DTA model
	Nickel oxide	**Graphite**	**Alumina**						
A	86	14	0	10	12	230	Ar	10	Q600-TA
B	86	14	0	360	12	230	Ar	10	Q600-TA
C	12.8	2.10	85	720	12	230	Ar	10	Q600-TA

dimensions of the porosity and the presence of nickel particles in the alumina body. The density of prepared composites was measured using the immersion method (Archimedes method). The porosity percentage was then calculated according to the measured density and composite body dimensions. The optimal amount of the dispersant to have a slurry with the desired fluidity was determined by a rotary viscometer (Anton Paar –physical mcr 301).

2. 3. Nickel Oxide Reduction Mechanism   To investigate the reduction mechanism of carbothermic reduction of nickel oxide and to analyze the reactions that occur during heating of the SM1 and SM2 samples, the powder samples (containing graphite, nickel oxide, and alumina) without gel casting were prepared following the conditions given in Table 3 and analyzed by TG-DTA.

3. RESULTS AND DISCUSSIONS

3. 1. Characterization of Composite
3. 1. 1. Slurry Rheology and Dispersant Amount
The graph of viscosity changes in Figure 1 shows that with an increase in the amount of dispersant in the slurry containing 50 V% of the solid, the viscosity first decreases until the viscosity reaches a minimum value in the slurry containing 2.5 wt % dispersant. Figure 1 displays that increasing the dispersant amount excess than 2.5 wt %, slightly increases the slurry viscosity. The reason for this increase is that in the slurry containing 3.20 wt % of the dispersant, the slurry particles are saturated with the dispersant and the free ions in the slurry increased with viscosity [31]. It is observed that the viscosity curve of 1.8 % TPP in the range of 40-110 1/s is lower than the viscosity curve of 2.5 % TPP. That is related to the measurement error of the viscometer. Therefore, the 2.5 wt % dispersant is an optimum amount for the preparation of gel casting slurry.

3. 1. 2. Phase Analysis   The XRD patterns of SM1 and SM2 samples after the sintering process are shown in Figure 2. The XRD patterns show the alumina (α-alumina), metallic nickel, and nickel aluminate spinel are present in the composites. As can be seen in the XRD pattern of SM1, the metallic nickel main peak (45 degrees) is more intense than it in the XRD pattern of SM2. It confirms that mechanical activation of the nickel oxide and graphite mixture has improved the nickel oxide reduction (metallic nickel production) process. Nickel aluminate spinel is a blue to green pigment. The presence of this phase caused the color of the prepared composite to be green-blue. The formation of this phase has no negative effect on the properties of alumina-nickel composite. Nickel aluminate spinel has catalytic
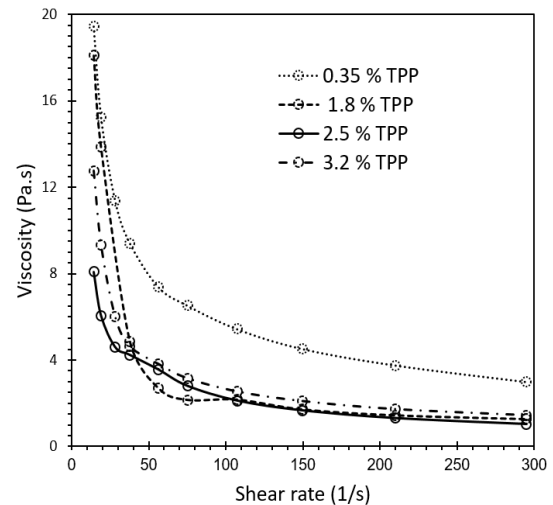

Figure 1. Rheological behavior of the gel casting slurry (50 V% of solid and 1 wt % of gelatin) containing the various amounts of dispersant

properties and is used in methane production process from hydrogen [32]. It has been suggested that the formation of nickel aluminate spinel in alumina-nickel catalysts increases the catalyst life [17].

3. 2. Composite Microstructure   The SEM images in Figure 3 show the porosities in the structure of the SM2 sample. In these images, porosities with dimensions up to 50 microns can be observed. The results showed that the SM1 sample, in which alumina was milled for a shorter time, had more porosity than the SM2 sample. The porosities of SM1 and SM2 samples were 64 and 48% by volume, respectively. The longer milling time in the SM2 sample reduced the particle size and thus reduced the porosity in the sample.
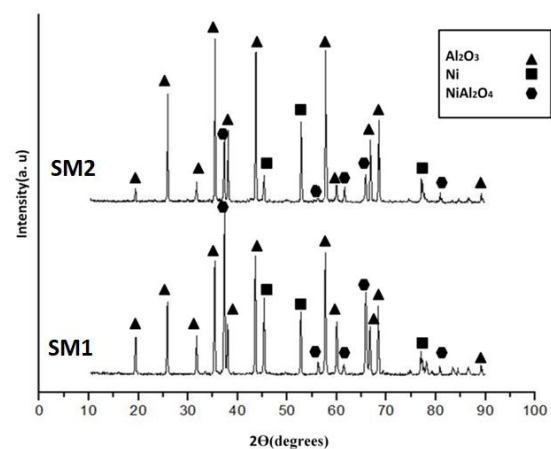

Figure 2. The XRD Pattern of SM1 and SM2 samples after the sintering process

Figure 4 shows the SEM images of the SM2 sample at a higher magnification. According to these images, the presence of nickel particles and a small amount of nickel aluminate spinel in the alumina field are quite clear. In Figure 4a, part of the alumina body is shown as a continuous phase, which indicates the proper connection and sintering of alumina after the sintering process. Nickel particles are seen in a light color. Figure 4b refers to the part of the composite that is deeper point from the surface. Figure 4c shows the nickel particles in nanometer dimensions. Alumina-nickel composites containing nickel nanoparticles have desired magnetic, optical, mechanical, and catalytic properties [5, 10]. Therefore, nickel nano-particles production by the method used in this research is a great advantage.
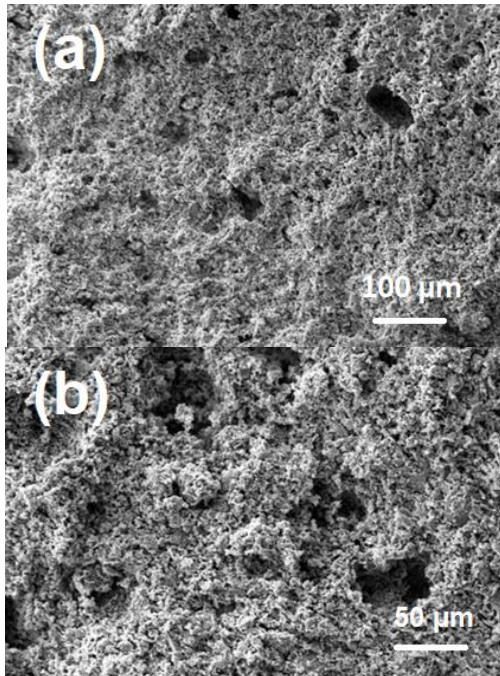
Figure 3. Porosities created in alumina-nickel composite (SM2) made by gel casting and reduction with graphite powder
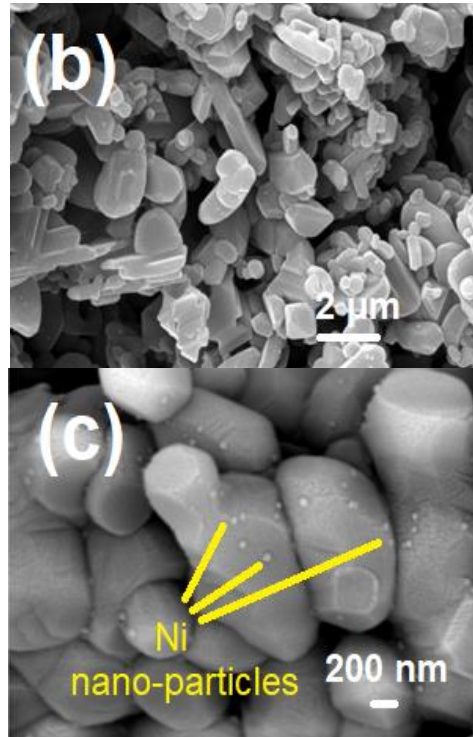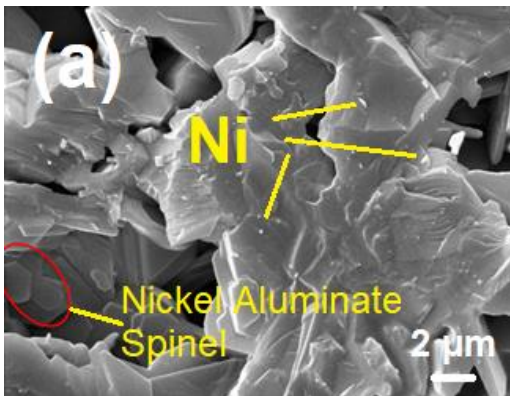
Figure 4. a) Structure of alumina-nickel composite-SM2, b) Structure of alumina-nickel composite-SM2 in the deeper point from the surface, c) Structure of alumina-nickel composite-SM2 containing Ni nano-particles

3. 3. Mechanism of Carbothermic Reduction of Nickel Oxide   The TG-DTA analyses of sample A are shown in Figure 5. It is seen that weight loss starts at 100 °C, which is related to the release of water absorbed by the powder. The weight loss continues up to 400 °C, which is related to the complete removal of bond water and volatiles. From 400 to 500 °C the weight is constant and no reaction occurs.
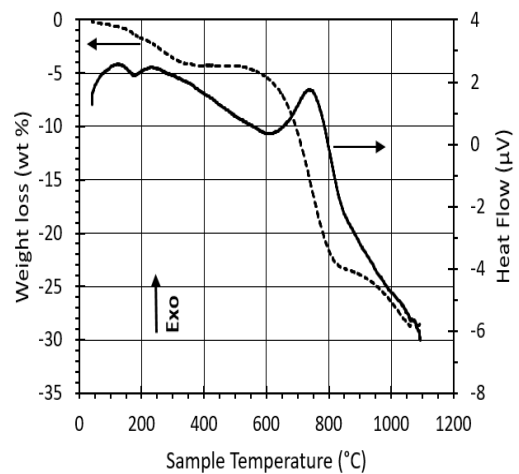
Figure 5. The TG-DTA curves of sample A

The reduction mechanism of most metal oxides with carbon, when there is no transition phase between the two materials, is described in two steps. In the first step (reaction 1), which is a slower step, the surface of the nickel oxide particles reacts with solid carbon. In the second step (reaction 2), the remained nickel oxide particles react with the CO gas resulted from reaction 1 [33]. Weight loss begins again at 500 ° C, which corresponds to the beginning of the reduction process of nickel oxide with graphite (Figure 5).

$$NiO + C = Ni + CO_{(g)} \tag{1}$$

$$NiO + CO_{(g)} = Ni + CO_{2\,(g)} \tag{2}$$
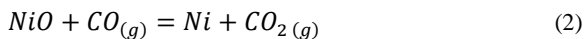
As can be seen in Figure 5, the rate of reaction 1 is initially slow. The diffusion of solid into solid (graphite and nickel oxide) is still low. As the temperature raised to 630 °C the reaction rate increased. Other studies have reported that the reaction of solid carbon with nickel oxide accelerated at high temperature close to 630 °C [34].

The solid-solid reaction takes place up to about 810 °C, and the slope continues to increase up to 810 °C. Here the second phase of the reaction, i.e. the reduction of nickel oxide with CO, begins and the rate of the reduction is reduced. There are two possible reasons for this decline. The first reason is that this temperature is the same as the temperature of CO formation; various studies have concluded that although CO itself is a reducing agent of nickel oxide, its formation initially slows down the reduction of nickel oxide with solid carbon. It is not clear why the presence of CO formation is an obstacle to the reduction reaction [33-35]. The formation of CO may consume some of the system energy and thus slow down the nickel oxide reduction process. The second reason is that at the beginning of CO formation, i.e. at a temperature of about 810 °C, the CO pressure has not yet reached a level that supports to react effectively. As a result, the reduction reaction as a whole was slowed down [33].

The TG-DTA analyses of sample B in Figure 6 show that due to the longer mechanical activation of sample B than sample A, the reduction reaction is initiated at a lower temperature (390 °C) than sample A (630 °C). According to Figure 6, in sample B, the onset temperature (775 °C) of the reaction rate decline is also lower than it in sample A (810 °C). It can be said that due to the reduction of nickel at a lower temperature and due to the catalytic role of nickel, the beginning of the carbon monoxide formation has also started from a lower temperature [35].

According to TG curves in Figures 5 and 6, the overall weight losses at 800 °C for samples A and D are 22 and 29 wt %, respectively. The loss of weight is equivalent to oxygen removal of the specimens during

NiO reduction. This confirms that the mechanical activation not only decreases the reduction temperature but also increases the metallic nickel production.

To investigate the effect of alumina in the reduction process, a thermal analysis was performed for the sample containing alumina (sample C) (Figure 7). A comparison of Figures 7 and 5 shows that the presence of alumina does not affect the reduction process. In general, the peaks in Figure 5 (sample A) are clearer than in Figure 7 (sample C) because sample A contains only graphite and nickel oxide. The slope of Figure 7 is due to the high thermal resistance of alumina resulted in a high heating rate during thermal analysis [36].
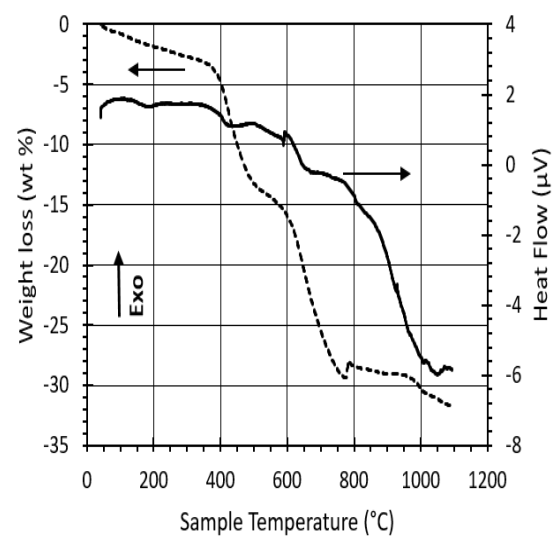

**Figure 6.** The TG-DTA curves of sample B
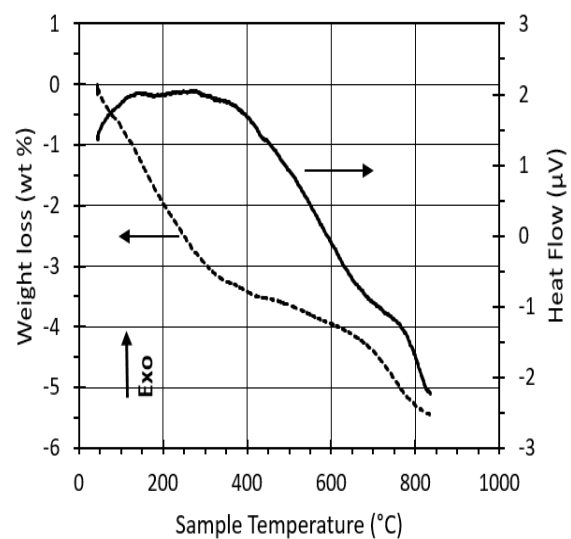
Figure 7. TG-DTA curves of sample C

4. CONCLUSION

The following conclusions were obtained from this research:

1. The optimum amount of tripolyphosphate sodium as a dispersant for preparation of a slurry with 50 V% of solid (alumina, graphite, and nickel oxide) was 2.5 wt %.

2. The porosity of the sample made with 12 h ball-milled alumina was 48% and it was 64 % in the sample made with 20 min ball-milled alumina.

3. The presence of nickel seems to reduce the temperature of CO formation during the Boudouard reaction due to its catalytic effect.

4. Due to the mechanical activation of the graphite and nickel oxide mixture for 6 h, more nickel was reduced than the inactivated sample.

5. In addition to alumina and nickel nano-particles, the sample also contained nickel aluminate spinel.

6. The mechanical activation of raw materials decreased the NiO reduction temperature and increased the metallic Ni production.

5. REFERENCES

1. Saindane, U. V., Soni, S., Menghani, J. V. "Dry Sliding Behavior of Carbon-Based Brake Pad Materials." *International Journal of Engineering, Transactions B: Applications*, Vol. 34, No. 11, (2021), 2517-2524. DOI: 10.5829/ije.2021.34.11b.14

2. Saindane, U. V., Soni, S., Menghani, J. V. "Studies on Mechanical Properties of Brake Friction Materials Derived from Carbon Fibres Reinforced Polymer Composite." *Materials Today: Proceedings*, Vol. 47, No. 17, (2021), 5760-5765. DOI: 10.1016/j.matpr.2021.04.079

3. Dehaghani, M. T., Ahmadian, M. "Fracture Mechanism of CoCrMo Porous Nano-Composite Prepared by Powder Metallurgy Route." *International Journal of Engineering, Transactions A: Basics*, Vol. 31, No. 1, (2018), 19-24. DOI: 10.5829/ije.2018.31.01a.03

4. Nekokar, N., Pourabdoli, M. "Isothermal Redox Kinetics of Co_3O_4-Fe_2O_3 Nano-Composite as a Thermochemical Heat Storage Material.", *International Journal of Engineering, Transactions B: Applications*, Vol. 32, No. 8, (2019), 1200-1209. DOI: 10.5829/ije.2019.32.08b.17

5. Niihara, K., Kim, B. S., Nakayama, T., Kusunose, T., Nomoto, T., Hikasa, A., Sekino, T. "Fabrication of Complex-Shaped Alumina/Nickel Nanocomposites by Gel Casting Process." *Journal of the European Ceramic Society*, Vol. 24, No. 12, (2004), 3419-3425. https://doi.org/10.1016/j.jeurceramsoc.2003.10.027

6. Kim, B. S., Sekino, T. , Nakayama, T. , Kusunose, T., J. S. Lee, K. Niihara. "Mechanical and Magnetic Properties of Alumina/Nickel Nano Composites Prepared by Pulse Electric Current Sintering." *Journal of Ceramic Society of Japan*, Vol. 111, No. 1295, (2003), 257-460.

7. Kritikaki, A., Tsetsekou, A. "Fabrication of Porous Alumina Ceramics from Powder Mixtures with Sol–Gel Derived Nanometer Alumina: Effect of Mixing Method." *Journal of the European Ceramic Society*, Vol. 29, (2009),1603-1611. DOI: 10.1016/j.jeurceramsoc.2008.10.011

8. Sekino, T., Nakajima, T., Ueda, S., Niihara, K. "Reduction and Sintering of a Nickel-Dispersed-Alumina Composite and its

9. Properties" *Journal of the American Ceramic Society*, Vol. 8, (1997), 1139-1148. https://doi.org/10.1111/j.1151-2916.1997.tb02956.x

9. Sekino, T., Nakajima, T., Niihara, K. "Mechanical and Magnetic Properties of Nickel Dispersed Alumina-Based Nanocomposite." *Materials Letters*, Vol. 29, (1996), 165-169. https://doi.org/10.1016/S0167-577X(96)00136-X

10. Roy, B., Martinez, U., Loganathan, K., Datye, A. K., Leclerc, C.A. "Effect of Preparation Methods on the Performance of Ni/Al_2O_3 Catalysts for Aqueous-Phase Reforming of Ethanol: Part I-Catalytic Activity." *International Journal of Hydrogen Energy*, Vol. 37, (2012), 8143-8153. https://doi.org/10.1016/j.ijhydene.2012.02.056

11. Zhao, A., Ying, W., Zhang, H., Ma, H., Fang, D. "Ni-Al_2O_3 Catalysts Prepared by Solution Combustion Method for Syngas Methanation." *Catalysis Communications*, Vol. 17, (2012), 34-38. https://doi.org/10.1016/j.catcom.2011.10.010

12. Koclar, G. S. "Gelcasting of Alumina Ceramics with Gelatin and Carrageenan Gum and Investigation of Their Mechanical Properties." M.Sc. Thesis, Materials science and engineering, Izmir Institute of Technology, 2013.

13. Dhara, S., Kamboj, R. K., Pradhan, M., Bhargava, P. "Shape Forming of Ceramics via Gel Casting of Aqueous Particulate Slurries." *Journal of Bulletin of Materials Science*, Vol. 6, (2002), 565-568. DOI: 10.1007/BF02710552

14. Pabst, W. , Gregorová, E. , Havrda, J. **,** Týanová, E. Gelatin casting and starch consolidation of alumina ceramics", Book chapter in Ceramic Materials and Components for Engine*s*, WILEY-VCH Verlag GmbH, 2001, pp. 587-592.

15. Omatete, O. O., Janney, M. A., Nunn, S. D. "Gel Casting: From Laboratory Development to Industrial Production." *Journal of the European Ceramic Society*, Vol. 17, (1997), 407– 413. https://doi.org/10.1016/S0955-2219(96)00147-1

16. Tari, G. "Gel Casting Ceramics: A Review." *American Ceramic Society Bulletin*, Vol. 82, No. 4, 43-46.

17. Becerra, A. M., Castro-Luna, A. E. "An Investigation on the Presence of $NiAl_2O_4$ in a Stable Ni on Alumina Catalyst for Dry Reforming." *Journal of the Chilean Chemical Society*, Vol. 2, (2005), 465-469. http://dx.doi.org/10.4067/S0717-97072005000200005

18. Cheng, H., Yang, J. F., Zhang, N. L. "Fabrication and Characterization of Hierarchical Porous SiC Ceramics via Gel Casting and Carbothermal Reduction Between Carbon and SiO." *Journal of the Ceramic Society of Japan*, Vol. 128, No. 9, (2020), 589-594. DOI: DOI:10.2109/jcersj2.20063

19. Zygmuntowicz, J., Piątek, M., Miazga, A., Konopka, K., Kaszuwara W. "Dilatrometric sintering study and Characterization of Alumina-Nickel Composites." *Processing and Application of Ceramics*, Vol. 12, No. 2, (2018), 111-117. DOI:10.2298/PAC1802111Z

20. Ndinisa, S. S., Whitefield, D. J., Sigalas, I. "Fabrication of Complex Shaped Alumina Parts by Gel Casting on 3D Printed Moulds." *Ceramics International*, Vol 46, No. 3, (2020), 3177-3182. https://doi.org/10.1016/j.ceramint.2019.10.021

21. Zygmuntowicz, J., Zielant, D., Suchecki, P., Konopka, K., Kaszuwara, W. "Fabrication of Al_2O_3-Ni Graded Composites by Centrifugal Casting in an Ultracentrifuge.", *Composites Theory and Practice*, Vol. 18, No. 3, 174-179.

22. Kedzierska-Sar, A., Starzonek, S., Kukielski, M., Falkowski, P., Rzoska, S. J., Szafran, M. "Gelcasting of Al_2O_3–W Composites: Broadband Dielectric Spectroscopy and Rheological Studies of Tungsten Influence on Polymerisation Kinetics, *Ceramics International*, Vol. 45, No. 12, 15237-15243. https://doi.org/10.1016/j.ceramint.2019.05.012

23. Chen, H., Shunzo, S., Zhao, J., Di, Z. "Pressure Filtration Assisted Gel Casting in Translucent Alumina Ceramics

Fabrication.", *Ceramics International*, Vol 44, No. 14, 16572-16576. DOI: 10.1016/j.ceramint.2018.06.079

24. Zygmuntowicz, J., Wiecinska, P., Miazga, A., Konopka, K., Szafran, M., Kaszuwara, W. "Thermoanalytical Studies of the Ceramic-Metal Composites Obtained by Gel-Centrifugal Casting." *Journal of Thermal Analysis and Calorimetry*, Vol. 133, No. 1, (2018), 303-312. https://doi.org/10.1007/s10973-017-6647-z

25. Shahbazi, H., Shokrollahi, H., Tataei, M. "Gel-Casting of Transparent Magnesium Aluminate Spinel Ceramics Fabricated by Spark Plasma Sintering (SPS)." *Ceramics International*, Vol. 44, No. 5, (2018), 4955-4960. DOI: 10.1016/j.ceramint.2017.12.088

26. Lv, L., Lu, Y., Zhang, X., Chen, Y., Hou, W., Liu, W., Yang, J. "Preparation of Low-Shrinkage and High-Performance Alumina Ceramics via Incorporation of Pre-Sintered Alumina Powder Based on Isobam Gelcasting." *Ceramics International*, Vol 45, No. 9, 11654-11659. https://doi.org/10.1016/j.ceramint.2019.03.039

27. Zhang, M. et al. "High-Strength Macro-Porous Alumina Ceramics with Regularly Arranged Pores Produced by Gel-Casting and Sacrificial Template Methods." *Journal of Materials Science*, Vol. 54, No. 14, (2019), 10119-10129. https://doi.org/10.1007/s10853-019-03576-8

28. Montanaro, L., Coppola, B., Palmero, P., Tulliani, J. M. "A Review on Aqueous Gel Casting: A Versatile and Low-Toxic Technique to Shape Ceramics." *Ceramics International*, Vol. 45, No. 7, (2019), 9653-9673. DOI: 10.1016/j.ceramint.2018.12.079

29. Esfahani, H. B., Yekta, B. E., Marghussian, V. K. "Rheology and Gelation Behavior of Gel-Cast Cordierite-Based Glass Suspensions." *Ceramic International*, Vol. 38, (2011),1175-1179. DOI: 10.1016/j.ceramint.2011.08.046

30. Chan, C. F. , Argent, B. B. , Lee, W. E. "Influence of Additives on Slag Resistance of Al_2O_3-SiO_2-SiC-C Refractory Bond Phases Under Reducing Atmosphere." *Journal of the American Ceramic Society*, Vol. 81, (1998), 3177-3188. https://doi.org/10.1111/j.1151-2916.1998.tb02754.x

31. Kim, H. M., Venkatesh, R. P., Kwon, T. Y., Park, J. G. "Influence of Anionic Polyelectrolyte Addition on Ceria Dispersion Behavior for Quartz Chemical Mechanical Polishing." *Colloids and Surfaces A: Physicochemical and Engineering Aspects*, Vol. 411, (2012), 122-128. https://doi.org/10.1016/j.colsurfa.2012.07.009

32. Ding, C., Liu, W., Wang, J., Liu, P., Zhang, K., Gao, X., Ding, G., Liu, S., Han, Y., Mac, X. "One Step Synthesis of Mesoporous NiO–Al_2O_3 Catalyst for Partial Oxidation of Methane to Syngas: The Role of Calcination Temperature." *Fuel*, Vol. 162, (2015), 148-154. https://doi.org/10.1016/j.fuel.2015.09.002

33. Lebukhova, N. V., Karpovich, N. F. "Carbothermic Reduction of Copper, Nickel, and Cobalt Oxides and Molybdates." *Inorganic Materials*, Vol. 8 (2008), 1003-1007. DOI: https://doi.org/10.1134/S0020168508080207

34. L'vov, B. V. "Mechanism of Carbothermal Reduction of Iron, Cobalt, Nickel and Copper Oxides." *Thermochimica Acta*, Vol. 360, No. 2, (2000), 109-120. DOI: 10.1016/S0040-6031(00)00540-2

35. Yang, H., McCormic, P.G. "Mechanically Activated Reduction of Nickel Oxide." *Metallurgical and Materials Transactions B*, Vol. 29, (1998), 29, 449-455. https://doi.org/10.1007/s11663-998-0123-x

36. Haines, P. J., Principles of thermal analysis and calorimetry, The Royal Society of Chemistry, Cambridge, 2002.

Persian Abstract

چکیده

اثر میزان پراکنده ساز (تری پلی فسفات سدیم) بر ویسکوزیته ژل و فعال سازی مکانیکی مواد اولیه، ترکیب مخلوط مواد اولیه و اتمسفر احیا روی کامپوزیت های تهیه شده و مکانیسم احیا NiO مورد بررسی قرار گرفت. مشخص شد که 2/5 درصد وزنی پراکنده ساز برای یک سوسپانسیون ژل با 50 درصد حجمی جامد متشکل از آلومینا، گرافیت و اکسید نیکل مقدار بهینه ای است. نتایج XRD محصول احیا و سینتر شده (در دمای 1500–1200 درجه سانتیگراد) نشان داد که اسپینل آلومینا، نیکل و آلومینات نیکل در کامپوزیت تهیه شده وجود دارد. تخلخل کامپوزیت ساخته شده با آلومینای آسیاشده به مدت 4 ساعت، 48 درصد و تخلخل کامپوزیت تهیه شده با آلومینای آسیاشده به مدت 20 دقیقه، 64 درصد بود. نتایج TG-DTA نشان داد که دما و مکانیسم احیا به زمان آسیاکاری مواد اولیه بستگی دارد. آنالیز حرارتی نشان داد که فعال سازی مکانیکی مواد اولیه باعث کاهش دمای احیا NiO و افزایش تولید نیکل فلزی می شود.

Theoretical Analysis on the Behavior of Reinforced Industrial Shed Structures with Shape Memory Alloys

H. Hosseinnejad[a], M. A. Lotfollahi-Yaghin[*b], Y. Hosseinzadeh[b], A. Maleki[a]

a Department of Civil Engineering, Maragheh Branch, Islamic Azad University, Maragheh, Iran
b Civil Engineering Faculty, University of Tabriz, Tabriz, Iran

A B S T R A C T

Shape memory alloys (SMAs) are functional materials that feature shape memory effects and super-elasticity. These features have made SMAs efficient materials for reinforcement and improvement of the stability of a structure. The present study investigated the effect of local post-tensioning with SMAs to improve the load-carrying capacity of tapered steel industrial sheds. For this purpose, ABAQUS software was used to predict the flexural strength and load-bearing capacity of the alloys. The effects of the diameter and the post-tension force applied to the SMA tendons were investigated. The results showed that external post-tensioning using SMA tendons is an effective way to increase the load-carrying capacity of industrial sheds. In the maximum load capacity of the frame for the steel and SMA tendons increased by 36 and 60%, respectively. The performance of the sheds was improved by local post-tensioning, which can reduce the weight of the structures.

doi: 10.5829/ije.2022.35.01a.22

1. INTRODUCTION

Industrial metal structures have been used for a wide nge of applications in different factories; such as poultry houses and aircraft hangars to sport stadiums. This means that it is necessary to improve and reinforce existing industrial metal structures to enhance their performance and stability. In the past, post-tensioning technology has been extensively used to reinforce concrete and metal structures; however, the effects of post-tensioning on industrial sheds have not yet been investigated. The improvement of the load-carrying capacity of tapered steel industrial sheds using post-tensioning technology also has not been investigated.

The high cost of installing new sheds has made it necessary to develop ways of reinforcing steel industrial sheds. The post-tensioning method is an available approach to strengthening an existing structure to cope with an increase in service loading. In this technology, some parts of the structure are reinforced in order to increase the total load-carrying capacity of the structure.

In the past two decades, post-tensioning has been commonly used to improve the performance of steel and concrete structures [1-12]. Nunziata [13] investigated the behavior of post-tensioned steel beams through experimental analysis. The results indicated that post-tensioning resulted in a 15% decrease in the weight of the structure.

Post-tensioned beams have technical and financial advantages over more simply fabricated structures. Studies have examined the use of post-tensioning cables in earthquake-resistant structural steel moment-resisting frames [14-17]. Nazir [18] applied post-tensioned cables to a bridge with a curved steel beam. Their results indicated that post-tensioning increased the load-carrying capacity of the structure as a suitable and affordable approach to the reinforcement of existing steel structures.

In the post-tensioning technique, prestress is introduced with the use of tensioning tendons because, when tendons are grouted, re-tensioning is impossible. Researchers have explored prestressing techniques that employ SMAs to overcome this disadvantage of conventional prestressing. SMAs possess physical and mechanical features that make them successful

*Corresponding Author Email: m.alilotfollahiyaghin@gmail.com (M. A. Lotfollahi-Yaghin)

candidates for use in structural engineering applications. They can regain their original shape after being deformed up to 6 to 8% as a result of underlying reversible solid-solid phase transformation. SMAs have shown promise, especially for applications in which the added value is more important than purely economic considerations. Some of the advantages of SMAs include bio-compatibility, usefulness for a variety of applications, and good mechanical properties, such as strength and corrosion resistance [21].

Park et al. [19] performed a numerical study using ABAQUS software to investigate the effect of post-tensioning method to increase the flexural strength and load-carrying capacity of I-shaped steel beams. The results indicated that the external prestressing technique creates a stiffer steel beam by applying suitable prestresses when parameters are appropriately combined. Taoum et al. [20] applied local post-tensioning to a steel beam for reinforcement of damaged steel bridges and I-shaped beams. The results showed that post-tensioning technology could be extensively used for steel beams due to its low cost and ease of preparation. Ghannam et al. [15] studied the effect of post-tensioned cables for strengthening steel frames (simple, double-bay, and double-story frames) using ANSYS finite element (FE) method. The results of the FE models indicated that the use of post-tensioned cables significantly increased the load capacity of the steel frame. The post-tensioning force must be designed to ensure that the connections remain safe after post-tensioning. In other words, the structural connections must also be considered for the design of post-tensioning forces.

The development of materials research has led to intelligent materials such as metals (e.g. shape-memory nickel-titanium alloy), ceramics, and SMAs, which can alter their properties to adapt to changes in the environment. Several studies have focused on the application of SMAs to structures [21–24]. A review of the use of SMAs in civil engineering applications can be found by Chang and Araki [25]. Shrestha et al. [26] evaluated the behavior of concrete structures optimally equipped with SMAs as they are being used along with plastic hinge of the beams. For this purpose, a reinforced concrete (RC) beam, a 2D RC frame, and a 3D RC building were considered, which were tested in previous studies under cyclic loading and on a shaking table. Daghash and Ozbulut [27] studied the cyclic behavior of composite materials reinforced with super-elastic NiTi SMA wires using uniaxial tensile tests. The results of the tests indicated that the SMA-FRP composites can recover from relatively high strains upon unloading and also revealed very high damage strains. Strieder et al. [28] performed an experimental study on the behavior of concrete beams post-tensioned with steel-based SMAs. They found that the

serviceability behavior of a concrete beam improved by the application of a second thermal activation at different temperatures and stress states for activation along the SMA strip. The study on application of shape memory alloys in had been done previously with different methods. This new material have the unique ability to sustain large deformations and returned to their original shape upon stress applied for superelastic SMA or by heating the SMA. Shape memory alloys due to their benefits of superelasticity and shape-memory effect have been successfully used in a number of industries and civil engineering such as pre-stressing, pre-tensioning, post-tensioning, SMA based dampers, etc. The benefits of using SMAs in pre-stressing are:

 Active control on the amount of pre-stressing with increased additional load-carrying capacity.

 No involvement of jacking or strand-cutting.

 No elastic shortening friction and anchorage losses over time.

Conventional pre-stressing of concrete members by pre-tensioning wires requires jacking and release of pre-stressing strands, which causes crack at the end of the girders during strand cutting. So, if we use SMA for pre-stressing, than jacking or strand-cutting are not required. A literature review showed that many studies have been done in the field of strengthening concrete structures using SMA, which shows the significant effect of SMA in increasing the bearing capacity of these members. However, this method has not been used in the case of steel structures, which was the main purpose of the present study. The main advantages are that the SMA bars do not need ducts nor anchorages and have no friction during pre-stressing or post-stressing.

A review of previous studies has shown that the application of post-tensioning to steel structures became a common way to reduce the cost and weight of structures. The use of high-strength steel tendons and post-tensioning can allow a decrease in the size of the steel elements and increase the load-carrying capacity of the structures. In recent years, the application of the post-tensioning method to steel structures has been investigated; but the application of this method to improve the characteristics of industrial sheds has not been considered. The present study investigated the use of this method as well as the application of SMA tendons as reinforcing structures using FE simulations using ABAQUS software. The effects of the diameter and the post-tension force applied to the SMA tendons were investigated. The results showed that external post-tensioning using SMA tendons is an effective way to increase the load-carrying capacity of industrial sheds. For the maximum load capacity of the frame, the steel and SMA tendons had an increase of 36 and 60%, respectively. The performance of the sheds was

improved by local post-tensioning, which can reduce the weight of the structures.

2. NUMERICAL SIMULATION

2. 1. 3D Model Details   As shown in Figure 1, an industrial shed of 20 m in length with a height that varies from 7 m at the supports to 9 m at the midspan was investigated. The slope of the roof in all models is 20%. The type of steel used is ST275. The cross-section of the rafter and column is I-shaped and has a variable cross-section. In all the studied models, the lateral bearing system in the transverse direction is considered as a normal bending frame and in the longitudinal direction, a simple frame with a conventional converging brace is assumed. For analysis and design of the industrial shed structure, ETABS2018 software was used depending on American code AISC 360-10 and the steel profile will be analyzed by using both LRFD design provisions according to AISC 360-10 and ASCE 7-16. Beams and columns are considered as beam elements to carry their weight, additional dead load, and the live load as gravity distributed pressures. The design loading combinations are the number of combinations of the prescribed response cases for which the building is to be checked/designed. In the LFRD method design shall be performed according to AISC Committee [29]:

$$R_u \leq \phi R_n \tag{1}$$

where R_u is required strength using LRFD load combinations, R_n is nominal strength, and ϕ is the resistance factor. The performance characteristics of the designed sections obtained based on the LFRD method in ETABS software is shown in Figure 1. As can be seen, the designed frame has a good performance.

2. 2. Modeling in ABAQUS   In the current study, the effect of local post-tensioning technology on the performance of steel industrial sheds has been investigated. For this purpose, an industrial steel shed was designed in ETABS software based on the LFRD method and this structure then was simulated in ABAQUS. The results were used to apply monotonic loading to study the effects of diameter of the elements, type of material and post-tensioning force on the performance of structure.

The structure was of grade S275 steel with an elastic modulus of 187 MPa, the yield stress of 275 MPa, the ultimate strength of 430 MPa and failure strain of 0.33. The structure was meshed using 3D C3D8R elements. The convergence of meshing was checked for the selection of a suitable mesh density to improve analysis precision and reduce computing time. Based on the

(a)

(b)
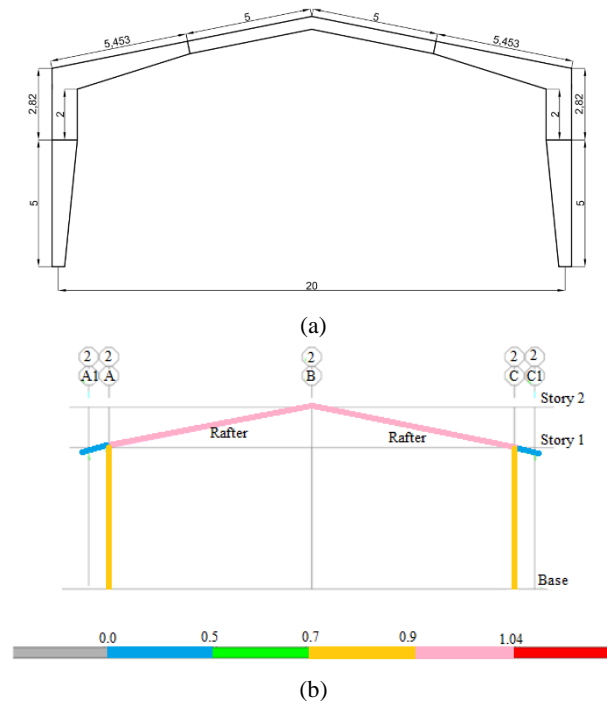
Figure 1. (a) Geometric characteristics of the tapered steel industrial shed used in finite element analysis, (b) The performance characteristics of the designed sections

initial results of the analysis, 0.02 cm was chosen as the size of the elements. The bolt load method was used for applying the post-tension load. Analysis was performed under displacement control. The boundary conditions were simulated as joint supports below the columns. Figure 2 shows the employed details of the FE model. The Newton–Raphson incremental iterative solution method was used to solve the equations in nonlinear FE analysis.

2. 3. Mechanical Features of SMA Tendons   As stated, the novelty of this study was the reinforcement of steel industrial sheds using SMA tendons under

Figure 2. Employed details of the FE model

external post-tensioning. The reversible phase change of SMAs in intelligent materials composed of gold-cadmium (Au-Cd) was first observed by Chang and Read [30]. Nili Ahmadabadi et al. [31] reorted the shape memory properties in nickel-titanium (Ni-Ti) alloy. At present, several types of SMA have been developed and used by different researchers.

Ni-Ti alloy, known as Nitinol, has many applications in practical engineering because of its high thermomechanical and thermoelectric characteristics. SMAs have two main phases, austenite and martensite, that are stable at low and high strain levels, respectively [34, 35]. The austenite and martensite phases can be mediated by heat or tension (See Figure 3). At the macroscopic scale, SMAs show two types of behavior: shape memory and super-elasticity. The shape memory effect requires a minimum temperature for returning to its former shape. The super-elastic effect provides reversibility of total deformation of SMAs under a minimum required temperature. The mechanical properties of the Nitinol used in the current study are presented in Table 1. The stress-strain curve for the Nitinol SMA is presented in Figure 4. In the current study, the area, A_{SMA}, and length, L_{SMA}, of the corresponding SMA are calculated as:

Figure 3. Super-elastic and shape memory effect [32]

Figure 4. Stress-strain behavior for SMA used in present work [33]

$$A^{SMA} = \frac{F_y}{\sigma_s^{AS}} \qquad (2)$$

$$L^{SMA} = \frac{E^{SMA} A^{SMA}}{K} \qquad (3)$$

where F_y is the yielding force, K is the axial stiffness and E^{SMA} is the elastic modulus of the SMA material under a stress level of σ_S^{AS}, at which point it enters the inelastic range (i.e., initiates forward transformation).

2. 3. Design of Experiments   Determining the design parameters employing experimental analysis by trial and error is time-consuming and costly. FE analysis can lead to reduce costs and overcome design obstacles. The design of experiments (DOE) technique allows process characterization, optimization and modeling in FE simulations [35]. Because it is important to identify the effective parameters and rank them from the highest to lowest priority, the main purpose of DOE is to investigate how the parameters affect the output of the process [36, 37].

In the current study, DOE was performed using response surface methodology (RSM) with a D-optimal design in order to determine the correlation between the outputs and the input parameters. The maximum displacement of the frame and maximum stress were considered as responses. The material properties, diameter and post-tension force applied to the tendons were modeled using the FE method and experiments designed in Design-Expert software. Table 2 shows the values of the parameters. Design Expert determined the design matrices according to the values of the geometric parameters on three levels (1, 0, 1). These design

TABLE 1. Mechanical properties of Nitinol (Ni-Ti) used in the current study [33]

Material properties	Value
Forward transformation stress (σ_{Ms})	400 MPa
Forward transformation stress (σ_{Mf})	500 MPa
Reverse transformation stress (σ_{As})	250 MPa
Reverse transformation stress (σ_{Af})	150 MPa
Plastic stress (σ_P)	700 MPa
Young's modulus (austenite) (E_P)	70 GPa
Young's modulus (martensite) (E_M)	40 GPa
Modulus of plasticity	3 GPa
Maximum transformation strain (ε_L)	5%
Poisson's ratio (austenite)	0.33
Poisson's ratio (martensite)	0.33

TABLE 2. Values of investigated geometric parameters

| Parameters	Level		
	1	0	-1
Tendon material	Steel	-	SMA
Tendon diameter	20mm	12.5mm	5mm
Post-tension force	40kN	20kN	0N

matrices then were used to perform 18 runs of FE data in order to determine a correlation between the input parameters and the responses.

3. RESULTS

In the results of nonlinear static FE analysis on the structure, the validity of the FE model was examined prior to studying the post-tension effect.

3. 1. Validation   Since there are no studies available in the open literature that examined the post-tensioning of steel tapered beams. The experimental results of post-tensioning I-shaped beams with steel rebars has been reported by Taoum et al. [20] which is used for validation. The results of the present work were compared with the control beam reported by Taoum et al. [20] and the moment-deflection curve of both results are shown in Figure 5. As illustrated, the FE model predicted the behavior of the I-shaped steel beams with reasonable accuracy at a maximum error of less than 10%. It is concluded that the developed model is capable of studying the performance of the post-tensioned structures.

Figure 6 compares the final deformation of the beam obtained from our FE modeling and the experimental results reported by Taoum et al. [20]. The application of the force resulted in a plastic hinge in the middle section


Figure 6. Stress distribution (Pa) of the beam obtained from finite element simulation and the experimental data reported in literature [20]

of the beam in the upper flange and local buckling at the place of loading. Comparison of the FE method and the experimental results for the deformation of the beam revealed that the FE model predicts the deformation of the post-tensioned beam at high accuracy [20].

3. 2. Post-tension with SMA Tendons   To ensure that finite element results produce the appropriate accuracy, we conducted a convergence analysis by changing elements size from comparatively coarse to excessively refined meshes i.e. 1mm to 20cm. Figure 7 shows the results for element sizes ranging from 1 mm to 20 cm for sample of No. 1. The results show that elements size of 2 mm is in agreement with an acceptable convergence.

Figure 5. Moment-deflection curve obtained from literture [20] and, the results obtained by the presented finite element model
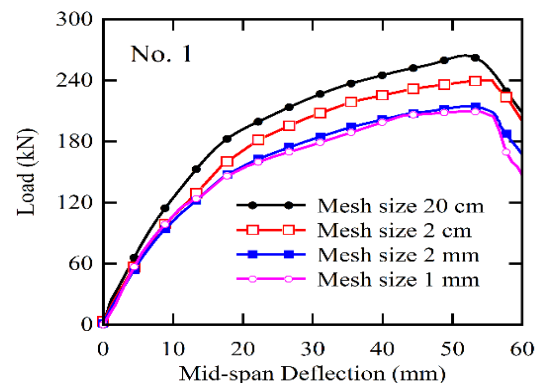

Figure 7. Comparison results between different mesh sizes for sample No.1

Since it was confirmed that our FE model is accurate, it was used to investigate the applicability of SMA tendons to improve the performance of tapered industrial sheds. Figure 8 shows the deformation of steel industrial sheds in samples No. 1, 3, 10, and 12. As listed in Table 3, samples 1 and 3 have been reinforced with SMA tendons with post-tension forces of 10 and 40 kN, respectively. Samples No. 10 and 12 have been reinforced with steel tendons at post-tension forces of 10 and 40 kN, respectively. Figure 8 shows that the maximum displacements in samples No. 1 and 10 were 15.5 cm and 20.4 cm, respectively. Whereas the maximum displacement for samples No. 3 and 12 were 6.8 cm and 10.3 cm, respectively. The SMA tendons caused an increase in the equivalent stiffness of the structure, which decreased the maximum displacement of the structure. The important result of this work is that the displacement of the steel industrial sheds decreased as the post-tension force increased. For example, the SMA tendons with post-tension forces of 10 and 40 kN resulted in 73% and 83% improvement in performance after post-tensioning, respectively.

The load-deflection curves are shown in Figure 9 for three types of steel industrial sheds at a post-tension force of 10 kN; without post-tensioning (sample 0), post-tensioning with SMA tendon (sample 1), post-tensioning with steel tendon (sample 10). As shown in this figure, the load decreased sharply after the peak load for all samples. The results showed that the post-tension approach significantly improved the performance of the steel industrial shed. The load capacity for samples 0, 1 and 10 were 85, 220, and 135 kN, respectively. The SMAs and steel tendons resulted in a 36% and 60% increase in the load capacity of the frame. It was found that the SMA tendons resulted in a two-fold increase in the load-carrying capacity in comparison with steel tendons under equivalent conditions. The performance of the SMA-tendon reinforced frame was similar to that of the steel-tendon reinforced frame in deflections of less than 5 mm.

TABLE 3. Design matrices for modeling geometric parameters

No.	Material	D (mm)	F (kN)
0			0
1			10
2		5	20
3			40
4	SMA		10
5		15	20
6			40
7			10
8		20	20
9			40
10			10
11		5	20
12			40
13			10
14	Steel	15	20
15			40
16			10
17		20	20
18			40

However, an increase in the deflection resulted in a significant increase in the equivalent stiffness of the post-tensioned structure with SMA tendons due to their super-elastic characteristics and the phase change of such alloys under large deflections.

The influences of the effective parameters on the performance of steel industrial sheds based on the experimental design matrices (See Table 3) are presented in Figures 10 and 11. The results revealed that the geometric characteristics and the applied post-tension force also affected the performance of the sheds. In general, an increase in the element diameter and post-tension force significantly increased the load-carrying capacity. At a constant tendon diameter, high post-tension forces did not affect the load-carrying capacity of the frames. For example, for an SMA tendon with a diameter of 5 mm, the load-carrying capacity of the structure increased up to 53% with an increase in the post-tension force from 10 to 40 kN in comparison with samples without post-tensioning. Similar results were observed for post-tensioning with steel tendons. Figure 9 showed that an increase in the post-tension force from 10 to 40 kN for a steel tendon with a diameter of 5 mm increased the load-carrying capacity of the structure by more than 45% in comparison with the sample without post-tensioning. The results also indicated that the post-

Figure 8. Deformation (m) of steel industrial sheds, (a) No.1, (b) No. 3, (c) No. 10, (d) No. 12.
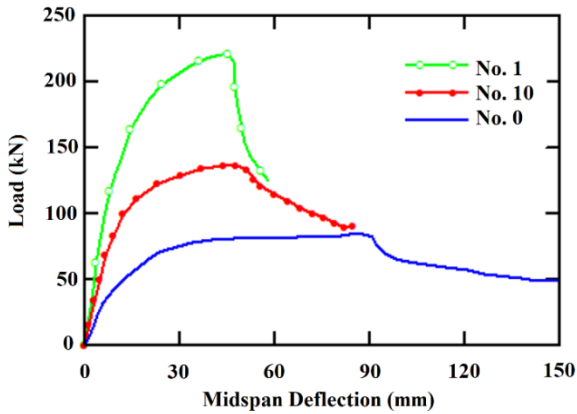
Figure 9. Load-deflection curve for three samples of No. 0, No.1, and No.10
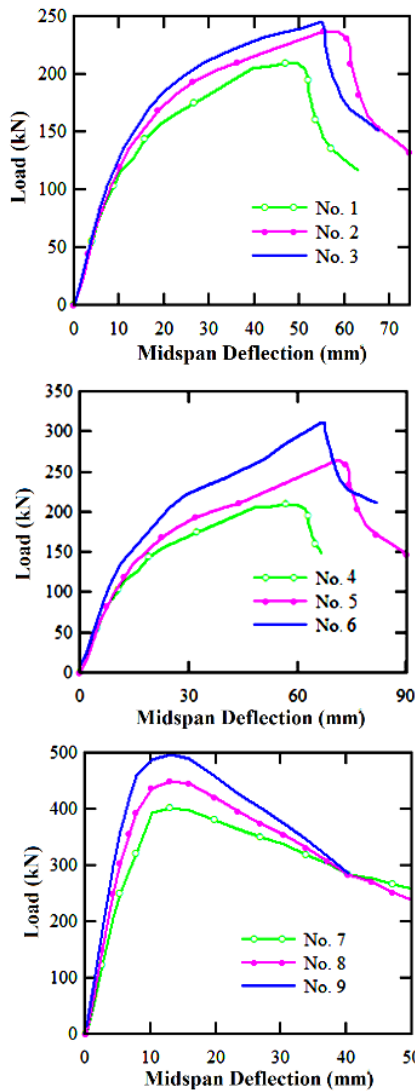
Figure 10. Load-deflection curve for the samples of post-tensioned industrial sheds by SMAs tendons
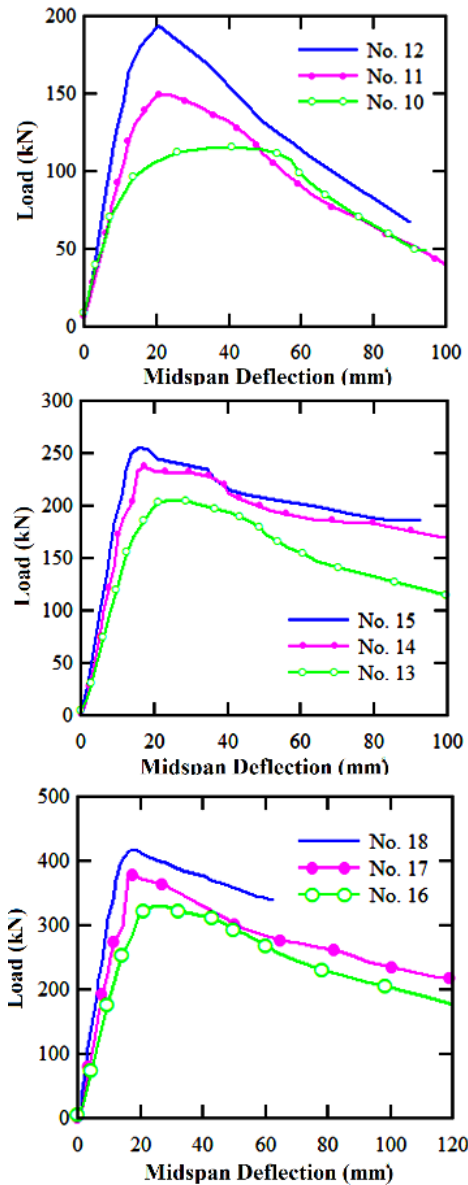
Figure 11. Load-deflection curve for the samples of post-tensioned industrial sheds by steel tendons

tension force is more effective in the SMA tendons rather than the steel tendons.

According to Table 3, samples No. 1 and No. 3 are reinforced with shaped memory tendons with 10kN and 40kN post-tensioning forces, and samples No. 10 and No. 12 are reinforced with steel tendons with 10kN and 40kN post-tensioning forces, respectively. Based on the results, it can be seen that the maximum deflection created in No. 1 and No. 10 samples is 45.5cm and 20.4cm, respectively. Tthese values for samples No. 3 and No.12 are 56.8cm and 20.5 cm, respectively. As can be seen, in the general case, the use of SMA tendons increases the equivalent stiffness of the structure and

thus reduces the maximum deflection and deformation created in the structure. The remarkable result is that the effect of SMA tendons on the reduction of steel frame deflection increases with an increase in post-stress force. For example, the use of SMA tendons for post-tension forces equal to 10kN and 40kN increases the performance of using the post-tensioning method by 73% and 83%, respectively, compared to similar samples of steel tendons.

4. CONCLUSIONS

The current study examined the effect of post-tensioning on an industrial shed using local post-tensioning technology and SMA steel tendons. Response surface methodology and design of experiments methods with D-optimal designs were used for the selection of effective parameters. The experimental results on post-tensioned I-shaped beams with steel rebars were used for validation. The FE model was employed to predict the behavior of I-shaped steel beams with reasonable accuracy at a maximum error of less than 10%. The obtained results of the present work indicated that the external post-tensioning method significantly increased the load-carrying capacity of an industrial shed. The SMA tendons increased the equivalent stiffness and decreased the maximum displacement of the structure. They also caused greater improvement in the performance of the structure rather than the steel tendons. The SMA tendons produced a two-fold increase in the load-carrying capacity in comparison with steel tendons under equivalent conditions. The steel and SMA tendons increased the maximum load capacity of the frame 36% and 60%, respectively. The geometric characteristics and applied post-tension force affected the performance of the steel industrial sheds. An increase in the element diameter or post-tension force significantly increased the load-carrying capacity of the sheds. The use of local post-tensioning can improve the performance of structures, decrease the weight of the structure, and also is more cost-effective.

5. REFERENCES

1. Naghipour M., Nemati M., Doostdar H. "Experimental study and modeling of reinforced concrete beams strengthened by post-tensioned external reinforcing bars", *International Journal of Engineering,Transactions A: Basics* Vol, 23, No. 2 (2010), 127-144.

2. Tassi, G., Rózsa P., "Forces in prestressed concrete bridges constructed by free cantilevering" *Periodica Polytechnica Civil Engineering*, Vol. 36, No. 3, (1992), 355-361.

3. Farkas G., Gyorgyi J., Lovas A., Misteth E., "Load-bearing capacity of IMS floors affected by cable corrosion" *Periodica Polytechnica Civil Engineering* 36, (1992), 271-282.

4. Maleki V. A., Mohammadi N. "Buckling analysis of cracked functionally graded material column with piezoelectric patches" *Smart Materials and structures,* Vol**.** 26, No. 3, (2017), 34-56. doi:10.1088/1361-665X/aa5324

5. Afshan S., Theofanous M., Wang J., Gkantou, M., Gardner L. , "Testing, numerical simulation and design of prestressed high strength steel arched trusses", *Engineering Structures,* Vol**.** 183, (2019) 510-522. doi: 10.1016/j.engstruct.2019.01.007

6. Landge S., Bhagat U., Bhaisare S., Prakash, V. and Khedikar, I.P., "Analysis and Design of Pre-stressed Concrete I-Girder Bridge" *International Research Journal of Engineering and Technology* Vol. 5, No. 5, (2018), 45-67.

7. Sirimontreea S., Keawsawasvong S., Thongchom C., Jongvivatsakul P., Noroozinejad Farsangi E., "Experimental investigations on strengthened reinforced concrete columns under monotonic axial loading". *International Journal of Engineering, Transactions B: Applications,* Vol. 34, No. 5, (2021), 1124-1131. doi: 10.5829/ije.2021.34.05b.06

8. Jahanghiry R., Yahyazadeh R., Sharafkhani N., Maleki V. A. "Stability analysis of FGM microgripper subjected to nonlinear electrostatic and temperature variation loadings" *Science and Engineering of Composite Materials,* Vol. 23, No. 2, (2016), 199-207. https://doi.org/10.1515/secm-2014-0079

9. Ghaderi M., Maleki V. A., Andalibi K., "Retrofitting of unreinforced masonry walls under blast loading by FRP and spray on polyurea" *Cumhuriyet Science Journal,* Vol. 36, No. 4, (2015), 462-477.

10. Mohammadi H., Esfahani M., Riyazi M., "Behavior of coupling beams strengthened with carbon fiber reinforced polymer sheets", *International Journal of Engineering,Transactions A: Basics*, Vol. 20, No. 1, (2007), 49-58.

11. Maghsudi A.A., Askari D.Y. "Ultimate unbonded tendon stress in CFRP strengthened post-tensioned indeterminate I-beams cast with HSCs" *International Journal of Engineering,Transactions A: Basics,* Vol. 28, No. 3, (2015) :350-359. doi: 10.5829/idosi.ije.2015.28.03c.03

12. Heydari T, Gerami M., "Multi-stage performance upgrade of steel moment frames by post-tension connections" *International Journal of Engineering,Transactions B: Applications,* Vol. 34, No. 5, (2021), 1132-1144. https://dx.doi.org/10.5829/ije.2021.34.05b.07

13. Nunziata V. "Prestressed steel structures design : a new frontier for structural engineering" Costruzioni Acciaio Struttura E Architetto 128, (1999), 965-975.

14. Abedi Sarvestani H "Cyclic behavior of hexagonal castellated beams in steel moment-resisting frames with post-tensioned connections" *Structures* 11, (2017), 121-134. doi: 10.1016/j.istruc.2017.05.001

15. Ghannam M, Mahmoud NS, Badr A, Salem FA "Effect of post tensioning on strengthening different types of steel frames" *Journal of King Saud University-Engineering Sciences* Vol. 29, No. 4, (2017), 329-338. doi: 10.1016/j.jksues.2016.07.001

16. Zhao Z., Jian X., Liang B., Liu H., "Progressive collapse assessment of friction damped post-tensioned steel frames based on a simplified model" *Structures* 23, (2020), 447-458. doi: 10.1016/j.istruc.2019.09.005

17. Sanches R., Mercan O., Roberts B. "Experimental investigations of vertical post-tensioned connection for modular steel structures" *Engineering Structures* 175, (2018), 776-789. doi: 10.1016/j.engstruct.2018.08.049

18. Nazir C.P. "Prestressed steel arch bridge" *Journal of the Institution of Engineers. India. Civil Engineering Division,* Vol. 84, (2003), 72-76.

19. Park S., Kim T., Kim K., Hong S.N. "Flexural behavior of steel

I-beam prestressed with externally unbonded tendons" *Journal of Constructional Steel Research,* Vol*.* 66, No. 1, (2010), 125-132. doi: 10.1016/j.jcsr.2009.07.013

20. Taoum A., Jiao H., Holloway D. "Upgrading steel I-beams using local post-tensioning" *Journal of Constructional Steel Research,* 113, (2015), 127-134. doi: 10.1016/j.jcsr.2015.06.012

21. Esmaeili J., Andalibi K., Gencel O., Maleki F. K., Maleki V. A. "Pull-out and bond-slip performance of steel fibers with various ends shapes embedded in polymer-modified concrete" *Construction and Building Materials,* Vol. 271, (2021), 121-131. https://doi.org/10.1016/j.conbuildmat.2020.121531

22. Mir Mohammad Sadeghi S., Hoseini S., Fathi A., Mohammadi Daniali H. "Experimental hysteresis identification and micro-position control of a shape-memory-alloy rod actuator" *International Journal of Engineering, Transactions A: Basics,* Vol. 32, No. 1, (2019), 71-77. doi: 10.5829/ije.2019.32.01a.09

23. Balak Z., Abbasi S. M., "Effect of the Primary Microstructures during training producers on TWSME in NiTi alloys (Technical note)", *International Journal of Engineering, Transactions B: Applications,* Vol. 25, No. 4, (2012), 337-342. doi: 10.5829/idosi.ije.2012.25.04b.10

24. A. Roohbakhsh Davaran, S.A. Sadrnejad, "A 3d micro-plane model for shape memory alloys", *International Journal of Engineering, Transactions A: Basics,* Vol. 21, No. 1, (2008), 17-30.

25. Chang W.S., Araki Y. "Use of shape-memory alloys in construction: A critical review" *Proceedings of the Institution of Civil Engineers-Civil Engineering*, Vol. 169, No. 2, (2016), 87-95. doi: 10.1680/jcien.15.00010

26. Shrestha K.C., Araki Y., Nagae T., Koetaka, Y., Suzuki, Y., Omori, T., Sutou Y., Kainuma R., Ishida K. "Feasibility of Cu-Al-Mn superelastic alloy bars as reinforcement elements in concrete beams". *Smart Materials and Structutres* Vol. 22, (2013), 12-24. doi: 10.1088/0964-1726/22/2/025025

27. Daghash S.M., Ozbulut O.E. "Characterization of superelastic shape memory alloy fiber-reinforced polymer composites under tensile cyclic loading". *Materials & Design,* Vol. 111, (2016), 504-512. doi: 10.1016/j.matdes.2016.09.034

28. Strieder E., Aigner C., Petautschnig G., Horn, S., Marcon, M., Schwenn, M., Zaman O., Castillo P., Wan-Wendner, Bergmeister, K. "Strengthening of reinforced concrete beams with externally mounted sequentially activated iron- based shape memory alloys". *Materials (Basel)* Vol. 12, (2019), 345-367. doi: 10.3390/ma12030345

29. AISC Committee. Specification for structural steel buildings (ANSI/AISC 360-10). *American Institute of Steel Construction*, *Chicago-Illinois* (2010).

30. Chang L.C., Read T.A. "Plastic Deformation and Diffusionless Phase Changes in Metals — the Gold-Cadmium Beta Phase". *JOM,* Vol. 3, (1951), 47-52. doi: 10.1007/bf03398954

31. Nili Ahmadabadi M., Shahhoseini T., Habibi-Parsa M., Haj-Fathalian, M., Hoseinzadeh-Nik, T., Ghadirian, H. "Static and cyclic load-deflection characteristics of NiTi orthodontic archwires using modified bending tests". *Journal of Materials Engineering & Performance,* Vol. 18, (2009), 793-796. doi: 10.1007/s11665-009-9488-5

32. Fukuta T., IIba M., Kitagawa Y., Sakai Y. "Experimental study on stress-strain property of shape memory alloy and its application to self-restoration of structural members". In Proceedings of 13th World Conference of Earthquake Engineering: 1-9. (2004)

33. Fang C., Yam M.C.H., Lam A.C.C., Zhang Y. "Feasibility study of shape memory alloy ring spring systems for self-centring seismic resisting devices". *Smart Materials and Structutres* Vol. 24, (2015), 75-94. doi: 10.1088/0964-1726/24/7/075024

34. Alkan S., Sehitoglu H. "Prediction of transformation stresses in NiTi shape memory alloy" *Acta Materialia,* Vol. 175, (2019), 182-195. doi: 10.1016/j.actamat.2019.06.009

35. Xu X., Zhang Y., Luo Y. "Self-centering eccentrically braced frames using shape memory alloy bolts and post-tensioned tendons" *Journal of Constructional Steel Research,* Vol. 125, (2016), 190-204. doi: 10.1016/j.jcsr.2016.06.017

36. Freddi A., Salmon M. "Design of experiment". In *Design Principles and Methodologies* Springer (2019), 127-158. doi: 10.1007/978-3-319-95342-7_6

37. Condra, L. W., Reliability Improvement with Design of Experiments: Revised and Expanded. CRC Press, 2018.https://doi.org/10.1201/9781482270846

Persian Abstract

چکیده

آلیاژهای حافظه‌دار شکلی، مصالحی با عملکرد تابع شرایط اعمال بار و تغییرشکل بوده و می‌توانند تغییرشکل‌های بزرگ را تحمل نمایند. در اعضای متشکل از این مصالح، عضو با از بین رفتن تنش ایجاد کننده تغییرشکل، به حالت اولیه خود بر می‌گردد. از آلیاژهای حافظه‌دار شکلی برای تقویت و بهبود رفتار و پایداری سازه‌های فولادی استفاده می‌شود. در مطالعه حاضر به بررسی اثر پس کشیدگی موضعی به منظور افزایش ظرفیت باربری قابهای شیب‌دار فولادی با استفاده از میله‌های فولادی و میله‌های ساخته شده از آلیاژهای حافظه‌دار شکلی پرداخته شده است. به این منظور، از نرم افزار آباکوس برای پیش بینی مقاومت خمشی و ظرفیت باربری قابهای شیب‌دار فولادی تقویت شده با این دو نوع مصالح، استفاده شده است. در مطالعه حاضر، تاثیر قطر و مقدار نیروی پس‌تنیدگی اعمال شده به میله‌های فولادی و تاندون‌های متشکل از آلیاژهای حافظه‌دار شکلی مورد بررسی قرار گرفته است. نتایج حاصل نشان می‌دهد که پس‌تنیدگی خارجی با استفاده از تاندون‌های آلیاژهای حافظه‌دار شکلی، روشی موثر برای افزایش ظرفیت باربری قابهای شیب‌دار فولادی است. میله‌های فولادی و تاندون‌های آلیاژهای حافظه‌دار به ترتیب باعث افزایش 36 و 60 درصدی در ظرفیت باربری قابها و بهبود عملکرد قابهای شیب‌دار فولادی با پس‌تنیدگی موضعی می‌شوند. همچنین استفاده از پس‌تنیدگی موضعی سبب کاهش وزن قابها می‌گردد.

Effect of Steps Height and Glass Cover Angle on Heat Transfer Performance for Solar Distillation: Numerical Study

M. R. Assari*[a], R. Mirzavand[a], H. Basirat Tabrizi[b], A. Jafar Gholi Beik[a]

a Department of Mechanical Engineering, Jundi-Shapur University of Technology, Dezful, Iran
b Department of Mechanical Engineering, Amirkabir University of Technology, Tehran, Iran

ABSTRACT

Productivity and heat transfer in the stepped solar still by varying the glass cover angle and steps height were numerically investigated. In order to obtain the productivity and heat transfer coefficient, mass, momentum, energy, and diffusion equations were applied for simulating the distillation process. Further, the numerical simulation validated by existed experimental data. Simulation results indicated the highest freshwater production in comparison with experimental set up condition, which is at the step height 4cm and glass cover angle 60.23°, belongs to the step height of 5.5cm with 1400 mL/m²h, namely 91% increase and much less for the step height of 1cm with 350 mL/m²h, namely 52% decrease. Most increase in Nusselt number obtained for the angle of 55° with Nu=12.03 with 29% increase and much less for the angle of 65° with Nu=8.16 with 12% decrease. In addition, most and less variation of the heat transfer coefficient obtained for the step height of 5.5cm with h_c=4.04 W/m² K, with 39% increase and for the step height of 1cm with h_c=2.18 W/m² K, with 24% decrease, respectively.

doi: 10.5829/ije.2022.35.01a.23

NOMENCLATURE

C	concentration [k mol / m³]	**Greek Symbols**	
C_p	specific heat [kJ/kg K]	β	thermal expansion factor[1/K]
D	molecular diffusion coefficient [m²/s]	$β^*$	species expansion factor [m³/k mol]
g	gravity [m/s²]	ΔT	difference between water and glass[K]
H	mean distance between water and glass [m]	φ	relative humidity
h	heat transfer coefficient [W/m² K]	ω	humidity ratio
k	thermal conductivity [W/m K]	μ	dynamic viscosity [kg/m s]
L	length [m]	ρ	density [kg/m³]
ṁ	productivity [mL/m² h]	**Subscripts**	
Nu	Nusselt number	a	air
P	absolute pressure [Pa]	c	convection
Ra	Rayleigh number	g	glass
T	temperature [K]	i	diffusive species index
u	x axis velocity [m/s]	l	left
v	y axis velocity [m/s]	m	mean temperature
x	direction	n	normal direction
x′	parallel direction with glass	r	right
Y	mass fraction of water in wet air	sat	saturation
y	direction	w	water

1. INTRODUCTION

There are two potential in the solar irradiation, i.e. its light and heat. The sunlight can be converted into electrical power by means of photovoltaic (PV) modules [1-5]. Moreover, its thermal energy can be also used to produce electricity by solar thermal power plants [6, 7]. Besides, the thermal energy of sun also can be utilized

*Corresponding Author Institutional Email: *assari@ jsu.ac.ir* (M.R. Assari)

directly for thermal objectives, e.g. in solar chimney [8, 9], air heating [10, 11], solar dryers [12, 13], solar water heaters [14-16]. Another interesting applications of the solar heat is solar desalination, which is studied in this study. Providing potable water which is a serious challenge these days; although oceans and seas cover about 70 percent of earth, however, most are salty and not suitable for consumption, not only for drinking even for farming. Scientist and engineers proposed various method for purification of water, most common method is reverse osmosis. Some of the methods have advantages and disadvantages which were discussed by researchers and could be found in the literatures [17-19]. Since most water treatment methods use considerable amount of energy and subsequently electricity, therefore using renewable energy such as solar energy, seems more reasonable and promising. Many experimental and numerical researches were reported in this field. Most recent work to be continued these days and some of the related ones will be reviewed here. de Paula and Ismail [20] numerically investigated on heat and mass transfer on an inclined solar still. Their results indicated that for high Rayleigh numbers an increase in cavity inclination causes the Nusselt and Sherwood numbers and the condensation rate to increase. Kabeel et al. [21] reported a comprehensive review article about tubular solar still and the advanced design techniques in tubular solar still which aimed to improve the yield of stills. Gazar et al. [22] showed that the fractional model has more accuracy compare with the classical model and hybrid nanofluid rises daily productivity by 27.2% in summer and 21.7%, in winter compare to the still without the nanofluid. Hedayati et al. [23] studied on the exergy performance evaluation of basin type double slope solar equipped with PV/T collector. The PV/T collector improves the freshwater production during the sunshining hours of the day by preheating the saline water and utilization of phase change material (PCM) makes it possible to produce freshwater at the night. Khalilmoghadam et al. [24] investigated on a system of energy recovery using PCM and pulsating heat pipe. Their result showed an increase in productivity also decreases cost per liter of water. Sivaram et al. [25] studied on the effect of external condenser on the stepped solar still to improve productivity. Their results have shown an increase in the overall efficiency of still by 10.6% in summer and 12.2% in winter. Higher performance was observed in winter than summer when the passive external condenser was added with the stepped evaporator and found inverse for the stepped solar still without condenser. Bouzaid et al. [26] numerically analyzed the thermal performances for a cascade solar desalination still with baffles on basins. The performance of the still investigated and compared with the ordinary model; the results indicated that the design allows an increase in the production. Rahbar and Esfahani [27] estimated productivity of single slope solar still numerically and their results compared with experimental data. Rahman et al. [28] studied

numerically triangular solar collector based on double diffusion natural convection model and achieved local and average heat and mass transfer coefficient using dimensionless numbers. El-samadony et al. [29] investigated on influence of glass cover inclination angle on radiation heat transfer rate within the stepped solar still and presented a theoretical analysis of the radiation heat transfer rate inside the stepped solar still. In addition, radiation shape factor between the hot saline water and glass cover for the stepped solar still computed. It was found that the influence of the radiation shape factor on the thermal performance predictions is significant. Most experimental works indicated minimum depth of water in the basin lead to more efficiency of solar still. Stepped solar stills by providing maximum cross section and minimum depth and less chamber volume in comparison with one basin solar still with one or double slope are more desirable for more productivity. Gawande et al. [30] studied on the shape of absorber surface and performance of the stepped type solar still by utilizing convex, concave absorber instead of flat absorber and indicated increase in the productivity of 57% and 29%, respectively. The effect of tilt angle on the productivity of a solar still was experimentally studied by Cherraye et al. [31]. The experiments were performed in arid climate of Ouargala city, Algeria. Different angles of 10° to 45° were tested. As results, it was reported that the inclination angles of 20° for summer and spring, and 30° for autumn and winter, were the optimum values. Ashtiani and Hormozi [32] studied the stepped solar still based on entropy generation, their results indicated that the number and height of the stepped were effective parameters for irreversibility and entropy generation. The effect of different environmental parameters and operational parameters on the system productivity were discussed, e.g., the decrease in humidity increases the productivity, the wind velocity significantly reduces the $(T_i–T_o)$ difference temperature, which adversely affects the productivity of the system, and the cloud coverage affects the solar radiation intensity.

Present study aims to demonstrate numerical simulation with some modifications on the reported theoretical study. The reported theoretical study was mostly based on the experimental measurement. Hence, obtaining experimental data requires lots of time and expensive setup in terms of cost and operation. Obviously changing in the experimental setup is another problem for optimizing of solar still performance, contrary the numerical method has not any of this hardship. However, in the presented method only temperature is the main input value that one needs and the rest such as mass fraction of water vapor in air can be obtained from psychrometric chart or using some reported correlation. To the best of the authors knowledge numerical study on the stepped solar still for estimating the productivity, heat transfer coefficient and Nusselt number have not yet fully been investigated. In this research, after comparing the proposed numerical

simulation with the reported experimental and theoretical study, the geometry optimization by varying the glass cover angle and steps height were reported. Therefore, this study soughts various and possible scheme to increase the productivity of freshwater in the stepped solar still by changing the geomety and seeking the thermal behavior and consequently productivity to achieve maximum and optimal production.

2. MODELING

Consider solar still is in equilibrium condition with an ambient and since there is, no external force such as pump and blower use in the passive solar, only natural convection occurs in the solar still cavity. Two-dimensional steady state governing equations on the moist air inside cavity, mass, momentum, and energy conservations are [33, 34]:

$$\frac{\partial u}{\partial x} + \frac{\partial v}{\partial y} = 0 \tag{1}$$

$$u\frac{\partial u}{\partial x} + v\frac{\partial u}{\partial y} = -\frac{1}{\rho}\frac{\partial p}{\partial x} + \nu\left(\frac{\partial^2 u}{\partial x^2} + \frac{\partial^2 v}{\partial y^2}\right) \tag{2}$$

$$u\frac{\partial v}{\partial x} + v\frac{\partial v}{\partial y} = -\frac{1}{\rho}\frac{\partial p}{\partial y} + \nu\left(\frac{\partial^2 v}{\partial x^2} + \frac{\partial^2 v}{\partial y^2}\right)$$
$$+ \beta_T g(T - T_0) + \beta_C g(C - C_0) \tag{3}$$

which β_T and β_C are: $\beta_T = -\frac{1}{\rho}\left(\frac{\partial \rho}{\partial T}\right)_p$, $\beta_C = -\frac{1}{\rho}\left(\frac{\partial \rho}{\partial C}\right)_p$

$$u\frac{\partial T}{\partial x} + v\frac{\partial T}{\partial y} = \alpha\left(\frac{\partial^2 T}{\partial x^2} + \frac{\partial^2 T}{\partial y^2}\right) \tag{4}$$

$$u\frac{\partial C_i}{\partial x} + v\frac{\partial C_i}{\partial y} = D_{w-a}\left(\frac{\partial^2 C_i}{\partial x^2} + \frac{\partial^2 C_i}{\partial y^2}\right) \tag{5}$$

Equation (5) can be rewritten as Equation (6):

$$\frac{\partial}{\partial x}(\rho u Y_i) + \frac{\partial}{\partial y}(\rho v Y_i) = -\left(\frac{\partial}{\partial x}(J_i)_x + \frac{\partial}{\partial y}(J_i)_y\right) \tag{6}$$

Y_i is mass fraction of water vapor in wet air $(Y_i = \frac{\rho_i}{\rho})$ and the relation between density and concentration is $(C_i = \frac{\rho_i}{M_i})$ and $\vec{J}_i$ defines by Equation (7):

$$\vec{J}_i = -\rho D_{w-a}\left(\hat{i}\frac{\partial}{\partial x}Y_i + \hat{j}\frac{\partial}{\partial y}Y_i\right) \tag{7}$$

Equations can be solved simultaneously for velocity, temperature, and concentration of water vapor. The

boundary condition for velocity, temperature, and concentration are:
For cover glass:

$$\mathbf{u} = \mathbf{v} = 0, \mathbf{T} = \mathbf{T_g}, \mathbf{Y_i} = \mathbf{Y_g}\Big|_{T=T_g, \varphi=100\%} \tag{8}$$

For steps basin:

$$u = v = 0, T = T_w, Y_i = Y_w\Big|_{T=T_w, \varphi=100\%} \tag{9}$$

For other walls:

$$u = v = \frac{\partial T}{\partial x} = \frac{\partial Y_i}{\partial x} = 0 \tag{10}$$

Note that for the concentration value in boundaries, Psychrometric chart was used in $\varphi=100\%$ and then the mass fraction in specific temperature defined as follows:

$$Y_i = \frac{\omega}{1+\omega} \tag{11}$$

which ω is the specific humidity and one can use:

$$\omega = 0.622\frac{\varphi P_{sat}}{P - \varphi P_{sat}} \tag{12}$$

Numerically solving above equations and using temperature and concentration profile, one can obtain the productivity of solar still and Nusselt number as follows [27,35]:

$$\dot{m} = \frac{-3600 \times \rho \times D_{w-a}}{L_g}\int_0^{L_g}\frac{\partial Y_i}{\partial y}\Big|_g dx' \tag{13}$$

$$\overline{Nu} = \frac{-H}{L_g(T_w - T_g)}\int_0^{L_g}\frac{\partial T}{\partial n}\Big|_g dx' \tag{14}$$

The convective heat transfer coefficient could be calculated using definition as [36]:

$$h_c = \frac{Nu \times k}{H} \tag{15}$$

3. DESIGN GEOMETRY AND SIMULATION PROCEDURE

Two-dimensional geometry of solar still which was used by Kabeel et al. [37] has been used for comparing the trend which is shown in Figure 1.

Step 1 has 10cm length and steps 2, 3, 4, each one has 12.5cm. Also, the offset height of each step increases 4.5cm. Front side length is 4.4cm and back side is 15cm. All walls are considered in the adiabatic condition except the top cover (glass) and steps (water surface). In this simulation, the air is assumed completely humid $\varphi=100\%$ and the properties are shown in Table 1. Moreover, the maximum solar radiation of 1050 W/m^2 was assumed
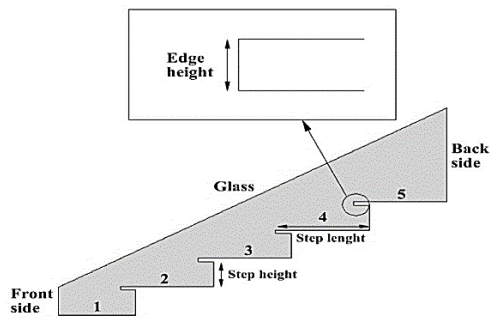
Figure 1. Sketch of stepped solar still geometry

and can be found in literature [37]. In this study, back side, H_1=15cm, front side, H_r=4.4cm, step1 length 10 cm, step 2, 3, 4, 5 length 12.5cm, step height 4cm, edge height 0.5 cm, and depth 200 cm were taken and temperatures variation were shown in Table 2.

4. SOLUTION PROCEDURE AND MESH INDEPENDENCY

Since this is an internal flow case, Rayleigh number can be determined as:

$$\text{Ra} = \frac{\rho^2 g \beta c_p H^3 \Delta T}{k\mu}, \quad H = \frac{(H_l + H_r)}{2} \qquad (16)$$

where H_l and H_r are the length of front and back side, respectively. By substitute the physical parameters in the above equation the Rayleigh number obtained to be less than 10^8; therefore, the flow regime is laminar in this study. SIMPLE algorithm was used for pressure-velocity coupling. Besides, PRESTO scheme was suitable and used for pressure interpolations due to the natural

TABLE 1. Properties of humid air [35]

Quantity	Expression, T (ºC)
Specific heat, C_p	$999.2+0.1434 \times T_m+1.101 \times 10^{-4} \times T_m^2-6.758 \times 10^{-8} \times T_m^3$
Density, ρ	$353.44/(T_m+273.15)$
Thermal conductivity, k	$0.0244+0.7673 \times 10^{-4} \times T_m$
Viscosity, υ	$1.718 \times 10^{-5}+4.62 \times 10^{-8} \times T_m$
Expansion factor, β	$1/(T_m+273)$
Species expansion coefficient, β_c	$[M_a/M_v-1]/\rho=0.513$
Diffusion coefficient, D_{a-w}	$0.26 \times 10^{-4} \times (101.325/P) \times (T/298)^{3/2}$

TABLE 2. Thermal condition and geometry parameters used [37]

Case	1	2	3	4
Time	12 pm	13 pm	14 pm	15 pm
T_w(ºC)	76	74	74.5	67
T_g(ºC)	46	44	43	41

convection vortices in the solar still. The momentum, energy, and species equations were discretize using second-order upwind scheme [38]. The discretized and linearized equations were solved by iterative method and the convergency criterion was 10^{-7} for all equations except for continuity equation, which was 10^{-4}. After convergency hourly productivity per unit area, Nusselt number, and convective heat transfer coefficient were determined. Figure 2 shows the implemented meshing which was tetrahedral and structured. Table 3 shows effect of mesh elements and nodes on the Nu, productivity, and heat transfer coefficient and in Figures 3 and 4 the simulation results by changing in the number of mesh are shown.

Further the simulation results compared with the reported experimental data and theoretical analysis [36] are shown in Figure 5 and Table 4. As shown in figure and table, the maximum productivity errors between this simulation and for the reported experiment is 30% and for the theoretical method is 13%. Therefore, this simulation indicates similar trend, however the reported study uses mostly experimental data.

4. PARAMETRIC STUDIES

Simulations were obtained as stated in Table 2 for 12:00 p.m. Velocity profile inside the solar still chamber is
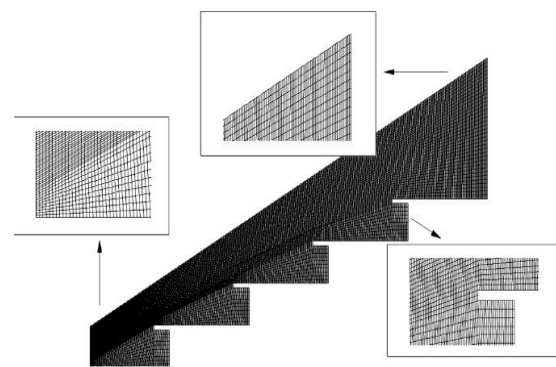
Figure 2. Meshing

TABLE 3. Number of mesh elements

| Number of mesh elements	88783	131752	193388	253538	340983	365955
Number of mesh nodes	89910	133132	195036	255415	343160	368205
Nusselt number	10.5	10.1	9.9	9.74	9.83	9.81
Productivity [mL/m²hour]	805	795	790	760	735	732
Heat transfer coefficient [W/ m² K]	3	2.94	2.87	2.85	2.81	2.8
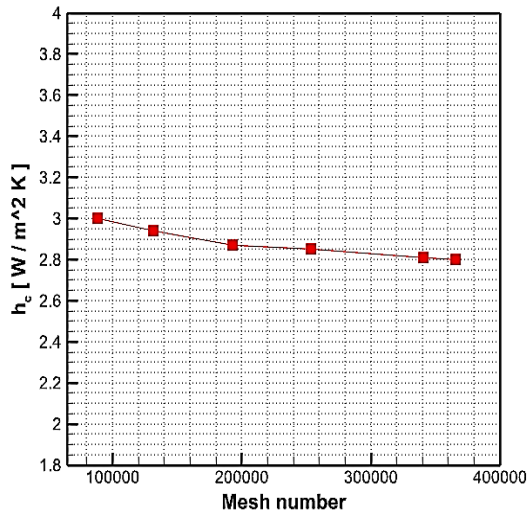
Figure 3. Heat transfer coefficient between water surface and glass vs mesh number
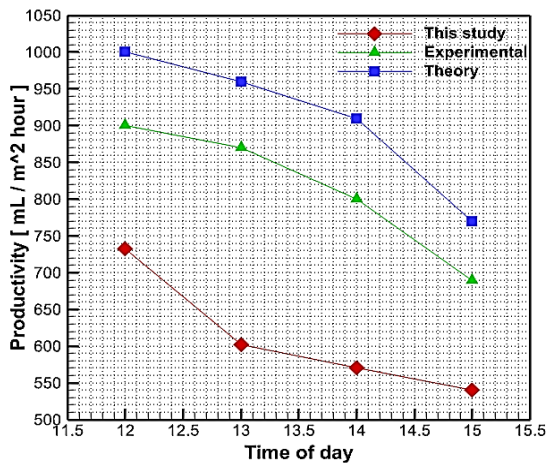

Figure 4. Nusselt and productivity vs mesh number
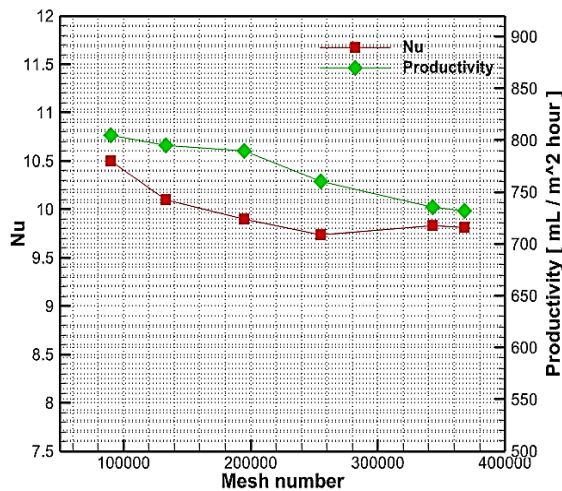

Figure 5. Productivity this simulation with experimental and theoretical reported model [37]

TABLE 4. Comparison of productivity for this simulation with the reported experiment and modeling [37]

Time	12 pm	13 pm	14 pm	15 pm
Productivity of experiment [37] (mL/h.m²)	900	870	800	690
Productivity of modeling [37] (mL/h.m²)	1000	960	910	770
Error with exp. (%)	11	10	14	12
Productivity of this simulation (mL/h.m²)	732	602	570	540
Error with exp. (%)	19	31	29	22

shown in Figure 6. Since the temperature of steps is more than glass temperature as expected, a natural heat transfer convection occurs inside solar still.

Figure 7 shows the temperature profile and circulation of the fluid inside the solar still. All big vortexes in the figure are counter clockwise and physically satisfy the thermal condition in the solar still because the glass cover has lower temperature than mean temperature of the humid air.

Figure 8 depicts the water vapor fraction contour. As one knows from thermodynamic point of view that the air with higher temperature has capability for mixing with much more amount of water vapor and for this reason the mass fraction of water near the steps are more than glass surface.
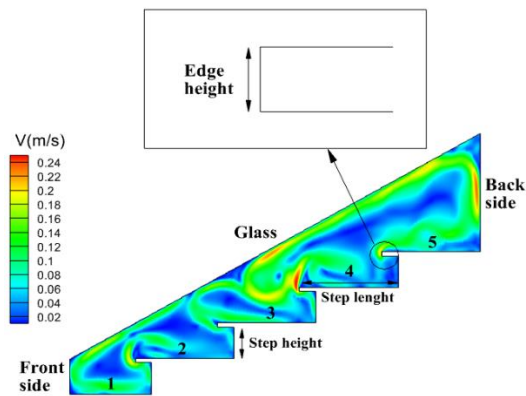

Figure 6. Velocity profiles inside the stepped solar still
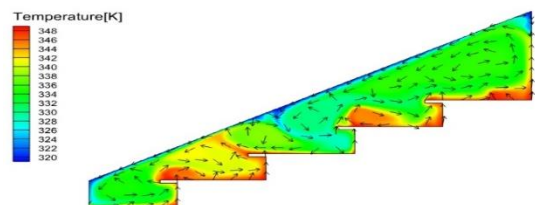

**Figure 7.** Temperature profile inside the solar step
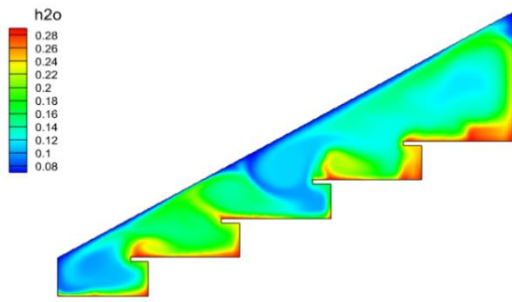
Figure 8. Water vapor mass fraction profile inside the solar still

5. EFFECT OF VARIATION OF GLASS COVER ANGLE

In Figure 4 the experimental model glass cover angle was reported 60.23°; therefore, simulations were extended and preformed for different angles, i.e. 55°, 57°, 62°, and 65°. It can be seen from Figure 9 that velocity profiles vary significantly by changing the angles. since the natural convection is the most important phenomenon in the passive solar stills, variation in the productivity, Nusselt number, and heat transfer can be expected to be significant. Figure 10 shows the productivity and Nusselt number in terms of glass angle. Increase in the productivity and decrease in the Nusselt number were observed and their quantitative values are given in Table 5.
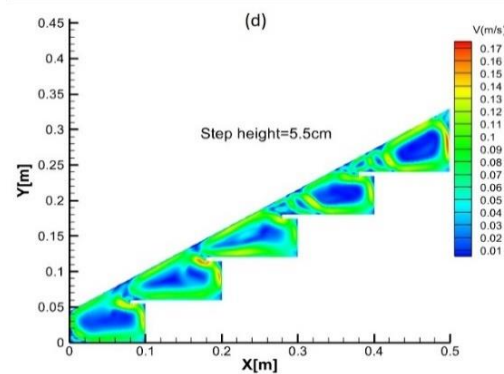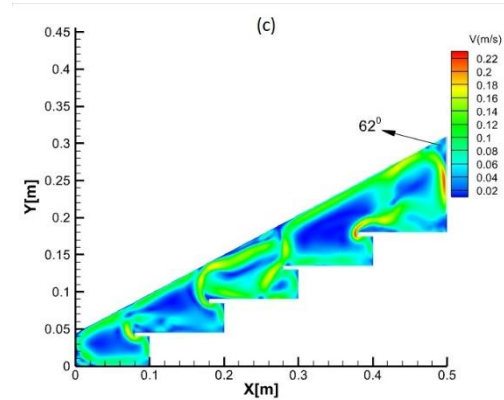
Figure 9. Velocity profile in solar still for different angles
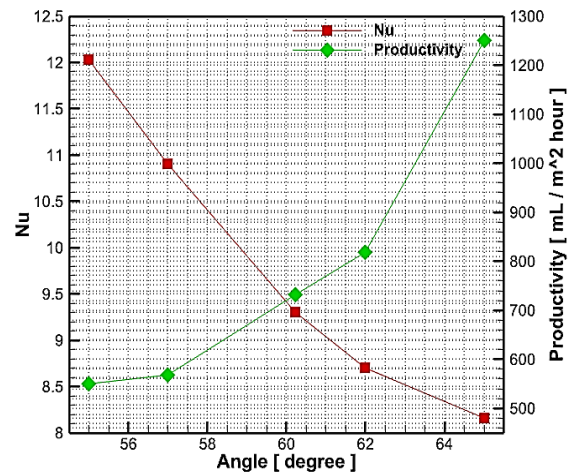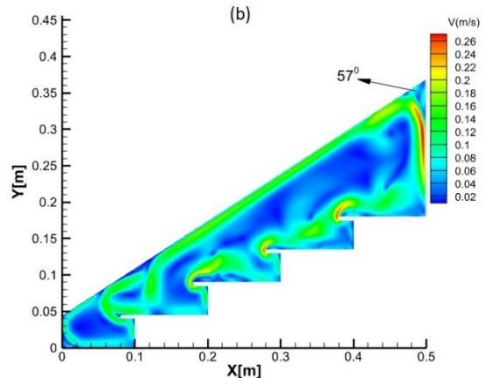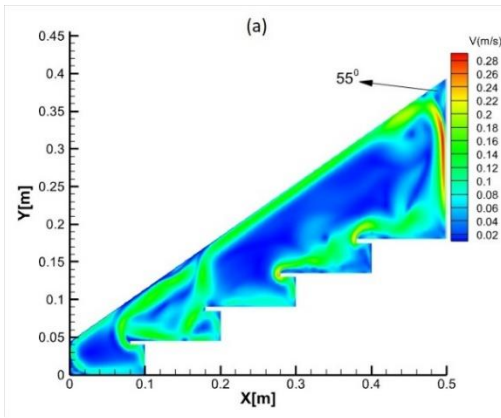
Figure 10. Nu & productivity vs angle of head

**TABLE 5.** Nusselt number and productivity vs variation of angle of the head

Angle of the head in degree	Nu	Productivity (mL/m² h)
55	12.03	550
57	10.9	568
60.23 (Exp. model [37])	9.3	732
62	8.7	818
65	8.16	1250

Figure 11 shows the heat transfer coefficient and mean distance between steps and glass versus angle of the head. As shown in the Nusselt number in the figure with decreasing trend, heat transfer coefficient increases by increasing angle of the head.

Similarly, Table 6 indicates values of the heat transfer coefficient and mean distance between steps and glass beside their variations versus angle of the head changes. As can be seen by decreasing the angle value, the mean distance between steps and glass (H) increases and heat transfer coefficient decreases and vice versa.

Another fluid flow property which variation of that offer meaningful relation with productivity and heat transfer, is vorticity of fluid flow. Figure 12 shows vorticity versus variation of angle of the head or the glass cover angle. Productivity, convective heat transfer coefficient and vorticity all have incremental trend by increasing angle, also one can notice from figure, which the bigger angle of the glass cover causes smaller chamber of solar still and then more vortex to be able to form. In general, by increasing the glass cover angle of solar still, the chamber became smaller and more vortexes appeared and these vortexes lead to enhance the heat transfer and productivity.
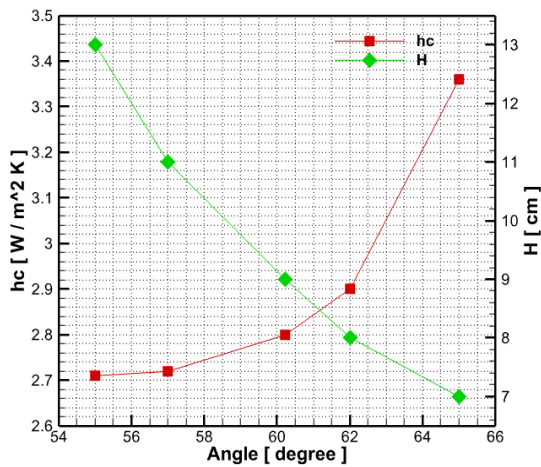
Figure 11. Heat transfer coefficient and mean distance between steps and glass (H)

**TABLE 6.** Heat transfer coefficient and mean distance between steps and glass (H) versus angle of the head

Angle of the head in degree	Heat transfer coefficient [W/m² k]	H(cm)
55	2.71	13
57	2.72	11
60.23 (Exp. Model [37])	2.8	9
62	2.9	8
65	3.36	7
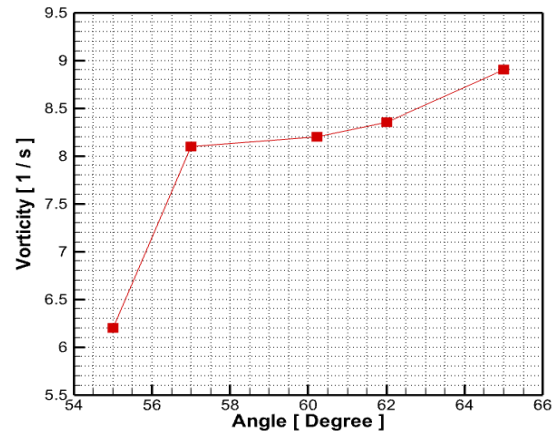
Figure 12. Vorticity vs angle of the head of solar still

6. EFFECT OF HEIGHT OF STEPS

Figure 13 shows for steps height of 1 to 5.5cm and compares to experimental model [37], which is 4cm. With increasing the step height, the cavity of solar still becomes smaller and as expected smaller chamber gives better heat transfer and also more productivity. As seen in figure, the velocity profiles are very different with respect to either experimental model (Figure 6) and each other.
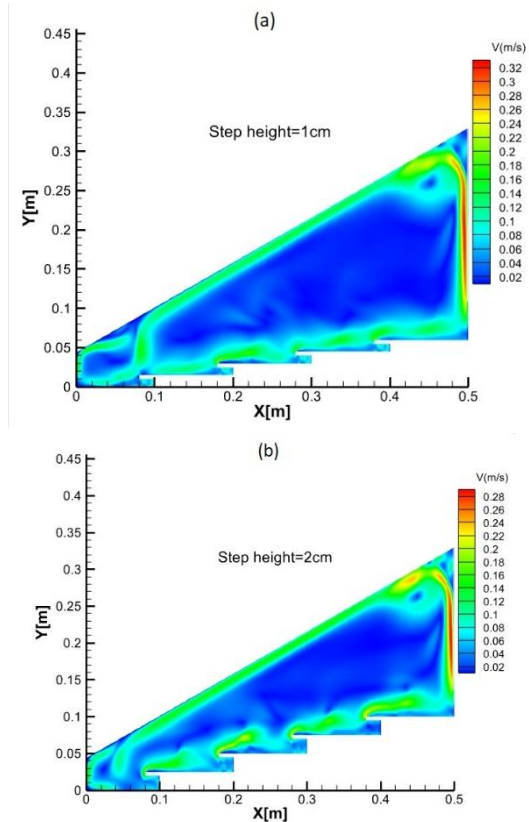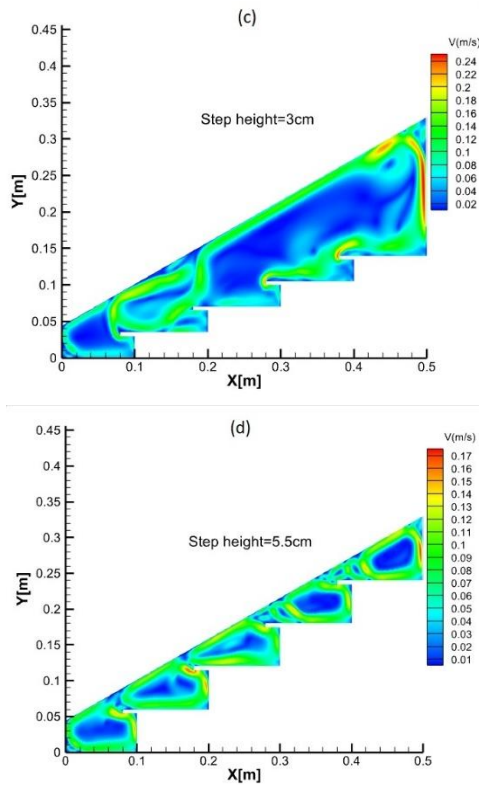
Figure 13. Velocity profile in solar still for various step height of (a) 1 cm, (b) 2 cm, (c) 3 cm and (d) 5.5 cm

Figure 14 shows the Nusselt number and Productivity for the above cases. As seen in figure, by increasing the steps height, the productivity increases and the Nusselt number decreases. This behavior caused by creation of vortexes and decrease mean distance between the steps and glass simultaneously. Table 7 illustrates the quantitate values and variation of them. Further, the convection heat transfer coefficient and the mean distance between steps and glass (H) plotted versus the steps height and are shown in Figure 15.
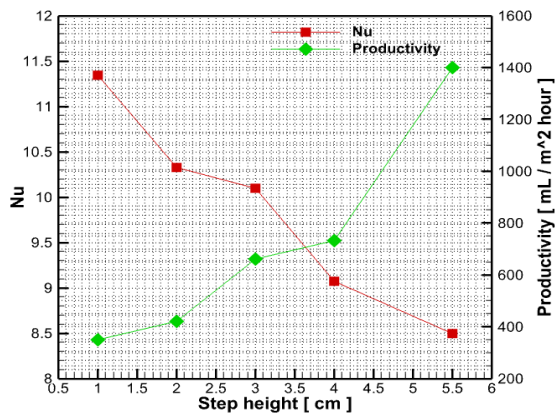
Figure 14. Nusselt and productivity vs steps height of solar still

TABLE 7. Nusselt number and productivity for various step height

Step height (cm)	Nusselt number	Productivity (mL/m² h)
1	11.34	350
2	10.33	420
3	10.1	660
4 (Exp. model [37])	9.07	732
5.5	8.5	1400
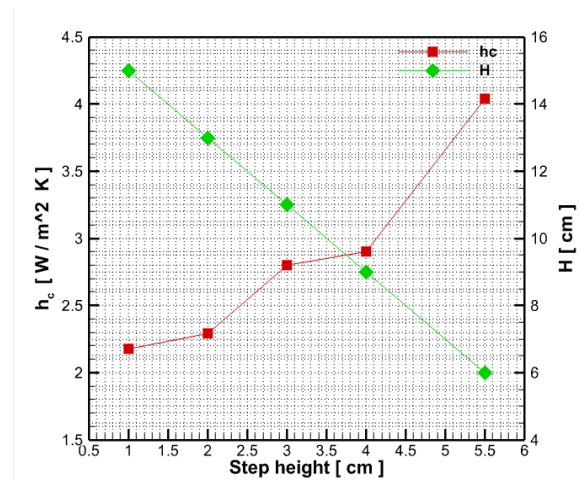
Figure 15. Heat transfer convection and mean distance between the steps and glass (H)

Their quantitative values for each case are shown in Table 8. Vorticity of fluid in this case, is shown in Figure 16 and it can be seen that like productivity and h_c have incremental trend by increasing the step height and this behavior is due to smaller space for wet air circulation. It means the vortexes on the steps must have more variation in their path direction and this variation lead to more heat and mass transfer. Hence, the productivity and h_c increase by increasing the step height and vice versa.

TABLE 8. Heat transfer coefficient and mean distance between steps and glass (H) for various step height

Step height (cm)	Heat transfer coefficient [W/m² K]	H (cm)
1	2.18	15
2	2.29	13
3	2.8	11
4 (Exp. model [37])	2.9	9.07
5.5	4.04	6
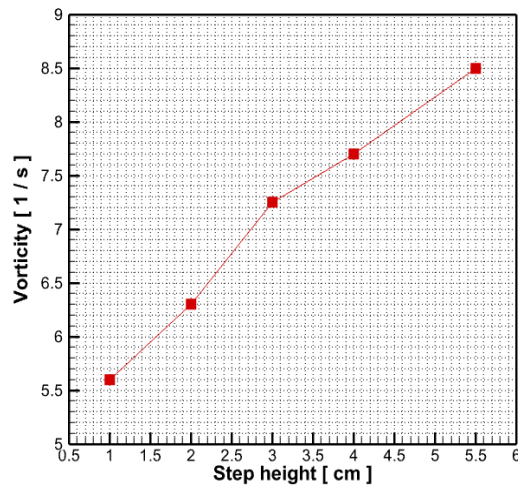
Figure 16. Vorticity variation vs step height of solar still

- Nusselt number varies as the solar still geometry changes, this variation is having reverse effect with h_c and direct effect with mean distance between water and glass (H). The largest Nusselt was obtained is 11.34 for H=15cm and the least Nusselt is 8.5 for H=6cm.
- The maximum freshwater production occurs for the step height of 5.5cm which was 1400 mL/m²h. Therefore, due to the experimental restrictions for changing the angle of glass cover, it is better to use this parameter to enhance the productivity.
- It was noticed that anywhere the vorticity increases, the heat transfer coefficient and the productivity increase too. Therefore, a physical conclusion can be inference from this numerical calculation is that vortexes are the main mechanism that affected on the heat transfer and productivity.

7. CONCLUSIONS

In this study, numerical simulation was performed on the stepped solar still to estimate the productivity and heat transfer criteria. For this purpose, mass, momentum and energy equation with species transport equation solved simultaneously, then by using mass fraction and temperature profiles and also Equations (13) and (14) productivity and Nusselt calculated. After validating the trend between this simulation with the reported experimental data and theoretical model, the variation in the geometry, the productivity and heat transfer coefficient were investigated. Results shows heat transfer and productivity extremely affected by change geometrical parameters which here discussed about glass cover angle and step heights. Some significant results which obtained are as follow:

- Geometry is one of the main factors in the productivity; the less space in solar still is equivalent to more productivity and vice versa. Therefore, based on this simulation by changing in the angle of the head of solar still, the productivity increases up to 70% and reaches to 1250 mL/m²h and by variation of the step's height increases up to 91% and reaches to 1400 mL/m²h. It was shown that the step height variation is more efficient in productivity because it gives higher increase in the productivity.
- Nusselt number unlike heat transfer coefficient decreases with decreasing solar still cavity volume and vice versa. Simulation indicated for up to 57° cover angle, the Nusselt decreased and heat transfer coefficient (h_c) significantly increased. The heat transfer coefficient varies from 2.72-3.36 W/m² K, Nusselt from 10.9 to 8.16. Hence, there should be an optimum point and needs more investigation.

8. REFERENCES

1. Hajipour, B., Hasheminejad, S. and Haghgou, H., "Extracting technical specifications of a solar panel type to design a 10 mw hybrid power plant", *International Journal of Engineering, Transactions A: Basics*, Vol. 32, No. 4, (2019), 562-568. doi: 10.5829/IJE.2019.32.04A.14

2. Firoozzadeh, M., Shiravi, A.H. and Shafiee, M., "Thermodynamics assessment on cooling photovoltaic modules by phase change materials (pcms) in critical operating temperature", *Journal of Thermal Analysis and Calorimetry*, Vol. 144, No. 4, (2021), 1239-1251. doi: 10.1007/s10973-020-09565-3

3. Shiravi, A.H., Firoozzadeh, M. and Lotfi, M., "Experimental study on the effects of air blowing and irradiance intensity on the performance of photovoltaic modules, using central composite design", *Energy*, Vol. 238, (2022), 121633. doi: 10.1016/j.energy.2021.121633

4. Firoozzadeh, M., Shiravi, A.H., Lotfi, M., Aidarova, S. and Sharipova, A., "Optimum concentration of carbon black aqueous nanofluid as coolant of photovoltaic modules: A case study", *Energy*, Vol. 225, (2021), 120219. doi: 10.1016/j.energy.2021.120219

5. Shiravi, A.H. and Firoozzadeh, M., "Thermodynamic and environmental assessment of mounting fin at the back surface of photovoltaic panels", *Journal of Applied and Computational Mechanics*, Vol. 7, No. 4, (2021), 1956-1963. doi: 10.22055/JACM.2020.32529.2076

6. Safari, M. and Torabi, F., "Improvement of thermal performance of a solar chimney based on a passive solar heating system with phase-change materials", *Energy Equipment and Systems*, Vol. 2, No. 2, (2014), 141-154. doi: 10.22059/EES.2014.9892

7. Khan, M.S., Abid, M. and Ratlamwala, T.A.H., "Energy, exergy and economic feasibility analyses of a 60 mw conventional steam power plant integrated with parabolic trough solar collectors using nanofluids", *Iranian Journal of Science and Technology, Transactions of Mechanical Engineering*, Vol. 43, No. 1, (2019), 193-209. doi: 10.1007/s40997-018-0149-x

8. Moosavi, L., Zandi, M., Bidi, M., Behroozizade, E. and Kazemi, I., "New design for solar chimney with integrated windcatcher for space cooling and ventilation", *Building and Environment*, (2020), 106785. doi: 10.1016/j.buildenv.2020.106785

9. Karimipour-Fard, P. and Beheshti, H., "Performance enhancement and environmental impact analysis of a solar

chimney power plant: Twenty-four-hour simulation in climate condition of isfahan province, iran", *International Journal of Engineering, Transactions B: Applications*, Vol. 30, No. 8, (2017), 1260-1269. doi: 10.5829/ije.2017.30.08b.20

10. Zina, B., Filali, A., Laouedj, S. and Benamara, N., "Numerical investigation of a solar air heater (sah) with triangular artificial roughness having a curved top corner", *Journal of Applied Fluid Mechanics*, Vol. 12, No. 6, (2019), 1919-1928. doi: 10.29252/jafm.12.06.29927

11. Ahmadzadehtalatapeh, M., "Performance study of a solar integrated central heating system of a residential building using trnsys-an hourly simulation model (research note)", *International Journal of Engineering, Transactions C: Aspects*, Vol. 27, No. 3, (2014), 457-466. doi: 10.5829/idosi.ije.2014.27.03c.14

12. Siqueira, A., Krink, N., Pereira, F., Villela, F., Silva, G. and Moura, A., "One-dimensional mathematical model for solar drying of beds of sludge", *Journal of Applied Fluid Mechanics*, Vol. 11, No. 5, (2018), 1407-1419. doi: 10.29252/jafm.11.05.28823

13. CV, S. and AR, U.S., "Drying kinetics of muscat grapes in a solar drier with evacuated tube collector", *International Journal of Engineering, Transactions B: Applications*, Vol. 27, No. 5, (2014), 811-818. doi: 10.5829/idosi.ije.2014.27.05b.18

14. Assari, M., Basirat Tabrizi, H., Parvar, M. and Alkasir Farhani, M., "Experimental investigation of sinusoidal tube in triplex-tube heat exchanger during charging and discharging processes using phase change materials", *International Journal of Engineering, Transactions A: Basics*, Vol. 32, No. 7, (2019), 999-1009. doi: 10.5829/ije.2019.32.07a.13

15. Mandal, S., Singh, P., Kumar, S. and Mishra, S., "Parametric investigation of cuo-doped charged nanofluid in solar water heater", *International Journal of Environmental Science and Technology*, (2020), 1-10. doi: 10.1007/s13762-020-03017-z

16. Warke, A., Auti, A., Pangavhane, D. and Ubale, A., "Experimental and theoretical study of thompson seedless grapes drying using solar evacuated tube collector with force convection method", *International Journal of Engineering, Transactions C: Aspects*, Vol. 28, No. 12, (2015), 1796-1801. doi: 10.5829/idosi.ije.2015.28.12c.13

17. Assari, M.R., Basirat Tabrizi, H., Parvar, M. and Forooghi Nia, M., "Performance of rotating solar still with rotating external reflectors (research note)", *International Journal of Engineering, Transactions C: Aspects*, Vol. 32, No. 6, (2019), 884-892. doi: 10.5829/ije.2019.32.06c.13

18. Assari, M., Tabrizi, H.B., Shafiee, M. and Khavar, Y.C., "Experimental performance of desalination system using solar concentrator, nano-fluid, and preheater tube accompanying phase change material", *Iranian Journal of Science and Technology, Transactions of Mechanical Engineering*, (2020), 1-12. doi: 10.1007/s40997-020-00383-4

19. Assari, M., Basirat Tabrizi, H., Parvar, M. and Esfandeh, E., "Experimental study of solar desalination performance due to water depths, flow rates, and using heat recovery from disposed brine", *International Journal of Ambient Energy*, (2021), 1-24. doi: 10.1080/01430750.2021.1999324

20. de Paula, A.C. and Ismail, K.A., "Parametric study, modeling, and numerical solution of an inclined solar still", *Computational Thermal Sciences: An International Journal*, Vol. 12, No. 5, (2020). doi: 10.1615/ComputThermalScien.2020026430

21. Kabeel, A., Harby, K., Abdelgaied, M. and Eisa, A., "A comprehensive review of tubular solar still designs, performance, and economic analysis", *Journal of Cleaner Production*, Vol. 246, (2020), 119030. doi: 10.1016/j.jclepro.2019.119030

22. El-Gazar, E., Zahra, W., Hassan, H. and Rabia, S.I., "Fractional modeling for enhancing the thermal performance of conventional solar still using hybrid nanofluid: Energy and exergy analysis", *Desalination*, Vol. 503, (2021), 114847. doi: 10.1016/j.desal.2020.114847

23. Hedayati-Mehdiabadi, E., Sarhaddi, F. and Sobhnamayan, F., "Exergy performance evaluation of a basin-type double-slope solar still equipped with phase-change material and pv/t collector", *Renewable Energy*, Vol. 145, (2020), 2409-2425. doi: 10.1016/j.renene.2019.07.160

24. Khalilmoghadam, P., Rajabi-Ghahnavieh, A. and Shafii, M.B., "A novel energy storage system for latent heat recovery in solar still using phase change material and pulsating heat pipe", *Renewable Energy*, Vol. 163, (2021), 2115-2127. doi: 10.1016/j.renene.2020.10.073

25. Sivaram, P., Kumar, S.D., Premalatha, M., Sivasankar, T. and Arunagiri, A., "Experimental and numerical study of stepped solar still integrated with a passive external condenser and its application", *Environment, Development and Sustainability*, (2020), 1-29. doi: 10.1007/s10668-020-00667-4

26. Bouzaid, M., Ansari, O., Taha-Janan, M., Mouhsin, N. and Oubrek, M., "Numerical analysis of thermal performances for a novel cascade solar desalination still design", *Energy Procedia*, Vol. 157, (2019), 1071-1082. doi: 10.1016/j.egypro.2018.11.274

27. Rahbar, N. and Esfahani, J.A., "Productivity estimation of a single-slope solar still: Theoretical and numerical analysis", *Energy*, Vol. 49, (2013), 289-297. doi: 10.1016/j.energy.2012.10.023

28. Rahman, M., Öztop, H.F., Ahsan, A., Kalam, M. and Varol, Y., "Double-diffusive natural convection in a triangular solar collector", *International Communications in Heat and Mass Transfer*, Vol. 39, No. 2, (2012), 264-269. doi: 10.1016/j.icheatmasstransfer.2011.11.008

29. El-Samadony, Y., El-Maghlany, W.M. and Kabeel, A., "Influence of glass cover inclination angle on radiation heat transfer rate within stepped solar still", *Desalination*, Vol. 384, (2016), 68-77. doi: 10.1016/j.desal.2016.01.031

30. Gawande, J.S. and Bhuyar, L.B., "Effect of shape of the absorber surface on the performance of stepped type solar still", *Energy and Power Engineering*, Vol. 5, No. 8, (2013), Article ID:37361,9 DOI:10.4236/epe.2013.58053

31. Cherraye, R., Bouchekima, B., Bechki, D., Bouguettaia, H. and Khechekhouche, A., "The effect of tilt angle on solar still productivity at different seasons in arid conditions (south algeria)", *International Journal of Ambient Energy*, (2020), 1-7. doi: 10.1080/01430750.2020.1723689

32. Ashtiani, S. and Hormozi, F., "Design improvement in a stepped solar still based on entropy generation minimization", *Journal of Thermal Analysis and Calorimetry*, Vol. 140, No. 3, (2020), 1095-1106. doi: 10.1007/s10973-019-08580-3

33. Azizi, K. and Keshavarz Moraveji, M., "Computational fluid dynamic-two fluid model study of gas-solid heat transfer in a riser with various inclination angles", *International Journal of Engineering, Transactions A: Basics*, Vol. 30, No. 4, (2017), 464-472. doi: 10.5829/idosi.ije.2017.30.04a.02

34. Akbar, F.R. and Arsana, I., "Effect of wire pitch on capacity of single staggered wire and tube heat exchanger using computational fluid dynamic simulation", *International Journal of Engineering, Transactions B: Applications*,, Vol. 33, No. 8, (2020), 1637-1642. doi: 10.5829/ije.2020.33.08b.22

35. Dwivedi, V. and Tiwari, G., "Comparison of internal heat transfer coefficients in passive solar stills by different thermal models: An experimental validation", *Desalination*, Vol. 246, No. 1-3, (2009), 304-318. doi: 10.1016/j.desal.2011.12.023

36. Shiravi, A.H., Shafiee, M., Firoozzadeh, M., Bostani, H. and Bozorgmehrian, M., "Experimental study on convective heat transfer and entropy generation of carbon black nanofluid turbulent flow in a helical coiled heat exchanger", *Thermal Analysis and Calorimetry*, Vol. 145, No. 2, (2021), 597-607. doi: 10.1007/s10973-020-09729-1

37. Kabeel, A., Khalil, A., Omara, Z. and Younes, M., "Theoretical and experimental parametric study of modified stepped solar

still", ***Desalination***, Vol. 289, (2012), 12-20. doi: 10.1016/j.desal.2011.12.023

38. Keshtkar, M., Eslami, M. and Jafarpur, K., "Effect of design parameters on performance of passive basin solar stills considering instantaneous ambient conditions: A transient cfd

modeling", ***Solar Energy***, Vol. 201, (2020), 884-907. doi: 10.1016/j.desal.2008.06.024

Persian Abstract

چکیده

در این مقاله، مطالعه‌ای عددی در حوزه‌ی بهره وری و انتقال حرارت در آب شیرین کن خورشیدی پلکانی با تغییر زاویه پوشش شیشه و ارتفاع پله‌ها مورد بررسی قرار گرفته است. بدین منظور از معادلات پایستگی جرم، حرکت، انرژی و انتشار استفاده شد. علاوه بر این، شبیه سازی عددی با داده های تجربی موجود تایید شده است. نتایج شبیه سازی نشان داد که بیشترین میزان تولید آب شیرین در مقایسه با شرایط راه اندازی آزمایشی که در ارتفاع پله 4 سانتی متر و زاویه پوشش شیشه ای 60.23 درجه است، متعلق به ارتفاع پله 5.5 سانتی متر با $1400 \ mL/m^2 \ h$ یعنی افزایش 91 درجه و بسیار کمتر است. برای ارتفاع پله 1 سانتی متر با 350 میلی لیتربرمترمربع ساعت، یعنی 52 درجه کاهش می یابد. بیشترین افزایش عدد ناسلت برای زاویه 55 درجه با $Nu=12.03$ با افزایش 29 ٪ و بسیار کمتر برای زاویه 65 درجه با $Nu=8.16$ با کاهش 12٪ بدست آمد. علاوه براین، بیشترین وکمتر تغییر ضریب انتقال حرارت برای ارتفاع پله 5.5 سانتیمتر با $h_c=4.04 \ W/m^2K$، با 39 ٪ افزایش و برای ارتفاع پله 1 سانتی متر با $h_c=2.18 \ W/m^2K$، با 24٪ کاهش یافت.

International Journal of Engineering

J o u r n a l   H o m e p a g e :   w w w . i j e . i r

A Method of Strip Footings Design for Light Structures on Expansive Clays

Z. Farid*a, N. Lamdouara, J. Ben Bouziyaneb

a Ecole Mohammadia d'Ingenieurs, Mohammed V University in Rabat, Rabat, Morocco
b Ecole Hassania des Travaux Publics, Casablanca, Morocco

A B S T R A C T

Shallow stiffened footing, in particular the Vierendeel typology, are considered as a design techniques for structures on expansive soils which have proven their success as challenging solutions; combining economy and safety. The current study is investigating an analytical model for preliminary design of strip footings for light structures on expansive soils, in particular the Vierendeel beam. The developed model is used to calculate, through soil–structure interaction analysis, the algebraic expressions for the bending moment and the footing displacement at any point on the footing. The method is based on a simplification of the clayey ground reaction (Pi) and structure geometry and is derived from an integration of the beam-on-Winkler mound equation. The analytical model is then used to assess the effect of the structure loads on the contact state between the structure and the clayey ground (full or partial contact) as well as the impact of this contact state on the value of the maximum bending moment inside the beam. The results underlines the influence of the construction load on the contact state between the foundation and the swelling soil. The results shows that the bending moment in the footing strongly depends on the contact state between this footing and the clayey ground.

doi: 10.5829/ije.2022.35.01a.24

NOMENCLATURE

Pi	Soil Pressure (KPa)	Δ	Permissible deflection of the footing (m)
y	Free-field soil movement (assumed to occur in the absence of the footing) (m)	L	Footing length (m)
Y	Maximum soil swell (m)	C	Detachment index, which is defined as the ratio of the footing length in contact with the soil to the total length of the footing ($0 \leq C \leq 1$)
f	Footing deformation (m)	E	Young's modulus of the material constituting the beam (KPa)
k	Soil swell stiffness (KPa/m)	I	Quadratic moment of inertia of the cross section (m4).

1. INTRODUCTION

Since engineers realized that special precautions are required when building on expansive soils, many designs of foundations have been developed in an attempt to overcome the negative impact of swelling soils [1-3]. These usually consist of methods that avoid expansive soil layers and load the building onto an underlying stable layer [4]. Shallow stiffened footing, as Vierendeel ones, are also widely used and can be laid directly on expansive soils because of their structural capacity to resist the expansive movement of the ground [5-7].

Actually, due to its simplicity of construction, shallow stiffened footing are considered to be, in many cases, a better cost saving solutions compared to the pile-beam foundation system, especially for lightweight structures such as one and two-story residential and commercial buildings as noted in literature [8, 9]. According to the classification of the Moroccan Guide on design measures for foundations in the North of the Kingdom, a shallow stiffened footing is the best solution for structures built on expansive soils in morocco and over the world. It ensures a high to very high level of protection to the buiding against the differential heave of the foundation subsoils. Negative impacts are avoided or,

Corresponding Author Email: zineb.farid@gmail.com (Z. Farid)

at least, reduced to low cracking of the building, hardly visible on the outside and easily repairable.

However, while the design of a pile-beam foundation may be based on conventional procedures well established in soil mechanics [10], the design of stiffened footings continues to be a major problem in the field of expansive soil mechanics. It is due to considerable complexity in quantifying precisely the behavior of a swelling soil, and modeling of the structure which interacts with this soil movement. This is so difficult that many codes of practice for the design of slabs, such as the Israeli draft code [11], deliberately avoid giving firm recommendations for the design of shallow reinforced footings. Most commonly, strip footings are designed from experience [8].

The objective of this paper is to develop an analytical model for calculating a strip footing, Vierendeel type, resting on a soil mass subjected to swelling movements. The developed model presents theoretical solutions for deflection and moment along the strip, taking into account the phenomenon of clay soil-structure interaction. Althoug it involves a number of simplifications, e.g. it considers a uniform section strip and assumes that the shape of the soil movement profile beneath the building can be predicted, the method presented herein should provide a basis for preliminary design of strip footings on expansive soils.

The building's mechanical behaviour is modeled using Euler–Bernoulli beam theory, and the soil's behaviour is modeled with a Winkler approach. The focus of this study is on the simplification of the swelling soil reaction expression $Pi(x)$ under the building. Indeed, the literature review revealed a lack of simplified and practical models for determining the reaction of expansive ground along the soil-structural contact surface from the results of simplified laboratory tests. The existing soil – structure interaction models for expansive soils are mostly based on experimental, sometimes heavy, test results [12-14]. and require complex numerical methods by using finite element modeling software [5, 15, 16].

Therefore, the challenge is to use the proposed model to investigate two fundamental questions for the understanding of the complex behavior of the swelling soil-structure system and yet very limited studies exist in the literature:

❖ Effects of applied load on the contact state between the footing and the clayey ground (full or partial contact). This aspect is little explored in the scientific literature [5, 8-17].

❖ The impact of this contact state on the design of the foundation especially on the value of the maximum bending moment inside the footing *which is an original part of this work.*

This analysis is carried out through a case study of a shallow foundation placed superficially on swelling clay soil in Ouarzazate city, located in the south of Morocco and subjected to different loading (w) cases (w = 30 KPa, 50 Kpa, 100 Kpa, 150 Kpa and 200 KPa).

2. MATERIALS AND METHODS

In the current study, the behavior of the expansive soil-structure system is modeled using the concept of beam on swelling dome proposed by Chen [5],

The most frequent situation of shallow foundations on swelling soils will be examined in this work, namely the swelling of the soil under the center of the foundation (central heave).

 In order to take into account, in this model for the worst-case scenario, the foundation seating depth is taken equal to zero.

The principles of the resistance of materials are used to calculate the foundation. The equations for this problem are based on the balance of forces involved; principle of action and reaction.

The study of soil behavior is carried out using the techniques of soil mechanics.

For the iterative calculation of the parameters "*C*" and "*a*" (defined in section 4.2. of this paper) of the model presented below, an algorithm has been developed, using the Python language.

The graphical representations are obtained using autoCAD and Excel software.

2. 1. Description of the Model   Figure 1 shows the distance under a building undergoing suction variations caused by humidification of the clayey soil under the effect of a water source located at a depth H below the middle of the foundation.

This change in suction content (Figure 1) leads to a differential settlement of the building and the ground between the center and edges (illustrated in Figures. 2a and 2b), and may in some cases lead to detachment of foundation from clayey ground (Figure 2b).

The problem is to determine the distribution of swelling soil reaction under the building, beam deflection and bending moment along the beam for a specified distribution of «free-field» movements.

The current study proposes to analyze the behaviour of a typical foundation, Vierendeel placed superficially on swelling clay soil. This variant consists of intersecting rigidified continuous beams. Each of these Vierendeel beams consists of two continuous members connected by vertical uprights (stiffening posts) embedded and thus forming a square mesh network (Figure 3). For building modeling, the plan of the structure can be divided into overlapping rectangles. So that in the current study, the analysis will be carried out on a rectangular dimensions of length (L) with fixed section, constant rigidity EI,
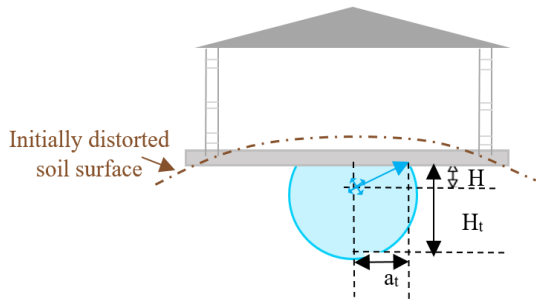
Where "at" is a width of the active area and "Ht" is the active depth over which the suction variation is not negligible.

Figure 1. Suction change under the center of the foundation (central heave)
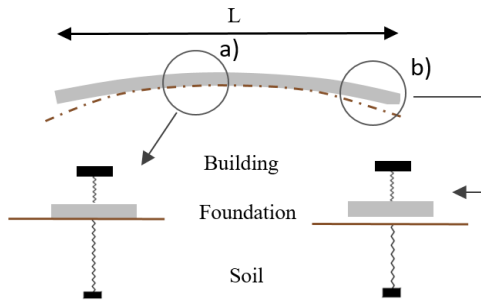
Figures 2. Simplified model for a soil–foundation interaction (a) Contact between soil and foundation (b) detachment of foundation from soil
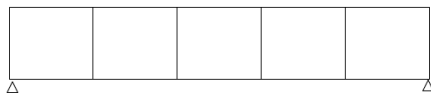
Figure 3. Outline of the Vierendeel type

Young's modulus E and tolerating a maximum admissible deflection Δ.

In this work, the soil–foundation interaction is investigated by exploiting the model developped by

Farid et al. [23]. The problem considered is shown in Figure 4, which is based on the following points:

- The soil is assumed to be an isotropic, elastic half space and the variability beneath the building of the modulus of reaction, noted k is not considered. The behaviour of the expansive soil-structure system is modelled using the concept of beam on swelling dome proposed by Chen [5].

- To make the analysis general, the beam loading is modelled by a linear perimeter distribution W (KN / m) (wall loads), a linear distribution acting in the center of the building (partitions) P (KN / m) and a uniform distribution w (KPa) and a vertical distribution Pi(x) that corresponds to the swelling soil reaction under the building (Figure 4). For the modelling of the studied system, a linear representation is chosen for the soil reaction under the frame Pi (KPa).

2. 2. Constitutive Equation of the Model and Resolution Procedure   As proposed by Winkler soil model [24], the expression of the ground reaction Pi, induced by the interaction between the swelling soil and the structure, is declined as follows:

$$Pi= k \, (y-f) \tag{1}$$

In the current study, the following expression of the soil reaction modulus k (KPa) determined from the swelling tests is retained :

$$k = \frac{\sigma_a}{y_0 - y_a} \tag{2}$$

where σ_a is the pressure applied to the test specimen, y_0 is the amplitude of the free swelling of the soil and y_a is the amplitude of the swelling of the soil under the applied pressure σ_a.

The distribution along footing for the free deformation of soil, called "swelling domes", is approximated by the Lytton equation [5, 15-18] as follows:

$$y \, (x) = (\frac{2x}{L})^m Y \tag{3}$$
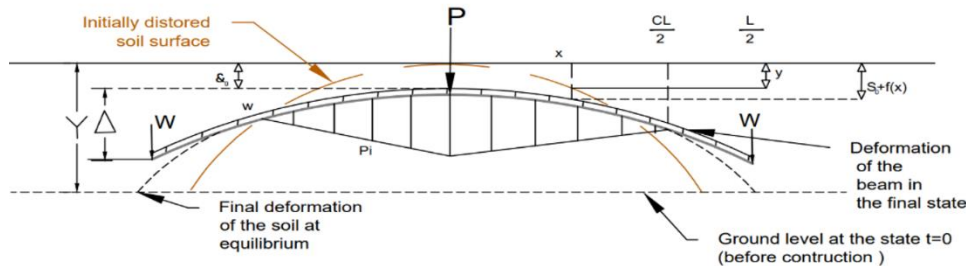
Figure 4. Definition of the building load, ground reaction and the building and ground deflections. For centre Heave (normal or dry season)

The exponent "m" in Equation (3) is an empirical coefficient reflecting the form of the "Swelling dome", which depends on the length of the foundation (L) and the depth of the active area of the clayey ground (H) (Figure 1) and takes values between 2 and 20. The following expression for the form factor "m" Equation (4), established by Mitchell [8] from analytical solutions of the steady state diffusion equation, is adopted in this study:

$$m = 1{,}5 \frac{L}{Ht} \tag{4}$$

Inspired by the models of Chen [5] and Mitchell [8] the expression for beam deformation is declined as follows:

$$f(x) = \left(\frac{2x}{L}\right)^a \Delta \tag{5}$$

In Equation (5), an exponent of this equation "a" is an integer.

To model the soil-foundation system response, as a first approximation, the contact state between the ground and the foundation can be considered partial.

At any point of intersection between the soil profile and the footing profile, the soil displacement equals the footing displacement. Equation (6) is used to ensure compatibility between y(x), f(x) and δ_0:
With δ_0 is the settlement at point x = 0 .

$$f(x) = y(x) - \delta_0 \tag{6}$$

Thereafter, the analysis will be limited to half of the beam due to the symmetry of the problem. Thus, the strip footing behaves like a console beam of maximum length L/2 and embedded at its origin x = 0.

According to the principles of the resistance of materials, if the footing is in equilibrium, and has lost contact with the soil over a certain length of footing, then three simultaneous equations are established :

1. In the final state, the superstructure loads must equal the soil forces over the length of footing in contact with the soil:

$$\sum F = P + \frac{w*L}{2} + W = \int_{-CL/2}^{CL/2} Pi(x)\, dx \tag{7}$$

2. At any point x of the beam, the bending moment due to the external loads and soil reaction must equal to the bending moment corresponding to the curvature of the footing:

$$M(x) = M(x)_{ext} \tag{8}$$

3. The equation of the beam deflection is a second-order differential equation that relates the vertical deflection f(x) and the bending moment M(x) in the x-abscised cross section:

$$M(x) = - \frac{EI * df(x)^2}{dx^2} \tag{9}$$

4. Taking into account the relationship between the shear force and the bending moment (the Euler-Bernoulli theorem):

$$V(x) = \frac{dM(x)}{dx} \tag{10}$$

The four equations can be used to determine the distribution of soil reaction along the length of footing in contact with the soil, thereby enabling the determination of the bending moment to permit a footing design. Figure 4 shows the applied load (W, w and P), ground reaction (pi(x)) and the building deflection (f(x)).

3. RESULTS

The calculation of the swelling soil reaction Pi(x) under the building, induced by the interaction between the swelling soil (modeled by springs) and the structure at static equilibrium, can be obtained by applying the least squares method to the expression of the soil reaction Pi resulting from Equation (7). The result is declined as follows:

$$\textbf{Pi(x)} = \textbf{Pi max} \left(\frac{-2}{CL} x + 1\right) \tag{11}$$

With Pi max = k$((C)^m Y - (C)^a \Delta)$.

where Pi max denotes the maximum value of the contact pressure of the swelling soil (the wettest zone) and C the detachment index.

When there is detachment, the reaction of the ground Pi (x) is zero throughout.

In a state of final equilibrium, the expressions of bending moment M(x), shear force V(x) and beam deflection are established by applying the relevant boundary conditions to Equations (7), (8) and (9). Equations (12) and (15) give the bending moment, Equations (13) and (16) give the shear force, Equations (14) and (17) give the footing displacement, wich when added to δ0 give the total footing movement:

- For $0 \leq x \leq \frac{CL}{2}$ *(contact between the ground and the foundation)*

$$M1(x) = \frac{b*Pimax}{3*CL} x^3 + b * \left(\frac{w}{2} - \frac{Pimax}{2}\right) x^2 + b * \left(\frac{(CL*Pimax)}{4} - \frac{wL}{2} - W\right) x + b * \left(\frac{wL^2}{8} + \frac{WL}{2} - \frac{(CL)^2 Pimax}{24}\right) \tag{12}$$

$$\textbf{V}_1\textbf{(x)} = \frac{Pimax*b}{CL} * x^2 + b*(w - Pimax)x + b*\left(\frac{CL*Pimax}{4} - \frac{wL}{2} - W\right) \tag{13}$$

$$\textbf{f1}(x) = \frac{b}{EI} \left(\frac{Pimax}{60*CL} x^5 - \frac{(Pimax-w)}{24} x^4 + \left(\frac{(CL*Pimax)}{24} - \frac{wL}{12} - \frac{W}{6}\right) x^3 + \left(\frac{wL^2}{16} + \frac{WL}{4} - \frac{(CL)^2 Pimax}{48}\right) x^2\right) \tag{14}$$

Wile for $\frac{CL}{2} \leq x \leq \frac{L}{2}$ *(loss of contact between the soil and the foundation)*

$$M_2(x) = \frac{b*w}{2} x^2 - b*\left(\frac{wL}{2} + W\right) x + b * \left(\frac{w L^2}{8} + \frac{WL}{2}\right) \tag{15}$$

$$V_2(x) = V_1\left(\frac{CL}{2}\right) + w*b*\left(x - \frac{CL}{2}\right) \tag{16}$$

$$f_2(x) = \frac{b}{EI}\left(\frac{w}{24} x^4 - \left(\frac{wL}{12} + \frac{W}{6}\right) x^3 + \left(\frac{wL^2}{16} + \frac{WL}{4}\right) x^2 - \frac{(CL)^3 Pimax}{192} x - \frac{3*Pimax}{640} (CL)^4\right) \tag{17}$$

where W (KN/m) is a linear perimeter distribution (wall loads), w (KPa) is a uniform distribution of superstructure loads and Pi max is the maximum value of the contact pressure of the swelling soil given by Equation (11). Furthermore, L (m) is a footing length and C is the detachment index ($0 \le C \le 1$).

4. APPLICATIONS

For the purpose of this article, the results of the model developed above are used to investigate the influence of building load on the contact state between the clayey ground and the foundation first and then the impact of this contact state on the value of the maximum bending moment inside the beam. In this section, a reference case is defined. This case corresponds to a building characterized by a length L = 9 m and having an admissible deflection $\Delta = 0.009$ m. The loading system is reduced to an equivalent uniform load w (KPa) (corresponding to the building self-weight and the loading service). Several loading scenarios will be examined (w = 200 kPa, 150 KPa, 100 KPA, 50 KPa and 30 KPa). The beam is considered placed on the surface (the most critical case) on a layer of soil of the city of Ouarzazate, south of Morocco. It is specified that the studied site is located north of Ouarzazat city, belonging to the High Atlas. The soil mass is characterized by a rigidity k (KPa / m), undergoing a maximum free swelling Y = 0.160 m (Figure 4) and a depth of the active zone Ht (m) under the effect of a water source located at a depth H = 0.5m beneath the middle of the foundation.

4. 1. Effect of the Construction Loads on the Contact State between the Swelling Soil and the Foundation   In this section, the effect of the construction loads on the contact state between the swelling soil and the foundation is evaluated analytically using the method proposed by Farid et al. [17], wich is briefly recalled below:
To decide whether there is full or partial contact, the following approach is suggested:

• If the total structural load $\sum F_{sup}$ is less than the value of the "Detachment Factor", which is estimated by $Fd = \frac{Lk}{4} (Y - \Delta)$, then a theoretical loss of contact between the clayey soil and the foundation can be expected at x $= \frac{CL}{2}$.

The surface rate engaged in the shallow footing - expansive soil interaction can then be equal to CL.

• If not, no detachment occurs and C=1.

Table 1 summarizes values of the soil reaction modulus k (KPa/m), for each value of the equivalent load of the structure w (KPa). The values of the parameter k are estimated from the results of oedometric laboratory tests carried out on samples of swelling soils taken from the experimental site which is the subject of this study (Figure 5), located in Ouarzazate city , by means of Equation (2).
Once all parameters defining the "Detachment factor" are known, the prediction of the swelling soil/ foundation contact state can be made by comparing the respective values of the superstructure forces and the "Detachment factors" for different values of the uniform load w (KPa). The results are synthesized in Table 2.

Thus, perfect soil - foundation contact is expected for structures with a load exceeding w = 166.7 KPa. A value for which the detachment factor and the superstructure forces take the same value Fd = Fsup = 750.1 KN/m. Thus, for less loaded structures (w = 150 KPa; 100 KPa; 50 KPa and 30 KPa) partial separation would occur.

4. 2. Deformations of the Soil-foundation System in the Final Equilibrium State   This analysis is extended below in order to determine the deformations of the soil-foundation system in the final equilibrium state as well as the extent of the soil-structure contact surface under different values of structural loads w (KPa).

TABLE 1. Soil reaction modulus k (KPa) for different values of construction loads

Construction loads w(KPa)	w=200	w=150	w=100	w=50	w=30
Soil reaction modulus k (KPa/m)	2247.2	2142.9	2041	2000	2000
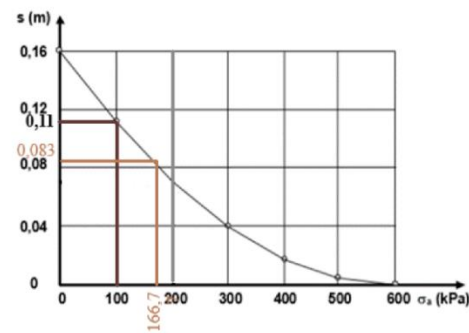
Figure 5. Result of an oedometer swelling test, cited by Ejjaouani [7]

TABLE 2. Contact state between the foundation and the clayey ground according to the construction loads

Uniform load w (KPa)	200	150	100	50	30
Superstructure forces (KN/m) $F_{sup} = \frac{w*L}{2}$	900	675	450	225	135
Detachment factors (KN/m) $F_d = \frac{Lk}{4}$ $(Y - \Delta)$	763.5	728	679.5	707.8	849.4
Contact state	No lift-off	Lift-off	Lift-off	Lift-off	Lift-off

To do this, the design parameters (m, C and a) which appear in Equations (3), (5), (14) and (17) are evaluated. **Value of the form factor «m»**   The form factor "m" is evaluated for an active zone of depth Ht by Equation (4). To remain in conformity with the case treated by Ejjaaouani [9], the most critical case with an active zone depth Ht equal to 2.8 m (corresponding to a width of the active zone at equal to half of the half beam) is treated. The depth of the active zone Ht (illustrated in Figure 1) can be evaluated by the following expression:

$H_t = H + \sqrt{at^2 + H^2} = 2,80$ m

So, according to Equation (4):

$m = \frac{1,5*9}{2,8} = 4,82$

Values of parameters «C» and «a»   Values of the detachment index "C" and the parameter "a" can be conveniently undertaken by Newton's method.

In the current study, for the determination of values of parameters "C" and "a", an algorithm has been developed using the Python language. Indeed, an iterative procedure is carried out and it starts by assuming an initial value to the parameter "a", then calculating the value of "C" by Equation (8) (using the expression of the soil reaction Pi (x) given by Equation (11)). The values of the footing deformation f (x) at two different points of the beam , obtained by using Equations (5) and (14) , allow the assumed value of «a» to be checked from the following equation:

$a = \ln(\frac{f1(x1)}{f1(x2)}) / \ln(\frac{x1}{x2})$ (18)

The correct value of "a" is then obtained by a process of trial and error, which can be undertaken quickly on a small programmable calculator.

Figure 6 summarizes the algorithm explained above for obtaining the values of parameters «C» and «a».

Table 3 summarizes values of parameters "C" and "α", obtained by using the Python language, as well as the extent of the contact between the clayey soil and the
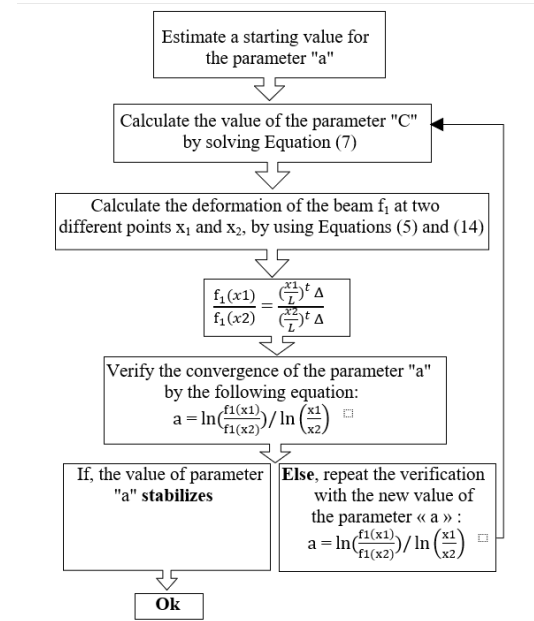
Figure 6. The proposed algorithm for obtaining the values of parameters « C » and « a »

TABLE 3. Parameter values "C" and "a" and the soil-foundation contact extent according to the load of the structure

| Structural load w (KPa)	150	100	50	30
α	1.91	1.91	1.91	1.90
Detachment index C $(0 \leq C \leq 1)$	0.99	0.93	0.83	0.77
Contact length: swelling ground / footing CL (m)	8.91	8.37	7.47	6.93

foundation for different loading scenarios w (150 KPa; 100 KPa; 50 KPa and 30 KPa), by adopting the approach described above.

Figures 7 to 10 show the final deformations of soil and beam resulting from the swelling soil-structure interaction under different values of w.

For the range of values of k, Y and Δ considered in this analysis, the results of this study illustrated in Figures 7 to 10 show that the extent of the soil-structure contact area increases when the building load w increases. Thus, the console part of the beam is shortened with the load; going from 1.035m for a structure loaded with 30 KPa (Figure 10) to less than 5 cm for a more heavy structure, loaded more than 150KPa (Figure 7).

Also, these Figures show that the final building deformation (due to load and suction variation) increases when the building load w increases. Meanwhile a structure loaded at more than 150 KPa would consume more than 15 cm of the free swelling of the clayey soil (before construction), a light structure loaded at less than
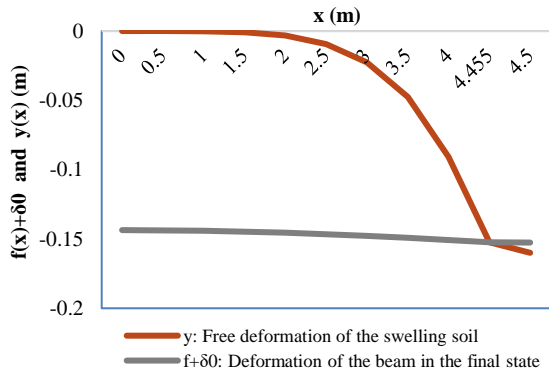
Figure 7. Final state of the soil and the beam loaded at w = 150 KPa

**Figure 8.** Final state of the soil and the beam loaded at w = 100 KPa
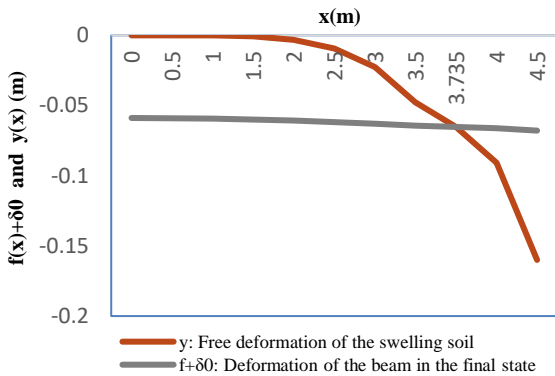
Figure 9. Final state of the soil and the beam loaded at w = 50 KPa

50 MPa would consume less than 6 cm of the free swelling of the clay soil.

4. 3. Impact of the Swelling Ground - Foundation Contact State on the Bending Moment inside the Footing   In this section, the impact of the swelling soil /footing contact state on the design of the foundation

Figure 10. Final state of the soil and the beam loaded at w = 30 KPa

is examined by comparing the maximum bending moment induced inside the footing in the two scenarios: "possibility of detachment of the foundation from the clayey ground" and "perfect contact" according to the approach explained below.

a. By adopting the model tolerating the detachment of the structure from the ground (detachment of the foundation from the ground object of this study, for structures loaded less than 166.7 KPa), the maximum bending moments M_{max} inside the beam is determined using Equations (12) and (15), developed in this article.

The distribution of the bending moment inside the beam, resulting from the application of Equations (12) and (15), is presented in Figure 11 below, for the different values of the equivalent load w (30 KPa, 50 KPa, 100 KPa and 150 KPa).

This figure shows that the resulting bending moment inside the beam (due to load and suction variation) is maximum in the mid-section of the beam and becomes zero at the edges of the foundation.

This figure also shows that the resulting bending moment inside the beam increases with increasing weight of the structure. So that a structure loaded at less than 30MPa would have a maximum moment of less than 147 KN.m while a foundation loaded at more than 150 KPa would be stressed by a maximum moment exceeding 513 MPa.

b. By adopting the idea that the clayey soil / footing contact is always maintained (independently of the load of the structure w (KPa)), the bending moment M (x) induced inside the footing will be calculated, for the same values of workloads used in the previous calculations (w = 150KPa; 100 KPa; 50 KPa and 30 KPa), using the model developed by Ejjaaouani [7], which exploits the Filonenko-Borodich model.

The maximum values of the bending moments induced in the beam in the two scenarios (contact with or without separation) are summarized in Table 4 below:
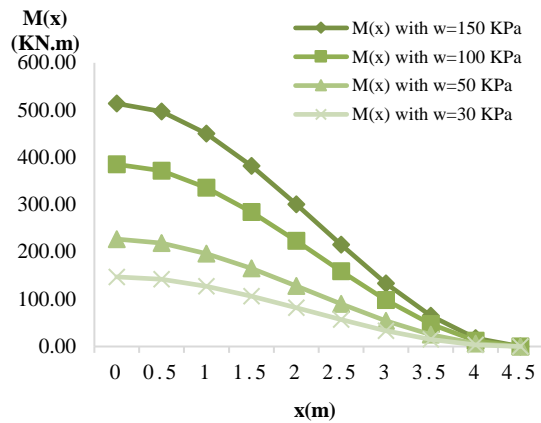
Figure 11. Bending moment along the loaded half-beam at w = 30 KPa, 50 KPa, 100 KPa and 150 KPa

TABLE 4. Maximum values of bending moments: "perfect contact" scenario and "possibility of separation" scenario

Structural load w (KPa)	200	150	100	50	30
Maximum bending moment (KN.m) «Perfect contact» scenario Model H. Ejjaaouani [9]	455.62	341.72	227.82	113.91	68.34
Maximum bending moment (KN.m) «Possibility of separation» scenario Z. Farid, N. Lamdouar and J. Ben Bouziyane [23]	455.62	513.80	385.17	227.18	147.21
Deviation (%)	0	33	41	50	53

The results of this analysis show a difference between the determined values of the maximum bending moments inside the beam in the two scenarios. This difference increases with the decrease in the value of the work load. Thus, for structures loaded more than 150 KPa a deviation of less than 33% can be expected while a deviation exceeding 50% can be considered for light structures (w ≤ 50 KPa).

5. DISCUSSION

A method of analysis is developed for the design of shallow footing on expansive soil, suitable for routine use by practitioners (design offices and geotechnicians). An approach that is both safe and reliable, although it involves a number of simplifying assumptions as justified above.

The swelling of the soil under the center of the foundation (central heave) was examined in this work. The most frequent and an inevitable situation of swelling of the clayey soil because of the variation in the water state of the clay soil under the building due to the thermo-osmosis effect due to the thermal gradient between the soil in the middle of the building footprint and at the ends.

The example treated as an application of the method in this article brings out the following conclusions:

This study clearly reveals that the contact state between the foundation and the swelling soil depends on the structure load. The lighter a structure is, the more likely detachment occurs. Reversely, the increase in the load of the structure always tends to widen the footprint of soil-structure contact. This result is in agreement with the results of the parametric study detailed by Farid et al. [17].

The same tendency of a decrease in the contact surface between the swelling soil and the structure compared to the decrease in the weight of the foundation structure is observed.

On the other hand, the approach assuming that "the soil-structure contact is always maintained because of the plastic behaviour of the supporting clay soil" as explained by Ejjaaouani [7] does not prove to be generally applicable, at least for light structures (loaded to less than 166 MPa, under the conditions of the case study discussed above).

The method of this article makes it possible to precisely define the length of the swelling soil - foundation contact length (equal to CL), a key parameter in the design study of any foundation. This is possible thanks to a numerical resolution of Equations 5, 8, 11 and 14 by Newton's method. In this work, this analysis was conducted by using the Python language to create functions with fewer lines of code. It is well known that the Python language has one of the most mature package managers (PyPI) and is the most widely used language in modern data science by both beginners and experts alike.

The comparison of maximum values of bending moments induced in footing in the case of a perfect contact scenario (independently of the value of the structure load) and in the second case where the detachment of the structure from the support soil is tolerated shows that: the bending moment in the footing strongly depends on the contact state between this footing and the clayey ground. Indeed, the second scenario leads to a more conservative maximum bending moment. Also, it was noted that the difference between the determined values of the maximum bending moments in the 2 scenarios increases with the decrease in the value of the load of the structure. Thus, a deviation exceeding 50% can be considered for light structures (w ≤ 50 KPa). These results are in harmony with the recommendations of BRAB [15], which specifies that the greater the soil

support is given to the beam the lower the bending moment induced in the beam is.

As illustrated in Figure 16, the decrease in bending moment with decreasing structural loads is clearly illustrated. This is consistent with the fact that the bending moment induced in the footing, under the effect of the swelling soil-structure interaction, is only the result of the difference between the load of the structure and the pressure of swelling ground contact.

It should be noted that in this study, the soil and building parameters (k, Y, Δ, L and w) were assumed to be independent, although they could be correlated for real buildings. This possible correlation was not taken into account.

In addition, the single-layer code, adopted in this work (assuming a uniform behaviour of the soil over the entire height of the clay layer), can lead to a detachment of the structure even for an average frame load. Especially since in this approach, the effect of the foundation bed depth is not taken into account. Therefore, one would expect that the method proposed in this article would be improved by adopting a multi-layered approach taking into account the evolution of the suction depth and the bedding depth of the foundation in order to achieve a less conservative bending moment.

6. CONCLUSION AND OUTLOOKS

A new soil-structure interaction analytical model was developed for the design of a shallow footing on expansive soil, especially the Vienendeel Type. The behavior of swelling soils was modeled using the concept of linearization of the clayey ground reaction integrated into a soil–structure interaction model that is based on the idealized Winkler model for the soil and an elastic Euler–Bernoulli beam concept for the building. The model can be used to calculate the the final deflection of a building and the bending moment at any point on the footing.

The method presented herein, althoug it involves a number of simplifications, should provide a basis for preminiraly design of strip footings on expansive soils. Most commonly designed from experience.

The analytical model was then used to investigate the effects of applied load on the contact state between the footing and the clayey ground (full or partial contact) and the impact of this contact state on the design of the foundation especially on the value of the maximum bending moment inside the footing which is an original part of this work which is an original part of this work. The results showed that the value of the maximum bending moment inside the foundation is very influenced by the contact state between the foundation and the clayey ground retained in the analysis of the system.

This research could be extended in the future by exploiting a more complete and precise database on the damaged houses. The developed model could be improved by adopting a multi-layered approach taking into account the evolution of the suction depth and the bedding depth of the foundation.

7. REFERENCES

1. Hait, P., Sil, A. and Choudhury, S., "Damage assessment of reinforced concrete buildings considering irregularities (research note)", *International Journal of Engineering, Transactions A: Basics*, Vol. 32, No. 10, (2019), 1388-1394, doi: 10.5829/ije.2019.32.10a.08.

2. Snethen, D., "Three case studies of damage to structures founded on expansive soils", in Fifth International Conference on expansive Soils, Adelaide, South Australia. (1984), 218-221.

3. Wei, X., Gao, C. and Liu, K., "A review of cracking behavior and mechanism in clayey soils related to desiccation", *Advances in Civil Engineering*, Vol. 2020, (2020), doi: 10.1155/2020/8880873.

4. Holland, J. and Richards, J., "The practical design of foundations for light structures on expansive clays", in Proc., 5th Int. Conf. on Expansive Soils, ACT: Institution of Engineers Australia. Vol., No., (1984), 154-158.

5. Chen, F.H., "Foundations on expansive soils, Elsevier, Vol. 12, (2012).

6. Gromko, G.J., "Review of expansive soils", *Journal of the Geotechnical Engineering Division*, Vol. 100, No. 6, (1974), 667-687, doi: 10.1061/AJGEB6.0000059.

7. Ejjaaouani, H., "Interactions of foundations and expansive soils: Pathology, calculations and experimental studies", Ecole des Ponts ParisTech, (2008),

8. Mitchell, P.W., "The design of shallow footings on expansive soil", (1984),

9. Pons Poblet, J.M., "The vierendeel truss: Past and present of an innovative typology", *Arquitetura revista*, Vol. 15, No. 1, (2019), 193-211, doi: 10.4013/arq.2019.151.11.

10. Liu, Y. and Vanapalli, S.K., "Load displacement analysis of a single pile in an unsaturated expansive soil", *Computers and Geotechnics*, Vol. 106, (2019), 83-98, doi: 10.1016/j.compgeo.2018.10.007.

11. Zeitlen, J.G. and Komornik, A., "A foundation code for expansive soil conditions", in Expansive Soils, ASCE. (1980), 609-616.

12. Suresh, R. and Murugaiyan, V., "Influence of chemical admixtures on geotechnical properties of expansive soil", *International Journal of Engineering, Transactions A: Basics*, Vol. 34, No. 1, (2021), 19-25, doi: 10.5829/ije.2021.34.01a.03.

13. Abbas, H.O., "Laboratory study on reinforced expansive soil with granular pile anchors", *International Journal of Engineering*, Vol. 33, No. 7, (2020), 1167-1172, doi: 10.5829/ije.2020.33.07a.01.

14. AG, S. and Mudavath, H., "Soil shrinkage characterization of low plasticity soil using digital image analysis process", *International Journal of Engineering*, Vol. 34, No. 10, (2021), doi: 10.5829/ije.2021.34.10a.02.

15. Board, N.R.C.B.R.A. and Administration, U.S.F.H., "Criteria for selection and design of residential slabs-on-ground, National Academy of Sciences, (1968).

16. El Brahmi, J., Lamdouar, N. and Zoukaghe, M., "Integral equation formulation of the displacement vector for unsaturated expansive soils by boundary element method", *Innovative Infrastructure Solutions*, Vol. 3, No. 1, (2018), 1-7, doi: 10.1007/s41062-017-0106-3.

17. Farid, Z., Lamdouar, N. and Bouziyane, J.B., "A new simplified prediction method of the contact state between shallow foundations and swelling ground", *Civil Engineering Journal*, Vol. 7, No. 5, (2021), 880-892, doi: 10.28991/cej-2021-03091697.

18. Carrier III, W.D., "Pipeline supported on a nonuniform winkler soil model", *Journal of Geotechnical and Geoenvironmental Engineering*,   Vol. 131, No. 10, (2005), 1301-1304, doi. https://doi.org/10.1061/(ASCE)1090-0241(2005)131:10(1301)

Persian Abstract

چکیده

پایه های مستحکم کم عمق ، به ویژه گونه شناسی Vierendeel ، به عنوان یک تکنیک طراحی برای سازه های روی خاک وسیع در نظر گرفته می شوند که موفقیت خود را به عنوان راه حل های چالش برانگیز ثابت کرده اند. تلفیق اقتصاد و ایمنی مطالعه حاضر در حال بررسی یک مدل تحلیلی برای طراحی اولیه پایه های نواری برای سازه های سبک در خاکهای وسیع ، به ویژه تیر Vierendeel است. مدل توسعه یافته برای محاسبه ، از طریق تجزیه و تحلیل تعامل خاک و ساختار ، عبارات جبری برای لحظه خمش و جابجایی پایه در هر نقطه از پایه استفاده می شود. این روش بر ساده سازی واکنش خاک رس (Pi) و هندسه ساختار استوار است و از ادغام معادله تپه تیر بر وینکلر مشتق شده است. سپس از مدل تحلیلی برای ارزیابی تأثیر بارهای سازه بر وضعیت تماس بین سازه و سطح خاک رس (تماس کامل یا جزئی) و همچنین تأثیر این حالت تماس بر مقدار حداکثر گشتاور خمش داخل استفاده می شود. پرتو. نتایج بر تأثیر بار ساختمانی بر وضعیت تماس بین فونداسیون و خاک متورم تاکید می کند. نتایج نشان می دهد که گشتاور خمش در پایه به شدت به وضعیت تماس بین این پایه و سطح خاک رس بستگی دارد.

AIMS AND SCOPE

The objective of the International Journal of Engineering is to provide a forum for communication of information among the world's scientific and technological community and Iranian scientists and engineers. This journal intends to be of interest and utility to researchers and practitioners in the academic, industrial and governmental sectors. All original research contributions of significant value focused on basics, applications and aspects areas of engineering discipline are welcome.

This journal is published in three quarterly transactions: Transactions A (Basics) deal with the engineering fundamentals, Transactions B (Applications) are concerned with the application of the engineering knowledge in the daily life of the human being and Transactions C (Aspects) - starting from January 2012 - emphasize on the main engineering aspects whose elaboration can yield knowledge and expertise that can equally serve all branches of engineering discipline.

This journal will publish authoritative papers on theoretical and experimental researches and advanced applications embodying the results of extensive field, plant, laboratory or theoretical investigation or new interpretations of existing problems. It may also feature - when appropriate - research notes, technical notes, state-of-the-art survey type papers, short communications, letters to the editor, meeting schedules and conference announcements. The language of publication is English. Each paper should contain an abstract both in English and in Persian. However, for the authors who are not familiar with Persian, the publisher will prepare the latter. The abstracts should not exceed 250 words.

All manuscripts will be peer-reviewed by qualified reviewers. The material should be presented clearly and concisely:

- *Full papers* must be based on completed original works of significant novelty. The papers are not strictly limited in length. However, lengthy contributions may be delayed due to limited space. It is advised to keep papers limited to 7500 words.
- *Research* notes are considered as short items that include theoretical or experimental results of immediate current interest.
- *Technical notes* are also considered as short items of enough technical acceptability with more rapid publication appeal. The length of a research or technical note is recommended not to exceed 2500 words or 4 journal pages (including figures and tables).

Review papers are only considered from highly qualified well-known authors generally assigned by the editorial board or editor in chief. Short communications and letters to the editor should contain a text of about 1000 words and whatever figures and tables that may be required to support the text. They include discussion of full papers and short items and should contribute to the original article by providing confirmation or additional interpretation. Discussion of papers will be referred to author(s) for reply and will concurrently be published with reply of author(s).

INSTRUCTIONS FOR AUTHORS

Submission of a manuscript represents that it has neither been published nor submitted for publication elsewhere and is result of research carried out by author(s). Presentation in a conference and appearance in a symposium proceeding is not considered prior publication.

Authors are required to include a list describing all the symbols and abbreviations in the paper. Use of the international system of measurement units is mandatory.

- On-line submission of manuscripts results in faster publication process and is recommended. Instructions are given in the IJE web sites: www.ije.ir-www.ijeir.info
- Hardcopy submissions must include MS Word and jpg files.
- Manuscripts should be typewritten on one side of A4 paper, double-spaced, with adequate margins.
- References should be numbered in brackets and appear in sequence through the text. List of references should be given at the end of the paper.
- Figure captions are to be indicated under the illustrations. They should sufficiently explain the figures.
- Illustrations should appear in their appropriate places in the text.
- Tables and diagrams should be submitted in a form suitable for reproduction.
- Photographs should be of high quality saved as jpg files.
- Tables, Illustrations, Figures and Diagrams will be normally printed in single column width (8cm). Exceptionally large ones may be printed across two columns (17cm).

PAGE CHARGES AND REPRINTS

The papers are strictly limited in length, maximum 6 journal pages (including figures and tables). For the additional to 6 journal pages, there will be page charges. It is advised to keep papers limited to 3500 words.

Page Charges for Papers More Than 6 Pages (Including Abstract)	
For International Author ***	$55 / per page
For Local Author	100,000 Toman / per page

AUTHOR CHECKLIST

- Author(s), bio-data including affiliation(s) and mail and e-mail addresses).
- Manuscript including abstracts, key words, illustrations, tables, figures with figure captions and list of references.
- MS Word files of the paper.